HELLENIC REPUBLIC
National and Kapodistrian University of Athens
EST. 1837

SCHOOL OF SCIENCE

DEPARTMENT OF GEOLOGY AND GEOENVIRONMENT

DIVISION OF GEOPHYSICS - GEOTHERMIC

Ph.D. Thesis

Application of geophysical technique to the investigation of tectonic structures in urban and sub-urban environments. A case study in Athens basin.

SPYRIDON DILALOS

Geologist - Geophysist, M.Sc.

Athens, 2018

HELLENIC REPUBLIC
National and Kapodistrian University of Athens
EST. 1837

SCHOOL OF SCIENCE

DEPARTMENT OF GEOLOGY AND GEOENVIRONMENT

DIVISION OF GEOPHYSICS - GEOTHERMIC

Ph.D. Thesis

Application of geophysical technique to the investigation of tectonic structures in urban and sub-urban environments. A case study in Athens basin.

SPYRIDON DILALOS

Geologist - Geophysist, M.Sc.

(Register number: 121)

Athens, 2018

Advisory Committee

Dr. Ioannis Alexopoulos, Assistant Professor, National and Kapodistrian University of Athens, **Supervisor**

Dr. Stylialos Lozios, Assistant Professor, National and Kapodistrian University of Athens

Dr. Georgios Apostolopoulos, Associate Professor, National Technical University of Athens

Examining Committee

Dr. Ioannis Alexopoulos, Assistant Professor, National and Kapodistrian University of Athens

Dr. Stylialos Lozios, Assistant Professor, National and Kapodistrian University of Athens

Dr. Georgios Apostolopoulos, Associate Professor, National Technical University of Athens

Dr. Nikolaos Voulgaris, Professor, National and Kapodistrian University of Athens

Dr. Andreas Tzanis, Associate Professor, National and Kapodistrian University of Athens

Dr. Efthymios Lekkas, Professor, National and Kapodistrian University of Athens

Dr. Andreas Tsatsaris, Associate Professor, University of West Attica

I **dedicate** this Ph.D. Thesis to

- ✓ My **beloved parents**, **brother** and **sister**,

for their continuous support

- ✓ My beautiful **wife, Sofia**,

for her endless support

- ✓ My precious **son**,

who recently came into my life

«**Geophysics** is an applied science
allowing us to see and explore the **unseen**,
whatever it might be.
It is very important to finally manage
to get the "**real image**" of the unseen
and not "just" an image.
The true **passion** and **love** of a geophysist,
will be his **guide** to this achievement»
My belief

"Research is formalized curiosity. It is poking and prying with a purpose."
Zora Neale Hurston

"The pursuit of PhD is an enduring daring adventure."
Lailah Gifty Akita

PREFACE – ACKNOWLEDGEMENTS

In the context of this Ph.D. Thesis, the gravity method has been applied in an effort to contribute to the delineation of the complex geotectonic subsurface structure of Athens basin, an urban area that suffered from economic damage and several casualties during the catastrophic earthquake of 7th September 1999. It is not only the most populated city of Greece with almost 4 million people, but it also my residence city. Therefore, this Ph.D. challenge was a great opportunity for me to investigate it in order to reveal new data that might be useful for its safety against earthquake damage.

A first approach of this Ph.D. Thesis, slightly different, was initially assigned to me by Dr. Taxiarchis Papadopoulos, Professor of National and Kapodistrian University of Athens, who has been retired. I sincerely thank him for his trust. Beyond that, Dr. Ioannis Fountoulis, Associate Professor of National and Kapodistrian University of Athens, was initially member of the advisory committee but unfortunately, he deceased unexpectedly. He had helped me a lot in the beginning with the geology of my study area and I think he was a great loss for the science of geology.

I would like to thank from the bottom of my heart my supervisor, Dr. Ioannis Alexopoulos, Assistant Professor of National and Kapodistrian University of Athens, who has been supporting and guiding me continuously for so many years, not only during this Ph.D. Thesis but also as a graduate and post-graduate student. I feel so grateful for his great confidence to me and his wise advice concerning not only the application of geophysics or text configuration but also the way of thinking in science and life. I have gained a lot of things from his long-range experience on applied geophysics.

I would like to express my gratitude to Dr. Stylianos Lozios, Assistant Professor of National and Kapodistrian University of Athens and member of the advisory committee for his crucial guidance regarding the complex geological regime of the Athens basin. His geological knowledge for the area was extremely helpful. I would like to thank him for all the valuable geological conversations we had, trying to evaluate the results of the gravity processing.

I am also grateful to Dr. Georgios Apostolopoulos, Associate Professor of National Technical University of Athens and member of the advisory committee, for his support and continuous guidance regarding the processing of the gravity measurements and the way I should handle them. His remarks during the Ph.D. thesis were very important for its completion and were based on his great experience on gravity processing.

I would also like to thank sincerely Dr. Nikolaos Voulgaris, Professor of National and Kapodistrian University of Athens and member of the examining committee for his valuable advice during the elaboration of this Ph.D. thesis.

I am also grateful to Dr. Andreas Tsatsaris, Associate Professor of the University of Western Attica and member of the examining committee for his crucial guidance and tips regarding the Building Correction calculation and the kind provision of data. This part of my Ph.D. thesis would not be complete without his valuable contribution.

I would also like to thank the two other members of the examining committee, Dr. Andreas Tzanis, Associate Professor of National and Kapodistrian University of Athens and Dr. Efthymis Lekkas, Professor of National and Kapodistrian University of Athens for their accurate remarks.

I would also like to express my gratitude to Mr. Stylianos Chailas, Geophysist and staff of Geophysics-Geothermic department, for the kind data provision of the established gravity base in the University, which was crucial for the establishment of my gravity base network. Moreover, I do thank him for his remarks and tips regarding the gravity field acquisition and processing, based on his long-term experience on gravity measurements.

I would like to sincerely thank Dr. Emmanouel Vassilakis, Assistant Professor of National and Kapodistrian University of Athens, for his kind provision of several kinds of geological data that were the starting point for construction of the geodatabase of this Ph.D. Thesis.

I am also grateful to Dr. Kouli Aikaterini, Associate Professor of National and Kapodistrian University of Athens, for kindly providing me the necessary equipment for the laboratory density measurements. In that way the whole procedure was simplified and the measurements were more reliable.

I would like to express my deepest gratitude to Dr. Serafeim Poulos, Professor of National and Kapodistrian University of Athens. By providing me the opportunity to join his scientific projects, I was able to support part of the economic needs during this Ph.D. I would also like to thank him for the kind provision of the DGPS equipment.

I do thank my friends and colleagues Mr. Georgios Goumas and Mr. Anastasios Stavrou for their kind concession of geological core samples retained from Athens basin, extremely valuable for the density laboratory measurements of this thesis. I would also like to acknowledge the 'Geoerevna Test Laboratories – O.T.M. S.A.' for their allowance to execute selected density laboratory measurements with Mr. Georgios Goumas, using their equipment in order to evaluate my laboratory measurements. Additionally, I would also like to thank my friend and colleague, Mr. Alkiviadis Gkouvailas, for mentioning field geological remarks that he had already gathered.

I would also like to acknowledge Dr. Kyriakos Georgiou, Professor of National and Kapodistrian University of Athens for the kind concession of a 4x4-jeep type vehicle, for a few days, in order to acquire gravity stations in inaccessible areas and rough roads.

I would also like to acknowledge the Forest Service of Parnitha and chief forester Mr. Ioannis Ziaziaris for the kind permission to access the restricted forest roads of Parnitha Mountain in order to acquire gravity measurements in the National Park.

I am deeply grateful to all my friends and colleagues for helping me in the difficult task of acquiring the great number of field measurements. They spent several days in the roads of Athens basin, under harsh conditions. For that reason, I would like to thank my colleagues Mrs. Elena Kaplanidi, Mr. Dimitrios Michelioudakis, Mr. Spyridon Mavroulis and my friends Mrs. Eleftheria Drosopoulou and Mr. Spyridon Papaelias. I would also like to thank Mrs. Georgia Mitsika for her kind contribution during the construction of the 3D fence illustrations.

One of the most valuable contributions for this Ph.D. thesis was the one of my supportive wife Sofia Achtypi. Her contribution was multidisciplinary. In the beginning, she helped me the most in the field acquisition for the majority of the gravity measurements. Even though she is not a geologist and therefore she had no field experience, she overcame any possible fear and followed me even to the roughest location in order to collect the necessary data. Beyond that, due to the fact that she is an experienced English teacher, she helped the most for the text correction and language editing of this Ph.D. thesis. Therefore, I want to express my deepest gratitude and love for her valuable contribution.

Last but not least, I would like to express my gratitude to my beloved mother, my deceased father, my brother and my sister, who have been supporting and encouraging me all these years. I am grateful for their understanding, patience and economic support they offered me without second thought.

Table of Contents

LIST OF FIGURES

LIST OF TABLES

EXTENDED ABSTRACT

On 7th September 1999, a 5.9R earthquake occurred in Greece metropolis, Athens city, causing enormous damage in almost 70,000 buildings with almost 100 of them collapsing. More than 2,000 injuries were recorded along with 143 dead people and at least 100,000 homeless people. Although many major earthquakes had occurred during the last 100 years in the greater area of Athens basin, this one caused the most damage. The 7th September 1999 earthquake had its epicenter at a fault that had not generated severe earthquakes until then.

Geologically, Athens basin is a complex neotectonic graben, covered with post-alpine sediments, elongated in a NE-SW direction. The surrounding mountains as well as the interior hills of the basin are structured by alpine formations, which are separated tectonically by a large-scale detachment zone in two rock types. At the eastern margin, the metamorphic formations of *Attico-Cycladic Unit* are located, comprising the relatively autochthonous geotectonic unit. At the northern and western margins, the unmetamorphic formations appear, known as the *Ypopelagoniki Unit*. The metamorphic formations of Attico-Cycladic massif that we come along are mainly marbles, schists and dolomites, dips towards NW under the unmetamorphic formations (mainly limestones and shales), with a general trace direction NE-SW. The hills located in the basin are mainly constituted by semi-metamorphic rocks (mainly sandstones, schists, tuffs, limestones) that belong to the allochthonous units of Athens and Alepovouni. Overlying the four (4) different geotectonic alpine units and the detachment zone, there are the recent post-alpine sediments, covering the majority of Athens basin.

In the context of this Ph.D. thesis, the gravity method has been applied for the subsurface investigation of the geotectonic structure of the urban and sub-urban areas of Athens basin, taking into account all the limitations of the increasing coverage by artificial structures (buildings, stadiums, roads, playgrounds, public services station etc.). It is expected to contribute by either verifying fault zones already mapped as possible/covered or even revealing new concealed (blind) faults which could affect the city in the future by generating disastrous earthquakes.

The density of the existing geological formations in the Athens basin was determined combinational with laboratory measurements on surface samples and cores, with the application of the Nettleton method across hills and with additional seismic velocity information. The information from all three methods was compared and evaluated in order to end up with a specific density value for each geological formation.

In the context of this gravity survey, data from 1,122 gravity measurements were finally gathered, including the grid gravity stations, Nettleton profiles and the established gravity base network. The corresponding Differential Global Positioning System (dGPS) measurements were also carried out for the determination of their exact coordinates. All the

necessary corrections (drift, tide, latitude, free-air, terrain, Bouguer) were applied on the acquired gravity data in the context of the standard data reduction and the calculation of the final Bouguer Anomaly Map. A method for calculating the additional Building Correction, necessary for such urban areas is also presented. The regional-residual separation was performed with Fourier Analysis and Filtering, based on the Power Spectrum Analysis data, which in our case indicated anomaly sources of two different depths.

In the context of the qualitative interpretation, we took advantage of the derivatives methods in order to enhance the structural edges. Thereby, we produced several structural maps by applying most of the enhancement techniques, such as the Total Horizontal Derivative (THDR), the First Vertical Derivative (VDR), the Second Vertical Derivative (SVDR), the Analytical Signal (AS), Tilt (Tilt) and the Theta (cos Tilt). Their results were extremely helpful, providing severe indications for the delineation of the structural framework of the area.

The final evaluation of the gravity survey is based on the quantitative interpretation, from which we try to determine some specific parameters, such as the location, depth, shape and density contrast of the subsurface geological bodies. This kind of information is obtained from several sources. First, we have obtained information for the depths according to the results of the 3D Euler deconvolution. Afterwards, by producing several 3D density models of the subsurface, we have gathered data concerning mostly the shape, depth and density contrast of the source bodies causing the determined gravity anomalies. Finally, we have the interpretive geological 2.75-D density models, where we compare the gravity response of the geological sections with the observed ones. These geophysical-geological profiles provide a subsurface “image” of the geological and tectonic structure.

The application of the gravity method in urban and sub-urban areas of Athens basin is considered more than successful and informative for our case. The importance of this Ph.D. thesis is considered multidisciplinary since it contributes not only to the immiscibly geological and tectonic knowledge but also to the geophysical knowledge, with the thorough study, application and evaluation of the innovative Building Correction. Although the differences of the final Residual Anomaly for many gravity stations were negligible, before and after the Building Correction, significant ones have been revealed, with values reaching up to 0.19 mGal.

Beyond that, an important correlation between published isoseismal contours the 7-9-1999 earthquake and the produced residual or structural maps has been revealed, where the most damaged areas are also presented with low gravity anomaly values. This could mean that we might have one new innovative scientific way to locate and define the most dangerous and susceptible to potential earthquake damage areas, especially in urban zones, where the collection of the necessary data is difficult and because of that, they have already published in an international scientific journal.

Finally, the immiscibly geological and tectonic data obtained from this Ph.D. thesis refer to depths up to 2,500 meters. Important data regarding the thickness of the geological formations covering the basin were retrieved. The location and extent of important tectonic structures have been revealed, such as the *West Cycladic Detachment System*, upthrusts and overthrusts, extended parallel folds or even supra-detachment basins. Beyond that, we were able to identify and propose new locations of blind faults or even verify and modify the location of already proposed as concealed faults zones from older geological researches, which was practically the initial purpose of this Ph.D. thesis.

Keywords: Urban Geophysics, Gravity Method, Building Correction, Athens Basin, 3D Density Modelling, Structural Map

ΕΚΤΕΝΗΣ ΠΕΡΙΛΗΨΗ

Στις 7 Σεπτεμβρίου 1999, ένας ισχυρός σεισμός μεγέθους 5,9R πραγματοποιήθηκε στην πρωτεύουσα της Ελλάδος, την Αθήνα, προκαλώντας υλικές ζημιές σε περίπου 70.000 κτίρια, εκ των οποίων περίπου 100 τελικά κατέρρευσαν. Πάνω από 2.000 άτομα τραυματίστηκαν, 143 εντοπίστηκαν νεκροί και τουλάχιστον 100.000 άνθρωποι έμειναν άστεγοι. Παρότι τα τελευταία 100 χρόνια έχουν καταγραφεί αρκετοί ισχυροί σεισμοί στην ευρύτερη περιοχή της λεκάνης των Αθηνών, αυτός ήταν ο πιο καταστροφικός. Το επίκεντρο του σεισμού της 7^{ης} Σεπτέμβριου 1999 εντοπίζεται σε μια ρηξιγενή ζώνη που μέχρι τότε δεν ήταν γνωστή γιατί δεν είχε προκαλέσει ισχυρούς σεισμούς μέχρι τότε.

Γεωλογικά, η λεκάνη των Αθηνών είναι ένα περίπλοκο επίμηκες νεοτεκτονικό βύθισμα, διεύθυνσης ΒΑ-ΝΔ, που καλύπτεται από μεταλπικά ιζήματα στο μεγαλύτερο μέρος της. Τα περίγυρα όρη καθώς και λόφοι που βρίσκονται στο εσωτερικό της λεκάνης δομούνται από αλπικά πετρώματα, τα οποία χωρίζονται τεκτονικά σε δύο διαφορετικούς τύπους από μια μεγάλη ζώνης τεκτονικής αποκόλλησης. Στα ανατολικά περιθώρια, εντοπίζεται η σχετικά αυτόχθονη *Αττικο-Κυκλαδική Ενότητα* με μεταμορφωμένα πετρώματα. Στα βόρεια και δυτικά περιθώρια εντοπίζεται η αμεταμόρφωτη *Υποπελαγονική Ενότητα*. Τα μεταμορφωμένα πετρώματα που απαρτίζουν την Αττικό-Κυκλαδική μάζα στην περιοχή είναι κυρίως μάρμαρα, σχιστόλιθοι και δολομίτες, τα οποία βυθίζονται προς τα ΒΔ κάτω από τους αμεταμόρφωτους σχηματισμούς των ασβεστόλιθων και κλαστικών του Παλαιοζωικού. Οι λόφοι στο εσωτερικό του λεκανοπέδιου δομούνται από ημι-μεταμορφωμένα πετρώματα (κυρίως ψαμμίτες, σχίστες, τοφφίτες και ασβεστόλιθους) που ανήκουν στις αλλόχθονες ενότητες των *Αθηνών* και *Αλεποβουνίου*. Υπερκείμενα και των τεσσάρων αυτών αλπικών ενοτήτων εντοπίζονται τα πρόσφατα μεταλπικά ιζήματα τα οποία και καλύπτουν το μεγαλύτερο μέρος του λεκανοπέδιου Αθηνών.

Στο πλαίσιο της παρούσας διδακτορικής διατριβής, η βαρυτική μέθοδος εφαρμόστηκε για τη διερεύνηση της υπεδαφικής δομής των αστικών και περιαστικών περιοχών του λεκανοπέδιου των Αθηνών, λαμβάνοντας υπόψη όλους τους περιορισμούς που προκύπτουν από την αυξημένη κάλυψη του από ανθρωπογενείς κατασκευές (κτίρια, στάδια, δρόμους, παιδικές χαρές, σταθμοί μέσων μαζικής μεταφοράς κ.ά.). Τα αποτελέσματα της αναμένεται να συνεισφέρουν είτε στην επιβεβαίωση ρηξιγενών ζωνών που έχουν ήδη αποτυπωθεί ως πιθανές είτε στον εντοπισμό νέων καλυμμένων ρηξιγενών ζωνών που θα μπορούσαν μελλοντικά να επηρεάσουν την πόλη των Αθηνών προκαλώντας κάποιο καταστροφικό σεισμό.

Η πυκνότητα του κάθε γεωλογικού σχηματισμού της περιοχής καθορίστηκε συνδυαστικά από εργαστηριακές μετρήσεις επιφανειακών γεωλογικών δειγμάτων και πυρήνων γεωτρήσεων, από την εφαρμογή της μεθόδου Nettleton κατά μήκος τοπογραφικών εξάρσεων καθώς και από στοιχεία σεισμικών ταχυτήτων. Η συνδυαστική αυτή πληροφορία

συγκρίθηκε και αξιολογήθηκε προκειμένου να αποδοθεί μια χαρακτηριστική τιμή πυκνότητας για κάθε γεωλογικό σχηματισμό.

Στο πλαίσιο της βαρυτικής έρευνας, συγκεντρώθηκαν δεδομένα από 1.122 θέσεις βαρυτικών μετρήσεων, συμπεριλαμβανομένων βαρυτικών σταθμών καννάβου, τομές Nettleton και τις βαρυτικές βάσεις του δικτύου που ιδρύθηκε. Οι αντίστοιχες μετρήσεις Διαφορικού GPS πραγματοποιήθηκαν προκειμένου να καθορισθούν με ακρίβεια οι συντεταγμένες των θέσεων. Εφαρμόστηκαν όλες οι απαραίτητες διορθώσεις (drift, παλιρροιακές, γεωγραφικού πλάτους, ελευθέρου αέρα, τοπογραφικές, πλάκας Bouguer) και κατασκευάστηκε ο Χάρτης Ανωμαλίας Bouguer. Επιπλέον, περιγράφεται ενδελεχώς η διαδικασία υπολογισμού της διόρθωσης λόγω του όγκου των κτιρίων, απαραίτητη για βαρυτικές μετρήσεις σε αστικές περιοχές. Ο διαχωρισμός της τοπικής ή υπολειπόμενης (residual) ανωμαλίας Bouguer από της ευρείας (regional) πραγματοποιήθηκε με Ανάλυση και εφαρμογή φίλτρων Fourier, βασιζόμενη στην φασματική ανάλυση των δεδομένων, που στην συγκεκριμένη περιοχή κατέδειξε δύο διαφορετικά βάθη για τις μάζες που προκαλούν τις ανωμαλίες.

Για την ποιοτική ερμηνεία των βαρυτικών δεδομένων που συγκεντρώθηκαν, οι παράγωγοι τους χρησιμοποιήθηκαν για την ενίσχυση των τεκτονικών γραμμών. Κατασκευάστηκαν αρκετοί χάρτες «τεκτονικών γραμμώσεων» (structural maps) εκμεταλλευόμενοι τις παραγώγους, όπως αυτοί της Ολικής Οριζόντιας Παράγωγου (THDR), της Πρώτης Κατακόρυφης Παράγωγου (VDR), της Δεύτερης Κατακόρυφης Παράγωγου (SVDR), του ‘Αναλυτικού σήματος’ (Analytic Signal) και της ‘Κλίσης’ (Tilt). Τα αποτελέσματα ήταν ιδιαίτερα χρήσιμα, προσδίδοντας σοβαρά στοιχεία για την σκιαγράφηση του τεκτονικού ιστού του λεκανοπέδιου.

Η τελική αξιολόγηση των βαρυτικών δεδομένων στηρίχθηκε στην ποσοτική ερμηνεία τους, μέσω της οποίας προσπαθούμε να καθορίσουμε κάποιες χαρακτηριστικές παραμέτρους, όπως η θέση, το βάθος, το γεωμετρικό σχήμα και η διαφορά πυκνότητας των υπεδαφικών γεωλογικών σχηματισμών. Αυτού του είδους τα στοιχεία συγκεντρώθηκαν από διάφορες πηγές. Αρχικά, πληροφορίες βάθους συλλέχθηκαν από τα αποτελέσματα της 3D αποσυνέλιξης Euler. Έπειτα, με την κατασκευή των 3D μοντέλων κατανομής της υπεδαφική πυκνότητας, συλλέξαμε στοιχεία κυρίως για το γεωμετρικό σχήμα, το βάθος και τη διαφορά πυκνότητας των γεωλογικών σωμάτων που προκαλούν τις βαρυτικές ανωμαλίες. Επιπλέον, κατασκευάστηκαν 2,75D γεωλογικές-γεωφυσικές τομές, συγκρίνοντας την βαρυτική απόκριση των γεωλογικών μοντέλων με αυτή των μετρήσεων, από τις οποίες προέκυψε μια υπεδαφική απεικόνιση της γεωτεκτονική δομής.

Η εφαρμογή της βαρυτικής μεθόδου σε αστικές και περι-αστικές περιοχές του λεκανοπέδιου Αθηνών θεωρείται παραπάνω από επιτυχής, προσφέροντας αρκετές νέες πληροφορίες. Θεωρούμε πολυπαραμετρική τη συνεισφορά της παρούσα διδακτορικής διατριβής, δεδομένου ότι συνεισφέρει όχι μόνο στην αμιγώς γεωτεκτονική γνώση της

περιοχής αλλά και στην γεωφυσική γνώση, μέσα από την εκτενή εφαρμογή και αξιολόγηση της Διόρθωση Κτιρίων (Building Correction). Παρότι σε πολλές θέσης βαρυτικής μέτρησης προέκυψαν σχεδόν αμελητέες διαφορές στην τοπική ανωμαλία Bouguer, πριν και μετά την εφαρμογή της Διόρθωσης Κτιρίων, σε κάποιες θέσεις υπολογισθήκαν τιμές ως και 0,19 mGal.

Επιπλέον, παρατηρήθηκαν έντονες συσχετίσεις μεταξύ δημοσιευμένων ισόσειστων καμπύλων από το σεισμό της 7-9-1999 και των βαρυτικών χαρτών τοπικής ανωμαλίας και 'τεκτονικών γραμμώσεων' που παρήχθησαν, με τις πληγείσες περιοχές να εντοπίζονται εντός των περιοχών χαμηλών βαρυτικών τιμών ανωμαλίας. Θα μπορούσαμε να πούμε ότι είναι νέα επιστημονική προσέγγιση, σχετικά με τον εντοπισμό και σκιαγράφηση επικίνδυνων περιοχών, επιρρεπών σε αυξημένες καταστροφές από σεισμικό γεγονός, ειδικά εντός αστικών ζωνών όπου η συλλογή επιστημονικών δεδομένων θεωρείται πιο δύσκολη. Εξαιτίας της σημαντικότητας της, η συγκεκριμένη επιστημονική προσέγγιση έχει ήδη δημοσιευθεί σε επιστημονικό περιοδικό.

Τέλος, τα νέα γεωλογικά και τεκτονικά δεδομένα που προκύπτουν από την εκπόνηση της παρούσας διδακτορικής διατριβής φτάνουν σε βάθη της τάξεως των 2.500 μέτρων. Σημαντικά στοιχεία σχετικά με την εκτίμηση των παχών γεωλογικών σχηματισμών έχουν προκύψει. Πληροφορίες για τη θέση και την έκταση σημαντικών τεκτονικών δομών αναδείχθηκαν, όπως για το *Σύστημα Οριζόντιας Ολίσθηση Δυτικών Κυκλάδων*, επωθήσεις και εφιππεύσεις, εκτεταμένες οριζόντιες πτυχώσεις καθώς και λεκάνες supra-detachment. Επιπλέον, σχετικά και με το τελικό στόχο της παρούσας διδακτορικής διατριβής, συγκεντρώθηκαν αρκετά στοιχεία ώστε να μπορέσουμε είτε να εντοπίσουμε και να προτείνουμε νέες θέσεις ρηξιγενών ζωνών είτε να επιβεβαιώσουμε και να τροποποιήσουμε ήδη προτεινόμενες ρηξιγενείς ζώνες από παλαιότερες γεωλογικές έρευνες.

Λέξεις-κλειδιά: Αστική Γεωφυσική, Βαρυτική Μέθοδος, Διόρθωση Κτιρίων, Λεκανοπέδιο Αθηνών, 3D Μοντέλα Πυκνότητας, Χάρτες 'τεκτονικών γραμμώσεων'

1. GENERAL

1.1. INTRODUCTION AND STUDY PURPOSE

On 7th September 1999, a 5.9R earthquake occurred in Greece metropolis, Athens city, causing enormous damage in almost 70,000 buildings with almost 100 of them collapsing. More than 2,000 injuries were recorded along with 143 dead people and at least 100,000 homeless people (Bouckovalas & Kouretzis, 2001). Although many major earthquakes had occurred during the last 100 years in the greater area of Athens basin, this one caused the most damage. The 7th September 1999 earthquake had its epicenter at a fault that had not generated severe earthquakes until then

Especially in urban and fully residentially developed areas, knowledge on the existence of concealed active faults is absolutely valuable because the damage distribution of an earthquake is usually related to the tectonic structures of the area. Unfortunately, since the areas are covered with artificial surfaces, such as buildings, industrial infrastructures, roads and generally concrete, the geological research is quite complicated, with the obtained information being restricted to quite older observations, geological maps, boreholes and data.

The application of geophysical methods can contribute to the geological and tectonic adumbration of the subsurface. The geophysical methods are subject to the contrast of the measured physical property (e.g. density for gravimetry, resistivity for geoelectrical, magnetic susceptibility for magnetics etc.). This means that the choice of the appropriate method should be primarily based on the evaluation of the local geology/lithology and its predictable range of variation, along with the scope of the investigation. Beyond these two basic factors (geology and scope), several others can be taken into consideration, such as the type of environment, including the type of the survey area (urban areas, mountains, fields, forest areas, marine etc.), the morphology of it (e.g. steep relief) or general obstacles for the field acquisition (e.g. power sources and current cables, roads, rivers, dense vegetation).

The purpose of this Ph.D. thesis is the application of the gravity method for the subsurface investigation of the geotectonic structure of the urban and sub-urban areas of Athens basin, taking into account all the limitations of the increasing coverage by artificial structures. It is expected to contribute by either verifying fault zones already mapped as possible/covered or even revealing new concealed (blind) faults which could affect the city in the future by generating disastrous earthquakes.

Although gravity method is considered to be a traditional approach, the processing of the acquired gravity data will be carried out with the state-of-the-art techniques (e.g. 3D modelling), along with the innovative method introduced for the Building Correction.

1.2. LOCATION - MORPHOLOGICAL DATA - LAND USE OF STUDY AREA

The study area (Fig. 1.1) covers almost 740 km^2 including the Athens basin that hosts the metropolis of Greece with population up to 4 million people and its greater area. It is surrounded by the mountains of *Aigaleo* (468 m) and *Poikilo* to the West, *Parnitha* (1,413 m) to the NNW, *Penteli* (1,108 m) to NE and *Hymettus* (1,027 m) to the East, while it is also surrounded by the *Saronikos Gulf* to the SW.

Figure 1.1. The location of Athens basin, which is the study area, is indicated with the red polygon.

The Athens basin is an oblong basin with NE-SW direction that presents a relatively low elevation ranging from the sea level up to almost 300-350 meters. At the central part of the basin, an axis of discontinuous hills with direction NE-SW is observed. The hills from north to south are *Tourkovounia-Galatsi* (339 m), *Lycabettus* (278 m), *Strefi* (163 m), *Akropolis* (156 m), *Filopappou* (147 m), *Areios Pagos* (115 m), *Skoyze* (67 m), *Sikelias* (79 m), *Ardittos* (131 m) and *Katsipodi* (129 m). One more, almost parallel axis of hills exists at the western margin of the basin, down to the eastern foothills of the *Poikilo-Aigaleo* Mountains, represented from north to south by *Tafos Gyftissas* (183 m), *Petroupolis* (205m), *Aspra Xomata* (239 m), *Profitis Ilias Haidari* (189 m), *Kaniaris* (262 m) and *Karavas*. Moreover, at the area of *Piraeus*, there are two more hills, the one of *Kastella* (87 m) and the one of *Piraiki* (48 m).

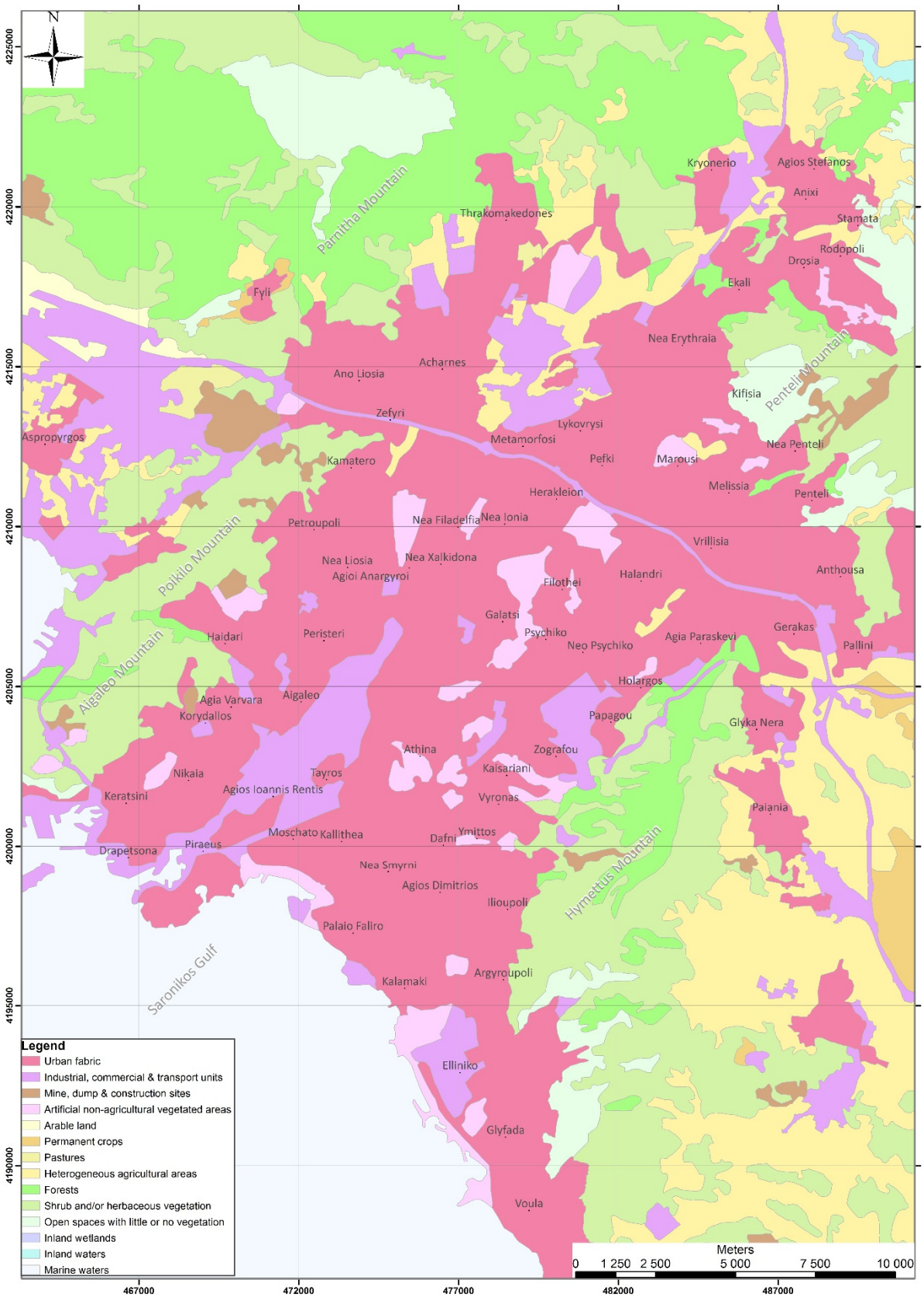

Figure 1.2. Simplified land cover map of the study area, based on CORINE 2012 data.

As far as the types of land coverage are concerned, based on Antoniou (2000), the urban area of the basin is 62%, from which the 35% is corresponding to areas with building coverage of 80-100% (*Downtown, Zografou, Haidari, Nea Smyrni, Ilioupoli, Piraeus, Faliro*) and the other 27% is corresponding to areas of lower building coverage supplemented with uncovered areas and urban green areas.

Taking into consideration the land cover data presented in Figure 1.2 provided by CORINE 2012 project (EEA, 2012), the areas of artificial surfaces cover a 54.5% of our study area, the agricultural areas cover 7.2%, the forests and semi-natural areas 38.2% and the inland waters 0.07%.

1.3. URBAN GEOPHYSICS

According to Fenning *et al*. (1994), Urban Geophysics is carried out in the context of the built environment and is usually practiced in surroundings dominated by structures, buildings, roads and concrete rather than the more familiar soils and geological strata of 'green field' sites.

Fenning *et al*. (1994) pointed that the practitioner of urban geophysics operates in a dynamic environment, in which anomalous, noisy and vibrating metal objects, such as vehicles, frequently pass in and out of the survey area while electrical power sources concealed in adjacent buildings operate to an unknown schedule. Additionally, based on Liu & Chan (2007), apart from the cultural noise, there are more difficulties such as the limited time for conducting the geophysical surveys, the regulatory constraints and the requirement for traffic management. Beyond these, special approaches and methods of interpreting the data are therefore required sometimes (Henderson, 1992).

In our modern world, rapid urbanization and industrial growth are the characteristics of several areas. Several geophysical applications can contribute significantly to the evolvement of these urban areas. Some up-to-date examples are the seismic microzonation, the detection of groundwater supplies, the salination of subsurface aquifers, the management of the waste disposals, the investigation of possible subsurface environmental contamination, forensic investigations (crime scenes) and geotechnical issues such as the excavation of the subway lines, road construction and even bridge paddling. And for cities with great history, such as Athens, geophysics can contribute a lot by investigating and revealing buried archaeological monuments.

Due to this rapid urban development and the lack of the appropriate geological knowledge of the older times, several cities were established over concealed active fault zones. They are practically established on potential threats since they can generate disastrous earthquakes that will probably lead to major economic damage and human casualties. Several cities have suffered for such social-economic damage, such as San Francisco in 1906 and Tokyo in 1923 (Xu *et al.,* 2015).

The **deep** geophysical research in urban areas is quite difficult to be developed (Xu *et al.,* 2015). It is almost prohibitive to apply the **electromagnetic** and **magnetic** methodologies due to the effects from the countless power sources and current cables. **Geoelectrical** methods are also difficult to carry out, since most of them require space and straight long lines to measure on. The **seismic** methods are widely applied in urban areas (Hutchinson *et al*., 2009; Krawczyk *et al*., 2012; Symeonidis *et al*., 2005) but it is quite expensive most of the times. On the other hand, as Miller (2003) states, buildings and infrastructure in urban areas are susceptible to vibration damage from a range of sources, both natural and anthropogenic. The **gravity** methodology can be applied in urban areas for deeper investigation but the field measurements should be planned with caution, taking into consideration the traffic, the construction vibrations and the building effects.

2. GEOLOGICAL DATA

The main purpose of our investigation in the Athens basin is to delineate the geological and tectonic subsurface structure, due to the damage caused by the major earthquake of 7th September 1999 (M_w=5.9R), with the contribution of gravity method.

First, we gathered all the bibliographic geological data regarding the greater Athens basin (papers, maps, technical studies etc.). Afterwards, all the references were re-evaluated and along with the personal field observations that were gathered, the final geological structure was determined and is described thoroughly in the following sections.

All these data (digital or not) had been imported in a Geographic Information System (GIS), in which they were digitized (if necessary), corrected, homogenized, categorized in layers and processed, creating a very important geodatabase. Almost all the maps presented in this Ph.D. thesis were constructed with the contribution of this geodatabase and GIS.

2.1. BIBLIOGRAPHIC DATA

Geo-tectonically, the Athens basin is located in the Northwestern area of the present active volcanic arc. The greater area is practically a transitional zone between the highly active areas of Corinth-Viotia and the low deformation area of Cyclades and South Attica (Mariolakos & Papanikolaou, 1987; Papanikolaou & Lozios, 1990).

The first attempt to categorize Attica geo-tectonically was made by Philipson (1898), who placed the Northern Attica in the East-Greece zone and the Southern Attica in the Attico-Cycladic zone. Later, Ktenas (1923) included Attica in the middle system of Attico-Cycladic crystallic massif. Renz (1940) considered that the limestones of Parnitha and the central hills of Athens were categorized in the Parnassos-Gkiona zone. Laureotiki's area was also set by Marinos & Petrascheck (1956) in Attic-Cycladic mass, while Tataris (1966) considered the area of Aigaleo as a horst of Ypopelagoniki zone. "Attica" autochthonous unit, located in the central area of Athens basin, was introduced by Papanikolaou (1986), underlying the units of East-Greece, Layrio and Almyropotamos. On the other hand, Katsikatsos (1977) considered that the autochthonous metamorphic formations of Attica belong to the extension of Olympos-Ossas zone and Krania-Elassona zone. Finally, the most recent aspects of authors (Jacobshagen *et al*., 1978; Durr *et al.*, 1978, Kilias *et al.*, 2004; Ring, 2007) categorize the Southern-Eastern area of Attica in the Attico-Cycladic massif and the Northern-Western area in Ypopelagoniki zone.

Based on Papanikolaou & Lozios (1990), the greater area of Attica is controlled by fault zones of WNW-ESE direction, along with the NNE-SSW perpendicular ones. Geologists consider as the most important structure of the greater area, the tectonic contact between metamorphic and unmetamorphic geological formations, with a NE-SW direction. Some authors (Katsikatsos *et al.,* 1986; Papanikolaou, 1986) believe that this important tectonic

contact is identified with Kifissos River course (Fig. 2.28). Their aspects are scientifically enhanced by specific structures of Saronikos gulf, adumbrated with seismic tomography by Drakatos *et al.* (2002; 2005).

Although many researchers have studied the geological and tectonic regime of Athens basin, there are still open questions and "grey" zones, due to the fact that most of them are based on the lithological stratum proposed by Lepsius (1893), who produced a detailed map of Athens and central-Southern Attica in scale 1:25,000. Bittner (1880) also described the geological formations of Attica before Lepsius (1893).

Renz (1908; 1909) described the geology of Parnitha Mountain, Negris (1912; 1913) evolved with the geology of Athens basin and the surrounding mountains. Moreover, Kober (1929) introduced the term of tectonic caps through the construction of geological sections for Athens basin. More detailed geological maps of the area were produced by other researchers (Niedermayer, 1971; Sindowski, 1949), while other authors dealt mostly with the Neogene formations study (Freyberg, 1951; Charalabakis, 1952). Many more papers were published for the geology of Athens basin (Clement, 1976; Dounas & Gaitanakis, 1981; Marinos, 1937; 1955; Marinos *et al.,* 1971; 1974; Paraskeyaidis & Chorianopoulou, 1978; Petrascheck and Marinos, 1953; Sindowski, 1950; Skounakis, 1972; Tataris, 1966; 1972).

Many of the authors investigated the surrounding mountains of Athens basin. Lozios (1990; 1993) studied thoroughly the metamorphic formations of NE Attica and Penteli Mountain. Additionally, Baziotis (2008) and Baziotis *et al.* (2004) continued the description of the petrology of the metamorphic formations of Attica. Tataris & Sideris (1989) analyzed the areas of Aigaleo Mountain and Salamis Island, Lekkas & Lozios (2000) described Hymettus structure, while Parnitha's Mountain structure was designated Mariolakos & Fountoulis (2000a; 2000b).

Beyond that, Lekkas *et al.* (1998) produced a neotectonic map of the greater East Attica area. On the contrary, Papadeas (2002) proposed a quite different aspect for Athens geology collocating a stratum of carbonate formations in alteration with shales or gneiss. Papanikolaou *et al.* (2002) published a detailed geological-geotechnical study of Athens basin, giving emphasis on the Neogene formations and their tectonic structure and Papanikolaou *et al.* (2004b) referred to the structure of the allochthonous system of the so-called "Athens Schists". Spanos (2012), tried to clarify the geodynamical evolution and deformation facies of the Athens area.

During the Athens' metro excavation, a great deal of data for the shallow geological structure came up (Leoutsakos *et al*., 2008; Marinos *et al.,* 2004; 2006; 2009).

Other authors, focused more on the tectonic analysis either of the surrounding mountains, like Parnitha (Chatoupis & Fountoulis, 2004; Mariolakos *et al.*, 2001b), or in a more general aspect, like Krohe *et al.* (2009) dealing with the detachment faults. Some researchers emphasized on specific areas or faults, like Papanikolaou *et al.,* (2008) and Papanikolaou & Papanikolaou (2007), who drew attention to emphasis on the NE area above the Athens basin

and *Afidnes* Fault Zone or like Ganas *et al.* (2005), where the DEM morphometry has been used to identify fault zones.

Important information from the submarine neotectonic maps of Saronikos Gulf (Papanikolaou *et al.,* 1989a) and Southern Evoikos (Papanikolaou *et al.,* 1989b) has been gathered, connecting the surface with subsurface structure.

Finally, Foumelis (2009), Foumelis *et al.* (2009; 2013) and Parcharidis *et al.* (2006), studied the surface deformation of the greater area of Athens basin, based on Differential GPS measurements and Radar Interferometry, trying to explain the damage of the earthquake that occurred in Athens in 1999 and delineate the tectonic structure of the basin.

2.2. GEOLOGICAL STRUCTURE OF THE STUDY AREA

Athens basin, as a complex neotectonic graben, is almost 3605km^2 without counting the surrounding mountains, covered with post-alpine sediments. It is elongated in a NE-SW direction, surrounded by Parnitha (NW), Penteli (NE), Hymettus (E), Aigaleo-Poikilo (W) Mountains, while at South it is facing to the sea and Saronikos Gulf. Across the central area of the basin, spread in a NE-SW direction, a number of hills are revealed. A similar axis of hills is located, with the same NE-SW direction, at the western area of the basin, at the foothill of Mountains Aigaleo and Poikilo.

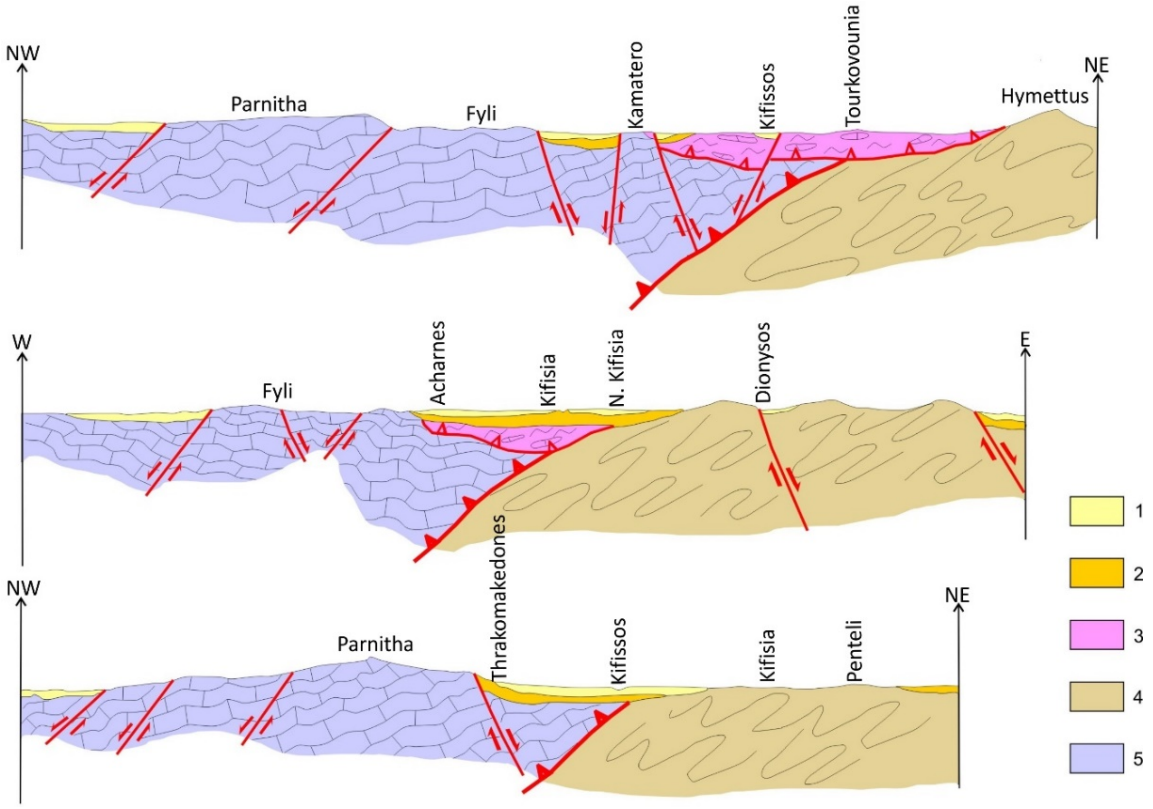

Figure 2.1: Representative geological sections illustrating the geotectonic regime of the Athens basin area. 1: Alluvium, 2: Neogene, 3: Allochthonous unit, 4: Autochthonous Metamorphic Unit, 5: Ypopelagoniki unit. (*Papanikolaou et al., 1999*)

The surrounding mountains and hills of the basin are structured by alpine formations, which are separated tectonically by a large-scale detachment zone (Papanikolaou *et al*., 2002; Papanikolaou & Papanikolaou, 2007), in two rock types. At the eastern margin, the metamorphic formations of Attico-Cycladic massif are located, comprising the relatively autochthonous geotectonic unit. At the northern and western margins, the unmetamorphic formations appear, known as the Ypopelagoniki unit. The metamorphic formations of Attico-Cycladic massif that we come along are mainly marbles, schists and dolomites, dips towards NW under the unmetamorphic formations (mainly limestones and shales), with a general trace direction NE-SW. The hills located in the basin are mainly constituted by semi-metamorphic rocks (mainly sandstones, schists, tuffs, limestones) that belong to the allochthonous units of Athens and Alepovouni (Fig. 2.1)

Overlying the four (4) different geotectonic alpine units and the detachment zone, there are the recent post-alpine sediments, covering the majority of Athens basin. Practically these sediments are lacustrine, lacustrine-terrestrial or even fluvio-marine.

In the context of this Ph.D. thesis, the adopted geological structure of the study area (Fig. 2.2) that will be described thoroughly in the subsequent sections was based on a combination of the following references:

- Geological-Geotechnical mapping of Papanikolaou *et al.* (2002), slightly simplified concerning the post-alpine categories. The inner area of Athens basin is described in detail.
- IGME Geological Map "*Athina-Elefsis*"1:50,000 (Katsikatsos *et al.*, 1986).
- IGME Geological Map "*Athina-Peiraias*"1:50,000 (Gaitanakis, 1982).
- IGME Geological Map "*Kifisia*"1:50,000 (Katsikatsos, 2002).
- IGME Geological Map "*Koropi-Plaka*"1:50,000 (Latsoudas, 1992).
- Lozios (1993), Ph.D. thesis, describing the metamorphic formations of Penteli Mountain.
- Personal field observations.

2.2.a. Alpine Formations

The alpine formations of the study area structure the basin's surrounding mountains and the axis of hills in the basin. Based on lithostratigraphic and tectonic criteria, four (4) geotectonic units seem to constitute the Athens geological structure (Fig. 2.1).

The tectonically lower and relatively autochthonous unit is the one of Metamorphic formations, located at Hymettus (Fig. 2.3) and Penteli (Fig. 2.4) Mountains. At the eastern margin of the basin, overlying the metamorphic unit, we observe the "*Alepovouni*" unit, with low metamorphism rocks, whereas at the western margin, the "*Ypopelagoniki*" unit is dominant forming the Mountains of Parnitha (Fig. 2.5) and Poikilo-Aigaleo (Fig. 2.6), with a volcano-sedimentary sequence at the base and carbonate rocks on the top. Finally, the *"Athens*" unit is overlying above all the aforementioned units, comprised of limestones, clay-sandstones and ophiolites.

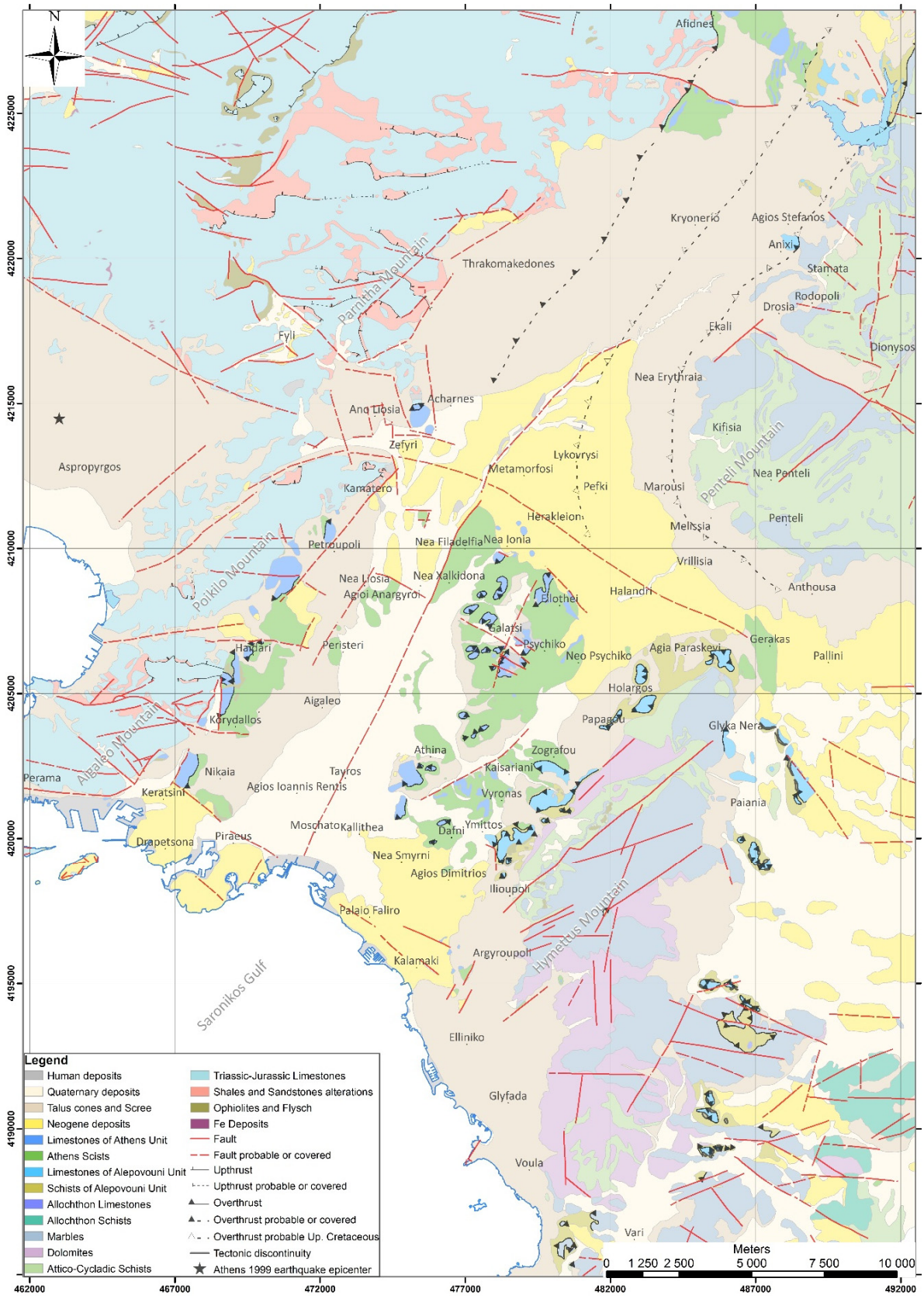

Figure 2.2: Geological and Tectonic Map of Athens basin (simplified and modified based on *Gaitanakis, 1982; Katsikatsos, 2002; Katsikatsos et al., 1986; Latsoudas, 1992 and Papanikolaou et al., 2002*).

Figure 2.3: View of Hymettus Mountain (photograph taken from west)

Figure 2.4: Penteli Mountain (photograph taken from south)

Figure 2.5:Parnitha Mountain (photograph taken from south)

Figure 2.6: Poikilo and Aigaleo Mountains (photograph taken from north-east)

2.2.a.1. Metamorphic Unit

The mountains of Penteli (Fig. 2.4) and Hymettus (Fig. 2.3) consist of the metamorphic formations of Attico-Cycladic massif zone, constituting the relative autochthonous of Athens basin. Therefore, they are considered to be the tectonically lowest geological formations of the study area.

Based on bibliographic data the unit could be subdivided in the following parts:

i. "*Varis"* Unit comprised of the formation "*Vari's Dolomites"* (Fig.2.7) and the formation *"Pirnari Schists"* (Lepsius, 1893; Lekkas & Lozios, 2000).
ii. The overlaying *"Hymettus"* Unit, formed by the *"Lower Marble"*, the "*Upper Marble"* (Fig.2.7) and the *"Kaisariani Schists"* (Lepsius, 1893).
iii. *"Penteli"* Unit (Lozios, 1993).

In between the above sub-units, ophiolites are also located.

Figure 2.7: Marbles (M) and Dolomites (D) at tectonic contact, over Hymettus Mountain (*Papanikolaou et al., 2002*).

The Metamorphic Unit consists of a complicated system of nappes, controlled by high-pressure and low-temperature metamorphism (Spanos, 2012). The main metamorphic rock types appearing in the area are marbles, schists, dolomites and dolomitic marbles.

The ***Marbles*** (*M*), located on mountains Penteli and Hymettus are characterized by the age of Mesozoic. They are white, grey-white, grey compact with well-formed crystals, medium to thick bedded, sometimes reduced to thin-bedded (Figs. 2.8). Due to the high grade of metamorphism fossils are constrained (gastropods, rudists, algae), indicating ages between Triassic and Cretaceous. Their thickness can reach the 500 meters for the "*Lower marble*" (Photiades, 2001) and the 250 meters for the "*Upper marble*".

Figures 2.8: Marbles (*M*)

The ***Schists*** *(Sch)*, underlying the Marbles are comprised of several types, like micaceous, chloritic, quartzose and amphibolitic (Figs. 2.9). Meta-laves and meta-tuffs can also be

observed. The "*Kaisariani Schists"* (Figs. 2.10), a subcategory of the *Schists,* construct the Hymettus Mountain and over 300 meters thickness. They are mainly micaceous and green schists (metamorphic basic rocks) with intercalation of marbles. Schists occupy the biggest part of the Penteli Mountain volume. On the contrary, Schists are observed in a quite smaller percent on the Hymettus Mountain. Regarding their age, there is no clear data for Penteli, except of the fact that they should be at least Triassic age, due to their tectono-stratigraphic position. The same age seems to dominate for the Hymettus Mountain due to older findings of remains.


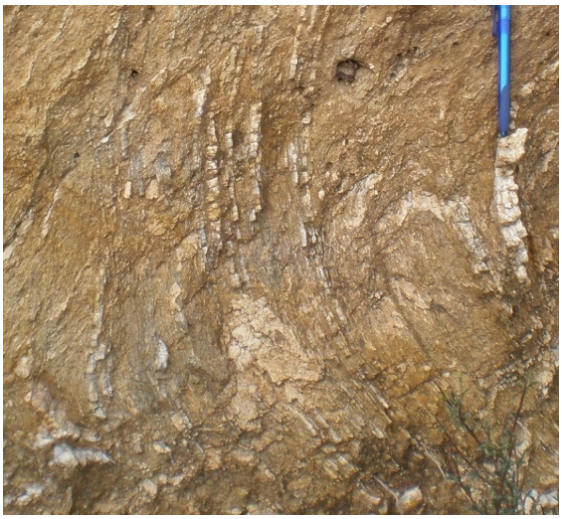

Figures 2.9: Schists (*Sch*)


Figures 2.10: Kaisariani Schists (*Sch*)

At the central, western and northern part of Hymettus Mountain, the medium-bedded, white and grey, granular to crystalline ***Dolomites*** (*D*) and ***Dolomitic marbles*** mainly appear(Figs. 2.11), with at least 200 thickness. Their base is clastic, known as *"Varis Schists"*. They are calcitic, micaceous schists with quartzose lens inside. Their age has been determined through algae, as Triassic and they are observed with thickness of at least 100 meters.

Figures 2.11: Dolomites (*D*)

2.2.a.2. Ypopelagoniki Unit

The formations of *Ypopelagoniki Unit* form the Mountains of Aigaleo-Poikilo (Fig. 2.6) and Parnitha (Fig. 2.5). They are underlying the *Athens Unit* across the western margins of the Athens basin, with their contact being hardly visible due to the post-alpine deposits that cover it. *Ypopelagoniki Unit* is also overlying (somewhere in the middle of the Athens basin) the *Metamorphic Unit*.

The major formation of Ypopelagoniki is carbonate rocks, known as ***Triassic-Jurassic Limestones*** (*T-J*). They are white to light grey or even reddish, unbedded to thick-bedded, crystalline, intensely broken into pieces and karstic limestones and dolomitic limestones. Their thickness can be a few hundreds of meters.

Figures 2.12: Triassic-Jurassic Limestones (*T-J*)

At the base of the limestones, a clastic sequence called ***Shales and Sandstones Alterations*** (*C-P*) can be found at the Northern Poikilo Mountain and the Southern edge of Parnitha. It is

comprised of shales, pelites, sandstones, quartz conglomerates, tuffs, tuffites, greywackes, laves and even bio-clastic limestones in the form olistoliths, from the fossils of which the age has been determined as Upper Carboniferous-Permian. The *Shales and Sandstones Alterations* formation is generally observed as tectonical intercalations between the *Limestones*, due to the increased thrusts. Therefore, in some areas (Ano Liosia and Kamatero) the clastic sequence is located above the limestones.

Figures 2.13: Shales and Sandstones Alterations (*C-P*)

2.2.a.3. Alepovouni Unit

The *Alepovouni* Unit is mainly observed across the eastern basin and western foothills of Hymettus Mountain, from the northern area to the area of Argyroupoli. It is located tectonically impacted (tectonic breccia is observed), between the underlying *Metamorphic Unit* and the overlying *Athens* Unit, with 100-200 meters thickness.

It consists of low metamorphism formations that structure the small hills at the mountain's foothills (*Tsako, Korakas, Alepovouni, Koutalades, Zoodoxos Pigi, Kopanas* and other smaller). The biggest part is covered by the post-alpine sediments, while its biggest surface exposure is located near the Panepistiomioupoli and the cemetery of Kaisariani.

The upper part consists of compact unbedded to thick-bedded crystalline **limestones** (*CAl*) of Mesozoic (Figs. 2.14). At specific locations, they evolve to platy limestones. On the other hand, the lowest part of the stratigraphic column is comprised of metamorphic to semi-metamorphic layers of **micaceous schists and phyllites** (*SchAl* - Figs. 2.15). Intercalations of platy gray to brownish limestones and pieces of metamorphic basic and ultrabasic rocks are also observed. The upper part of limestones is tectonically overlying the lower one and seprentinites with intensely schistosity (serpentinised peridotites) are also located.

Figures 2.14: The Limestones of Alepovouni Unit (*CAl*)

Figures 2.15: Schists and Phyllites of Alepovouni Unit (*SchAl*)

2.2.a.4. Athens Unit

The formations of *Athens* Unit are covering almost the whole extension of Athens basin, although they are located on surface only on the upper parts of the hills existing at the central and western areas of the basin. The post-alpine sediments of the basin are covering the major extension of *Athens* unit, especially along the greater area of *Kifissos* river flow.

It is considered to be the tectonically upper stratigraphic unit of Athens basin forming a coverage with successive imbrications. Along the eastern foothills of Aigaleo and Poikilo Mountains, it is observed overlying tectonically on the *Ypopelagoniki* Unit, forming an elongated zone of hills (*Tafos Gyftissas, Petroupoli, Latomeia Aspra Homata, Profitis Ilias Haidari, Korydallos, Mikros Karavas and Megalos Karavas*). Moreover, at the central area of

Athens basin, it is located tectonically overlying the Alepovouni and formations of the Metamorphic Unit. Again, an axis of hills (*Tourkovounia, Lycabettus, Strefi, Akropolis, Filopappou, Areios Pagos, Sikelias, Ardittos* and *Katsipodi*) is controlled by *Athens* Unit's formations.

The geotectonic unit can be discriminated in two separate lithostratigraphic parts, due to their different paleogeopgraphic conditions and tectonic deformation. The upper part is tectonically overlying the lower one, with an almost horizontal tectonic contact. A **tectonic breccia** of 1-1.5 meters thickness is usually observed there, visible at the central hills of *Acropolis, Areios Pagos* and *Lycabettus,* but also at the western hills of *Profiti Ilia Haidari, Korydallos* and *Karavas*.

The upper part mainly consists of unbedded to thick-bedded, neritic ***limestones***, evolving at specific locations to dolomitic limestones (*CA*). Along the foothills of Aigaleo and Poikilo Mountains, they are located varying from grey to bluish, thick-bedded with pieces of rudists and foraminifera (Fig. 2.16-left). On the other hand, at the central hills of the basin whitish to grey, thick-bedded to unbedded and locally platy ones are found (Fig. 2.16-right). Their thickness can reach up the 250 meters.

Figures 2.16: The Limestones of Athens Unit (*CA*)

The lowest part of the unit is quite complicated and is known as ***Athens Schists*** nappe (Marinos *et al*., 1971; 1974), with almost 200 meters thickness. It is comprised of unmetamorphic clastic sediments, such as sandstones, pelites, clays, sandstone marls, greywackes, tuffs and argillic schists. Platy limestones and chert nodules also exist (Figs. 2.17). At the area of *Petroupoli*, it is observed with reddish and green tuffs and tuffites, marls and schists alternating. Southern, at *Aspra Homata* area, it is characterized by brownish schistose pelites, schists, sandstones, marls and platy limestones. On the other hand, the central hills of the basin are structured by epigenetic metamorphic formations, such as phyllites and micaceous schists, along with facies of schistose pelites, marl, schists and intercalations of platy limestones.

Figures 2.17: Athens Schists mélange (*SchA*)

The unit has been characterized as a complex mélange without internal geometry, because of its continuous tectonical alterations of its parts, the mixture of its formations, the complete absence of stratigraphic sequence and the existence of pieces of basic and ultrabasic formations. Furthermore, two main folding directions have been identified, one NW-SE dipping to NE and another NE-SW dipping to NE (Poll & Theodoropoulos, 1971).

2.2.a.5. Ophiolites (O)

In almost all the pre-mentioned alpine geotectonic units of Athens basin, fragments of basic and ultrabasic rocks are detected, especially along tectonic contacts of the nappes, such as the one of the *Athens Schists* overlying the *Ypopelagoniki* limestones or between the imbrications of the Athens Unit limestones.

The majority of these basic and ultrabasic rocks are altered **serpentinites**, probably originated from an ophiolitic complex. They can easily be observed at the western basin on the *Petroupoli, Latomeia Agiou Nikolaou, Korydallos, Profiti Ilia Haidari* and Karava hills. Beyond them, they also appear on *Tourkovounia* hill (central basin) along with **basaltic spilites** in pillow-lavas form and altered diabase.

Another group of ophiolites is also located along the western foothills of Hymettus Mountain, either between the upper (limestones) and lower (phyllites) part of *Alepovouni* Unit or in the mass of phyllites itself (*Korakas* hill). Here, they are comprised mainly of **diabasic** type of rocks. On the other hand, near *Panepistiomioupoli* serpentinized peridotites are observed.

Finally, a third group of basic and ultrabasic rocks is observed in the *Kaisariani Schists* of the Metamorphic Unit, in the form of intercalations and consists of **peridotites**.

2.2.b. Post-alpine Formations

The post-alpine formations occupy the biggest part of Athens basin, lying and covering uncomfortably the underlying alpine formations. They can be discriminated in the older ones, with Neogene age, and the more recent ones, belonging to the Quaternary. Normally, the Quaternary formations are covering the Neogene ones.

In the framework of this Ph.D. thesis, some simplification groupings of the post-alpine formations have been made (Figure 2.2) based on their response on the gravity measurements and their litho-stratigraphic characteristics. Nevertheless, we will describe thoroughly their component subcategories based on Papanikolaou *et al*. (2002).

2.2.b.1. Human Deposits (Hm)

Human or Anthropogenic deposits can be discriminated in two types concerning the Athens basin. The first category includes all kind of materials that have been used for landfills or in the context of creating artificial landscapes, breakwaters, piers etc. They might include artificial materials, like cement block, demolition wastes, quarries excavations etc.

The other type of human deposits is the one for restoration of abandoned quarries. The materials placed are uneven, containing sand, clays, pebbles etc.

2.2.b.2. Loose Quaternary Deposits (Q)

In this category, many different types of loose sediments from the Quaternary period have been sorted. This grouping has been mainly based on the relative low densities that characterize these formations.

i. Alluvium deposits

The majority of them are the fluvial deposits of *Kifissos* River and its tributaries. They are comprised of clays, mud and loose conglomerates, with lateral transitions. Their contact and limits with the underlying formations are ambiguous because of their deposition way and the human interference. Their thickness is usually a few meters, but it increased along the *Kifissos River* flow, where they can be up to 30 meters (Koukis & Sabatakakis, 2000).

ii. Marshy deposits

Their main extension is located in the area of *Faliro*, between the estuaries of *Kifissos* and *Ilissos Rivers*. They are plastic clays and muds with organic traces and a few meters thickness.

iii. Coastal deposits

They are comprised of sand and unconnected pebbles originated from the wave forces. We can observe them at the area of *Agios Kosmas*, with limited thickness.

iv. Diluvial deposits

Diluvial deposits are formed from the weathering products of the surrounding rocks and more specifically, they contain detailed material (mud and clays) including subsurface fragments. They can be observed mainly close to argillic schists of *Athens* Unit due to their easy weathering. Their thickness begins from a few centimeters but they can reach up to 5 meters, especially in the central area of the basin (*Zografou, Patissia, Dafni, Neos Kosmos* and *Downtown*).

2.2.b.3. Pleistocene Talus cones and Screes (Pt.sc)

They are placed linear along the mountain slopes, consist of **screes** and cohesive **talus cones**. Sometimes they may indicate the existence of fault zones that contributed to their formation (Goumas, 2006; Papadopoulos *et al.*, 2003; 2007).

Their texture depends on the source geological formation, providing the including materials. Their cohesion may vary, but in general, they are semi-cohesive formations, with some layers of increased cohesion (Figs. 2.18). Their thickness can reach up to 30 meters.

Their coverage of Athens basin is quite extensive, covering the foothills of the surrounding mountains. They are located at the foothills of *Aigaleo* and *Poikilo* Mountains (*Korydallos, Nikaia, Haidari, Peristeri* and *Ilion*), *Parnitha* Mountain (*Thrakomakedones, Varibobi* and *Kryoneri*), *Penteli* Mountain (*Drosia, Ekali, Nea Erythraia, Kifisia, Melissia*) and *Hymettus* Mountain (*Argyroupoli, Ilioupoli, Pagkrati, Zografou, Papagou, Holargos, Agia Paraskevi*). Beyond them, they have been deposited at the bottoms of the central hills of Akropolis, Lycabettus and Tourkovounia.

In some locations of the Athens basin (*Thrakomakedones* and *Glyfada*), extended depositions of screes in the form of big talus cones or **fans** can be observed. Their material supply is originating from a punctual/local source. They can be discriminated from the main category due to their large extension that consists of them discrete litho-stratigraphic units.

They have a typical horizontal gradation, with coarse-grained facies at their proximal areas and more detailed at their distal areas. They illustrate vertical alterations of coarse-grained and detailed facies, based on the increased or decreased flow feeding. They are quite cohesive and sometimes they can reach the cohesion of rock formations. Their limits are uncertain since they move and increase during their evolution, depending on their material supply.

Their thickness is varying, following the expected range of a fan, which means thinner to the top, bottom and periphery but thicker to the central-axial area. For example, *Glyfada's fan*, range from 2 meters to more than 50 meters in the center. For the fan of *Thrakomakedones* area, its thickness is expected to be more than 100 meters, but geophysical surveys in the area indicated a total thickness of post-alpine deposits of almost 800 meters (Papadopoulos *et al.,* 2007).

Figures 2.18: Pleistocene Talus cones and Screes (*Pt.sc*). The upper two images are from Parnitha Mountain foothills and the two lower ones from Hymettus Mountain foothills.

2.2.b.4. Neogene Formations (Ng)

All the Neogene formations have been grouped in one package, called the *Neogene deposits*, in the framework of this Ph.D. thesis, (Figure 2.2). Nevertheless, they will be described separately for better geological knowledge of the area.

i. Pliocene Marine deposits (Plm)

Two main outcrops of Pliocene Marine deposits have been detected in Athens basin, one in *Piraeus* peninsula and the other one at *Alimos* area.

In *Piraeus peninsula*, the stratigraphic sequence from the bottom to top includes sandstones marls, brecciоconglomerates, marly limestones with sandstone intercalations and whitish limestones full of fossils (Figs. 2.19).

At *Alimos* area, they are observed as alterations of conglomerates with good gradation, sandstones and marls.

Figures 2.19: Pliocene Marine deposits (*Plm*) in Piraeus peninsula

ii. Pliocene Terrestrial deposits (Pll)

They are undisturbed sediments of sand and clay, with thin (5-20cm) intercalations of lignite (Fig. 2.20). They can be detected with thickness of a few decades meters, dip of bed no more than 5^{o} and reddish to yellowish colors.

They are characterized by their quite smooth surface relief, while their main surface extensions are located at the areas of *Metamorfosi, Filothei Marousi, Halandri and east of Acharnes.*

iii. Upper Miocene Marine Limestones (Msc)

These Marine Limestones are characterized by different facies such as brecciated, sandy, coral or oolithic limestones (Fig. 2.21). They are grey-white or yellowish, with ambiguous dips.

They are detected in small outcrops, mainly on the hilltops, such as the ones of *Kallithea*, *Palaio Faliro* and *Trahones-Alimos* (*Pani* hill).

Figure 2.20: Pliocene Terrestrial deposits (*Pll*) at Halandri area.

Figure 2.21: Upper Miocene Marine Limestones (*Msc*) at Pani hill

Figures 2.22: Upper Miocene Coastal deposits (*Msm*) at Alimos area.

iv. Upper Miocene Coastal deposits (Msm)

This kind of coastal deposits embraces several lithologies in alterations, such as clays and mud with schist rubbles, sandy marls, conglomerates, breccia with sandy texture and cohesive brecciоconglomerate with boulders (Figs. 2.22). Their thickness is estimated to be up to a few decades of meters and their dips of beds range from 20^{o} to 40^{o}.

They are usually overlying on the Upper-Miocene limestones and their main extension is in the southern basin covering a great part of *Kallithea, Nea Smyrni, Agios Dimitrios, Palaio Faliro* and *Alimos*.

v. Upper Miocene Terrestrial and Lacustrine deposits (Msl)

This formation consists of terrestrial and lacustrine facies. The terrestrial facies include reddish clays and conglomerates while the lacustrine ones are comprised of marly limestones, sandy marls and green marls with lignite intercalations.

Generally, they are intensely disturbed formations (reducing to East), with varying dips of beds and even bed bending. On the contrary, in some areas they are located undisturbed.

Their main surface exposures are in the northern areas of Athens basin, such as *Anthoupoli, Aspra Homata, Nea Liosia, Agioi Anargyroi, Neo Herakleion, Pefki, Thrakomakedones* and even northern in *Fyli.* The lacustrine facies can be easily observed at *Kalogreza, Neo Herakleion* and *Agios Vasileios*, while the terrestrial facies dominate in the area between *Hymettus* and *Penteli* Mountains.

Figures 2.23: Upper Miocene Terrestrial and Lacustrine deposits (*Msl*)

2.3. TECTONIC – NEOTECTONIC STRUCTURE

In this section, we will analyze and discuss in detail the tectonic structure that controls the Athens basin area (Fig. 2.2). The information is based mainly on the applied research of Papanikolaou *et al.* (2002) that re-evaluated all the bibliographic data until then, along with new field observations and data. The contribution of geophysical researches (Alexopoulos *et al.,* 2001; Louis *et al.,* 2002b; Papadopoulos *et al.,* 2003; 2007) to the delineation and identification of important fault zones had also been helpful, since many of them remain covered by the post alpine sediments of the basin.

It is important to mention that through the detailed tectonic and neotectonic analysis of the area we can understand their contribution to the damage distribution during a severe earthquake but also predict in a way their response to future seismic events (Fountoulis, 2004; Lozios *et al.,* 2004).

The alpine tectonic regime is controlled mainly by low-angle fault zones, observed between the limits of the alpine geotectonic units of the Athens basin (Papanikolaou *et al.*, 2004b).

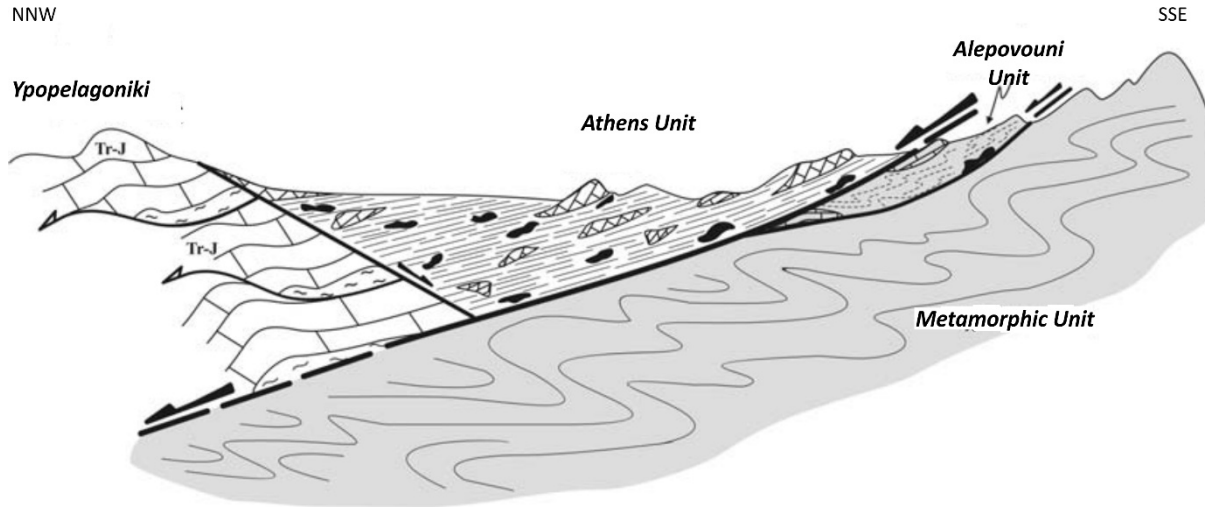

Figure 2.24: Schematic illustration of the tectonic structure of Athens basin (*Papanikolaou et al., 2004b*)

The *Alepovouni* unit is delimited by two low-angle fault zones, one with the relative autochthonous underlying Metamorphic Unit accompanied with a layer of tectonic rock and one with the overlying *Athens* Unit, along which intense schistosity can be observed. Both of them dip to Northwest. The tectonic contact between the *Athens* and *Alepovouni* Units is almost identical with the west margin of *Hymettus* and *Penteli* Mountains. It is considered to be a major tensile detachment zone, where metamorphic formations adjust to unmetamorphic ones, leading to the rise of the metamorphic up to the surface (Katsikatsos, 1977; Katsikatsos *et al.*, 1986; Papanikolaou, 1986; Xypolias *et al.,* 2003). Similar dynamic and

kinematic characteristics are observed at the tectonic contact between *Alepovouni* and Metamorphic Unit.

The *Athens* unit is also overlying the *Ypopelagoniki* Unit with a normal low-angle fault zone. Its dip is the opposite of those between *Athens* Unit and Metamorphics, dipping to Southeast.

2.3.1. Tectonic Analysis

A statistical approach of the faults' direction (Antoniou, 2000) indicated two dominating fault directions, these of 80-110^{o} (WNW-ESE to E-W) and the almost perpendicular ones of 0-50^{o} direction (NNE-SSW to NE-SW). These fault systems are considered to be the major ones, while we can observe secondary fault systems with directions of 60-70^{o} (SE-NW), 320-330^{o} (SW-NE) and 340-360^{o} (SSW-NNE). Based on Mariolakos *et al.* (2001b), similar fault directions are observed on *Parnitha* Mountain but with the secondary systems being more frequent.

More recent fault systems with directions WNW-EWE and NNW-SSE interrupt the continuity of the prementioned major systems. The fault systems of directions NNE-SSW and NE-SW are identified with the directions that the geotectonic units evolve, while the E-W and WNW-ESE frames are connected with shear zones. All these fault systems with different dynamic and kinematic characteristics participated in the neotectonic evolution of the area (Papanikolaou *et al.,* 2004a).

The determination of the kinematic characteristics is quite difficult since there are few locations with geological healthy fault surfaces where the friction lines are maintained. The same problem occurs with the determination of the fault throw, since the urban area of Athens minimizes the chance of a clear undisturbed (by artificial structures) geological observation.

The majority of the fault zones are almost perpendicular, with clockwise and counterclockwise characteristics of horizontal slide. The older fault systems present almost horizontal friction lines with WNW-ESE direction under tectonic micro-breccia. On the other hand, the most recent fault systems are dipping, with friction line dip direction of 70-80^{o} at NNE-SSW direction (Papanikolaou *et al.,* 1988; 2002). Finally, some fault systems were activated between the two prementioned systems, with sidelong friction lines.

Several characteristics, like the quantification of the fault throws along with the post-alpine formations thickness, the sedimentation's rhythm or the palaiogeographic evolution, indicate that there was no fixed vertical movement along the marginal fault zones. This is based on the movement complexity of the fault systems, leading to movements that are rotary along the horizontal axis of the fault blocks (Papanikolaou *et al.,* 1988). The contribution of the horizontal rotary movement, along with the scalar arrangement of the fault frame and the simultaneous rotations along the horizontal axes indicate a tensional shear field (Mariolakos & Papanikolaou, 1987).

The marginal fault zones that determine the boundaries between the alpine and post-alpine formations are based on *en echelon* faults, determining the general fault direction.

2.3.2. Neotectonic Macrostructure

The geometry of the neotectonic structure seems quite complicated due to the complex geotectonic processes from the Upper Miocene until now. The asymmetries of the hydrographic network along with the displacements of morphological axes and the geographical distribution of the flattening areas indicate the tectonic influence on the relief configuration (Mariolakos *et al.,* 2001b; Chatoupis & Fountoulis, 2004).

The western margin of Athens basin along the Mountains *Aigaleo, Poikilo* and *Parnitha* is mapped out by fault zones of NNE-SSW direction (Fig. 2.2), delimiting the post-alpine formations and especially the Pleistocene fans and talus cones. Secondary fault zones contributing to this delineation have directions of NE-SW, NNW-SSE and even E-W.

On the contrary, at the eastern margin and at Mountains *Hymettus* and *Penteli* no marginal faults are observed to delineate the post-alpine sediments. A less complicated situation is observed here, shaping the metamorphic formations of the area based on different tectonic evolution. Fault systems of NNE-SSW and NE-SW directions have been identified in the alpine formations. Intense in-depth erosion and minor morphological discontinuity are detected at the upper fault block of Hymettus, combined with weathered planar surfaces dipping 50-60^{o} to NW and sidelong friction lines (Papanikolaou *et al.,* 2002). At *Penteli* Mountain, the fault zones seem to be constrained only at directions N-S, except for its northern margin which has a WNW-ESE direction.

At the northern area of mountain *Parnitha,* a fault zone of NW-SE direction is detected, forming the post-alpine basin of *Fyli* (Fig. 2.2). Relatively outside of the Athens basin limits, but with quite important impact, there is the Fault zone of *Thriassio*, with WNW-ESE direction. Steep morphological discontinuities and in-depth erosion can be noticed on the upper block. Beyond that, the nearby Neogene formations present large dip values (Mariolakos & Fountoulis, 2000a; 2000b).

The macrostructure frame of Athens basin is based not only on the marginal fault zones but also on large-scale inner structures. One of the most important is the one along the *Kifissos* river flow, with NNE-SSW direction, separating the basin in two sub-areas with individual neotectonic and palaiogeographic evolution (Fig. 2.2). There are several indications supporting this separation, such as the number and geometry of the faults, the type of the existing geological formations, the morphological discontinuities, the hydrographical network asymmetries and even the surface outcrops of the alpine formations at the eastern part but not at the western (fully covered by post-alpine sediments). The fault zones at the eastern part are observed with several directions, including NNE-SSW, NNW-SSE, NW-SE, NE-SW, E-W and S-N.

One more variation between the northern and the southern areas has been identified, based mainly on the observed post alpine sediments facies, the existence or no of fault zones and the alpine bedrock emergence (Papanikolaou *et al.,* 2004b). Practically the limit between these two areas is a fault zone of WNW-ESE direction (Fig. 2.2), extending from the area of *Zefyri* (located between *Poikilo* and *Parnitha* Mountains) to the area of *Agia Paraskevi* (located between the *Hymettus* and *Penteli* Mountains). This great fault zone seems to expand to the west at the northern margin of *Thriassio* plane and to the east at the northern margin of *Mesogeia* plane. The northern part includes the *Penteli* and *Parnitha* Mountains, with WNW-ESE extent and Neogene lacustrine-terrestrial sediments. The southern part contains the *Hymettus* and *Aigaleo* Mountains with NNE-SSW extent along with marine sediments. Moreover, alpine outcrops are observed at the southern part, but not in the northern. It is important to mention that this zone is considered to be a great-scale *en echelon* fault (Mariolakos & Fountoulis, 2000a; 2000b), with its throw differentiating. This great-scale fault zone is directly correlated with the evolution of the hydrographic network (Pavlopoulos *et al.,* 2005).P;

A second order graben between the mountains of *Parnitha* and *Aigaleo* is formed, based on smaller scale faults of NNW-SSE direction (Fig. 2.2), developed in the basin of *Ano Liosia* (Lekkas *et al.,* 2001). Based on borehole data from Lekkas *et al.* (2001), along the southern margin the fault throw is 50 meters, while at the eastern margin it is more than 100 meters, bringing in contact the *Ypopelagoniki* limestones with the Neocene marls.

2.3.3. Faults description

Following the pattern of the applied research by Papanikolaou *et al.* (2002), the Athens basin (Fig. 2.2) can be divided in four sections, based on their neotectonic and palaiogeographic evolution. The division is controlled by the great-scale fault zone of Zefyri-*Agia Paraskevi*, its perpendicular one of *Kifissos* and the marginal faults of the basin (Fig. 2.2).

NW Section

It can be subdivided in two smaller sections, the NE and the SW, based on an elongated NNW-SSE alpine outcrop between *Menidi* and *Ano Liosia*.

In this section, close to the margins, the majority of the fault zones are observed. On the contrary, at the central and northern part of the section no fault zones can be observed at least at the surface, possibly due to their coverage by the post alpine sediments.

At *Thrakomakedones* greater area, many marginal faults (sometime *en* echelon) have been identified, with directions ENE-WSW or E-W, delimiting the alpine and post-alpine formations. There are fault planes dipping 60-70^{o} to SSE, with friction lines and even tectonic breccia. They have caused obvious morphological anomalies, scalar elevation reduction of the flat areas, directly connected to the alteration of stratigraphy of the local fan.

The SW part, known as the small basin of *Ano Liosia*, faced the greatest damage during the earthquake of 1999. It is a second-order neotectonic graben, developed in the tectonic horsts of *Parnitha* and *Aigaleo* Mountains and the NW margin of Athens basin.

The western edge of the great-scale fault zone *Zefyri-Agia Paraskevi* and another one are the northern margin of the *Aigaleo* Mountain, covered by the scree, with directions ENE-WSW and WNW-ESE. Its fault throw has been estimated at least 100 meters at the eastern part, bringing in contact the *Ypopelagoniki* limestones with the Neogene marls.

At the southern margin of *Parnitha* Mountain, there is a fault zone of WNW-ESE direction, dipping to SSW and delimiting the post-alpine sediments from the alpine bedrock. Boreholes indicated that its throw is more than 130 meters. Moreover, the east and west margin of the graben is bounding the alpine bedrock with the scree along a NNW-SSE direction and a dip to WSW. Its 100 meters fault throw was also provided by borehole data.

The west marginal fault zone of *Ano Liosia* small basin controls the alpine formation, buried under a few meters of scree (max 20m) while the east margin controls scree of large thickness. At the southern margin, a small ESE-ENE fault zone has been detected, covered by alluvium deposits.

At the interior of the tectonic horst, there are fault zones forming a smaller scale horst on the Neogene of a WNW-ESE direction at south and NNW-SSE at north. The fault throw is estimated at 20-50 meters. The NE and W margins of this horst is created by NNW-SSE and WNW-ESE faults.

SW Section

The most important fault zones are located on the NE area of the *Aigaleo* Mountain's horst. Its NE margin is controlled by a 3-4 *en echelon* faults of NNW-SSE direction and 100 meters length each, dipping 70-80^{o}, joined together with smaller faults of ENE-WSW faults. It delimits the *Ypopelagoniki* limestones with the Neogene deposits that are observed very close to the fault dipping up to 60-70^{o} dropping to 10-20^{o} farther. It seems that this zone is extended to NNW.

A major marginal fault zone of *Aigaleo* mass, with NE-SW direction, delimits the alpine formations of *Ypopelagoniki* and the Neogene-Quaternary sediments. Southernmost, it alters to a complex system of NNE-SSW or N-S or even NW-SE faults, with more alpine outcrops. They set the limits between the alpine bedrock and the scree and Neogene formations or between the Neogene deposits and the scree. One other important system of E-W faults, with horizontal movement component, has been identified at this margin, crossing the *Aigaleo* mass, creating perpendicular valleys and E-W direction structures. Although fault planes exist, the friction lines have not been preserved.

At the interior of this section, smaller faults of NNE-SSW, E-W or ESE-WNW directions have been detected, delimiting the scree, alluvium or Neogene deposits. Beyond that, at *Nea*

Filadelfia the only residual fault planes of *Kifissos* fault zone can be observed, delimiting the *Athens* Unit with the Neogene or alluvium deposits.

Close to *Piraeus,* a NW-SE a system of faults bounds the Neogene formations. The NW edge dips to SW, separating the alpine formations from the Neogene, while the SE edge dips to NE separating the Neogene from the alluvium deposits.

NE Section

In this section of Athens basin, no major faults have been detected except for the marginal ones, probably due to their coverage by post alpine sediments. The north edge of *Kifissos* fault system (4-5 *en echelon* faults of NE-SW direction) crosses the Neogene sediments.

The east extension of the *Zefyri-Agia Paraskevi* fault zone, with WNW-ESE direction, crosses the Neogene deposits. At the eastern area, there is the large marginal fault zone of Penteli, with N-S direction, covered by talus cone and bounding the metamorphic formations. Moreover, at its NE edge, there is also a part of the north marginal fault of *Penteli*, with NWN-ESE direction, delimiting the metamorphic rocks from the talus cones and alluvium deposits.

SE Section

There are several faults and fault zones at the *Hymettus* margin, with NNE-SSW and NW-SE directions. A major fault zone of NNE-SSW separates the marbles from the schists or scree. There is an intense erosion in-depth, with residual fault planes dipping 50-60^{o} to NW. Northernmost, two more faults of similar direction have been identified, the one of which delimits the dolomites and the scree. Southernmost, a system of parallel NNE-SSW faults forms the margin.

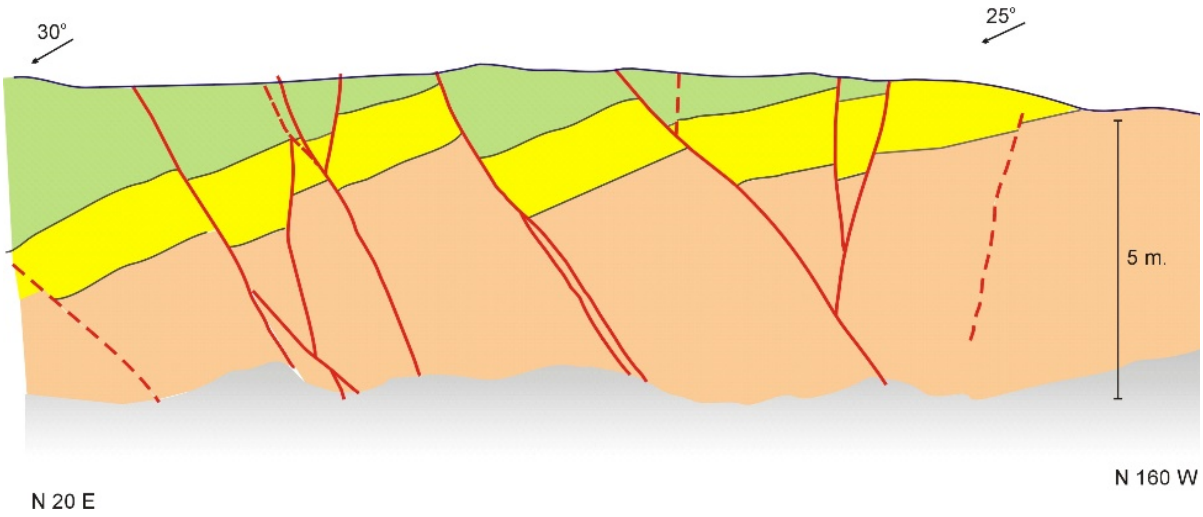

Figure 2.25: A system of synthetic and antithetic normal faults bending the Neogene formations (*Papanikolaou et al., 2002*)

At the interior of this section, there are more faults and faults zones crossing the allochthonous units. Their main direction is NW-SE along with secondary ones like NNE-SSW, NE-SW or even N-S.

Near the coastal zone, a few more faults have been found, with NNE-SSW direction, delimiting small alpine outcrops and scree or with NW-SE direction, located in the Neogene sediments, almost parallel to the coastline. Sometimes they are characterized from a system of synthetic and antithetic normal faults (Fig.2.25) of a general ENE-WSW direction, bending the Neogene formations.

2.3.4. Faults' classification

Papanikolaou *et al.* (2002) and Ganas *et al.* (2004) estimated the prospective potency of the delineated fault zones, based on their geometric, kinematic and dynamic characteristics.

The fault zones with E-W and WNW-ESE directions are considered to be active and practically they delineate post alpine structures on the western area of the basin, where the earthquake of 1999 took place. Some of them are the fault zones of *Perama, Fyli* and *Thriassio*.

Their extensions to east with the same geometry, at the inner part of the basin, up to the fault zone of Kifissos River, are characterized as possible active and they contribute a lot to the neotectonic evolution of the area. Some examples of them are the fault zone of *Zefyri-Agia Paraskevi*, with WNW-ESE direction and the one of *Haidari*, crossing the *Aigaleo* Mountain. There are also the marginal faults of *Poikilo* and *Parnitha* mountains, with NNE-SSW direction. As possible active, Papanikolaou *et al.* (2002) have characterized the fault zone of *Kifissos* River. Finally, the north marginal fault Zone of *Penteli* Mountain, with WNW-ESE direction, has also characterized as possible active.

The eastern part of the basin has limited fault zones that have been characterized by Papanikolaou *et al.* (2002) as active. The same authors with some additions by Foumelis (2009) described in detail the **most important active fault zones** of the greater area of Athens basin (Fig. 2.2).

***Perama* Fault Zone:** Located at the SW part of the basin, it delimits the *Aigaleo* Mountain from the *East Saronikos Gulf* basin, with direction WNW-ESE. Its extension to west can be observed at *Salamina* Island and it is characterized as active due to its tectonic and morphotectonic characteristics (Mariolakos *et al.,* 2001a; Theocharis, 2001).

***Thriassio* Fault Zone:** It delimits the *Parnitha's* horst from the *Thriassio* basin, with a direction WNW-ESE. It is practically composed of smaller *en echelon* faults of E-W direction. Their planes can be observed dipping 50-70^{o} to SSW but few friction lines have been preserved. It is considered as an active zone, with similar orientation with underwater active zones. An observed sharp morphological discontinuity is delimitated due to the vertical fault throw, along with Quaternary talus cones and fans that have been placed.

***SE Parnitha* Fault Zone:** Northern of the *Thriassio* fault zone and at the inner part of the *Parnitha* Mountain, fault zones of WNW-ESE and NW-SE direction exist, bounding smaller post-alpine grabens and affecting the morphotectonic characteristics of the region. This results in lowering the *Parnitha* in relation to the *Thriassio* basin. The *Fyli* Fault Zone is included, with NW-SE direction dipping 60-70^{o} to the SW. A few fault planes with friction lines can be identified.

***Dionysos* Fault Zone:** It delimits the metamorphic formation of *Penteli* from the northern post-alpine basins and its direction is WNW-ESE. Here also steep morphological relief is detected along with in depth erosion on the arising fault block of *Penteli*. A lot of fault planes are spotted with friction lines and dips 60-80^{o} to the NNE, revealing the counterclockwise component.

***Haidari* Fault Zone:** Located between the *Aigaleo* and *Poikilo* Mountains, with E-W direction, causing a horizontal displacement to the hydrographical watershed of NNE-SSW direction and to geological contacts of both alpine and post-alpine. The friction lines have been vanished due to the erosion. Its kinematic characteristics can be related to the great-scale fault zone of *Zefyri-Agia Paraskevi* with the addition of a horizontal component movement.

***Zefyri-Agia Paraskevi* Fault Zone:** It is covered by post-alpine sediments and has a general WNW-ESE direction. The differentiation of the lithological facies of the post-alpine sediments and the impact on the hydrographical network revealed its existence. It seems that it is the extension of the northern active margin of *Thriassio* basin. It is quite impressive that during the Alkyonides earthquake (1981), the majority of the severe damage was observed along its trace.

***East Parnitha* Fault Zone:** It is delimiting the *Parnitha* relief from the Athens basin, with direction NE-SW, considered as a marginal fault zone with a few planes spotted. The friction lines have been preserved revealing the counterclockwise horizontal movement component. It is correlated to the enormous talus cone of *Thrakomakedones* and sharp morphological discontinuities.

***East Poikilo* Fault Zone:** It runs along the eastern margin of the *Poikilo* Mountain with NE-SW direction, separating the *Ypopelagoniki* alpine formations from the post-alpine sediments. Fault planes with dipping 60-70^{o} to SE can be found but with lack of friction lines.

***West Poikilo* Fault Zone:** It is located between the *Poikilo* Mountain and an axis of hills of *Thriassio* basin, with NE-SW direction. It could be the extension of the *East Parnitha Fault Zone*. The morphological discontinuities along with the different elevation of the Neogene deposits revealed its existence. Westernmost the east margin of *Thriassio* basin is located (Drakatos *et al.,* 2002; Papadopoulos *et al.,* 2003; Pyrli, 2001), sub-parallel to its direction.

***Kifissos* Fault Zone:** As we have already mentioned this zone is totally covered by post-alpine sediments, except for an area at *Nea Filadelfia*, where parts of fault planes have been identified, adjoining the *Athens* Unit with Neogene sediments. Northernmost it is composed of *en echelon* faults of NE-SW direction, with great dips to NW.

***Ekali* Fault Zone:** Another covered fault zone, with S-N direction, dipping to west and delineating the west margin of *Penteli* Mountain. Only parts of the fault planes can be found.

***Afidnes* Fault Zone:** It is an E-W normal fault, which downthrows to the north and bounds the Afidnes Quaternary basin. Some geomorphological characteristics indicate its recent activity (Papanikolaou *et al.,* 2008; Papanikolaou & Papanikolaou, 2007).

It seems that generally the active fault zones of Athens basin have a WNW-ESE direction, revealing that the area is subject to a NE-SW tension. This can be related to the observation of Papanikolaou & Lozios (1990) that the active E-W faults of East Korinthiakos are connected to the active WNW-ESE and NW-SE fault zones of South Evoikos, through a transgressive zone of altering the direction, which seems to be Athens basin.

2.3.5. Paleogeographic evolution

Regarding the geomorphology and paleogeographical evolution of Athens basin, many researchers published their aspects about Athens basin during the last years (Gournellos & Maroukian, 1990; Papanikolaou *et al.,* 2004a; Pavlopoulos, 1992; Pavlopoulos *et al.*, 2005). The area of *Piraeus* and *Faliro* has been thoroughly investigated with the contribution of borehole data or/and geophysical techniques (Apostolopoulos *et al.,* 2014; Goiran *et al.*, 2011; Triantaphyllou *et al.*, 2016; Vandarakis, 2013; Vandarakis *et al.,* 2016), due to the rapid alterations of the paleogeographical relief. There are implications by these authors that *Piraeus* was an island 7-5 thousand years ago. Skylodimoy (2002) studied the geomorphology of the SW coastal zone.

The short description that will be presented in the following sections is mainly based on Papanikolaou *et al.* (2002) and Papanikolaou *et al.* (2004b).

Upper Miocene

The relief of that period (10-6 million years ago) at the interior of the basin was more intense, with continuous alterations of mountain ranges and valleys. An axis of hills was located at the center of the basin the residuals of which formed the hills of *Tourkovounia*, *Lycabettus* and *Filopappou*. At the region, the masses corresponding to *Aigaleo, Poikilo, Parnitha, Penteli* and *Hymettus* Mountains had started forming (Fig.2.26a).

The coastline was northernmost, close to *Filopappou* hill. This means that the areas of *Piraeus, Moschato, Glyfada* and *Nea Smyrni* were covered by sea and marine sediments were gathered. The area of *Agios Dimitrios* was probably a river debouchment, deposing marine-terrestrial sediments.

Northernmost, the two greater areas of *Halandri, Vrilissia, Marousi, Pefki, Metamorfosi*, *Ano Liosia, Acharnes, Thrakomakedones* and *Dafni, Haidari, Peristeri, Agioi Anargyroi, Petroupoli*, *Kamatero* were temporal lakes. Their extension was differentiating based on the torrents supply.

Fault zones of NNE-SSW direction were upthrowing the masses of the region, especially the west ones. The *Zefyri-Agia Paraskevi* fault zone seems that had a great role that period, by upthrowing the northern part of the basin and blocking the water exit to the sea, contributing to the lake formation.

Upper Pliocene

During this period (4-2 million years ago), the status is similar to the one of Upper Miocene. The surrounding masses of the mountains exist, along with the hills at the interior of the basin and the temporal lakes, but to smaller extent (Fig.2.26b). At the central area among *Petroupoli, Nikaia, Holargos* and *Ilioupoli* the sedimentation has stopped.

The active fault zones of Upper Miocene had stopped upthrowing the mountains. Their weathering procedures have started, creating small talus cones. The *Zefyri-Agia Paraskevi* fault zone is still active.

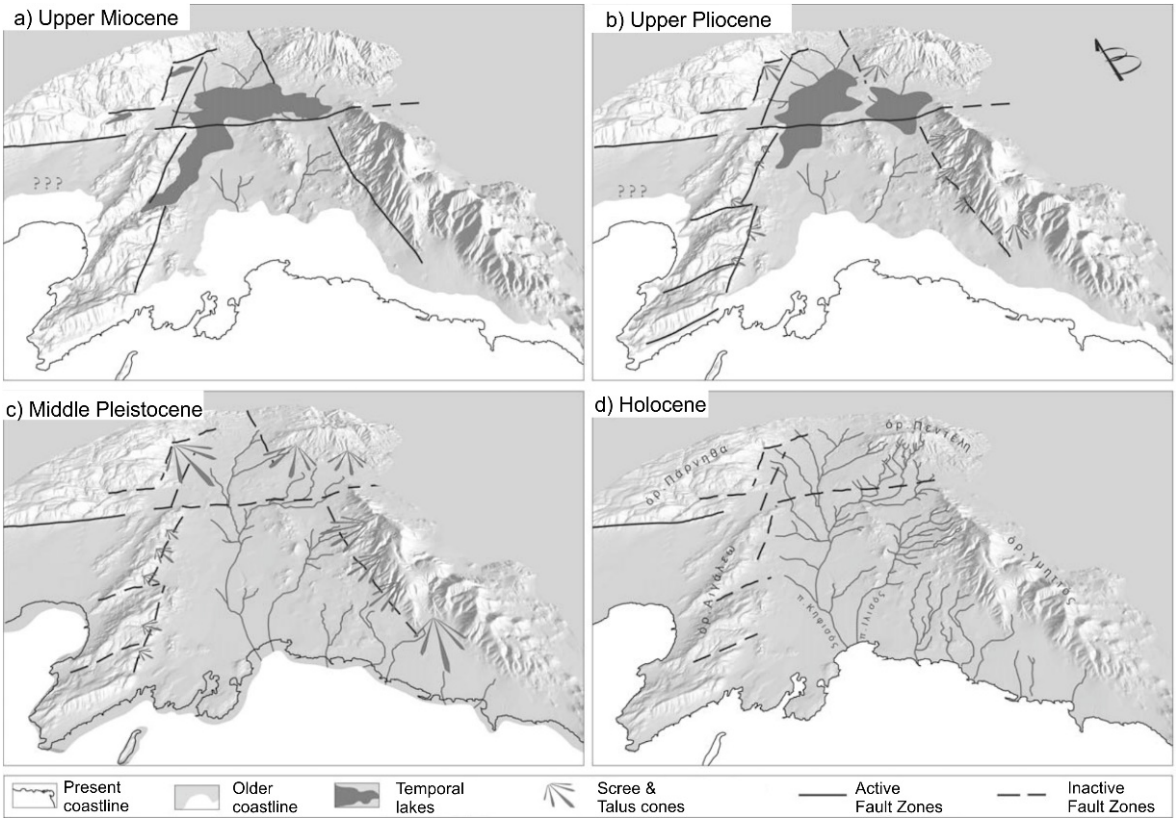

Figures 2.26: Paleogeographic representations of Athens basin (*Papanikolaou et al., 2004a*)

Middle Pleistocene

The status of this period (800-500 thousands years ago) is quite similar to the present. The relief of the interior basin was also smoother and neither the central block of hills existed nor the periodical lakes, since the water flew to the sea, through the *Kifissos* River (Fig.2.26c). The coastline was very close to the present one.

The surrounding mountains were still weathering leading to talus cones and scree creation, with those of *Thrakomakedones* and *Glyfada* being quite large in extension. The tectonic activity was mainly spotted at the western part of the basin.

Upper Pleistocene

During this period, the climate changed rapidly (glacial and interglacial periods), affecting the Athens basin evolution through the sea level fluctuation. During the last glacial period, the reduction of the sea level to -120m, led to land advance and the islands of *Aegina* and *Salamina* were attached to the inland and the Athens basin (Mariolakos & Theocharis, 2001).

The relief of the hills and mountains was similar to the present and the *Kifissos* River was flowing southernmost, in the new land of *Saronikos* Gulf.

Holocene

The form of Athens basin (Fig.2.26d) during the last 3-5 thousands years remain almost the same, where the relief has been reduced a little. The smooth interior of the basin, covered by Neogene and alluvium deposits, is interrupted by the remaining hills. The hydrographical network is asymmetrical.

The tectonic activity has been restrained out of the basin, mainly at *Parnitha* Mountain and *Thriassio* plane. The fault zones of *Aigaleo* and *Poikilo* Mountains along with the one of *Kifissos* are still considered as important ones.

According to Goiran *et al.* (2011), during the period 8,700-7,500 years ago, the area of *Faliro* was a swallow sea-lagoon, Piraeus was connected to the mainland by a narrow isthmus, and there was a sandy beach ridge in the southern part of the lagoon (Fig. 2.27a). During the period 6,800-5,400 years ago, *Piraeus* was an island in the center of a shallow marine bay (Fig. 2.27b), while during the period 4,800-3,500 years ago, a wide lagoon was created with beach barriers separating it from the sea (Fig. 2.27c). The lagoon was filled with fluvial sediments and finally, around 2,500 years ago, only a freshwater marsh was left at the north of *Piraeus*, connecting it to the mainland (Fig. 2.27d). Moreover, the marshlands north of the beach ridges were filled with coarse materials (Goiran *et al.*, 2011)

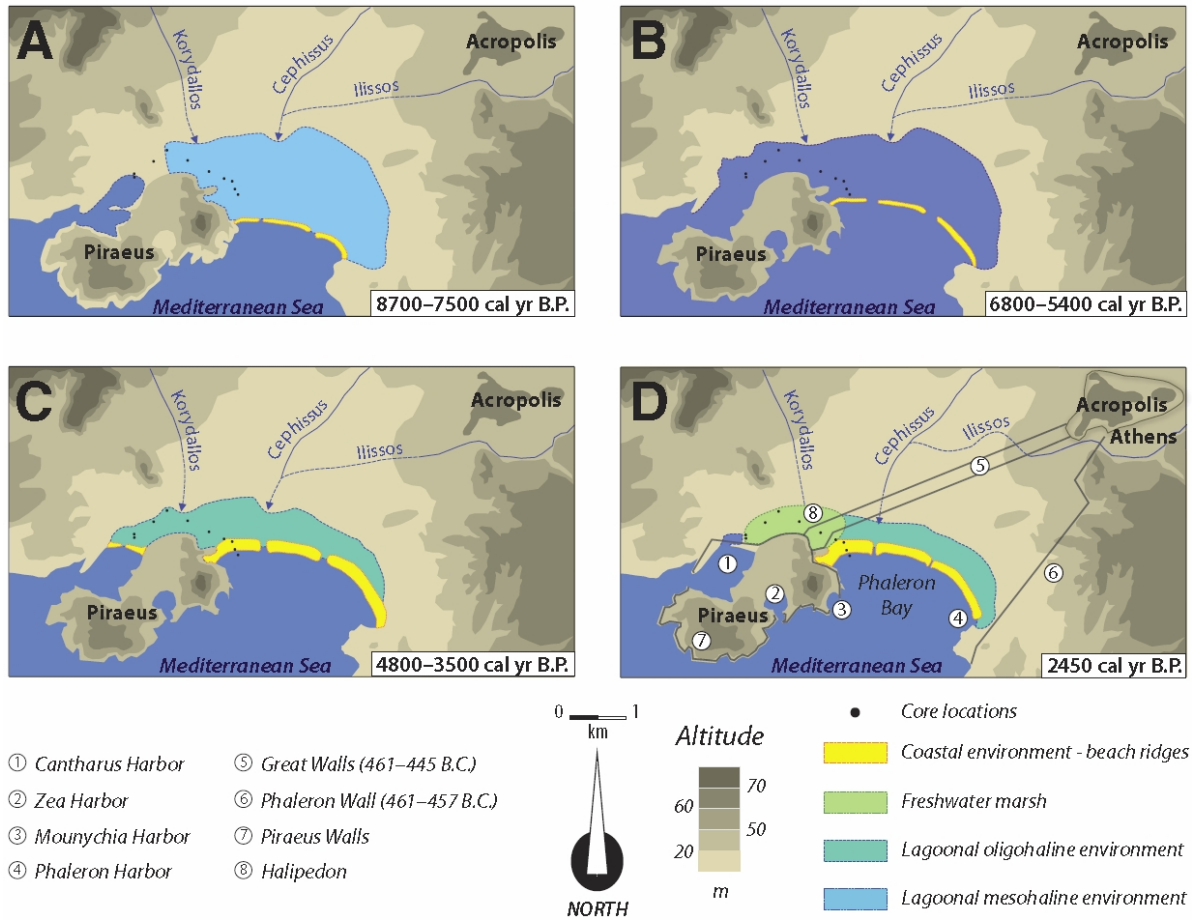

Figures 2.27: Paleogeographical evolution of Piraeus during Holocene by Goiran *et al*. (2011).

2.4. HYDROGEOLOGICAL CONDITIONS

The detailed mapping of the natural flow of the drainage network of Athens basin is quite difficult due to the human interferences. Several parts of the drainage system have been both covered and enclosed in artificially flow paths or redirected in order to build. Nevertheless, Alexouli-Livaditi *et al.* (2007), Bathrellos *et al.* (2016) and Papanikolaou *et al.* (2002) describe in detail the hydrographical network of Athens basin and its streams. Furthermore, Koumantakis *et al.* (1997), created a database of all the registered hydro-boreholes located in Athens basin (Fig. 2.28).

In Athens basin two main river systems can be identified, *Kifissos* and *Ilissos*, along with three other minor ones (Fig. 2.28).

Kifissos River is classified based on Horton, as a 5th class system, draining the 85% of the basin and having a hydrological basin of almost 370km^2. It has an axial flow of NNE-SSW direction, with no tectonic influence and it has a dendritic shape. It flows meandric in the Neogene deposits until 5 kilometers before the debouchment, where intense in-depth erosion is dominating. It has a main branch, called *Podoniftis*, flowing from *Penteli* Mountain, with direction to SSW and then WSW.

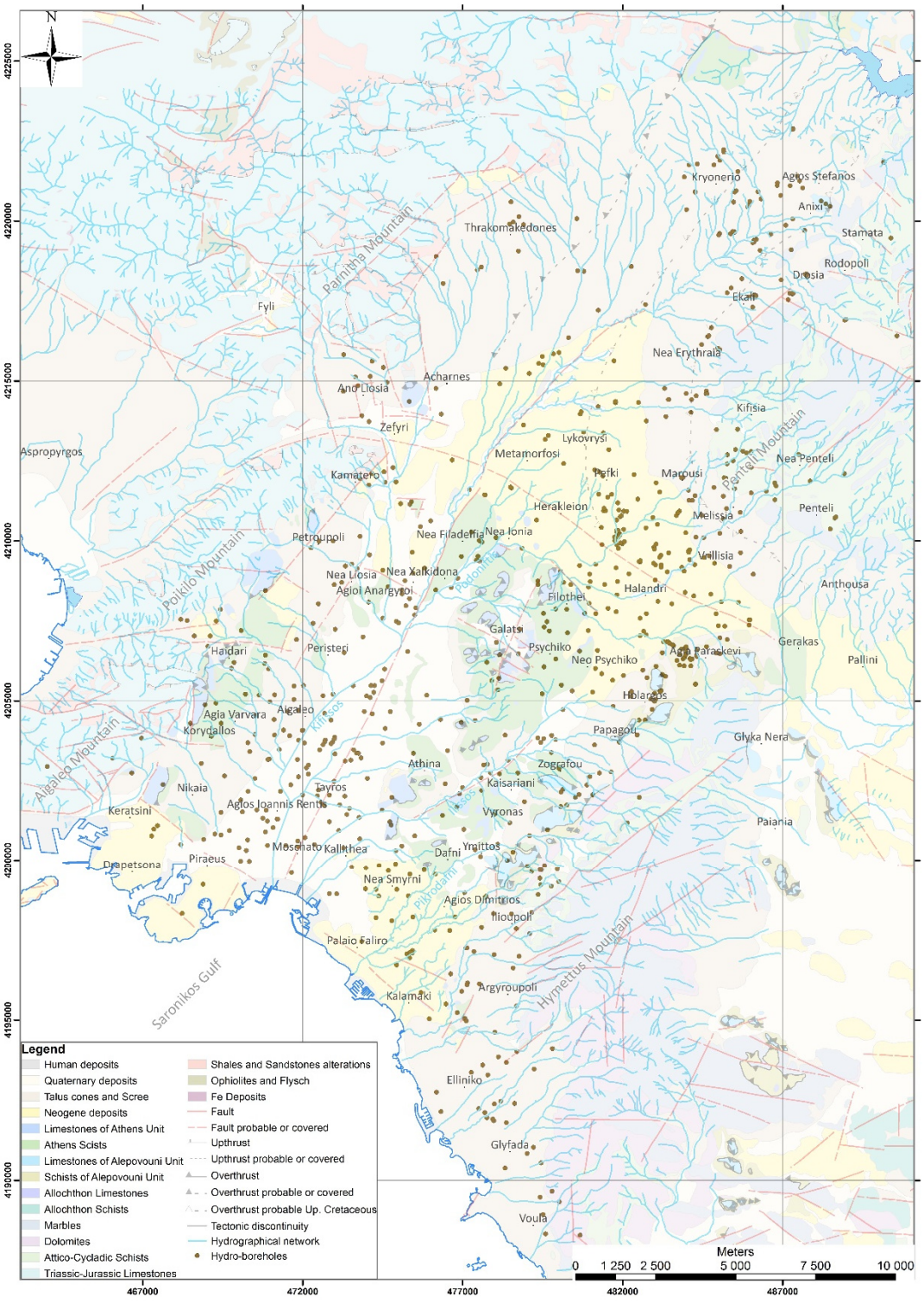

Figure 2.28: The hydrographical network of the greater area of Athens basin, along with hydro-boreholes (brown dots) by Koumantakis *et al*. (1997).

Ilissos River is classified based on Horton, as a 4th class system, flowing among the *Hymettus* Mountain, the *Tourkovounia, Lycabettus* and *Acropolis* hills, discharging to the area of *Faliro*, creating extensive marsh deposit areas. It has an elongated dendritic shape and great asymmetry, since the majority of its branches come from east (*Hymettus* Mountain).

Three more minor river systems discharge the SW area of *Hymettus* Mountain. The biggest one is called *Pikrodafni*, flows from *Kareas* through the areas of *Ilioupoli, Dafni, Nea Smyrni* and *Kalamaki*. It is a 4th class system based on Horton, with elongated dendritic shape and characteristics of asymmetry to west. All of these systems present great in-depth erosion.

Finally, many authors (Bathrellos *et al.,* 2016; Dounas *et al.,* 1976; Kounis, 1981; 1998; Kounis & Kounis, 2010; Marinos *et al.*, 2006; 2008; 2009; Stamatis *et al.,* 1994) have discussed several issues on hydrogeological conditions of the geological formations of Athens and their transmissibility, especially for the formation of *Athens Schists* (SchA).

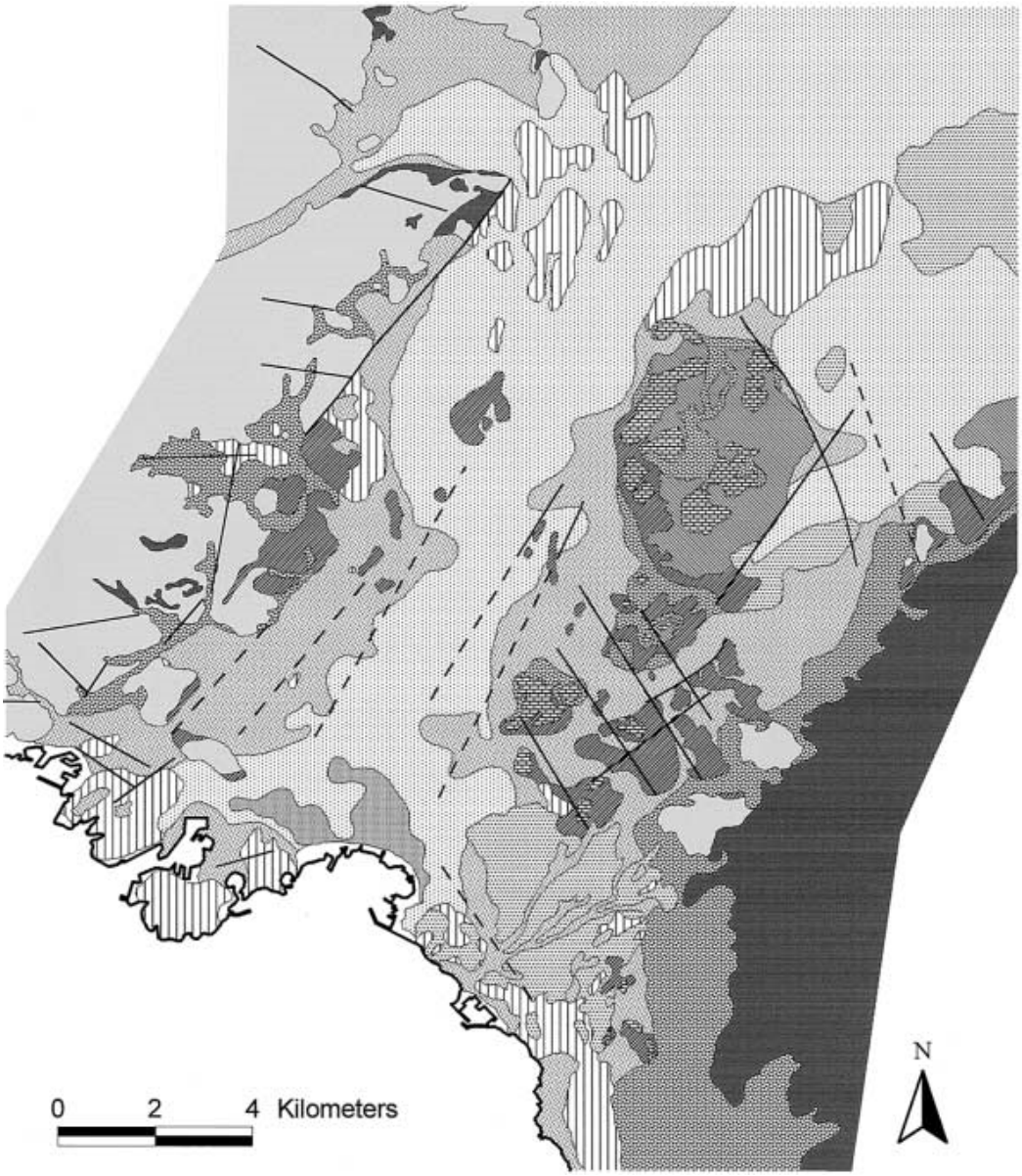

Figure 2.29: Geotechnical map of Athens basin (*Koukis & Sabatakakis, 1999*).

1: Coarse-grained recent deposits, 2: Fine-grained recent deposits, 3: Loose coastal deposits, 4: Scree, 5: Red loams & Conglomerates, 6: Marly formations, 7: Crest limestones, 8: Schist-Sandstone-Marly series, 9: Athens Schist

2.5. GEOTECHNICAL CHARACTERISTICS

Many authors (Antoniou, 2003; Antoniou *et al.*, 2008; Koukis & Sabatakakis, 2000; Karfakis & Loupasakis, 2006; Kynigalaki *et al.,* 2010; Marinos *et al*., 2004; Papanikolaou *et al*., 2002; Sabatakakis, 1991; Stamatis *et al.,* 1994) studied the geotechnical characteristics of the Athens basin. The characteristics of the formations and especially the density play significant role in the gravity measurements response.

One the most complete researches for the geotechnical regime of Athens basin was presented by Sabatakakis (1991), who constructed a detailed geotechnical map of Athens basin, in scale 1:25.000 (Fig. 2.29), based on the uniformity in lithological character and structural arrangement. There was also the criterion of the geological age, categorizing the older formations based on their lithogenesis and the recent sediments based on the grain size. Therefore, eleven geotechnical units came up. According to Sabatakakis (1991) these are: 1) mixed recent deposits with domination of fine-grained materials, 2) mixed recent deposits with domination of coarse-grained materials, 3) sand silts and soft clays, 4) scree, 5) loams and conglomerates, 6) marly formations, 7) crest formations, 8) schist-sandstone-marls, 9) Athens schists mélange, 10) limestones, 11) marbles and schists.

After a few years, Koukis & Sabatakakis (2000) enriched the data and published updated geotechnical maps and data. Beyond that, Antoniou (2003) and Antoniou *et al.* (2008) presented a GIS platform that manages the obtained geotechnical data of Athens.

2.6. SEISMICITY AND SEISMIC HAZARD

Although many earthquakes had occurred during the last 100 years in the greater area of Athens basin, no severe one was reported. Because of that, the area was considered to be of low seismicity (Ganas *et al.,* 2000; Papadimitriou *et al*., 2002; Voulgaris *et al*., 2000). In fact, based on Ambraseys (1996), only the nearby areas (50-100 km) were considered dangerous for a disastrous event.

On 7th September 1999, a 5.9R (M_s) earthquake occurred about 20 kilometers from the center of Athens city (Fig. 2.2), causing enormous damage to almost 42,847 buildings, 66.6% of all buildings, with 28 of them collapsing (Pomonis, 2002). Furthermore, around 80,000 families became temporarily homeless, more than 2,000 injuries were recorded along with 143 dead people (Pomonis, 2002). A few papers regarding the seismic vulnerability assessment were published (Bouckovalas & Kouretzis, 2001; Eleftheriadou *et al.,* 2012; Baltzopoulou *et al.,* 2012; Pomonis, 2002), discussing in detail the economic consequences of this earthquake. Beyond that, some authors (Deligiannakis *et al.,* 2016; Farangitakis *et al.,* 2016) produced seismic hazard maps for Athens basin, mostly through the application of GIS and taking into consideration several parameters.

In spite of the moderate magnitude of 5.9R, the intensity reached the value of IX (Ganas *et al.,* 2000; Papadimitriou *et al*., 2000; 2002; Rondoyanni *et al.,* 2000) and the peak ground acceleration reached values of 0.3 and 0.5g (Ganas *et al.,* 2000).

Due to the significance of this earthquake and its extensive damage, many authors studied thoroughly all kind of seismic parameters and factors of the main event and the aftershock sequence, with several techniques, producing several papers (Baumont *et al*., 2002; 2004; Delibasis *et al.,* 2000; Ganas *et al.,* 2000; Louvari & Kyratzi, 2001; Papadimitriou *et al.,* 2002; Papadopoulos *et al.,* 2000a; 2000b; Papanastassiou *et al*., 2000; Papazachos *et al.,* 2001; Rondoyanni *et al.,* 2000; Sargeant *et al.,* 2002; Stavrakakis *et al*., 2002; Tselentis & Zahradnik, 2000a; 2000b; Voulgaris *et al*., 2000; 2001).

The majority of the scientific publications indicate that the activated fault was normal, with WNW-ESE direction (around 105^{o}), 10-20 km long, dipping to SSW with 55-60^{o} and with counter-clockwise component. The focal depth solutions vary between 8 and 17 kilometers, depending on the applied technique. Nevertheless, there was no surface trace of the fault (Papadimitriou *et al.,* 2000) based on field observations (Mariolakos *et al.,* 2000), the absence of shallow (<2km) aftershocks (Pyrli, 2001; Voulgaris *et al*., 2000) or based on Differential Interferometry data (Foumelis, 2009; Kontoes *et al.,* 2000; Parcharidis & Foumelis, 2005).

Beyond the seismic parameters, the identification of the fault zone and its characteristics, the caused damage and its distribution was deeply investigated by many researchers (Andrianakis *et al.,* 1999; Lekkas, 2001; Rondoyanni *et al.,* 2000; Tzitziras *et al.,* 2000). The largest intensity values are located at the western and northwestern areas of Athens basin (*Acharnes, Ano Liosia, Kifisia, Tatoi, Kamatero, Ilion, Peristeri* and *Aigaleo*). The intensity values range from VII to IX based on the modified Mercalli-Sieberg scale, shaping isoseismal contours that are elongated in a NE-SW direction (Fig. 2.30), similar to the *Kifissos* Fault zone, which seems to have played an important role. Lekkas (2001) also presented an isoseismal contour map, based on EMS-1998, with maximum intensity value of X (Fig. 2.31).

Additionally to the prementioned papers, many other were published regarding the site characterization and the ground conditions (Assimaki 2004; Assimaki *et al.,* 2005a; 2005b; 2005c; Bouckovalas *et al.,* 2002; Bouckovalas & Kouretzis, 2001; Elenas; 2003; Hutchings *et al.,* 2007; Ioannidou *et al.,* 2001; Marinos *et al.,* 2001; Roumelioti *et al*., 2003a; 2003b; 2004). The horizontal ground acceleration was determined reinforced by almost 40% in stiff soil, compared to the alpine soft rock (Bouckovalas & Kouretzis, 2001). Bouckovalas *et al.* (2002) estimated the maximum horizontal ground acceleration up to 0.49-0.57g for soil formations and up to 0.35-0.42 for rock formations.

It is obvious (Figs. 2.30 & 2.31) that the most severe damage occurred on recent geological formations, like alluvium deposits and loose scree or close to streams. Minor damage was observed in areas covered by scree. Moreover, the damage is restricted to the western area of the *Kifissos* Fault zone.

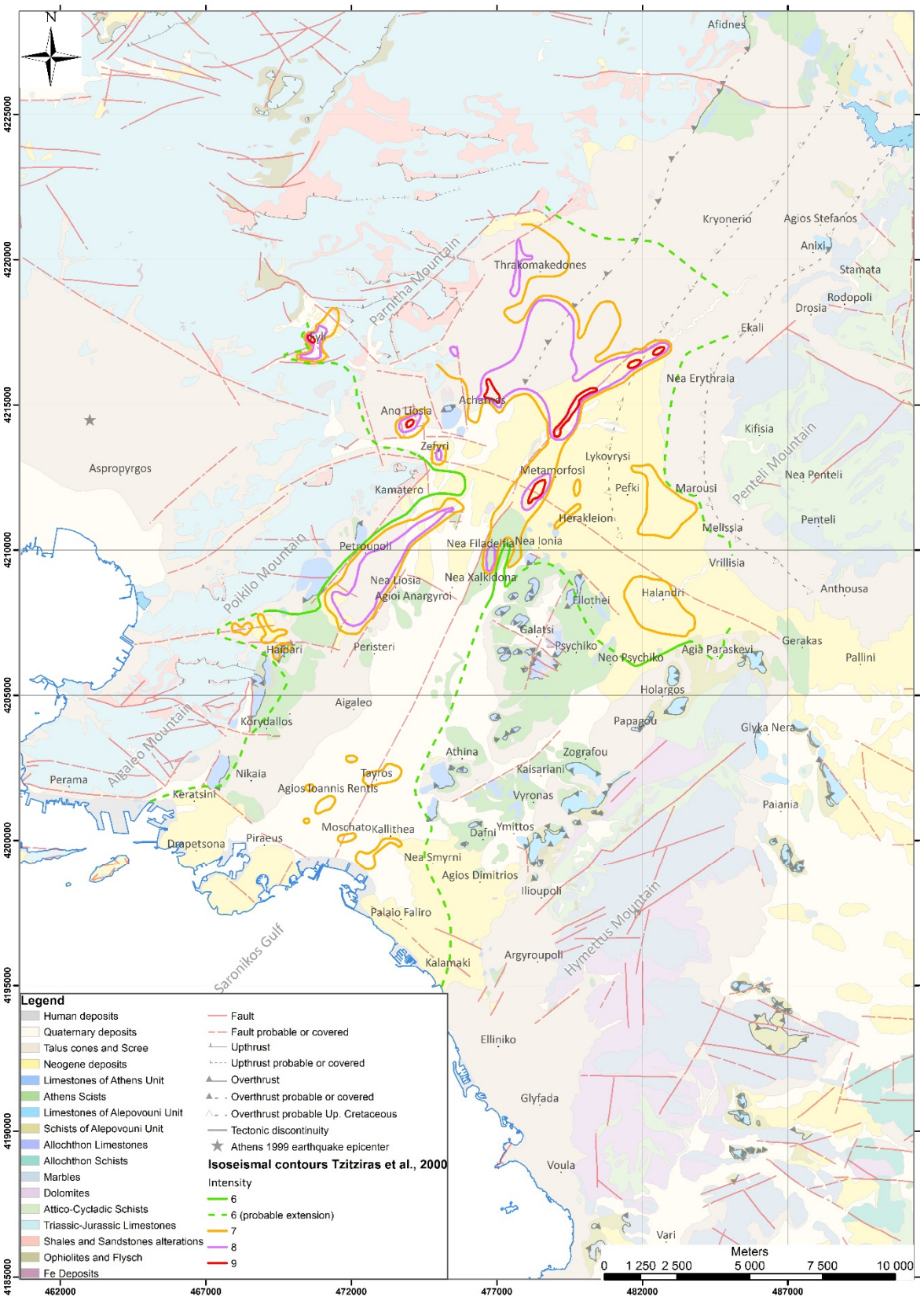

Figure 2.30: Isoseismal contours by Tzitziras *et al*. (2000).

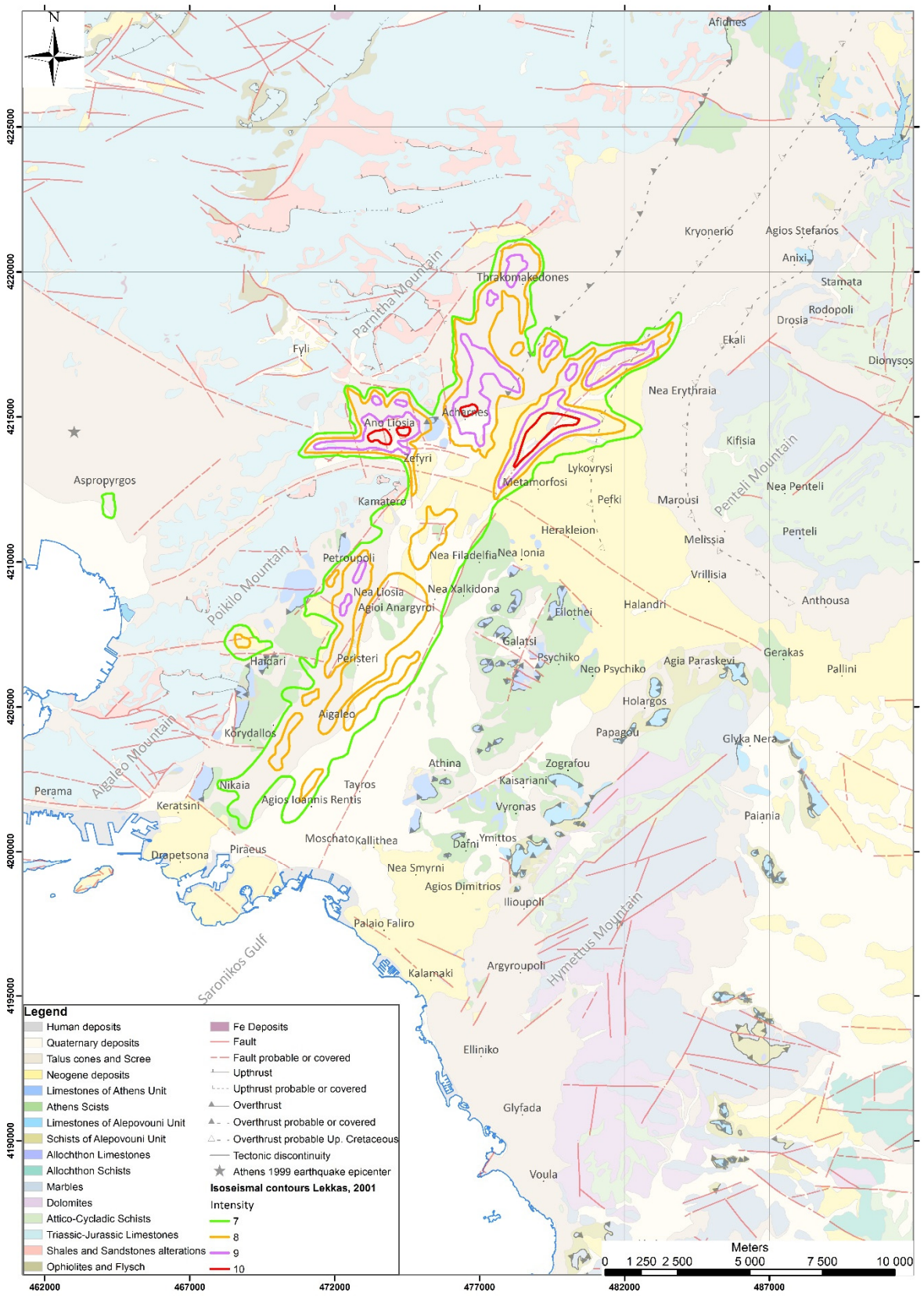

Figure 2.31: Isoseismal contours by Lekkas (2001) based on EMS-1998

3. GRAVITY METHOD THEORY

Gravity method is based on the fact that we have variations of the subsurface lithology. This means that measuring their physical properties will result in corresponding variations. In this case, the density of the formations influences their gravitational attraction. By investigating the spatial relative differences in gravity acceleration, we gather information about the lithological changes, both vertical and lateral.

3.1. PHYSICAL PRINCIPLES

The basic physical principles of gravity are the key of understanding the way that gravity method works. Therefore, we will refer to some fundamental elements of gravity method.

3.1.a. Universal Law of Gravitation

The force of gravitation is expressed by Newton's universal law. Consider two small masses m_1 and m_2, separated by a distance r. Newton's law states that each of these masses attracts the other by a specific force **F**, which is proportional to the product of the two masses and inversely proportional to the square of the distance r, separating the centers of the two masses:

$$\boldsymbol{F} = G\frac{m_1 m_2}{r^2}$$

where G is the universal gravitational constant, which is equal to 6.672×10^{-11} $N \cdot m^2/kg^2$ (in SI units). The force ***F*** is attractive.

3.1.b. Acceleration of Gravity

In geophysical application of the gravity method, we are more concerned about the accelerations than with forces. Newton's second law of motion states that the change of momentum of a small mass is proportional to the applied force ***F*** and it is expressed via the equation:

$$\boldsymbol{F} = ma$$

where a defines the acceleration given to the mass m.

By combining the previous two equations together, we get the gravitational acceleration a of the mass m_2, due to the attraction of the mass m_1, ending up with the equation:

$$a = G\frac{m_1}{r^2}$$

where G is the universal gravitational constant and r the distance between the two small masses. If m_1 is the mass of the Earth M, then a becomes the acceleration of gravity g. So, given that R is the radius of the Earth, the equation will be:

$$g = G\frac{M}{R^2}$$

The value of *g* at the Earth's surface is about 980 cm/s^2 or 9.8 m/s^2 (in SI units). The unit cm/s^2 is called a *Gal*, in honor of Galileo, who measured first the acceleration of gravity at Pisa. The changes on the acceleration of gravity due to the geological structures are quite small and for their measurements milli*Gal (mGal)* are used.

The common gravimeters used in geological-geophysical researches have a sensitivity of about 0.01 *mGal (10^{-3} Gal)*. Modern gravimeters or micro-gravimeters can measure with accuracy up to 5 *μGal (10^{-6} Gal)*.

3.1.c. Gravitational Potential

3.1.c.1. General

Gravitational fields are considered conservative. This means that moving a mass in that kind of field from point A to B, is independent of the path and depends only on the start and end points. In the case that the mass after a certain path returns to its starting point, the consumed energy is considered zero. In other words, the sum of kinetic (motion) and potential (position) energy is constant in a closed system.

The gravitational potential, *U*, is the potential energy of the unit mass in such a gravitational field. The force that gives rise to such conservative fields can be derived from a scalar potential function, known as Newtonian potential or three-dimensional potential. So, the acceleration is a three-dimensional vector. That in Cartesian coordinates (*x, y, z*) is expressed through the gradient as:

$$\nabla U(x,y,z) = -\frac{\boldsymbol{F}(x,y,z)}{m_2} = -g\ (x,y,z)$$

In spherical coordinates, the previous equations take the form:

$$\nabla U(r,\theta,\varphi) = -\frac{\boldsymbol{F}(r,\theta,\varphi)}{m_2} = -g\ (r,\theta,\varphi)$$

Or alternatively, we can use the equation:

$$\nabla U(r,\theta,\varphi) = \int_{\infty}^{r} (\nabla U)dr = -\int_{\infty}^{r} g dr$$

that states the work done a mass from very long distance/infinity to a specific point at a distance *r* away from the mass that produces the gravitational field.

The gravitational attraction of a mass body comes from the combination of countless individual discrete particles. In order to calculate the gravitational acceleration of that object at a certain point, we have to use a vector sum of the accelerations of all the individual particles, where each one has a different direction. Assuming *m* to be the mass of the particle at a distance *r*, the following equation is used:

$$g = -G\frac{m_1}{r_1^2} - G\frac{m_2}{r_2^2} - G\frac{m_3}{r_3^2} - \cdots$$

The expression for the calculation of the gravitational potential, *U*, is given by:

$$U = -G\frac{m_1}{r_1^2} - G\frac{m_2}{r_2^2} - G\frac{m_3}{r_3^2} - \cdots$$

Therefore, the mass is represented as a continuous mass distribution and not as individual discrete elements. Nevertheless, we can divide it into smaller discrete elements and given that the density is known, the element's mass can be calculated along with its contribution to the potential. For a certain body point having coordinates *(x, y, z*), we assume a density *ρ (x, y, z)* and a distance *r (x, y, z)*, in order to calculate the gravitational potential of the body by the equation:

$$U = -G \iiint_{x\,y\,z} \frac{\rho\,(x,y,z)}{r\,(x,y,z)}\,dxdydz$$

The values outside a sphere, at a distance *r* from its center, can be considered the same as its entire mass, *M*, concentrated at its center:

$$U = -G\frac{M}{r}$$

$$g = -G\frac{M}{r^2}$$

3.1.c.2. Derivatives

Sometimes in gravity processing the derivatives of the potential are applied, by differentiating the potential, in order to isolate anomalies. Derivatives magnify the near-surface elements by increasing the power of the linear dimension in the denominator. This is because gravity effect varies inversely to the distance in square. Practically, the gravimeters measure the vertical gravity.

The first derivative of g is given by the equation:

$$\partial g/_{\partial z} = -\,\partial^2 U/_{\partial z} = -U_{zz} = -G\rho \iiint_{x\,y\,z} \left(\frac{1}{r^3} - \frac{3z^2}{r^5}\right) dxdydz$$

The second derivative of g is given by the equation:

$$\partial^2 g/_{\partial z^2} = -\,\partial^3 U/_{\partial z^3} = -U_{zzz} = -3G\rho \iiint_{x\,y\,z} \left(\frac{5z^3}{r^7} - \frac{3z}{r^5}\right) dxdydz$$

We can also take the derivatives along the *x* and *y* axes, producing the horizontal gradient of gravity, usually determined from gravity profiles or maps, as the rate of change of g, with horizontal displacement. Regarding for example the *x*-axis, we take:

$$U_{xz} = -\,\partial g/_{\partial x} = -3G\rho \iiint_{x\,y\,z} \left(\frac{xz}{r^5}\right) dxdydz$$

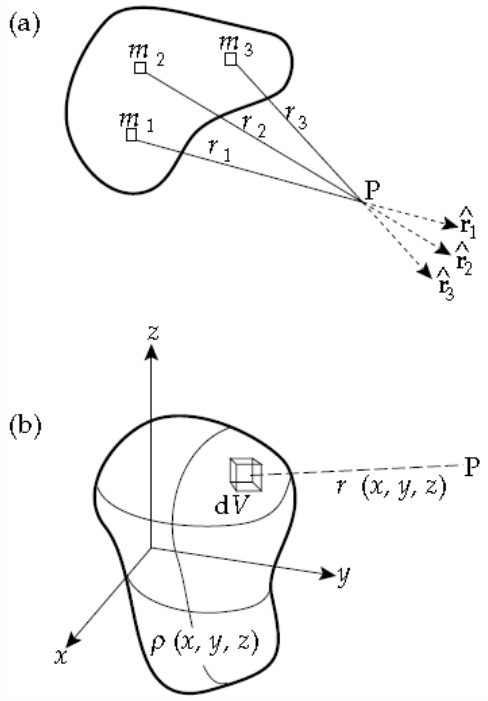

Figure 3.1: Each particle of a small body is gravitational attracted to different directions (*Lowrie, 2007*).

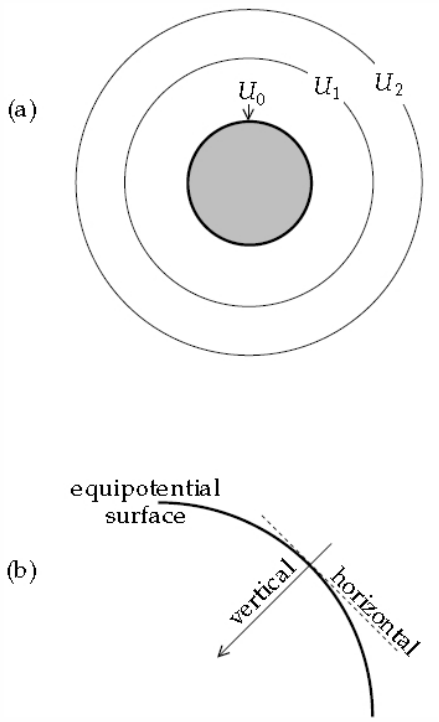

Figure 3.2: Equipotential surfaces (above for a spherical mass) (*Lowrie, 2007*).

3.1.c.3. Equipotential Surface

Given a small mass with spherical shape, the gravitational potential varies only with the distance *r* from its center and nothing else. Consequently, at a certain distance r_1, the potential will be U_1, at distance r_2 will be U_2 etc. Therefore, at this distance there will be surface, called equipotential surface since it is characterized by the constant potential. The total of equipotential surfaces practically form a set of concentric spheres, with the one for distance *r=0,* corresponding to the outer surface of the spherical mass. Since we are dealing with equipotential surfaces, by moving from one point to another on such a surface, produces no change in the potential or no work done. If no work is done, then the force and acceleration of the gravitational field must be perpendicular to the equipotential surface, in vertical direction.

3.1.d. Earth's Gravity Field

3.1.d.1. Figure of the Earth

Nowadays, it is known that the real shape of the Earth is not a perfect sphere, since its true surface is uneven and irregular. Therefore, the gravitational attraction of the Earth is not constant, over its surface. The figure of the Earth is shaped by the equipotential surface of gravity that coincides with the mean sea level. So, the real shape of the Earth is a spheroid or oblate ellipsoid, since it flattens at the poles and bulges at the equator. In 1980, the

International Association of Geodesy, adopted the *Geodetic Reference System (GRS80)*, based on the most detailed data of that time. The equatorial radius is R_e=6,378.16 kilometers and the polar one is R_p=6,356.755 kilometers, providing a resulting polar flattening factor equal to 1/298.25. Because of that, larger gravitational attraction is observed at the poles. More specifically, the gravity is 5.3 Gal larger, almost 0.5% of the average value of g, equal to 980 Gal.

Because of the flattening of the Earth, the distribution of its mass is not simply dependent on radius. The flattening of the polar is the deforming cause of the centrifugal acceleration, which is maximum at equator and minimum at polar.

The Earth is rotating around its axis, producing a centrifugal force at the points of its surface. The potential of gravity of Earth or geopotential is practically the sum of the gravitational and centrifugal potentials.

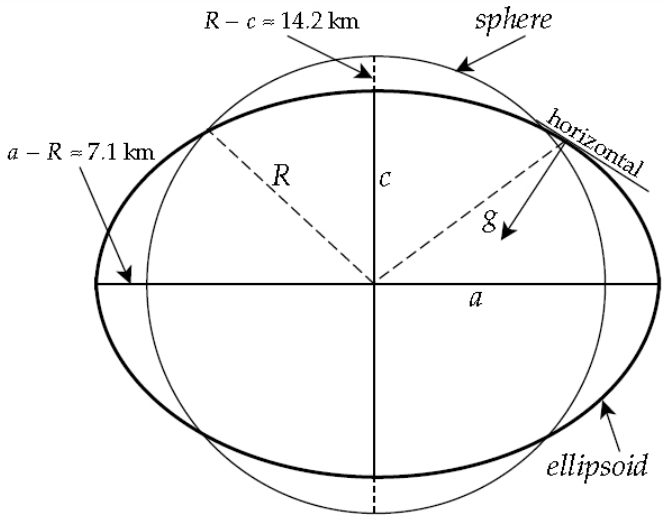

Figure 3.3: Earth's real shape, compared to a sphere (*Lowrie, 2007*).

3.1.d.2. Reference Spheroid and Normal Gravity

The reference ellipsoid is an oblate ellipsoid that approximates the mean sea level surface (geoid), while the land above it has been removed. The *International Reference Ellipsoid* has been adopted as the standardized reference figure of the Earth.

The theoretical value of gravity on this rotating ellipsoid called Earth can be computed by differentiating the gravity potential. Standard formulas have been developed and recognized by unions of geodesists, even since 1930, relating the theoretical (*normal*) gravity *g* to the latitude φ of a gravity station, giving the theoretical gravity over the reference ellipsoid. They allow calculation of normal gravity at any latitude with an accuracy of 0.1 mGal. The normal gravity formula is important, because it provides the theoretical variation of normal gravity (g_n) with latitude on the surface of the reference ellipsoid. The most recent formula, established in 1984, based on the World Geodetic System (WGS84) is the following:

$$g_n = 978{,}032.67714 \frac{1 + 0.00193185138639 sin^2\theta}{(1 - 0.00669437999013 sin^2\theta)^{0.5}}\ mGal$$

where ϑ is the geodetic latitude.

3.1.d.3. The Geoid

The *International Reference Ellipsoid* is approximate to the equipotential surface of gravity, but practically is only a mathematical approach. The physical equipotential surface of gravity is known as *geoid* and it reflects the true distribution of the underlying mass. It is the equipotential surface of the actual gravitational field.

The geoid and the ellipsoid would be identical if the Earth was filled with rocks up to the sea level, in order to have the same density. But in the reality, we have continents and seawater. The differences with the ellipsoid are small, usually 50-100 meters, with some exceptions.

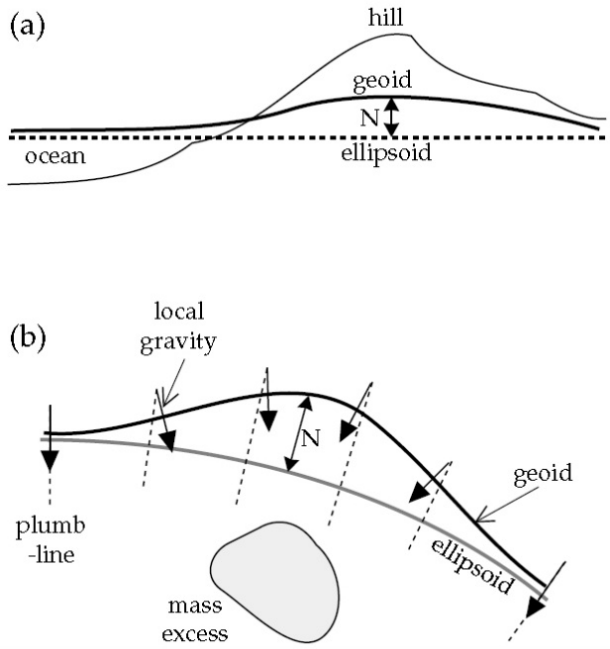

Figure 3.4: (a) Difference between geoid and ellipsoid and (b) A mass below ellipsoid elevates the geoid above it (N is a geoid undulation) (*Lowrie, 2007*).

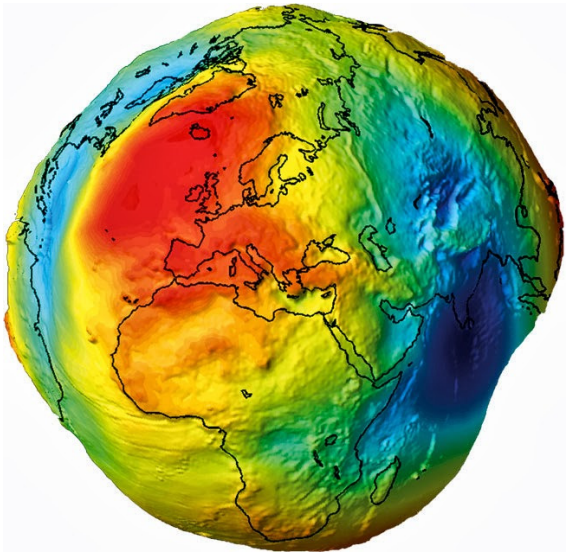

Figure 3.5 : Geoid (http://deepearthscience.blogspot.gr)

The simplified figure of the Earth practically allows only the variation in depth and not lateral. Therefore, over the continents, the geoid is affected by the rock mass above the sea level, appearing with an upward attraction. On the contrary, above seawater (oceans) we observe a downward attraction due to the low density of the water (Fig. 3.4). These local displacements of the geoid, above or below the ellipsoid, are called geoid undulations (Fig.3.4). Due to the uneven topography and the heterogeneous mass distribution of the Earth, the geoid is a bumpy equipotential surface (Fig.3.5).

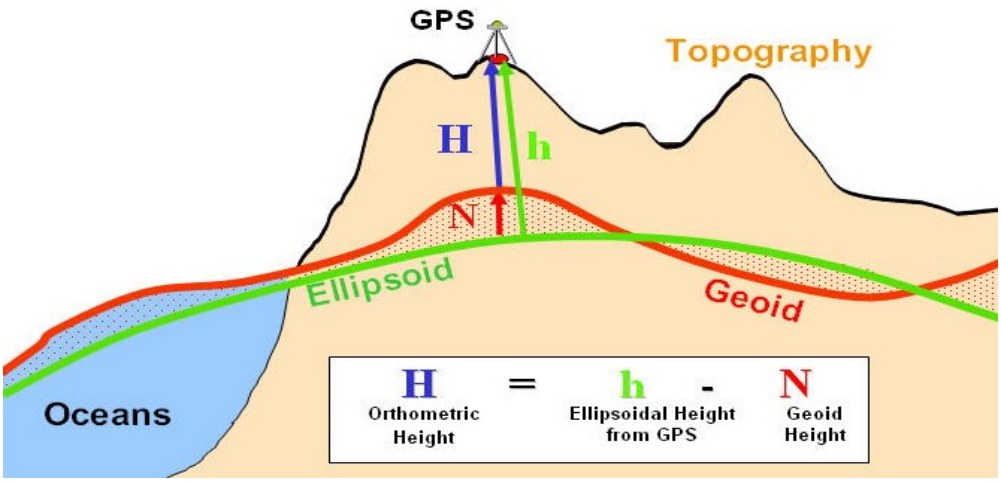

Figure 3.6: The orthometric height, H, measured from the geoid, the ellipsoidal, h, from the ellipsoid and N is the geoid height.

GPS measurements usually provide the ellipsoidal height, *h*, above reference ellipsoid (Fig.3.6). However, the orthometric height, *H*, above the mean sea level or in other words the geoid (Fig.3.6), is the one used in gravity investigation. Taking into consideration that geoid models evolve continuously, we will take different orthometric height if we change the geoid model used. Orthometric height may be common in gravity investigation, but the height above the ellipsoid, *h*, is used for the latitude and free-air corrections. To convert the ellipsoidal height, *h*, to an orthometric one, *H*, the height *N* of the geoid is required (Fig.3.6).

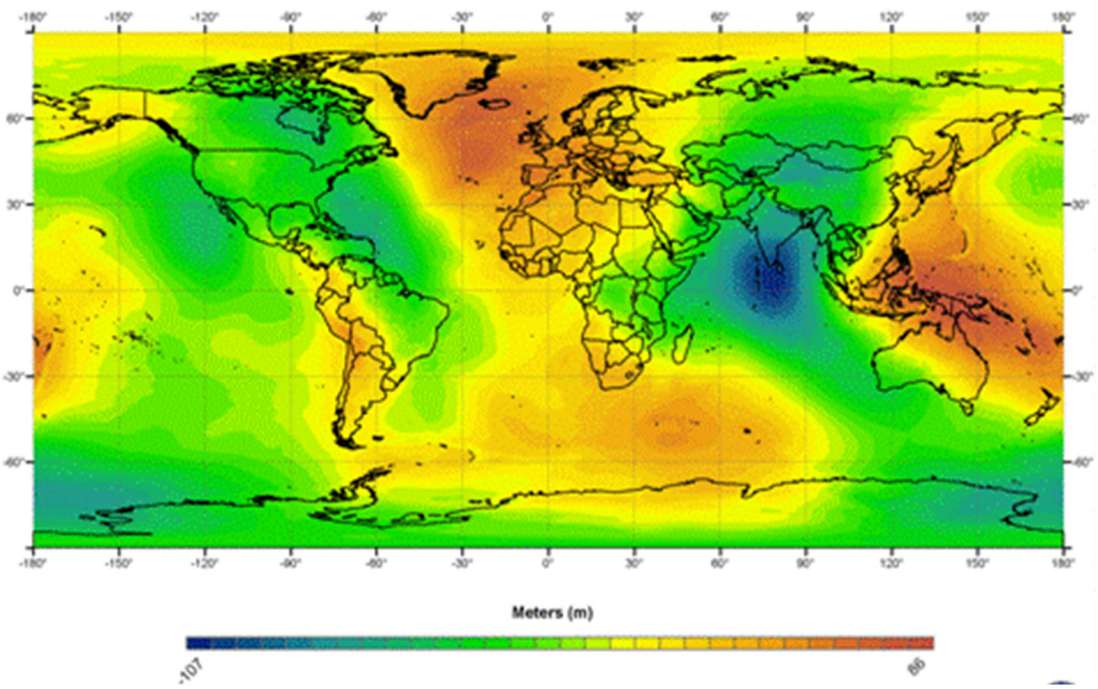

Figure 3.7: The EGM08

(*http://earth-info.nga.mil/GandG/wgs84/gravitymod/egm2008/egm08_wgs84.html*)

The current domain Earth's Gravity Model is *EGM08* and the previous one, was the *EGM96*. The *EGM08* is provided as a grid of free-air gravity or a set of harmonic coefficients. The long-wavelength part contains GRACE satellite data up to order n=150, equal to λ=270 km.

3.1.e. Gravity Units

The SI units of g (vertical acceleration due to gravity) is m/s^2, but traditionally the geophysicists use the unit 1 cm/s^2=1 Gal (*named after Galileo*). For the gravity exploration surveys and contouring the most practical unit is **mGal = 10^{-3}Gal** = 10^{-5} m/s^2 which is more often used for micro-gravity surveys the μGal=10^{-6} Gal. Moreover, the 'gravity unit' has been used in the past, where 1 g.u. = 0.1mGal = 10^{-6} m/s^2.

Modern gravity meters can obtain up to 1 μGal (10^{-9} Gal) reading accuracy. The usual accuracy desired in common land field measurements is of 0.01 mGal while in marine measurements increases up to 1 mGal. In oil and gas exploration, accuracy of less than 0.2 mGal is important for the investigation of the local anomalies, while in basins the sediments can produce variations of a few hundreds mGal.

3.2. GRAVITY MEASUREMENTS

Gravity exploration began during the first period of the twentieth century, while the first oil-gas discovery was based on a successful torsion-balance research, in coastal Texas (LaFehr, 1980).

The main contribution of gravity in geology is to locate and adumbrate source anomalies that can be related to geological formations of interest. Gravity measurements are used at a wide range of scales and for several purposes.

On a global scale, gravity measurements contribute to the investigation of the details of the gravity field. On exploration scale, gravity method is applied to oil, gas and mineral explorations. Salt domes can be identified, leading to hydrocarbon geological traps. Also, regional gravity networks adumbrate the large-scale geometry of the tectonic plates. Of course, gravity measurements have contributed a lot in the adumbration of geometry of basins all over the world. Beyond that, we can find shallow applications of gravity, such as in archaeology, detection of sub-surface cavities, investigation of weapons.

Data collection instruments and methods have been evolved all the time. Each type of instruments has its own characteristics and capabilities. Land surveys evolve in accuracy and airborne or satellite data contribute to regional investigation. Depending on the target, each time the appropriate instrument and type of survey should be chosen.

3.2.a. Gravity meters

Gravity meters are separated in two categories, the absolute and the relative ones. An absolute instrument measures the local value of gravity at every gravity station. They can

measure from zero to the total terrestrial gravity *g*. They are more expensive, much bigger and time-consuming for a precise measurement.

A relative instrument measures the difference in gravity between gravity stations and usually is tied up to a base where the absolute value of gravity is known. These kinds of instruments are usually required for exploration purposes, since they are considered more accurate and easy to operate.

3.2.a.1. Absolute Measurements

An absolute gravity meter practically determines the gravitational acceleration based on measurements of displacement or time. The classical method of absolute measuring is with a pendulum, based on the measurement of the period of a freely swinging pendulum. The compound pendulum, described by Henry Kater in 1818 is the most popular and precise absolute instrument. The accuracy of the pendulum measurements depend on precise measurement of the pendulum's dimensions and dynamic interaction with its support. To obtain a sensitivity of about 1 mGal, it is required to determine the period with an accuracy of about 0.5 μs, which nowadays is quite easy by using a precise atomic clock.

Figure 3.8: The modern FG5-X Absolute Gravimeter, by Micro-g LaCoste

During 1906, at Potsdam, Germany, a package of precise measurements of the acceleration were carried out, resulting in a value of 981274 ± 3 mGal that has been adopted as the international standard for measurements all over the world. The Potsdam's standard base was then tied up to many national networks, with local bases founded at airports. Therefore, the network of absolute gravity bases evolved worldwide. In 1971, a new standard for the international gravity measurements was adopted, known as the 1971 International Gravity Standardization Net (IGSN71 by Morelli *et al.,* 1974). There was a difference of almost 15 mGal between the IGSN71 and the Potsdam standard. For that reason, combining old and recent data sets, require caution.

3.2.a.2. Relative Measurements

The most common gravity measurements are carried out by relative gravimeters, which are more precise and easy to handle. The basic aspect is that each new gravity measurement is compared with a standard base value.

i. Pendulums

Pendulums were used during the 18th and 19th century in the first researches for declaring the dependency of gravity by the position. Their accuracy is limited to almost 0.25 mGal.

For a pendulum of given length *L* that freely swing with a period *T,* only the measurement of the length and time is required for the determination of gravity *g.* a point mass is suspended by the string.

ii. Torsion Balance

Two equal masses *m* are separated horizontally and vertically by rigid bars, supported by a torsion fiber with an attached mirror, measuring the rotation due to the deflection of a light beam. The deflection of the torsion balance beam comes from the vertical and horizontal changes of the gravity field. Practically they are gravity gradiometer meters used a lot in oil exploration even since 1918. They are more sensitive to near-sensor changes of mass, having an advantage in sensitivity of the topography effects.

iii. Spring Gravimeters

Spring gravimeters measure the change in the equilibrium position of a certain mass as a result of gravity change between gravity stations. The first spring gravity meters were based on the application of Hooke's law and they were known as '*stable type*. They were extremely sensitive to external effects, such as pressure and temperature.

The displacement of the mass is proportional to the change of gravity. Therefore, the small mass *m* suspended from a spring of length l_0 causes it to stretch to a new length *l*. The length change of the spring is proportional to the restoring force of the spring and for that, the value of gravity *g* is, when *k* is the elastic constant of the spring:

$$F = mg = -k(l - l_0)$$

As we mentioned already, the gravimeter has to be calibrated in a known location. If it measures at another location, the spring's extension will logically change and by that, the gravity change can be computed.

The stable type gravimeters were replaced by the *unstable* or *astatized* types, at which an additional force acts in the same direction of gravity, opposing the restoring force of the spring. That is called a state of unstable equilibrium, which provides them with greater sensitivity.

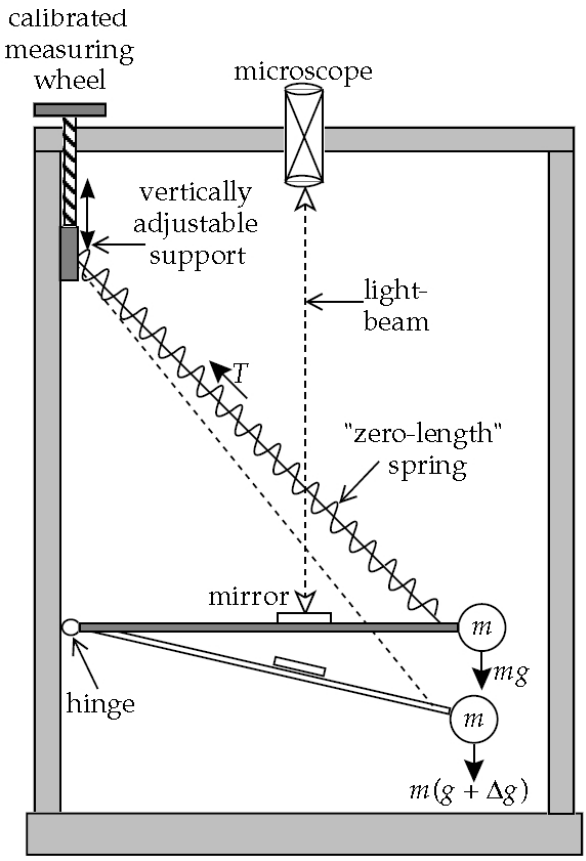

Figure 3.9: Operation principles of unstable type gravimeter

Figure 3.10: Scintrex Autograv CG-5 gravimeter

Characteristic examples of unstable gravity meters are those with *zero-length spring* (Fig. 3.9), such as those that were first launched by *LaCoste & Romberg*. They are considered as the most classic and popular relative instruments, with accuracy up to 20 μGal. These gravity meters have a helical type spring, with such a small length that could be considered as zero. This kind of springs stretches against its restoring force with a gravity increase and the extension increases due to the built-in pre-tension. Other popular *zero-length spring* gravimeters are the *Worden* and the *Scintrex* (Fig. 3.10).

How does an unstable gravimeter work (Fig. 3.9)? A mass *m* is supported by a horizontal rod with an attached mirror. The rod's position can be observed by a light-beam reflected in a microscope. When the gravity changes, the zero-length spring changes length and the rod also moves, which is reflected in the microscope. An adjusting screw on the top of the meter changes the position of the upper attachment of the spring, altering its tension and restoring the rod to the horizontal position. This screw is calibrated in units of gravity change, such as mGal. These gravimeters can reach a sensitivity of about 0.01 mGal in a few minutes. In most modern instruments, the mechanism described above, is enclosed in an isolated box with standard temperature. Moreover, electronic data acquisition has been introduced, with digital signal enhancement along with embedded GPS for location and timing.

iii. Vibrating-string Gravimeters

An elastic string suspends vertically with a mass at the end of it and vibrates with frequency proportional to the square root of the local gravity field. Vibrating-string gravimeters are smaller but with large dynamic range. Considering that they are less sensitive to platform movements, they are mostly used in marine measurements.

iv. Superconducting Gravimeters

Superconducting gravimeters are stationery instruments, not portable for field measurements, but with very high precision. They are usually used to record very small temporal gravity variation, such as the ones caused by the earth tides. A magnetic field is produced by an electric current in a helium ring. A conducting sphere is suspended in that field. Any small variations of gravity will cause a change of position in the equilibrium.

3.2.b. Types of Gravity Field Surveys

Since almost 1930, due to the development of the new gravimeters types, such as the torsion balance and spring gravimeters, the data collection became easier and more accurate. Nowadays this revolution leaded to instrument configurations not only for the common land gravity measurements but also for marine, airborne or even satellite ones. For almost each type of exploration survey, there is a solution, an appropriate gravimeter and some standard procedures that need to be followed.

3.2.b.1. Land Surveys

Since almost 1930, when gravimeter evolved, more than 10 million stations have been acquired worldwide (Nabighian *et al.*, 2005). Regarding the land surveys, even impervious places have been investigated, with gravity measurements in jungles and marshes, on glaciers and on extremely rugged topography.

Depending on the purpose of the gravity survey and the expected depth and size of the target, the appropriate station spacing will be defined. For land surveys, it varies from 20 km to 5 meters or even to less than 1 meter (for micro-gravity). For oil exploration, one station per 2-4 km^2 is satisfactory, due to the larger geological structures. In mineral exploration, the station spacing could be 15-50 meters. In microgravity surveys such as searching for cavities or for archaeological purposes, the spacing will be close to 1 meter.

The required accuracy of the gravity measurements can be achieved if we obtain a precision of 5-10 cm in elevation determination and 30 m in latitude determination.

Borehole gravity measurements, requires the instrument to be measured along a borehole. It contributes to the determination of the subsurface formations density.

3.2.b.2. Marine Surveys

The first oceanographic researching gravity measurements were carried out since the 1950s. The earlier LaCoste & Romberg gravity meters swung freely in gimbals, but as the

instruments were mounted on a stabilized platform, unwanted motion effects were produced. There are two ways for marine gravity measurements.

The first method, known as static, a gravimeter is lowered to the seabed, usually to depths up to 200 m. It is preferred for inland waters and coastal areas. The instrument is enclosed in a pressure-housing box and supported on a squat tripod with disk feet and the whole system weighs up to 300 kg. The meter is automatically leveled, readings are taken remotely and the connection to the ship is obtained through a cable. The meter must be raised up to the surface in order to move to the next station.

A second method is the dynamic one, with gravity meters on shipboard, mounted on an elaborate gyro-stabilized platform. Due to the velocity that might have an instrument, the centrifugal force acting on it is different. Therefore, a correction for the velocity must be applied, called *Eötvös* correction. Wave motion causes vertical accelerations that are less than 10.000 mGal in good weather conditions. Since their periods are shorter than 60 s, this poses a substantial filter design problem for that kind of systems.

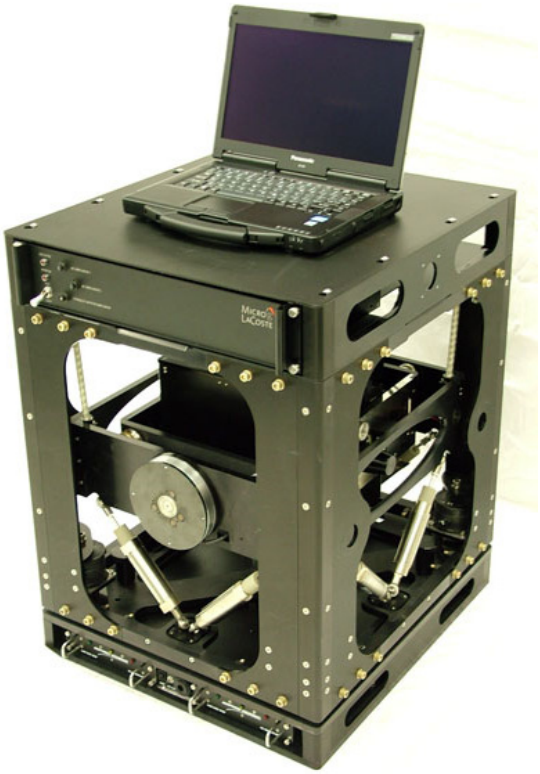

Figure 3.11: The MGS-6 Gravity Meter on gyro stabilized platform

Figure 3.12: The AIRGrav gravimeter with several gyroscopes to keep stable

3.2.b.3. Airborne Surveys

Airborne gravity measurements include the major difficulty originating from the large and rapid changes in observed gravity due to the aircraft altitude, its acceleration and roll. Even thought it was considered impossible to collect good quality airborne data, DGPS systems overcome any difficulties in measuring motional effects (acceleration). There is also a gyro-

stabilized platform holding stable the meter. Nowadays airborne gravity gradient surveys, manage to measure the gradient of the Earth's gravitational field, which is independent of the aircraft's acceleration.

3.2.b.4. Satellite Gravity

A new type of gravity measurements introduced in 1978 with Seasat mission. Satellite radar altimetry began its great contribution, by mapping the global marine geoid, its first vertical derivative and the marine free-air gravity field. The altimeter was designed to measure sea-surface topography in order to collect information for the relief caused by water displacement, like large-scale ocean currents.

The most recent dynamic satellite missions are the GRACE and GOCE, help define with accuracy the long wavelength part of the global model. They measure the gravity field at the satellite height using ranging and gradiometer systems.

The mean sea surface is practically the geoid, an equipotential surface of the Earth's gravity field. The gravity response is the first vertical derivative of the equipotential surface. The marine gravity field can be computed by the sea-surface topography (Sandwell & Smith, 1997). Therefore, the difference between the geoid and the mean sea surface has to be corrected.

Since the first satellite mission, enormous amounts of data have been gathered. Despite the relatively long-wavelength resolution, they are considered invaluable.

3.2.b.5. Gravity Gradiometry

Conventional gravity meters measure a single (vertical) component of the gravity field vector. Gravity gradiometers measure the gravity gradient, or in other words, how the gravitational acceleration changes over distance in both horizontal and vertical directions. Full-tensor gradiometers measure changes in the z-, y- and z- directions for all three components of the gravity field g_x, g_y and g_z.

A simple way of measuring the vertical gradient is by using specially designed tripods that lead to acquisition of gravity measurements with constant height difference. The first gravity gradiometer was the torsion balance, made in 1886, by Baron von Eötvös. Two weights were suspended from a torsion fiber at unequal heights, on which different forces were applied due to their spatial differences. Modern gravity gradiometers, known as full-tensor, have been recently developed. Some of them consist of 12 accelerometers, with three spinning disks, measuring the Earth's gravity differences. The development of gravity gradiometers contributed a lot to the systems based on moving platforms, like airborne or marine operations, where advanced corrections are required due to the movement and acceleration.

Horizontal gradients are measured in Eötvös units, where 1 Eötvös (E) = $10^{-9}s^{-2}$. This is practically the $1/10^{th}$ of a microGal/m or better the $1/10^{th}$ of an mGal/km. Geological sources range at +/- 200 E (Fairhead, 2015).

3.2.c. Standard Field Operations

Like all field surveys, in gravity ones general guidelines have to be applied. These include safe working conditions and acquiring appropriate permissions to survey on special occasions (security concerned areas, public areas etc.). Moreover, standard operating procedures should be developed (ASTM, 1999) for precise measurements.

Obviously, planning a priori each day stations is more than desirable and helpful. Furthermore, the appropriate survey documentations are very important, including information about members of the crew, station's details (code, roads, description etc.), reading time, instrument height, affecting factors (vibrations, traffic etc.), weather conditions, local terrain corrections.

The station spacing and the number of desired stations of each campaign is determined by the investigated subsurface target (size and depth). An 'empirical' rule says that the station spacing should not be more than half the expected target burial depths (LaFehr & Nabighian, 2012; Long & Kaufmann, 2013). Stations might be planned on either profiles or grid, depending on the target.

Starting a new survey, permanent base stations have to be established carefully. This can be accomplished by tying up the new base to the national base-station network with known absolute values and ideally to the IGSN71 (Morelli, 1974). Thorough description of the bases is also required. Every new gravity station is acquired in loops, starting and ending with a base measurement. Each loop should not exceed a period of 3 hours, for precise drift correction of the measurements.

Relatively to the reading procedure, great care should be given. The gravity stations should be located on stable ground, away from signal noise and traffic. Great care must be given on the correct levelling of the instrument. Slow and stable handling of the instrument is necessary. At every station, a couple of readings are required to ensure the repeatability and quality measurement. The micrometric screw must be turned always in the same direction during the measurement. Additionally, a percent of 5% repeat gravity stations is preferred.

The coordinates of each gravity stations (x, y and elevation) should be determined with high precision (5-10 cm). Modern Differential GPS systems permit an accuracy of centimeter in height, which gives an accuracy of about 3 μGal in Free-air correction or 2 μGal in Free-air plus Bouguer correction (Jacoby & Smilde, 2009). For latitude correction, a 10 m point uncertainty, imports a <10μGal uncertainty (Jacoby & Smilde, 2009).

If we keep up to the pre-mentioned survey standards, we can achieve resolutions between 1 and 20 μGal for land measurements (LaFehr & Nabighian, 2012).

3.3. STANDARD DATA REDUCTION

Lateral variations in the density of rocks cause variation in the gravity field measured. The aim of gravity surveys is to investigate that kind of variations and discover the nature of them and the anomalies related to them.

This cannot be accomplished directly by the gravity field measurements, since they are affected by unwanted effects, like topography, location, the tides, the instrument drift, and the so-called Bouguer slab, which have to be removed. Earth tides can produce variations of up to 0.3 mGal in a day while barometric pressure only 0.003 mGal per day (Jacoby & Smilde, 2009).

The observed gravity at a given location is practically the sum of several components. Some of them are considered as time-variant, some as time-invariant and some as permanent. Based on these the observed gravity can be formulated as followed:

$$g_{obs} = g_n + g_h + g_{tm} + g_g$$

where,

- g_{obs} is the observed gravity.
- g_n is the normal gravity, calculated by the normalized Earth's ellipsoid (latitude correction).
- g_h is the gravity change due to the point elevation *h* above the reference surface (free-air correction).
- g_{tm} is the gravity effect due to the topographic mass, located between the reference surface and the actual physical surface of the Earth. It depends on the elevation and density distribution (includes the Bouguer and terrain corrections).
- g_g is the gravity variation due to interior deviations of the Earth's subsurface geology. It is usually the target of the gravity research. Based on that, in order to determine the geologic anomaly, the equation will be:

$$g_g = g_{obs} - g_n - g_h - g_{tm}$$

Gravity data reduction is a process that begins from the field measurement at a specific gravity station processes and removes all the unwanted effects ending up with a gravity anomaly value. The basic procedure remains almost the same for the last 75 years. Gravity corrections are being applied to theoretical (normal) gravity value calculated on the reference ellipsoid in order to bring the theoretical value up to the elevation of the measurement, before it is subtracted from the measure value as was put forth by Nabighian *et al*. (2005). In this way, the gravity anomaly value is defined at the location of measurement rather than on the ellipsoid or geoid.

In order to proceed to the standard reduction procedure, specific data is required for each gravity station, such as the measuring time and date, the drift rate, the meter constant, the

station latitude and elevation and an absolute value at the established base station of the survey.

3.3.a. Tidal Correction

Gravimeters are sensitive enough to record the changes in gravity due to the movement of the Sun and Moon, producing the tide and depended on latitude and time. This means that during one day's field measurements the gravimeter is influenced by the tidal attraction, produced by the Earth tides. The tidal gravity variations originate not only directly from the attraction of the Moon and Sun but also from the elastic deformation of the ground surface and loading the ocean tides. The lunar effects are twice the solar ones.

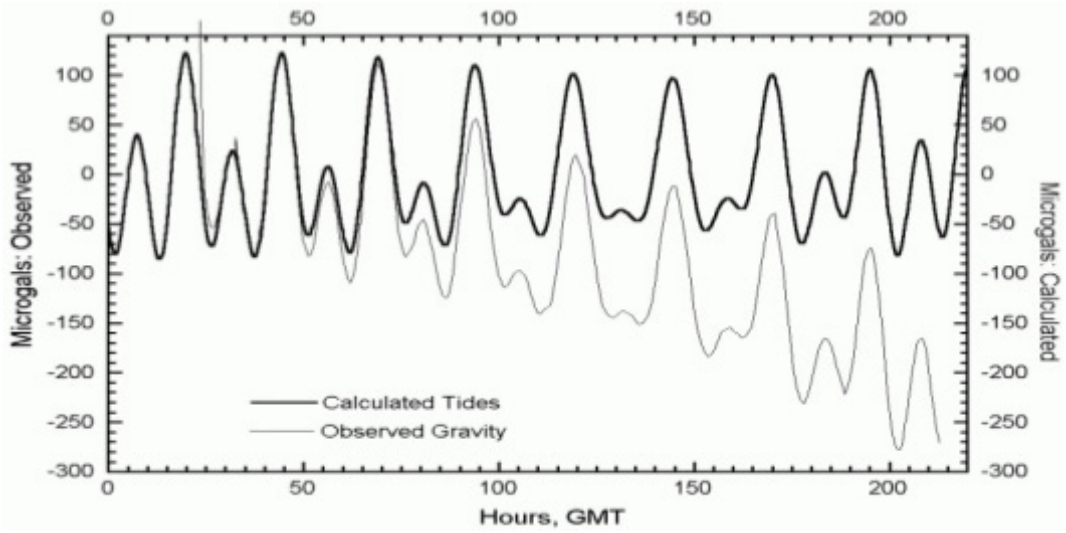

Figure 3.13: Tidal Correction diagram

Fortunately, their effect can be precisely computed for any location and time. The only requirement is the reading time again. The range of the tidal effect could range up to 0.3 mGal for a six hours period, but in general, they are less intense. They removal can be obtained through the same process followed for the drift correction, described in the previous paragraph.

3.3.b. Drift Correction

Repeating reading of a gravimeter during a day, even at the same location will give different values, since the response of the internal spring alters with time. This phenomenon is called "instrument drift" and it is partly due to thermally induced changes affecting the elastic properties of the spring. Although they are minimized by enclosing the spring mechanism in a shielded environment with stable temperature, the changes occur. Modern gravimeters have very little drift, while on the other side the older gravimeters improve with age and their drift lowers after some years of operation.

The drift correction can be obtained by reoccupying the established gravity bases during the day survey. This means that the field measurements should be acquired in loops, with a base reading at the start and the end. The reoccupying period should not exceed the 3-4 hours. Of course, the shorter the reoccupying time at the base, the more precise correction will be calculated, a drift curve will be produced and based on that, all the gravity stations of the day will be corrected. The only essential information for the production of the drift curve is the recording of the precise measuring time and the instrument reading at the gravity stations and the base. The drift correction should be applied after the tidal reduction.

In order to avoid erratic changes in the drift curve of the gravimeter, the handling and transportation of the instrument has to be smooth, precautious and stable. The spring must be always clamped during any movement or transportation.

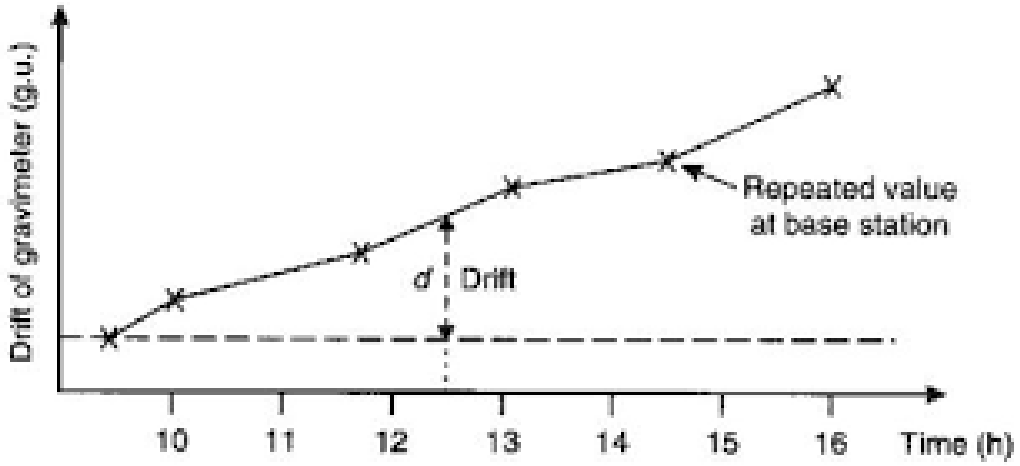

Figure 3.14: Drift Correction diagram

3.3.c. Latitude Correction

The Earth's rotation and the equatorial bulge lead to increase of the gravity with latitude. Centrifugal acceleration is maximum at the equator. As we have already mentioned in §3.1.d.2 normal gravity (calculated on the reference ellipsoid) increases from equator to pole. The latitude correction deducts the normal gravity field from the observed value in order to eliminate the gradient effect that would be caused.

For local surveys, often a constant latitudinal or horizontal gradient is assumed. Therefore, the latitude correction (Δg_L) in these cases is calculated by the following equation, where φ is the station latitude:

$$\Delta g_L = 0.812 sin2\varphi \; mGal/km$$

An accuracy of 0.01 mGal for the latitude correction can be achieved providing that the gravity station location is determined with precision of about 10 meters or less. Nowadays this can be easily determined with the contribution of the Differential GPS systems.

3.3.d. Free-Air Correction

Gravity decreases proportionally to the inverse square of distance from the Earth's center. Because of that, it is essential to correct for changes in elevation between stations to reduce the field reading to a datum surface (Fig. 3.15c). Notice that the free-air correction ignores the material existing between the station and the datum surface. The following equation calculates the free-air correction from each gravity stations, based on its elevation *h*:

$$\Delta g_{FAC} = 0.3086\, mGal/m$$

The free-air correction is added (positive) to the observed gravity when the gravity station is above the datum surface (sea level) and deducted when it is below it. Free-air correction can be quite large. For an accuracy of 0.01 mGal in calculation, the elevation must be determined with an accuracy of 3 cm.

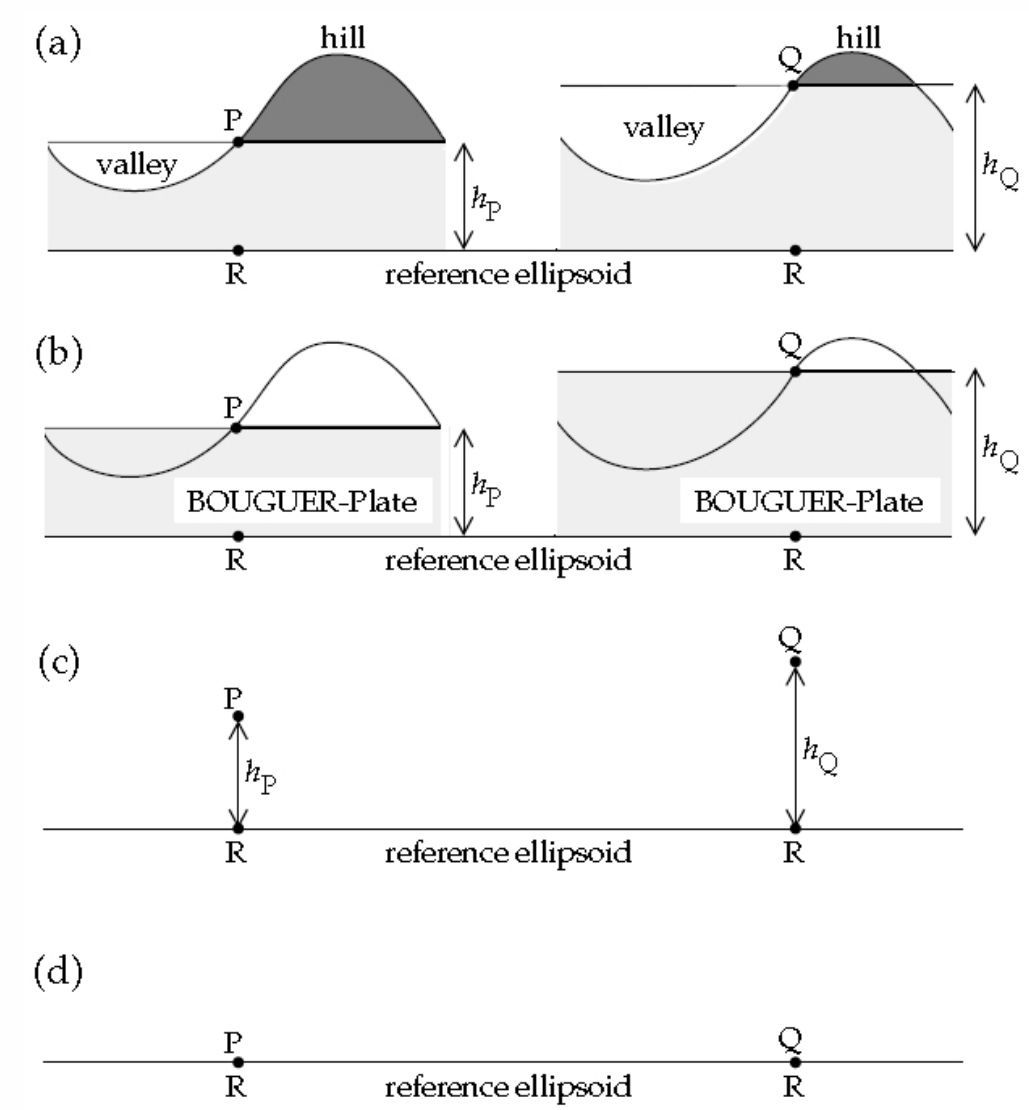

Figure 3.15: After (a) Terrain correction, (b) Bouguer (plate) correction, (c) Free-air correction, gravity measurements on stations P and Q have been reduced to the theoretical gravity at R (d), on the reference ellipsoid (*Lowrie, 2007*).

It is important to clarify that by applying the free-air correction, we do not reduce the data to a datum, where we would have measured there. Practically, we calculate the decrease of the observed value produced by the fact that gravity station is located farther from the Earth's center.

3.3.e. Bouguer Correction

The Bouguer correction removes the attraction of the rock layer whose thickness is the elevation difference between the measurement location and the reference surface (Fig. 3.15b). This is modelled as a uniform (constant density) horizontal slab with large extent. Bouguer Correction is calculated through the equation:

$$\Delta g_B = 2\pi G\rho h = 0.04192 \cdot \rho \ \ mGal/m = 0.112 mGal/m$$

where ρ is the slab density, in gr/cm^3, h the station elevation and G the gravitational constant. If we consider an average value of rocks equal to 2.67 gr/cm^3 and embedded it the equation we will end up to the last part of the equation above.

The Bouguer correction has to be subtracted from the observed value when the station is above the datum and added when it is below. The main effect of the Bouguer correction is to remove large gravity differences between neighboring stations at different elevations.

When only a flat plate is taken into account for the mass, the anomaly is called Simple Bouguer Anomaly. If we have topographic deviations, these are removed through a topographic correction. Therefore, when both the flat plate effect and the topographic effect of mountains and valleys are removed, the result is the Complete Bouguer Anomaly. So, the Simple Bouguer Anomaly (*SBA*) is defined as:

$$SBA = g_o - g_n + \Delta g_L + \Delta g_{FA} - \Delta g_B$$

where, g_o the observed gravity, g_n the normal gravity, Δg_L the latitude correction, Δg_{FA} the Free-air Correction and Δg_B the Bouguer Correction. In this case, we apply also, the Terrain Correction (Δg_T) described in the next paragraph and we will take the Complete Bouguer Anomaly (*CBA*):

$$CBA = g_o - g_n + \Delta g_L + \Delta g_{FA} - \Delta g_B + \Delta g_T$$

3.3.f. Terrain Correction

Topographic variations also affect the gravity measurements. Hills above the gravity station produce an upward pull on the measurement that is not included in the calculated Bouguer correction (Fig. 3.15a). The component of the hill attraction is upwards in vertical direction, decreasing the value of the gravity at the measurement station. When there is a valley, the lack of mass compensates the lack of attraction, which was assumed during the Bouguer correction. This means that the valley not only does not produce a downward attraction but also reduces the observed attraction. For these reasons, the terrain correction is always positive.

The classic method of calculating terrain corrections requires detailed topographic data. The procedure is to divide the area into compartments and calculate the average elevation of each one, compared to the one of the gravity station. Hammer (1939) introduced the Hammer chart zone, where the area is separated by concentric circles (the center is the station) and radial lines in sectors (Fig. 3.16). Specific radial distances and number of equal sectors have been established (Table 3.1). The outer radius extends to 21 kilometers from the station.

The calculation in the older times was accomplished with the contribution of transparent sheets, estimated from the mean elevation of the contours within it. The procedure was time consuming and tedious, but nowadays the terrain corrections are calculated automatically through specialized software. They separate the area in prisms, based on the general idea of the Hammer charts and they use Digital Elevation Model (DEM). In cases with rough terrain near the gravity stations, additional field topographic information may be imported to the program manually. In mountainous areas, the correction value can be more than 50 mGal, while in areas with alteration in elevation of ±200 meters the correction values are close to 2 mGal.

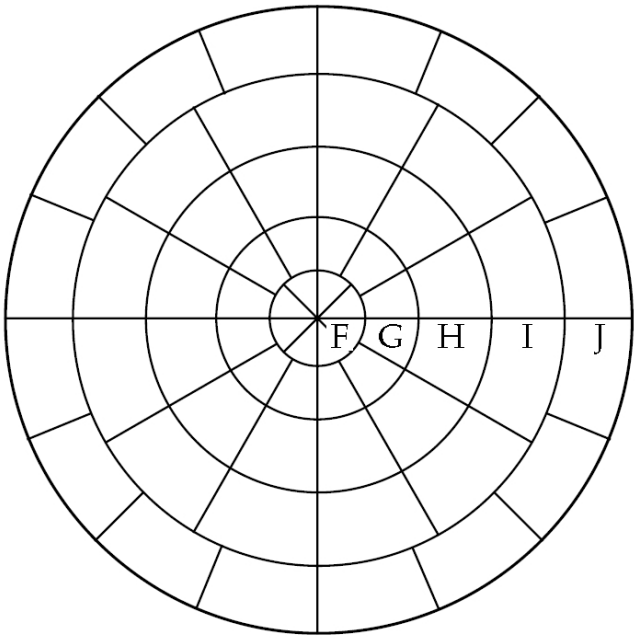

Figure 3.16: Hammer zones chart (*Hammer, 1939*).

Zone	Inner radius (m)	Outer Radius (m)	Sectors
A	0.0	2.0	1
B	2.0	16.6	4
C	16.6	53.6	6
D	53.3	170.1	6
E	170.1	390.1	8
F	390.1	849.9	8
G	849.9	1530	12
H	1530	2615	12
I	2615	4469	12
J	4469	6653	16
K	6653	9903	16

Table 3.1: Radius distances of first Hammer chart zones

3.3.g. Isostatic Correction

On global scale, the Bouguer anomalies have an inverse correlation with the station elevation. In mountainous areas, they are generally negative, while in oceans positive. These variations originate from the Earth's density variations, indicating denser material beneath the ocean areas and less dense in mountainous continents. This implies that higher topography entails thicker crust and deeper Moho.

Isostasy is the tendency of vertical mass balance with the topography in the upper few hundred kilometers of the Earth. The effect is important mostly in large-scale surveys or globally, like the ones considering the depth of Moho.

Isostatic corrections have been proposed through the contribution of simplified isostatic models, like those of Airy and Pratt (Fig. 3.17). Airy claimed that mountains have roots and Pratt that crustal density varies horizontally.

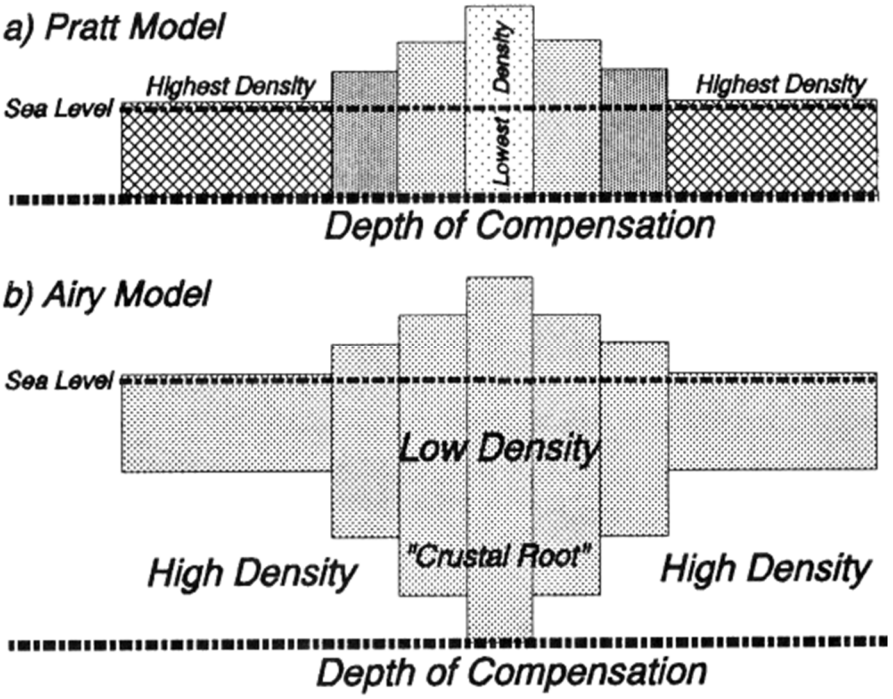

Figure 3.17: Pratt and Airy Isostasy models. (*Lillie, 1999*)

3.3.h. Additional Corrections

In some cases of gravity surveys with advanced characteristics, additional corrections may be needed, depending on the occasion.

3.3.h.1. Eötvös Correction

In all kinds of gravity measurements acquired on moving vehicles or platforms, like ships and airplanes, the motion of the instrument modifies the effect of the Earth's rotation, which is already treated as if the gravity meter was at rest. This phenomenon is called Eötvös effect.

The Eötvös effect is given from the following equation:

$$E = 2V\omega cos\varphi sin a$$

where V is the vehicle velocity, a is its direction with respect to the North, ω is the Earth's rotation and φ is the latitude. The actual centrifugal acceleration, V^2/R, acting on the gravity meter has to be added to this. It is independent of direction but nearly constant in each survey.

The value of Eötvös correction can be quite large, ranging for a ship, from almost 5 mGal to even more than 75 mGal, depending on the velocity and latitude of the survey.

3.3.h.2. Bullard B Correction

The Bullard B reduction corrects the fact that the simple Bouguer plate contains material mass laterally beyond the Earth, but not where the Earth's surface dips below the plate (Fig. 3.18).

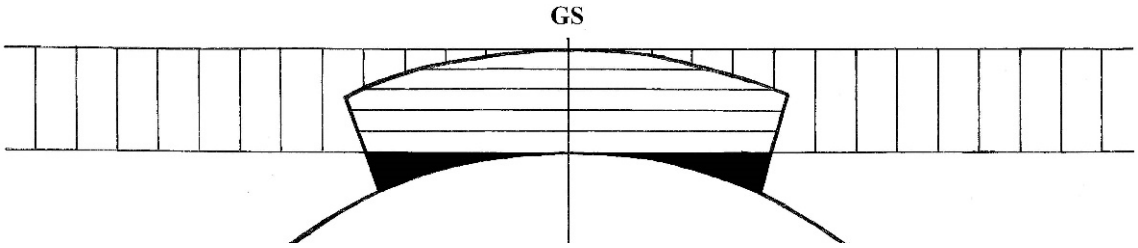

Figure 3.18: Geometry of spherical cap related to infinite Bouguer plate. (GS) is the Gravity Station. (*Nowell, 1999)*

The Bullard B correction modifies the Bouguer slab Correction to the fact that has a surface radius of 167 km and same thickness as the infinite plate. This is equivalent to removing all the plate above the Earth's surface and beyond 167 km, whether above or below and adding the part of the cap below the plate (Fig. 3.18 – black area). The part of the spherical cap (with horizontal lines in it) is common to both the plate and the cap. This means that it does not have to participate in the correction.

The Bullard B can be calculated with the equation:

$$B = 2\pi k\rho(\mu h - \lambda R)$$

Where *R* is the Earth's radius to the station (the elevation from sea surface must be added), μ and λ dimensionless coefficients and ρ the density.

3.3.h.3. Atmospheric Correction

The attraction of the atmosphere is included in the ellipsoidal normal gravity provided by the International Gravity formula of 1980. When the atmosphere's mass exists in uniform elliptical shells, there is no reflection of the overlaying atmosphere in the observed gravity value. However, a decreasing factor should be added to the observed value of gravity.

A formula for the atmospheric correction was suggested by Wenzel (1985), with accuracy up to 0.01 mGal for the first 10 km elevation, provided by the equation:

$$\Delta g_{atm} = 0.874 - 9.9 \times 10^{-5}h + 3.56 \times 10^{-9}h^2 \ (mGal)$$

Where *h* is the height above sea level (in m).

3.3.h.4. Building Correction

The mass of buildings existing near a gravity station produce an upward attraction, which decreases the observe value of gravity. This means that a correction must be calculated and added to the measurement reading. This kind of correction is usually applied in micro-gravity surveys, where lower scale anomalies are being investigated.

Mention that the older buildings have an average density twice than the modern ones. Several researchers have already proposed methods to calculate and correct the building effect, either by modelling the buildings like prisms (Debeglia & Dupont, 2002; Radogna *et al.,* 2003) either by using modern technologies like LIDAR data and photogrammetry (Dilalos *et al.*, 2018; Panisova *et al*, 2012).

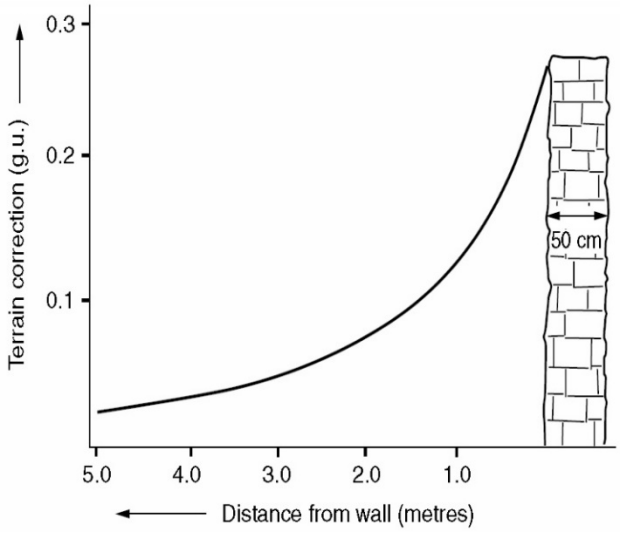

Figure 3.19: Effect of a thick stone-wall (0.5m) on the gravity field (*Milsom & Eriksen, 2011*)

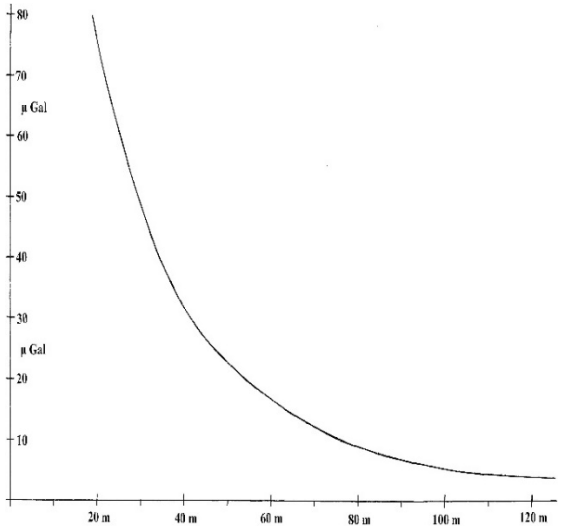

Figure 3.20: Effect of a 27m square building, 100m high, average density 0.34 gr/cm3. Horizontal axis is distance from the center of the building (*Nowell, 1999*).

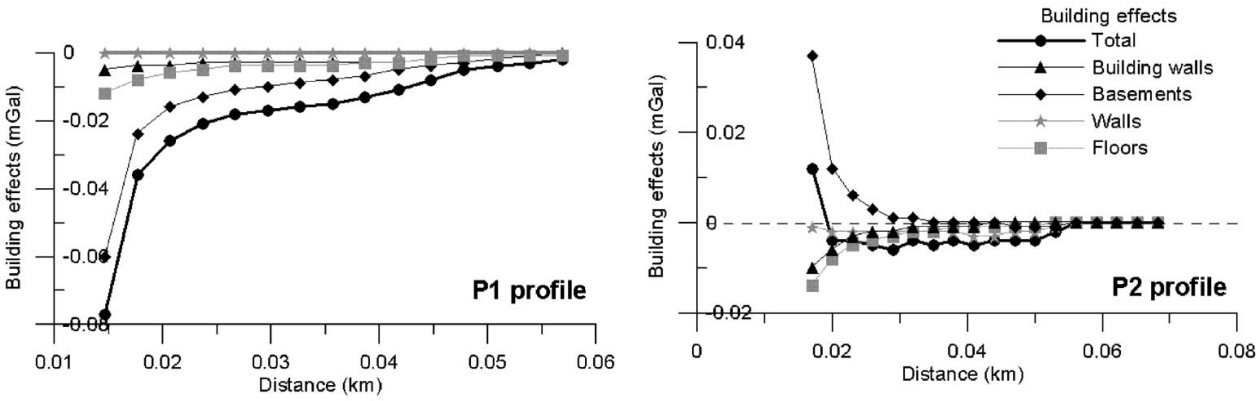

Figure 3.21: Building Effects (*Debeglia & Dupont, 2002*).

3.3.h.5. Marine Corrections

Special corrections might be required for water-bottom surveys or in cases where the meter is on tripod (shallow lakes). In such cases, the reference datum might be below the water bottom, which means that the elevation must be threatened accordingly.

Underwater locations are negative, so the free-air and Bouguer corrections are reversed in sign in regard with land measurements. Moreover, for the upward attraction of the overlying water layer the term $0.043 \cdot d$ is proposed for seawater.

Since the ship surveys are considered to be located on the reference datum, the free-air correction will be zero. Tidal correction in open sea cannot be estimated correctly and for that, the Bouguer correction will be formulated as:

$$\Delta G_{B-ship} = 2\pi k h_3(\rho - 1.03) = 0.0419\ mGal\ (\rho - 1.03)h_3$$

where h_3 is the water depth from the ship.

3.4. MANAGEMENT OF GRAVITY ANOMALIES

The term Anomaly is common in geophysical terminology, but each time the type of the anomaly should be specified, for example Bouguer Anomaly. The differences are referred and compared to certain reference models, depending on the purpose and scope. A Gravity Anomaly is defined as the difference between observed and normal gravity.

Typically, the anomaly should be determined by at least a set of observation points and not a unique point. Consequently, such anomalies can be detected either on map contouring of discrete points or in profiles, where continuous fields are presented.

During the processing steps, the gravity field measurements are treated in that way of revealing the gravity anomalies. After the field data examination for errors and the data reduction procedure described in §3.3, their visual representation follows. Maps of several parameters can be produced and processed in order to define any possible anomalies that will contribute to the subsurface determination. In many cases, the data processing includes a filtering procedure. Even statistical methods can be applied in order to focus on certain aspects, such as the gradients.

3.4.a. Visual Representation

As we have already mentioned, several types of maps and grids can be produced during the gravity processing, usually after the application of a filter type.

3.4.a.1. Smoothing

The collected data is affected by random or stochastic errors of certain distribution, almost Gaussian (Jacoby & Smilde, 2009). The first step, where we intend to remove the data noise is called *Smoothing*, which can be carried out in many ways, such as by manual inspection along with the appropriate drawing, moving average or by applying statistical methods.

A simple way is to average the values of points in overlapping areas, using weighing average factors. In a circle of certain radius for example, the mean value of all the included points can be assigned to the center of the circle. However, in local surveys of which the aim is the identification of discontinuities and short-wavelength anomalies, smoothing must be carried out with great caution. For smoothing through computer applications, a rectangular coordinate system is preferred.

3.4.a.2. Mapping and Gridding

Gridding data is quite crucial, if we realize that many crucial filtering procedures will be based on that, such as the regional-residual separation. Gravity data usually are either collected along profiles, such as ship tracks, or based on grids with uneven distribution. After the data reduction to the level of gravity anomalies, usually gridding the data for filter application is necessary. Therefore, either as scattered points or as profiles the best gridding method is *minimum curvature* (Briggs, 1974). Only in cases with parallel profiles (ships), an aliasing reduction is also essential along with line levelling methods.

Through minimum curvature gridding, the data points will be joined in the smoothest possible way. This method estimates grid values at the nodes of a coarse grid (usually eight times the final grid cell size) by using inverse distance averages of the actual data within a specified search radius (Fairhead, 2015). If there is no data within the pre-defined search radius, then the search radius will increase until the average of all data is used. Then, iterations are being made to adjust the grid to fit the actual data points nearest to the coarse grid nodes. By the time an acceptable fit is accomplished, the coarse cell size is divided in 2, and the process is repeated. The procedure is repeated until the surface is divided to the final grid cell size.

Usually the grid size is half of the data density. The smaller the grid size the most time-consuming. If the cell size is quite larger than the optimum one, a de-aliasing filter should be applied. Great care should be given on a good station distribution.

Another method for gridding, mostly for land gravity surveys, is the *natural neighbor* (Sambridge *et al.*, 1995). If we have regularly distributed gravity stations, both *natural neighbor* and *minimum curvature* methods can be applied with quite similar results. *Minimum curvature* is considered to be more “true” to the data values than *natural neighbor* is, but its inherent ability to follow trends is smaller.

Moreover, *kriging*, is another gridding method, based mostly on statistical analysis of the data calculating values at grid nodes, based on the whole dataset in order to generate a variogram. The procedure includes determining all differences between every data point pair, averaging values for same distance and plotting the averages as a function of distance. It is not as smooth as the previous mentioned methods, but based on Pilkington & Shamsipour (2014) it can be applied for noise removal.

Generally, in order to grid profile data, it is recommended to use a cell size of 1/4 or 1/5 of the line spacing to minimize the short wavelength information.

3.4.b. Anomaly Separation

The first step of gravity processing is the data reduction procedure, as we have already analyzed it in §3.3. The gravity anomaly generated after this step, is the Bouguer Anomaly. This Bouguer Anomaly contains superposed anomalies from several sources.

The deep large sources produce long wavelength anomalies and they are known as *regional* anomalies. They are contributing to the large-scale structure of the Earth. Beyond them, shallower and smaller sources exist and produce anomalies with short wavelength characteristics and they are known as *residual* or *local* anomalies.

Therefore, depending on the aim of the gravity research, one of these two fields needs to be removed. For example, for basin surveys, the regional field must be calculated and removed, in order to isolate the residual anomaly field.

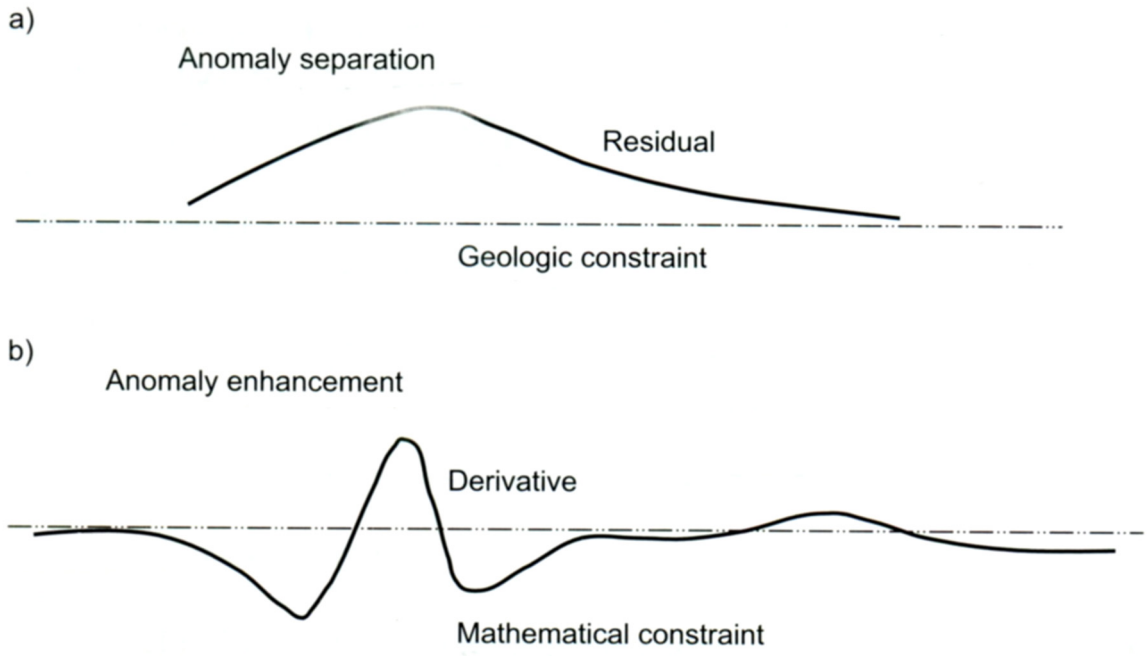

Figure 3.22: (a) Anomaly separation versus (b) anomaly enhancement (*LaFehr & Nabighian, 2012*)

This part of gravity data processing is suffering from the ambiguity problem but on the other hand, it is an important step in the interpretation procedure. Many methods have been adopted for the regional-residual separation, such as the graphical approaches, mathematical filters and geological filters. The choice of the appropriate method is not always easy or objective. Even for spectral filters, the choices of the wavelengths that will be set are somewhat arbitrary.

Anomaly separation and data enhancement seem similar or even use similar techniques but they are not. They have different units and they serve different purposes (Fig. 3.22).

3.4.b.1. Graphical method

It is the oldest and simplest method. At a Bouguer gravity anomaly profile (Fig. 3.23) or map (Fig. 3.24), the regional gravity field can be visually fitted to the anomaly as a smooth curve or contour respectively, drawn by the interpreter. The value originated from this curve/contour

is subtracted point by point from the Bouguer anomaly one, in order to calculate and finally isolate the residual anomaly (curve or contour).

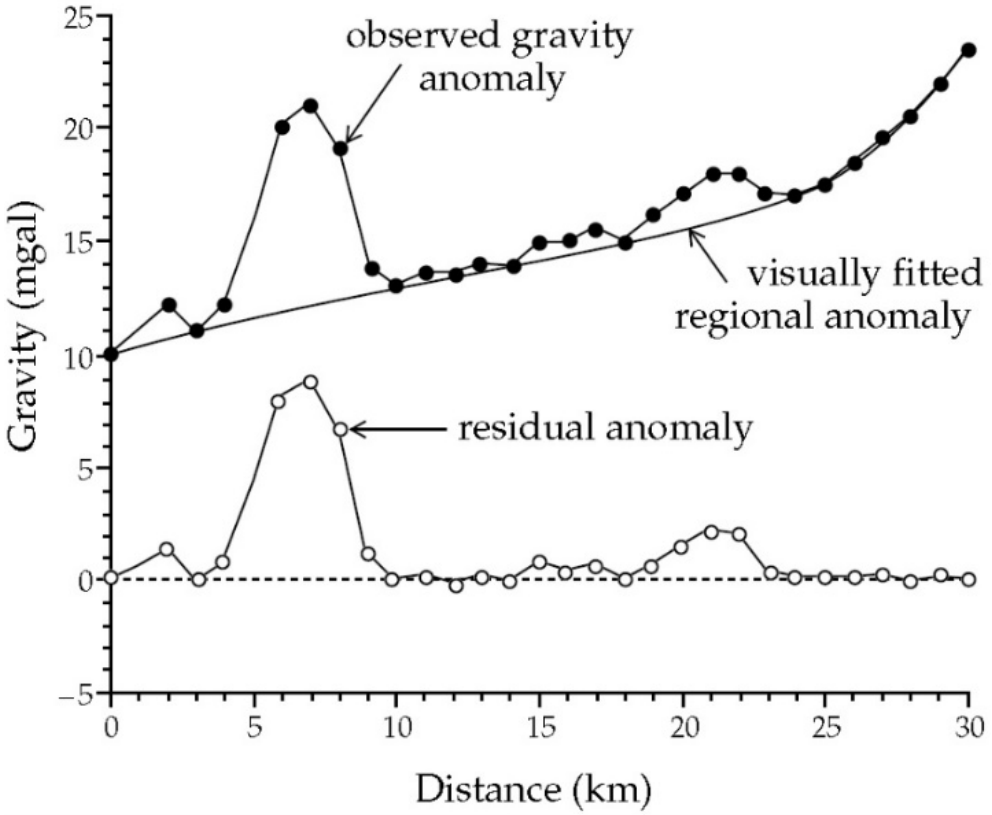

Figure 3.23: Graphical method of fitting the regional anomaly of a gravity profile and isolating the residual anomaly (*Lowrie, 2007*)

This approach requires experienced interpreters, since the choice of a regional is quite empirical with subjective characteristics and uncertainties. However, good results have been derived from its application.

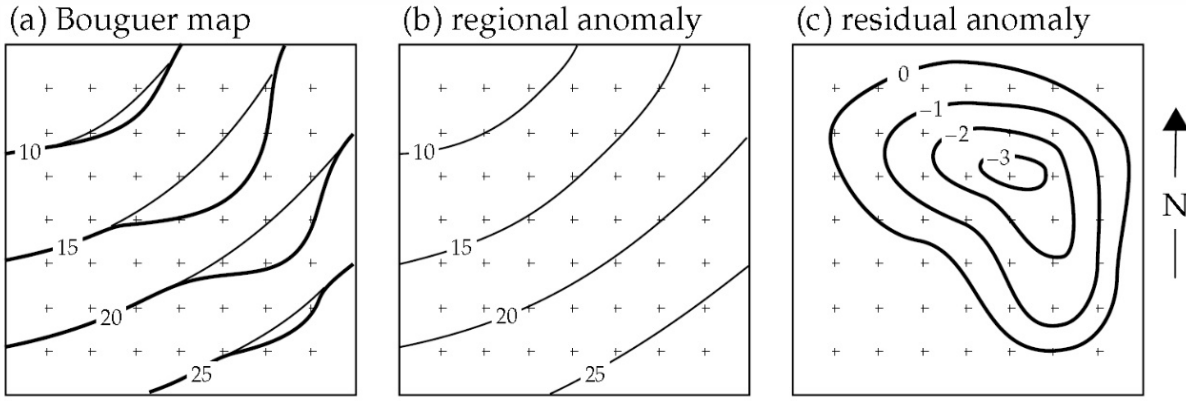

Figure 3.24: Graphical method of calculating and removing the regional anomaly field from a Bouguer map in order to isolate the residual anomaly (*Lowrie, 2007*).

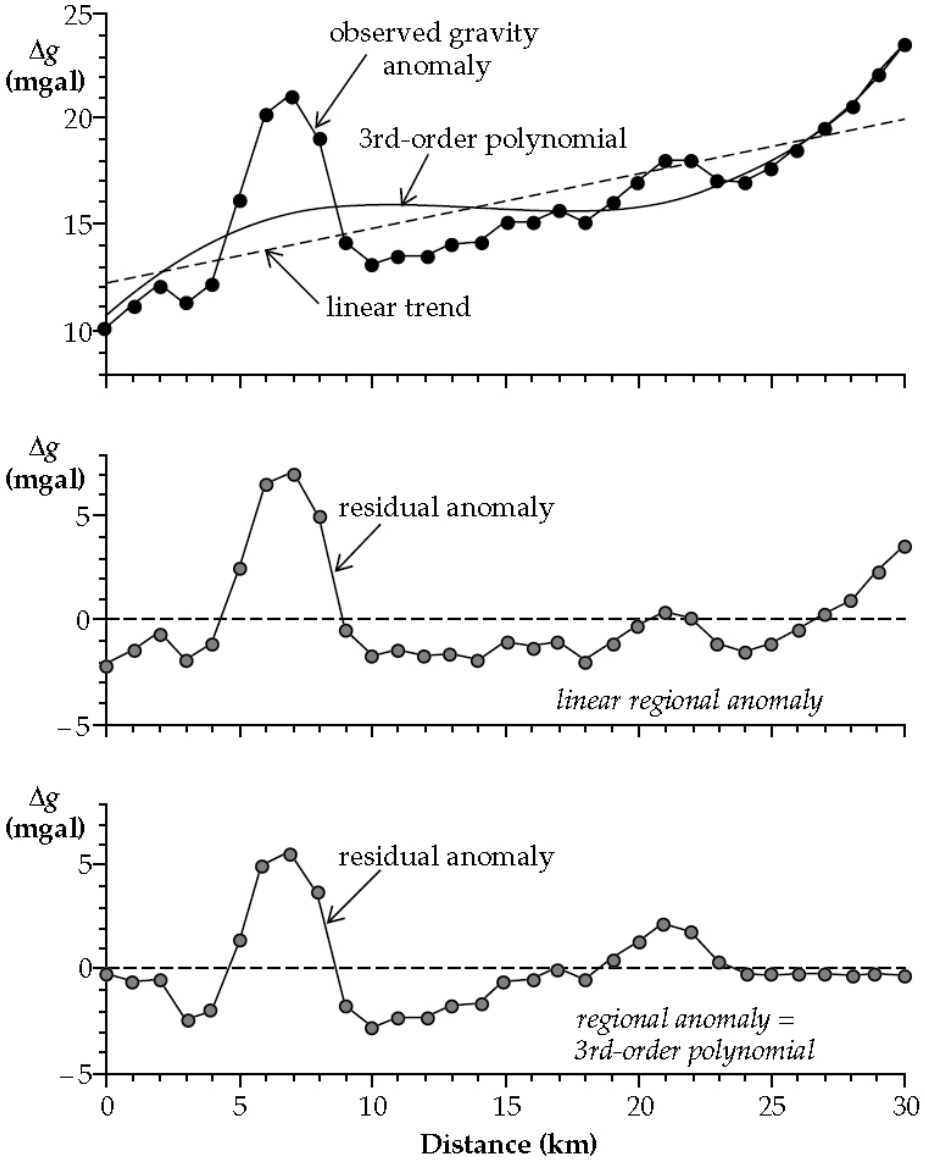

Figure 3.25: Removal of regional field based on a smooth polynomial curve, fitted to the observed gravity anomaly by the least-squares method (*Lowrie, 2007*)

3.4.b.2. Polynomial fitting

An alternative method for anomaly separation is the polynomial fitting, based on the least squares method applied on the observed gravity data. The higher the order of the polynomial, the better it will fit the observation data (Fig. 3.25). Great care should be given as the polynomial order increases because from a point and further it will have no geological meaning. For that reason, the interpreter should judge and choose the lowest appropriate order that represents better the regional trend. Moreover, the curve should pass through the gravity data values in a way that the residual anomalies will have both negative and positive values.

The polynomial fitting, is applied on line and grid based data. For maps, it will be represented as a smooth surface or plane. The expressions used for the procedure are the following, where Δg is the regional gravity:

$$\Delta g_R = \Delta g_0 + \Delta g_1 x + \Delta g_2 x^2 + \Delta g_3 x^3 \dots + \Delta g_n x^n \; for \; profile \; data$$

$$\Delta g_{(x,y)} = \Delta g_0 + \Delta g_{x1} x + \Delta g_{y1} y + \Delta g_{x2} x^2 + \Delta g_{y2} y^2 \dots + \Delta g_{xy} xy \; for \; grid \; data$$

A common problem with polynomials is that the edged do not behave well. For that reason, their application should be constrained to data covering the entire map area.

3.4.b.3. Upward/Downward Continuation

In some occasions, the original observation surface need to be moved to another surface level, in order to compare it for example with another data set. The transfer of the gravity data to higher (upward continuation) or lower (downward continuation) level can be accomplished mathematically, in order to attenuate or emphasize anomalies with short wavelengths respectively. It can be applied either in space or frequency domain.

With the *upward continuation*, we can enhance the deeper anomalies (*regional*), due to the reduction of the shallow responses, since shallower sources have shorter wavelengths. It can be achieved by using the Fourier transformation, but considering the values to be on a relatively flat surface. Upward continuation is quite stable procedure, with values ranging from zero at infinite frequency to one at zero frequency. However, it contains ambiguities basically for the level that will move up.

On the other hand, we can move the data surface to a lower level (*downward continuation*), in order to enhance the shallower sources. However, it should be applied along with the appropriate tapering filters for regularization in order to avoid the embedding of noise. The values range from one at zero frequency to infinity at infinite frequency.

3.4.b.4. Derivatives

Although the derivatives are not anomaly-separation methods, we will mention that the first and second vertical derivative are applied a lot to emphasize the signals from the shallow sources (short-wavelength) and they are applicable in both space and frequency domains. Tapering filters should be applied also in order to avoid the embedding of noise.

3.4.b.5. Matched filtering

Matched filtering can help locating the signal in a data set, if the spectrum of the expected signal is known. The matched filter has the same spectrum as the desired signal. Therefore, it is used to separate data in several components, representing the different source depths.

3.4.b.6. Finite-element

This method differentiates from the others because there are no regional computations entered in the observed data over the anomalous zones (Mallick *et al.*, 2012). A rectangular or square element is superimposed on the gravity survey area in a way that all zones of interest will be included. The regional field is assumed in a form of a weighted sum of the discrete values at the vertices or nodal points.

The regional computation is based on discrete regional points of the given data set and the anomalous zones are kept inside the element. Moreover, the computation is considered independent of a priori assumptions regarding the depth of shallow or deeper structures (Mallick *et al.*, 2012).

3.4.b.7. Frequency/Wavenumber domain Filtering

Gravity anomaly evolves in the space domain, since it varies with the distance. Therefore, for spatial distribution, the wavenumber $k=2\pi/\lambda$ is the equivalent for the frequency in time series, expressed in the terms of wavelength λ, providing the distance between the peaks of a sine wave. Its variation is considered to be periodic, expressed by a *Fourier series* constituted of discrete harmonics, constituted of sine or cosine functions multiples of the fundamental wavenumber.

Gravity grid data can be resolved from space domain to frequency/wavenumber domain by using the *Fast Fourier Transform (FFT)*. The wavenumber domain has positive (real) and negative (imaginary) values. Therefore, the representation is centered about zero wavenumbers. On the other hand, *convolution* is *w*hen the gravity data function is multiplied by a filter function that generates a new function.

Applying *Fast Fourier Transform (FFT)* to a grid requires some preparation procedures for the grid. The first step is the first order *trend removal*, in order to avoid strong effects within the grid. The second step is the *grid fill*, during which the surrounding part of an irregular grid is being filled with dummy data, in order to allow FFT run. The most popular methods are maximum entropy and minimum curvature. Afterwards, the grid needs tapering on its edges, with coefficients 1 to 0, in a way that the final size grid will have 2^n values. The filtering procedure (*Fourier analysis - see below*) can follow and finally the grid needs to be transformed back to the space domain and trimmed back to the original one.

Fourier analysis is called the procedure of separating a complex anomaly into simpler periodic variations of different wavelengths. Practically we can determine the important discrete components of a signal in a way that gives us the ability to remove certain wavelengths, considered as unwanted. Generally, there are four types of frequency filters, based on their cutoff values that usually are defined at the half amplitude response of the filter (50%):

- The *Low Pass*, *which p*asses longer wavelengths than its cutoff value, leaving only the *regional* anomalies.
- The *High Pass*, which passes shorter wavelengths than its cutoff value, retaining only the *residual* anomalies.
- *The Band Pass*, which passes certain wavelengths, located between two cutoff values.
- The *Band Stop*, which stops certain wavelengths, located between two cutoff values.

Based on the pre-mentioned filter types, several standard filters have been proposed with specific characteristics. Some of the most popular will be described at the following section.

i. Butterworth filter

It is a very popular smooth filter in potential field surveys (Ali *et al*., 2017), excellent for applying straightforward high-pass and low-pass filters, because it has easy control of the roll-off degree while leaving the central wavenumber fixed. The roll-off is defined as a function of frequency determined by the filter order *n* (positive integer value). Larger values produce sharper cutoffs and consequently greater 'ringing' of the narrow anomalies. When the 'ringing' is intense, the degree should be minimized for a better result.

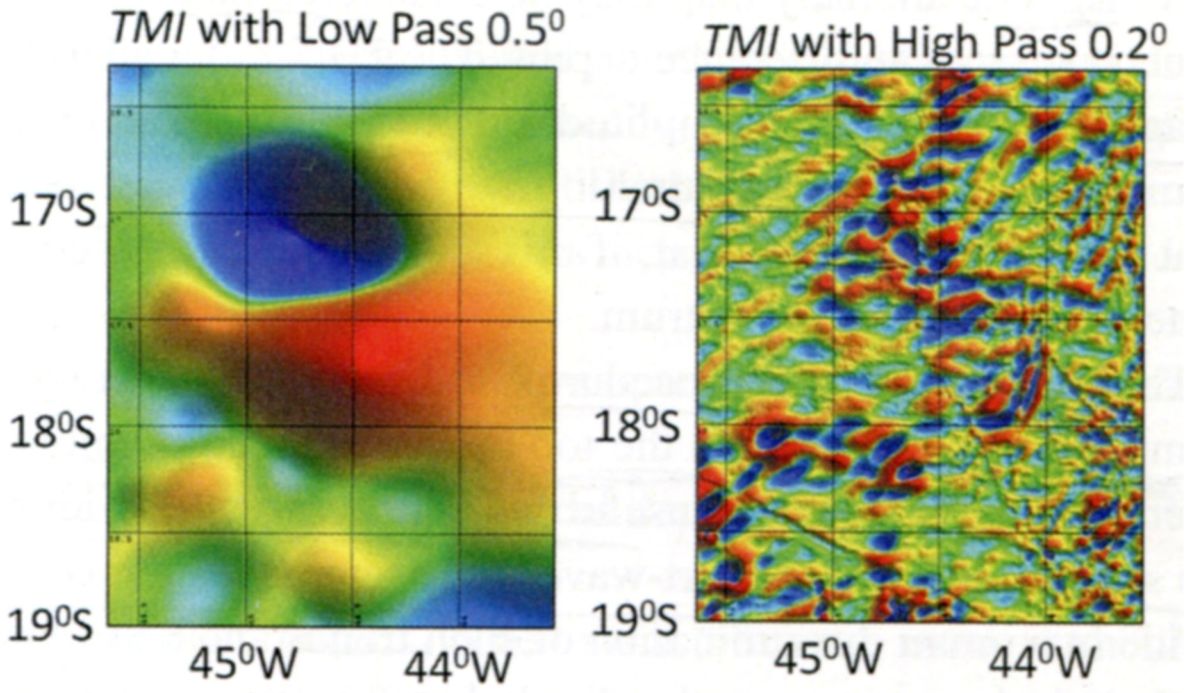

Figure 3.26: An example of the Butterworth filters application. The left picture is Low Pass filtering and the right is High Pass. (*Fairhead, 2015*).

ii. Cosine filter

This filter is commonly used for simple high-pass and low-pass applications since it has a smooth shape and does not differentiate the energy spectrum below the start of the roll-off. The required parameter is the determination of the width of the roll-off region, expressed as a fraction of the wavelength cutoff.

iii. Gaussian filter

Gaussian filter is one smooth filter used for low-pass and high-pass filtering (Fig. 3.27). It has a fixed bell-shaped response curve, which also describes the impulse response. There is no 'ringing' and the cutoff slope is not very steep. The only required parameter is only the cutoff wavelength.

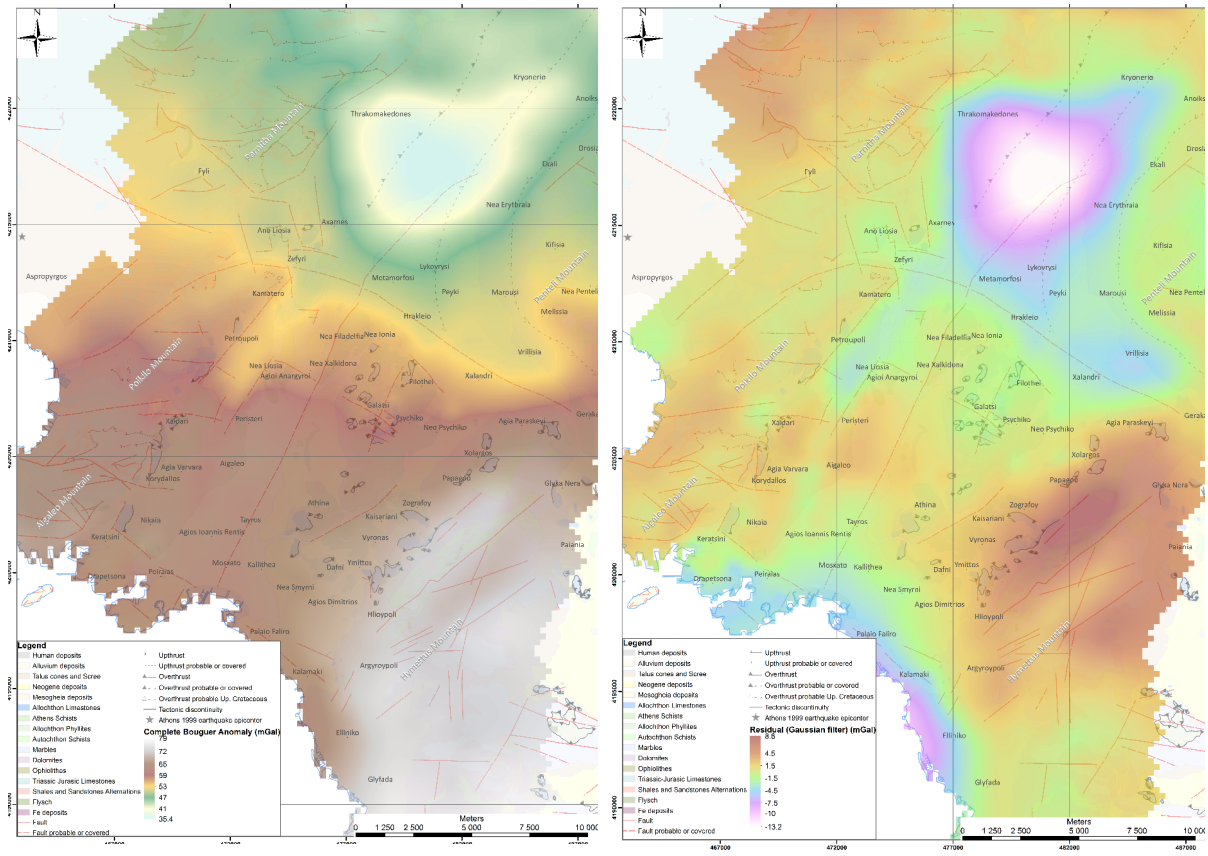

Figure 3.27: Example of the Gaussian filter application, as high-pass filter in order to isolate the residual anomalies (*Dilalos & Alexopoulos, 2017*).

iv. Strike filter

This filter is applied in the frequency domain in order to remove selected frequencies from the sector of XY frequency diagram, which is defined by its direction and angular width. While in the sector, it behaves like a *Butterworth filter*, at the edges the filter is faded using as *cosine filter*. Beyond the sector, there is no modification.

There are many more filters proposed by many authors, such as *Green's* concept of an equivalent-source layer, *Wiener* band-pass filter (Pawlowski, 1994), the *Directional Cosine filter*, for removing directional features of a grid, *Radially Symmetric* filters, for special-purposes.

3.4.c. Data Enhancement

Data enhancement practically incorporates the essential conditioning of the gravity data in order to proceed to the interpretation stage. Through the data enhancement, we enforce the identification of specific aspects of the spectral content of the data that will lead to better adumbration of the subsurface structure. Therefore, in order to gather elements for the final geological evaluation of the gravity data, several filters should be applied and evaluated. Data enhancement can be applied to both line and grid based records. They are also applicable to

space and frequency domains. Prior to generating derivatives aimed to structural and geological information, the steps of transform and filtering need to be undertaken in order to condition properly the data. The aim of this procedure is to enhance or isolate features in order to have a better image to evaluate geologically. The gravity response of a subsurface density body, assumed to be a point source, is proportional to $1/r^2$.

During the data enhancement, we need to take into consideration several things that might change or affect the final result. For example, the anomalies are usually boarder that the source, or close anomalies may interfere or the bigger anomaly may mask a smaller one very close to it. Due to these issues, we usually proceed to derivatives calculating, separating or isolating the wanted anomalies. Derivatives methods are excellent at enhancing the edges of the source bodies, which is very helpful in producing a structural map (Ali *et al.,* 2017; Fairhead, 2015).

There are also some geological controls affecting the ridge locations of the structural mapping produced through the data enhancement procedure, such as:

- The depth of body/structure: gravity anomaly depends on its distance from the source.
- Dip of contact: There is small variation along with the change of dip of contact.
- Not all parts of the zero level contour for *VDR, Tilt* and *Theta derivatives* refer to actual structural edges: Since faults have a specific length and zero contour continues until it closes on themselves, parts of them are artificial and do not respond to geological edges.
- Scale: Larger features may overlap smaller ones

3.4.c.1. Amplitude/Magnitude Derivatives

Although the term *derivative* is the most common, some authors also use the terms *slope* and *gradient* when referring to them. Generally, amplitude derivatives are used to map the lateral extent of the anomalous source and their edges, but they have limitations due to their dependence on density contrasts (large contrast leads to large anomaly and respectively).

Some of the most common derivatives are described below.

i. Total Horizontal Derivative (THDR)

This derivative is generally proposed for detecting structural edges. Calculating the full horizontal derivative on gravity anomalies on grid-based data, will display maximum ridges/horsts over the boundaries defined by faults or geological contacts (Fig. 3.28). If there is a good gravity station coverage, both large and small edges with both large and small density contrasts will be identified. If *B* is the residual or regional gravity field, its calculation is based on the following equation:

$$THDR = \sqrt{\left(\left|\frac{\vartheta B}{\vartheta x}\right|^2 + \left|\frac{\vartheta B}{\vartheta y}\right|^2\right)}$$

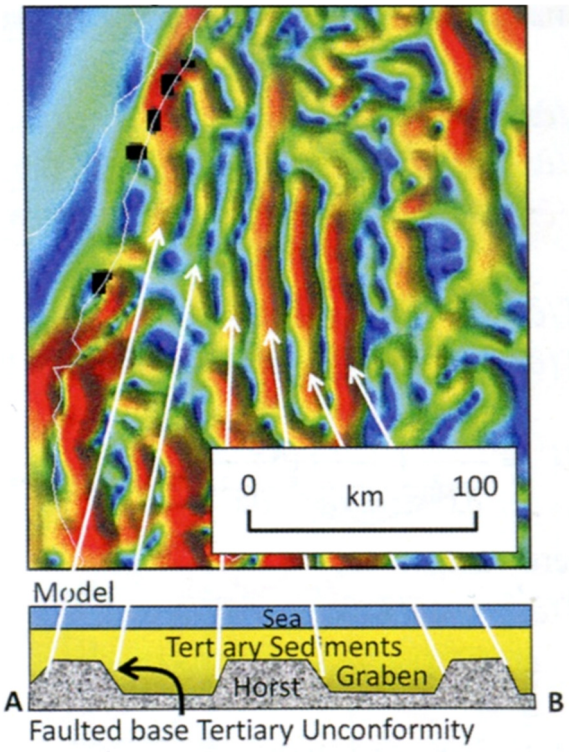

Figure 3.28: An example of THDR from Gulf of Thailand (Fairhead, 2015).

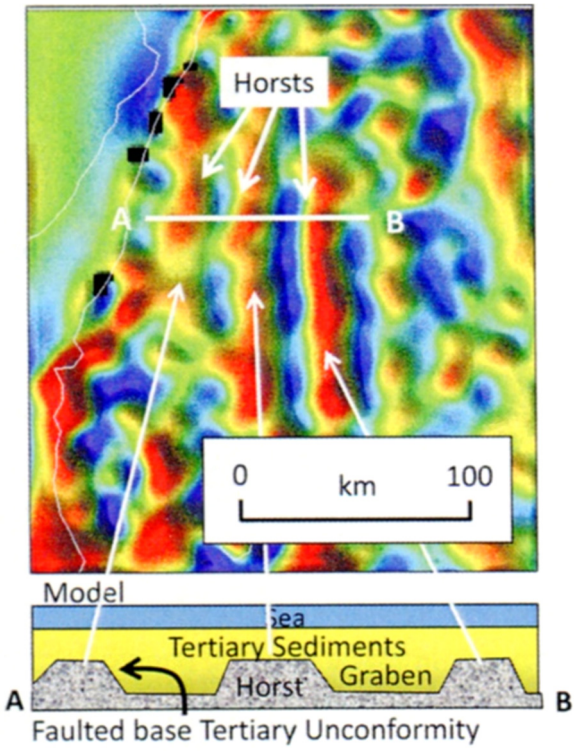

Figure 3.29: An example of VDR from Gulf of Thailand (Fairhead, 2015).

ii. First Vertical Derivative (VDR)

The *VDR* is considered to be an important derivative, since it is included in other derivatives also, such as the *Analytic Signal*, *Tilt*, *Theta* etc. It has good results for both location and edge detecting of shallow structures (larger values), since it is not sensitive to deep regional sources, because of their small vertical gradient (smaller values). The edges are identified from the zero level of the derivative, the source is identified from the maximum of the *VDR* itself and the structure also is characterized with positive or negative density (Fig. 3.29). Its definition is based on$-\vartheta T/\vartheta z$.

There are two methods of calculating the VDR. The first one is the FFT method, by analyzing the spectral content. The second method is the ISVD, a more stable method, where Laplace's equation is being used. Then, $VDR = \vartheta T/\vartheta z = \int \vartheta^2 T/\vartheta z^2 \vartheta z$. During the FFT method, noise might insert affecting the result, while with ISVD method there is no noise.

iii. Second Vertical Derivative (SVDR)

The *SVDR* identifies contacts over zero value levels, but it is also controlled by other parameters (Fig. 3.30). Although it is considered quite easy to calculate *SVDR*, the resulting maps may be noisy. For that reason, quantitative interpretation is limited to the determination of edges by the zero level. It is also depended on the grid size and the data distribution. Its calculation can be derived by using FFT or by using again the Laplace's equation. From maps It is calculated by $\vartheta^2 T/\vartheta x^2$ and$\vartheta^2 T/\vartheta y^2$.

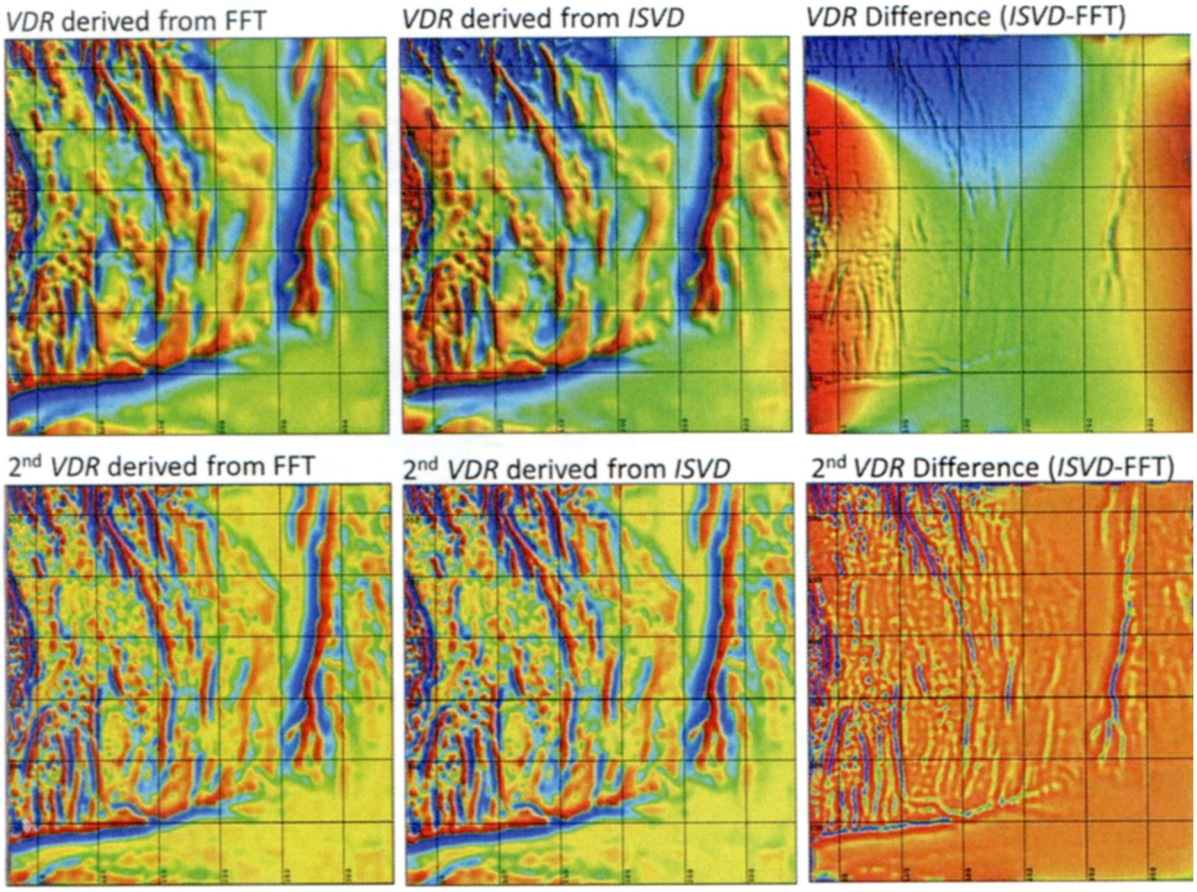

Figure 3.30: Comparison of VDR and SVDR, with FFT and ISVD method (Fairhead, 2015)

iv. Dip-azimuth Derivative

The *Dip-azimuth Derivative* method produces an image of false color shading series where all the 2D structures can be identified. Illumination counts a lot on this procedure, so practically four different color lighting directions should be used (from N, S, W and E).

v. Analytic Signal (AS)

Analytic Signal is not applied a lot to gravity measurements due to their sparser nature (compared to magnetics), which makes the calculation less reliable (Nabighian *et al*., 2005).

3.4.c.2. Phase derivatives

The data enhancement procedure is accomplished not only with the amplitude derivatives, but also with phase derivatives, which can also be very helpful. The most common of them are described below.

i. Local phase (ϑ)

The *local phase* anomaly can be used in line-based data and not in grid-based, due to its directional dependence of x. The *local phase* anomaly of a profile, in the x direction, practically contains two derivatives, the *VDR* (*ϑT/ϑz)* and the *horizontal gradient in the x direction* (*ϑT/ϑx)* and can be positive or negative. It is expressed by the equation:

$$\theta = tan^{-1}\left(\frac{\vartheta T}{\vartheta z}\Big/\frac{\vartheta T}{\vartheta x}\right)\ (in\ x\ direction)$$

ii. Tilt derivative (Tilt)

Tilt derivative was first introduced by Miller & Singh (1994), defined as the ratio of the *First Vertical Derivative (VDR)* to the *horizontal derivative (THDR)*. The *Tilt derivative* enhances all features in even way, resulting in edge mapping that are not biased toward the largest magnitude. It can be only positive and its zero level closely adumbrates the structural edges (Fig.3.31). It is preferred when we have to deal with small density contrasts, since it prevents the domination of the large ones. The following equations are used for *Tilt derivative*:

$$Tilt = ATAN\left(\frac{VDR}{THDR}\right)\ in\ radians\ (\pm 1.57rad) or\ degrees\ (\pm 90°)$$

The above equation will be changed to the following two depending on the data type:

$$Tilt = \sqrt{\left(\frac{\vartheta y}{\vartheta x}\right)^2}\ for\ profiles$$

$$Tilt = \sqrt{\left(\frac{\vartheta T}{\vartheta x}\right)^2 + \left(\frac{\vartheta T}{\vartheta y}\right)^2}\ for\ grid$$

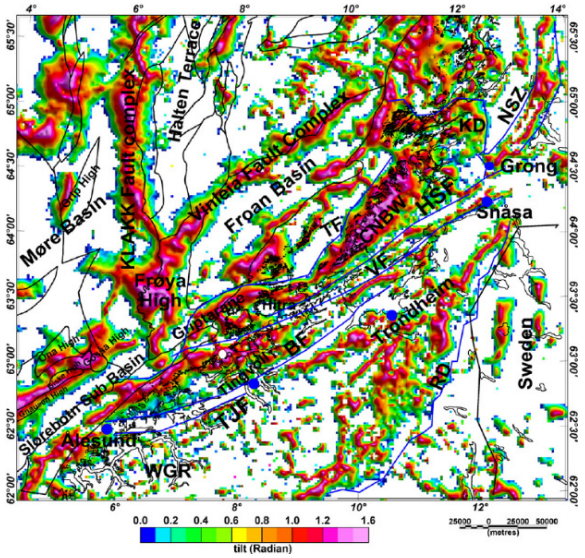

Figure 3.31: An example of Tilt derivative map. Only the positive components are shown, in order to see the structures more clearly (*Nasuti et al., 2011*)

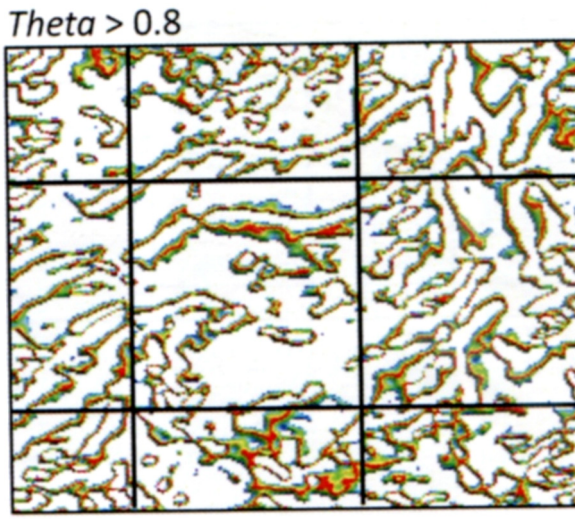

Figure 3.32: An example of Theta derivative of the Erindi area, Namibian. The values above 0.8 have been isolated. (*Fairhead, 2015*)

iii. Theta derivative (cos Tilt)

Practically, *Theta derivative* is the cos(*Tilt*), which means that when *Tilt*=0➔*Theta*=1. This can be very helpful to structural mapping, since edges will be tracked by the maximum values equal to 1, or at least >0.80 (Fig.3.32).

3.4.c.2. Grid Averaging

In several cases, the analytical method was applied based on mathematical operations, mostly on grid-based data. The average value of a circle of points replaces the gravity field at its center. The difference between the original and the average value, gives the residual value. It is considered an empirical procedure. Several types of 'rings' were used, such as 4-point rectangular grid, 8-point rectangular grid and 6-point hexagonal grid.

3.4.d. Interpretation and Depth determination

It is important to know that the interpretation of gravity anomalies is not unique, since different density distributions can produce similar or even same anomalies. The interpreter should always take into account the aim of the gravity survey, the possible target and of course the geological relations with the gravity data.

After all the necessary processing procedures described in the previous sections (data reduction, anomaly separation etc.), the isolated residual gravity anomaly has to be interpreted based on the subsurface mass distribution.

Depth estimation for gravity data is not as popular as for magnetic, since gravity anomalies are controlled by the corresponding anomalous mass, its center and overlying geological formations. All parameters of the gravity anomaly field are taken into consideration (amplitude, wavelength, gradient, phase) in order to gather information about the source parameters, such as the depth, the shape and the location. There is also a rule stating that gravity effects are proportional to the model length scale.

3.4.d.1. Gravity effect of simple shapes

The study and iterative modelling (Bhattacharyya, 1978) of the gravity effects of simple shapes, have contributed to understanding the kind of information that can be retrieved from the anomaly curves. For example, it has been investigated how the aspects of a gravity anomaly curve provide indications for the depth, shape, density contrast and total mass of the causative body.

The first methods used for depth determination, mostly for line-based gravity data, were based on measurements of specific parameters, such as the amplitude, slope and width of the anomaly curves. Depending on the shape of the causative body, which is simulated with simple geometric model patterns, such as sphere, cylinder, sheet etc., the corresponding equation for the depth determination was proposed.

In the following paragraphs, we present some examples of gravity anomaly curves that are generated due to the existence of simplified shaped causative sources. The first example (Fig.3.33) illustrates the gravity effect produced by a sphere of radius R and density contrast $\Delta\rho$, buried at depth z equal to 2 and 4 km below surface. This illustrates how the depth of the center of this spherical body affects the peak amplitude of the anomaly, resulting in smaller

amplitudes as the depth increases. Of course, for a given depth, different combinations of the density contrast *Δρ* and *R* can generate the same anomaly. This is due to the ambiguity of the gravity data.

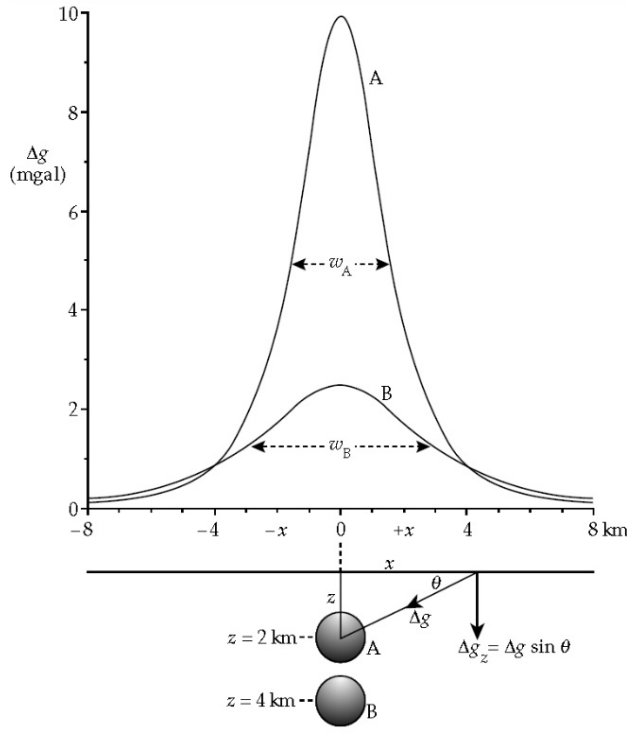

Figure 3.33: Gravity anomaly curves for spherical causative bodies of same radius R and density contrast Δρ, buried in different depths (*Lowrie, 2007*)

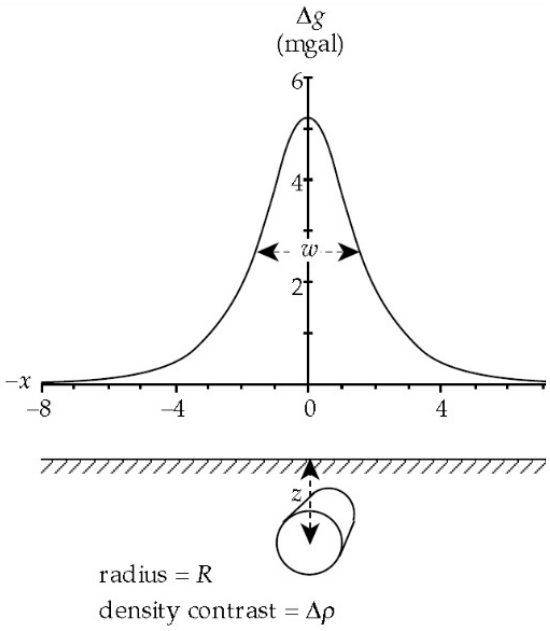

Figure 3.34: Gravity anomaly curve produced by an infinite horizontal cylinder (*Lowrie, 2007*)

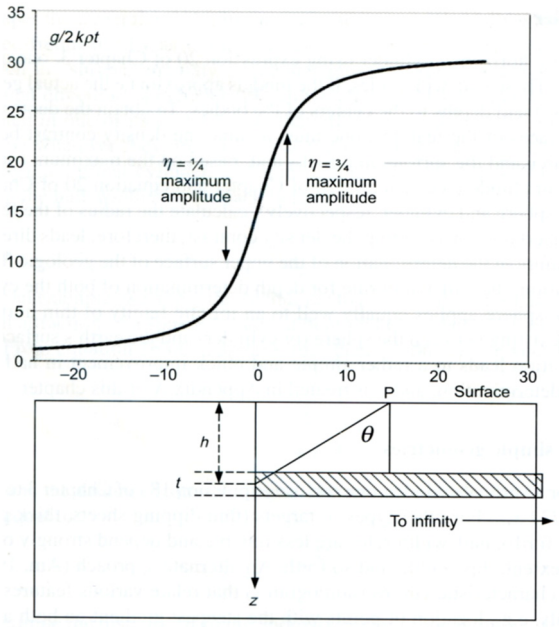

Figure 3.35: Gravity anomaly curve of a semi - infinite horizontal sheet (LaFehr & Nabighian, 2012)

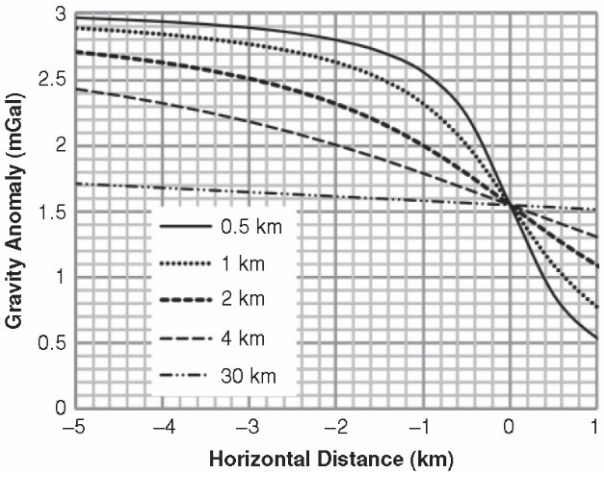

Figure 3.36: Gravity anomaly for a simple fault with variable depth (*Long & Kaufmann, 2013*).

Furthermore, an anomaly source mass simulated as an infinite horizontal cylinder produces similar anomaly curves (Fig. 3.34). On the other hand, a semi-infinite horizontal sheet produces a different anomaly curve, as it is illustrated in Figure 3.35, which variates with the depth of the fault (Fig. 3.36).

Of course, we have to take into consideration the fact that sometimes, an anomaly curve includes the combined effected of more than one causative body. For example, in Figures 3.37-3.38, we observe the anomaly curve originated from the combined anomaly of both sheets of a two-sided fault.

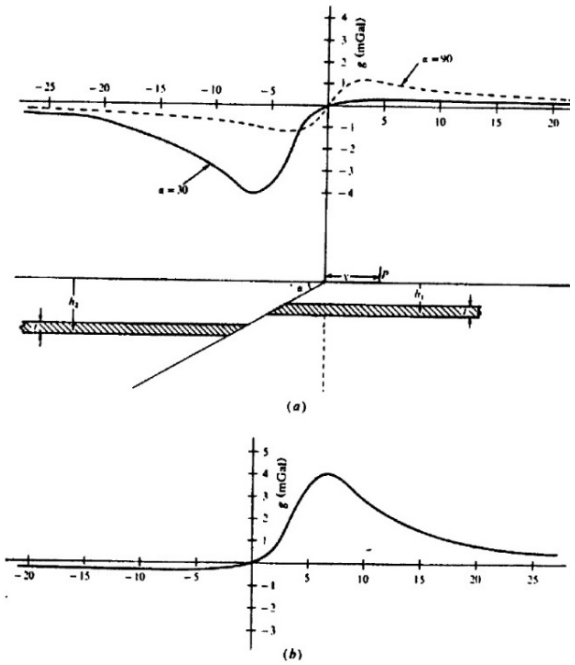

Figure 3.37: Two-sided fault anomaly. (*Telford et al, 1990*)

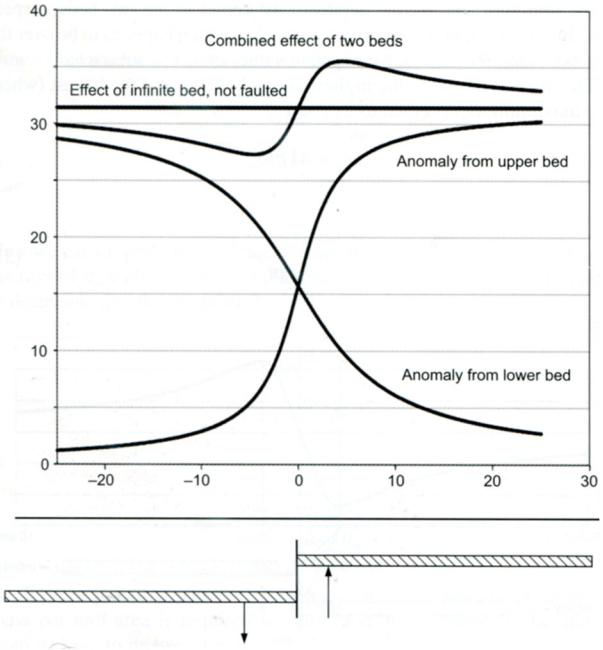

Figure 3.38: The combined gravity effect included in one gravity anomaly curve, due to a two-sided fault (*LaFehr & Nabighian, 2012*).

3.4.d.2. Standard Depth rules

A gravity anomaly curve, produced by a simplified source body shape, is generally characterized by a maximum value, Δg_{max}, located at x_{max}. Therefore, as $x_{1/2}$, we define the half width at the half value of the Δg_{max} (Fig. 3.39).

The most popular technique for depth determination of profile-based gravity data is the '*Half-Width rules*', proposed by (Henderson & Zietz, 1948). They are based on the half-maximum width $W_{1/2}$ of the anomaly curve and the depth is provided according to the estimated causative body shape, which will define the corresponding equation of Tables 3.2 & 3.3 that should be used.

Other techniques are generally based on the line of the maximum slope of the anomaly curve and its characteristics (Peters, 1949; Sokolov, 1956; Vacquier *et al.,* 1951 - Fig.3.40).

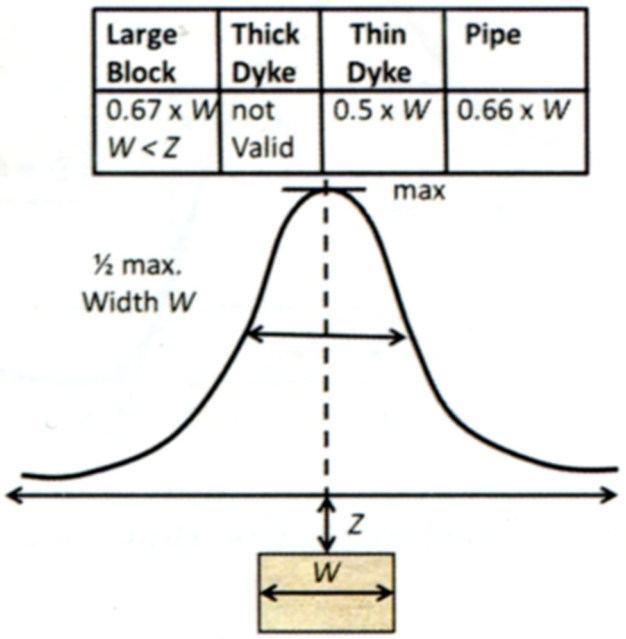

Figure 3.39: Half-maximum width rule for the depth determination of a gravity anomaly source. (*Fairhead, 2015*).

Shape of source body	Depth
Sphere	$h=1.305x_{1/2}$
Horizontal cylinder	$h=x_{1/2}$
Vertical cylinder	$h=1.732x_{1/2}$

Table 3.2: Half-width equations, depending on the anomaly mass shape

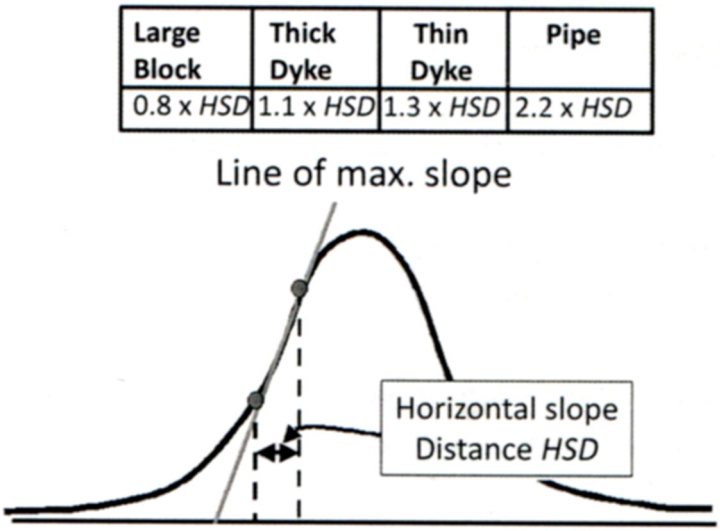

Figure 3.40: Half-maximum width rule for the depth determination of a gravity anomaly source. (*Fairhead, 2015*).

Shape of source body	Depth
Large block	h=0.8x*HSD*
Thick Dyke	h=1.1x*HSD*
Thin Dyke	h=1.3x*HSD*
Pipe	h=2.2x*HSD*

Table 3.3: Half-width equations, depending on the anomaly mass shape

3.4.d.3. Spectral Analysis

Through the procedure of *Fourier analysis*, we present the *Power Spectrum* of gravity data in a diagram of radially averaged power (squared amplitude) plotted against wavenumber (Fig. 3.41). The most popular practice is to plot the natural log of power against wavenumber, expressed in cycle per kilometer.

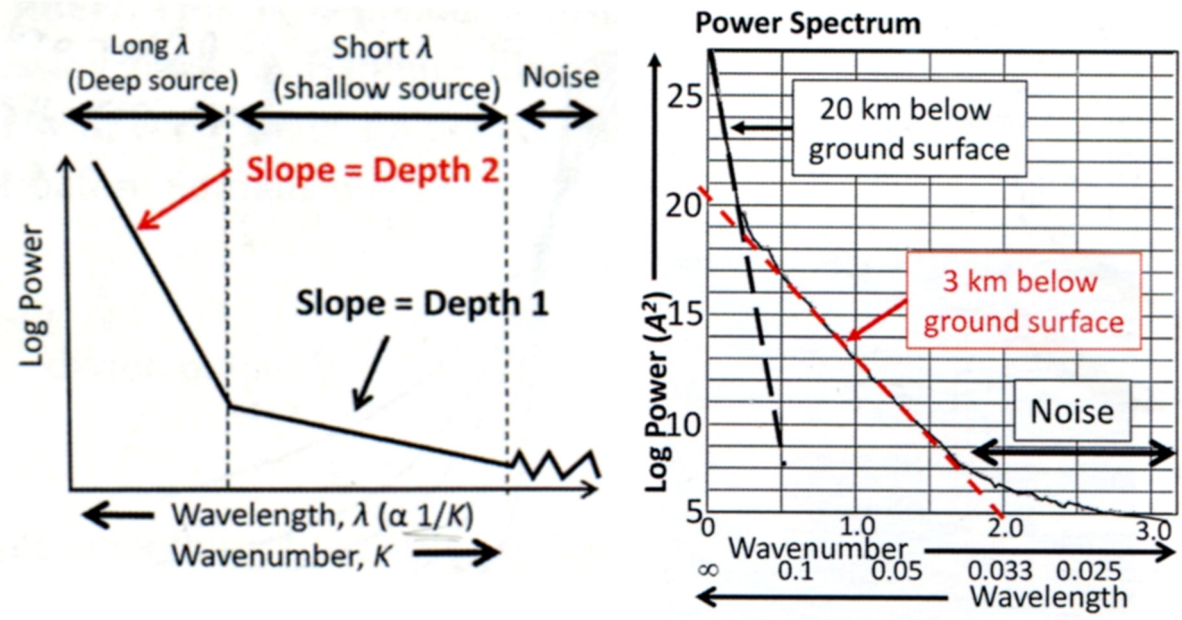

Figure 3.41: Power spectrum illustrating responses from different depths and the areas of noise. Two different examples (*Fairhead, 2015*).

The power spectrum method can contribute to the determination of cutoff wavelengths (Ali *et al*., 2017) during filtering for anomaly separation (regional-residual), separating responses from different depths of sources and the depth to top or bottom (Fig. 3.41). The depth determination is simple, since the slope of any straight-line segment of the diagram is twice the depth of the source's body top. The spectral analysis can be applied on both line-based and grid based data.

3.4.d.4. Euler Deconvolution

Euler deconvolution, proposed firstly by Hood (1965), is widely used in aeromagnetic interpretations and less in gravity ones. Although it does not require the knowledge of density variation or the direction of the anomaly body, namely an interpretation model, it is considered valid only for homogenous functions. This is the reason for its low popularity and application for gravity surveys. However, Euler deconvolution can illustrate contracts at a deeper level, according to the center of mass.

Practically Euler methods are considered as derivatives method of first, second or even third order. The method uses three orthogonal gradients of the gravity field along with the field itself, in order to determine the location and the depth of the target. Several Euler methods have been developed and will be briefly described in the following section.

i. Standard Euler

The *Standard Euler* (Reid *et al.*, 1990; Thompson, 1982) obtains its solutions by inverting Euler's homogeneity equation over an unchanging window of data at every grid point. It is considered to be a first-order derivative and its equation is:

$$(x - x_0)\frac{\vartheta G}{\vartheta x} + (y - y_0)\frac{\vartheta G}{\vartheta y} + (z - z_0)\frac{\vartheta G}{\vartheta z} = -N(B_Z - U_Z) = constant$$

where x_0, y_0, z_0 are the unknown coordinates of the causative body center, x,y,z the known coordinates of the observation point, B_Z an unknown constant background value for U_Z and N is the structural index of the source type (Table 3.4). The input parameters required are the window size and *Structural Index (N)*, maximum % depth tolerance and maximum distance to accept.

The application of Euler deconvolution method on grid-based gravity data of an nxn window provides an overdetermined equation system from which we can determine the desired information to solve the four unknown (x_0, y_0, z_0, N). The process is repeated for every window position, covering the entire grid and generating thousands of solutions, illustrated by circles of different depths according to the depth of the solution. An acceptance level should be set in order to remove the poor quality solutions.

Similar procedure takes place for line-based data, with an operator length moving along the profile with a certain rate, providing solutions at each step. The *Standard Euler* method is still considered to be the more reliable, but faces some limitations such as distinguishing anomalies from 2D and 3D structures, determining if the solution is reliable or poor.

Type of Body	SI
Sphere	2
Horizontal Cylinder	1
Line	1
Sheet edge / Fault	0

Table 3.4: Structural Index of simple bodies

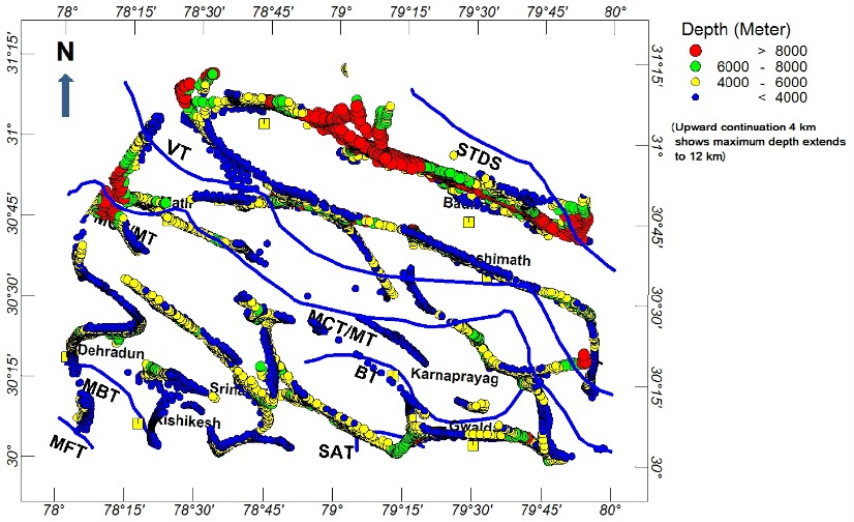

Figure 3.42: Map of Euler source depth solutions.

ii. Laplacian XY Euler

The *Laplacian XY Euler* (Fairhead *et al.*, 1994) is a first-order derivative method, using the Standard Euler method but minimizing the poor solutions (by 65%). It restricts the wavelengths with the application of the Laplacian filter of the *Total Horizontal Derivative* in order to determine the best window size. Moreover, the most reliable solutions are located directly over the anomaly source, which is at the maximum of the *THDR*.

iii. Tensor Euler

Tensor Euler method proposed by Mushayandebvu *et al.,* 2000, is a second-order derivative method, which practically uses all gravity-gradient tensor components (mainly from marine and airborne surveys). It removes interpolation errors from the grid and can invert structures using five independent tensors at the same time.

iv. Hilbert Euler

This method was proposed by Nabighian & Hansen (2001), modifying the extended Euler method for a 3D natural generalization, using Hilbert transforms. It is considered a more stable algorithm, providing at each point three equations instead of one.

3.4.d.5. Adapted Conventional tilt-depth method (tensor gravity)

This tensor method was proposed by Salem *et al.* (2011), it is a second-order derivative filter, using the *Adaptive Tilt-depth* for tensor gravity data, defined as:

$$\theta_a = tan^{-1}\left[\frac{G_{ZZ}}{\sqrt{G_{ZX^2}+G_{Zy^2}}}\right]$$

A scale value that is related to the nature of the source (2D or 3D) on the three components of the Full Tensor Gradiometer data (G_{ZX}, G_{zy}, G_{ZZ}) is being used.

The estimation of the depth and location of buried gravity bodies such as point, line or sheet is possible with this method, modifying the above equation properly. Moreover, it can also enhance the resolution of the tensor gravity anomalies produces by weak density contrast. The *Adaptive Tilt* is independent of the density variation effect since it consists of the ration of vertical and horizontal derivatives. Nevertheless, there is information contained regarding the wavelength content of the anomaly.

3.5. GRAVITY INVERSE 3D MODELLING

Gravity Inversion is the automated numerical procedure of iteratively constructing a subsurface model, based on the response of the observed gravity data and other reliable information. Practically through inversion, the best solution (misfit) of certain variables is expected. Moreover, the different components of a density model influence the one each other, affecting all variables. The clue is that during the inversion, the qualitative information turns into quantitative.

It is important to keep in mind that inversion generally does not have a unique solution. Here the contribution of the interpreter is crucial, since he will also take into account other constrains such as the geological regime. Nevertheless, the number of possible solutions can be reduced by fixing any known parameters evolving in the procedure (a priori information), such as the density or any source attribute.

The first gravity modelling approach executed with computers was based on the equations for 2D bodies of polygonal cross section, introduced by Talwani *et al*. (1959). Several

modifications of these equations led to the 2.5-D modelling (Saltus & Blakely, 1983; Webring, 1985). The first signs of 3D gravity modelling were by Talwani & Ewing (1960), evolved by Nagy (1966) with the rectangular prisms and Hjelt (1974) with dipping prisms. A generalized 3D inversion was introduced by Li & Oldenburg (1996, 1998, 2000; 2003), using the Tikhonov regularization along with a model objective function, measuring the structural complexity of the density contrast. A depth-weighing factor is contributing to setting a priori information and consequently improving the solution. The generalized 3D inversion allowed the gravity inversion to deal not only with the anomalies interpretation but also with the regional and continental problems.

The general case of gravitational attraction, where *ρ(Q)* is the density function at a point *Q(ξ,η,ζ)* inside a volume *V*, is provided by the equation:

$$g_z(x,y,z) = k \int_V \frac{\rho(\xi,\eta,\zeta)(\zeta - z)d\xi d\eta d\zeta}{[(\xi - x)^2 + (\eta - y)^2 + (\zeta - z)^2]^{\frac{3}{2}}}$$

or more compact

$$g_z(P) = \int_V \rho(Q) G_z(P,Q) dV$$

The vertical component of gravitational attraction of an observation point *P(x,y,z)* of distance *r* at point *Q*, is provided by Green's equation:

$$G_Z(P,Q) = \frac{1}{r^2}\frac{\zeta - z}{r} = \frac{\zeta - z}{[(\xi - x)^2 + (\eta - y)^2 + (\zeta - z)^2]^{\frac{3}{2}}}$$

Gravity inversion is carried out mainly in two ways, based either on the causative body geometry or on the density distribution. Generally, the density distribution inversion needs less input information and is applicable at different stages.

The data misfit is the most important part of the inversion. Even when a solution has been found, it is important to evaluate its quality. This means the consistency of the data and side conditions, the acceptability of the parametrization, the uncertainties characterizing the variables and the suitability of the problem for the specific case. Sometimes one single parameter needs to be evaluated and some others a combination of them.

Summarizing, there are four important elements concerning the inversion algorithm and the *a priori* information. These are:

i. The data misfit
ii. The model objective function (reference model and 3D weighing functions)
iii. The depth weighing factor
iv. The bound constraints

3.5.a. 3D Density inversion

The approach of the density inversion aims to determine the underground density distribution and contrasts, based on the surface observed gravity data. The procedure is controlled by some conditions, based on the types of structures and the accepted tolerances. The subsurface under the investigated area is divided in a large number of adjacent rectangular cells (Fig. 3.43) and during the inversion, a constant density for each cell is attempted to be determined. The datum at each study area is the sum of contributions from the all the cells.

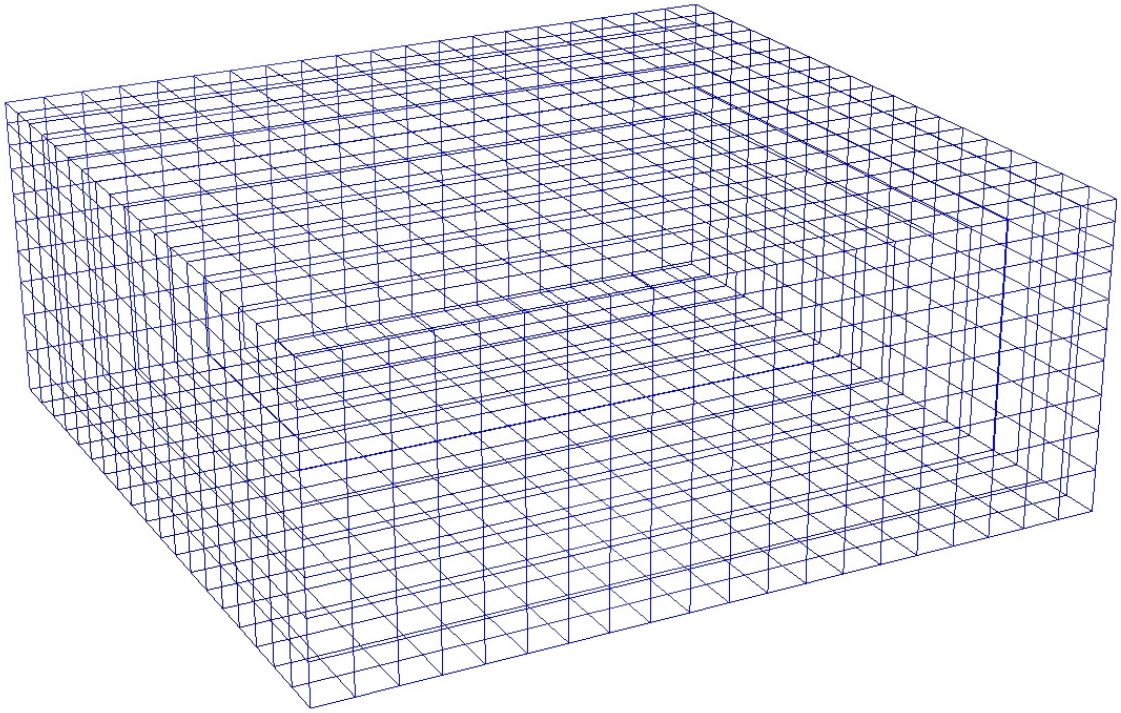

Figure 3.43: Division of the underground area of 3D gravity inversion in a large number of rectangular cells. A density value will be determined during the inversion.

i. The λ parameter

The majority of the algorithms for inversion are based on the Tikhonov regularization, (Tikhonov & Arsenin, 1977) during which the data fit a solution with a least model roughness. The structural characteristics of the model (type of boundaries, smoothness, possible dips etc.) need to be described for the proper function to be set. The model roughness can be reduced by minimizing the first order derivative of the density function.

Moreover, the embedded noise of the observed data (instrument noise, measurement errors etc.) has to be removed. Considering the noise is Gaussian (LaFehr & Nabighian, 2012), the data misfit has the expression:

$$\Phi_d = \sum_{i=1}^{i=n} \left(\frac{d_i - d_{i,calc}}{\sigma_i} \right)^2$$

where σ_i are the estimated standard deviations, d_i the observed data a location *I* and $d_{i,\,calc}$ the calculated model values at the same locations. Therefore, the function is minimized as following:

$$\Phi(\rho) = \Phi_d + \lambda\Phi_\rho(\rho)$$

where 0<λ<∞ is a constant called regularization parameter.

Very small values of λ lead to better data fit of the model without increased model complexity input. Accordingly, big values of λ will lead to larger data misfit. The proper λ for a gravity model should be chosen for an acceptable model. To obtain the most suitable value of λ, various values are used and then a diagram is created for the change of data misfit according to the change of λ (Fig. 3.44). Observing the diagram, we can figure out that for small values of λ, the model structures change a lot but the data misfit is not affected that much. The opposite takes place for large values. Therefore, the point between these two areas is considered to be the most appropriate.

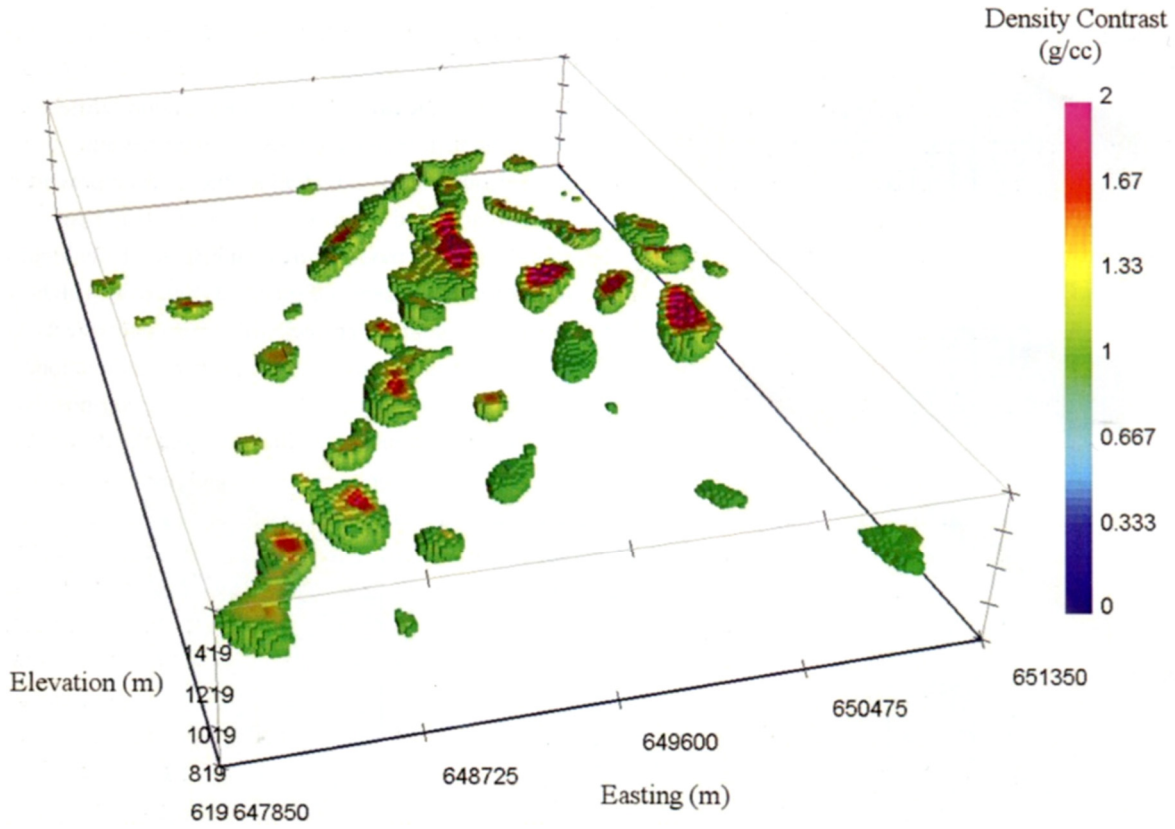

Figure 3.44: Density model inversion (*Li & Krahenbuhl, 2015*)

There is also the *Cross-Validation (GCV)* method (Golub *et al.,* 1979; Wahba, 1990) for the better determination of the parameter λ. It is obvious that the λ parameter is a crucial parameter for the determination of the model. Finally, it is important to mention that the inversion procedure should be carried out after the isolation of the residual anomaly.

ii. Depth Weighing Factor

The solutions of an inversion can be quite a lot. Therefore, any depth information and actual density distribution is more than helpful to the procedure, in order to constrain it somehow, minimizing the possible solutions.

For that reason, *generalized 3D inversion* and a depth-weighing factor was introduced by Li & Oldenburg (1996), as *a priori* information for a better solution formed as following:

$$w(z) = \frac{1}{(z + z_0)}$$

where z_0 is depended on the observation height and cell size.

For data collected on a relatively smooth elevation surface, the above weighing factor is simple and effective, but for rugged areas, the depth-weighing factor is not applicable.

iii. Bound Constraints

Except the depth-weighing factor, setting bound constrains on the model densities also minimizes the possible solutions and makes the procedure more stable. For example, there might be a known upper bound that will help in the inversion procedure. Taking into account that density contrasts usually have a well-defined range, the inversion is solved as inequality-constrained optimization (Li & Krahenbuhl, 2015).

iv. Density-based or Distance-based Weighing Factor

For gravity data acquired on rugged areas, instead of the non-applicable depth-weighing factor, we can apply a density-based weighing factor, by defining a root-mean square (RMS) density.

Otherwise, a weighing factor based on the distance between cells and observation locations can be applied.

v. Binary inversion

A special case of density inversion known as *Binary inversion* (Li & Krahenbuhl, 2015), is when the density at any location can take only one value between two possibilities, with two distinct values. Binary inversion method belongs to a category known as *lithologic inversions*, aiming to reconstruct distinct lithologic units with specific physical properties (Li & Krahenbuhl, 2015). This method was introduced by Krahenbuhl & Li (2006), developed for imaging salt domes using Tikhonov regularization. Moreover, they are applied in time-lapse studies (Krahenbuhl & Li, 2008) and studied for dynamic processes such as aquifer storage (Davis *et al.*, 2008).

Practically, it is a constrained inversion of high level during which the objective function subject is minimized, since the model parameters can get only one of the two possible values at each location.

3.5.b. 3D Geometric / Boundary inversion

The approach of the geometric inversion aims to determine the parameters (depth, width, dip etc.) of a geometric shape (sphere, cylinder, polygon etc.) assumed to be the target/source of anomaly, based on the observed data.

Many authors have dealt in the past with geometric inversion, starting with Bott (1960) who investigated the shape of the sedimentary basing simulating them with 2D rectangular blocks with known density contrast and Danes (1960) who investigated the determination of the top of a salt dome. Cordell & Henderson (1968) extended the inversion to 3D, while Parker (1972) and Oldenburg (1974) evolved in the Fourier (wavenumber) domain. Density-depth functions and other constrains proposed by many authors (Pedersen, 1977; Reamer & Ferguson, 1989; Barbosa *et al*, 1997) and applied in oil and gas exploration (Nagihara & Hall, 2001; Cheng *et al.,* 2003).

This method requires more known data than unknown factors and it is considered to be more simple than the density inversion but more time-consuming. Moreover, normalization of the data is usually essential because the variables (depth, width, dip etc.) have different kind of dimensions. For a problem with *n* unknown parameters to investigate, we have a single value of the objective function for each pair of these parameter values (LaFehr & Nabighian, 2012).

Monte Carlo techniques are being used in order to minimize the required time. According to them, various models are selected randomly from the many available. Therefore, for each model the forward problem and data misfit are being calculated. The interpreter should have a good knowledge of the area geology and the general limitation of this kind of inversion.

i. Cordell & Henderson method (3D)

Cordell & Henderson (1968) introduced the first 3D automated gravity modelling.

It is an iterative method executed in four steps:

i. Form the input Residual anomaly data in order to create the initial model.

The calculation of the source structure of a single body is calculated, based on the Residual anomaly data. The initial model is created by the determination of thickness at each grid node from the residual value and the Bouguer infinite slab equation.

Three types of starting model are proposed considering a horizontal reference plane as standard (Fig. 3.45): *Building-down* (e.g. for sedimentary basin)*, Building-up* (e.g. for granite intrusions) and *Building Symmetrically* (e.g. for horizontal intrusions).

ii. Calculate the gravity effect of the initial model

The gravity effect of the source body is calculated, usually considering the shape as vertical prism or line.

For a vertical prism with width *W*, height *T*, depth of top *d* the gravity effect at a point A, which is all over grid node locations is:

$$\Delta g_{vert.cyl} \cong 2\pi G\rho \left\{ T - \sqrt{(d+T)^2 + \frac{W^2}{\pi}} + \sqrt{d^2 + \frac{W^2}{\pi}} \right\}$$

and accordingly for a vertical line with height *T* and distance from the point *R*:

$$\Delta g_{vert.lin} = G\rho W^2 \left\{ \frac{1}{\sqrt{R^2 + d^2}} - \frac{1}{\sqrt{R^2 + (d+T)^2}} \right\}$$

iii. Modify the initial model, according to the differences between calculated response and observed data.

The alteration of the prism size at each grid size is essential in order to minimize the misfit.

iv. Repeat of steps ii & iii until the best fit is obtained.

The termination of the repeat process is achieved either by setting a maximum number of iteration or by setting a threshold value of RMS. Usually the first five iterations alter the model rapidly.

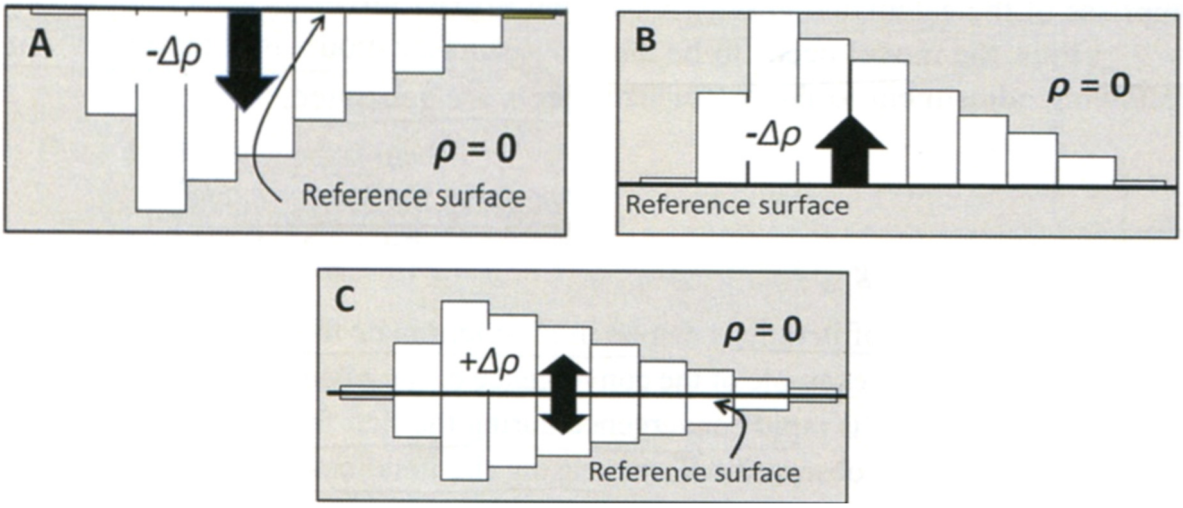

Figure 3.45: Types of building the initial model. (*Fairhead, 2015*).

ii. Enhanced Cordell & Henderson method (3D)

The original method of Cordell & Henderson (1968) has been modified by replacing the constant density with a linear density-depth function and for the gravity response of a right rectangular prism. This method was proposed mainly for the sedimentary basins cases (Fairhead *et al.* 2012; 2013), where the sediments' density increases with the depth while the basement density remains constant.

Therefore, for linear change of density contrast $\Delta\rho=\alpha_o+\alpha_1 z$ we have the equation:

$$\Delta g_z = \frac{G(a_0 + a_1 z) z \vartheta x \vartheta z \vartheta y}{(x^2 + y^2 + z^2)^{3/2}}$$

where the term a_1 will be negative for linear varying density with depth.

3.6. DENSITY

In gravity surveys, the physical quantity practically investigated is the density of the subsurface geological formations and its lateral variation. Density evolves in the data reduction procedure, in Bouguer correction (2.67 gr/cm^3) and terrain corrections. Furthermore, it is the most important parameter (or even constraint) in modelling procedure since it can control the shape, depth and magnitude of the anomaly.

The definition of density is the mass per unit of volume of the material. Several types of units are being used for the density determination, such as gr/cm^3, referred to c.g.s, or kg/m^3, referred to SI system. For gravity exploration, most researchers still use the c.g.s. units (gr/cm^3). The same will be applied in the frame of this Ph.D. thesis.

The *Bulk density* includes all types of possible voids and is usually referred for the shallower formations (depths <4km). The bulk density (ρ_b) is a function of the matrix density (ρ_m), the porosity φ and the fluid's density (ρ_φ) located in the pores:

$$\rho_b = \rho_m(1-\varphi) + \rho_\varphi \varphi$$

Tables of bulk densities for almost all rock types have been introduced by many authors (Blake, 2013; Cara, 1994; Carmichael, 1984; Clark, 1966; Dobrin, 1976, Gutenberg, 1929; Jung, 1961; Milsom & Eriksen, 2011; Sharma, 1986; Telford *et al*., 1990). Reevaluating and updating all these references, the densities of the most characteristic rocks, minerals and materials are presented in Tables 3.5-3.10.

Table 3.5: Post-alpine densities

Type	Range (gr/cm^3)	Average / dry (gr/cm^3)	Average / wet (gr/cm^3)	Type	Range (gr/cm^3)	Average / dry (gr/cm^3)	Average / wet (gr/cm^3)
Alluvium	1.50 - 2.00	1.55	1.95	Moraine	1.50 - 2.00	1.80	-
Clay	1.30 - 2.60	1.70	2.20	Sand	1.30 - 2.30	1.50	2.00
Gravel	1.50 - 2.10	1.70	2.00	Silt	1.40 - 2.00	1.45	1.90
Marl	2.30 - 2.50	-	-	Soil	1.20 - 2.40	-	1.90

Table 3.6: Sedimentary rocks densities

Rock type	Range (gr/cm^3)	Average / dry (gr/cm^3)	Average / wet (gr/cm^3)	Rock type	Range (gr/cm^3)	Average / dry (gr/cm^3)	Average / wet (gr/cm^3)
Anhydrite	2.90 - 3.00	-	-	Limestone	1.75 - 2.90	2.55	2.65
Chalk	1.80 - 2.60	2.00	-	Marlstone	2.20 - 2.50	-	-
Coal	1.10 - 1.80	1.32	-	Rock Salt	2.10 - 2.40	2.21	--
Dolomite	2.40 - 2.90	2.60	2.70	Sandstone	2.10 - 2.70	2.25	2.35
Gypsum	2.20 - 2.40	2.32	-	Shale	2.10 - 2.90	2.10	2.40
Lignite	1.10 - 1.25	-	-	Siltstone	2.10 - 2.60	-	-

Table 3.7: Igneous rocks densities

Rock type	Range (gr/cm^3)	Average (gr/cm^3)	Rock type	Range (gr/cm^3)	Average (gr/cm^3)
Andesite	2.40 - 2.80	2.61	Peridotite	2.80 - 3.40	3.15
Basalt	2.70 - 3.30	3.00	Phyolite glass	2.20 - 2.30	2.25
Basalt tuff	2.00 - 2.30	2.15	Porphyry	2.40 - 2.90	2.74
Calcareous tuff	1.60 - 1.70	1.65	Pumice	0.40 - 0.95	0.65
Dacite	2.30 - 2.80	2.58	Quartzdiorite	2.60 - 2.95	2.79
Diorite	2.70 - 3.00	2.85	Rhyolite	2.35 - 2.70	2.52
Gabbro	2.70 - 3.50	3.03	Trachyte	2.40 - 2.80	2.60
Granite	2.50 - 2.80	2.64	Trachyte lava	2.10 - 2.70	2.40
Granodiorite	2.67 - 2.80	2.73	Trachyte tuff	1.40 - 2.20	-
Lavas	2.80 - 3.00	2.90	Tuffstone	1.30	1.30
Obsidian	2.20 - 2.40	2.30			

Table 3.8: Metamorphic rocks densities

Rock type	Range (gr/cm^3)	Average (gr/cm^3)	Rock type	Range (gr/cm^3)	Average (gr/cm^3)
Eclogite	3.20 - 3.55	3.38	Quartzite	2.50 - 2.70	2.60
Gneiss	2.60 - 3.00	2.80	Schist	2.40 - 2.90	2.65
Marble	2.50 - 2.90	2.75	Serpentinite	2.50 - 2.80	2.60
Phyllite	2.70 - 2.80	2.74	Slate	2.70 - 2.90	2.80

Table 3.9: Minerals and Ores densities

Type	Range (gr/cm^3)	Average (gr/cm^3)	Type	Range (gr/cm^3)	Average (gr/cm^3)
Chalcopyrite	4.10 - 4.30	4.20	Hematite	4.90 - 5.30	5.10
Chromite	4.50 - 4.80	-	Iron	-	7.87
Copper	-	8.70	Magnesite	2.90 - 3.12	3.03
Corundum	3.90 - 4.10	4.00	Magnetite	4.90 - 5.30	5.10
Diamond	-	3.52	Mica	2.65 - 2.95	2.80
Epidote	3.25 - 3.50	-	Orthoclase	2.50 - 2.60	2.55
Feldspar	-	2.55	Pyrite	4.90 - 5.20	5.00
Gold	15.60 - 19.40	-	Quartz	2.55 - 2.75	2.65
Graphite	2.00 - 2.30	2.15	Sulfur	1.90 - 2.10	2.00

Table 3.10: Basic elements & Artificial densities

Type	Range (gr/cm^3)	Average (gr/cm^3)	Type	Range (gr/cm^3)	Average (gr/cm^3)
Air	-	0.00	Lignite	1.10 - 1.25	1.19
Fresh water	-	1.00	Petrolium	0.60 - 0.90	-
Ice	0.88 - 0.92	0.91	Brick	1.50 - 2.10	1.70
Sea water	1.01 - 1.05	1.03	Building waste	1.30 - 2.00	-
Asphalt	1.10 - 1.20	-	Cement	2.2 - 2.5	2.40

In Tables 3.5-3.10, wide ranges of *bulk density* are observed, especially for the sedimentary rocks and the reasons are:

i. The porosity (density increases as porosity decreases)
ii. The nature of their pore fluids
iii. Age (density increases with time – Fig. 3.46)
iv. Depth burial (density increases with depth, due to higher pressures, especially for shales – Fig. 3.47)
v. Degree of metamorphism (density increases with the degree of metamorphism, because the pore spaces are filled and the rock is recrystallized).

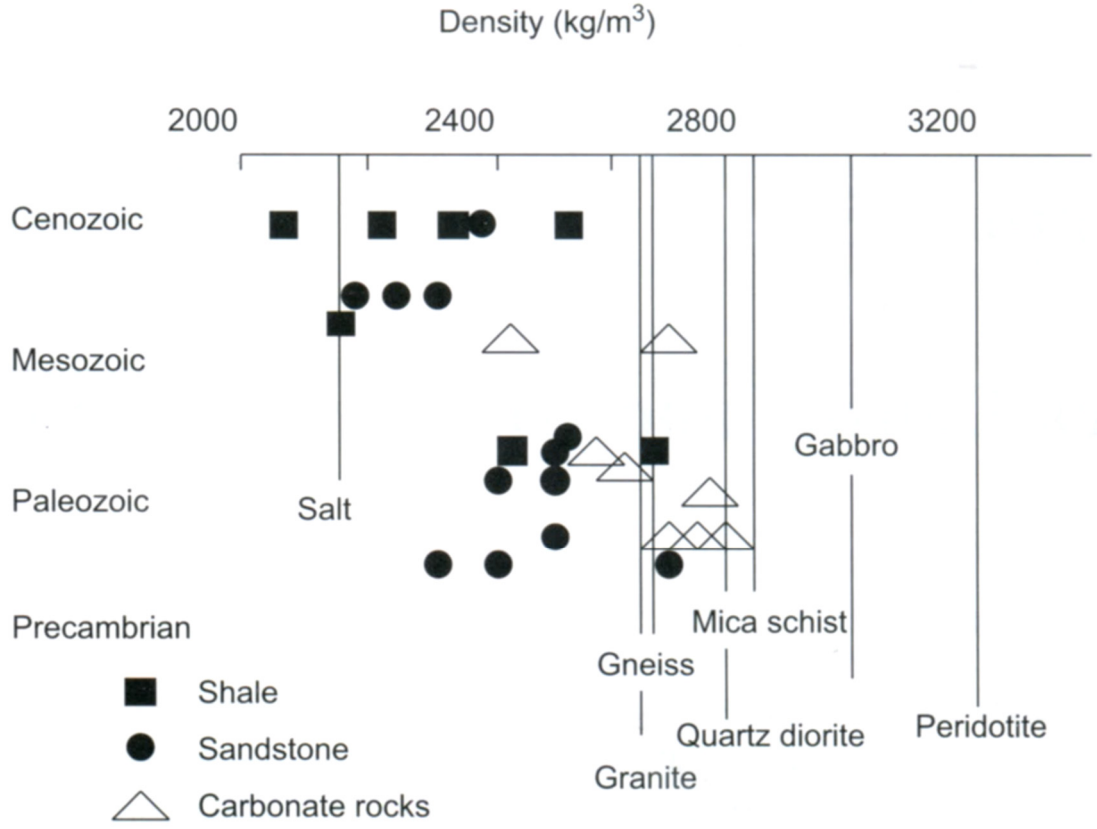

Figure 3.46: Rock densities compared to age (*LaFehr & Nabighian, 2012*).

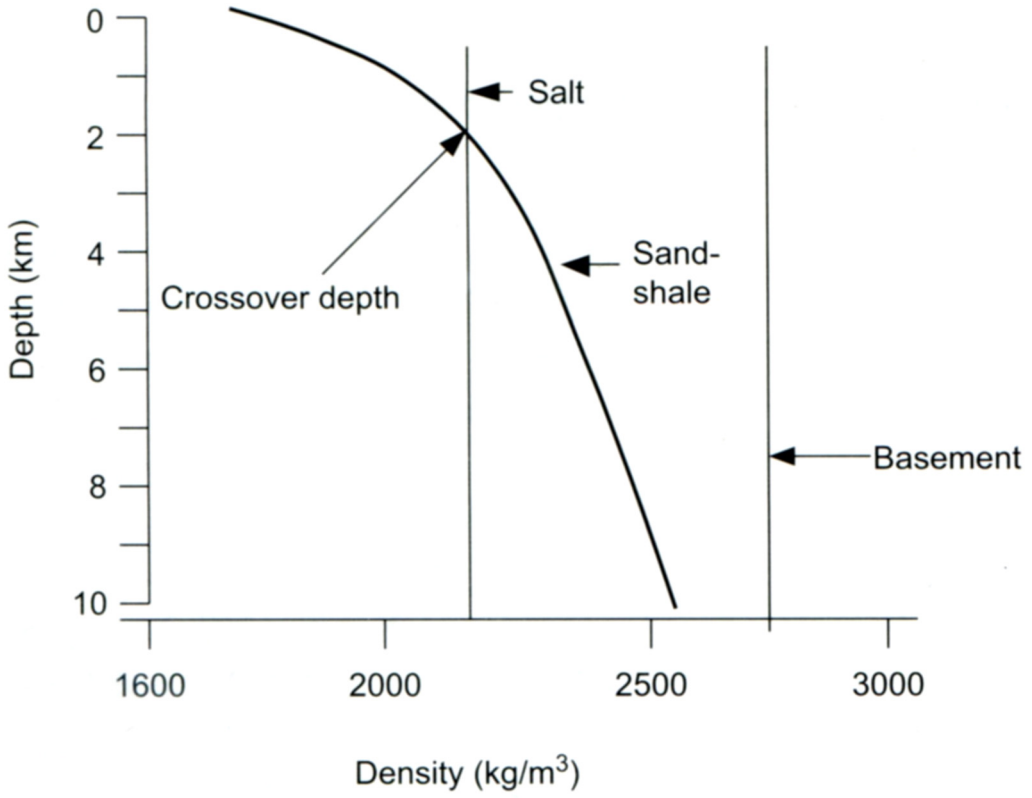

Figure 3.47: Density as a function of depth, over a salt dome (*LaFehr & Nabighian, 2012*). The depth where salt density equals to the one of the surrounding sands and shales is called crossover depth.

Generally, sedimentary rocks are less dense than igneous and metamorphic. The greater variation in density is related to their porosity and differs with depth. Volcanic rocks' density varies with composition, taking into account that the more basic will be correspondingly denser. Although igneous rocks are denser than sedimentary rocks, an overlap of density values exists between these two types. On the other hand, low-grade metamorphic rocks are generally denser than their equivalent sedimentary. Plutonic and metamorphic rocks have higher density as the degree of metamorphism increases.

Practically, density contrasts provide information about the anomaly sources and targets. For example, ore bodies are determined through positive gravity anomalies ($+\Delta\rho$) related to the environment. Similar positive anomalies can be produced by carbonate leading edges of thrust sheets, faults, anticlines and horst blocks. Negative gravity anomalies ($-\Delta\rho$) are usually detected over sedimentary basins. Finally, both positive and negative anomalies can be produced due to salt domes (depending on the surrounding environments), reefs (depending on porosity and depth) and kimberlite pipes (depending on country rock and weathering degree).

There are several ways to estimate or even better measure the density of the formations, such as borehole logging (gravity or gamma ray), laboratory measurements from outcrops' samples, seismic velocity etc.

3.6.a. Laboratory measurements

A simple way of calculating the density of the geological formations of the study area is the laboratory measurements of rock samples, cores and cuttings. It is recommended to collect some samples for density determination in all gravity surveys, especially as a reconnaissance procedure.

The whole procedure is based on Archimedes' principle. The density can be determined by weighing the sample or core in the air first (W_a) and then in the water (W_w). Therefore, the density (ρ_s) derives from the following equation:

$$\rho_s = \frac{W_a}{W_a - W_w}$$

Great care and high precision is needed during the weighing of the samples, especially for small ones. Additionally, many samples of each formation should be measured in order to have a good image of the formation's density range.

Surface rock samples cannot always ensure that they are representative of the geological formation due to weathering, but core samples tend to be representative enough. One disadvantage of this method is that differences might occur due to the differences of the atmospheric pressure in the field area and the laboratory.

This method can be applied mainly to rock type samples and not soil type, since they will be dissolved during the water weighing. Even rock type samples with high percentage of marl (e.g. marly limestone) may introduce great uncertainties during the weighing, since the marl will be melted.

3.6.b. Borehole gravity

One other method to derive density is the borehole gravimetry that can be quite accurate providing an accuracy of almost 5 μGal, based on Schmoker (1978) and LaFehr (1983).

The method evolves with gravity measurements in a vertical borehole at different depths. The gravity differences that will be derived through the procedure are produced because of the different elevation (depth) and Bouguer attraction. The deeper it gets the larger will be the gravity, since it gets closer to the Earth's center and simultaneously the upward Bouguer attraction gets bigger due to the increased material. The difference of two values in the borehole and the reduction to h_2 level (deeper), gives the following equation:

$$\Delta g = (0.3086 - 0.0838\rho \times 10^{-3})\Delta h \Rightarrow \rho = \left(3.683 - 11.93\frac{\Delta g}{\Delta h}\right) \times 10^{-3} gr/cm^3$$

The measurement is executed at the volume that is closest to the borehole. More specifically, 50% of the effect is produced by rock within of 0.7Δ*h* (h= the investigation radius) and 90% from within 5Δ*h*. Therefore, for measurements radius h≈5m, the volume that will be measured and affect the density will be 25m laterally of the borehole. As a result of that, the lateral depth of investigation is quite large and the density measurement is practically unaffected from any local alteration of the formation due to the drilling process (LaFehr, 1983).

3.6.c. Nettleton's method

A method for estimating the near-surface density of a closely spaced gravity stations profile over topographic relief (hill or even valley), that is not related with density variations was proposed by Nettleton (1939).

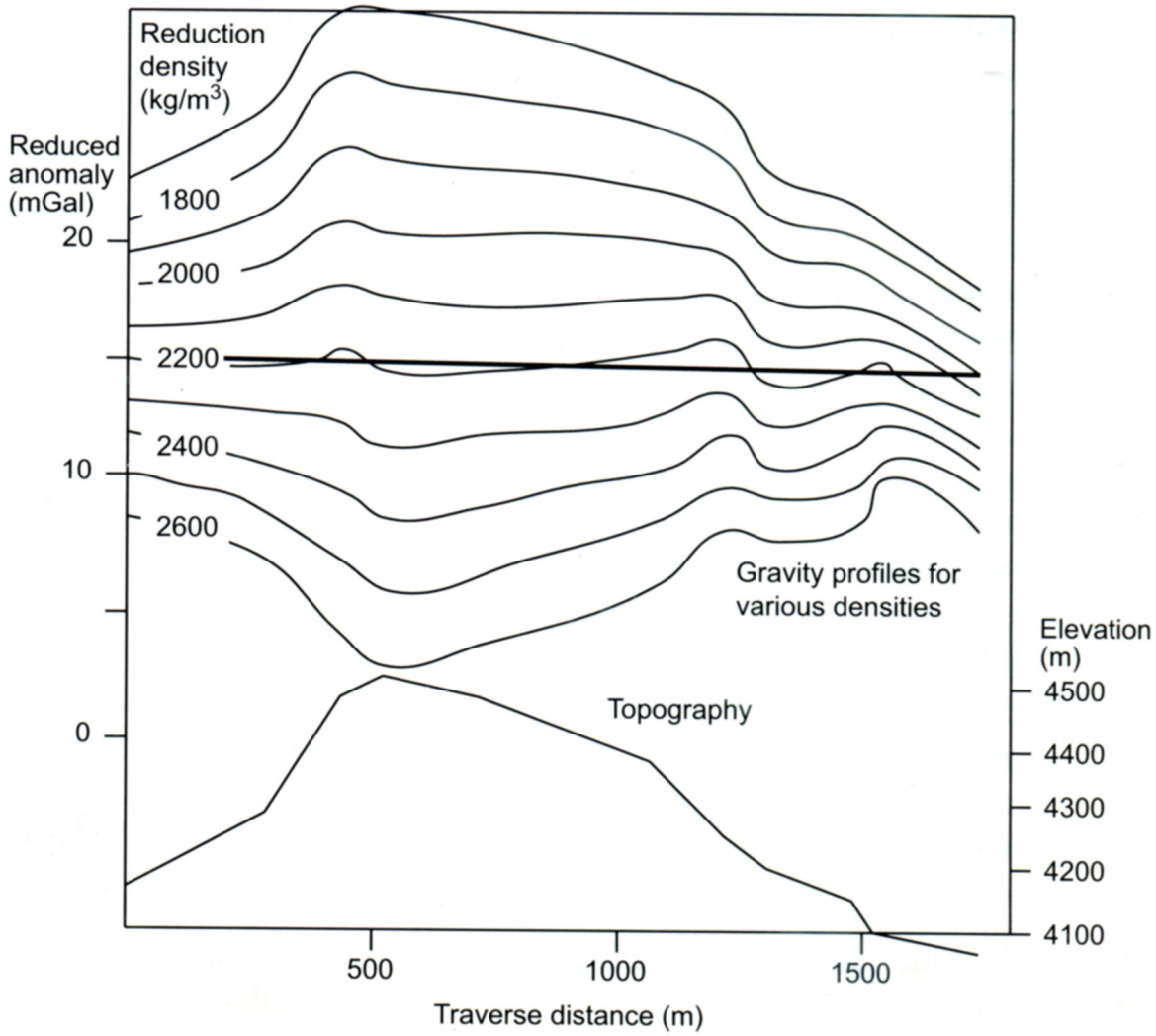

Figure 3.48: Nettleton's method for density determination (modified by *Nettleton, 1939*). The desired curved is the one with density 2.2 gr/cm^3

Within the scope of this method, the shape of the topography along the gravity profile is compared with the shape of the Bouguer gravity anomalies generated after assigning several values of density for the Bouguer and terrain correction (density dependent corrections) and

calculating the Complete Bouguer Anomaly. Taking into account that the terrain correction is less important than the Bouguer, we can neglect it and use the Simple Bouguer Anomaly.

When the assigned density is smaller than the true value, the curve will be illustrated as a positive image of the topography (Fig. 3.48). On the contrary, if the assigned density is larger than the true one, the curve will shape a negative image of the topography (Fig. 3.48). The gravity curve showing the minimum correlation with the elevation curve is the desired one and its assigned density is the correct one, since the appropriate reduction density will remove the elevation effect.

It is very important that the gravity profile cross a topographic relief (hill) with no lateral geological variations, such as contacts or faults, because it will affect the result. The best estimates of density are obtained in areas where the topography is within a single geologic unit with sharp topography variations due to recent stream erosion (Long & Kaufmann, 2013).

3.6.d. Seismic velocity conversion

Knowing the seismic velocities of the geological formations of the study area, can be very helpful. Many authors (Birch, 1960; 1961; Brocher, 2005; Carlson & Herrick, 1990; Christensen & Mooney, 1995; Gardner *et al.*, 1974; Ludwig *et al.*, 1970; Nafe & Drake, 1957; 1961) have introduced empirical curves relating the seismic velocity to the density of several geological formations. Therefore, we can compute the mean density of a body from its seismic velocity. Of course, we will have to take into consideration that differences will occur for higher temperatures and pressures (depths) and that when the seismic velocity increases, the density also increases.

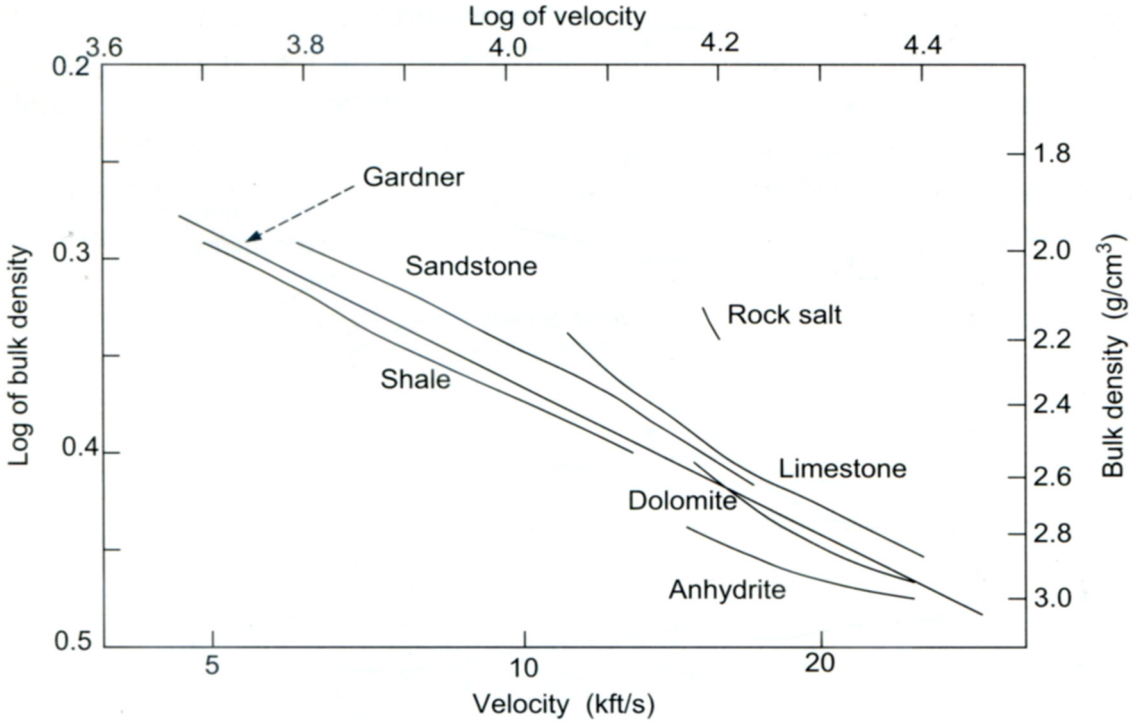

Figure 3.49: Velocity-density relationships (*Gardner et al., 1974*)

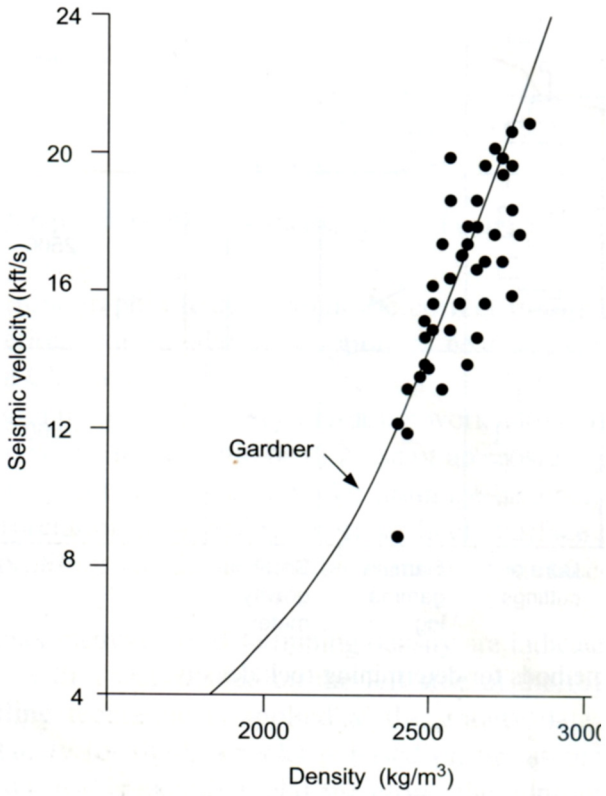

Figure 3.50: The Gardner velocity-density relationship curve (*Gardner et al., 1974*).

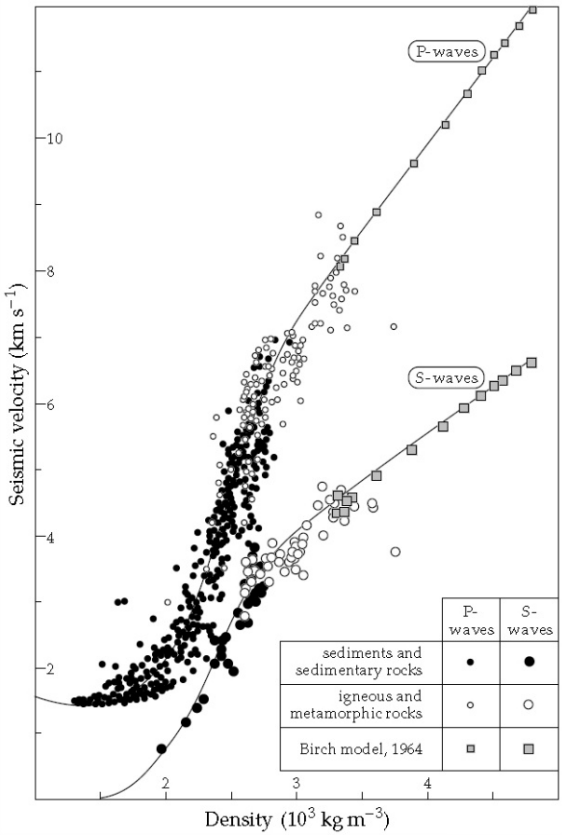

Figure 3.51: Compressional velocity for ocean sediments related to density (*Ludwig et al., 1970*).

The best empirical curve of velocity to density, for sedimentary rocks, is the one proposed by Gardner *et al.* (1974), derived from laboratory studies (Fig. 3.50):

$$\rho = 0.31 \cdot V^{0.25} \frac{gr}{cm^3}$$

where *V* is Velocity in m/s.

Due to the good response for shales and sandstone, Gardner's curve is extensively used in the oil and gas exploration (Fig. 3.49).

Birch (1960, 1961) proposed an almost linear relation, also derived from laboratory measurements, mainly on crystalline rocks under pressure and provided the equation:

$$\rho \approx a + bV_p \Rightarrow b \approx \Delta\rho/\Delta V_p$$

On the other hand, Nafe & Drake (1961), worked on unconsolidated marine sediments and basic igneous rocks, producing a non-linear relation (Fig. 3.51).

3.6.e. Gamma-gamma logging

The basis of the gamma-gamma logging is the Compton scatter of gamma rays by loosely bound electrons in the rock adjacent to the borehole. Electron density is approximately proportional to mass density although deviations exist.

The density probe contains a radioactive source of gamma rays, such as ^{137}Cs or ^{60}Co, radiating. The gamma rays photons hit the loosely bound electrons and are scattered. The scintillation receiver of the probe, counts the scattered radiation. The probe is pressed strongly on the borehole walls in order to collect properly the scattered radiation. Practically, the intensity of the received radiation is controlled by the density of the electrons and consequently by the density of the rock. A disadvantage of this method is that the gamma rays penetrate only 15-20cm into the rock.

3.7. ERRORS ASSESSMENT

During the whole procedure of a gravity survey and its processing, errors can affect the final accuracy. There are two types of errors, systematic and random ones. On the other hand, we could separate them in two other categories, the *Acquisition* errors and the *Processing* errors.

Obviously, the *Acquisition* errors correspond to the level of accuracy during all the field measurements (gravimetric and topographic). In detail, we can have the following errors:

- The reading of the meter and especially the estimation of the last digit may result to an error of ±0.005 mGal. Therefore, in order to keep it systematic, the 'reader' should be the same person during the whole campaign.
- Wrong levelling of the instrument can produce errors of about 0.015 mGal for a tilt of 0.01^{o} (Milsom & Eriksen, 2011).
- The horizontal coordinates' accuracy (x, y) of the gravity station has to be ±10m in order to have an error ±0.01 mGal. DGPS accuracy can reduce the error to ±0.0008 mGal (Long & Kaufmann, 2013).
- The elevation of the gravity station has to be ±10 cm accurate, in order to have an error ±0.02 mGal. DGPS can provide 12-18mm accuracy, minimizing the error to ±0.003 mGal (Long & Kaufmann, 2013).
- An inaccuracy of 2-3 cm for the instrument height can result in an error of ±10 μGal. Great care should be given in microgravity surveys.
- The atmospheric pressure provides an error of ±0.35 μGal per mbar (Milsom & Eriksen, 2011).
- Earthquakes produce errors of ±0.1 mGal and microseismicity 0.01-0.1 mGal (Milsom & Eriksen, 2011).

- Wind may vibrate the instrument, resulting to an errors 0.01-0.1 mGal (Milsom & Eriksen, 2011).
- Soft footing can introduce errors of ±5 μGal (Milsom & Eriksen, 2011).

Therefore, depending on the campaign type, the appropriate care should be given along with the observational check procedures. The repetition of the field measurement of each station (without moving the gravimeter) is a standard procedure, in order to minimize errors. Beyond that, if great variations are observed between the two values, a third or even a fourth measurement should be recorded, until the deviation is acceptable. Beyond that, it is considered a standard procedure that a small percentage of scattered stations (10-15 %) should be re-occupied at different time, during the campaign. Through this procedure, possible base tie errors and inconsistencies can be determined.

Great care should be given during the typing and copying of the data. Simple check procedures have to be introduced in the whole procedure, such as calculating the difference between the repeated values. Several other practical procedures can also be applied to check the quality of the data, such as the Elevation-Gravity Reading diagram, which should illustrate an almost linear relationship (Fig. 3.52). Values appearing with great offset of the linear trend line should be re-checked or even delisted from the database.

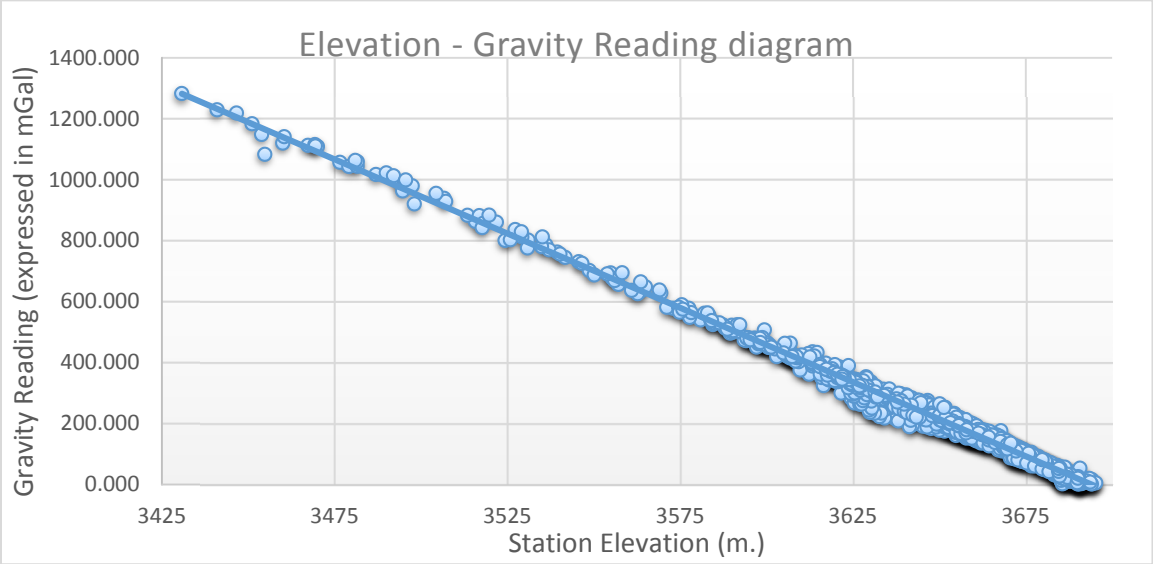

Figure 3.52: Elevation-Gravity reading diagram of this Ph.D. gravity data, used to check the reliability of the collected gravity data.

The *Processing* errors are mainly generated through the gravity data reduction. Therefore, the following errors can be observed:

- During the drift correction, error of ±0.02 mGal may rise (Goumas, 2006).
- The tide corrections can be calculated with an error ±0.0005 mGal (Goumas, 2006).
- The terrain corrections may introduce errors of ±0.15 mGal for areas with slight topography, or even ±7.5 mGal in mountainous areas (Long & Kaufmann, 2013).

4. APPLICATION OF GRAVITY METHOD IN ATHENS BASIN

There are numerous geophysical methods that someone could apply in order to contribute to the adumbration of the fault zone system of an area. The majority of them are subject to the contrast of the measured physical property (e.g. density for gravimetry, resistivity for geoelectrical, magnetic susceptibility for magnetics etc.) in order to reveal any anomalies that can be evaluated. This means that the choice of the appropriate method should be primarily based on the evaluation of the local geology/lithology and its predictable range of variation, along with the scope of the investigation. Beyond these two basic factors (geology and scope), several others can be taken into consideration, such as the type of environment, including the type of the survey area (mountains, urban areas, fields, forest areas, marine etc.), the morphology of it (steep relief) or even general obstacles for the field acquisition (current cables restricting electromagnetic methods; roads, rivers and dense vegetation cove restricting possible alignments).

In the context of this Ph.D. thesis scope, which is the investigation of the tectonic structures in urban and sub-urban areas the possible geophysical methods that can be applied are restricted a lot. **Athens basin** is covered with artificial constructions (buildings, stadiums, roads, playgrounds, public services station etc.) in a very large percent. This means that many geophysical methods cannot be applied in the area, such as electromagnetics, magnetics and geoelectrics due to the unlimited current cables and other systems affecting their functionality and reliability. Seismic methods have been applied in the past (Louis *et al*., 2002b; Papadopoulos *et al*., 2003; 2007) in selected areas. However, the land gravity measurements seem like the most cost-effective method for structural investigation in such environments and large areas (Dilalos & Alexopoulos, 2017; Xu *et al*., 2015; 2017).

Several papers have been published for the application of geophysical methods in **urban environments**, but mostly for shallow issues. For example we can find applications of the contribution of electrical and electromagnetic techniques for geomorphological and geotechnical issues (Birken *et al.,* 2002; 2006; Hong *et al*., 2018; Kim *et al*., 2017; Rossi *et al*., 2017; 2018; Saribudak, 2010; Sevil *et al.,* 2017; Sirles *et* al., 2009; Son *et al.,* 2017; Pazzi *et al.,* 2016), or according to seismic methods (Adly *et al.,* 2017; Becker *et* al., 2017; Hutchinson *et al.,* 2009; Krawczyk *et* al., 2012; Macau *et al.*, 2018; Martinez-Pagan *et al.*, 2018; Martinez & Mendoza, 2011; Wiener *et al*., 2014; Williams *et al.*, 2006; Whiteley & Stewart, 2008). Regarding the **gravity** methods, few microgravity surveys have been carried out in order to adumbrate the **bedrock** or locate **cavities** (Abbott & Louie, 2000; Calvo *et al.,* 2005; Castiello *et al*., 2010; Cueto *et al.*, 2018; Lamontagne *et* al., 2011; Radogna *et al*., 2003; 2004; Piroddi *et al.,* 2009; Thierry *et al*., 2005; Trogu *et al.,* 2012) and limited ones for **tectonic** investigations (Papadopoulos *et al*., 2007; Pamucku *et* al., 2014; Xu *et al*., 2015; 2017). Recently, Kobe *et al.* (2017) have even tried time-lapse gravity in sinkholes of an urban area in Germany.

Apart from the urban environments, **gravity** measurements have been extensively applied the last few years. Their main application is the structural / basin investigations (Ali *et al*., 2017; Arfraoui *et al*., 2011; Berrocal *et al*., 2004; Braitenberg *et al*., 2006; Chailas *et al.,* 2007; de Castro *et al*., 2014; Dilalos and Alexopoulos, 2017; Fernandez-Cordoba *et al*., 2017; Flinders *et al*., 2010; Haddad *et al*., 2001; Hamdi-Nasr *et al*., 2009; Karner *et al*., 2005; Madon and Watts, 1998; Onal *et al*., 2008; Sainz-Maza *et al*., 2017; Yuan *et al*., 2012; Zheng *et al*., 2006). Furthermore, gravity method is widely applied in natural resources exploration, such as the delineation of oil-gas and mineral reservoirs (Chen et *al*., 2015a; 2015b; Dufrechou *et al*., 2011; Hu *et al*., 2017; Kadirov, 2000; Martinez *et al*., 2013; Sander & Cawthorn, 1996; Wang *et al*., 2013) or the geothermal reconnaissance (Arzate *et al.,* 2018; Pearson-Grant *et* al., 2017; Saibi & Aboud, 2013). Additionally, it has been applied successfully in cavity determinations (Fais *et al.*, 2015; Leucci G. and De Giorgi L., 2010; Martínez-Moreno *et al.*, 2015) and in general engineering problems (Lamontagne *et al.*, 2011; Narayanpethkar *et al.*, 2007),

The application of geophysical methods in the area of Athens basin is limited due to restrictions of urban environment. Engineering and archaeological applications have been generally carried out (Apostolopoulos *et al*., 2014; Louis *et al*., 2002a; 2002b; Papadopoulos *et al*., 2001; Papaioannou, 2002; Symeonidis *et al.,* 2005, Tsokas *et al.,* 2008; Tsourlos & Tsokas, 2011). A few deeper investigations have been carried out with the application either geoelectrical methods (Alexopoulos et *al*., 2001), or combination of seismic and gravity methods (Papadopoulos *et al*., 2003; 2007).

4.1. DATA ACQUISITION OF STUDY AREA

The gravity data acquisition in an urban area like Athens basin, the metropolis of Greece, with population up to 4.5 million people is quite difficult. Athens city is covered with artificial constructions (buildings, stadiums, roads, playgrounds, public services station etc.) in a very large percent.

Taking into consideration that the gravity measurements are affected when they are executed very close to walls and buildings, we had to take great care that the gravity stations would be placed in “open” areas (squares, parks, fields, parking areas, homesites, wide pavements etc.), far from high buildings as much as possible (at least 60 meters). But also, we had to avoid the busy roads due to the oscillations they provoke to the gravimeter.

The author tried to minimize the problems of moving all day in a fully developed city like Athens, by choosing to acquire the gravity measurements during the summer months, where the most of the city residents leave for vacations, leading automatically to the reduction of traffic jam. Consequently, the time spent moving between the stations and the bases (in the context of drift correction) is rapidly reduced. Thereby, more measurements per day might be gathered, less vibrations are produced by vehicles (better measurement quality) and less suffering for the field crew.

In the framework of this Ph.D. thesis, more than 100 field days (of a two-person crew) were required, during the summers of 2013, 2014 & 2015, during which more than 8,400 kilometers were covered. The result of this is 1,122 gravity stations and more specifically:

- ✓ 807 gravity stations (§4.1.b & Fig. 4.3).
- ✓ 315 additional gravity points developed along 40 Nettleton profiles (§4.2.b & Fig. 4.3).
- ✓ An established gravity base network of 13 locations (§4.1.a & Fig. 4.3).
- ✓ 3 established topographical bases for the DGPS measurements (§4.1.c & Fig. 4.3).

All the above gravity measurements were acquired by the same observer (the author), in order to avoid divergences on way of reading the gravimeter, since a subjectivity is included regarding the determination of the last two digits from the nulling dial but also the final position of internal reading crosshair at the scale. Additionally, every gravity measurement was received at least twice in order to check the repeatability and credibility of the determined value. If the difference of these values were not in the defined limits, more repeating readings would be collected.

The whole map planning and management of the field surveys was based on the satellite images of Google Earth. Their accuracy is extremely high for such an urban environment and was very helpful locating the desired "open" spots for the gravity measurements in order to create or re-design the measurement grid. Its friendly environment provides numerous tools to plan and manage a field survey and its results. Additionally, its supported *kmz* files collaborate fully with the Geographic Information System platform used in this Ph.D. thesis, supporting all kind of essential thematic maps (geology, tectonism, relief contouring, geophysical & topographical stations, boreholes, density samples, processed gravity data and anomaly maps etc.) visualizing them with the satellite image as a background.

4.1.a. Gravity Bases Network Establishment

In every gravity campaign, a well-established network of gravity bases is required, taking into account that every 2-3 hours of measurements we must return and re-measure the value of the gravity base. This procedure provides the data that allows the subtraction of the drift effect of the instrument. The absolute gravity value has to be already calculated at each gravity station of this network in order to accomplish this.

Several authors (Berg & Thiruvathukal, 1965; Csapo & Volgyesi, 2002; Krynski *et al.*, 2013; Lagios, 1985; Robertson, 1965; Srivastava *et al*., 2015; Warsi, 1989) have discussed in the past the establishment of absolute gravity bases networks, in several areas of the world, mostly for quite larger areas.

Gravity bases must be linked together using the A-B-A-B-A ties (Jacoby & Smilde, 2009; Milsom & Eriksen, 2011) (Fig. 4.1), which practically means that a reading is made at base A and then as quickly as possible (for an assumed linear drift) another reading will be made at base B. Then, repeat measurements have to be made at bases A and B. The two measurement

sets between A-B, will provide their final difference. The difference value will be accepted only if the two individual differences are within the desired accuracy limit. If not, the procedure must be repeated. Apparently, the second reading at base B, can simultaneously be the first for the same procedure between bases B and C. We can also calculate the misclosures, which is the sum of the differences around each loop. In the context of our base network establishment, the loop (e.g. A-B) was repeated at least 3 times to improve the accuracy of the defined absolute value of gravity.

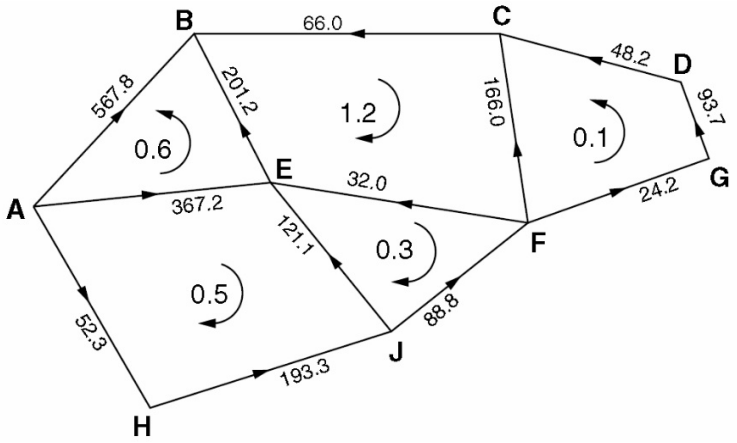

Figure 4. 1: Gravity Base network adjustment with its misclosures (*Milsom &Eriksen, 2011*)

Gravity base	Absolute gravity (mGal)	Deviation (mGal)	Easting (Egsa '87,m)	Northing (Egsa '87, m)	Elevation (m)	Order
UoA_Office	980,010.745	±0.00	480,948.310	4,201,848.100	252.000	i
UoA_Oulof	980,029.856	±0.03	478,772.001	4,202,445.816	134.792	i
Rouf	980,049.351	±0.04	473,639.680	4,202,590.600	20.239	ii
Psychiko	980,017.268	±0.03	480,288.710	4,206,831.900	179.091	ii
Nea Smyrni	980,043.877	±0.04	474,819.600	4,198,156.400	42.662	ii
Peristeri	980,044.151	±0.07	472,514.450	4,206,815.757	51.888	iii
Dilaveri	980,052.977	±0.08	469,013.766	4,200,694.898	7.536	iii
Kifisia	979,991.509	±0.04	483,373.599	4,212,901.998	287.379	iii
Filadelfia	980,029.065	±0.04	477,276.990	4,210,270.695	116.118	iii
Elliniko	980,039.123	±0.07	478,453.689	4,193,259.660	80.884	iii
Acharnes	980,017.082	±0.07	475,726.609	4,215,036.626	168.425	iv
Ekali	979,981.326	±0.07	485,997.896	4,217,756.564	344.891	iv
Vrilissia	979,997.111	±0.07	485,846.098	4,210,619.196	269.935	iv
Dafni	980,031.436	±0.05	468,050.208	4,206,980.671	109.281	iv

Table 4.1: Established gravity bases in Athens (Fig. 4.2) along with their determined absolute values.

Taking into account the traffic jam of this over-populated metropolis and the increased time that we would spend moving among the stations and the base re-measurements, we planned and established very cautiously a gravity base network, distributing spatially **thirteen (13) gravity bases** (Fig. 4.3), in a way that would be less time-consuming for the base loops. Most of them were located on squares that were close to main roads (*quick access*) but "quiet" at the same time (Figs. 4.2), providing in that way stable measurements, without traffic noise and vibrations from the vehicles.

Figures 4.2: Some of the established local gravity bases. Top left: "*Rouf*", Top right: "*Filadelfia*", Bottom left: "*Vrilissia*". The bottom right photograph illustrates the permanent marks of a base.

Each established base (Table 4.1) was characterized by 3 permanent marks on the ground (3 feet of the gravimeter plate-Fig. 4.2.) which sometimes were additionally engraved around for more enduring results. In that way, the re-measurements would always be at the exactly same point. Detailed sketches and photographs of each gravity base and its surrounding stable structural characteristics (columns, balusters, stairs, walls, yards etc.) were kept.

The entire gravity base network is referred to the IGSN'71 datum (Morelli *et al*., 1974) as it was tied with repeated measurements (ABABA type) to an already established gravity base in the University of Athens (Hipkin *et al*., 1988).

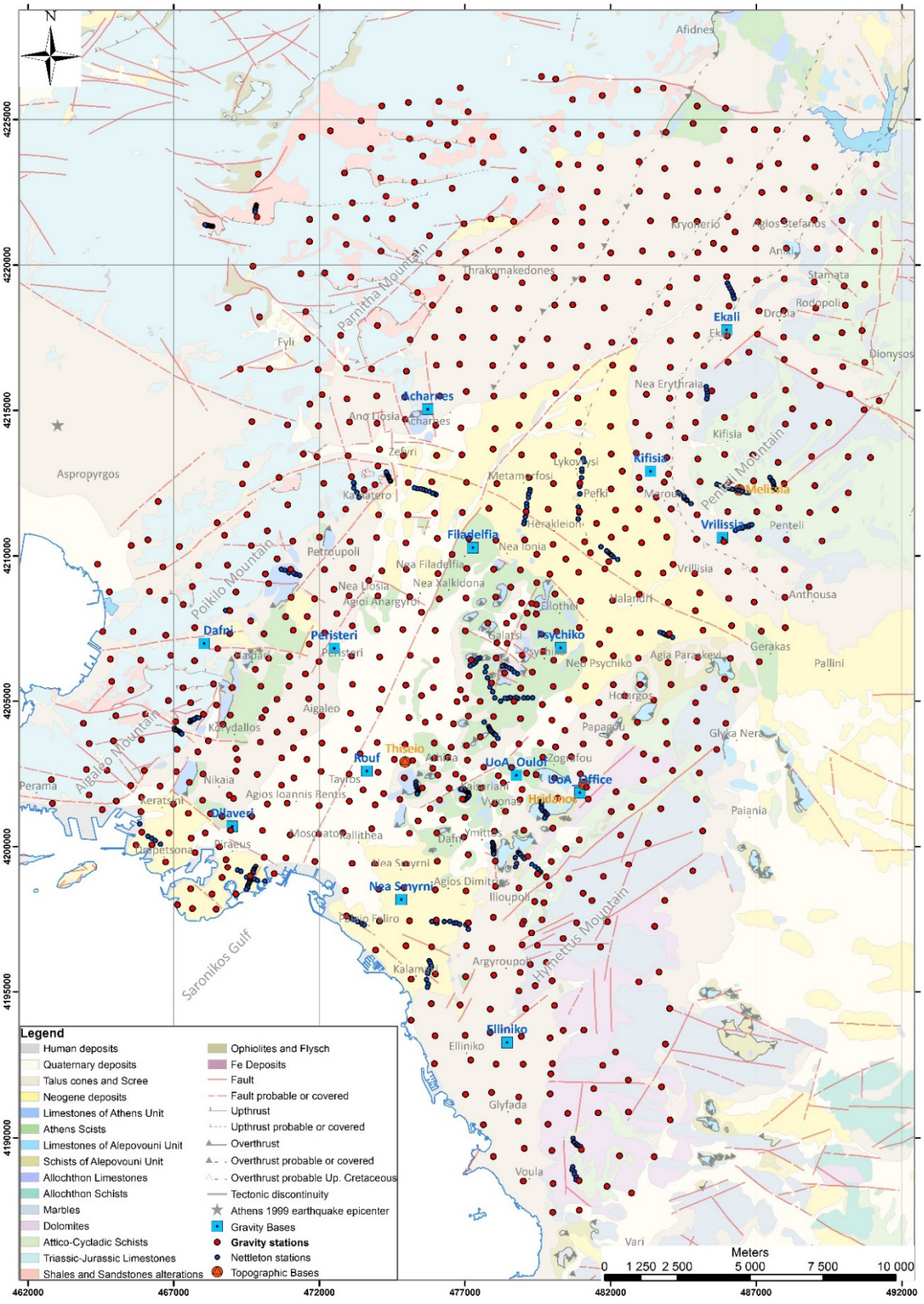

Figure 4.3: Gravity (red dots) and Nettleton (blue dots) stations acquired along with the established gravity (blue squares) and topographic (orange circles) bases.

4.1.b. Gravity Field measurements

As we have previously mentioned, Athens basin as an urban area, sets up several difficulties throughout the period of the field measurements. Great care had been given not only to the primary map planning, but also during the field measurements. The map determination of the gravity stations had to be organized very wisely, taking advantage of the high-accuracy space images of Google Earth.

For start, it is an area covered with artificial constructions (buildings, stadiums, roads, playgrounds, public services station etc.). Taking into consideration that the gravity measurements can be affected by walls and buildings, the gravity stations should be placed in "open" areas (squares, parks, fields, parking areas, playgrounds, homesites, wide pavements, cemeteries, roadsides etc.), far from high buildings as much as possible (Figs. 4.4). Beyond that, we also have to take care of the "open" spots that were very close or above of subway stations, since they are practical artificial "cavities", altering the 'initial' response of the subsurface.

Furthermore, such a metropolis always faces traffic congestion problems. This means that the necessary car routes between the gravity stations and bases will be time-consuming, minimizing also the final amount of collected data and possibly their quality. For that reason, the acquisition of the gravity data was carried out through the summer months, when the majority of the city residents depart for vacations. This leads automatically to traffic jam reduction and facilitation of the whole procedure. For precise and reliable measurements, it is recommended to avoid busy roads, as the oscillations produced nearby affect the gravimeter stability.

Taking into account the complicated geology of the area, the purpose of the research (tectonic structure) and the urban environment, the gravity measurements were organized on a **grid** and not along few traverses. This might obstruct the finding of the appropriate spots for measurement, but provides a horizontal two-dimension piece of information, leading to a final 3-D inversion model. The initial grid **station separation** was set to **1,000** meters. Due to the human constructions and all the city obstacles, many stations had to be relocated to the nearest executable point (limiting it within the first 100-200 meters if possible), trying also to minimize the building effects. Throughout the supplementary measurements sets (years of 2014 and 2015) gravity stations were added in-between the initial ones (2013), creating a denser grid at certain areas (down to 500 meters stations separation), in order to clarify the initial ambiguous image originating from the preliminary processing.

The gravity measurements were based on the "*close loop*" procedure. Every loop begins with a gravity base occupation (reading value and time), then a set of gravity stations is acquired (reading values and times) and finally the loop closes again with a gravity base measurement. The time taken for each loop should not exceed the three (3) hours, trying also to restrain the accuracy of the drift closure below 0.01mGal/hour. This procedure aims to

correct the instrument drift. Repetitive instrument readings were carried out (at least two), in order to ensure their credibility. Generally, the desired limit of the reading accuracy error was set at a maximum of 0.01mGal. Additionally, at least a 5% of them was reoccupied another day to check the repeatability of the reading.

Figures 4.4: Examples of "open" areas for acquiring urban gravity measurements (parks, fields, playgrounds, parking areas, squares, roadsides)

For each gravity station, detailed field notes were taken, such as the code of the station, the date, the area or even the address, the time and reading values and any useful observation (surface geology, affecting buildings, gas stations etc.). Additionally, the estimation of the terrain corrections within the first 53.5 meters from the reading point (Hammer zones A-C), was kept in specific form sheets.

The gravity database is comprised of **1,122 gravity stations** (Fig. 4.3) and it is divided in two categories. The main category counts the **individual 807 gravity stations** that were acquired in three phases (three summer periods). More specifically, during the summer of 2013, 500 gravity stations were planned and collected, covering the interior of Athens basin. The next summer (2014), 292 new gravity stations were acquired either on the surrounding mountains or on locations that made the grid denser. Finally, in the summer of 2015, fifteen (15) more gravity stations were acquired. The second category refers to the **315 Nettleton gravity stations,** gathered during the 2014 (297 points) and 2015 (18 more points), which were practically for the Nettleton profiles that were executed across selected topographical reliefs (hills). These Nettleton stations improve the final results at the hills, where they were executed.

4.1.c. Topographic Field Measurements

In the context of gravity data reduction, it is necessary to determine the coordinates of each acquired gravity station and base with high precision. More specifically, the horizontal coordinates are needed for the Tidal and Latitude corrections, while the Elevation is essential for the Free-Air, Bouguer and Terrain Corrections. The desired accuracy depends on the purpose of the survey each time. Therefore, in such a 'tectonic' survey, an elevation accuracy of ±10cm, producing a 0.1mGal error in Bouguer gravity (Milsom & Eriksen, 2011) is satisfactory. Nevertheless, the desired elevation accuracy for this gravity survey was set lower, to ±5cm (if it was applicable), in order to obtain an error of 0.01mGal in Bouguer.

In order to calculate the coordinates of each location of gravity measurement during this Ph.D. research, we used Differential Global Positioning System (dGPS). Taking into consideration that all the measurements were collected in an extensive urban environment, with high buildings and constructions that block the horizontal visibility and radio signals, the only reliable and highly accurate way (3 decimals) of determining the coordinates of a point is the Static technique of Differential Global Positioning Systems. It provides this level of accuracy even for antennas placed at a distance of up to 20 kilometers.

In general, the dGPS system is compiled by two different, dual-frequency antennas. The one antenna is used as a *reference base*, with known coordinates and the other one is used as the *rover*, measuring the coordinates of each gravity station. Both antennas are recording data from numerous satellites (usually 5-18) for the same time window, for a minimum of 15 minutes. The length of this common time window is based on the distance between the two

antennas (the larger the longer), the sky visibility (high buildings etc.) and the total number of satellites.

Therefore, a topographic base network was essential for the acquisition of the gravity measurements. For that reason, three (3) topographic bases with known coordinates were planned and established in the Athens basin (Fig. 4.3 & Figs. 4.5). These bases had to be placed in secure locations, since an expensive antenna would be left recording almost all day. Beyond that, the open sky view was essential, in order to track the satellites. Taking into account these specifications, the two bases were established on the floor of secured rooftops of apartment buildings in the areas of *Thisseio* (downtown) and *Melissia*. The third one was established in an enclosed area (*Iridanos*) in University of Athens Campus, on a bench.

Figure 4.5: Two of the established topographical bases. Left: *Iridanos* and Right: *Melissia*

Base	**Easting (Egsa '87,m)**	**Northing (Egsa '87, m)**	**Elevation (m)**	**Horizontal precision (m)**	**Vertical precision (m)**	**Type**	**Order (local)**
Thisseio	474,944.593	4,202,903.184	70.079	0.01	0.02	Rooftop Mark	i
Iridanos	481,087.872	4,202,140.151	249.545	0.02	0.04	Bench	ii
Melissia	486,420.753	4,212,255.510	393.108	0.05	0.08	Rooftop Mark	ii

Table 4.2: Established topographic bases, their coordinates and characteristics.

The Geodetic benches of the Hellenic Military Geographical Service (*Filopappou* and *Ardittos*) were used for the determination of the coordinates of the primary base of *Thisseio*, with an accuracy of 3 decimals (Table 4.2). Practically, the static survey method of dGPS systems was applied likewise, but this time the *reference base* was placed on the geodetic benches of the Hellenic Military Geographical Service (known coordinates) and the *rover* on the new-established local base of *Thisseio*. The common time of recording was a few hours, in order to maximize the final accuracy. Afterwards, the base of *Thisseio* was tied with the two other bases of *Iridanos* and *Melissia* (Table 4.2). The Hellenic Geodetic Reference System (*EGSA'87*) has been used for all the topographic measurements.

Figure 4.6: The Geodetic benches of the Hellenic Military Geographical Service of *Filopappou* (*left*) and *Ardittos* (*right*) that were used for the tie of the base of *Thisseio*.

4.1.d. Equipment

The equipment used during this Ph.D. thesis is practically separated in two major categories, the gravity and the topographical ones.

To begin with, the instrument used for the gravity data acquisition was the gravity meter LaCoste & Romberg G-496 (Figs. 4.7-4.8), owned by the division of Geophysics-Geothermics of the Department of Geology and Geoenvironment, National Kapodistrian University of Athens. It is a relative gravimeter of *zero-length* type, known for its reliability. It has a repeatability of 0.01mGal. This gravimeter is accompanied by its aluminum carrying case and its aluminum concave baseplate, where it is placed. The energy supply of the gravimeter for the reading light and the conservation of its inner temperature are supported by an external 12-volt battery.

A general levelling of the instrument is obtained by sliding it gently on the baseplate. Then the three leveling screws of the gravimeter are turned until the perfect levelling has been achieved. After the levelling of the instrument, the beam should be released by unclamping the knurled arrestment knob that keeps the spring locked and stable in order to prevent any damage during the transfers. After turning on the switch for the internal light, the instrument is ready for the measurement. The placement of the crosshair at the characteristic reading line is carried out by turning clockwise a nulling dial and observing it through the microscope eyepiece. Finally, the reading value is obtained from the counter (the 4-digit integer and the first decimal) and from the nulling dial (the last two decimal digit). It is important to mention that the counter readings need to be converted to milligals, based on the instrument's calibrations table, in order to proceed to the data reduction.

Figure 4.7: The gravimeter *LaCoste & Romberg G-496*, placed the concave plate.

Figure 4.8: Development of the gravimeter and dGPS *TopCon HiperPro* antenna (placed on the tripod over the gravimeter) at the field.

The second major category of the equipment refers to the instruments of the *Differential Global Positioning System (dGPS),* owned by the division of Geography-Climatology, of the Department of Geology and Geoenvironment, National Kapodistrian University of Athens. necessary for the determination of the coordinates of each gravity station. The system was compiled by two different (base and rover), dual-frequency TopCon HiperPro GPS receivers antennas (Fig. 4.8). They are able to collect data from up to 20 satellites of the GPS and GLONASS global navigation satellite systems (GNSS), improving the accuracy of any survey

point. The energy supply of the antennas is supported by internal batteries, providing power for at least 11 working hours. These antennas are attached and levelled on a tribrach that is mounted on the tripod placed on the ground (Fig. 4.8). All the data collected throughout the static survey method measurements, was processed via the *TopCon Tools* post-processing program in order to determine the final coordinates of all the survey points.

4.2. DENSITY DETERMINATION OF STUDY AREA

As we have already mentioned in §3.6, density is the physical quantity that controls the gravity response of each geological formation, based on its characteristics (e.g. porosity, age, metamorphism). It is very important for the final processing of the gravity data and the construction of the anomaly model, which will provide information about the volume, depth and general shape of the anomaly, since the same anomaly can be produced by many density distributions. The density is practically a strong constraint in the process.

In the context of this Ph.D. study, the density of the existing geological formations in the Athens basin (§2.2) was determined with 3 different ways (see §3.6), wherever it was possible. The laboratory measurements on surface samples and the Nettleton method were applied to almost every type of geological formation of the Athens basin.

4.2.a. Laboratory measurements

Several authors (Abzalov, 2013; Baptiste *et al.,* 2016; Boszczuk *et al.,* 2011; Damaceno *et al.,* 2017; Garcia-Perez *et al.*, 2018; Goumas, 2006; Onal *et al.,* 2008; Papadopoulos *et al.,* 2007; Parasnis, 1952; Whetton *et al*., 1956) have carried out laboratory measurements in order to determine the densities of the geological formations existing in their study area.

As we have previously discussed in §3.6.a, the bulk density of a rock geological sample can be calculated in the laboratory. A set of 3 measurements is required (Goumas, 2006; Parasnis, 1952), which are the $\boldsymbol{W_1}$ for the weight of the dry specimen measured in air, the $\boldsymbol{W_2}$ for weight of the saturated specimen measured in air and the $\boldsymbol{W_3}$ for weight of the saturated specimen measured in the water. More specifically, we can determine the dry density $\boldsymbol{\rho_d}$, the saturation density $\boldsymbol{\rho_s}$ and the granular one $\boldsymbol{\rho_g}$ with the following equations given that ρ_w is the water density (almost equal to 1 gr/cm^3):

$$\rho_d = \frac{W_1}{W_2 - W_3}\rho_w$$

$$\rho_s = \frac{W_2}{W_2 - W_3}\rho_w$$

$$\rho_g = \frac{W_1}{W_1 - W_3}\rho_w$$

Based on Long & Kaufmann (2013), the bulk density of a formation may be either dry or fluid saturated. Near the surface and especially above the water table the bulk density is

usually the dry one, while the saturated is for larger depths. On the other hand, Parasnis (1952), believes that the “field” density is somewhere between the dry and saturated one.

Figure 4.9: *Triassic-Jurassic Limestone* geological specimen for density calculation

Figure 4.10: Borehole core of *Athens Schist* for density calculation

It is common belief that for reliable determination of the densities, it is necessary to measure numerous samples for each geological formation, collected from several locations in order to calculate their average that will provide a representative value of the formation, since it is considered inhomogeneous. It is preferred that the samples are taken from borehole cores since they are more characteristic than the weathered samples from surface outcrops. Nevertheless, for formations that consist of various lithologies, we have to take into consideration the densities of all lithologies for the average ones of the formation itself, but even then, we might not be able to obtain a characteristic density of the formation (§4.2.b).

Figure 4.11: Weighing the dry specimen in air (W_1)

Figure 4.12: Weighing the saturated specimen dipped in water (W_3) with the aid of special kit.

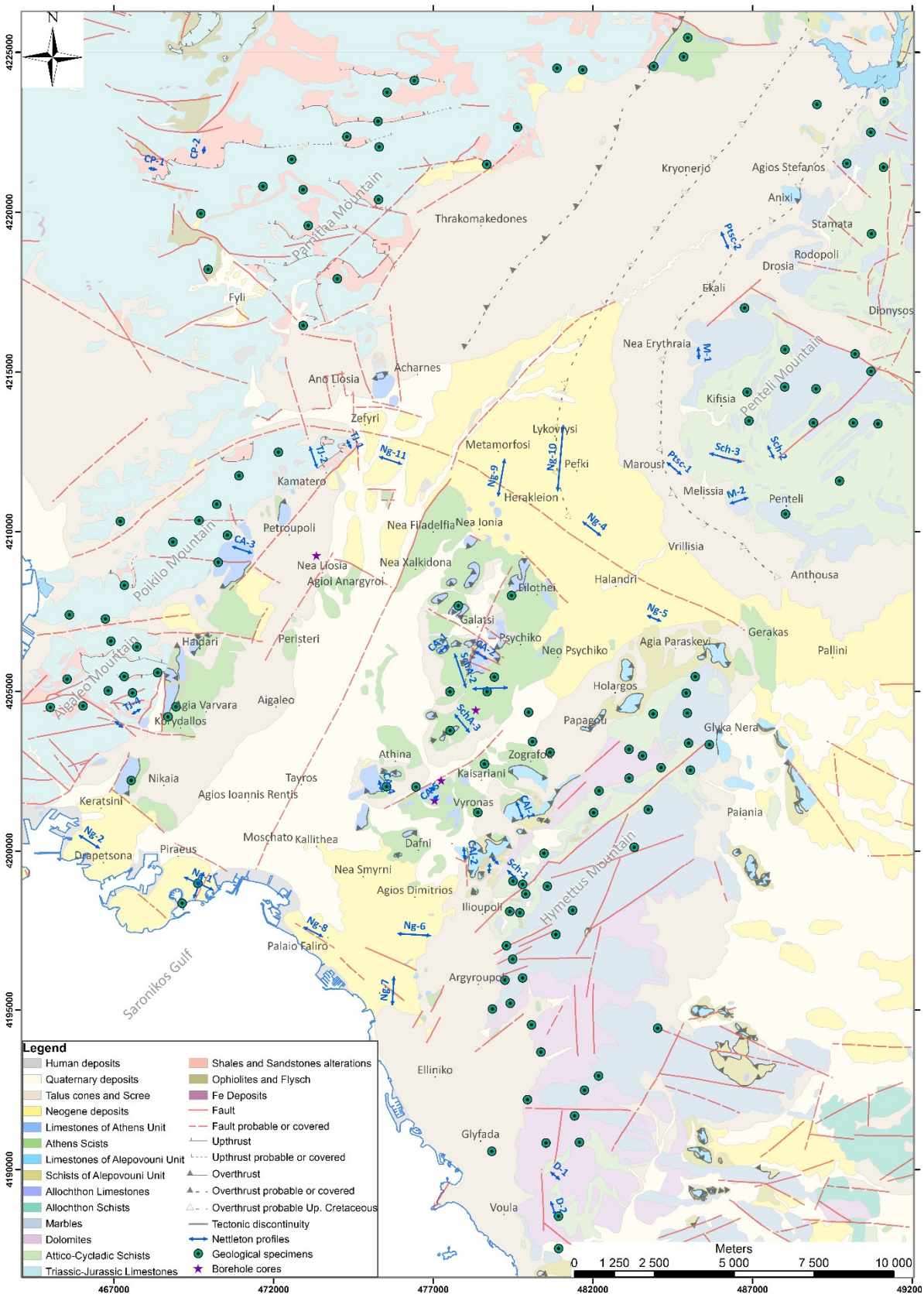

Figure 4.13: Locations of geological specimens and borehole cores used in laboratory measurements. The Nettleton profiles are also illustrated.

Geological formation/lithology	Number of specimens	Dry density ρ_d (gr/cm^3)	Saturation density ρ_s (gr/cm^3)	Grain density ρ_g (gr/cm^3)
Triassic-Jurassic Limestones (*T-J*)	60	2.66 ±0.04	2.68 ±0.04	2.70 ±0.04
Dolomites (*D*)	20	2.74 ±0.07	2.76 ±0.07	2.79 ±0.07
Marbles (*M*)	30	2.66 ±0.02	2.68 ±0.03	2.71 ±0.04
Schists (*Sch-Hymettus Mt*.)	11	2.43 ±0.05	2.54 ±0.03	2.76 ±0.02
Schists (*Sch-Penteli Mt*.)	5	2.57 ±0.05	2.68 ±0.10	2.94 ±0.29
Shales & Sandstones (*C-P*)	16	2.51 ±0.05	2.57 ±0.03	2.67 ±0.03
Limestones of Athens Unit (*CA*)	28	2.64 ±0.04	2.66 ±0.03	2.70 ±0.02
Limestones of Alepovouni (*CAl*)	21	2.64 ±0.04	2.66 ±0.02	2.70 ±0.01
Clastic Limestones of Athens Unit (*CmA*)	8	2.57 ±0.04	2.61 ±0.02	2.67 ±0.01
Athens Schists (*SchA*)	38	2.55 ±0.07	2.60 ±0.05	2.69 ±0.05
Schists of Alepovouni (*Sch-Al*)	13	2.19 ±0.09	2.36 ±0.08	2.61 ±0.10
Limestones (*Ng-Plm*)	5	2.55 ±0.04	2.59 ±0.05	2.67 ±0.07
Marly limestones (*Ng-Plm*)	12	2.45 ±0.05	2.52 ±0.04	2.63 ±0.02
Sandy marls (*Ng-Msm*)	18	1.60 ±0.09	1.91 ±0.12	2.36 ±0.24
Breccia & sand (*Ng-Msm*)	6	2.50 ±0.11	2.55 ±0.07	2.65 ±0.03
Reddish clays (*Ng-Msl*)	5	2.49 ±0.03	2.56 ±0.03	2.68 ±0.01
Limestones (*Ng-Msl*)	5	2.61 ±0.04	2.64 ±0.03	2.68 ±0.02
Marls (*Ng-Msl*)	6	1.72 ±0.07	1.96 ±0.14	2.29 ±0.31
Marly limestones & Sandy marls (*Ng-Msl*)	18	2.13 ±0.16	2.29 ±0.11	2.52 ±0.06
Clay & Sand (*Ng-Pll*)	5	-	2.16 ±0.04	-
Talus cones & Scree (*Pt.sc*)	1	2.28	2.39	-
Metabasic	9	3.05 ±0.04	3.10 ±0.03	3.20 ±0.03

Table 4.3: Average densities (W_1, W_2, W_3) of the geological formations or individual lithologies in Athens basin, derived from the laboratory measurements of surface outcrops specimens and borehole cores of this Ph.D. thesis.

In the framework of this Ph.D. thesis, laboratory density measurements were finally carried out on **364 geological specimens** (Appendix B)**,** collected from several locations of almost every formation existing in Athens basin (Fig 4.13). The majority of the measurements was executed by the author, based on small-size specimens (<200 gr), due to the weight limitation of the scale and the special "underwater" weighing kit. This precision scale had a readability of 0.001gr. It is important to mention that the samples came from both surface outcrops (Fig.

4.9) and boreholes cores (Fig.4.10). Beyond these, additional measurements of bigger size cores were carried out in certified geotechnical laboratory, with a more typical electronic scale, capable to weigh quite bigger specimens (up to 2,000 gr) and equipped with the "underwater" system (hook) under it. By weighing these bigger specimens, we gathered probably more characteristic density values of inhomogeneous formations, such as the *Athens Schists*, considered as a mélange.

Therefore, the procedure began when all the specimens were dipped in the water for 48 hours, in order to become saturated. Then, we were able to measure on the precision balance their weight W_2 in air and their weight W_3 dipped in distilled water (Fig. 4.12). Afterwards, they stayed for 24 hours in a kiln, at almost 100^{o}C to get completely dry, in order to measure their weight W_1 in air (Fig. 4.11). This procedure was followed for each specimen (Appendix B). Afterwards, the results of all the individual specimens were evaluated categorized per formation, in order to ignore any abnormal values for the calculation of the average formation density (Table 4.3), where almost 93% of the specimens were included. For the majority of the post-alpine sediments covering the Athens basin (§2.2.b), we were even able to calculate discrete densities for lithologies of the formations.

Beyond our own laboratory calculations of samples and cores gathered by the author, bibliographic references have also been collected (Table 4.4), regarding older density calculations in Athens basin, either for engineering purposes (Sabatakakis, 1991) or application of geophysical methods (Goumas, 2006; Papadopoulos *et al*., 2007). Comparing the bibliographic densities (Table 4.4) with the ones derived in the framework of this Ph.D. (Table 4.3), we can see that generally all the values are pretty close, except for the Schists and Athens Schists, where we can observe bigger differences.

Geological formation/lithology	**Papadopoulos *et al*., 2007.** (ρ_d in gr/cm^3)	**Sabatakakis, 1991** (ρ_d in gr/cm^3)	**Goumas, 2006** (ρ_d in gr/cm^3)
Triassic-Jurassic Limestones (*T-J*)	2.72±0.01	2.68	2.72 ±0.04
Marbles (*M*)	2.69 ±0.01	2.88	-
Schists (*Sch-Penteli Mt*.)	2.81±0.05	2.78	-
Shales & Sandstones (*C-P*)	2.57 ±0.03	-	-
Athens Schists (*SchA*)	2.65 ±0.02	2.51	-
Limestones of Athens Unit (*CA*)	-	2.68	-
Marls	2.01	2.07	-
Conglomerates	2.42	2.44	2.46 ±0.10
Marly Limestones	-	2.4-2.62	-

Table 4.4: Bibliographic densities for geological formations/lithologies of Athens basin

4.2.b. Nettleton Method (Density profile)

Several authors (Ali & Whiteley, 1981; Fernandez-Cordoba *et al.,* 2017; Goumas, 2006; Karastathis *et al.,* 2010; Parasnis, 1952) have applied this method in order to determine successfully the bulk density of geological formations. The densities estimated through this method are considered to be quite representative for the geological formations, very close to their bulk density, since it is applied in the real field conditions.

In Athens basin, we can observe many hills coming into view, where we applied the Nettleton (1939) profile method (§3.6.c) for the estimation of their bulk density. This method requires the execution of a profile of close gravity stations across a preferably gentle topographic relief (hill or valley), shaped by a geological formation, with no lateral variations. Based on Nettleton (1939), a simple slope is not enough given the fact that it is not possible to separate the contribution of density to the slope of the profile from the existing regional slope. It is preferable to select hills surrounded by post-alpine sediments.

During the data reduction procedure, different values of densities have to be assigned, producing corresponding reduced curves (*Complete Bouguer Anomaly)*. Subsequently, all these curves are compared plotted in a common graph in order to identify the one demonstrating the minimum correlation with the topography. For better results, the values obtained for each station are usually referenced to the first station of each profile. Especially for the profiles executed in the urban environment of Athens for this Ph.D. thesis, the data reduction procedure included also the necessary Building Corrections (§3.3.h.4). Additionally, the minimum correlation curve was identified with the aid of the correlation coefficient formula in worksheets and not just by optical estimation.

Within the scope of this Ph.D. thesis, totally **40 density profiles** (Fig. 4.13) were carried out, constituted of **315 gravity stations.** The selection of the location of the density profiles and their gravity stations were chosen after careful planning. Difficulties arose during the planning due to the urban environment (§4.1) and the quite complicated geology of Athens basin (§2.2). The distance of the stations was not stable, but was limited in order to investigate the near-surface formations only.

Almost all the geological formations of the Athens basin were investigated and their bulk densities were estimated. Unfortunately, the results of some profiles were not helpful and therefore were not included in the evaluation. The reason of these profiles being misrepresentative was probably due to their locations (not in the interior of the basin), close to mountain slopes and therefore influenced by the intense regional field. Unfortunately, the locations for planning and executing such density profiles were very limited.

For the process procedure, the assigned values of density ranged from 1.4 to 3.2 gr/cm^3 (Figs. 4.14-4.19), with reduced curves produced for every 0.05 gr/cm^3. After the evaluation of all the Nettleton profiles, the corresponding densities were determined (Table 4.5).

Geological formation/lithology	Density profiles	Density (gr/cm^3)
Triassic-Jurassic Limestones (*T-J*)	4	2.55-2.65
Dolomites (*D*)	2	2.60
Marbles (*M*)	2	2.60
Schists (*Sch-Hymettus Mt.*)	1	2.55
Schists (*Sch-Penteli Mt.*)	2	2.75
Shales & Sandstones (*C-P*)	2	2.35-2.45
Limestones of Athens Unit (*CA*)	7	2.50-2.55
Limestones of Alepovouni (*CAl*)	2	2.65
Athens Schists (*SchA*)	3	2.50-2.55
Schists of Alepovouni (*Sch-Al*)	2	2.55
Neogene Deposits / Several lithologies (*Ng*)	11	1.95-2.15 & 2.40
Talus Cones & Scree (*Pt.sc*)	2	*not identified*

Table 4.5: Representative densities determined by the application of Nettleton profile method (1939).

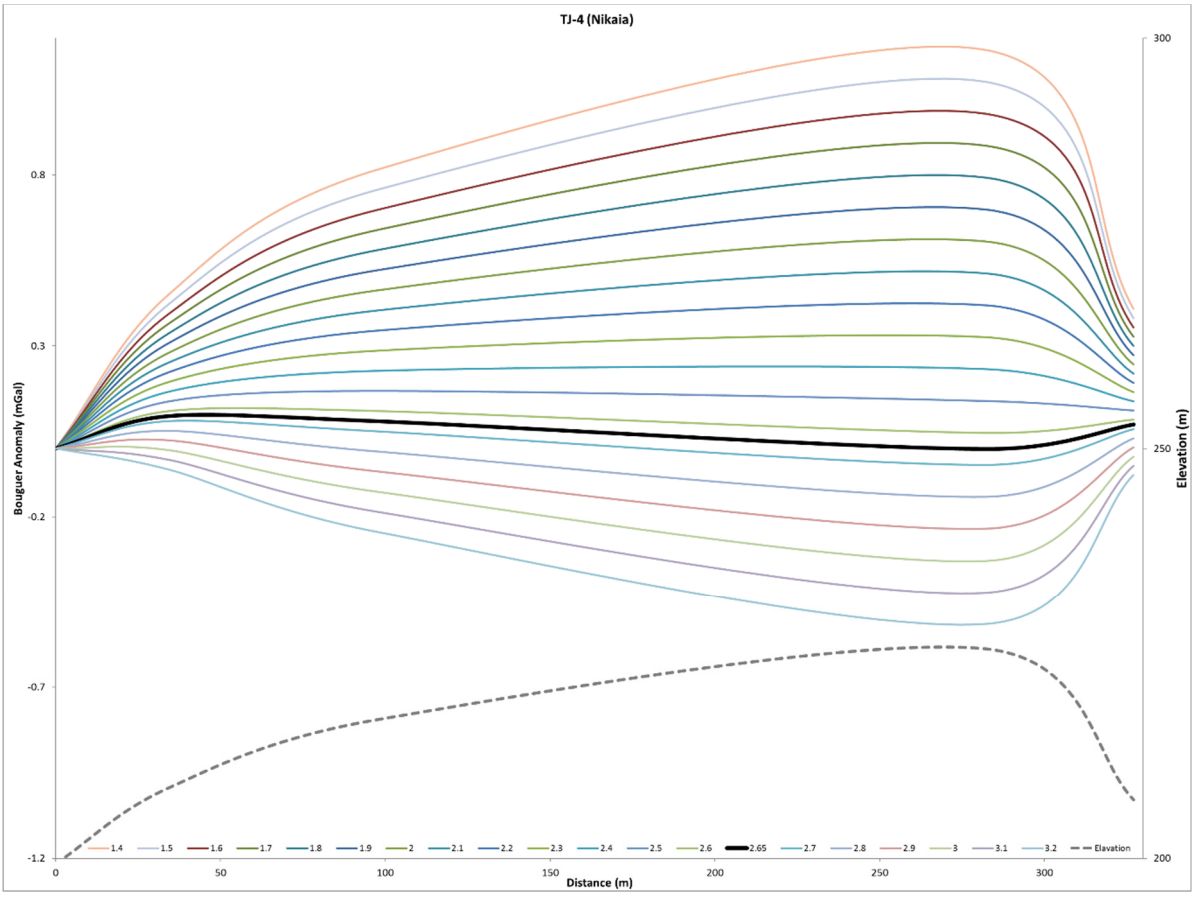

Figure 4.14: Nettleton profile of Triassic Limestones (*TJ*) at *Nikaia*.

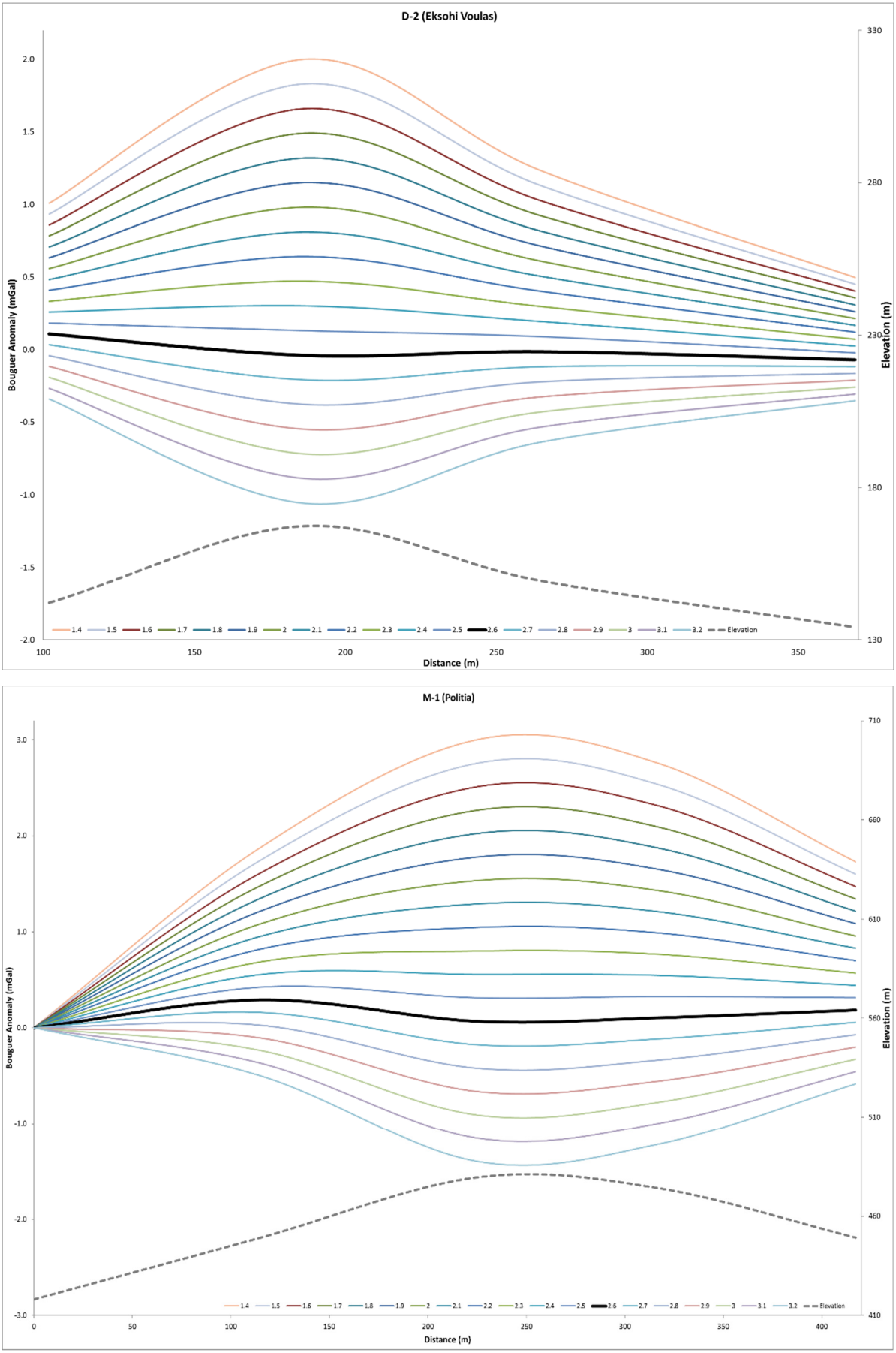

Figure 4.15: Nettleton profiles of Dolomites (*D*) at *Voula* and Marbles (*M*) at *Politia*.

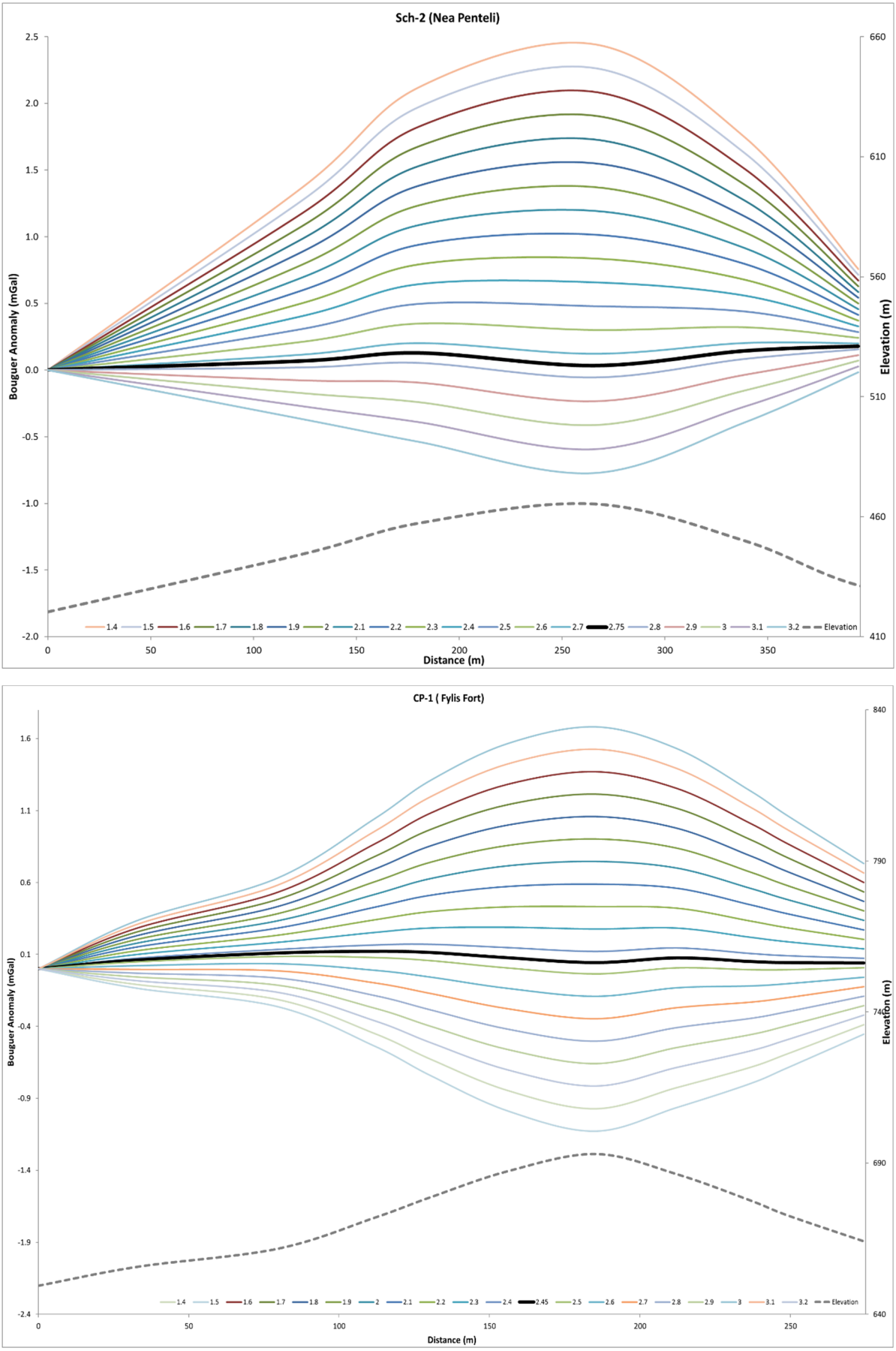

Figure 4.16: Nettleton profiles of Schists (*Sch*) at *Nea Penteli* and Shales-Sandstones (*C-P*) at *Fyli*

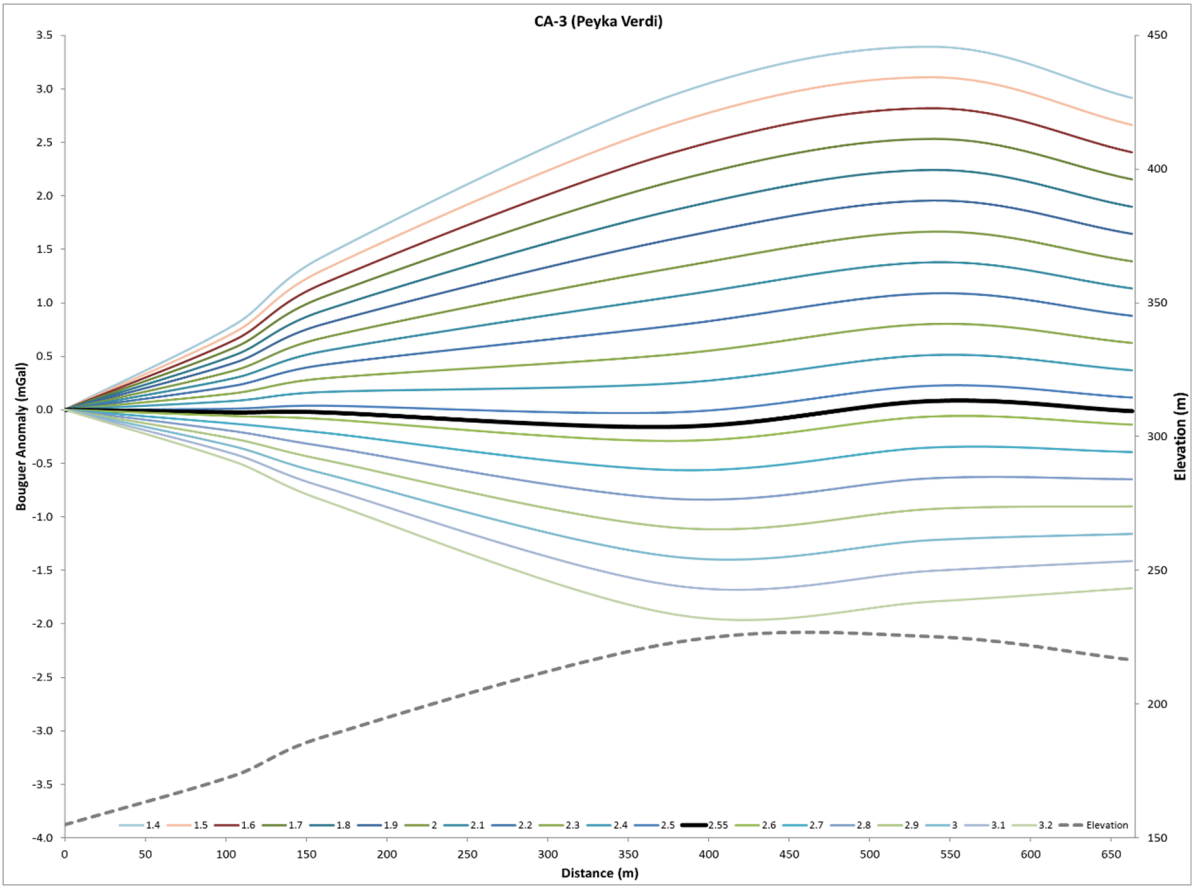

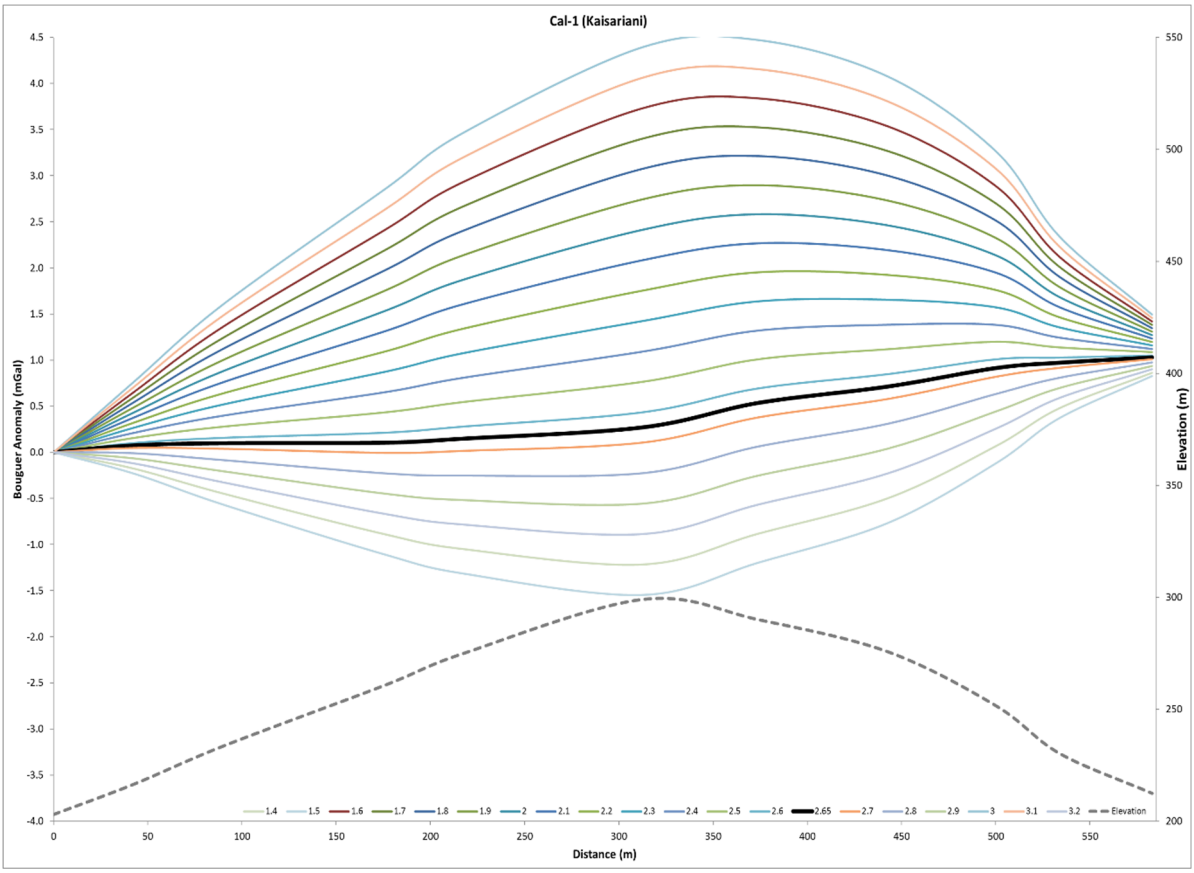

Figure 4.17: Nettleton profiles of Limestones of Athens Unit (*CA*) at *Peyka Verdi* and Limestones of Alepovouni (*CAl*) at *Kaisariani.*

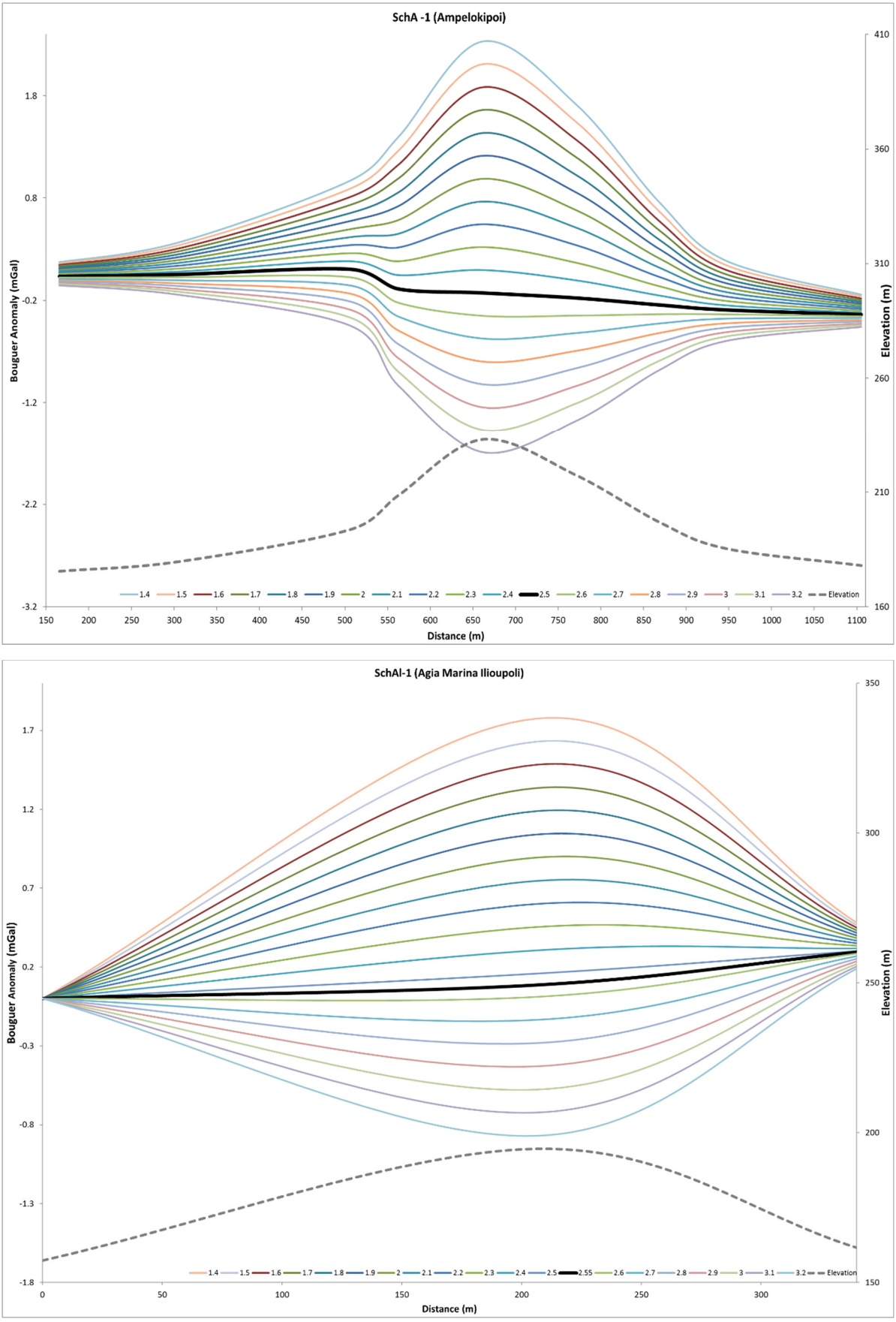

Figure 4.18: Nettleton profiles of Schists of Athens Unit (*SchA*) at *Ambelokipoi* and Schists of Alepovouni (*SchAl*) at *Ilioupoli.*

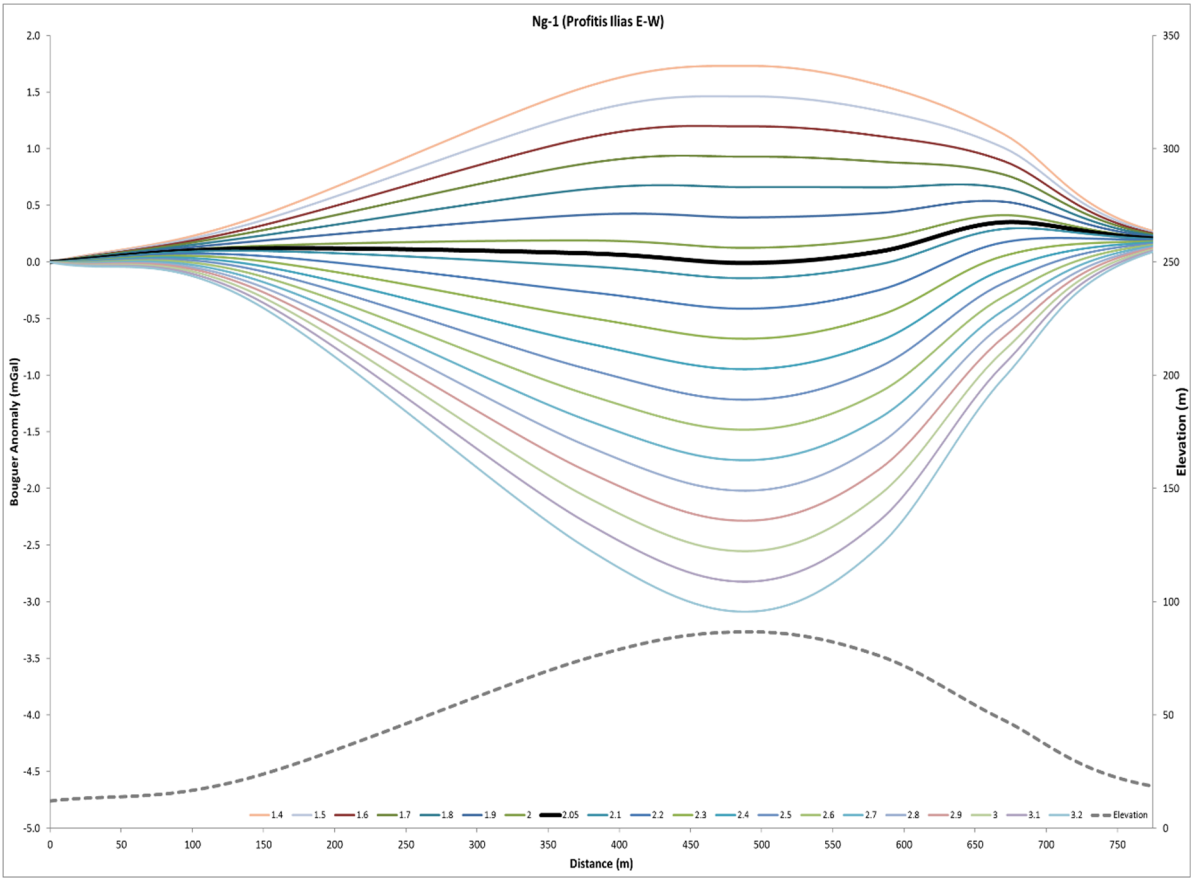

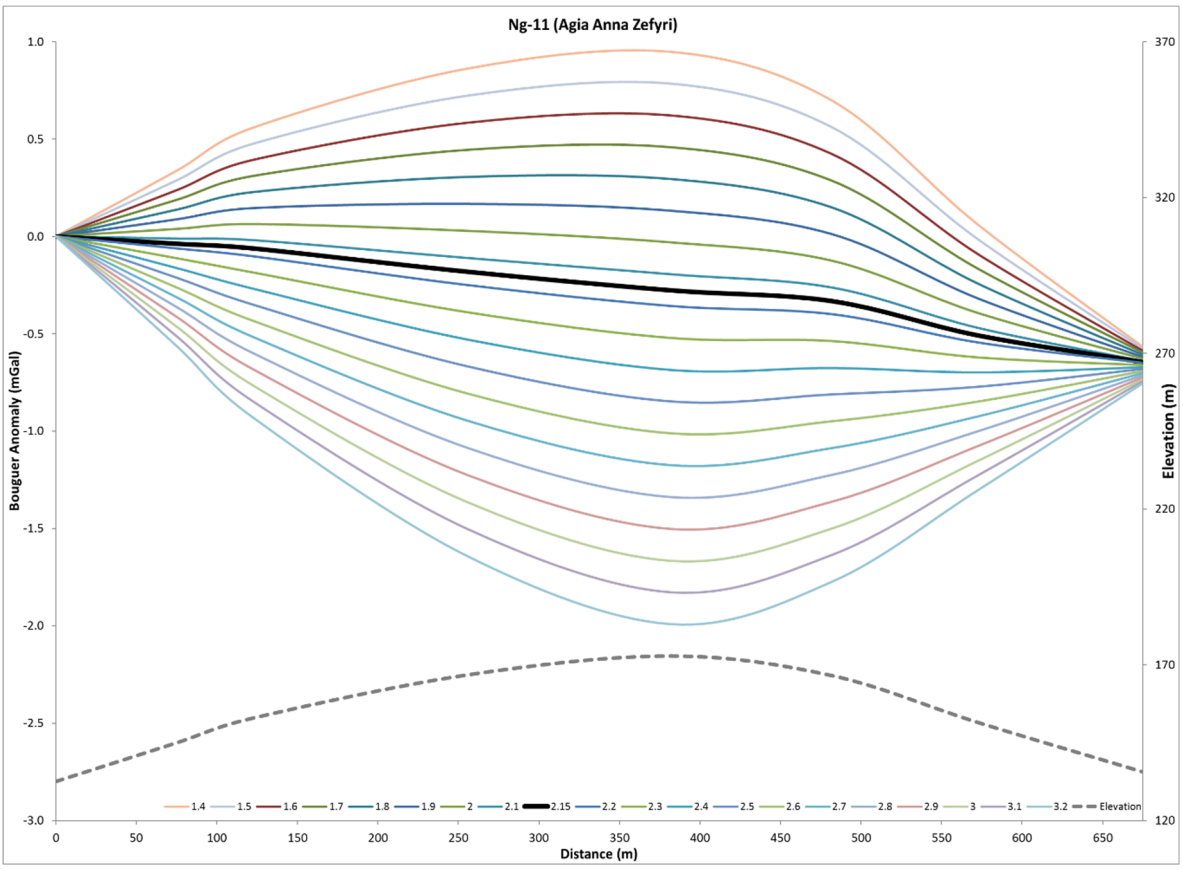

Figure 4.19: Nettleton profiles of Neogene Deposits (*Ng*) at *Piraeus* and *Zefyri.*

4.2.c. Seismic Velocity information

The density of a geological formation is related to its seismic velocity and has already been discussed in theoretical level in §3.6.d, where the most known published empirical curves of their relations have been presented. Many researchers (Ammirati *et al.*, 2018; Berrocal *et al.,* 2004; Chaubey *et al.,* 2002; Makris & Yegorova, 2006; Makris *et al*., 2013; Nakada *et al*., 2002; Sanchez-Rojas & Palma, 2014) have taken advantage of these empirical curves of density-velocity correlation in order to estimate the densities of several geological formations.

In the context of this Ph.D. thesis, we will estimate the density of geological formations, based on bibliographic seismic data regarding the Athens basin area. In Table 4.6, we can observe the densities derived by using three different empirical curves, described previously in §3.6.d (Brocher, 2005; Gardner *et al*., 1974; Nafe & Drake, 1961).

The majority of the provided velocities for Athens formation come from Louis *et al.* (2002b), by carrying out in-situ measurements on geological outcrops of *Ano Liosia* area. Afterwards, Symeonidis *et al.* (2005) executed refraction and surface waves tests above a borehole with known stratigraphy at *Glyfada* area. Additionally, Papadopoulos *et al.* (2001) carried out seismic tomography across boreholes with known stratigraphy at *Kalogreza* area searching for underground cavities. Finally, Papadopoulos *et al.* (2007) executed three long seismic refraction lines, across the Athens and Thriassio basin, illustrating their results. By checking the surface formations along these profiles and their near-surface seismic velocities, we managed to derive similar velocities with Louis *et al.* (2002b) for the Triassic-Jurassic Limestones (*T-J*) and the Talus Cones & Scree (*Pt.sc*).

Geological formation/lithology	**V_p** (in m/s)	**Density by Gardner *et al.*, 1974** (gr/cm^3)	**Density by Nafe & Drake, 1961** (gr/cm^3)	**Density by Brocher, 2005** (gr/cm^3)
Triassic-Jurassic Limestone (*T-J*)[1]	3,500-4,500	2.38-2.54	2.32-2.46	2.32-2.48
Shales & Sandstones (*C-P*)[1]	2,300	2.14	2.03	2.05
Talus Cones & Scree (*Pt.sc*)[1]	1,800-1,900	2.02-2.05	1.81-1.86	1.80-1.87
Neogene Deposits / Several lithologies (*Ng*)[1]	1,400-1,600	1.90-1.96	1.6-1.70	1.6-1.7
Loose Quaternary deposits (*Q-Al*)[1]	1,100-1,500	<1.93	<1.64	<1.6
Conglomerates[2]	2,080-2,270	2.09-2.14	1.95-2.05	1.94-2.02
Clays[3]	1,000-2,500	<2.19	<2.09	<2.1
Breccia[3]	2,500-3,000	2.19-2.29	2.09-2.22	2.1-2.21

Table 4.6: Densities calculated from the empirical curves of velocity-density correlation, based on by 1: in-situ measurements (Louis *et al.,* 2002b), 2: Refraction data (Symeonidis *et al.,* 2005) and 3: Cross-hole data (Papadopoulos *et al.,* 2001).

4.2.d. Comparison of Methods and evaluation results

Other authors in the past (Hammer, 1950; Parasnis, 1952; Whetton *et al*., 1956) have tried to define the rock densities by carrying out both laboratory measurements on specimens or cores and survey methods such as the Nettleton profiles. In such cases, the comparison was made between the saturated density derived from the laboratory measurements and the density derived by the density profile. Although Parasnis (1952) declared that laboratory measurements would be sufficiently accurate, he ended up adopting values that were the mean value of the two methods (laboratory measurements and density profiles). On the contrary, Hammer (1950) supported the idea that the density determination can be done better with the density profiles rather than by laboratory measurements on specimens. Similar aspects presented also by Whetton *et al.* (1956). The last two papers supported that the differences between the two methods can be associated with changes in saturation or mechanical changed during the drilling.

In our case, it seems that the application of Nettleton method for determining the density of the Athens formations proved valuable regarding the post-alpine formations (*Ng*), because they were either too unconsolidated to be measured in the laboratory or they were comprised of several different lithologies (§2.2.b). Each lithology has its own density that was calculated by laboratory measurements but the final representative value of the whole formation could not be estimated. The density profiles were equally helpful in the case of the Athens Schists (*SchA*), which are considered to be a mélange (Table 4.7).

Geological formation/lithology	**Adopted Density (gr/cm^3)**	**Dominant Method**
Triassic-Jurassic Limestones (*T-J*)	2.68	Laboratory
Dolomites (*D*)	2.76	Laboratory
Marbles (*M*)	2.68	Laboratory
Schists (*Sch-Hymettus Mt*.)	2.54	Laboratory
Schists (*Sch-Penteli Mt*.)	2.68	Laboratory
Shales & Sandstones (*C-P*)	2.57	Laboratory
Limestones of Athens Unit (*CA*)	2.66	Laboratory
Limestones of Alepovouni (*CAl*)	2.65	Lab & Nettleton
Athens Schists (*SchA*)	2.50	Nettleton
Schists of Alepovouni (*Sch-Al*)	2.36	Laboratory
Neogene Deposits / Several lithologies (*Ng*)	2.10	Nettleton
Talus Cones & Scree (*Pt.sc*)	2.30	Lab & Seismic
Loose Quaternary deposits (*Q-Al*)	1.60	Seismic

Table 4.7: Adopted densities of geological formations, used in gravity data processing.

On the other hand, the most carbonate formations, such as the Triassic-Jurassic limestones (*T-J*), the Dolomites (*D*), the Marbles *(M)* and the Limestones of Athens Unit (*CA*), were characterized by quite smaller densities based on the Nettleton profiles results and are not quite representative. This could be due to the increased weathering (Hammer, 1950; Whetton *et al.*, 1956), existing cavities or due to the regional anomalies (Hammer, 1950), given the fact that the density profiles of the first three (*T-J, D, M*) were carried out constrainedly close to mountain slopes and therefore regional anomalies. The same discordances, probably for similar reasons, are observed for the Shales & Sandstones (*C-P*), the Schists *(Sch)* - mainly for the ones of *Penteli* Mt. - and the Schists of Alepovouni (*Sch-Al*). For all these formations, the adopted densities were based on the laboratory measurements (Table 4.7).

In the case of the Loose Quaternary deposits (*Q-Al*) the only available density was derived based on seismic reference data, since it is obvious that no laboratory measurements can be executed. Moreover, the density of the inhomogeneous formation of Talus Cones & Scree (*Pt.sc*) was selected somewhere between the laboratory measurements and the density derived by the seismic data (Table 4.7), as long as the density profiles could not determine a proposed density.

4.3. DATA PROCESSING - QUALITATIVE INTERPRETATION

Given the fact that gravity measurements are affected by many parameters (topography, sea level, elevation etc.), that have already been described thoroughly in §3.3, we have to consume lots of time for the data processing in order to take the final result. The evolution of the computer science and the development of new algorithms, improve the situation. But the human parameter holds the major role, based on the decisions taken for several steps in the processing procedure (e.g. reduction density, gridding method, applied filters and their parameters).

The whole process can break in semi-individual parts, like the DGPS post-processing (§4.3.a), the gravity data preparation and visualization (§4.3.b), the data reduction with the application of all the essential corrections (§4.3.c), the data enhancement (§4.3.d), the anomaly isolation (§4.3.e), the 3D inversion (§4.4.c) and the production of the appropriate maps and sections (§4.4.a). Depending on the final scope of each gravity survey, some of these processing parts can be ignored, except for the absolutely basic data reduction. In the following sections, we will describe the practical operations made in the context of the data processing for this Ph.D. thesis, since the theoretical foundation has already been analyzed in chapter 3.

4.3.a. DGPS Data Processing

In §4.1.c we mentioned that the topographical measurements for the determination of the coordinates of every gravity measurement were carried out with the *static* method. The method was chosen due to the urban environment and the desired high accuracy. But this

method requires a post-processing procedure, during which the final horizontal and vertical coordinates are determined, with an accuracy of a few millimeters (3 decimals).

The post-processing was executed with the *TopCon Tools* program that provides you the environment for illustrating, processing and adjusting incorrected field DGPS observations. The input raw data (satellite recordings) are obtained from the internal storage space of the GPS receivers. After the calculation of the coordinates, a quality control is also available with several calculated parameters (horizontal and vertical precisions, deviations etc.). Additionally all kind of information is presented regarding the details of the acquisition, like the type of antenna, the antenna height and the way of measuring it, the recording duration etc.

The EGM96 geoid model was used to convert the ellipsoidal heights into orthometric heights, required for the gravity processing. The elevation mask was kept to 15^{o} and the system as GPS+. The coordinates of all the survey points were calculated based on the Hellenic Geodetic Reference System (*EGSA'87*).

4.3.b. Preparing and visualizing data

This step of the processing procedure intends to outline more reliable and unambiguous anomalies, with better visualization of the spatial data that will benefit the interpretation step. For that reason, simple inspections are essential in order to avoid foolish errors in the data input, since in our case the field hand-written data from the gravimeter (*Lacoste & Romberg D-496*) have to be typed in a worksheet database in the appropriate format. Of course, the counter readings of the instrument have to be converted in milliGalls, based on its calibration table. Apart from the database of the gravity stations, two more databases have to be created; one including the calculated coordinates of all the survey points (§4.3.a) and one more regarding the gravity bases and their absolute values.

The choice of the gridding method used for the spatial distribution of the data is very important since it can either outline the existing anomalies or distort the image. It should be chosen based on the type of the survey points (parallel profiles, scattered points etc.).

In our case, with the hundreds of scattered points spread to the greater area of Athens basin, the ideal gridding method was considered to be the *Minimum Curvature*, which interpolates the data in the smoothest possible way (§3.4.a.2) and has already been applied by many researchers during gravity surveys (Blaikie *et al.,* 2014; Crossley *et al*., 2004; Kay & Dimitrakopoulos, 2000; Louro & Mandovani, 2012; Mendonca & Silva, 1995; Shafie *et al*., 2014; 2016). The grid size was set initially to 500 meters at the first phase, where the stations were placed at distances of 1000 meters, but finally it was reduced to 250 meters because of the denser collected data. The parameters defining the stop of the iterative process for creating the grid were the maximum 100 iterations and the condition that 99% of the survey points were in the 1% of the data range.

4.3.c. Data Reduction and Bouguer Anomaly Calculation

The theoretical background of the gravity data reduction has been discussed extensively in §3.3. Therefore, in the following sections we will discuss the practical parameters and issues of the gravity survey of this Ph.D. thesis.

The whole gravity processing was carried out with the ***Oasis Montaj*** software by Geosoft, along with the necessary supplementary extensions, like the *Gravity & Terrain Correction*. The ***Oasis Montaj*** software is a powerful tool for visualization, analysis and processing data from potential fields. It has been widely used in the scientific community by many researchers (Araffa, 2012; Araffa *et al*., 2015a; 2015b; Blaikie *et al.,* 2014; Dilalos & Alexopoulos, 2017; Farhi *et al.,* 2016; Fathy *et al*., 2013; Fries *et al*., 2005; Louro & Mandovani, 2012; Shafie *et al*., 2014; 2016; Sultan *et al.,* 2009a; 2009b; Zahra & Oweis, 2016) taking advantage of the enormous processing and filtering tools.

4.3.c.1 Drift and Tidal Corrections

During the whole gravity survey in Athens basin, every 2-3 hours we were reoccupying the nearest established gravity base (§4.1.a) in order to calculate with good accuracy the drift correction of our instrument (§3.3.b). This means that practically the measurements were carried out in loops, where its start and end were defined by a base occupation.

The drift was calculated with the *Gravity & Terrain Correction* extension of the *Oasis Montaj* software, based on the closure error between the first and last reading in each loop based on the following equation:

$$drift = \frac{(base\ 2\ reading - base\ 1\ reading) - (base\ 2\ Absol.G - base\ 1\ Absol.G)}{(base\ 2\ time - base\ 2\ time)}$$

After the drift calculation, the closure errors had been evaluated and usually if the drift closure was more than 0.01mGal/hour, the measurements were acquired again in order to have qualitative data. Fortunately, this was very rare in our case.

Selecting the option to calculate the drift correction, the program calculates simultaneously the tidal effects and the corresponding correction (§3.3.a), based on the measurement time of each station and the program's database. The range of the calculated tidal corrections is from almost -0.1008 mGal to 0.1713 mGal.

Therefore, after the time-dependent corrections of the drift and earth tides, the Absolute Gravity Value of each survey point is calculated. This is also the procedure in order to determine the absolute values of the established gravity bases.

4.3.c.2. Latitude and Free-Air Corrections

The next step includes the latitude and free-air corrections, where the calculated coordinates of each gravity station are taken into account.

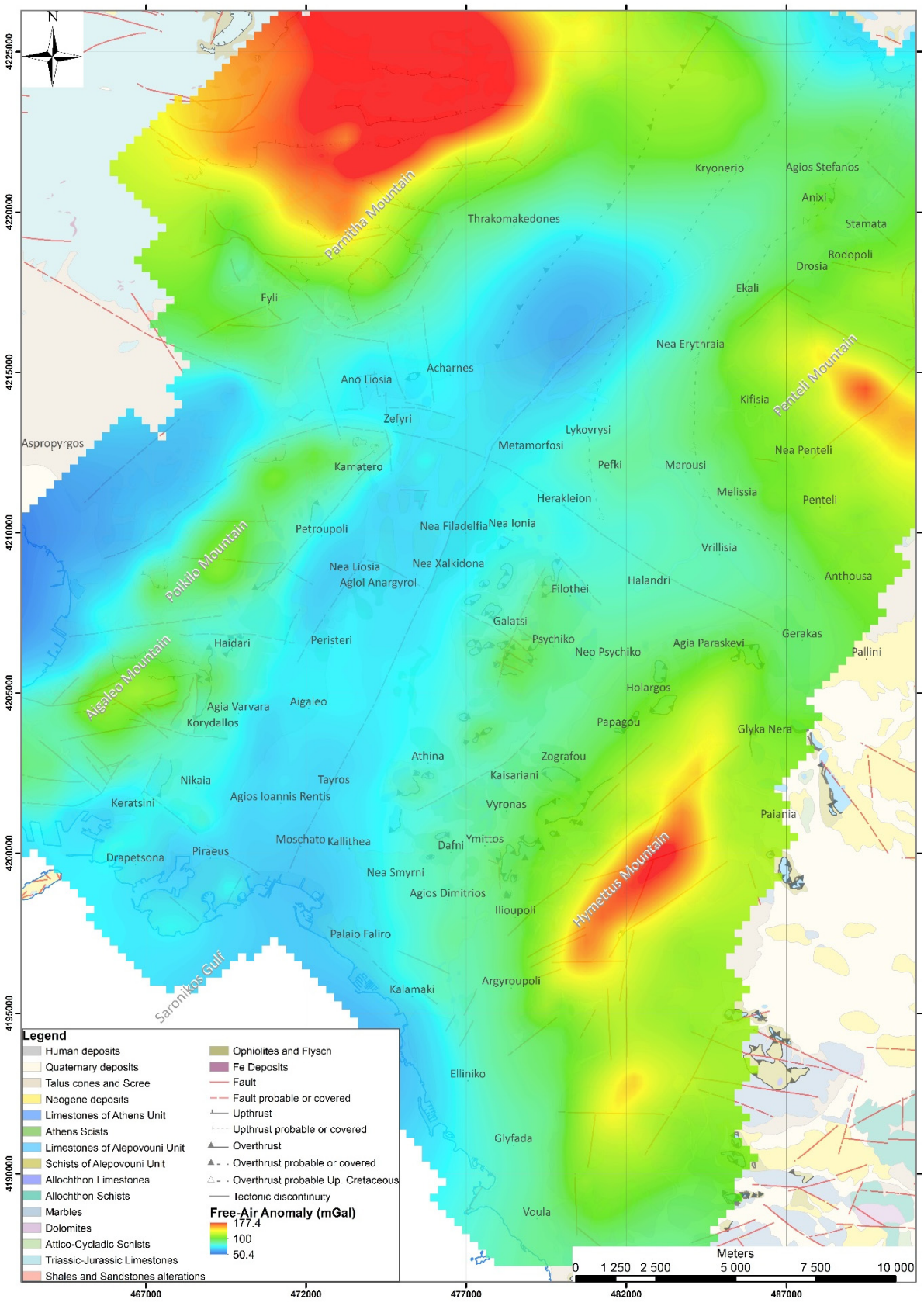

Figure 4.20: Free-Air Anomaly Map

For the calculation of the Latitude Correction, the normal gravity has to be determined first (§3.3.c). The program provides four different International Gravity Formulas (*IGF30, IGF67, GRS80 and WGS84*) for its calculation. We applied the **WGS84 formula**, which is internationally accepted by the International Union of Geodesy and Geophysics (IUGG) and it is considered to be the best one, since it takes into account the weight of the atmosphere. If ϑ is the geodetic latitude of the station, the normal gravity is calculated with the following equation:

$$g_{1984} = 9{,}780{,}320.67714\frac{1 + 0.00193185138639sin^2\theta}{(1 - 0.00669437999013sin^2\theta)^{0.5}}mGal$$

For the Free-Air Correction (§3.3.d) the formula finally selected between the proposed ones of the program is the following (*h* is the station elevation):

$$\Delta g_{FAC} = 0.308596h\ in\ mGal$$

The calculated Free-Air Anomaly of the survey points range from almost 50.4 mGal to 177 mGal (Fig. 4.20). The results are quite predictable, with the lower values located in the basins areas (smaller elevation) and the higher ones at the areas with greater relief, such as the surrounding mountains and the central hill axis.

4.3.c.3. Terrain Correction

As we have already discussed in §3.3.f the procedure for the calculation of the Terrain Correction is simple, based on the Hammer zones (Hammer, 1939), but time-consuming. The classic method required detailed topographic maps. Given the fact that Athens basin is an urban area, the greatest part of it is covered with artificial constructions (buildings, roads etc.). This means that the existing topographic maps, published by the Hellenic Military Geographical Service several years ago, are not efficient enough, because large-scale constructions provoke great changes in geomorphology, modifying the existing topography.

For that reason, recently updated DEM map (Fig. 4.21) had been used for the calculation of the essential terrain corrections, for a radius up to 21 kilometers for each station. These DEM maps have grid cell size equal to 5 meters and they were crosschecked with the DGPS field data (more than 1,100 points).

The terrain corrections were calculated through the *Gravity and Terrain Correction* extension of *Oasis Montaj* software, as many authors have already done (Araffa *et al*., 2015a; 2015b; Dilalos & Alexopoulos, 2017; Farhi *et al.,* 2016; Re *et al.,* 2016; Sultan *et al.,* 2009a). For the inner zones, up to a radius of 1.500 meters, the corrections were calculated based on a more detailed DEM with 5 meter cell spacing including the terrain relief and the bathymetry data of the nearby sea areas (e.g. *Saronikos Gulf*). The corrections for the zones between 1.5 and 21 kilometers were calculated from another coarse DEM, with 25 meter cell spacing. This is because the routine of the *Oasis Montaj* software calculates one regional terrain correction based on the coarse extended DEM and a local one based on the more detailed DEM, which

will be added to the regional one. In cases with severe relief, supplementary field topographic information for the inner zones was provided, since DEM could be inadequate.

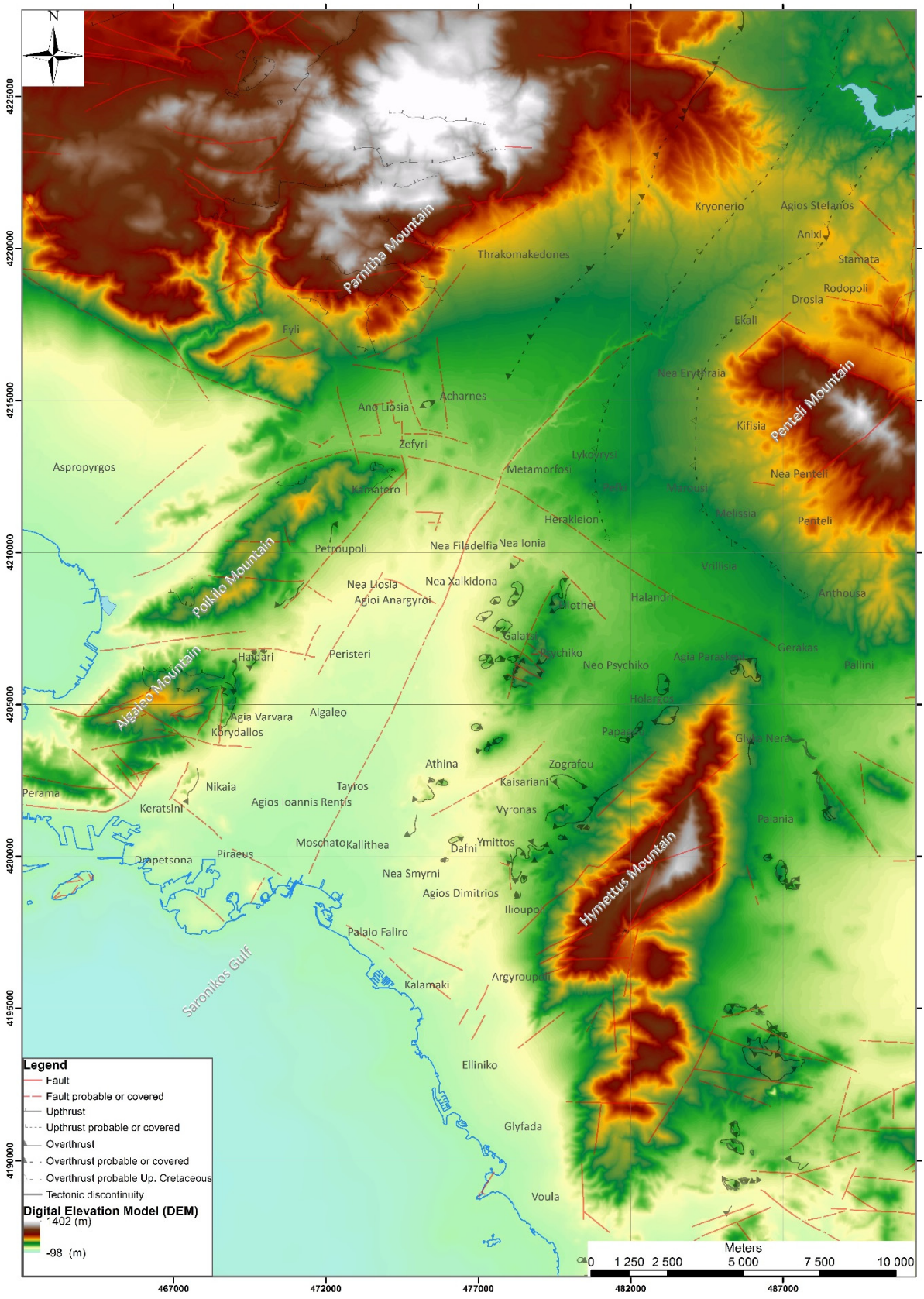

Figure 4.21: Digital Elevation Model (5m grid cell size) along with the tectonism of the study area

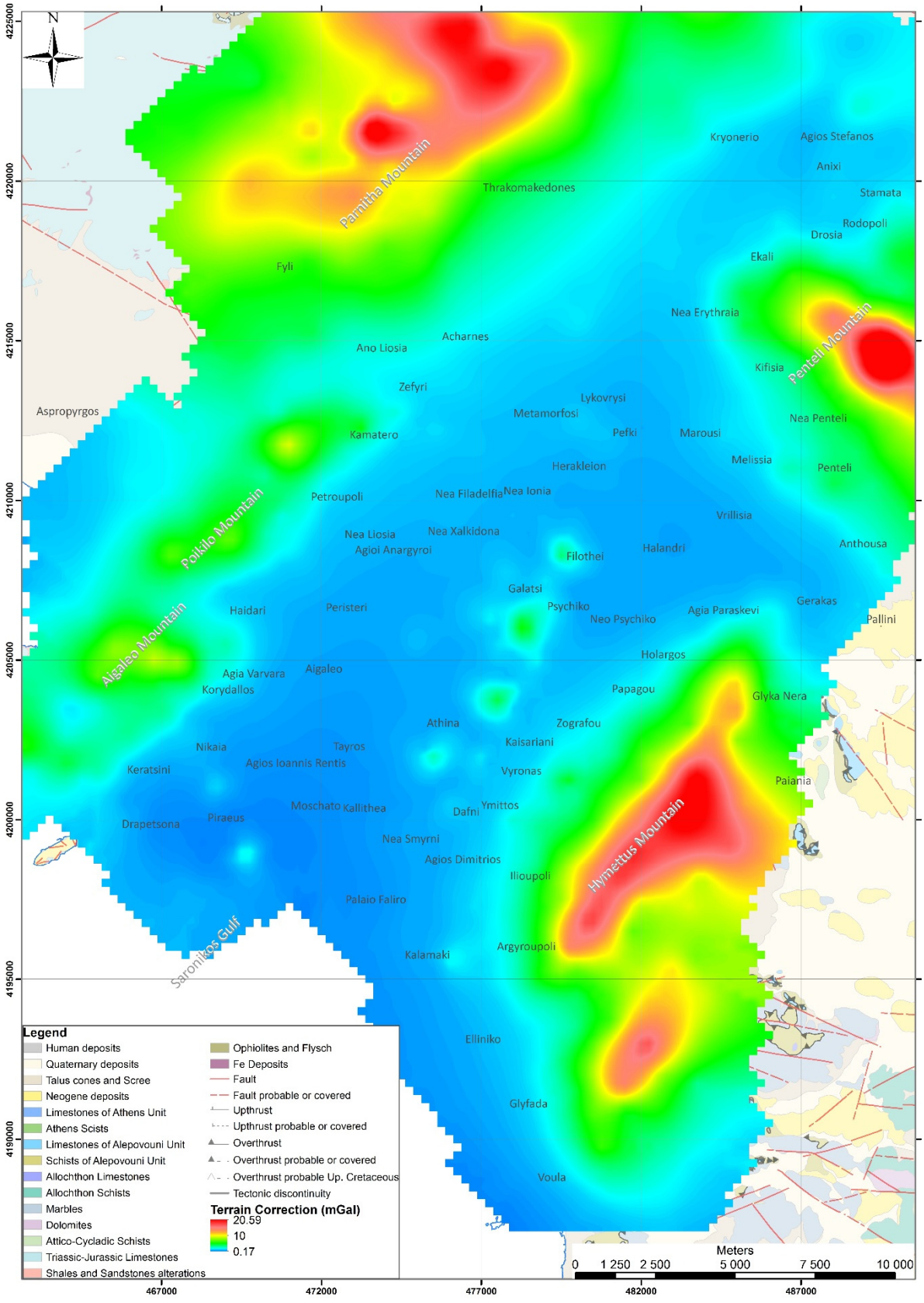

Figure 4.22: Distribution of Terrain Correction values.

Based on the manual of the *Gravity and Terrain Correction* extension (Geosoft, 2010) of *Oasis Montaj* software, the Terrain Corrections are calculated using a combination of the method described by Nagy (1966) and Kane (1962). The DEM is sampled to a grid mesh centered on the survey station to be calculated. The calculation of the correction is based on contribution of the *near* zone (1 cell radius ring from station), the *intermediate* zone (2-16 cell radius ring) and the *far* zone (more than 16 cells radius ring).

In the *near* zone, the effect of four slopping triangular sections is summed up, describing the surface between the station and the elevation at each diagonal corner. In the *intermediate* zone, the terrain effect is calculated using the flat topped square prism approach proposed by Nagy (1966) for every station. Moreover, for the *far* zone, it is calculated based on Kane's (1962) annular ring segment approximation to a square prism. Additionally, the DEM grid is reflected on its edges in order to ensure that the required radius for the correction will be ensured and beyond that, any dummy values will be first interpolated by the adjacent valid ones. Nevertheless, an edge correction will be calculated in order to account the distance between the station elevation and the grid average elevation beyond the DEM grid edge.

The Terrain Correction values that have been calculated range from 0.17 mGal to 20.59 mGal and their distribution (Fig.4.22) seems satisfying, since the bigger ones are located up to mountainous areas.

4.3.c.4. Building Correction

It has already been mentioned that the mass of buildings close to a gravity station produces an upward attraction (§3.3.h.4), distorting the reading value. Taking into consideration that Athens is a fully developed city with an enormous number of buildings (Figs. 4.23) and other anthropogenic constructions, we decided to quantify somehow this impact on the measurements, calculating a so-called *Building Correction*.

Several researchers have worked on the building effect and some of them have tried to quantify it. Most of them have based their calculations on Nagy (1966), who calculated the gravitational attraction of a rectangular prism. Radogna *et al.* (2003) carried out a micro-gravity study for the metro line of Lausanne city, where they calculated the building effects through a software. Detailed work for the correction of building effects is illustrated by Debeglia & Dupont (2002), by modelling the buildings with polygonal prisms. Additionally, Panisova *et al.* (2012) introduced a microgravity survey in the interior of a church, where photogrammetry has been used to estimate the gravitational effect of the church itself. Finally, Yu (2014) investigated the building effect, adjacent to a new-developed city and a line of buildings. He carried out several gravity profiles parallel to this building line, with increasing distance from them.

In the following sections, we will develop in individual steps the concept of quantifying the *Building Correction*.

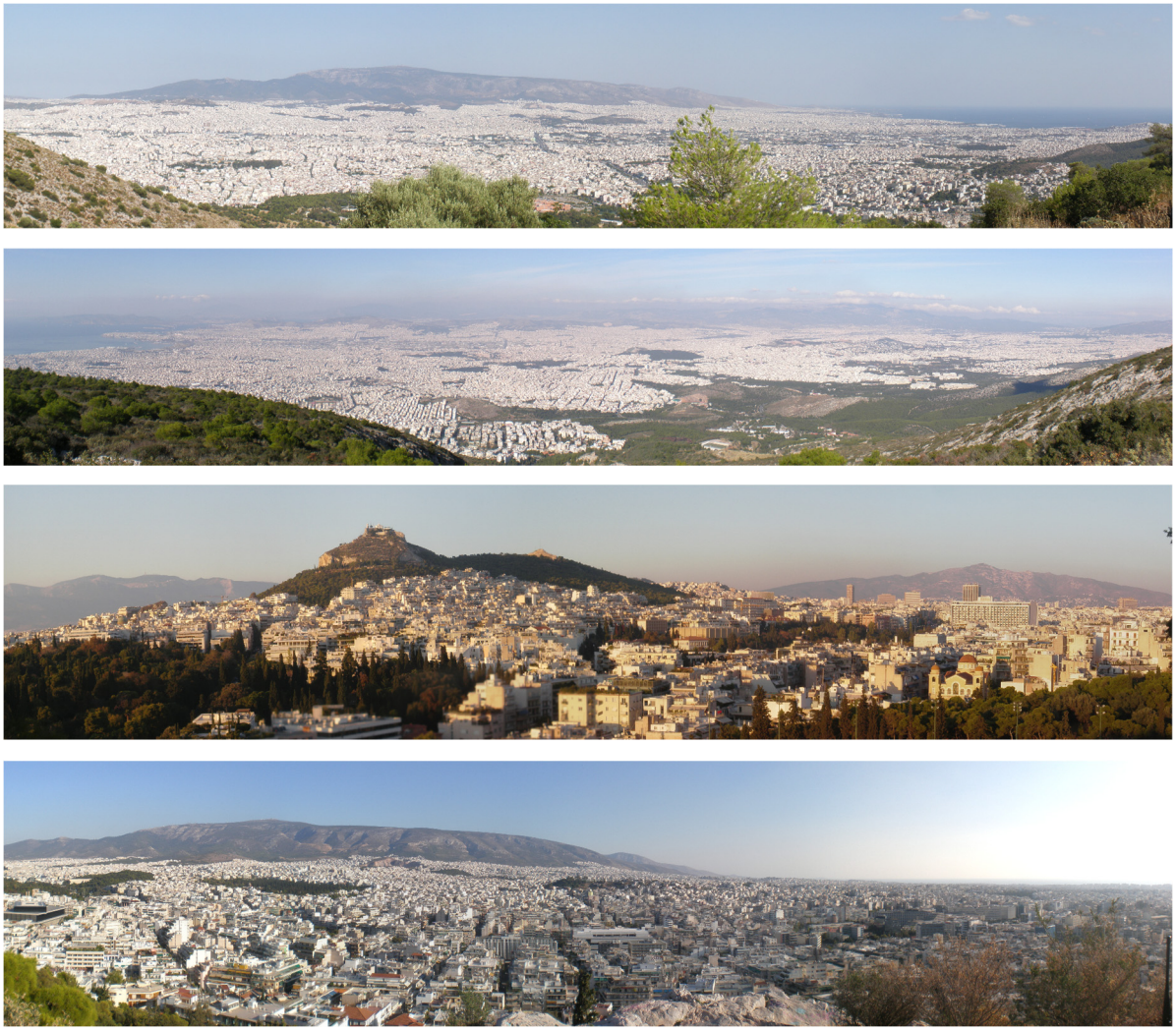

Figure 4.23: Panoramic photographs of the Athens basin study area, illustrating that is a city practically covered by buildings.

i. Determining the building coverage and volume

The first problem we have to deal with is to calculate the spatial coverage of the anthropogenic constructions and buildings in the area of interest. Beyond this, it is necessary to obtain data concerning the volume extension of these constructions. In other words, the information of their height extent is also essential, or at least an indirect approach to calculate it, such as the one based on the number of floors.

There are some methods to retrieve this kind of data. One common example is the town-planning maps that government services hold (Haala *et al*., 1998; Brenner, 2000; Radogna *et. al.*, 2003; Vosselman & Dijkman, 2001). Nevertheless, for such a big area of interest, like Athens basin (almost 720km^2), this seems impractical, endless and time-consuming.

For that reason, we chose a more simple, quick and precise method to calculate the building volume, for which two types of raster data is required. The first one is a detailed *Digital Elevation Model* (DEM), as the one used in the calculation of the Terrain Correction

(Fig.4.21) in the previous section. The second necessary package of data provides us with information about the maximum elevation of the covered area, including all the anthropogenic constructions. Many people tend to confuse it with a DEM, but the correct term is '*Digital Surface Model*' (DSM).

A *Digital Surface Model* (DSM) can be generated by high accuracy airborne LIDAR data (Jochem *et al.,* 2009; Sampath & Shan, 2007; Yan *et al.,* 2015; Yu *et al.,* 2010) or even with the contribution of UAV/drones (Eisenbeiss & Zhang, 2006; Remondino *et al.,* 2011; Tokunaga, 2015), but with the second one limited to relative small areas. Nowadays this information is taken advantage of in many cities of the world for several practical applications, in order to calculate the volume of the buildings and produce their 3D reconstruction (Baba *et al.,* 2014; Brédif *et al.,* 2013; Mongus *et al.,* 2014; Yan *et al.,* 2017).

LIDAR data gives us the maximum elevation points of the investigated area. This means that if a building exists, the elevation of its roof will be measured, as the maximum elevation/surface point. If not, it will measure the terrain elevation (same as in the DEM). Usually, such kinds of data are provided with a cell size of 0.8-1 meter. The DSM of Athens basin is presented in Figure 4.24, with a grid cell size of 5 meters. The white areas do not enclose any height information, due to either the absence of buildings (e.g. mountainous areas) or the existence of protected areas (e.g. military settlements).

Advanced toolboxes of a Geographic Information System and more specifically a raster calculator tool are required in order to isolate the buildings. We have to subtract the DEM elevations from the respective DSM elevations (DSM-DEM) (Ameri, 2000; Baba *et al.,* 2014; Brunn & Weidner, 1997; Dilalos *et al.,* 2018; Haala & Brenner, 1999; Jochem *et al.,* 2009; Weidner & Forstner, 1995). In that way, a new raster map will be produced, illustrating the spatial distribution of the heights of all the buildings and constructions in the study area. This is called '*Building Height Map*' (Fig.4.25), which practically provides the volume of the building (3 dimensions), based on the horizontal distribution (2 horizontal dimensions) of their heights (1 vertical dimension). Although, it might also contain information about the three heights, we consider it cleavable (Awrangjeb *et al.*, 2012; Brunn & Weider, 1997; Dilalos *et al.,* 2018; Haala & Brenner, 1999; Matikainen *et al.,* 2003; Priestnall *et al.,* 2000), since we are dealing with extremely smaller volumes, coverage and heights at the same time. Great emphasis must be given on the management of the two types of raster maps (DEM and DSM), their cell size and their spatial limits in order to have accurate and correct calculation of the building heights.

Observing the produced *Building Height Map* (Fig.4.25), someone can detect the areas with the higher buildings (up to 30 meters height), such as the greater area around the *Downtown*. In these areas, it is expected that the impact of the buildings to the gravity measurements will be larger. In this map also, the white areas do not provide any information, since we did not have DSM information that could be subtracted from the DEM.

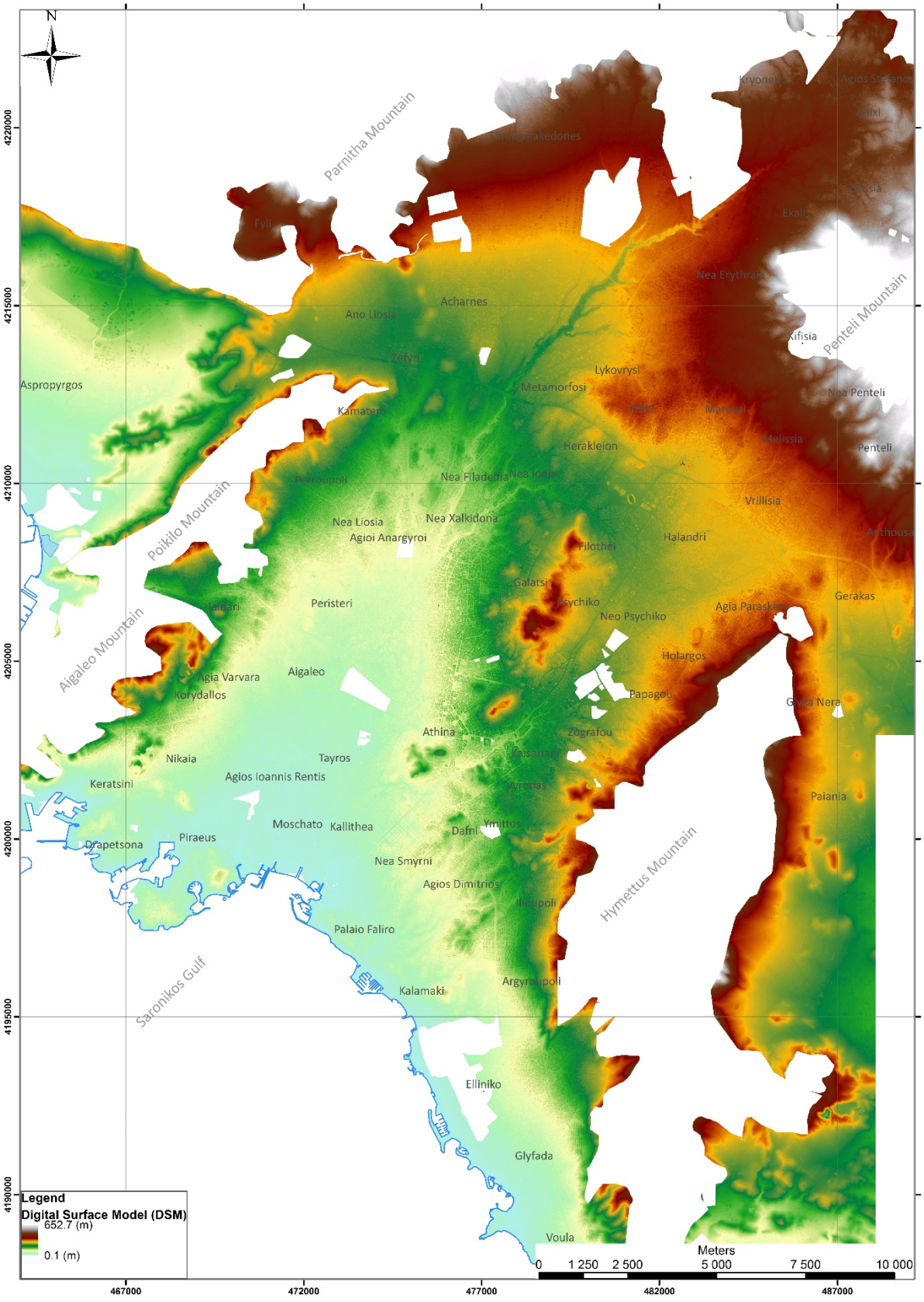

Figure 4.24: Digital Surface Model (DSM) of the Athens basin

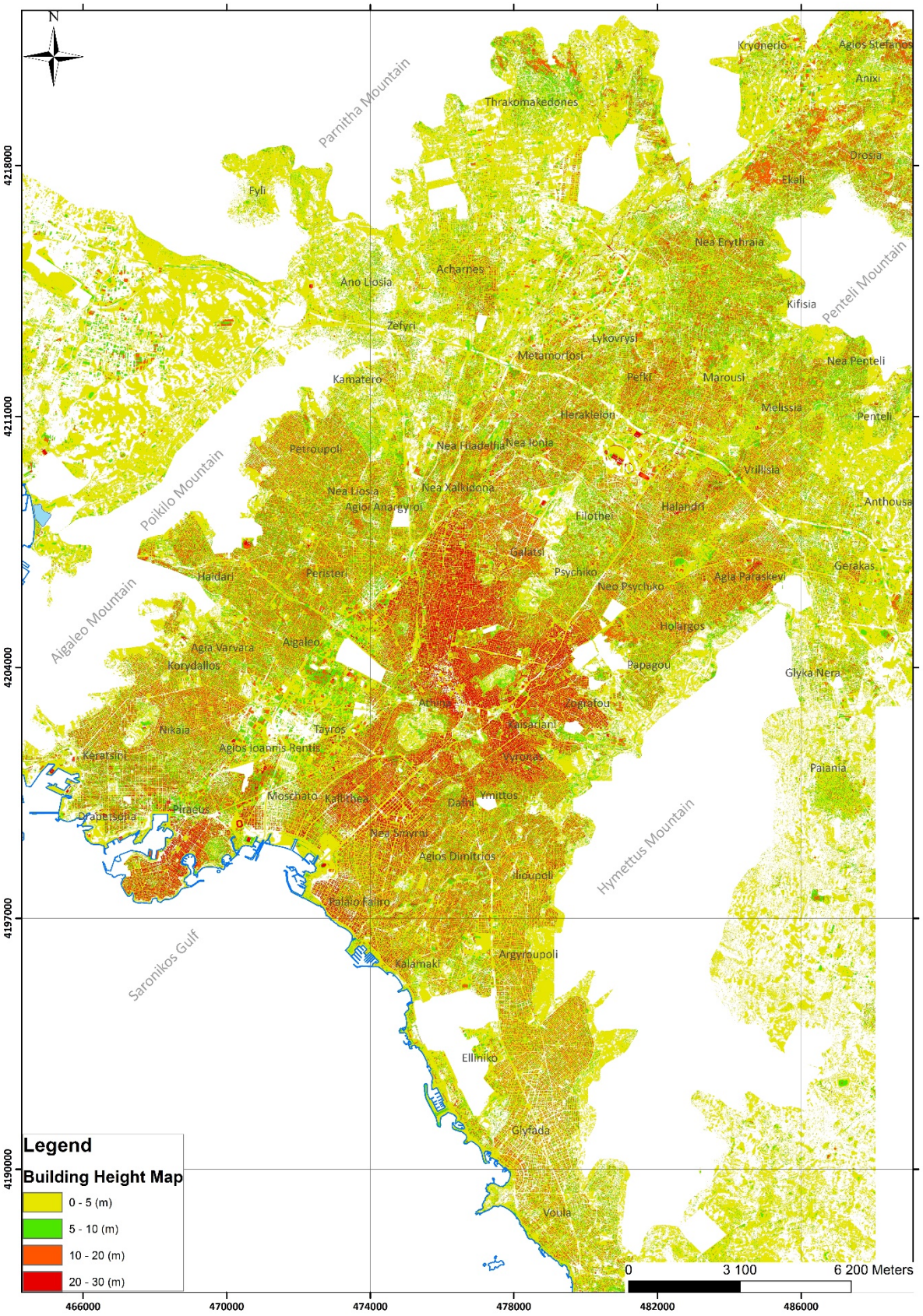

Figure 4.25: Building Height Map of Athens basin

ii. Building density calculation

In the previous paragraph, we managed to produce a map demonstrating the spatial distribution and height of all the buildings in the study area (Fig. 4.25). However, the mean density of these buildings is required, in order to calculate the desired Building Correction. In a typical city, different types of buildings exist, such as the ones made of stonewalls, wooden walls, concrete, reinforced concrete, aluminum and glass. In large-scale gravity researches, a mean density of the most common type of building has to be calculated. In the city of Athens, the most popular type of building is the one with reinforced concrete and brick walls.

Regarding the structure of this type of buildings and basic aspects of building construction, we have to take into consideration the gravitational attraction of the walls and floor slabs summative. We have to accept some common standards, like the fact that the thickness of the floor concrete slab is usually equal to 0.20 meter, the exterior brick wall thickness equal to 0.20 meters and the interior ones equal to 0.10 meter. Moreover, an average height of an apartment (floor to ceiling) is 2.70 meters.

After several volume calculations of structures, with a view to estimating the respective participation percent of each building material, it turned out that the concrete (slabs and pillars) contributes 10.5% to the building volume, the brick inner and outer walls 11% and the air occupy the rest 78.5% of the building. The above calculations were based on a "model" building of 100m^2 floor, taking into account the basic aspects we mentioned in the previous paragraph (wall and slab thickness). Therefore, for each floor that has 300m^3 volume, the slab occupies the 20m^3, the pillars almost 11.5m^3 and the basic walls 33m^3.

There is also an empirical type derived by the civil engineers, indicating that the required volume of concrete can be estimated by multiplying the area of the ground plan times 0.3-0.35. This comes to validate the pre-mentioned calculations.

Several densities concerning the reinforced concrete (ACI code 318; Blake, 2013; Chromčák *et al.,* 2016; Stoulos *et al.,* 2003) can be found. In the context of this Ph.D. thesis, the author chose a dominant density for the reinforced concrete, equal to 2.4 gr/cm^3. Regarding the density of the bricks (walls), a mean density equal to 1.7 gr/cm3 has been chosen, among several suggested values (Alawadhi, 2008; Ashby & Johnson, 2013; Chen *et al.,* 2011; Chromčák *et al.,* 2016; Kuranchie *et al.,* 2016; Stoulos *et al.,* 2003; Jung, 1961). Taking into consideration the contribution percent of each material, estimated in the previous paragraph, we can calculate the required building density.

Therefore, we can simply multiply the contribution percent of each material with its characteristic density with the aim of calculating the building's density. The mean density of reinforced concrete building has been calculated by the author equal to 0.44 gr/cm^3. Yu (2014) has also calculated a close building density equal to 0.459 gr/cm^3 using theoretical building models while Szeto (2006) calculated the building density equal to 0.58gr/cm^3 (±0.06), considering a box-like building. Therefore, we can consider our calculations valid.

iii. Calculation of Building Correction

We need two types of data, that is to say the volume of the buildings (Building Height Map – Fig. 4.25) and their mean density (0.44 gr/cm^3), in order to proceed with the calculation of the Building Correction (Dilalos *et al.,* 2018). The preparation and calculation for both parameters have already been discussed in the above sections of this thesis. The calculation procedure is similar to the one for the Terrain Correction, based on the classic Hammer zones (Hammer, 1939), and is carried out through the *Gravity and Terrain Correction* extension of *Oasis Montaj (Geosoft)*.

In terms of correlated procedure of Terrain Calculation, three parameters have to be changed, in order to obtain the desirable Building Correction. Firstly, the inner zone radius has been effectively reduced to 100 meters and the outer one to 1,000m, while during the Terrain Correction calculations, a radius of 1,500 meters and 21 kilometers respectively had been used. We chose these zone radiuses, because the building effect minimizes rapidly with the distance, until it is considered negligible (§3.3.h.4). Secondly, instead of an elevation input, the Building Height (Fig. 4.25) is required here. Thirdly, the reduction density given in the formula is not the classic Bouguer density (2.67 gr/cm^3) but the one calculated for the buildings, equal to 0.44 gr/cm^3.

With only these three different parameters, the procedure of the Building Correction calculations can be completed for each gravity station separately. Their spatial distribution of the quantified Building Correction is presented in Figure 4.26, based on the locations of the gravity stations. They range from 0 mGal (in suburbs and mountainous areas) to 0.24mGal, for stations surrounded by great volumes of buildings, like in the center of the city (*Downtown*). Therefore, generally we can observe that the highest values of Building Corrections are located in the areas with increased density of population (therefore higher buildings), such as the greater area of *Downtown, Zografou, Kallithea, Piraeus, Nea Smyrni, Marousi* etc., which is absolutely normal and foreseeable.

iv. Application of Building Correction

The next step is to apply the calculated Building Correction to the acquired gravity measurements. The reduction procedure is similar to the Terrain Correction. After the typical data reduction of the gravity measurements, the Simple Bouguer Anomaly comes up, as we will present in the following section (§4.3.c.5). Ordinarily, the Terrain Correction (TC) has to be added, in order to calculate the Complete Bouguer Anomaly (g_{CBA}).

However, in the case of an urban geophysical survey like ours, the Building Correction (BC) is also necessary to be added to the Simple Bouguer Anomaly (g_{SBA}) along with the typical Terrain Correction, in order to obtain the desired Complete Bouguer Anomaly (g_{CBA}), as it is indicated in the next section (§4.3.c.5).

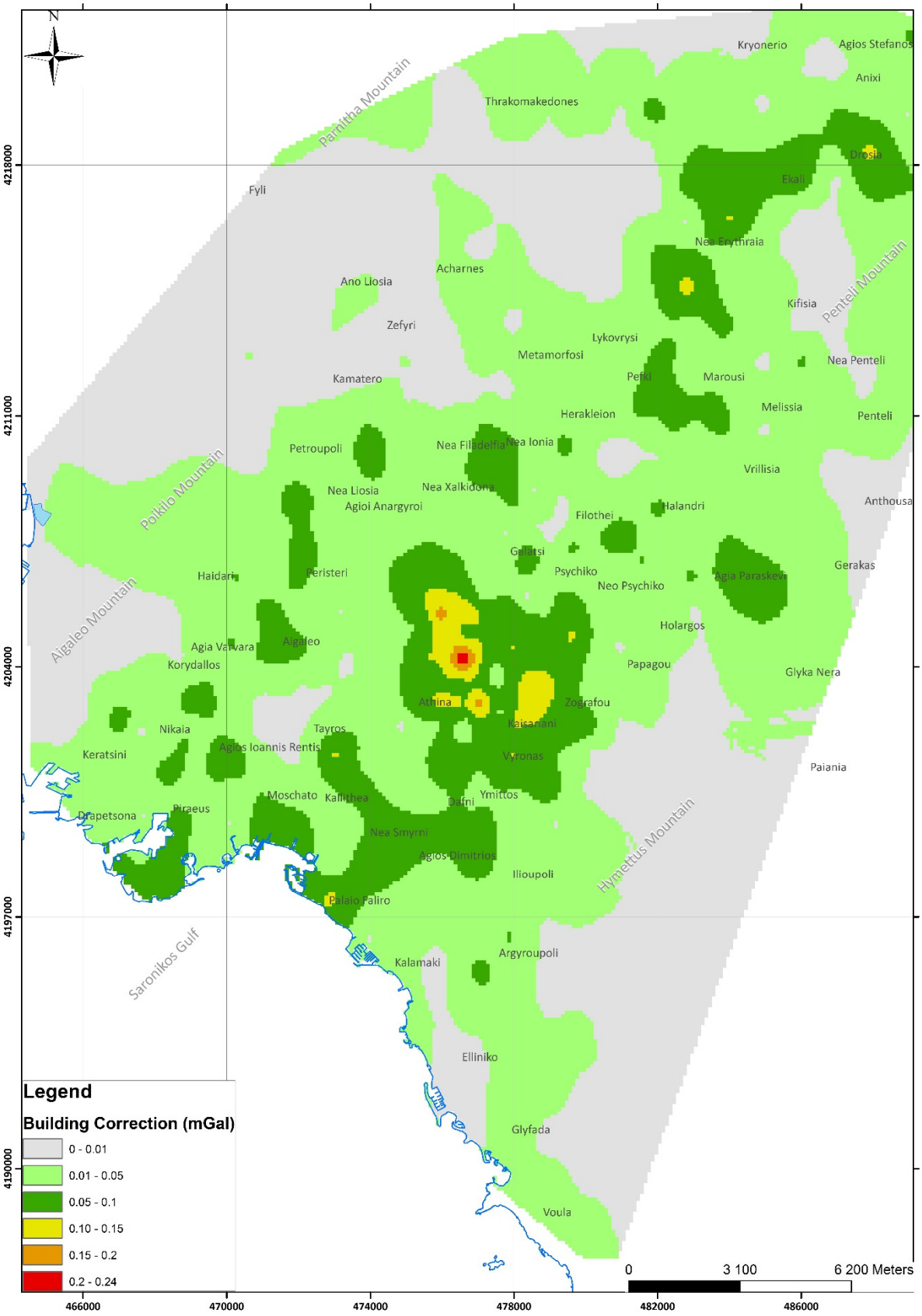

Figure 4.26: Building Correction distribution in Athens basin

4.3.c.5. Bouguer Correction

As we have already discussed in §3.3.e, the Simple Bouguer Anomaly (g_{SBA}) corrects only the attraction of the rock slab. The Complete Bouguer Anomaly (g_{CBA}) corrects additionally earth irregularities due to the terrain relief close to the measurement, which means that it embodies in the formula the Terrain Correction and in our case the Building Correction too (§4.3.c.4).

The calculations have been executed through the *Gravity and Terrain Correction* extension of *Oasis Montaj*. First, the Simple Bouguer Anomaly (g_{SBA}) is calculated with the following equation:

$$g_{SBA} = g_{FA} - 0.0419088\rho h + g_{curv}$$

where g_{FA} is the calculated Free-Air Anomaly in mGal (§4.3.c.2), ρ is the selected Bouguer density of the rock slab in gr/cm^3 and g_{curv} the Curvature correction (§3.3.h.2) applied, based on LaFehr's formula (LaFehr, 1991), in order to convert the geometry of the infinite slab to a spherical cap of radius equal to 166.735km.

Afterwards, the Complete Bouguer Anomaly (g_{CBA}) can be calculated based on the equation:

$$g_{CBA} = g_{SBA} + g_{TC} + g_{BC}$$

where g_{SBA} is the Simple Bouguer Anomaly, calculated above (in mGal), g_{TC} is the calculated Terrain Correction in mGal (§4.3.c.3) and g_{BC} is the calculated Building Correction in mGal (§4.3.c.4).

The assumed constant reduction density for the Bouguer correction was set up to 2.67gr/cm^3, used by several other researchers too (Casten & Snopek, 2006; Chailas *et al.,* 2007; Dilalos & Alexopoulos, 2017; Goumas, 2006; Hinze, 2003; Makris *et al.,* 2013; Papadopoulos *et al.,* 2007; Tontini *et al.,* 2016).

As we can see, the values of the Simple Bouguer Anomaly (Fig. 4.27) range from 25.8 up to 78.5 mGal, while the values of the Complete Bouguer Anomaly (Fig. 4.28) range from 35.4 up to 79.0 mGal. The main differences can be spotted over the greater areas of the *Parnitha*, *Penteli* and *Hymettus* Mountains, where the Complete Bouguer Anomaly has increased relatively to the Simple one.

An area of minimum values, with circular shape, is located in the northern suburbs, among the areas of *Thrakomakedones, Kryoneri, Ekali, Kifisia, Lykovrysi* and *Acharnes*. The Bouguer values seem to be increasing to the southern areas and especially over the mountain *Hymettus* where the maximum values exist. There is a transgressive zone with a general direction East-West, along which the values differentiate a lot, creating zones of smaller values between the general zone of larger values.

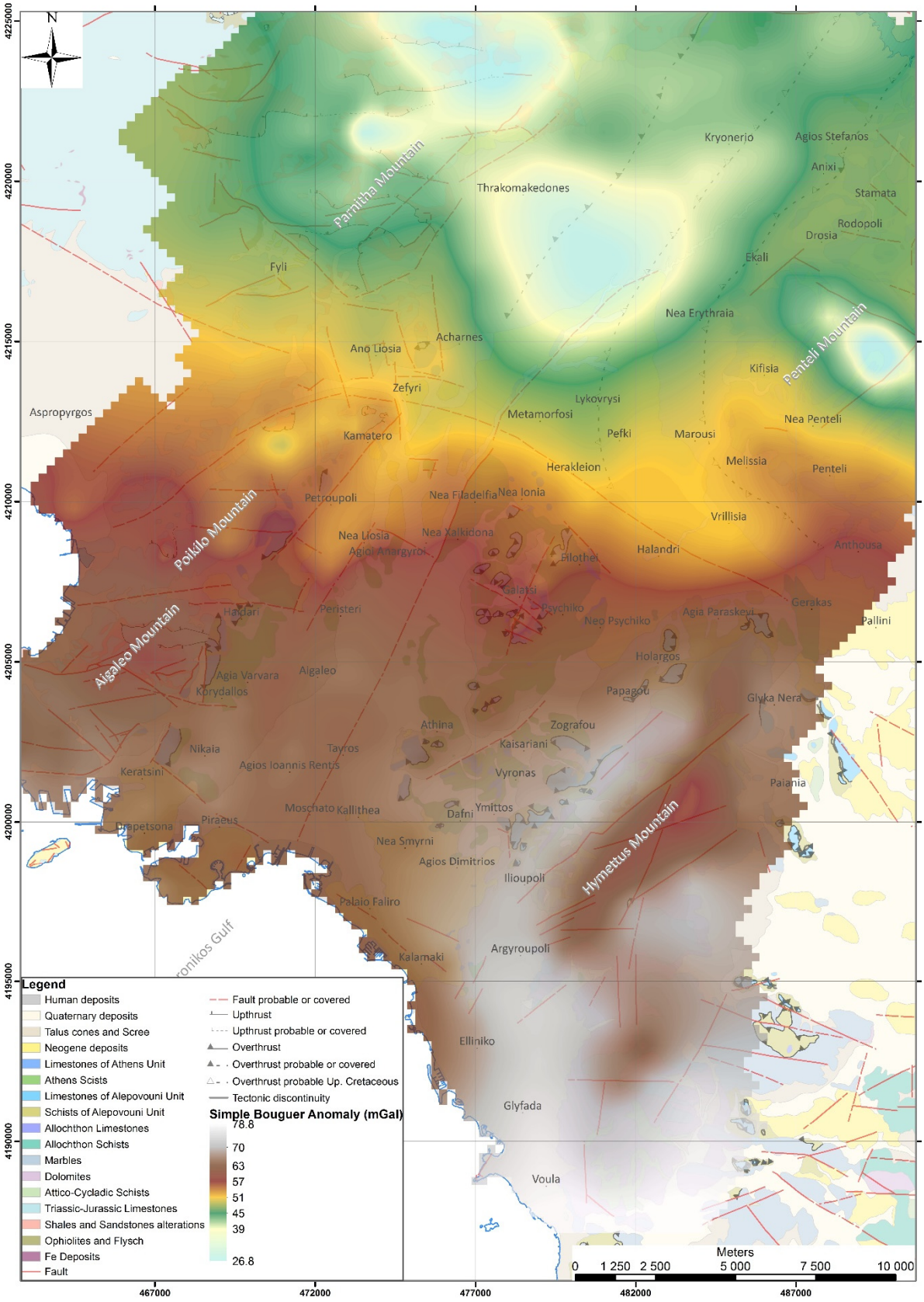

Figure 4.27: Simple Bouguer Anomaly map

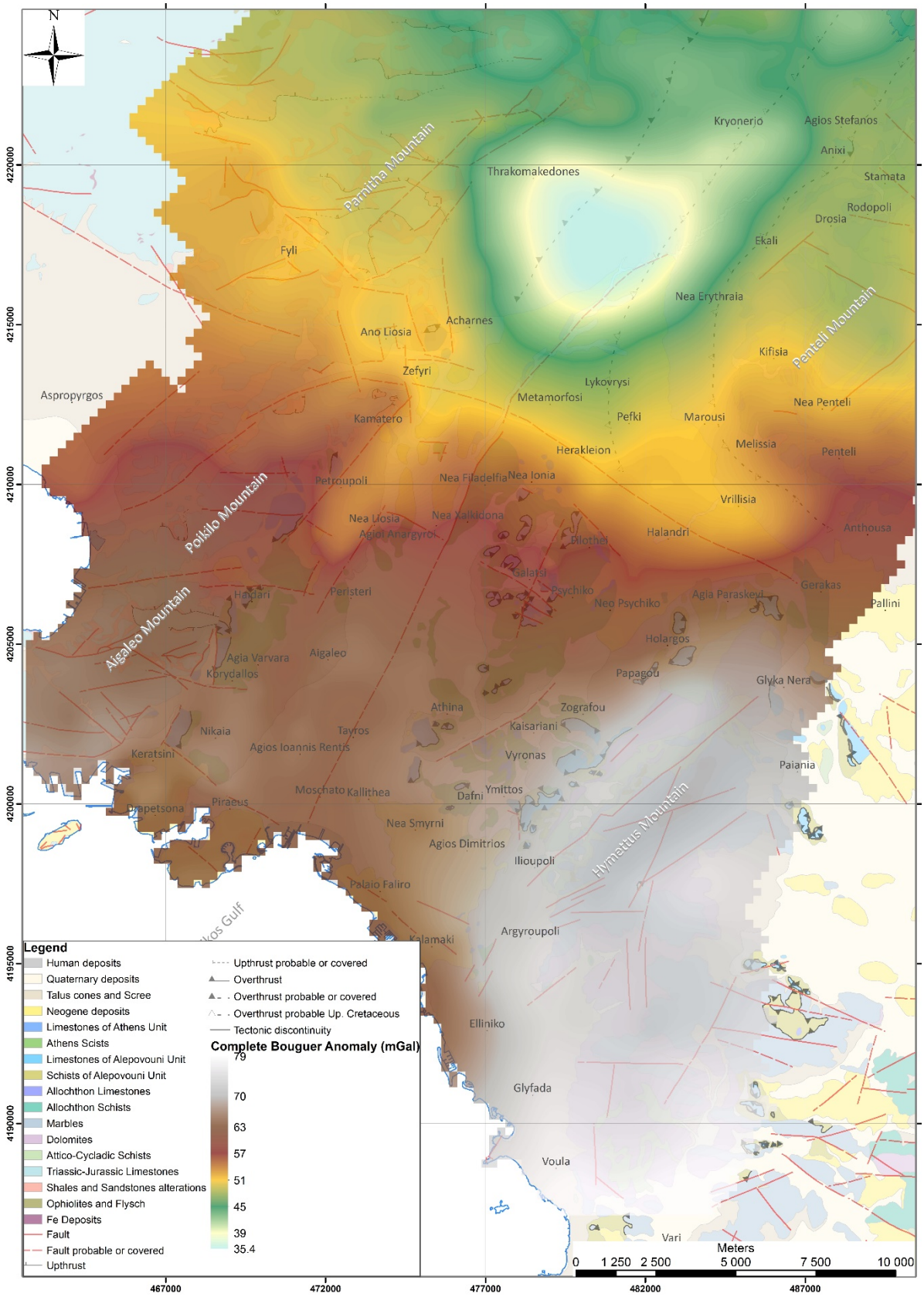

Figure 4.28: Complete Bouguer Anomaly map

4.3.d. Regional-Residual Separation

One of the classic problems for the researchers dealing with gravity measurements and processing is how to calculate and separate the regional gravity field from the residual field (Martínez-Moreno *et al*., 2015; Nettleton, 1954; Roach *et al*., 1993). The produced Complete Bouguer Anomaly map (Fig. 4.28) consists of both the regional and the residual (due to local structures) gravity field components.

There are quite a few filtering processes for the regional-residual separation (§3.4.b), each one with its pros and cons. The most popular ways are the graphical method, the derivatives (Gönenç, 2014), the upward continuation process (Jacobsen, 1987; Zeng *et al*., 2007), the polynomial fitting (Beltrao *et al*., 1991), the finite element approach (Mallick & Sharma, 1999; Mallick *et al*., 2012) and the application of Fourier filters (Anudu *et al*., 2016; Dilalos & Alexopoulos, 2017; Elkhodary & Youssef, 2013; Götze *et al*., 1994; Khamies & El-Tarras, 2010; Shafie *et al*., 2014; Syberg, 1972; Xu *et al*., 2009), which tend to be applied more nowadays.

In the context of this Ph.D. thesis, we chose to proceed to the regional-residual separation with **Fourier Analysis and Filtering**, since we consider it as the most reliable and up-to-date technique. The processing was carried out with the contribution of Oasis Montaj software and the *MAGMAP* extension, since the measurements were executed on a grid plan. Having a great spatial cover of the inner Athens basin but also of the surrounding mountains, would help calculate correctly the regional component.

For the application of filters in the Fourier domain (or wavenumber), a pre-processing procedure is required for the space domain grid. Therefore, the grid was prepared for the transformation by removing the first order trend (based on all points). Afterwards, there were the grid expansion and filling to rectangular size (based on maximum entropy prediction), so that it would be acceptable for Fast Fourier Transformation (FFT), in order to convert the space domain data to the Fourier domain. Depending on the value of the standard deviation parameter that we will choose, we can produce residual anomaly maps of different depths. After the frequency filtering, a post-processing inverse procedure is also essential, in order to return the data back to the space domain.

The separation of the regional and residual gravity fields was based on the information provided by the corresponding **Power Spectrum Analysis** of the gravity data (Complete Bouguer map - Fig.4.28), a common procedure executed before the Fourier filtering (Al-Banna & Al-Karadaghi, 2018; Ali *et al.,* 2017; Elkhodary & Youssef, 2013; Fernandez-Cordoba *et al.,* 2017; Gabtni & Jallouli, 2017; Gomez-Ortiz *et al.,* 2005; Hinze *et al*., 2013; Khamies & El-Tarras, 2010). The power spectrum, calculated by averaging all the grid elements at the wavenumber, can provide depth estimates of the anomaly sources (*h*), based on the following relation introduced by Spector & Grant (1970) for aeromagnetic data, where *S* is the slope of the least-squares line of each section of the spectrum:

$$h = S/4\pi$$

Observing the produced Radially Averaged Power Spectrum (Fig.4.29) originated from the Complete Bouguer Anomaly data, we can distinguish two different slopes fitting the data. This leads to the estimation of two different depths of the anomaly sources, which based on the above formula, are placed at 2.06km and 0.48km. The final part (yellow) is considered to be "noise" and has been ignored. Based on these depths, we can differentiate more easily the regional from the residual gravity field. Nevertheless, we have to mention that the presence of vertical and lateral variation in lithology and therefore density might produce a mix of gravitational responses (Ali *et al.,* 2017).

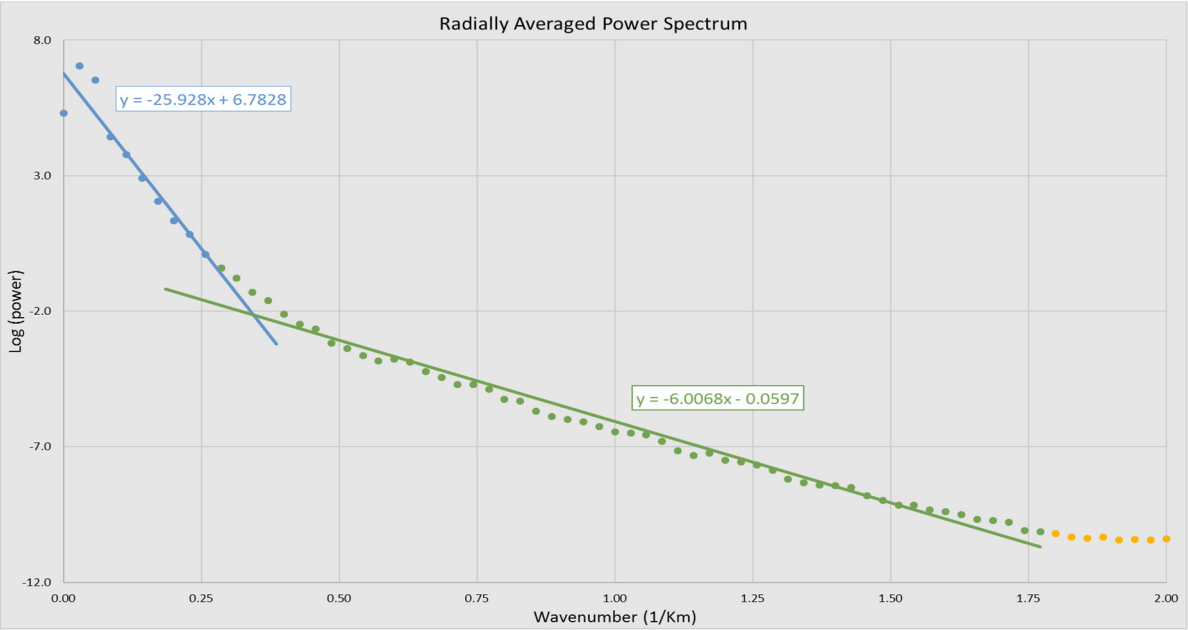

Figure 4.29: Radially Averaged Power Spectrum of the Complete Bouguer Anomaly of Athens basin.

First, a Bandpass filter was applied in order to remove the "noise" frequencies derived from the power spectrum. The next step is to proceed with the application of the **Gaussian filter**, which has been chosen as the most appropriate for this case, applied successfully in several other cases (Anudu *et al*., 2016; Damaceno *et al.,* 2017; deCastro *et al.,* 2011; 2014; Dilalos & Alexopoulos, 2017; Fernandez-Cordoba *et al.,* 2017). The calculation for the residual field is derived from the following formula:

$$L(k) = 1 - e^{\frac{-k^2}{2k_0^2}}$$

where k_0 is the standard deviation of the Gaussian function in cycles/ground unit (e.g. meters or kilometers), applying it as a smooth high-pass filter. Based on the above results of the power spectrum (Fig.4.29), we produced a residual map with a cutoff wavelength of 500m and standard deviation equal to 0.25 cycles/km (Fig 4.30). Beyond that, a second residual map of the basement, with standard deviation equal to 0.02 cycles/km (Fig 4.31) was produced, including the anomaly sources and information from deeper structures of the bedrock.

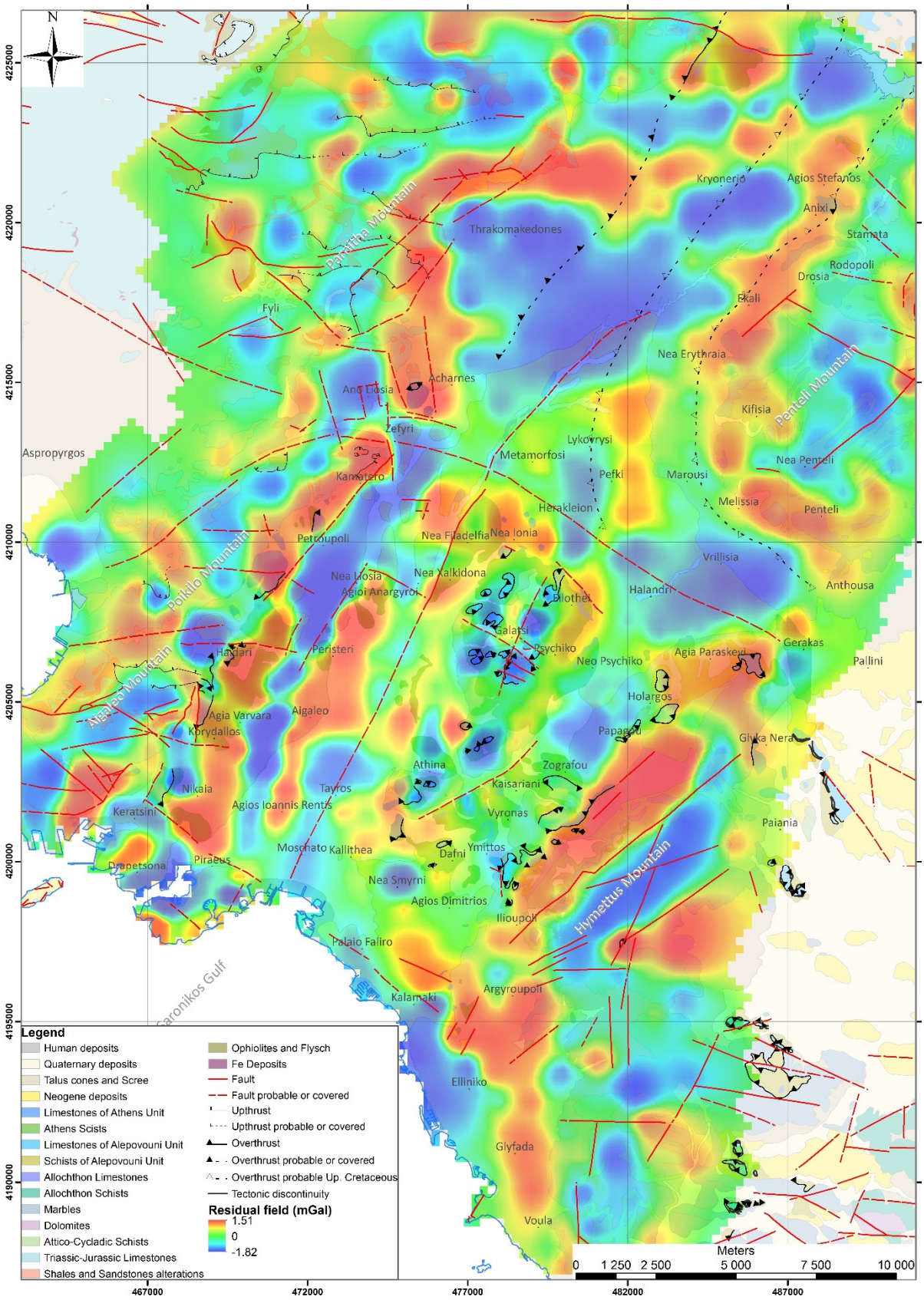

Figure 4.30: Residual Map of Athens basin with standard deviation equal to 0.25 cycles/km, illustrating the shallow anomaly sources.

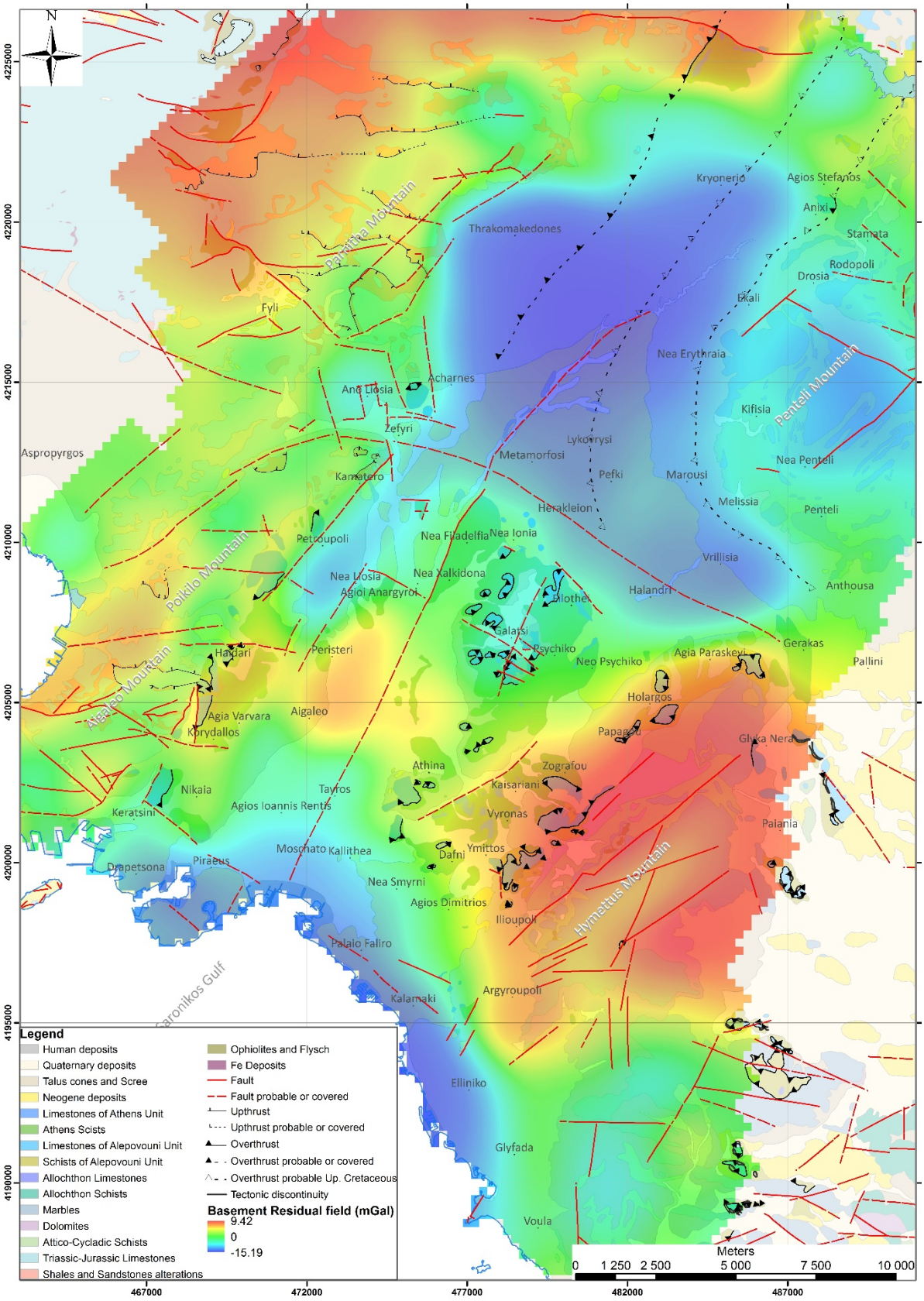

Figure 4.31: Residual Map of basement with filter standard deviation equal to 0.02 cycles/km, illustrating the deeper bedrock anomaly sources.

Starting from the residual map of the basement (Fig. 4.31), its values range from -15.2mGal to 9.4mGal, with deep and shallow structures contributing. We can observe two areas of minimum values (down to -15.2 mGal). The main one is located among the areas of *Thrakomakedones, Kryoneri, Drosia, Kifisia, Melissia, Vrilissia, Halandri, Herakleion, Metamorfosi* and *Acharnes*, with relatively circular shape, along with two linear extensions, one to the zone towards *Petroupoli* and *Agioi Anargyroi* and another one to the zone between *Nea Penteli* and *Rodopoli*. A second area of minimum values is located northern, almost parallel to the urban coastline, at the areas of *Piraeus*, *Palaio Faliro*, *Kalamaki* and *Elliniko* reaching a minimum anomaly value of -6.5 mGal. It could be said that there is a vestigial linear connection with the zone of *Petroupoli* and *Agioi Anargyroi*.

On the other hand, the maximum anomaly values are observed at the areas of the surrounding mountains *Hymettus* (up to 9.4 mGal), *Aigaleo-Poikilo* (up to 2.5-3 mGal) and *Parnitha* (up to 2-4 mGal). Moreover, an area of the inner basin appears with a maximum positive anomaly value of almost 2.7 mGal, located among the *downtown* of Athens city, the *Aigaleo* and *Peristeri* municipalities. The general direction of the area (WNW-ESE) is almost perpendicular to the general direction of the mountains Hymettus and Aigaleo (NNE-SSW), to which it seems to be connected.

Going up to the shallow anomaly sources and structures, the values of the residual map (Fig. 4.30) illustrating only the shallow anomaly sources range from -1.82mGal to 1.51mGal. Structures of high and low values of gravity are alternating, especially in the western area. The low gravity area (down to -0.9 mGal) among *Thrakomakedones, Kryoneri, Nea Erythraia* and *Acharnes* is spatially constrained relatively to the image of the basement residual (Fig. 4.31), surrounded by a zone of high gravity from west and north (southern foothills of *Parnitha Mt*.) with values up to almost 1mGal. A big linear zone of low gravity (down to -1.5mGal) has been revealed running across the areas of *Zefyri, Petroupoli, Peristeri, Aigaleo, Agios Ioannis Rentis* and ending up to the northern *Piraeus*. This zone is laterally constrained by two other linear zones of higher gravity (up to almost 1mGal), the westernmost running from *Zefyri, Kamatero, Haidari, Korydallos, Nikaia* to *Piraeus* and the other easternmost extending from *Agioi Anargyroi, Peristeri, Aigaleo* to *Agios Ioannis Rentis*.

Moreover, a zone of high gravity (up to 0.85mGal) is located along the areas of *Agios Stefanos, Ekali, Kifisia, Marousi, Melissia* and *Penteli*, almost identical with the probable overthrust of Upper Cretaceous. Additionally, at *Hymettus* mountain the high values zone of the basement residual (Fig. 4.31) in a “U” shape, has been separated in a central low zone (down to -0.85mGal), constrained by two high zones (up to 1.05mGal). The southern low zone (now down to -1mGal) of the basement residual (Fig. 4.31) has also been spatially constrained only to the area of *Kalamaki* and *Elliniko*.

The differences of these two maps might be useful during the geological and tectonic evaluation (§5.4), providing combined information from two “zones” of depth.

4.3.e. Structural Mapping - Edge detection

After the separation of the gravity field into residual and regional (§4.3.d), we can take advantage of the derivatives methods in order to enhance the structural edges (§3.4.c). The structural mapping is very common in the scientific literature the latest years (Al-Banna *et al.,* 2017; Ali *et al.,* 2017; Anudu *et al.,* 2016; Beiki, 2010; Cooper & Cowan, 2008; Eshaghzadeh, 2015; Elkhodary & Youssef, 2013; Ghosh, 2016; Hosseini *et al.,* 2013; Hsu *et al.,* 1996; Khalil *et al.,* 2014; 2015; Khamies & El-Tarras, 2010; Koumetio *et al.,* 2012; Martins-Ferreira *et al*., 2018; Nasuti *et al.,* 2012; Oruc, 2011; Wu *et al.,* 2017), since it has been very helpful in structural investigations. For that reason, we proceeded to this procedure in order to adumbrate the structural edges of Athens basin with the contribution of *Oasis Montaj* software.

There are several methods using the derivatives that can provide the desired enhancement of the structural edges (§3.4.c). The traditional ones are the **amplitude derivatives**, such as the Total Horizontal Derivative (*THDR*), the First Vertical Derivative (*VDR*), the Second Vertical Derivative (*SVDR*) and the Analytical Signal (*AS*). They are directly related and controlled by the lateral variation in density of the source bodies and therefore with the geology. On the other hand, we also have the local **phase derivatives**, such as the Tilt (*Tilt*) and the Theta (*cos Tilt*), which are independent of density.

In the context of this Ph.D. thesis, we applied most of the aforementioned edge enhancement techniques. Firstly, the results of the **Total Horizontal Derivative (*THDR*)** are illustrated in Figure 4.32 for the shallow sources and in Figure 4.33 for the deeper ones. The maximum values identify linear edges such as fault zones and contacts, especially for shallow structures, identifying large and small edges with large and small density contrasts (Fairhead, 2015). The THDR results for the shallow structures (Fig. 4.32), reveal three linear zones of maxima with general direction NE-SW. The major one extends from the area of *Piraeus, Nikaia, Aigaleo, Agioi Anargyroi, Zefyri* and ends up to *Thrakomakedones*. One other zone is observed along the axis of the central hills (*Filopappou, Lycabettus, Attiko Alsos, Tourkovounia*) and one along the western part of the *Hymettus* Mountain. Smaller maxima are also located along the area of *Kalamaki-Elliniko* and *Kryoneri-Agios Stefanos*. The same image, but more intense, is observed for the results of the basement sources (Fig. 4.33). The area among *Thrakomakedones, Ekali, Nea Erythraia* and *Acharnes* presents wider areas of maxima and so does the one of *Agia Paraskevi* and *Papagou*.

The results of the **First Vertical Derivative (*VDR*)** are illustrated in Figure 4.34 (shallow structures) and Figure 4.35 (basement structures). This technique is also more sensitive to the shallow structures. Parts of the zero crossing adumbrate the edge location while the maxima values outline the structure location providing simultaneously information for its positive or negative density and therefore for its dip. The negative values of the derivative has been removed in an effort to manage it more easily by illustrating only the structural edges (zero crossings) and the positive structures-possible horsts only (maxima).

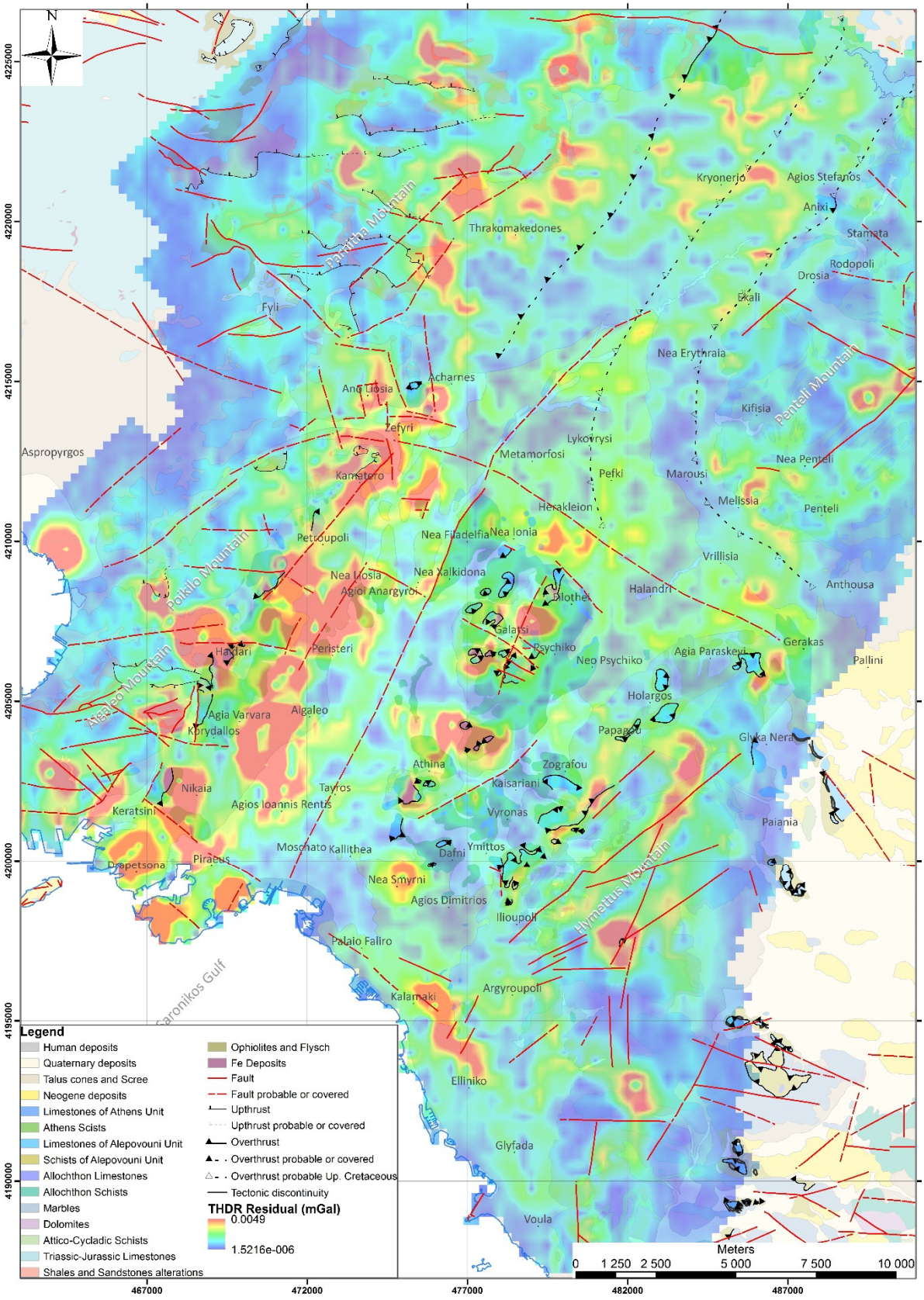

Figure 4.32: THDR of residual data (*shallow structures*). The maximum values identify linear edges

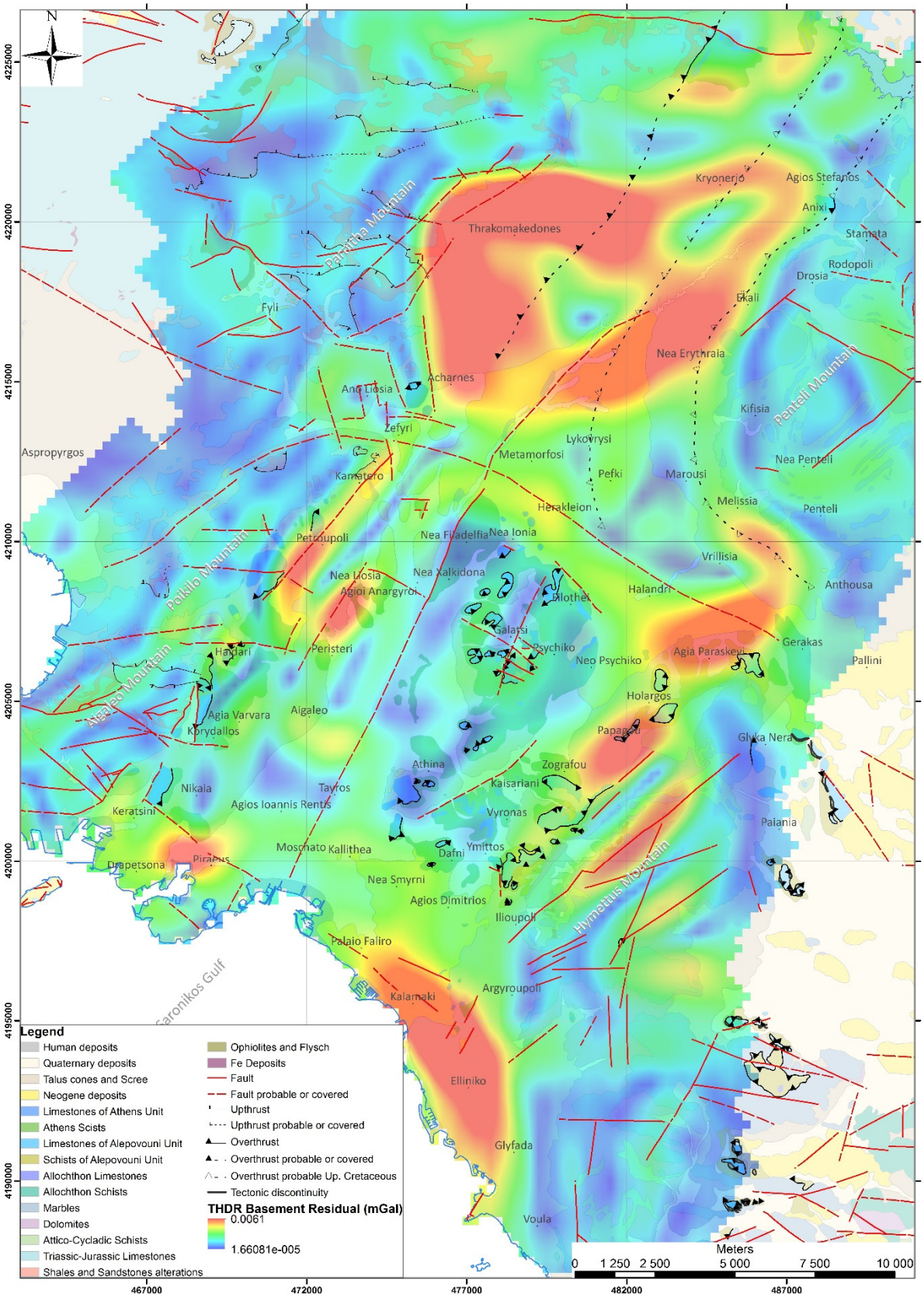

Figure 4.33: THDR of basement residual data (*deeper structures*). The maximum values identify deeper linear edges.

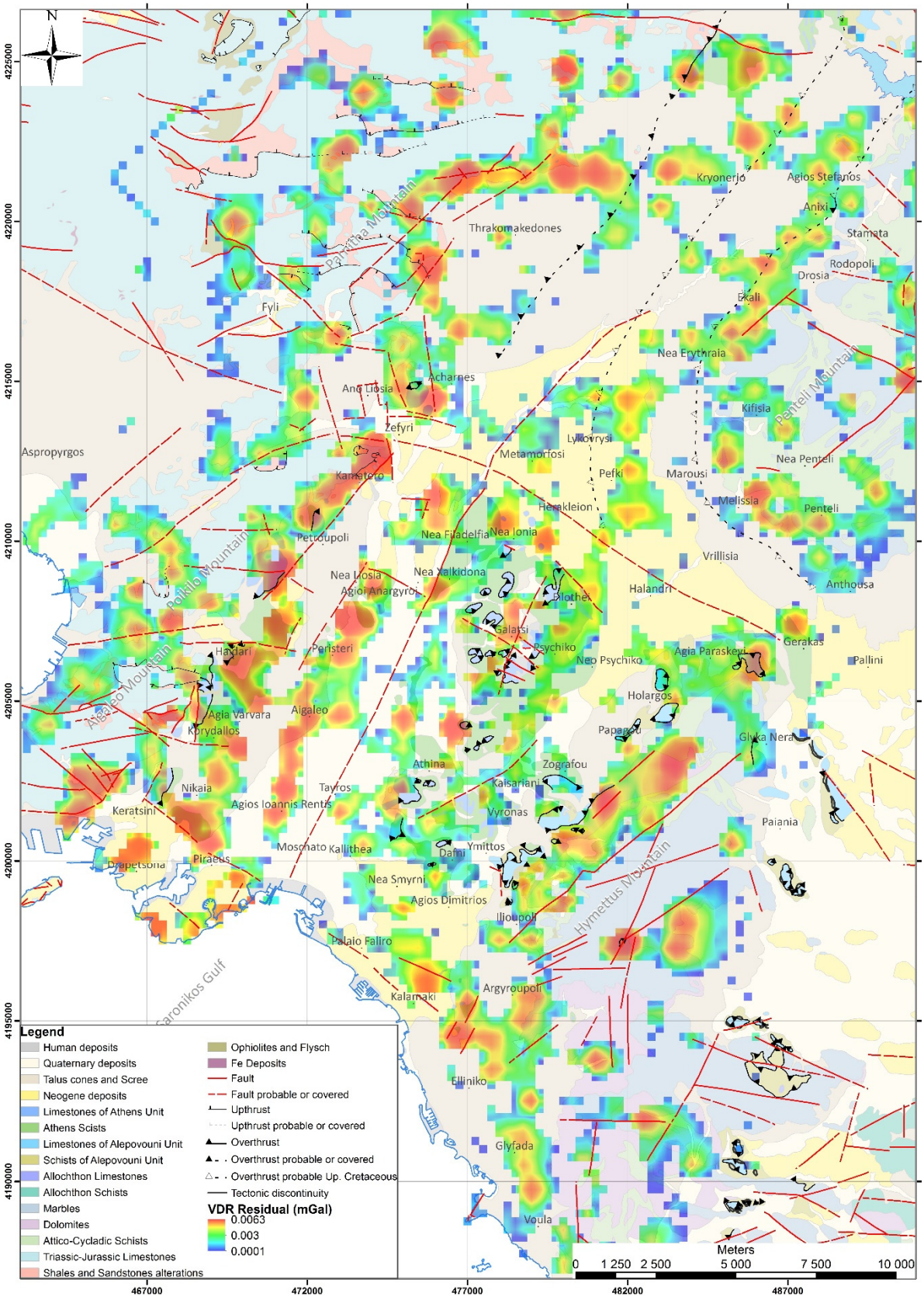

Figure 4.34: VDR of residual data (*shallow structures*). The zero crossing adumbrates the edge location while the maxima values outline the positive density structures.

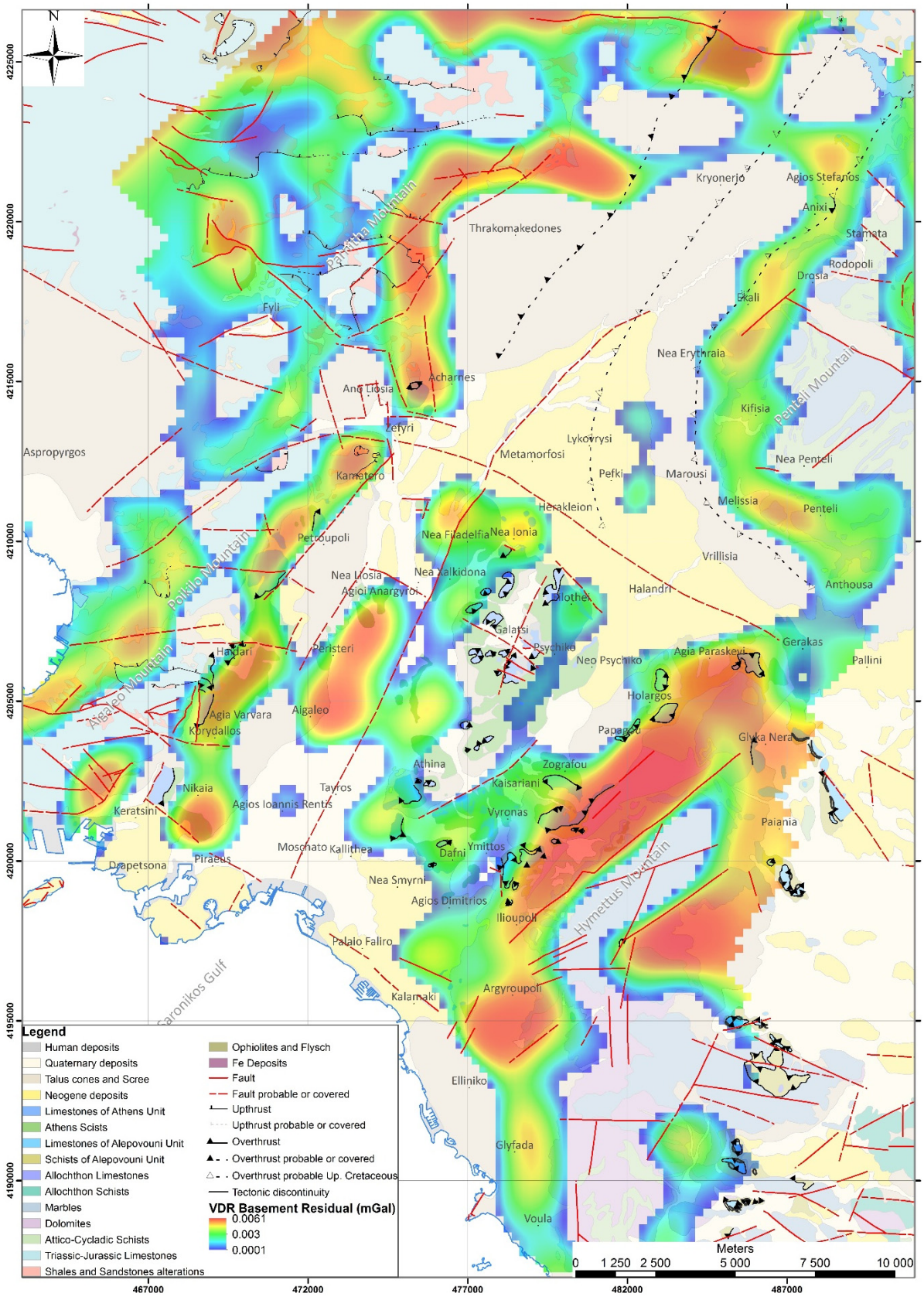

Figure 4.35: VDR of basement residual data (*deeper structures*). The zero crossing adumbrates the edge location while the maxima values outline the positive density structures.

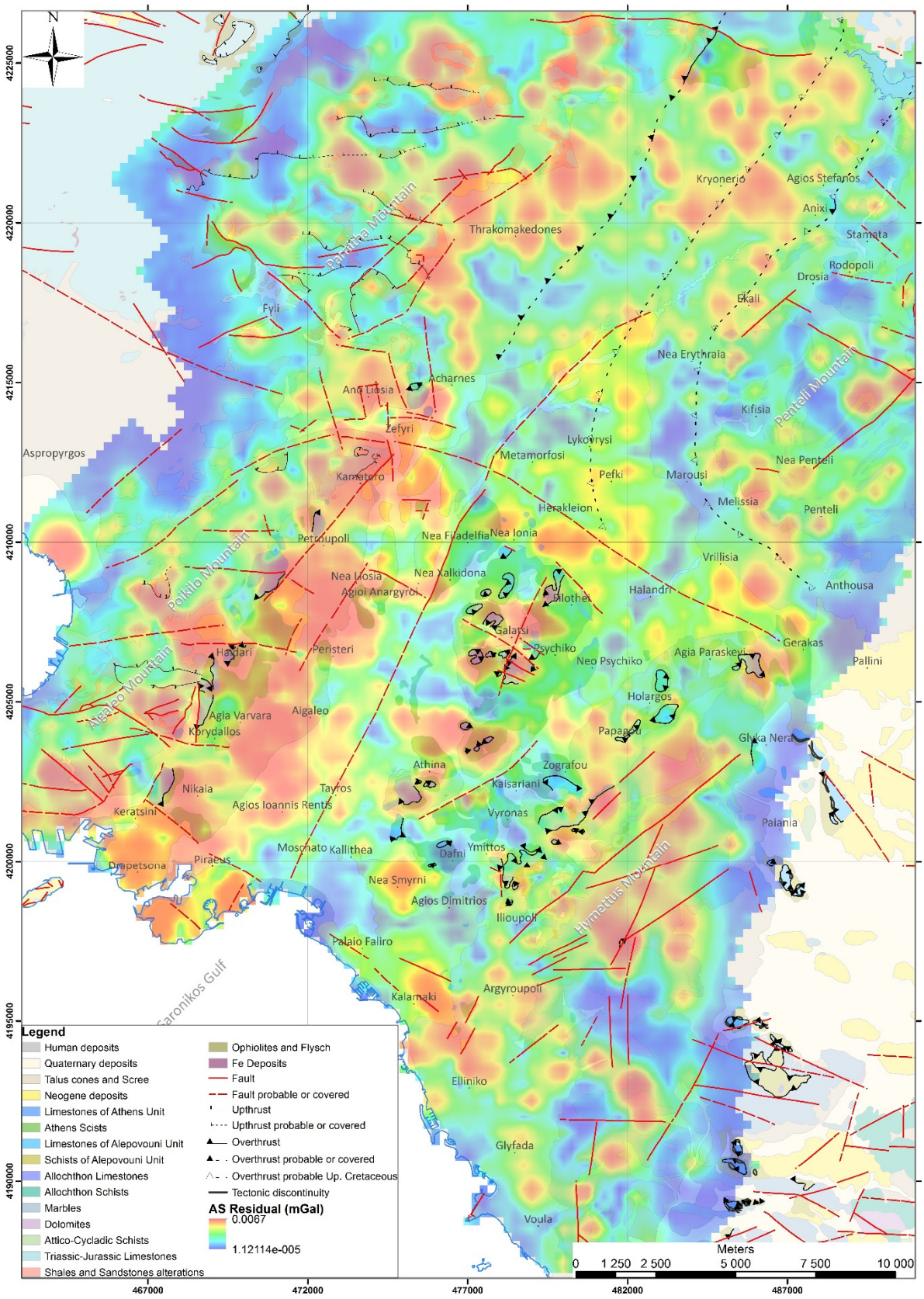

Figure 4.36: Analytic Signal of residual data (*shallow structures*). The maximum values outline the fault zones or contacts.

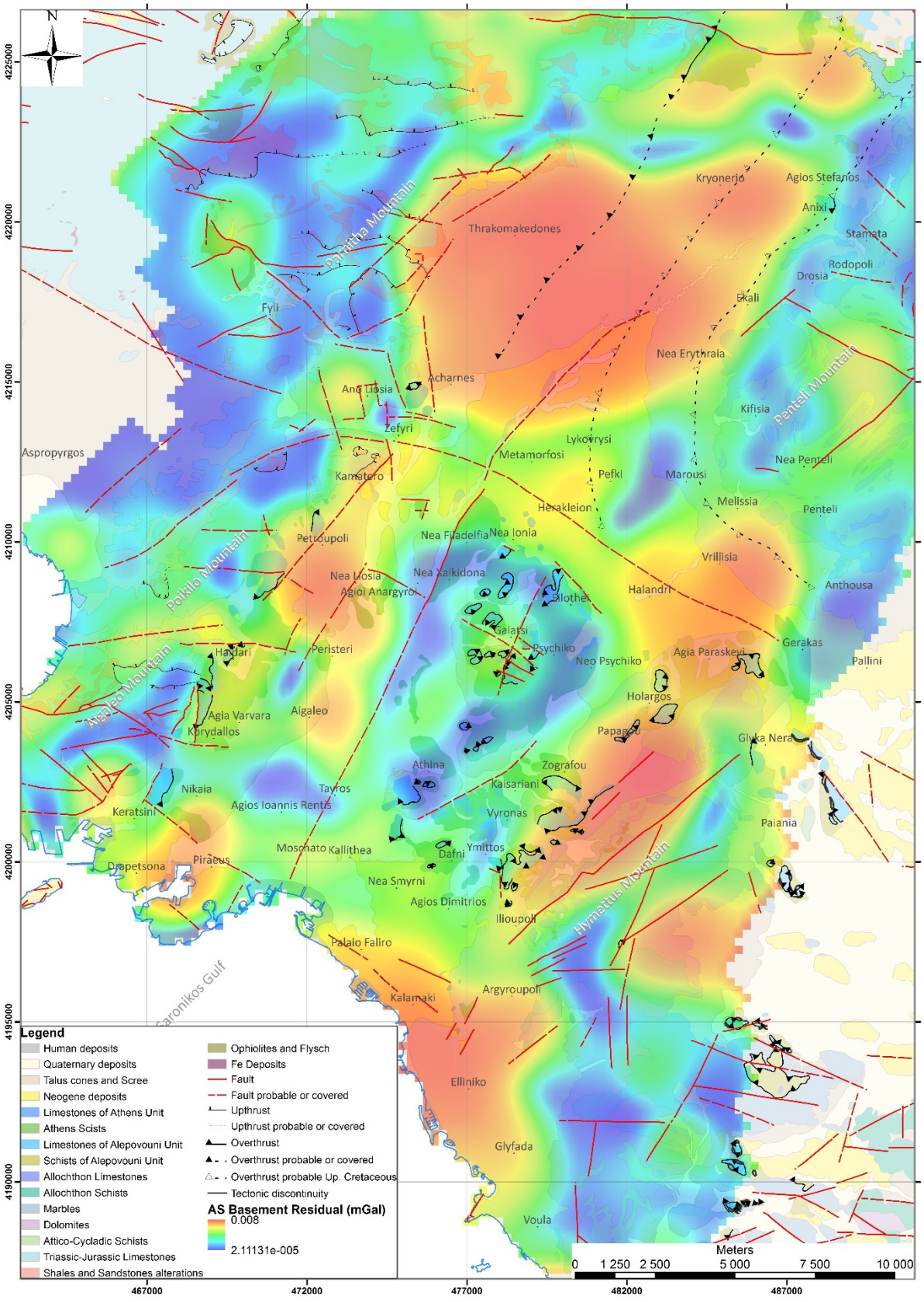

Figure 4.37: Analytic Signal of basement residual data (*deeper structures*). The maximum values outline the deeper fault zones or contacts.

The results of the VDR (Figs. 4.34-35) indicate almost the same edges as those of the THDR (Figs. 4.32-33), but providing also information for the relative block position (positive density bodies). However, in two areas it seems to clarify a little bit more the structural status. One of them is the western and southern part of *Penteli* Mountain and the other one is the western part of *Hymettus* Mountain, where severe indications reveal the existence of great structural edges. These maxima (positive structures-horsts) run along the same areas for both shallow and basement structures.

The last amplitude derivative applied in Athens basin was the **Analytic Signal (AS)**, observed in Figure 4.36 (shallow structures) and Figure 4.37 (basement structures). Practically, the maximum values outline the edges that THDR also have done and especially for the zone of the eastern foothills of *Aigaleo-Poikilo* and *Parnitha* Mountains. It also delineated similar zones with THDR on *Hymettus* Mountain and along the axis of hills in the basin interior. The produced Analytic Signal maps (Figs. 4.36-37) seem a little noisier, compared to that of THDR (Figs. 4.32-33).

Afterwards we move on to the application of the phase derivatives, by first calculating the ***Tilt* derivative** (Figs. 4.38-39), at which the zero crossing lines are related to the location of the structural edges and the maxima delineate the positive density structures (possible horsts). The results for both shallow and deeper structures reveal an almost identical image with the corresponding VDR maps (Figs. 4.34-35), with the same zones adumbrated but slightly more definite. The main difference between the two derivatives is that the *Tilt* one is independent of the density and relatively smoother. It also prevents the domination of the large density contrast edges (Fairhead, 2015).

Finally, the ***Theta* derivative** has been calculated based on the *Tilt* and is illustrated in Figure 4.40 (shallow structures) and Figure 4.41 (basement structures). Taking into account that it is practically the cosine of *Tilt* derivative, its maximum values (≈1) will delineate the structural edges. In the produced *Theta* maps of Athens basin (Figs. 4.40-41) we have isolated the values greater than 0.8 (the units are in radians), trying to produce more perspicuous images, with obvious linear structures, normally related to the structural edges. The *Theta* map for the shallow structures (Fig. 4.40) reveals exceptionally limited areas, regarding the results of all the derivatives applied. The map from the deeper bodies (Fig. 4.41) reveals sufficiently better the edges, which practically are identical with those of the prementioned structural maps.

Taking into consideration the results of all the derivative maps, extremely helpful indications have been revealed for the delineation of the structural framework of Athens basin. Many of the derived zones of edges are identified with either already mapped fault zones and contacts (*Hymettus* and *Parnitha* Mts., *Ippokrateios Politia)*, or with probable ones, especially in the westernmost basin (*Petroupoli-Kamatero, Aigaleo-Ilion, Haidari, Zefyri, Ano Liosia*), in *Piraeus*, in the southern foothills of *Parnitha* Mt. (*Acharnes, Thrakomakedones*) and the western foothills of *Poikilo* Mt. and even in central ones (*Zografou-Fix, Galatsi-Psychiko*).

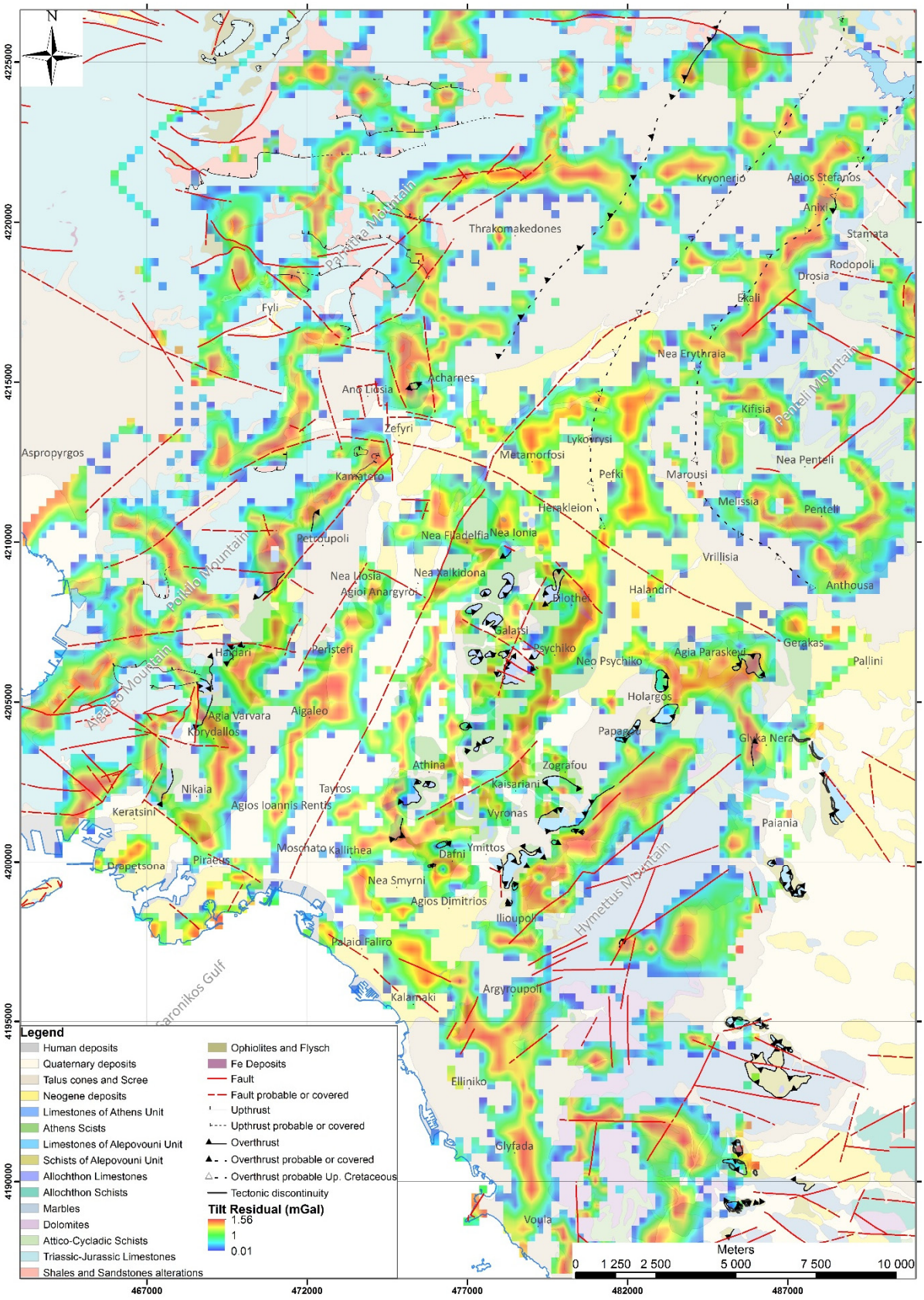

Figure 4.38: Tilt derivative of residual data (*shallow structures*). The zero crossing adumbrates the edge location while the maxima values outline the positive density structures.

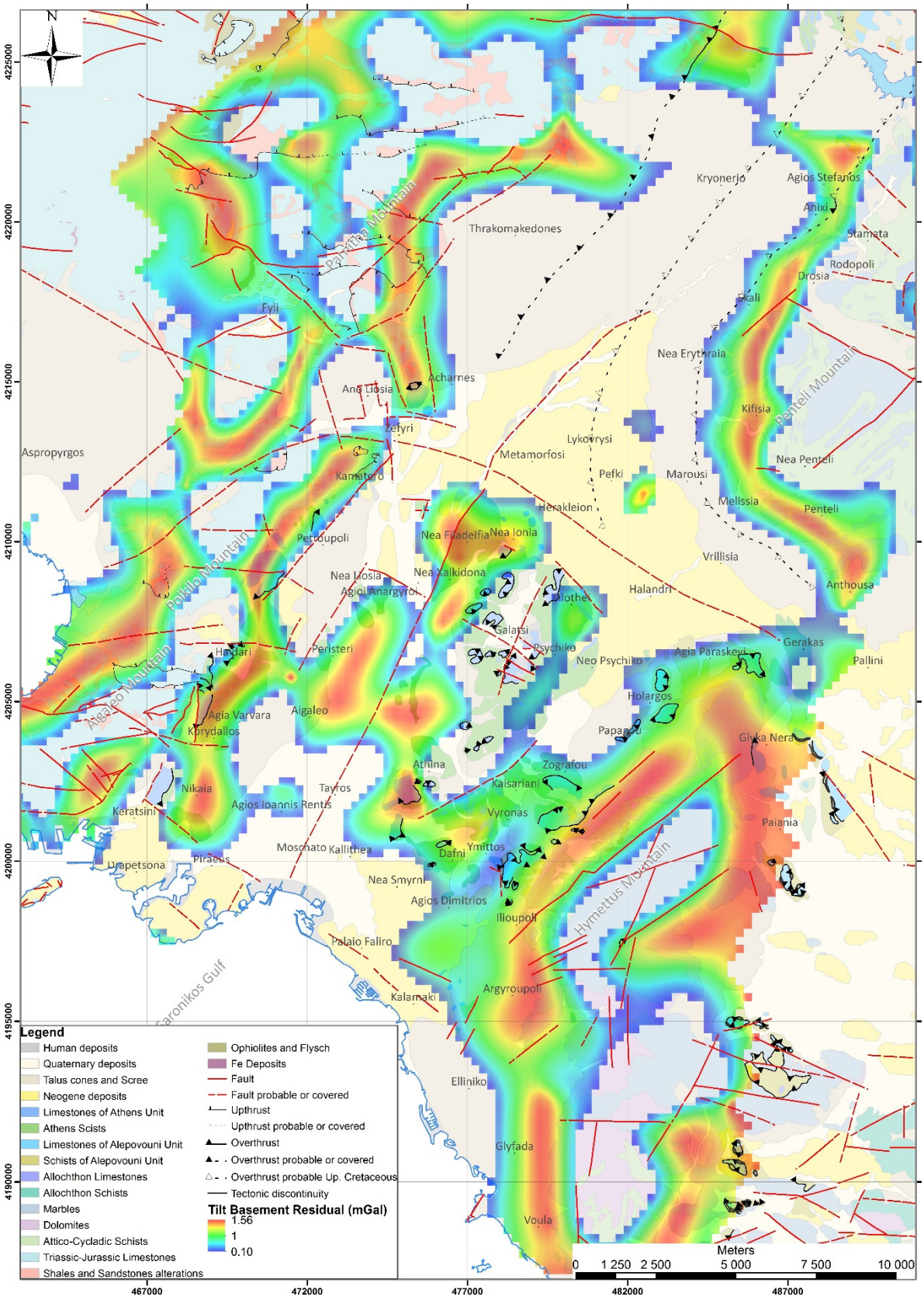

Figure 4.39: Tilt derivative of basement residual data (*deeper structures*). The zero crossing adumbrates the deeper edge location while the maxima values outline the positive density structures.

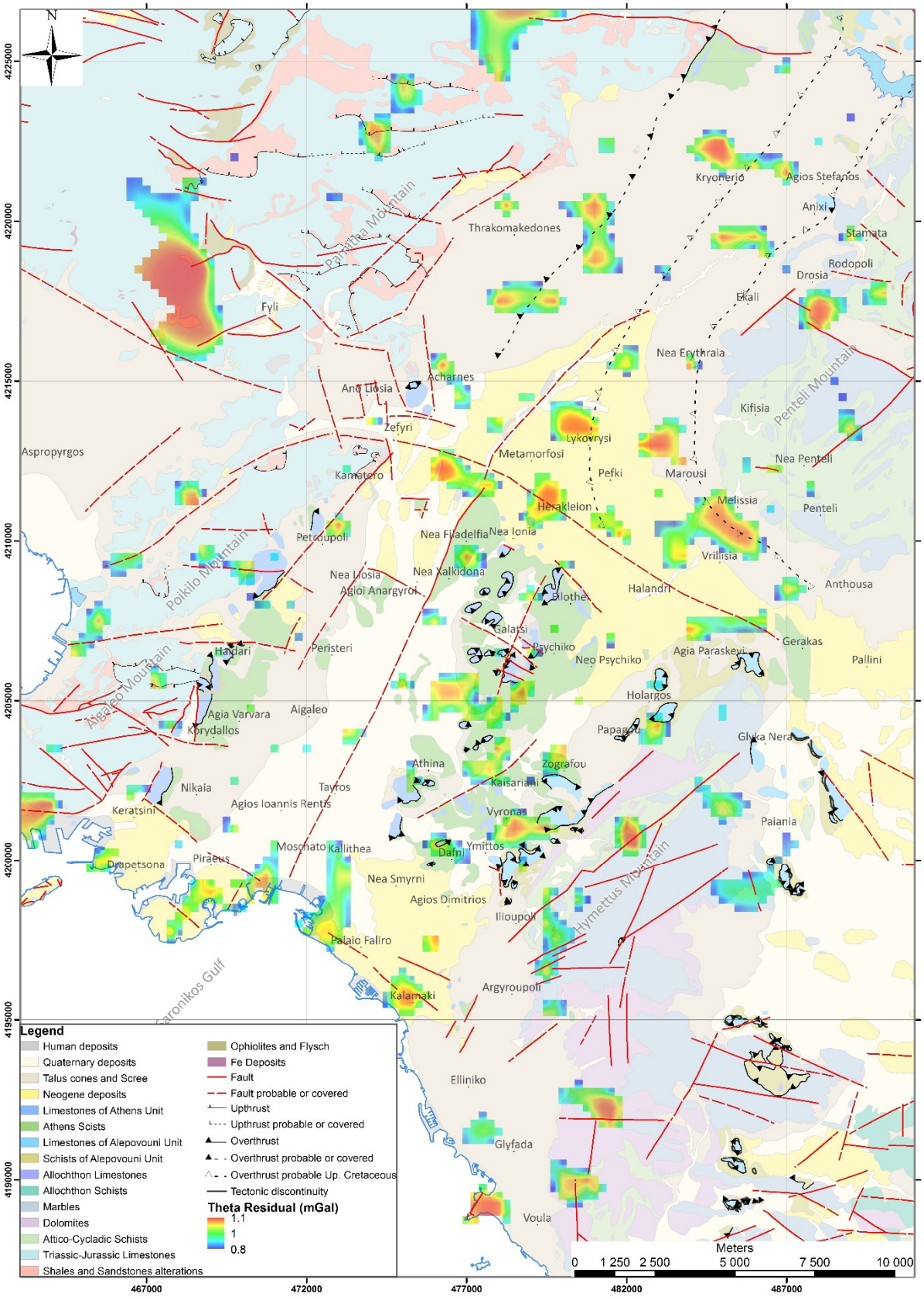

Figure 4.40: Theta derivative of residual data (*shallow structures*). The maximum values delineate the structural edges.

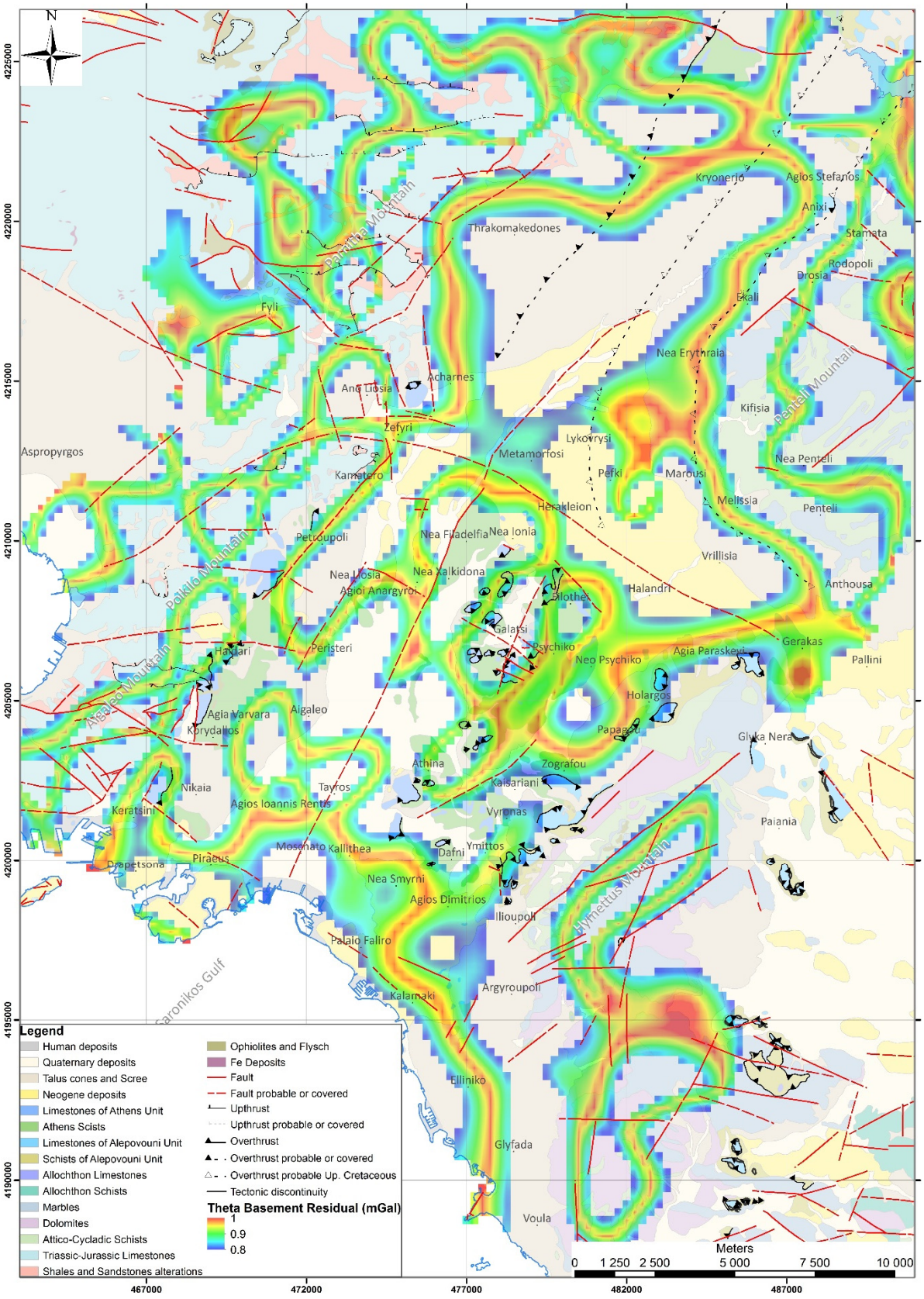

Figure 4.41: Theta derivative of basement residual data (*deeper structures*). The maximum values delineate the deeper structural edges.

Regarding the major fault zone of *Kifisos*, it seems that the southern section starting from *Agioi Anargyroi* ending to *Faliro*, has been verified in a way. In other words, from the VDR (Fig. 4.34) and *Tilt* (Fig. 4.38) maps of the shallow sources, we observe an area corresponding to a graben structure, since structural edges have been revealed edgeways. One of these two edge zones could be identified with Kifisos probable one, but slightly shifted in the E-W direction. This can also be confirmed by the low areas of the THDR (Fig. 4.32). The mapped part of the area *Agioi Anargyroi-Nea Filadelfia* has been partially revealed in the VDR (Fig. 4.34), Tilt (Fig. 4.38) and AS (Fig. 4.36) maps. The probable extension of *Kifisos* to the north (*Metamorfosi-Lykovrysi-Nea Erythraia*) might have been adumbrated only partially at the *Metamorfosi* area by the shallow VDR (Fig. 4.34) and Tilt (Fig. 4.38) maps. The outcomes of the THDR (Fig. 4.33) and Analytical Signal (Fig. 4.35) of the deeper bodies seem to reveal some indications for its northern extension to *Nea Erythraia* but in quite bigger depths.

Likewise, for the other major probable zone with direction almost E-W (*Zefyri-Agia Paraskevi*), we have systematic indications presented in almost all the derivative maps, but not for its total length. Therefore, we can verify its central section along *Metamorfosi-Herakleion -Halandri*, its western edge at *Zefyri* and its eastern one at *Agia Paraskevi-Gerakas.* Its probable extension to the west and southwest is confirmed only at the northwest foothills of *Poikilo* Mt. (*Homateri* area), but no indications have been revealed for its farther extension to *Neoktista* and *Koumoundourou Lake*.

Beyond these, we have severe indications verifying the overthrust of the Upper Cretaceous characterized as probable. This zone runs around the western and southern foothills of *Penteli* Mt., along *Agios Stefanos, Ekali, Nea Erythraia, Melissia, Penteli* and *Anthousa* and has been revealed in most of the structural maps. Especially in the VDR (Figs. 4.34-35) and *Tilt* (Figs. 4.38-39) maps, an edge zone is presented almost with identical trace with the zone already proposed as an Upper Cretaceous overthrust. The delineation is more obvious at the results derived from the basement data. Concerning the other proposed Upper Cretaceous overthrust, located west of the prementioned one, only the section along the areas of *Lykovrysi-Peyki* can also be observed in the derivative maps.

Of course, apart from the confirmation of several mapped faults (visible or covered), the structural mapping based on the derivatives has revealed several more locations of probable fault zones or contacts, which have not been proposed yet. There are some linear features that could easily match to faults or contacts. Some of these are along *Nikaia-Korydallos, Piraeus-Agia Varvara, Agios Ioannis Rentis-Aigaleo-Peristeri, Kalamaki-Elliniko-Glyfada, Nea Smyrni-Agios Dimitrios, Zografou-Neo Psychiko-Filothei, Thrakomakedones-Kryoneri-Agios Stefanos*, *Lycabettus-Strefi* hills and *Drapetsona*. Most of them could be characterized as extensions of adjacent mapped (visible or probable) structural edges.

Finally, one more major structural edge has been detected by most of the derivative maps and is clearly presented in the VDR (Figs. 4.34-35) and *Tilt* (Figs. 4.38-39). This zone is observed

at the east foothills of Hymettus Mt., along the areas of *Gerakas, Agia Paraskevi, Holargos, Papagou, Zografou, Vyronas, Kareas, Ilioupoli, Argyroupoli,* Glyfada and *Voula.* The overthrust of *Metamorphic Unit* above the *Alepovouni* one seems to justify the outcomes of the shallow structural maps, while the overthrust of the *Alepovouni Unit* above the *Athens* one produces the corresponding, more extended, results in the structural maps of the basement structures.

4.4. QUANTITATIVE INTERPRETATION

In the context of quantitative gravity interpretation, we shall try to determine some specific parameters, such as the location, depth, shape and density contrast of the geological bodies. Thus, gravity interpretation cannot be characterized by its uniqueness and absolute solution, due to its ambiguity problem, but any additionally data can constrain the quantification errors and limits.

There are two methods to approach the interpretation problem and these are the *direct* and *indirect*. The direct method involves that some parameters of the model are calculated based on the features of the observed anomaly. On the other hand, the indirect method is defined by the *trial and error* procedure, based on an initial model of mass distribution. The comparison of the model gravity effect with the real one helps to improve the model, leading to the determination of the most acceptable one, through an iterative procedure known as *inversion*.

The real aim of the gravity inversion is to define model bodies that could realistically correspond to geological structures. Therefore, gravity modelling is carried out in 2, $2^{1/2}$ (infinite structures), 2.75 and 3 dimensions, depending on the acquired data and the target of the research.

4.4.a. 3D Euler deconvolution - Grid Depth

Although Euler deconvolution (§3.4.d.4) is mostly applied for the magnetics, it can sometimes be applied well for gravity data (Keating, 1998) as an approximation. The only difference is that the calculated depth solutions for the gravity method are located at a deeper level, closer to the center of the mass, in regard with the ones of magnetics.

The outcome of the Euler deconvolution here is a map, illustrating the locations and depths of the geologic sources of gravity anomalies that have been identified in grid-based gravity data, like in several other cases (Chen & Zhou, 2005; Curto *et al.,* 2015; FitzGerald *et al.,* 2004*;* Khalil *et al.,* 2014; Martins-Ferreira *et al*., 2018; Naouali *et al.,* 2011; Nasr *et al.,* 2011; Nouraliee *et al.,* 2015; Tedla *et al.,* 2011). For the best results from Euler deconvolution Reid *et al.* (2014a; 2014b) discuss the avoidable errors during its application to gravity data and how to determine the required parameters (SI, window size, grid interval etc.). The grid cell of the processed data is important, since the minimum depths defined are about the same as the cell size.

One fundamental parameter for Euler deconvolution is the Structural Index (SI) value, which depends on the type of the source body (see Table 3.3). In the context of this study, we have calculated Euler depth solutions by using values equal to 0 (Figs. 4.42 & 4.44) and 1 (Figs. 4.43 & 4.45), since both are close to the fault/contact type that we want to delineate. Of course, the SI=0 is estimated to appear almost the twice the uncertainty of the one for SI=1, which appears depth uncertainty equal to 10% and horizontal one equal to 20%. Although several researchers have used non-integer values such as 0.5 for SI (Slack *et al.,* 1967; Tedla *et al.,* 2011), we decided not to, based on the comments of Reid *et al.* (2012; 2014b). Reid *et al.,* (2014a; 2014b) propose that the SI equal to -1 is the appropriate value for finite contacts and faults in gravity surveys, but it has not been embedded as a possible value in most software.

The window size was set to 15x15 grid points, trying to compromise with all the conflicting requirements (Reid *et al.,* 2014a), being as small as possible and greater than twice the acquired data grid spacing and simultaneously greater than half the desired depth of investigation, which here is at least 2-3 kilometers. Moreover, some eliminations of spurious solutions were executed, by setting some acceptable parameters, such as the maximum acceptable distance (7500m), the maximum depth tolerance (14%) and the maximum horizontal tolerance (35%).

The Euler deconvolution has been carried out with the *Euler3D* extension of *Oasis Montaj* software and more specifically with two different methods, the *Standard Euler* (Figs. 4.42-4.43) and the *Located* one (Figs. 4.44-4.45). The second one produces far fewer spurious solutions (Figs. 4.44-4.45) since it is based only at the areas with existing anomalies (picks) in the analytic signal and then proceeding to the Euler deconvolution solutions. The input grid data were the residual (Fig. 4.30) and the basement residual ones (Fig. 4.31). The generated Euler solutions from both input maps were merged and presented together in order to have a common solution image that will lead to an easier evaluation.

The produced solutions for the Structural Index zero (0) are located mainly around the main low-gravity spherical area (*Thrakomakedones, Kryoneri, Ekali, Nea Erythraia, Lykovrysi,* Acharnes) observed in the basement residual map, with depths mostly between 500 and 1,500 meters and some deeper (1,500-2,300m) at the southwest corner. Moreover, we observe solutions of depths ranging from 500 to 1,000 meters along two linear areas. The first area is located at the western foothills of *Hymettus* Mountain, from *Anthousa* to *Kaisariani* and the second one is located at the southern foothills of *Parnitha* Mountain, along *Agios Stefanos* and *Drosopigi*. Additionally, solutions for depths from 500 up to 1,500 meters are illustrated at the southern suburbs of Athens basin, along smaller linear areas, such as *Agios Ioannis Rentis-Moschato-Kallithea, Nea Smyrni-Agios Dimitrios, Kalamaki-Elliniko* and *Elliniko-Glyfada.* The solutions clusters are more extended and systematic in the Standard Euler technique, while the solutions in the Located Euler are constrained a lot. There are not large differentiates of depths and locations between the two methods.

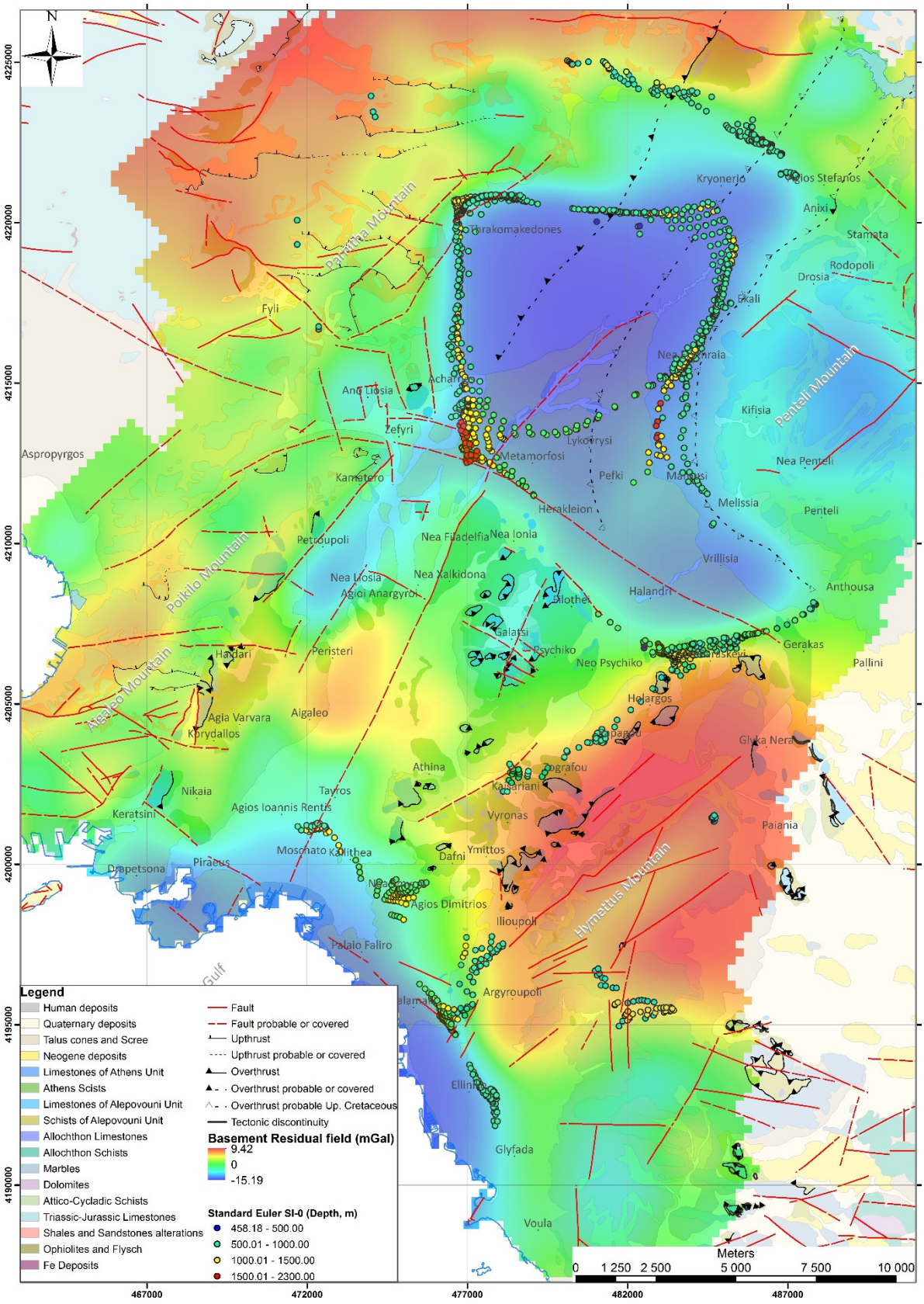

Figure 4.42: Standard Euler solutions (graduated symbols with depth) for Structural Index equal to 0 placed on the basement residual map.

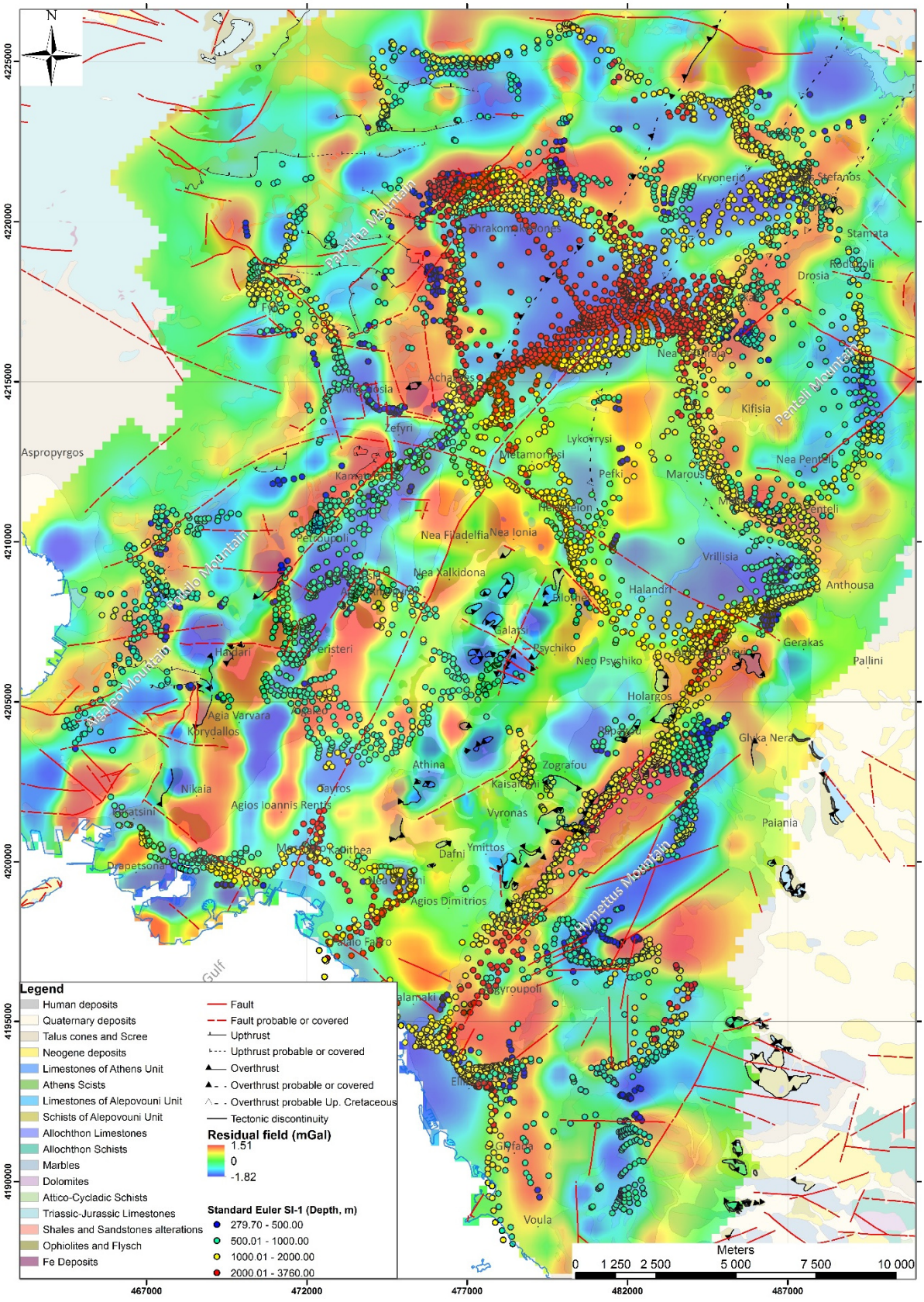

Figure 4.43: Standard Euler solutions (graduated symbols with depth) for Structural Index equal to 1 placed on the residual map.

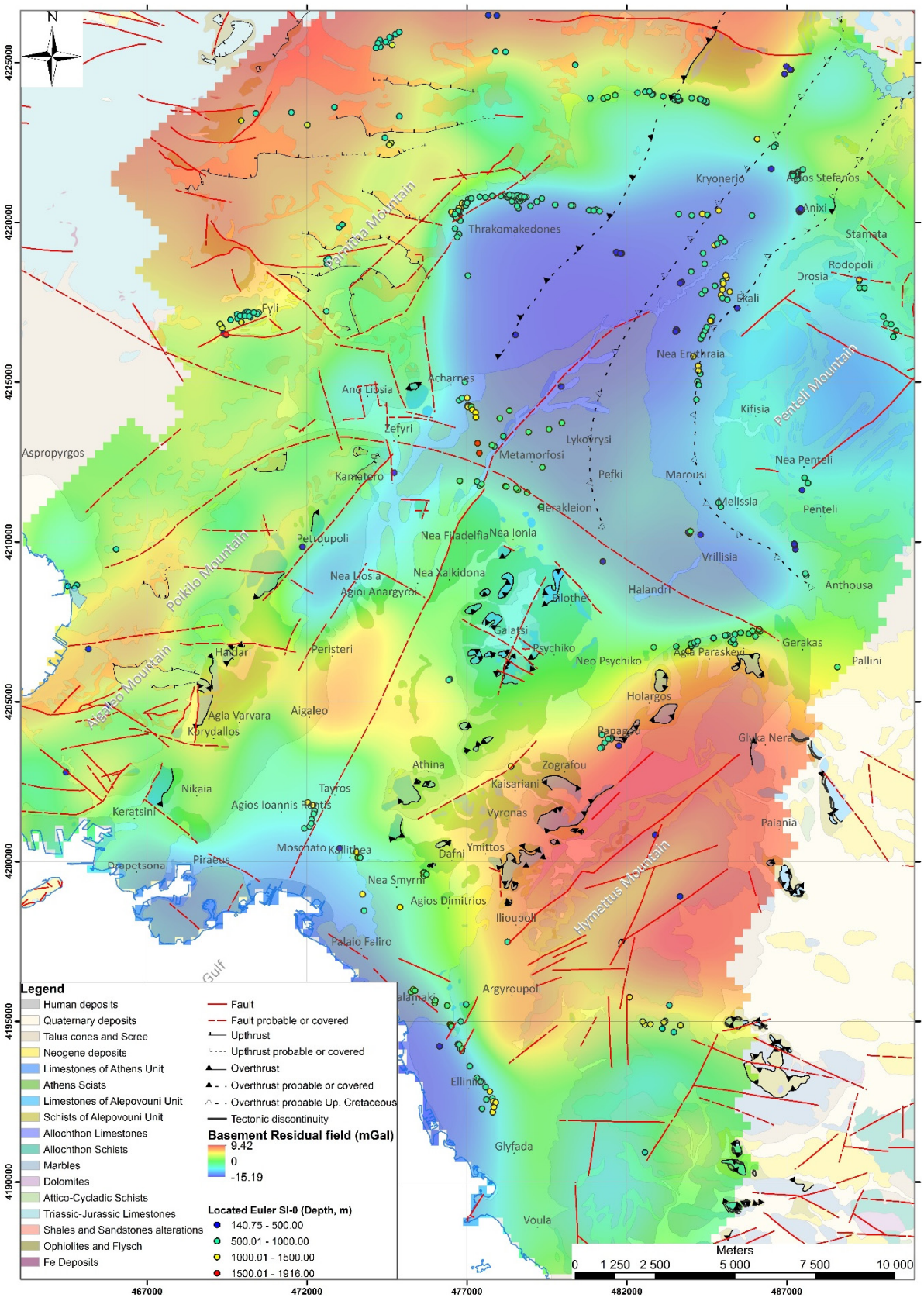

Figure 4.44: Located Euler solutions (graduated symbols with depth) for Structural Index equal to 0 placed on the basement residual map.

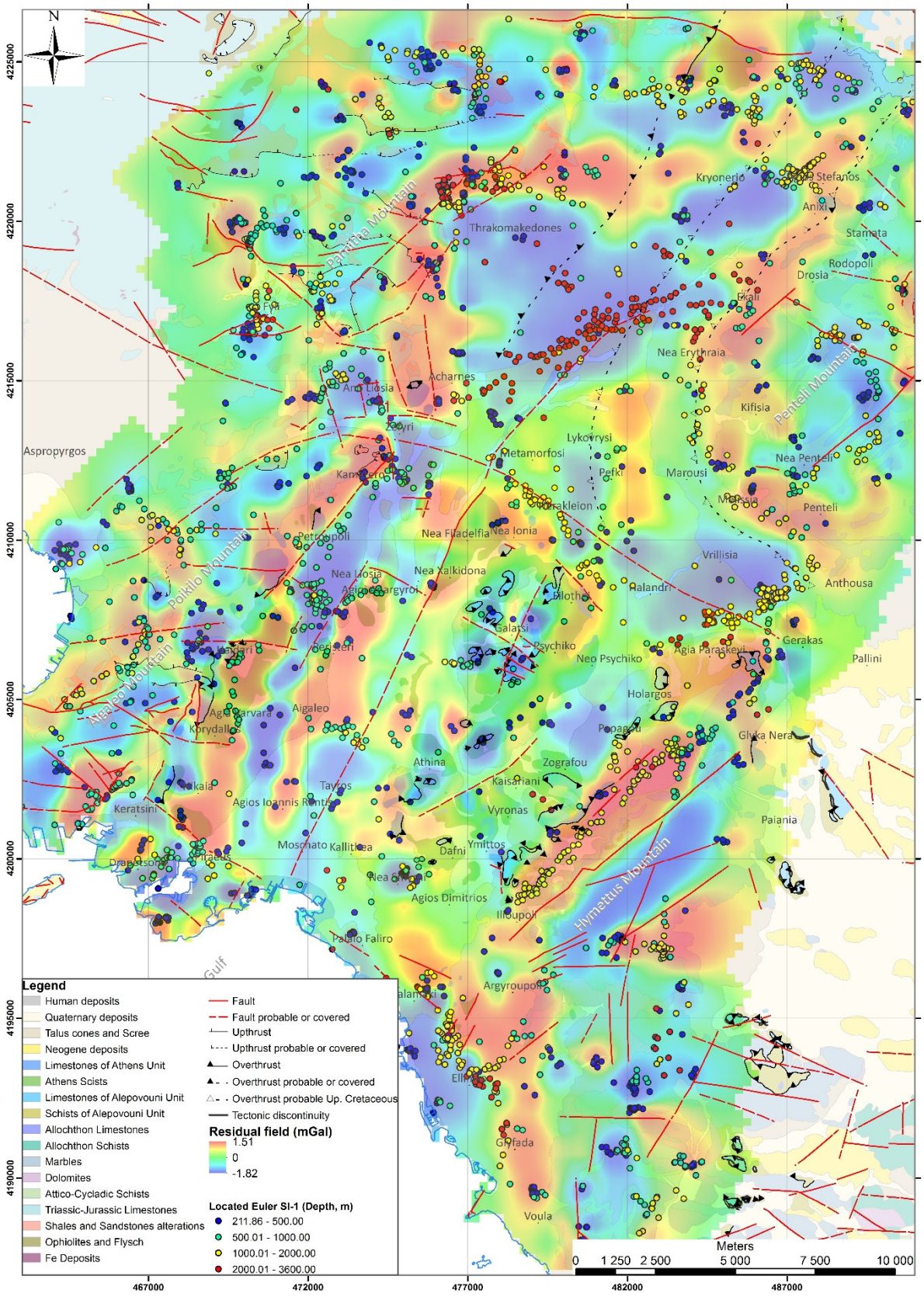

Figure 4.45: Located Euler solutions (graduated symbols with depth) for Structural Index equal to 1 placed on the residual map.

For Structural Index equal to one (1), the number of the produced Euler solutions is quite higher (Figs. 4.43 & 4.45), especially for the ones produced through the Standard Euler procedure. It seems that we have many correlations between the locations of the solutions and possible or existing fault zones. For SI=1, we can also observe great clusters of solutions around the margins of the main low-gravity area, like in solutions of the SI=0. The calculated depths are bigger, reaching up the 3,760 meters, when for the same area the SI=0 gave maximum depths close to 2,300 meters and quite restricted in swarm. Furthermore, the two linear areas of solutions, presented for SI=0 (Figs. 4.42 & 4.44), along the foothills of *Hymettus* and *Parnitha* Mountains, also appear with bigger calculated depths (up to 2,000m at *Hymettus* Mt. and up to 3,760m for *Parnitha* Mt.) and simultaneously expanded in length. This means that the one is running along *Anthousa-Agia Paraskevi-Holargos-Kaisariani-Argyroupoli-Kalamaki* and the other along *Agios Stefanos-Drosopigi-Karavola top*. For the linear areas located in the southern suburbs, we can also observe larger depths.

Beyond the clusters of solutions detected for both Structural Indexes 0 and 1 (discussed in the above paragraph), by setting SI=1 we observe new clusters of solutions, in other areas, located in the central and western part of the basin. More specifically, clusters of solutions for depths 500-1,000 meters are spotted along the zone *Zefyri-Kamatero-Petroupoli-Haidari, Keratsini-Drapetsona-Piraeus, Agioi Anargyroi-Peristeri, Aigaleo-Votanikos-Downtown-Psychiko*, *Penteli* and *Hymettus Mt.* For bigger depths (1,000-2,000m) along *Nea Penteli-Melissia-Marousi-Nea Erythraia, Agia Paraskevi-Halandri-Herakleion-Metamorfosi-Acharnes*, *Kryoneri-Agios Stefanos* and *Piraeus-Faliro-Moschato*. At the areas of *Fyli* and *Poikilo-Aigaleo* mountains, the depths of solutions range from 500 to 2,000 meters.

Generally, for both selected Structural Indexes (0 and 1) and for both applied Euler deconvolution methods (*Standard* and *Located*) the produced clusters of solutions seem to have great similarities with the structural maps of §4.3.e. (Figs. 4.32-4.41). Moreover, the depths calculated are ranging close to the source depths estimated by the Energy Spectrum Analysis (§4.3.d-Fig.4.29), except for some solutions of SI=1 that reach greater depths. Finally, it seems that the *Standard Euler* method is better, although it produces far more solutions than the *Located* one, which produces fewer. A good windowing of the solutions in order to remove the spurious ones will provide very good and reliable results.

4.4.b. 3-D Density Inversion Model

There are a few methods to estimate the shape of subsurface anomalous bodies (Abdelrahman *et al*., 2006; Essa, 2007; 2014). Inversion of the gravity data has been evolved rapidly during the last years (Andersson & Malehmir, 2018; Azizi & Saibi, 2015; Bersi *et al.,* 2016; Boszczuk *et al.,* 2011; Choi *et al.,* 2011; Commer, 2011; Damaceno *et al.,* 2017; Farhi *et al*., 2016; Martinez *et al.,* 2013; Prutkin *et al.,* 2011; Wang *et al.,* 2011; Wehr *et al.*, 2018), in order to quantify the gravity data and produce 2D geological-geophysical models and 3D, a

powerful tool for interpretation. 3D modelling of the gravity data provides us information concerning the volume of the anomalous sources and their geometry, possible connected to concealed faults in the area. The model is constructed based on a mesh of blocks/cells of equal dimensions, specified from the beginning, each one characterized by a certain value of density or density contrast. These values have been determined after a mathematical and computational procedure, aiming the minimum misfit (error) between the response of that model and the observed data.

All the density inversions within the context of this PhD thesis, have been carried out using the "*VOXI*" Earth modelling module (Azizi & Saibi, 2015; Farhi *et al.*, 2016; Martins-Ferreira *et al*., 2018; Weidmann *et al.,* 2016) of Oasis Montaj by Geosoft, integrated with the densities of the geological formations that have already been calculated (§4.2).

We applied the unconstrained 3D gravity modelling on both Complete Bouguer Anomaly data and the Residual anomaly data (0.02cycles/km) in order to compare the results, based on the fact that for the first case a trend removal procedure has to be first applied. Insignificant differences derived, proving that the trend removal procedure is reliable, since the inversion results were almost identical with those of the Residual data, where the regional field has already been removed with the FFT (§4.3.d). The desired absolute error was 5%.

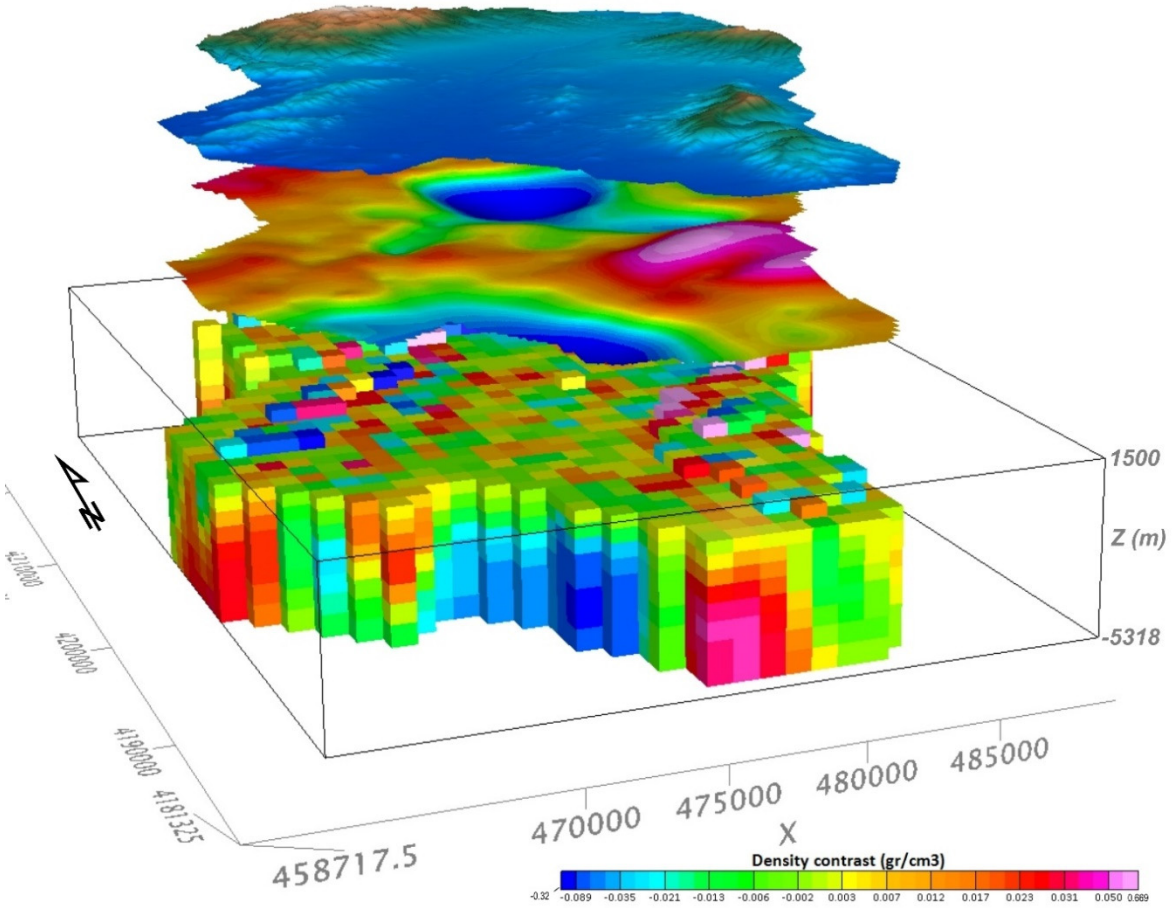

Figure 4.46. 3D gravity inversion of Athens basin, with cell size of 1000m. The upper plane is the area DEM and the lower is the grid of the Residual Anomaly (0.02 cycles/km).

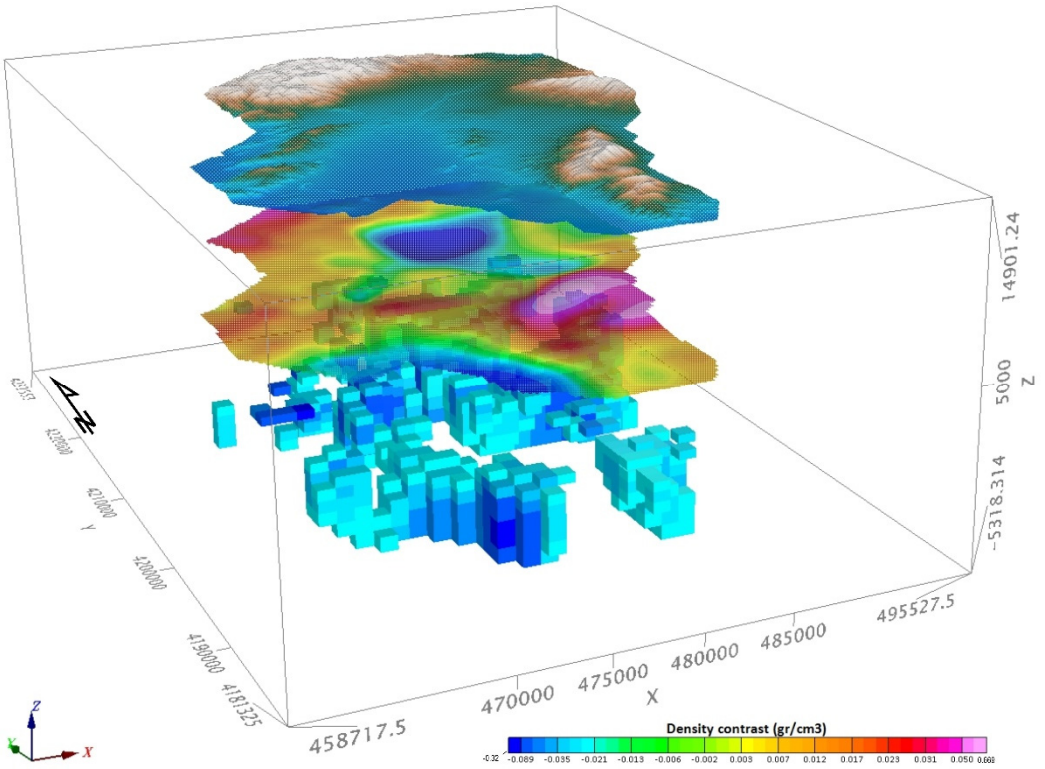

Figure 4.47. 3D gravity inversion (cell size 1000m), showing structures of low densities (density contrast from -0.32 to -0.02 gr/cm^3).

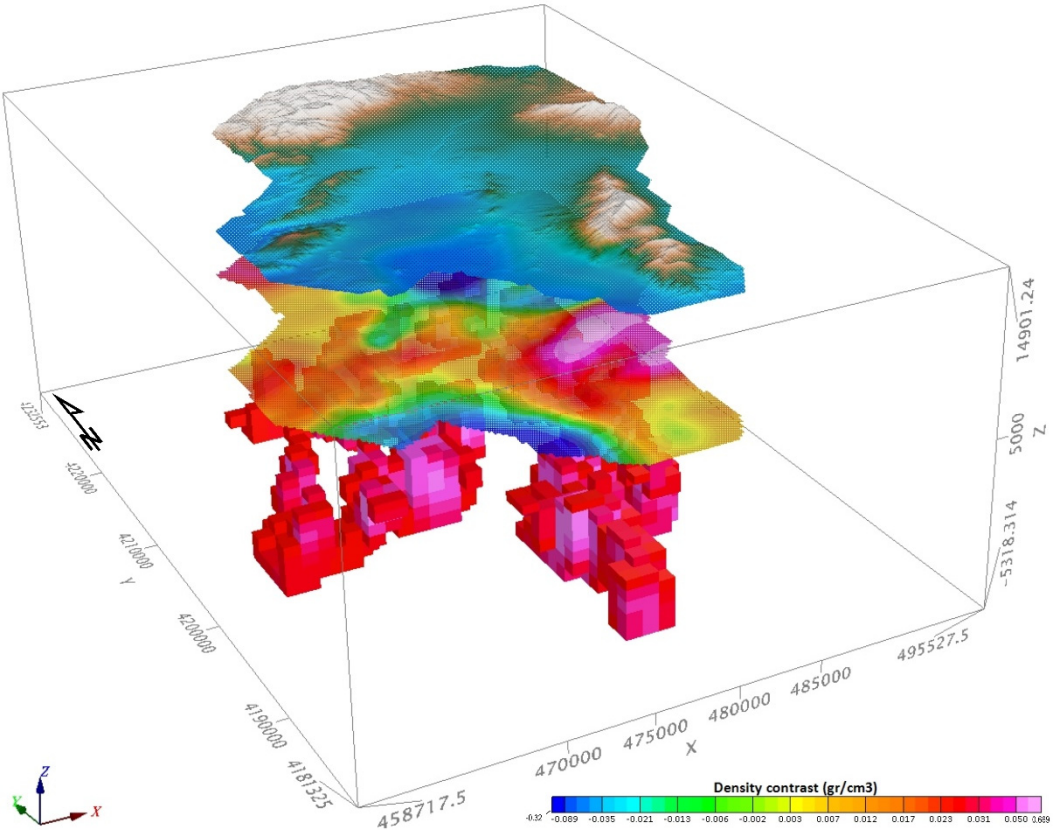

Figure 4.48. 3D gravity inversion (cell size 1000m), showing structures of low densities (density contrasts from 0.02 to 0.67 gr/cm^3).

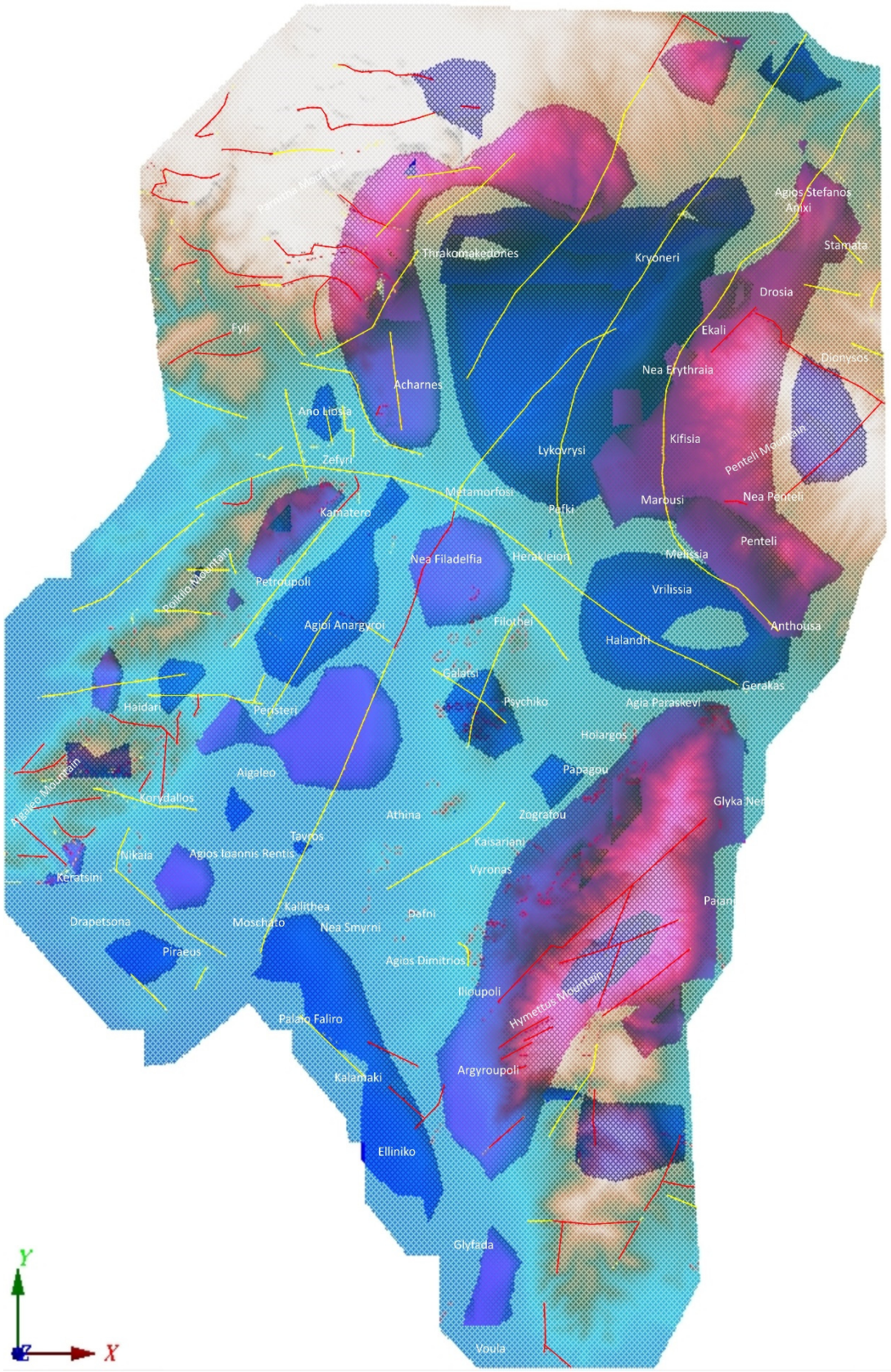

Figure 4.49. Ground plan of isodensity surfaces based on the 3D inversion model, along with the DEM of the area and the fault zones-tectonic zones (the red are the visible ones and the yellow are the possible ones). The blue isodensity surface surrounds areas with density contrast below -0.03 gr/cm^3 and the pink the areas above 0.03 gr/cm^3.

The subsurface was first discretized in a 3D block mesh, with 29 blocks in the 'X' direction, 40 in 'Y' direction and 11 blocks in the 'Z' direction, where all blocks have a cell size equal to 1000 meters for X-Y and 500 meters for Z direction (Fig. 4.46). Practically, the produced block mesh is constituted by a total of 12,760 blocks/cubic cells of individual density contrast. The minimum error was 0.1751. The density contrast ranges from -0.32 gr/cm^3 (bluish colors) to 0.669 gr/cm^3 (reddish colors), with a maximum depth of almost 6,800 meters (absolute elevation -5,300m).

In Figure 4.47, we have isolated the bodies with negative density contrast (ranging from -0.32 to -0.02 gr/cm^3) at the areas of *Thrakomakedones, Kryoneri, Drosia, Kifisia, Melissia, Vrilissia, Halandri, Herakleion, Metamorfosi, Acharnes*, *Petroupoli*, *Agioi Anargyroi, Piraeus*, *Palaio Faliro* and *Kalamaki* producing the low gravity anomalies in the Residual maps (4.30-4.31). On the other hand, in Figure 4.48, the bodies with positive density contrast (0.02-0.67 gr/cm^3), producing the high gravity anomalies, have been adumbrated below the areas of Mountains *Hymettus*, *Aigaleo-Poikilo*, *Parnitha* and the *downtown* of Athens city. These bodies define the geometric boundaries of the anomalies sources, producing either low or high gravity values. The DEM and the Residual maps have been positioned above the 3D model of the area for a better understanding.

Both types of bodies, with negative and positive values of density contrast, are being illustrated as isodensity surfaces in Figure 4.49. More specifically, areas with density contrast below -0.03 gr/cm^3 are surrounded by the blue isodensity surface and areas with density contrast above 0.03 gr/cm^3 with pink. The DEM of the area and the fault zones are also shown in an attempt to compare the produced 3D density model with the structural trending of the subsurface, mapped either as visible or possible (red and yellow color respectively).

Taking into consideration the anomalies already observed in the general model (Figs. 4.46-4.49), additional inversions were carried out for smaller areas, in order to reduce the cell size down to 500 meters (Figs. 4.50-4.53) or even 250 meters for the horizontal directions. This would provide greater detail of the final 3D density model and consequently better adumbration of the geometry of the source bodies. These inversions, with cell size 500 meters, were executed not only for the internal area of the basin, that is covered with post-alpine deposits, but also for the surrounding mountains of *Aigaleo-Poikilo* (Figs. 4.54-4.55)*, Hymettus* (Figs. 4.56-4.57)*, Parnitha* (Figs. 4.58-4.59) and *Penteli* (Figs. 4.60-4.61), since they also have intense structural trending.

The results of the 3D models are quite impressive and revealed important subsurface structures that might play important role for the seismotectonic structure of Athens basin. Several fault zones already mapped are verified by these models and more information about their characteristics might be gained (e.g. throw, depth and dip). But the most significant contribution of the 3D density models is that they also validate the existence of several fault zones mapped as possible (blind faults), based on other criteria.

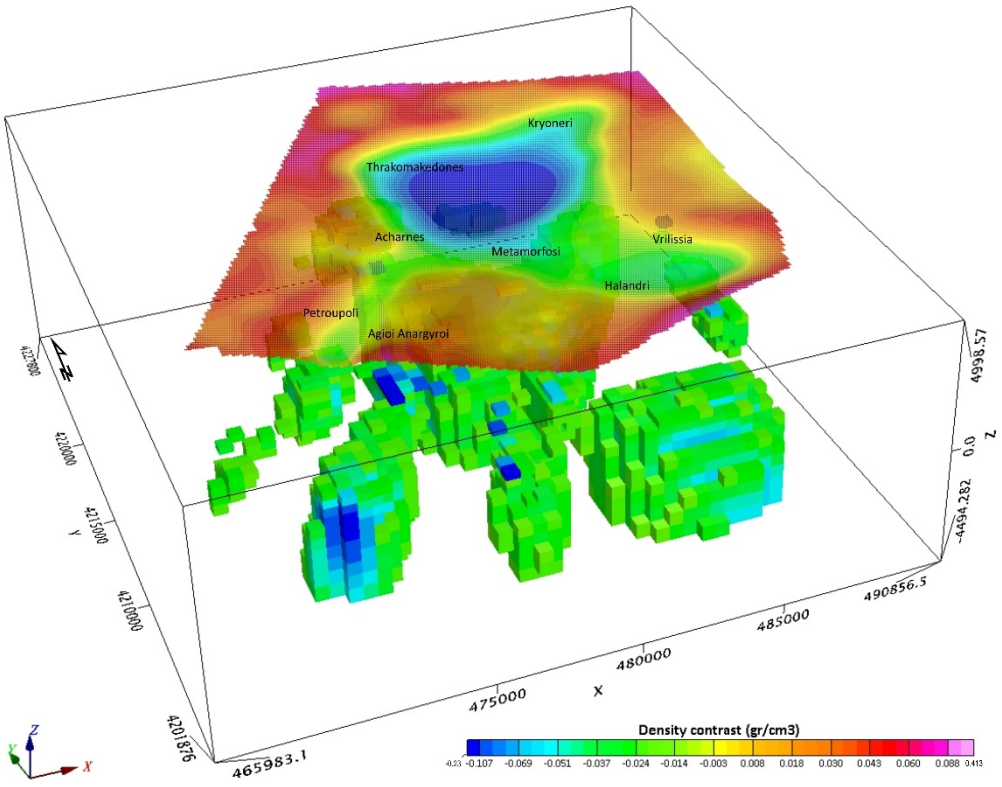

Figure 4.50. 3D gravity model (cell size 500m, mesh 42x45x17 blocks), showing structures of low densities (density contrast from -0.24 to -0.02 gr/cm^3) in the area of *Thrakomakedones, Acharnes, Drosia, Kifisia* and *Petroupoli.*

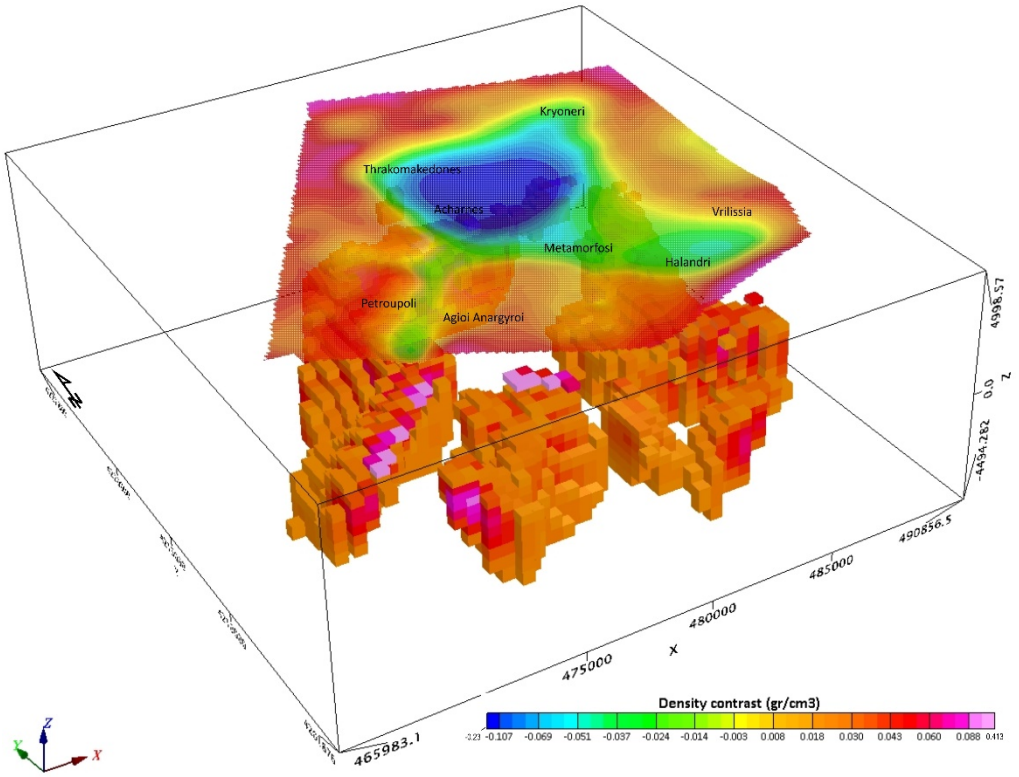

Figure 4.51. 3D gravity model (cell size 500m, mesh 42x45x17 blocks), showing structures of high densities (density contrast from 0.02 to 0.41 gr/cm^3) in the area of *Thrakomakedones, Acharnes, Drosia, Kifisia* and *Petroupoli.*

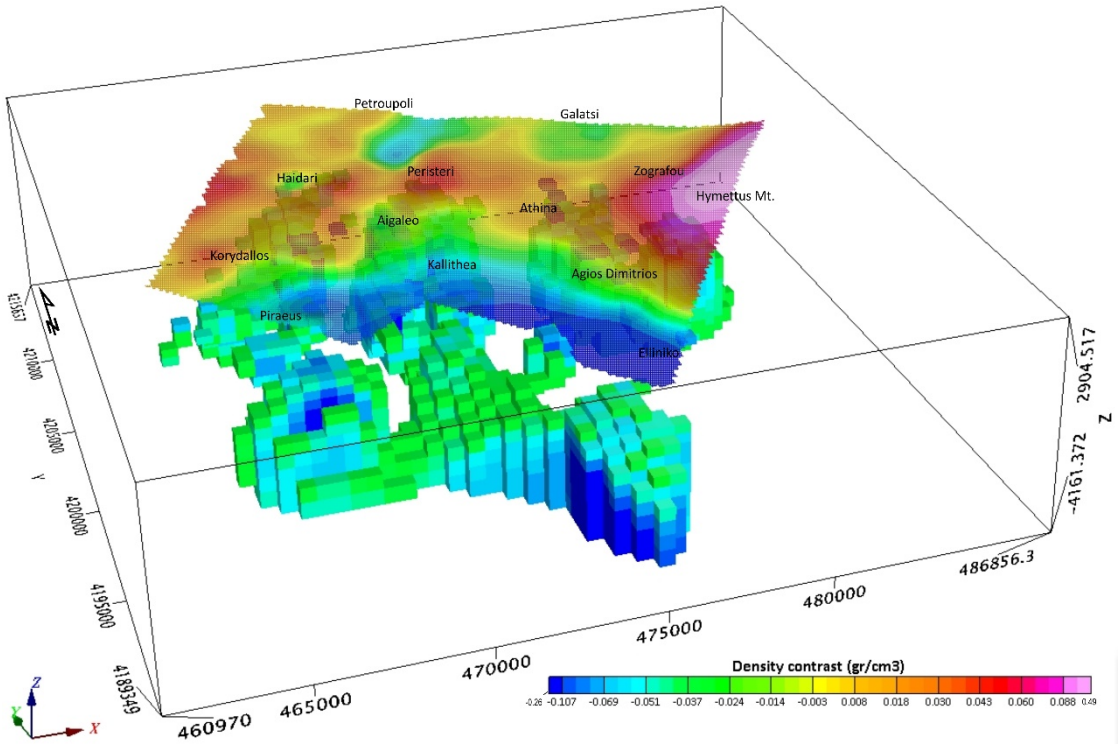

Figure 4.52. 3D gravity model (cell size 500m, mesh 44x46x13 blocks), showing structures of low densities (density contrast from -0.26 to -0.02 gr/cm^3) in the area of *Haidari, Peristeri, Downtown and Hymettus Mt*.

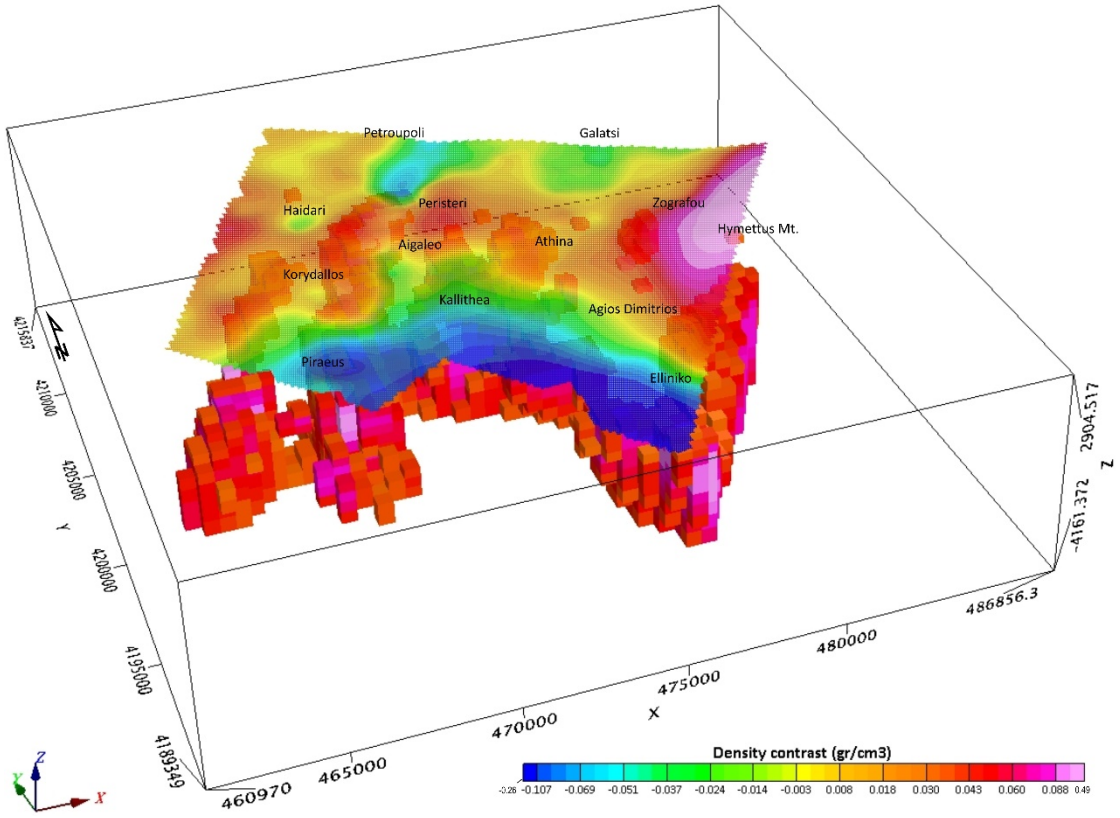

Figure 4.53. 3D gravity model (cell size 500m, mesh 44x46x13 blocks), showing structures of high densities (density contrast from 0.02 to 0.49 gr/cm^3) in the area of *Haidari, Peristeri, Downtown and Hymettus Mt.*

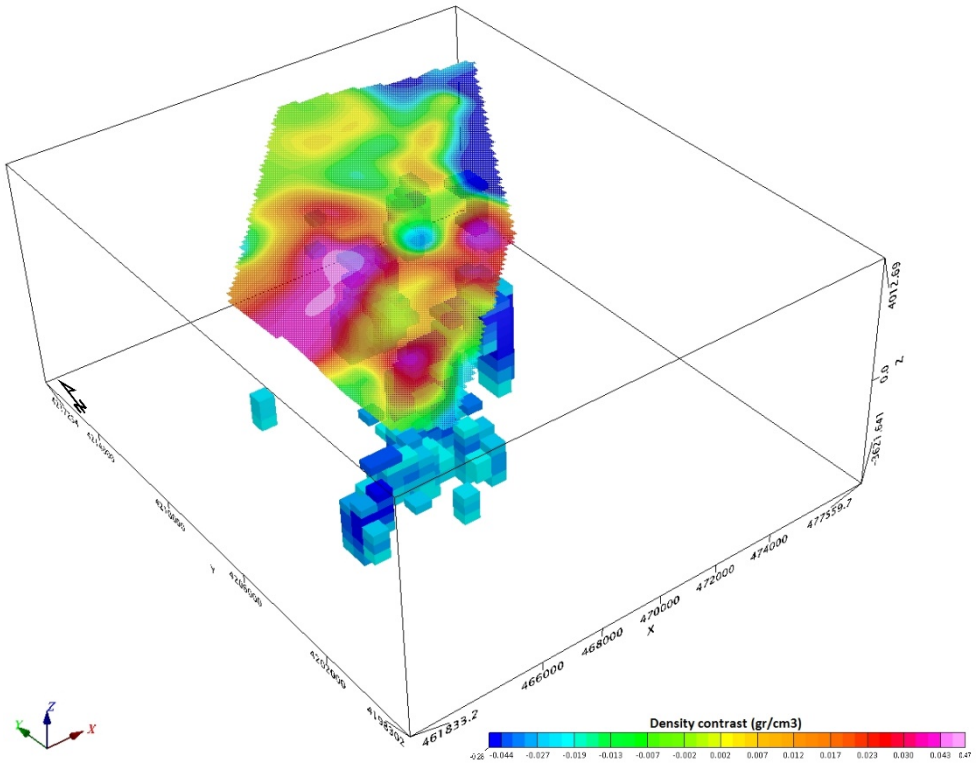

Figure 4.54. 3D gravity model (cell size 500m, mesh 27x33x12 blocks), showing structures of low densities (density contrast from -0.28 to -0.02 gr/cm^3) below *Aigaleo-Poikilo* Mountains.

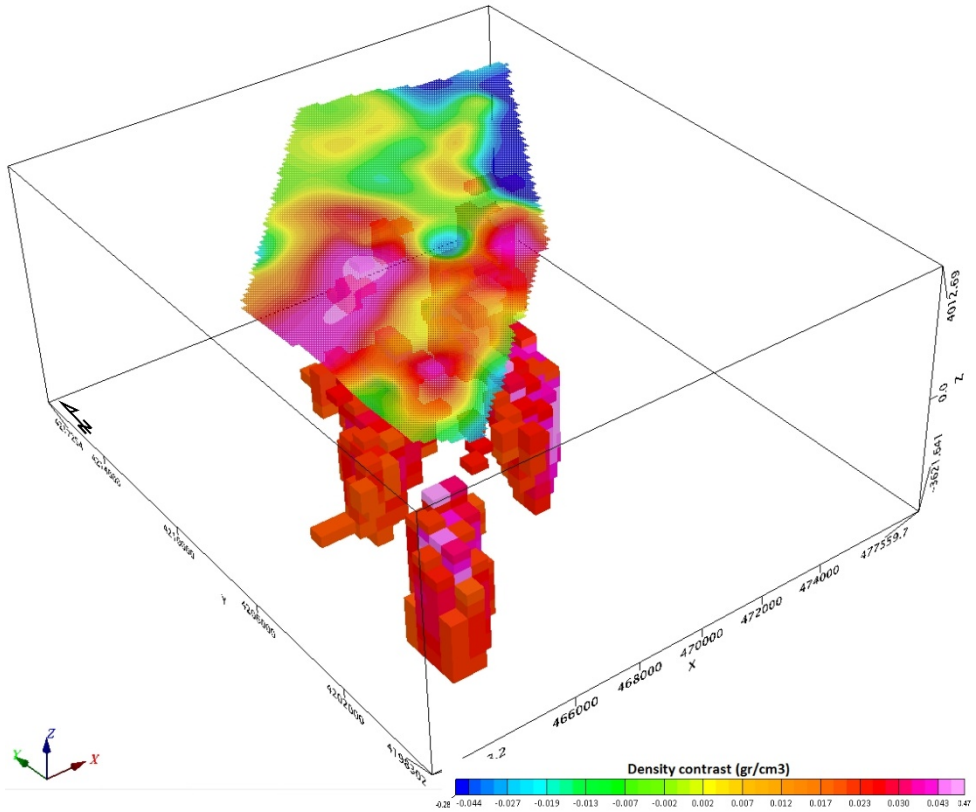

Figure 4.55. 3D gravity model (cell size 500m, mesh 27x33x12 blocks), showing structures of high densities (density contrast from 0.02 to 0.47 gr/cm^3) below *Aigaleo-Poikilo* Mountains.

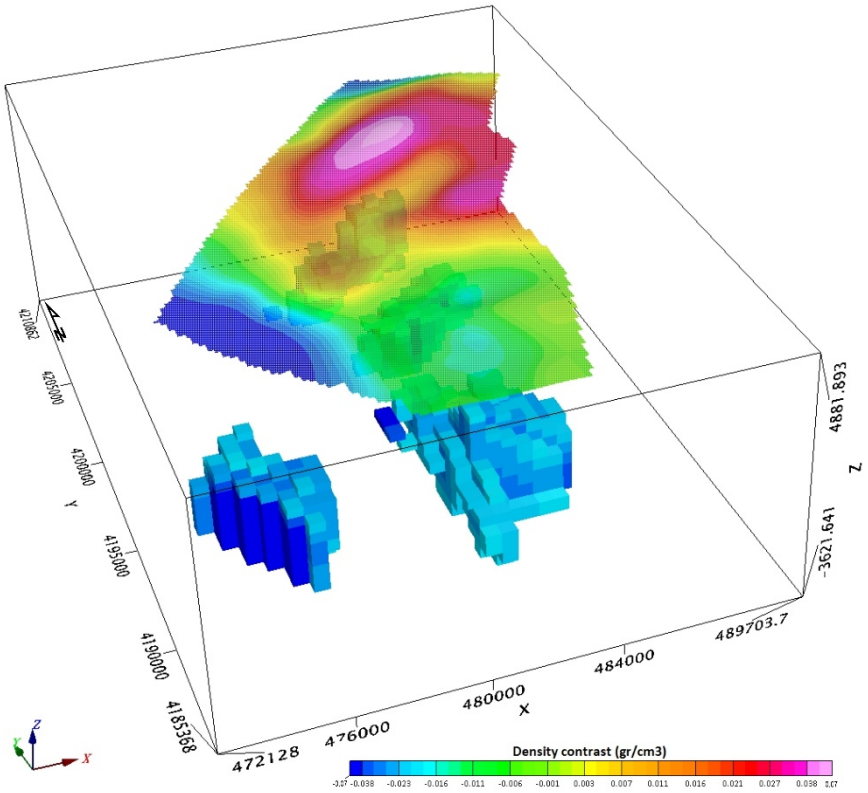

Figure 4.56. 3D gravity model (cell size 500m, mesh 30x44x15 blocks), showing structures of low densities (density contrast from -0.07 to -0.02 gr/cm^3) below *Hymettus* Mountain.

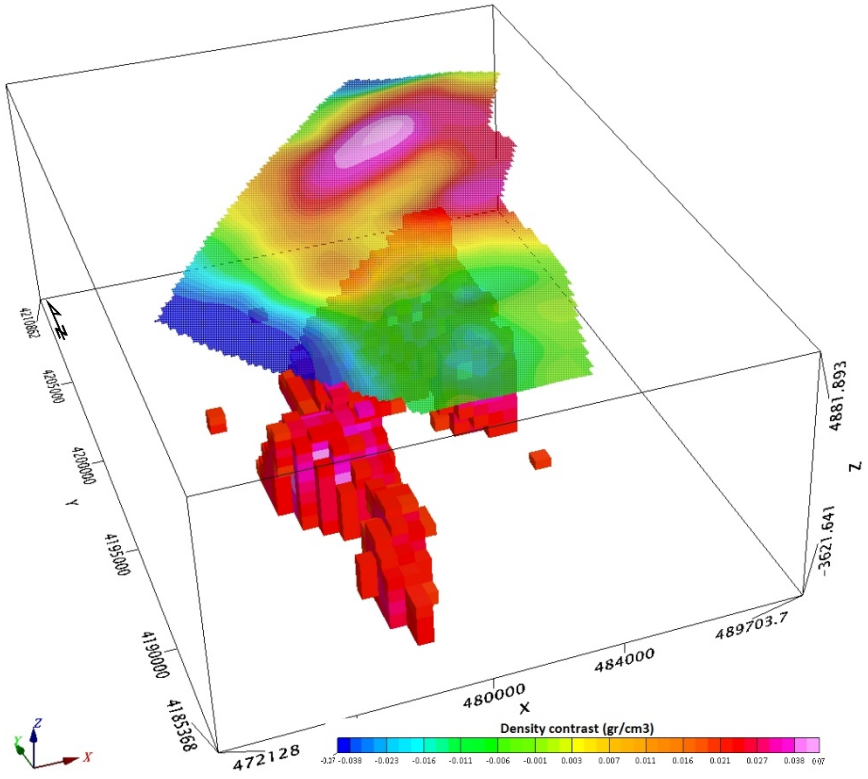

Figure 4.57. 3D gravity model (cell size 500m, mesh 30x44x15 blocks), showing structures of high densities (density contrast from 0.02 to 0.07 gr/cm^3) below *Hymettus* Mountain.

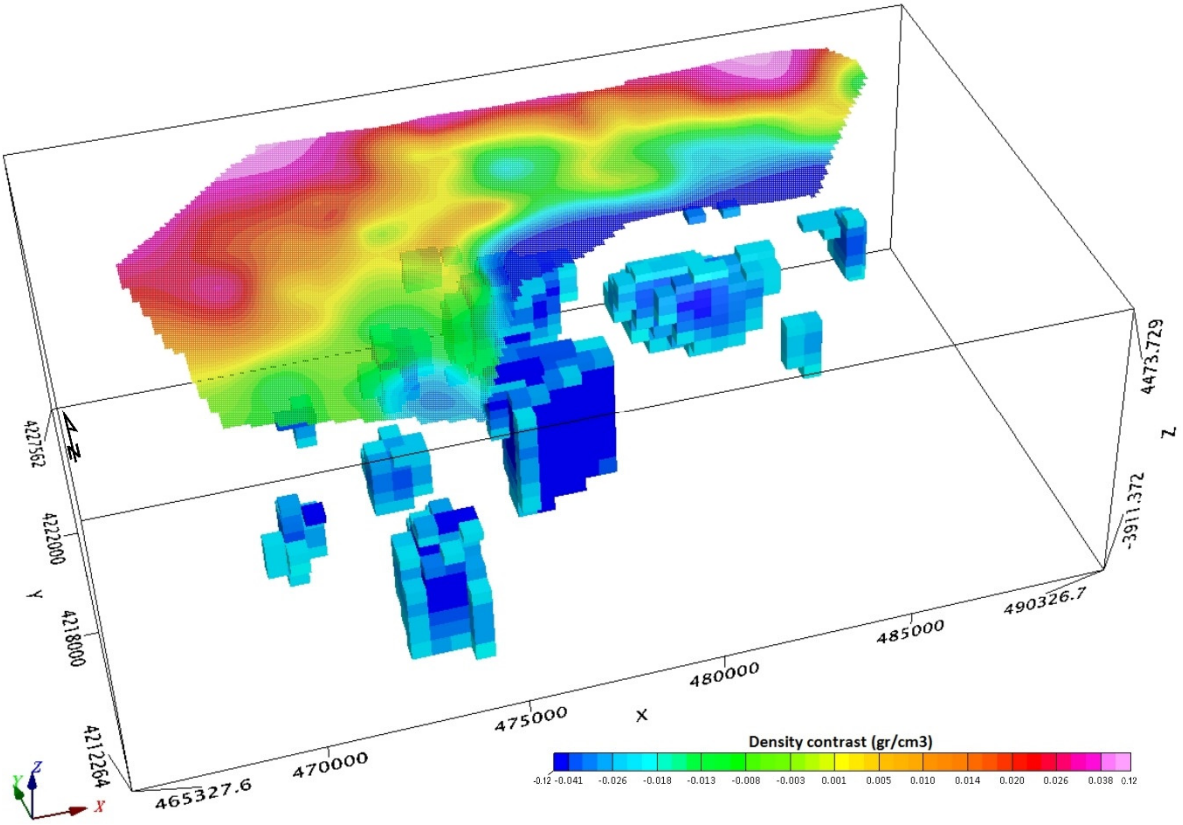

Figure 4.58. 3D gravity model (cell size 500m, mesh 44x26x16 blocks), showing structures of low densities (density contrast from -0.12 to -0.02 gr/cm^3) below *Parnitha* Mountain.

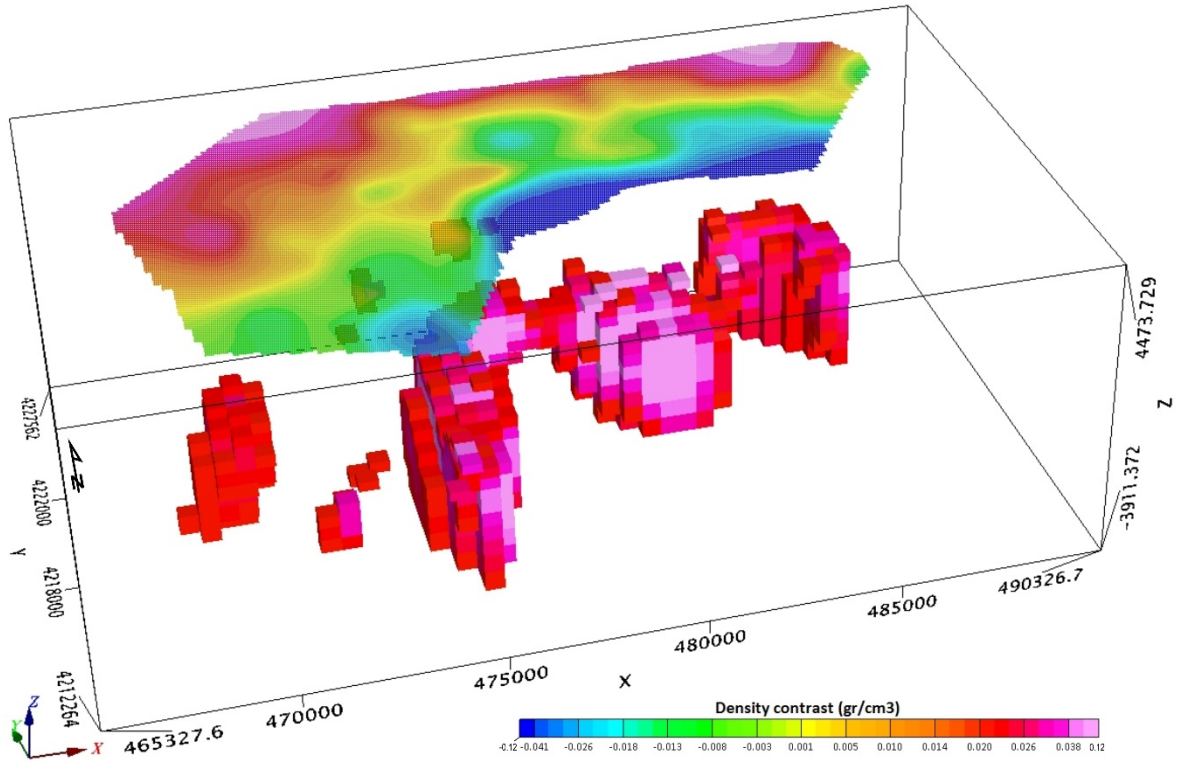

Figure 4.59. 3D gravity model (cell size 500m, mesh 44x26x16 blocks), showing structures of high densities (density contrast from 0.02 to 0.12 gr/cm^3) below *Parnitha* Mountain.

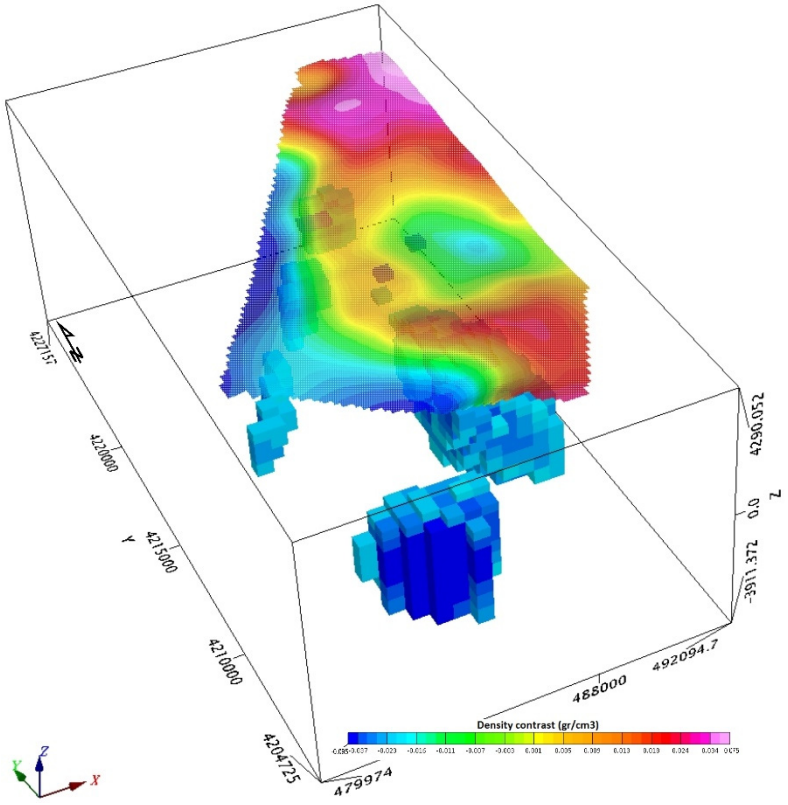

Figure 4.60. 3D gravity model (cell size 500m, mesh 22x40x15 blocks), showing structures of low densities (density contrast from -0.095 to -0.02 gr/cm^3) below *Penteli* Mountain.

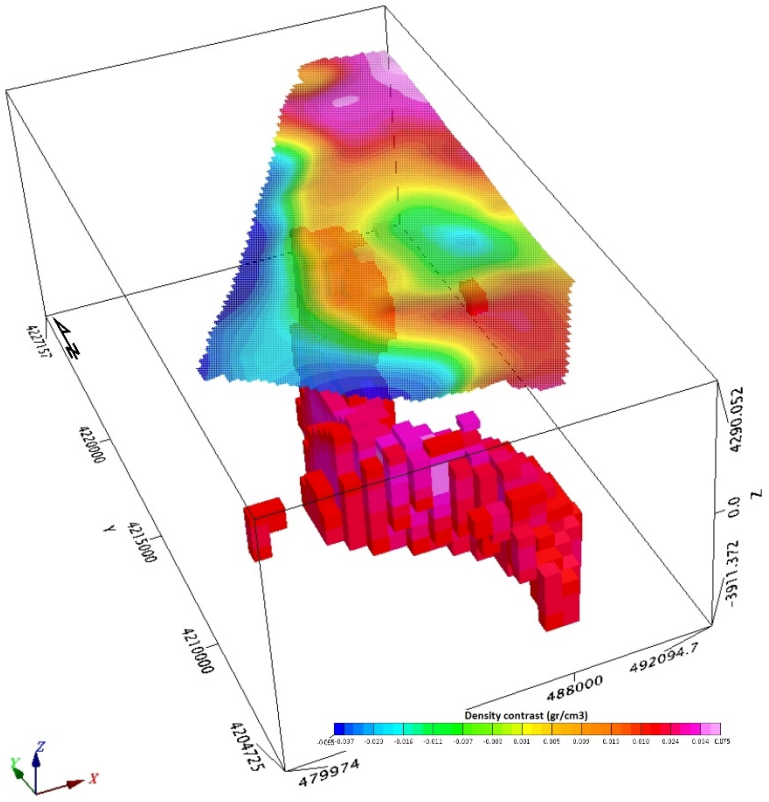

Figure 4.61. 3D gravity model (cell size 500m, mesh 22x40x15 blocks), showing structures of high densities (density contrast from 0.02 to 0.075 gr/cm^3) below *Penteli* Mountain.

In this section, we present all the 3D density models (Figs. 4.46-4.61) in a way that we can gather all the information concerning the geometry of the identified anomaly bodies. A first approach has already been presented in Figure 4.49, with the isodensity surfaces of the -0.03 gr/cm^3 (blue) and 0.03 gr/cm^3 (pink). This approach can also be supported by the 3D models presented in Figures 4.46-4.61, providing a complete understanding of the subsurface structure.

4.4.c. Interpretive geological 2.75-D density modeling

In 2D models we consider earth to be two-dimensional and because of that it is assumed to change with depth (Z) and in the direction of the profile (X) while there is no change in the strike direction (Y). Therefore, the models are considered to extend to infinity for the strike direction. Many publications present such 2D gravity models (Ayarza *et al.,* 2005; Cella *et al.,* 2007; Martelet *et al.,* 2004; Raum *et al.,* 2002; Yegorova *et al.,* 2008; Yuan *et al*., 2012) in order to understand the subsurface geological structure. Beyond that, there is also 2.5D modelling (Azab & Khadragy, 2013; Blaikie *et al.,* 2014; Mishra *et al.,* 2005; Sander & Cawthorn, 1996; ten Brink *et al.,* 2002; Yu-shan & Yuan-yuan, 2018)

In the context of this Ph.D. thesis, we have constructed 2.75D models of our gravity data, with the contribution carried by **GM-SYS**, a program by *Geosoft* for calculating the gravity response from a geological cross-section, compared to the observed field anomaly response. It is a reliable software that many authors have already used in their publications (Ammirati *et al.*, 2018; Azab & Khadragy, 2013; Blaikie *et al.,* 2014; Blecha *et al.,* 2009; Boubaya *et al.,* 2011; Kim *et al.,* 2009; Leader *et al.,* 2006; Rajasekhar & Mishra, 2008; Sultan *et al.,* 2011; Weidmann *et al.,* 2016). The models in GM-SYS are built with polygons that represent different geological formations and a density value is assigned at each one.

GM-SYS supports the 2.75D modelling, observed in many publications (Blecha *et al.,* 2009; Leader *et al.,* 2006; Park *et al.,* 2006; Smith *et al*., 2006). The 2.75D models can have 2D prisms asymmetrically positioned and extended at some distance from the line of the profile, in the strike direction. The model strike may also be tilted relative to the profile azimuth. Beyond the ends of these prisms, there are new ones of the same cross-section, but with different densities. It also allows independent specification of the locations of the two ends of the blocks (Geosoft, 2009).

Forward modelling includes the creation of a starting geological model and the calculation of its response. The Inversion procedure will change the proposed geological model in order to provide the best fit with the observed data response. Either the geometry of the models or their density can be modified in order to achieve the best fit between the calculated and the observed response. We can select up to 20 parameters (geometric dimensions or densities of blocks) to remain stable (fixed) during the inversion process, controlled by other types of data.

It is important to remind that gravity models are not unique and for that reason, we will obtain a better result if we have better starting models.

The observed gravity data for import in the GM-SYS software can be either Free-Air, Residual or Bouguer ones. Depending on the type of data, some parameters, such as the background density, have to be adjusted properly. For the case of importing Complete Bouguer data, the reduction value should be used for the background density.

The methods used to calculate the gravity response are based on Talwani *et al.,* (1959), Talwani & Heirtzler (1964) and Won & Bevis (1987). The 2D calculations are based on Rasmussen & Pedersen (1979). The GM-SYS inversion routine utilizes a Marquardt inversion algorithm (Marquardt, 1963) to linearize and invert the anomalies. Based on the GM-SYS manual (Geosoft, 2009), it uses a 2D, flat earth model, with each structural block extended to plus or minus infinity perpendicular to the profile. All models extend to ±30000 kilometers along the profile, in order to minimize the edge effects.

In Figure 4.62, the location of the profiles along the Athens basin, selected to create the interpretative geological-density 2.75-D models, is presented. A total of six (6) sections of total length equal to 133.5 kilometers in several directions have been chosen, trying to adumbrate the tectonic framework of the area in all directions. The density values assigned to each block/prism are based on the values we have already determined in §4.2. The Residual data (§4.3.d) have been imported in the software for the modelling, so the reduction density (2.67 gr/cm^3) has been declared as the background one.

The known geological data have been taken into consideration in order to create models that present logical geological structures. Of course, we have to remind that gravity modelling and inversion cannot produce unique solutions. Deep reliable borehole data have not been found in order to constrain the results. Seismic data (Papadopoulos *et al.,* 2007*)* have been recovered and compared with the gravity modelling in an effort to produce “unique” final interpretative models.

The proposed results of the interpretative geological-gravity 2.75-D sections are illustrated in Figures 4.63-4.68. In each of these figures, the upper part illustrates the observed residual gravity data (squares) along with the calculated one (line) that is based on the geological model, which is illustrated on the lower part of the figures. There has been an effort to maintain the colors used for the geological formations as they are in the main geological map (Fig. 2.2). The only exceptions concern the *Msl, Pll* and *Al* formations, which have been subdivided in the initial lithologies, due to the large density differences of the post-alpine lithologies. Each block, colored differently simulates a geological body, with a certain density quoted in the brackets. The sections are presented with a scale 1:2; therefore, there is a vertical exaggeration for better presentation and understanding.

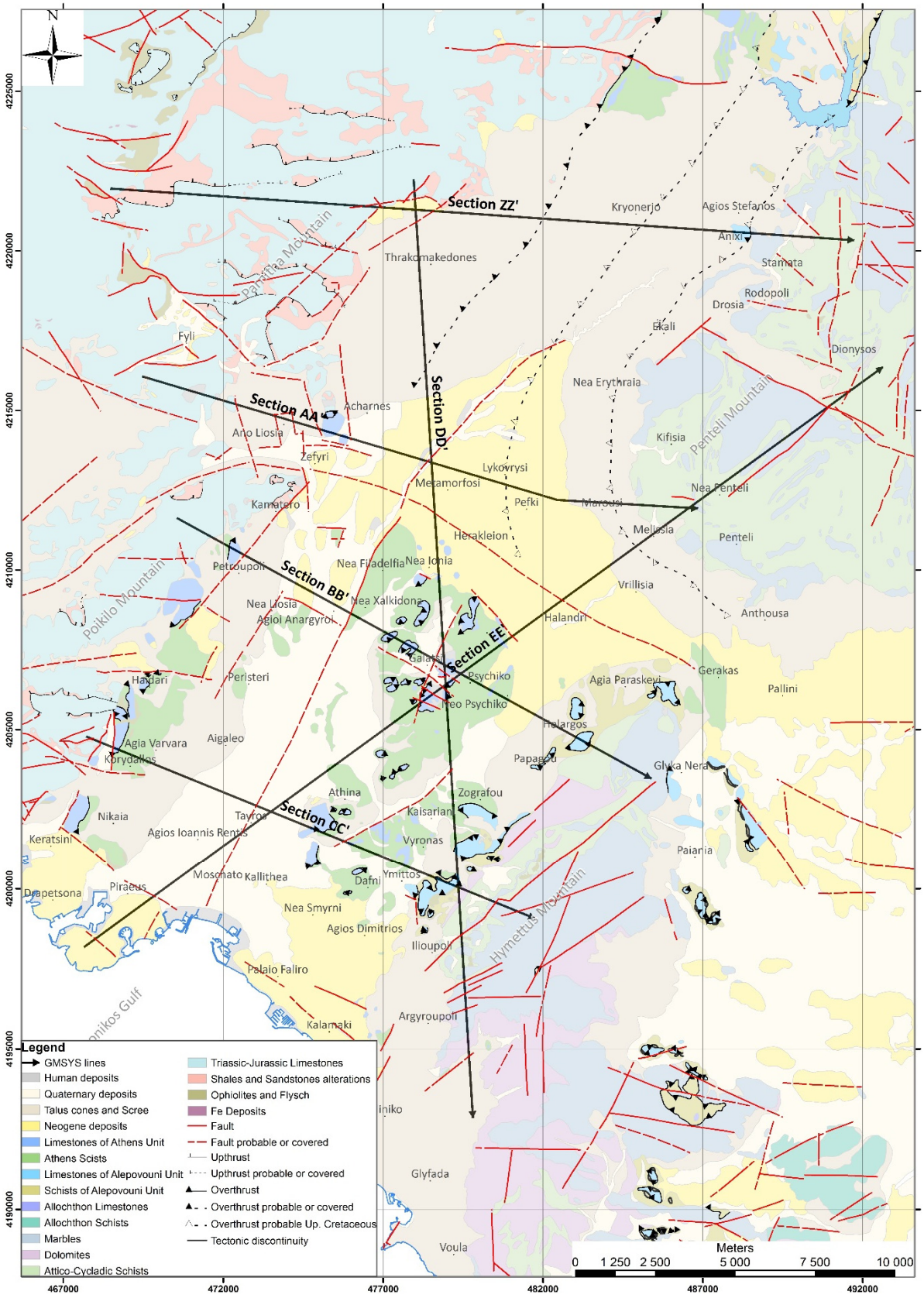

Figure 4.62. Locations of the profiles selected for the construction of 2.75D inversion models with GM-SYS.

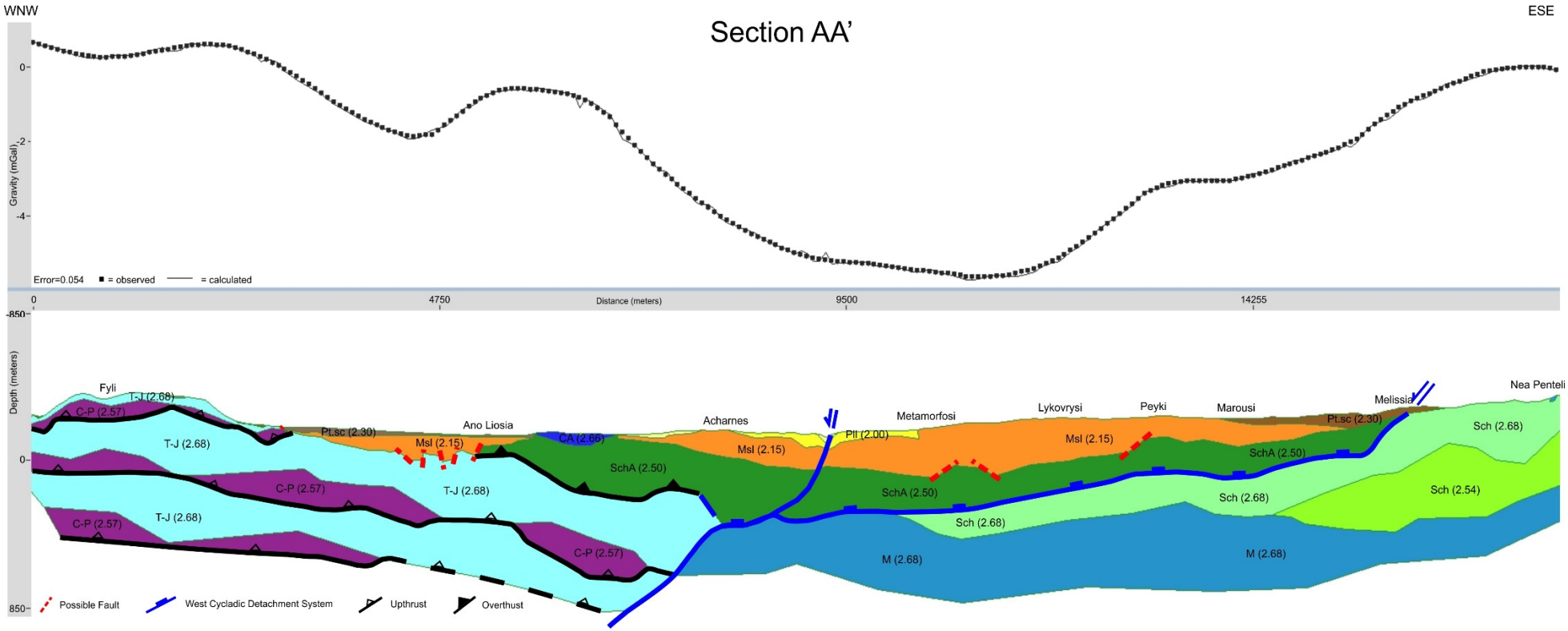

Figure 4.63. Interpretive geological 2.75-D profile modelling of Section AA', constructed with GM-SYS (scale 1:2). The observed (squares) and calculated (line) residual anomaly are observed, with a misfit equal to 0.054. Each geological polygon is characterized by the corresponding density value (in brackets) of the geological formation, determined in §4.2. The geological formations are the following:

T-J: Triassic-Jurassic Limestones (*Ypopelagoniki Unit*), **C-P**: Shales and Sandstones alterations (*Ypopelagoniki Unit*), **M:** Marbles (*Metamorphic Unit*), **Sch:** Schists (*Metamorphic Unit*), **SchA:** Athens Schists (*Athens Unit*); **CA:** Limestones (*Athens Unit*), **Msl:** Upper Miocene Terrestrial and Lacustrine deposits (*Neogene Formations*), **Pll:** Pliocene Terrestrial deposits (*Neogene Formations*), **Pt.sc:** Pleistocene Talus and Screes, **Al:** Alluvium deposits (*Loose Quaternary deposits).*

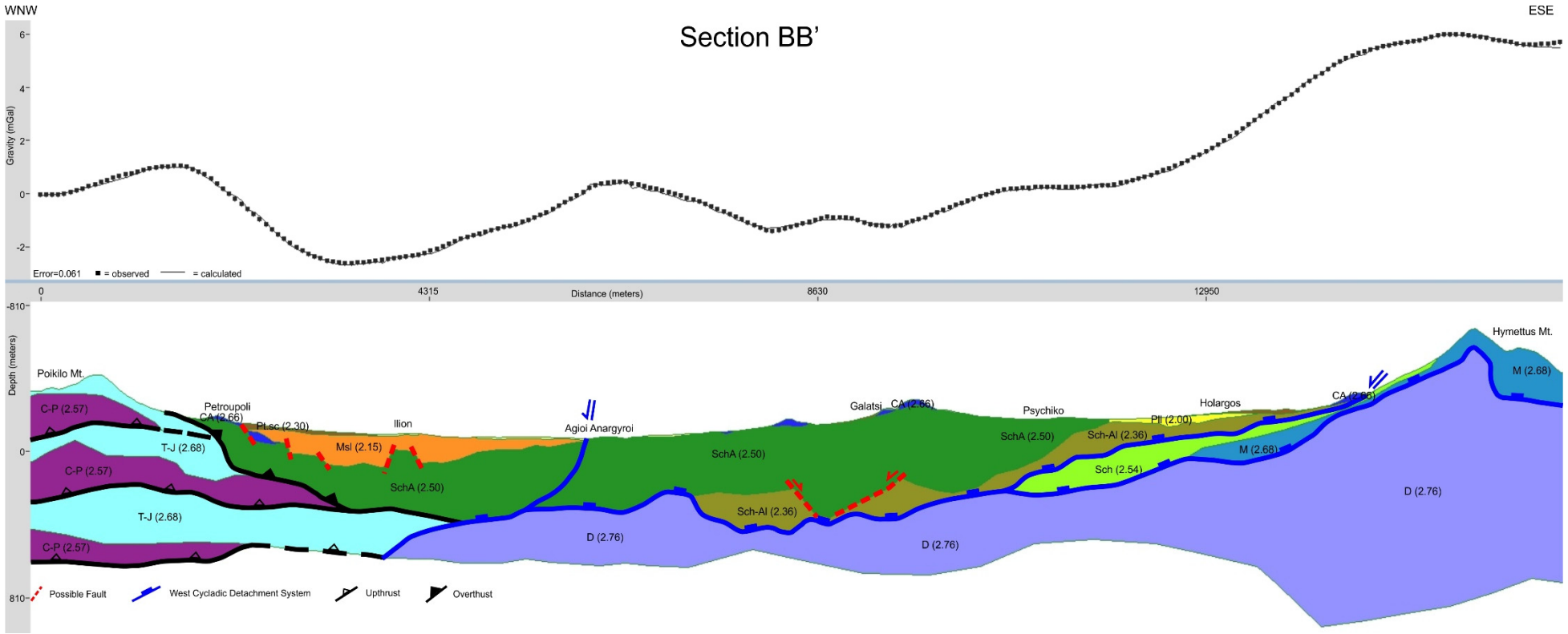

Figure 4.64. Interpretive geological 2.75-D profile modelling of Section BB', constructed with GM-SYS (scale 1:2). The observed (squares) and calculated (line) residual anomaly are observed, with a misfit equal to 0.061. Each geological polygon is characterized by the corresponding density value (in brackets) of the geological formation, determined in §4.2. The geological formations are the following:

T-J: Triassic-Jurassic Limestones (*Ypopelagoniki Unit*), **C-P**: Shales and Sandstones alterations (*Ypopelagoniki Unit*), **M:** Marbles (*Metamorphic Unit*), **Sch:** Schists (*Metamorphic Unit*), **D:** Dolomites (*Metamorphic Unit*), **SchA:** Athens Schists (*Athens Unit*), **CA:** Limestones (*Athens Unit*), **Sch-Al:** Schists (*Alepovouni Unit*), **Msl:** Upper Miocene Terrestrial and Lacustrine deposits (*Neogene Formations*), **Pll:** Pliocene Terrestrial deposits (*Neogene Formations*), **Pt.sc:** Pleistocene Talus and Screes, **Al:** Alluvium deposits (*Loose Quaternary deposits).*

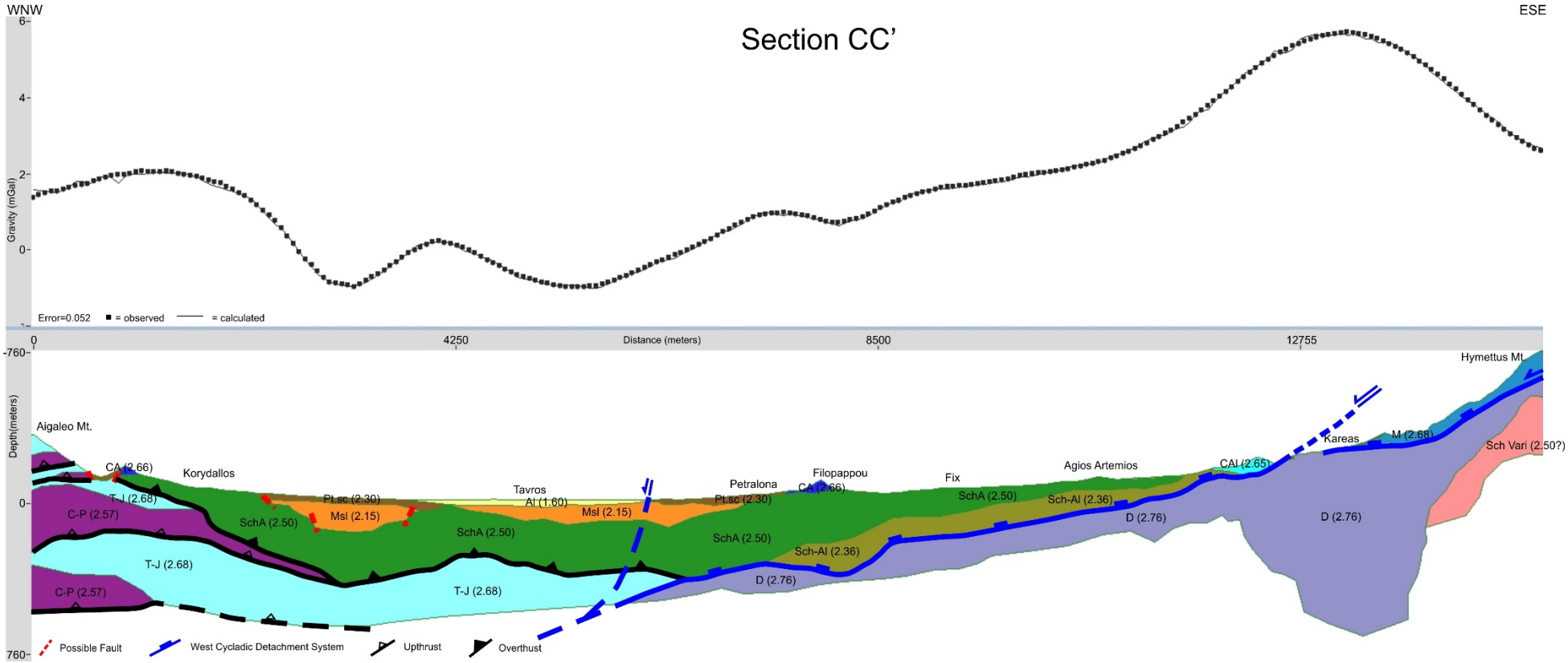

Figure 4.65. Interpretive geological 2.75-D profile modelling of Section CC', constructed with GM-SYS (scale 1:2). The observed (squares) and calculated (line) residual anomaly are observed, with a misfit equal to 0.052. Each geological polygon is characterized by the corresponding density value (in brackets) of the geological formation, determined in §4.2. The geological formations are the following:

T-J: Triassic-Jurassic Limestones (*Ypopelagoniki Unit*), **C-P**: Shales and Sandstones alterations (*Ypopelagoniki Unit*), **M:** Marbles (*Metamorphic Unit*), **Sch:** Schists (*Metamorphic Unit*), **D:** Dolomites (*Metamorphic Unit*), **Sch-Vari:** Varis Schists (*Metamorphic Unit*), **SchA:** Athens Schists (*Athens Unit*); **CA:** Limestones (*Athens Unit*), **Sch-Al:** Schists (*Alepovouni Unit*), **CAl:** Limestones (*Alepovouni Unit*), **Msl:** Upper Miocene Terrestrial and Lacustrine deposits (*Neogene Formations*), **Pt.sc:** Pleistocene Talus and Screes, **Al:** Alluvium deposits (*Loose Quaternary deposits).*

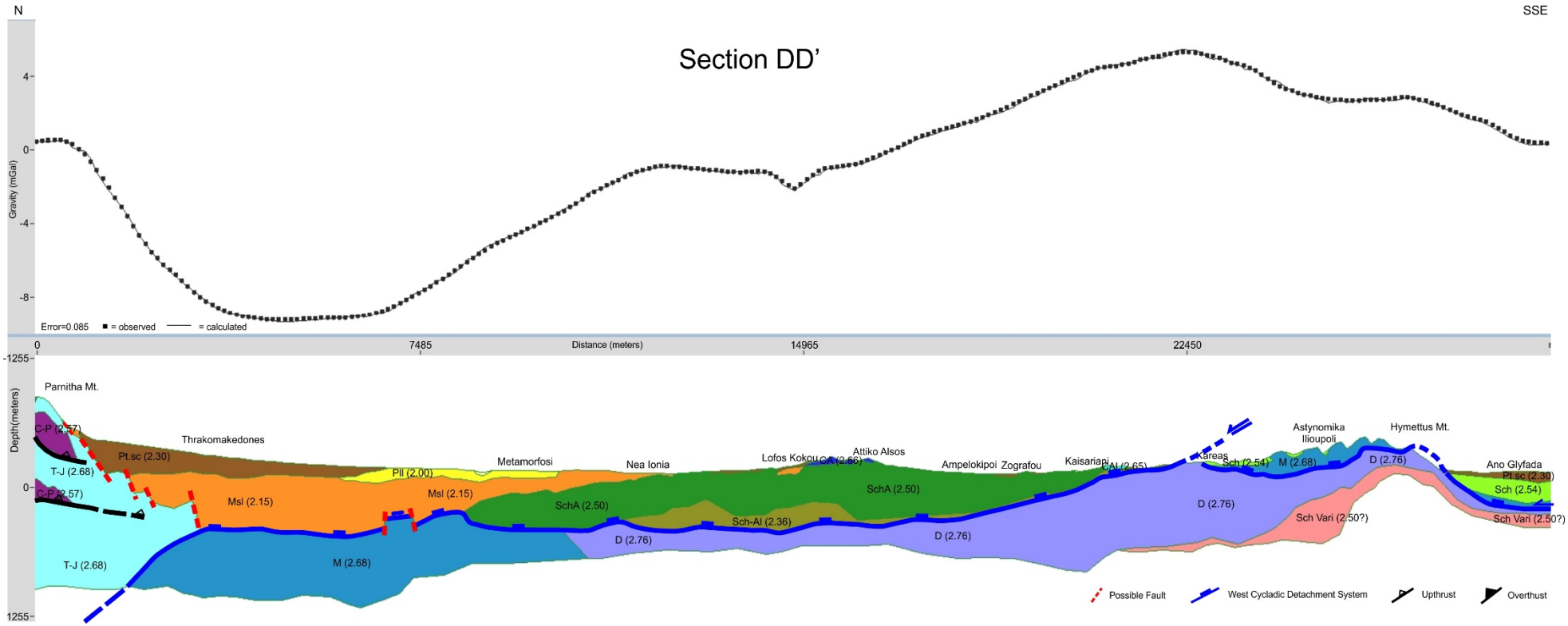

Figure 4.66. Interpretive geological 2.75-D profile modelling of Section DD', constructed with GM-SYS (scale 1:2). The observed (squares) and calculated (line) residual anomaly are observed, with a misfit equal to 0.085. Each geological polygon is characterized by the corresponding density value (in brackets) of the geological formation, determined in §4.2. The geological formations are the following:

T-J: Triassic-Jurassic Limestones (*Ypopelagoniki Unit*), **C-P**: Shales and Sandstones alterations (*Ypopelagoniki Unit*), **M:** Marbles (*Metamorphic Unit*), **Sch:** Schists (*Metamorphic Unit*), **D:** Dolomites (*Metamorphic Unit*), **Sch-Vari:** Varis Schists (*Metamorphic Unit*), **SchA:** Athens Schists (*Athens Unit*); **CA:** Limestones (*Athens Unit*), **Sch-Al:** Schists (*Alepovouni Unit*), **CAl:** Limestones (*Alepovouni Unit*), **Msl:** Upper Miocene Terrestrial and Lacustrine deposits (*Neogene Formations*), **Pll:** Pliocene Terrestrial deposits (*Neogene Formations*), **Pt.sc:** Pleistocene Talus and Screes, **Al:** Alluvium deposits (*Loose Quaternary deposits).*

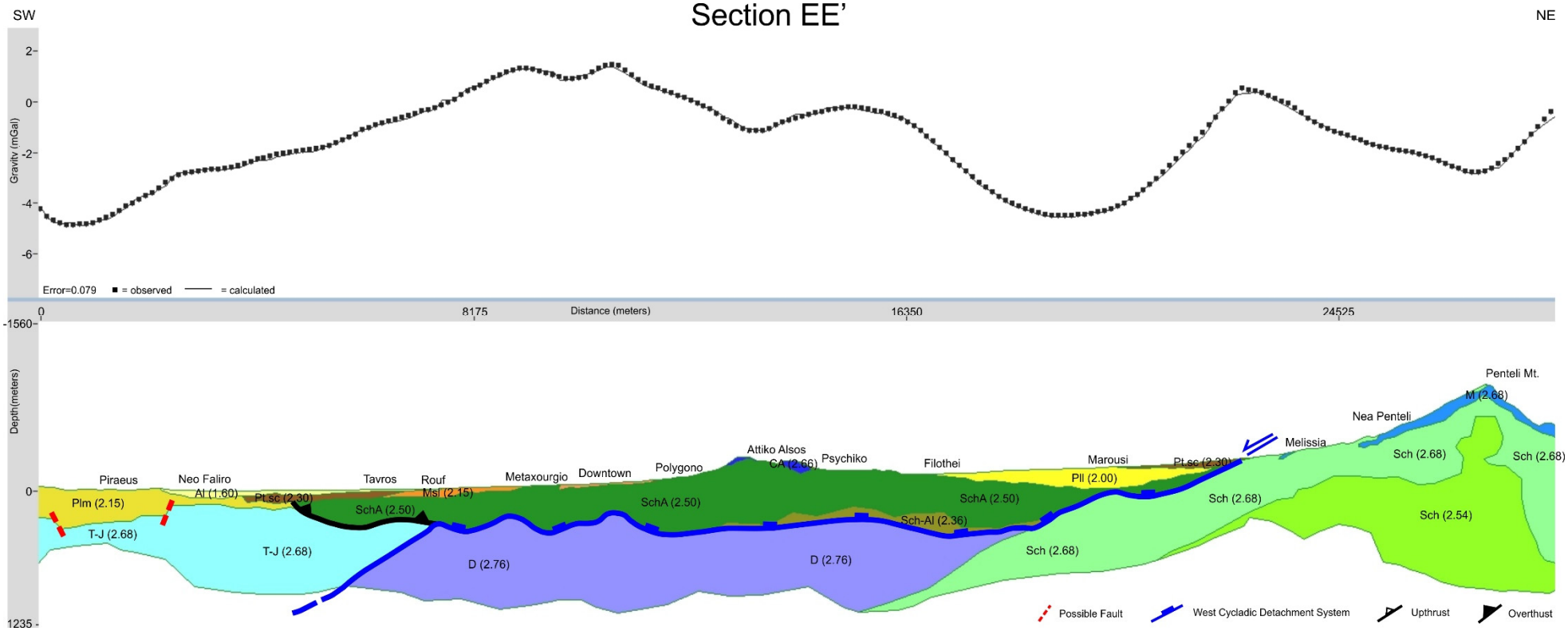

Figure 4.67. Interpretive geological 2.75-D profile modelling of Section EE', constructed with GM-SYS (scale 1:2). The observed (squares) and calculated (line) residual anomaly are observed, with a misfit equal to 0.079. Each geological polygon is characterized by the corresponding density value (in brackets) of the geological formation, determined in §4.2. The geological formations are the following:

T-J: Triassic-Jurassic Limestones (*Ypopelagoniki Unit*), **M:** Marbles (*Metamorphic Unit*), **Sch:** Schists (*Metamorphic Unit*), **D:** Dolomites (*Metamorphic Unit*), **SchA:** Athens Schists (*Athens Unit*); **CA:** Limestones (*Athens Unit*), **Sch-Al:** Schists (*Alepovouni Unit*), **Msl:** Upper Miocene Terrestrial and Lacustrine deposits (*Neogene Formations*), **Plm:** Pliocene Marine deposits (*Neogene Formations*), **Pt.sc:** Pleistocene Talus and Screes, **Al:** Alluvium deposits (*Loose Quaternary deposits).*

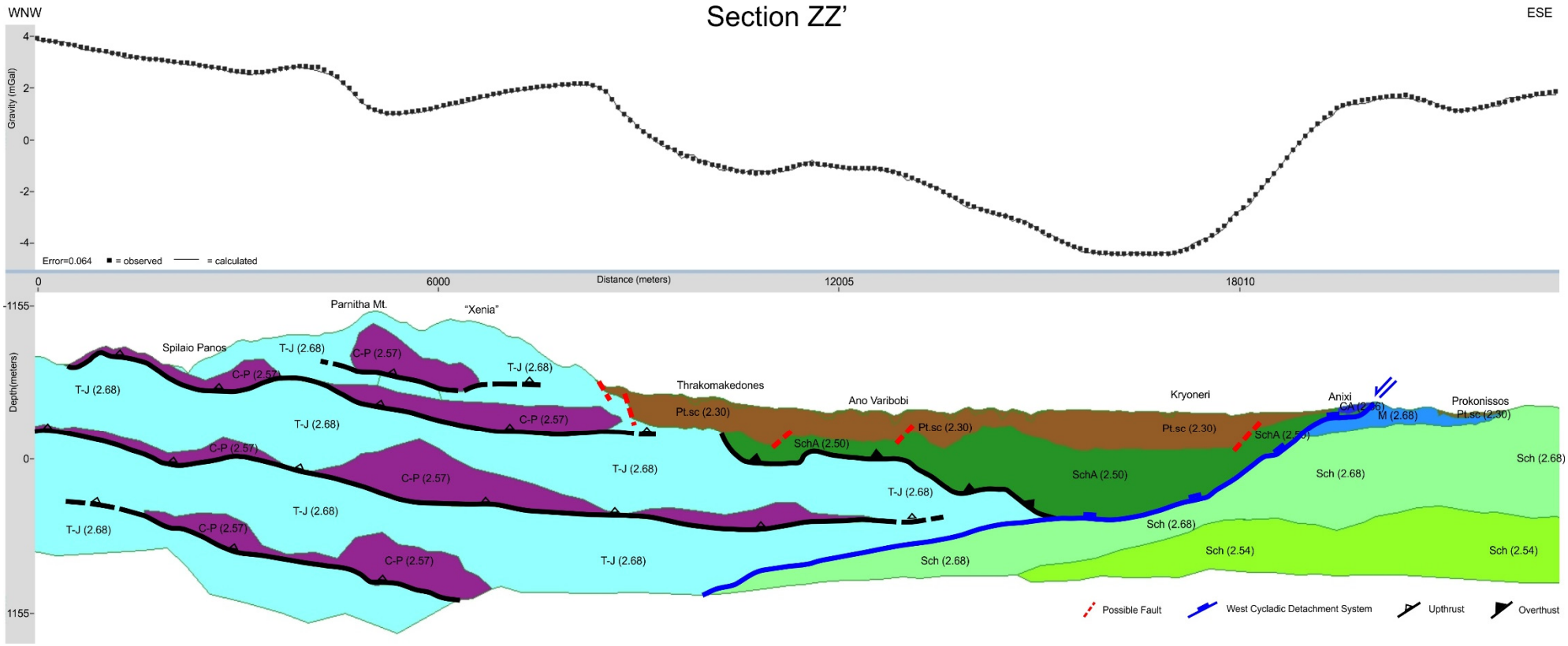

Figure 4.68. Interpretive geological 2.75-D profile modelling of Section DD', constructed with GM-SYS (scale 1:2). The observed (squares) and calculated (line) residual anomaly are observed, with a misfit equal to 0.064. Each geological polygon is characterized by the corresponding density value (in brackets) of the geological formation, determined in §4.2. The geological formations are the following:

T-J: Triassic-Jurassic Limestones (*Ypopelagoniki Unit*), **C-P**: Shales and Sandstones alterations (*Ypopelagoniki Unit*), **M:** Marbles (*Metamorphic Unit*), **Sch:** Schists (*Metamorphic Unit*), **SchA:** Athens Schists (*Athens Unit*); **CA:** Limestones (*Athens Unit*), **Pt.sc:** Pleistocene Talus and Screes.

In Section AA' (Fig. 4.63), the Neogene deposits (*Msl* and *Pll*) are observed with thickness up to 300 meters and excessive lateral coverage below the areas of *Ano Liossia*, *Acharnes* and *Lykovrysi*, producing the low values in the residual gravity field (down to -5.8 mGal). Several neotectonic fault zones might have been revealed, mostly along the Neogene deposits and their underlying alpine formations, especially at the areas of *Ano Liossia, Metamorfosi* and *Lykovrysi*. Underlying the Athens Schists (*SchA*) are detected, in the central part of the profile, with thickness up to 380 meters. They are observed either as an overthrust above the *Ypopelagoniki Unit* or as part of the *West Cycladic Detachment System*, moving upwards relatively to the underlying *Metamorphic* Unit. On the other hand, at the first part of the section three upthrusts of Triassic-Jurassic Limestones (*T-J*) and Shales and Sandstones alterations (*C-P*) seem to have been identified. Below the *Penteli Mountain*, it seems that the Schists (*Sch*) of the *Metamorphic Unit* are dominating over the Marbles (*M*) that are detected mostly at its western foothills. Moreover, no Dolomites (*D*) seem to be present. Somewhere between the 7-8th km of the section (*Acharnes)*, the detachment zone between the *Ypopelagoniki Unit* and the *Metamorphic* one seems to have been detected.

In Section BB' (Fig. 4.64), the Neogene deposits (*Msl* and *Pll*) are observed with relatively smaller thickness (up to 170 meters) and lateral coverage, below the areas of Petroupoli , *Agioi Anargyroi* and *Halandri*, producing the low values in the residual gravity field (down to -2.5 mGal). Several neotectonic fault zones might have been revealed, mostly along the Neogene deposits and their underlying formation of *Athens Schists*, between the areas of *Petroupoli* and *Ilion*. The Athens Schists (*SchA*) and the Schists of *Alepovouni Unit* (*Sch-Al*) cover a great part of the subsurface underlying the Neogene deposits, with great surface exposure also (outcrops) reaching a maximum thickness up to 500 and 225 meters correspondingly. They are observed either as an overthrust above the *Ypopelagoniki Unit* or as part of the *West Cycladic Detachment System*, moving upwards relatively to the underlying *Metamorphic* Unit. The first part of the section is dominated by the existence of at least three upthrusts of the Triassic-Jurassic Limestones (*T-J*) and the Shales and Sandstones alterations (*C-P*). In this profile, the Dolomites (*D*) of the *Metamorphic Unit* seem to dominate at the lower area below the basin (from a depth of 300 meters) and the *Hymettus* Mountain, with thickness up to 1300 meters*.* Beyond that, extended parallel folds of the *Metamorphic* Unit, a familiar structure in the area, have been adumbrated from this geological section. Below the Athens Schists (*SchA*), somewhere between the 3-5th km of the section a detachment zone between the *Ypopelagoniki Unit* and the *Metamorphic Unit* has been detected.

In Section CC' (Fig. 4.65), the Neogene deposits (*Msl*) are observed with relatively smaller thickness, up to 150 meters and lateral coverage below the area of *Agios Ioannis Rentis and Tavros*, producing the low values in the residual gravity field (down to -1 mGal). There is also a layer of 40-50 meters of Alluvium deposits (*Al*) and Pleistocene Talus and Screes (*Pt*.sc),

overlying. Few neotectonic fault zones have been revealed, mostly along the Neogene deposits and their underlying formation of *Athens Schists*, between the areas of *Korydallos* and *Tavros*. The Athens Schists (*SchA*) and the Schists of *Alepovouni Unit* (*Sch-Al*) cover a great part of the subsurface, underlying the Neogene deposits, with great surface exposure also (outcrops) reaching a maximum thickness up to 300 and 155 meters correspondingly. Along this section, they are also observed either as an overthrust above the *Ypopelagoniki Unit* or as part of the *West Cycladic Detachment System*, moving upwards relatively to the underlying *Metamorphic* Unit. The first part of the section is dominated by the existence of three or four upthrusts of the Triassic-Jurassic Limestones (*T-J*) and the Shales and Sandstones alterations (*C-P*). Furthermore, the Dolomites (*D*) of the *Metamorphic Unit* seem to dominate at the lower area below the basin (from depths of 350 meters) and the *Hymettus* Mountain, with thickness that reaches 950 meters. The Marbles (*M*) are also detected below *Hymettus Mountain,* while the Schists (*Sch*) have been restrained to a thin layer of a few meters. A structure similar to the one of extended parallel folds seems to appear among the formation of the *Metamorphic* Unit. The formation of Varis Schists (*Sch Vari*) is also illustrated underlying the Dolomites (*D*) in the end of the section. Somewhere below the Athens Schists (5-6th km of the section), the detachment zone between *Ypopelagoniki Unit* and the *Metamorphic one* is located.

In Section DD' (Fig. 4.66), the Neogene deposits (*Msl* and *Pll*) are observed with great thickness, up to 580 and 130 meters correspondingly, below the areas of *Thrakomakedones, Acharnes* and *Metamorfosi*, producing the low values in the residual gravity field (down to -9.3 mGal). They are forming this supra-detachment basin that is overlying on the Marbles (*M*) of the *Metamorphic Unit*. A layer of almost 310 meters of Pleistocene Talus and Screes (*Pt.*sc) partially overlying the *Msl* deposits. More particularly, below the area of *Thrakomakedones*, several neotectonic fault zones have been revealed, between the post-alpine deposits and the underlying formations of *Ypopelagoniki Unit*. The first part of the section is dominated by two upthrusts of the Triassic-Jurassic Limestones (*T-J*) and the Shales and Sandstones alterations (*C-P*). The Athens Schists (*SchA*) and the Schists of *Alepovouni Unit* (*Sch-Al*) cover a great part of the subsurface, underlying the Neogene deposits, with great surface exposure also (outcrops) reaching a maximum thickness up to 530 and 270 meters correspondingly. They are covering mostly the Dolomites (*D*) as part of the *West Cycladic Detachment System,* moving upwards relatively to the underlying *Metamorphic* Unit. The Marbles (*M*) and Schists (*Sch*) of the *Metamorphic Unit* are also detected below the greater area of *Hymettus Mountain* as long as below the area of *Thrakomakedones*. The Dolomites (*D*) of the *Metamorphic Unit* seem to dominate at the central area of the section, below the basin (from depths of 600 meters) and below the *Hymettus* Mountain, with thickness that reaches 750 meters. Underlying them, the formation of Varis Schists (*Sch Vari*) is also expected. Below the area of *Hymettus Mt.*, these metamorphic formations are revealed through extended parallel folds.

Somewhere below these Neogene deposits and the Athens Schists (1-2th km of the section), the detachment zone between *Ypopelagoniki Unit* and the *Metamorphic Unit* is expected.

In Section EE' (Fig. 4.67), the Neogene deposits are observed below the areas of *Piraeus (Plm)* and *Marousi (Pll),* with thickness, up to 250 and 200 meters correspondingly, producing the low values in the residual gravity field (down to -4.8 mGal). At the area of *Piraeus* and Neo Faliro a couple of neotectonic fault zones have been revealed at the basement of the post-alpine deposits. There is also a layer of 40-50 meters of Alluvium deposits (*Al*) partially overlying the *Plm* sediments at *Piraeus* area. The first part of the section is dominated by the existence of the Triassic-Jurassic Limestones (*T-J*). The Athens Schists (*SchA*), with great surface exposure (outcrops), also cover a great part of the subsurface, with maximum thickness up to 600 meters, mostly below the central area of the basin. The Schists of *Alepovouni Unit* (*Sch*-Al) have been determined with a thin layer of maximum thickness of 200 meters, below the Athens Schists. These two formations are located either as an overthrust above the *Ypopelagoniki Unit* or as part of the *West Cycladic Detachment System* (the *Sch-Al* formation mostly), moving upwards relatively to the underlying *Metamorphic* Unit. The Dolomites (*D*) of the *Metamorphic Unit* seem to dominate at the central area of the section, below the basin (from depths of 300 meters) and below the *Hymettus* Mountain, with thickness that reaches 750 meters. Below *Hymettus Mountain*, it seems that the Schists (*Sch*) are dominating against the Marbles (*M*), with their thicknesses reaching 1,750 and 100 meters correspondingly. Somewhere below the Athens Schists (6-8th km of the section), the detachment zone between *Ypopelagoniki Unit* and the *Metamorphic Unit* has been investigated.

In Section ZZ' (Fig. 4.68), a thick layer of Pleistocene Talus and Screes (*Pt*.sc) is observed at the central area of the section, below *Thrakomakedones, Kryoneri* and *Agios Stefanos* areas, with thickness up to 290 meters, producing the low values in the residual gravity field (down to -4.5 mGal). Especially, below the area of *Thrakomakedones*, several neotectonic fault zones have been revealed, between the Pleistocene Talus and Screes (*Pt*.sc) and the underlying formations of *Ypopelagoniki Unit*. The first part of the section is dominated by the existence of three or four upthrusts structured by the Triassic-Jurassic Limestones (*T-J*) and the Shales and Sandstones alterations (*C-P*). The Athens Schists (*SchA*) cover a great part of the subsurface, underlying the Pleistocene Talus and Screes (*Pt*.sc), with thickness up to 540 meters. They are positioned either as an overthrust above the *Ypopelagoniki Unit* or as part of the *West Cycladic Detachment System*, moving upwards relatively to the underlying *Metamorphic* Unit. Below *Penteli Mountain*, it seems that the Schists (Sch) are dominating over the Marbles (*M*), with thicknesses that reach 1350 meters and 175 meters correspondingly. On the contrary, the Dolomites (*D*) of the *Metamorphic Unit* have not been identified. Somewhere below these Quaternary deposits and the Athens Schists (9-10th km of

the section), the detachment zone between *Ypopelagoniki Unit* and the *Metamorphic Unit* has been identified.

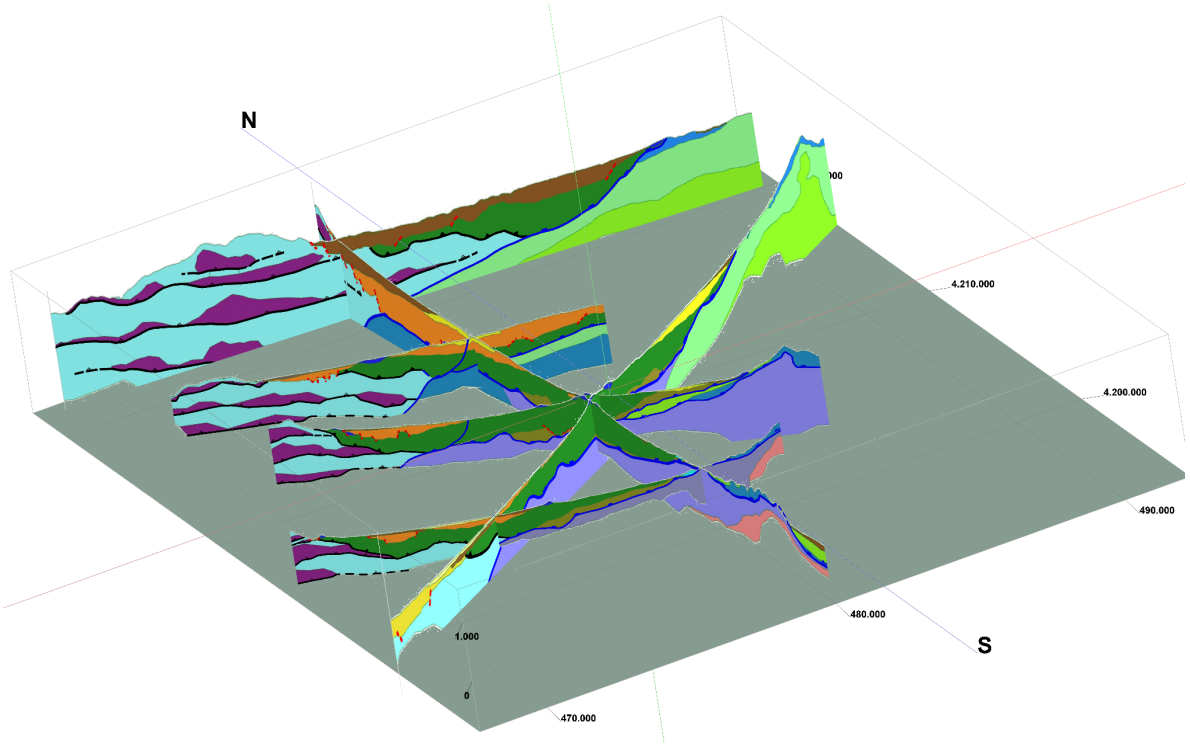

Figure 4.69. 3D illustration of the interpretative geological profiles (looking from SW)

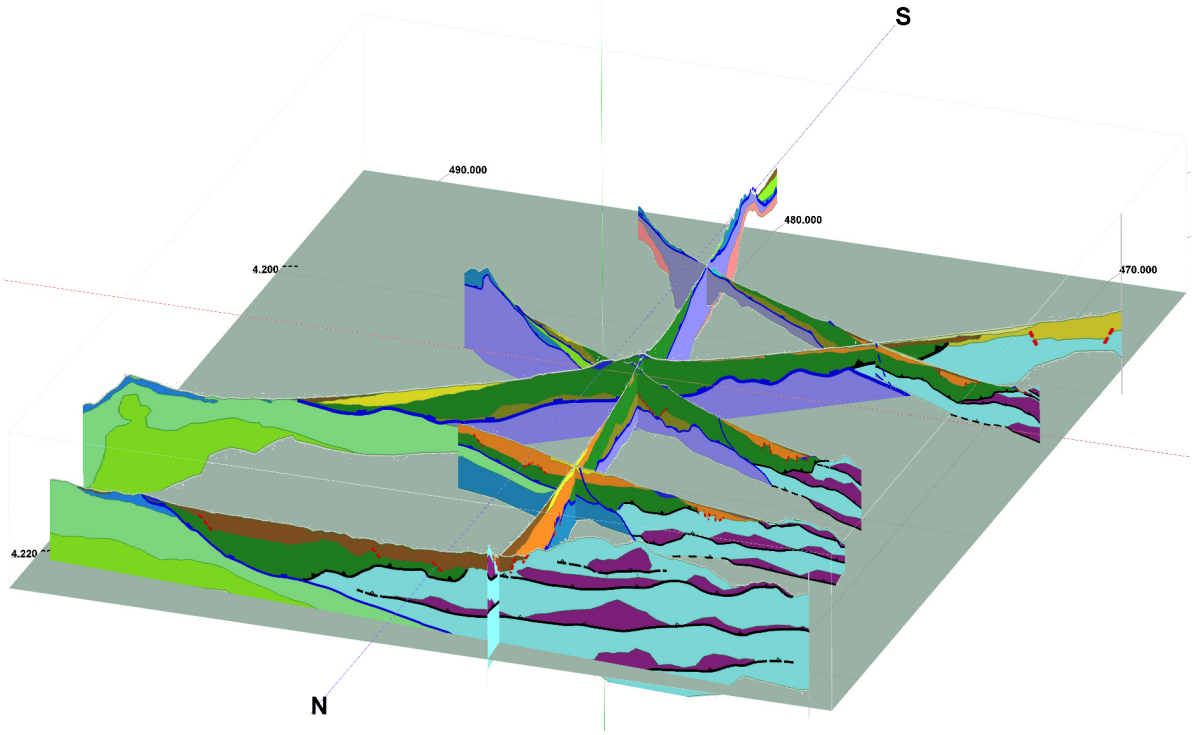

Figure 4.70. 3D illustration of the interpretative geological profiles (looking from NW)

Based on the above geological models illustrated in 3D in Figures 4.69-4.71, we can clarify the subsurface structure of Athens basin for depths up to 2,500 meters and gather information about important structural issues, such as the location of neotectonic faults and overthrusts or even for the major detachment zone between the metamorphic and non-metamorphic (*Ypopelagoniki*) units. Several important tectonic structures have been revealed, such as the part of the *West Cycladic Detachment System* and the extended parallel folds in the Metamorphic Unit. Moreover, several upthrusts of the Ypopelagoniki Unit have been investigated as well as a supra-detachment basin filled with post-alpine sediments, at the area between *Thrakomakedones* and *Metamorfosi*. All the results will be discussed and evaluated further in the following chapter (§5.4), gathering all the produced information from all types of maps and profiles of this chapter.

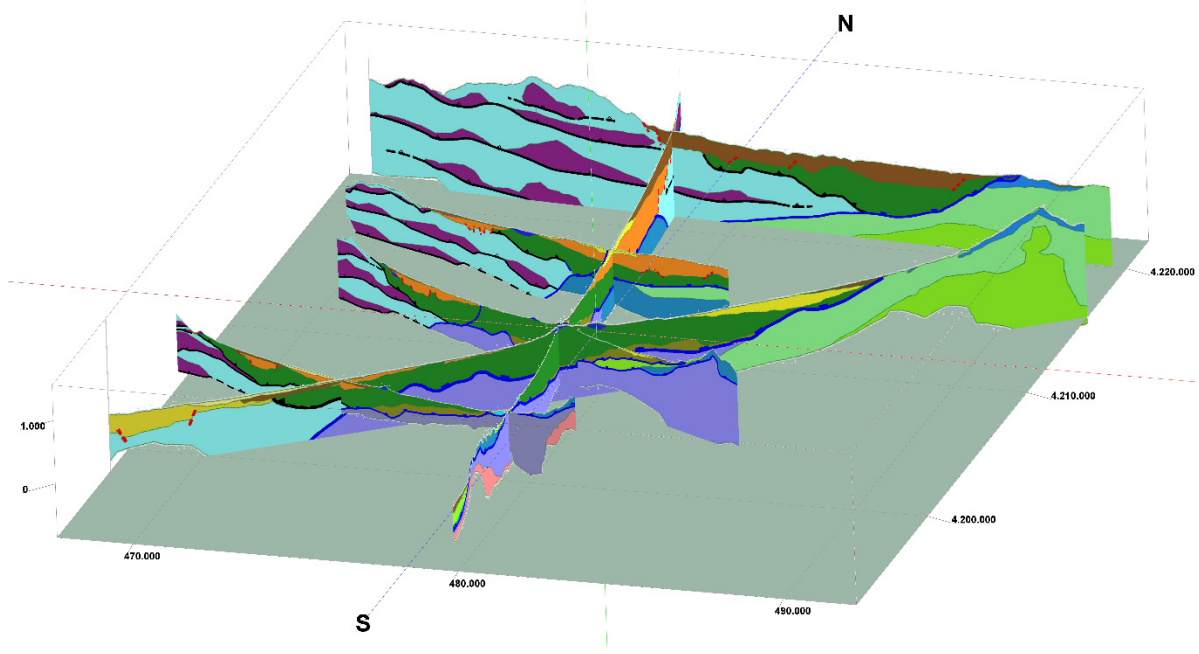

Figure 4.71. 3D illustration of the interpretative geological profiles (looking from SE)

5. CONCLUSIONS

In the context of this Ph.D. thesis, the urban gravimetry was selected in order to investigate the subsurface tectonic structure of Athens basin, the metropolis of Greece, given the fact that the area is covered with artificial structures. The application of the method, with the acquisition of 1,122 gravity stations, is considered to be not only successful but also geologically "precious" since it provided new subsurface data for such a complicated geological area that also happens to be the most populated and important city of the country.

The importance of this Ph.D. thesis is considered multidisciplinary since it contributes not only to the immiscibly geological and tectonic knowledge but also to the geophysical knowledge, with the thorough study and application of the Building Correction. For that reason, this chapter is divided in three sections. At first, we will discuss the geophysical contribution, with the application of the gravity method in urban areas and we will emphasize on the importance of the building corrections (§5.1). Furthermore, we will correlate the Bouguer anomaly maps with the isoseismal maps, presented in §2.6, revealing important findings (Dilalos & Alexopoulos, 2017). In the end, we will deal with the geological contribution, regarding the updated delineation of the tectonic structure in Athens basin.

5.1. GRAVITY METHOD IN URBAN AREAS AND THE IMPORTANCE OF BUILDING CORRECTIONS

Regardless of the increasing problems that we faced during the data acquisition, none of this was insuperable. The careful planning of the field campaign (determination of station locations) along with the appropriate precision and precautions during the data acquisition proved to be very important. Apart from this, the additional innovative Building Correction that we have calculated (§4.3.c.4) in order to remove the effect of the building volume on the gravity data, was a great contribution (Dilalos *et al.*, 2018).

In the following paragraphs, we will try to expose the significance of the Building Corrections. In Figure 5.1, the acquired gravity stations and their corresponding calculated Building Correction are illustrated in graduated symbols, based on their value. The Building Height Map has been used as background, providing the capability to correlate the Building Heights with the Building Correction. Therefore, it is obvious that the final image is absolutely logic, since the highest values of Building Correction correspond to gravity stations that are located in areas with increasing building volume, such as the downtown of the city and the area of Piraeus (red areas in Fig. 5.1). The gravity stations of the mountainous areas are not illustrated (white areas), since there was no need of Building Correction as there are barely any infrastructures. Because of that, the corrected gravity stations for the building volume are finally 863 from the total of 1,122.

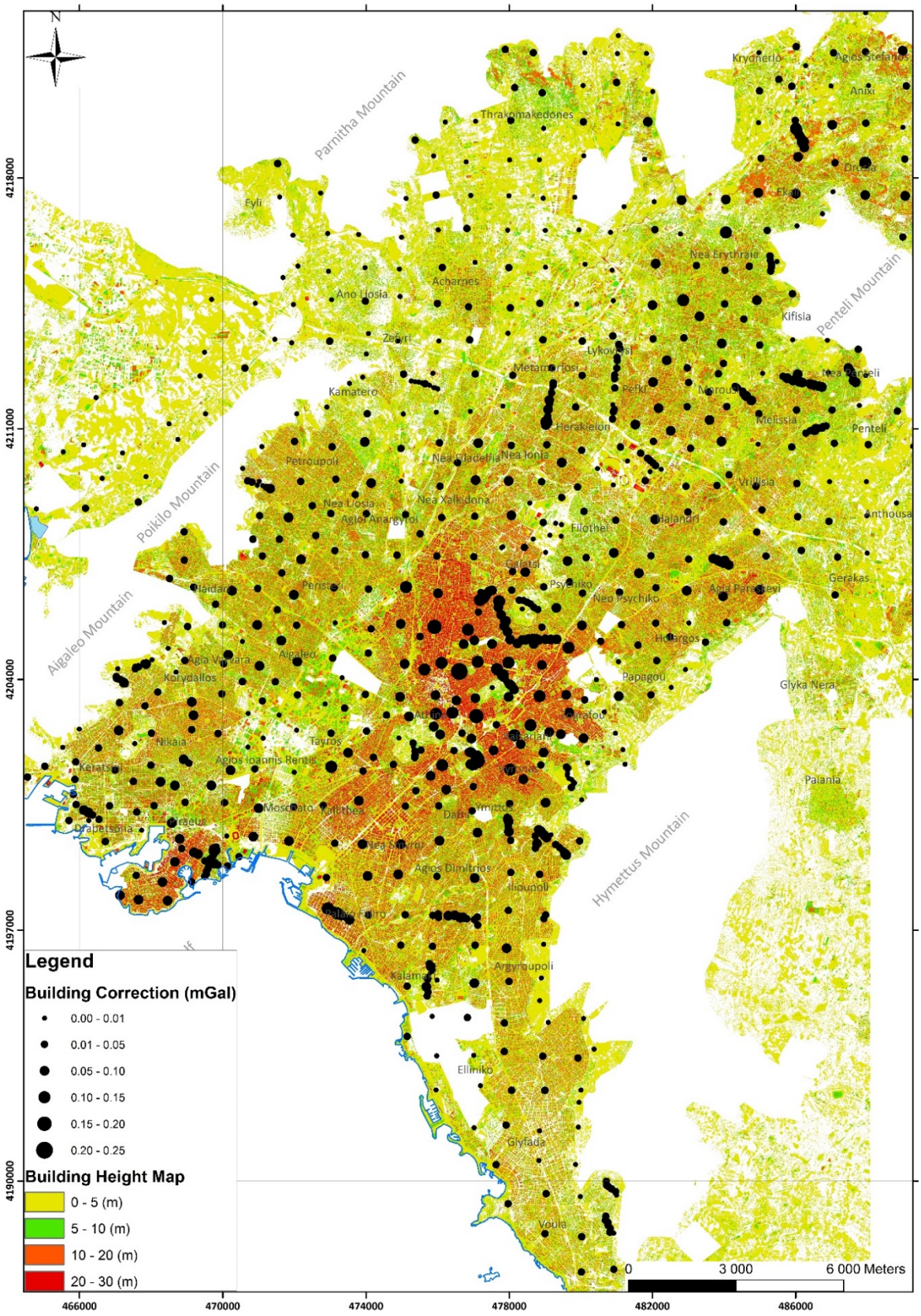

Figure 5.1. Building Height Map along with graduated gravity stations based on the values of Building Correction (in mGal).

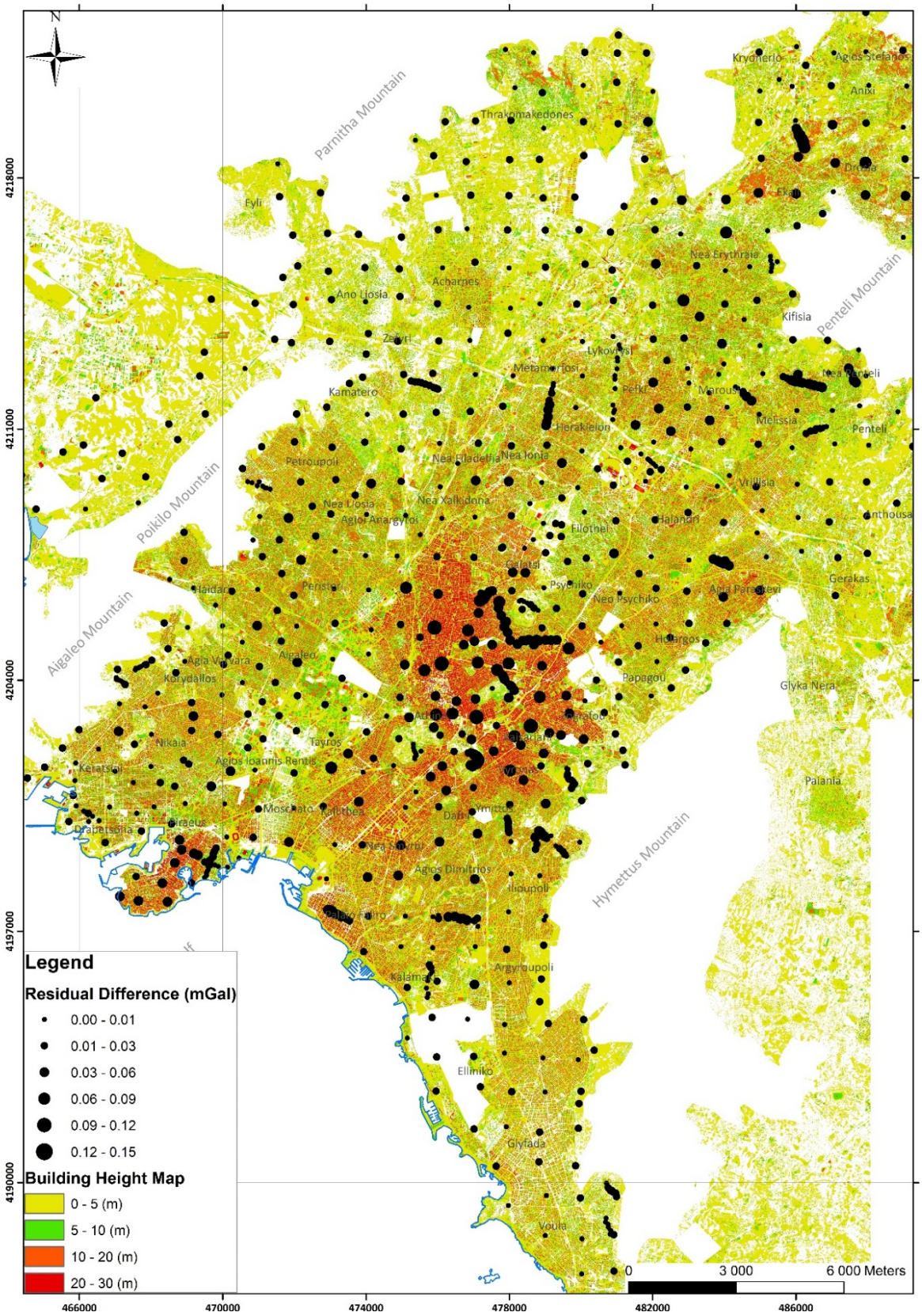

Figure 5.2.Building Height Map along with graduated gravity stations based on the final difference of the calculated Residual anomaly.

The Building Correction practically affects the final calculation of the Complete Bouguer Anomaly and consequently the one of the Residual Anomaly, which is basically the final processed data that we take into account for the subsurface modelling (§4.4). For that reason, the final difference in Residual Anomaly has been calculated (before and after the Building Correction) and is illustrated in Figure 5.2, with graduated symbols based on the difference values. The resulting image (Fig.5.2) is similar to the previous one (Fig. 5.1), with the most affected gravity stations located in areas with high building volume.

A statistical approach is provided in Figure 5.3, where a histogram distribution of the calculated Building Corrections is presented. The calculated values for the entire Athens basin and the 863 affected gravity stations begin from zero and reach values of almost 0.25 mGal. Almost 39.4% of them (340 of 863 stations) appear with values between zero and 0.02 mGal, which seem negligible. Nevertheless, the other 60.6% of the affected gravity stations (523 of 863) appear with higher and more significant values of Building Correction (Fig.5.3).

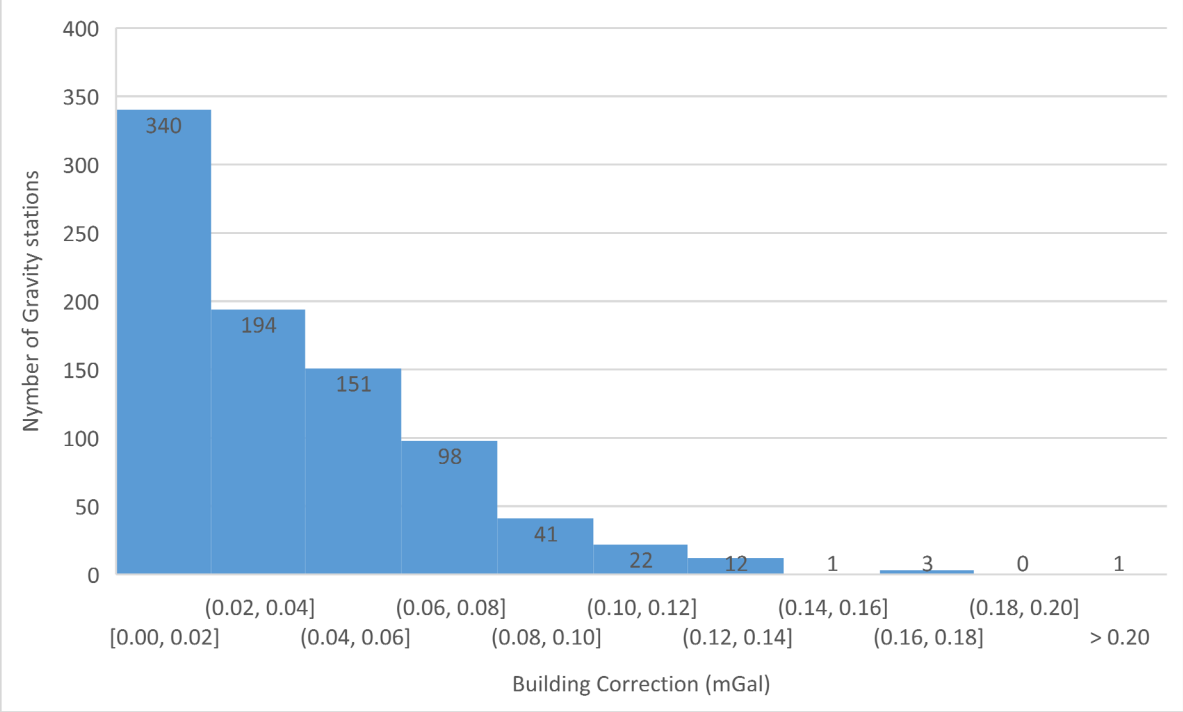

Figure 5.3. Building Correction values histogram distribution.

Furthermore, in Figure 5.4, we present the histogram distribution of the final difference values of Residual Anomaly, with and without the removal of the Building Corrections. It is evident that the 61.3% (529 of the 863 stations), revealed a final basement Residual Anomaly difference between zero and 0.02 mGal (after the removal of the Building Correction), which can be considered almost negligible. However, for the other 38.7% (334 of the 863 stations), we have more significant differences after the application of the calculated Building Corrections, with values reaching up to 0.19 mGal.

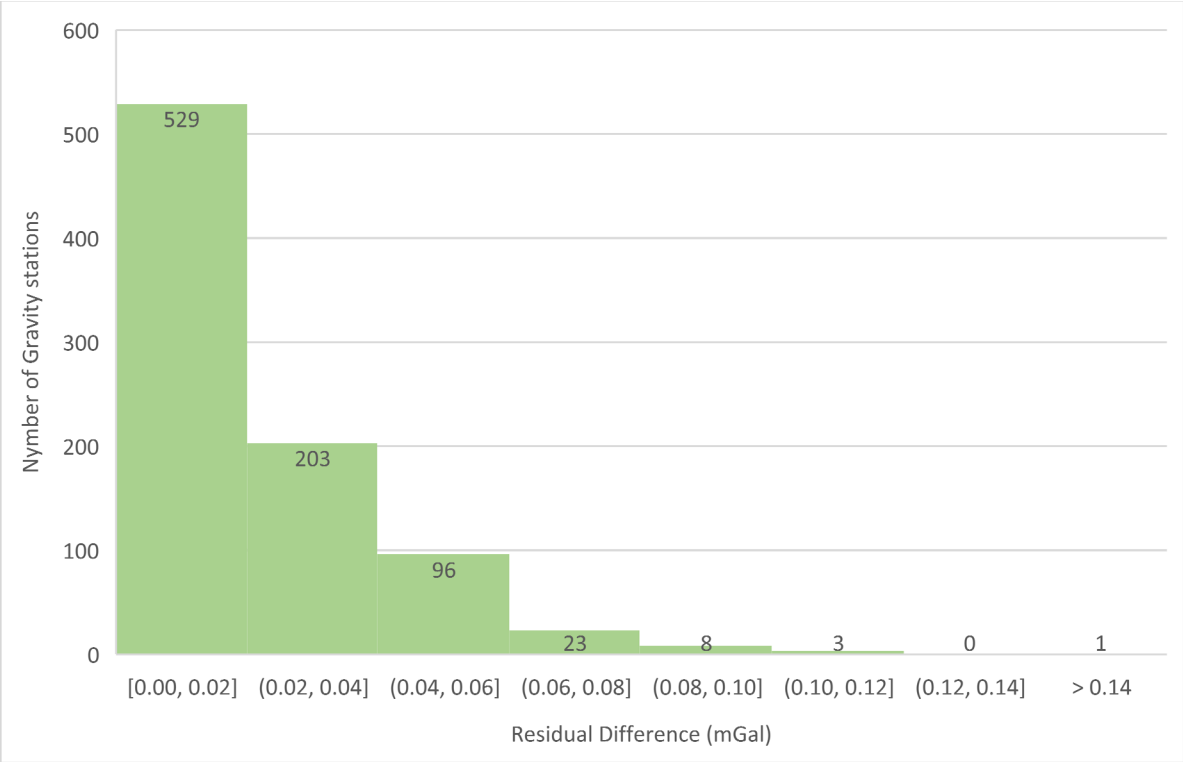

Figure 5.4. Histogram distribution of the basement Residual Anomaly Differences (before and after the Building Correction).

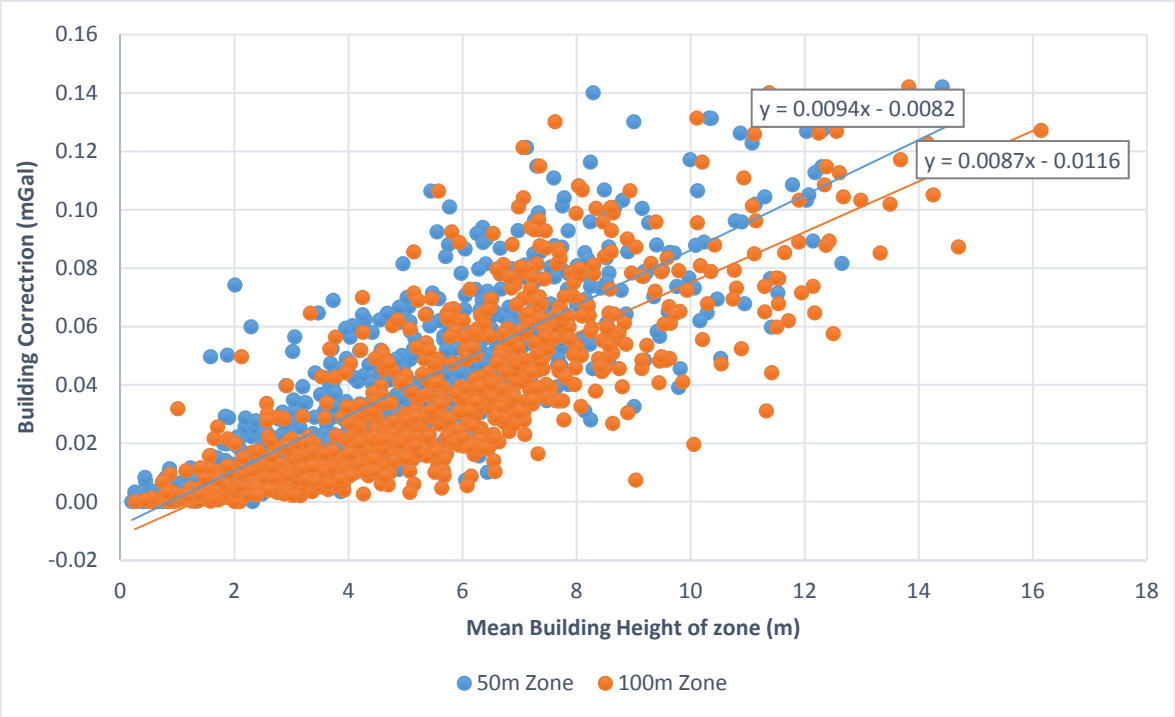

Figure 5.5. Correlation of mean Building Height with the respective calculated Building Correction. The blue dots refer to the 50 meters radius zone and the orange ones to the 100 meters one.

Finally, an attempt to correlate the Building Correction with the Height of the surrounding buildings is illustrated in Figure 5.5. Two different zones around the stations have been selected (similar to the Hammer zones of the Terrain Correction), one with radius equal to 50m and one other with radius 100m. These two zones were selected based on the general fact that the building effect decreases with distance (§3.3.h.4) but also taking into consideration the publications of Nowell (1999) and Debeglia & Dupont (2002). The mean Building Height has been calculated for each one of these zones, based on the data of the Building Height Map (Fig.4.25).

The calculated Building Corrections are presented in a diagram (Fig.5.5), correlated to the mean Building Height of the two radial zones mentioned above. The trend lines of the two datasets are also illustrated, revealing similar linear equations. Therefore, it seems that we could accept a generalized linear equation that would provide the Building Correction based on the mean Building Height of the acquisition area, as following:

$$BC_{50} = 0.0094 \cdot bh_{50} - 0.0082$$

$$BC_{100} = 0.0087 \cdot bh_{100} - 0.0116$$

where BC_{50} and BC_{100} are the Building Corrections, bh_{50} and bh_{100} the mean Building Height of the surrounding zone of the gravity station, for radius 50m and 100m respectively.

The mean Building Height can be retrieved either by simple field observations or by detailed digital data, like in this Ph.D. thesis. The final Building Correction for each gravity station is also affected by the volumes of the buildings beyond the zone of 100 meters but the impact is considered negligible.

It is important to clarify that the proposed correction is not taking into consideration the existence of any basement of the buildings. This is based on the fact that previous studies (Debeglia & Dupont, 2002; Yu, 2014) revealed that the basement effect beyond the 44 meters is negligible. In the context of this research, we tried to keep a distance of 75m from the buildings. Additionally, the DSM data cannot provide information concerning the basement existence.

5.2. COMPARISON OF ISOSEISMAL AND BOUGUER ANOMALY MAPS

A Residual anomaly map is practically determined by the local scale geotectonic structures. Likewise, the damage distribution of an earthquake, presented by the isoseismal contours, is usually related to the tectonic structures of the area (fault directions etc.). Consequently, the qualitative interpretation of both maps seems to be related. We compare the residual anomaly maps (for both 0.25 and 0.02 cycles/km) that had already been produced (Figs. 4.30-4.31), with the isoseismal maps (Figs. 2.30-2.31), by Lekkas E. (2001) and by Tzitziras *et al*. (2000). The comparison was made by overlying the maps (Figs. 5.6-5.9) and it is obvious that there are great similarities. Specifically, we observe that the most damaged areas, mapped

out by the isoseismal contours, seem to be clearly adumbrated by the areas that have the lowest values in the Residual anomaly map (Figs. 5.6-5.9), produced after the gravity survey in the Athens basin.

This could mean that we might have one new innovative scientific way to locate and define the most dangerous and susceptible to potential earthquake damage areas (Dilalos & Alexopoulos, 2017), especially in urban zones, where the collection of the necessary data is difficult. Subsequently, gravity studies could be taken into consideration in order to minimize future damage and deaths in urban environments. They could adumbrate zones of increasing risk after an earthquake.

At a first view of them (Figs. 5.6-5.9), someone could say that the isoseismal contours are located mainly in the areas where we have minimum values (bluish colors). The most impressive part of identicalness for both residual maps is the zone between *Petroupoli* and *Nea Liosia* (Figs. 5.6 & 5.8), where Tzitziras *et al*. (2000) present a separate lobe of isoseismal contours with maximum intensity equal to 8. This lobe seems to be identical to a similar lobe of minimum anomaly values observed in the Residual anomaly map. The isoseismal contours at this location seem to be hedged by the greater residual gravity values. Additionally, the main circular shaped area below *Thrakomakedones, Acharnes, Lykovrysi, Nea Erythraia* and *Metamorfosi*, with minimum residual anomaly values, seems to "enclose" the majority of high intensity isoseismal contours. Basically, almost all the isoseismal contours with intensity more than 7, are located in the areas with minimum residual anomaly values for both deeper and shallow structures (Figs. 5.6 & 5.8 respectively). Likewise, at the areas of *Haidari* and *Fyli* we mostly observe the existence of a small area of low gravity values at the residual map for of 0.25 cycles/km (Fig.5.8). Almost no isoseismal contours are observed in the areas of maximum residual gravity field values.

Regarding the isoseismal map of Lekkas E. (2001), the contours seem to be more continuous and denser (Figs. 5.7 & 5.9), with a general direction NE-SW. Here also, the isoseismal contours with intensity more than 8 appear in the areas of the main circle of low residual anomaly values, among *Thrakomakedones, Kryoneri, Ekali, Kifisia, Lykovrysi* and *Acharnes*. The zone among *Petroupoli, Kamatero* and *Nea Liosia* has good identicalness, but not as good as the contours by Tzitziras *et al*. (2000) and is also extended southern to the areas of *Aigaleo, Peristeri, Agios Ioannis Rentis, Korydallos* and *Nikaia*. On the other hand, here we have better fit of low residual anomaly values (no minimum, just low) in the area of *Ano Liosia* and *Zefyri*, where new high intensity isoseismal contours appear by Lekkas E. (2001). The only 'misfit' is the area along *Peristeri* and *Aigaleo*, where although the author (Lekkas, 2001) impressed the existence of isoseismal contours of values 7 and 8, the residual maps for both deeper and shallow structures, high values reveal in this zone. The area of *Fyli* is not characterized by isoseismal contours by this author.

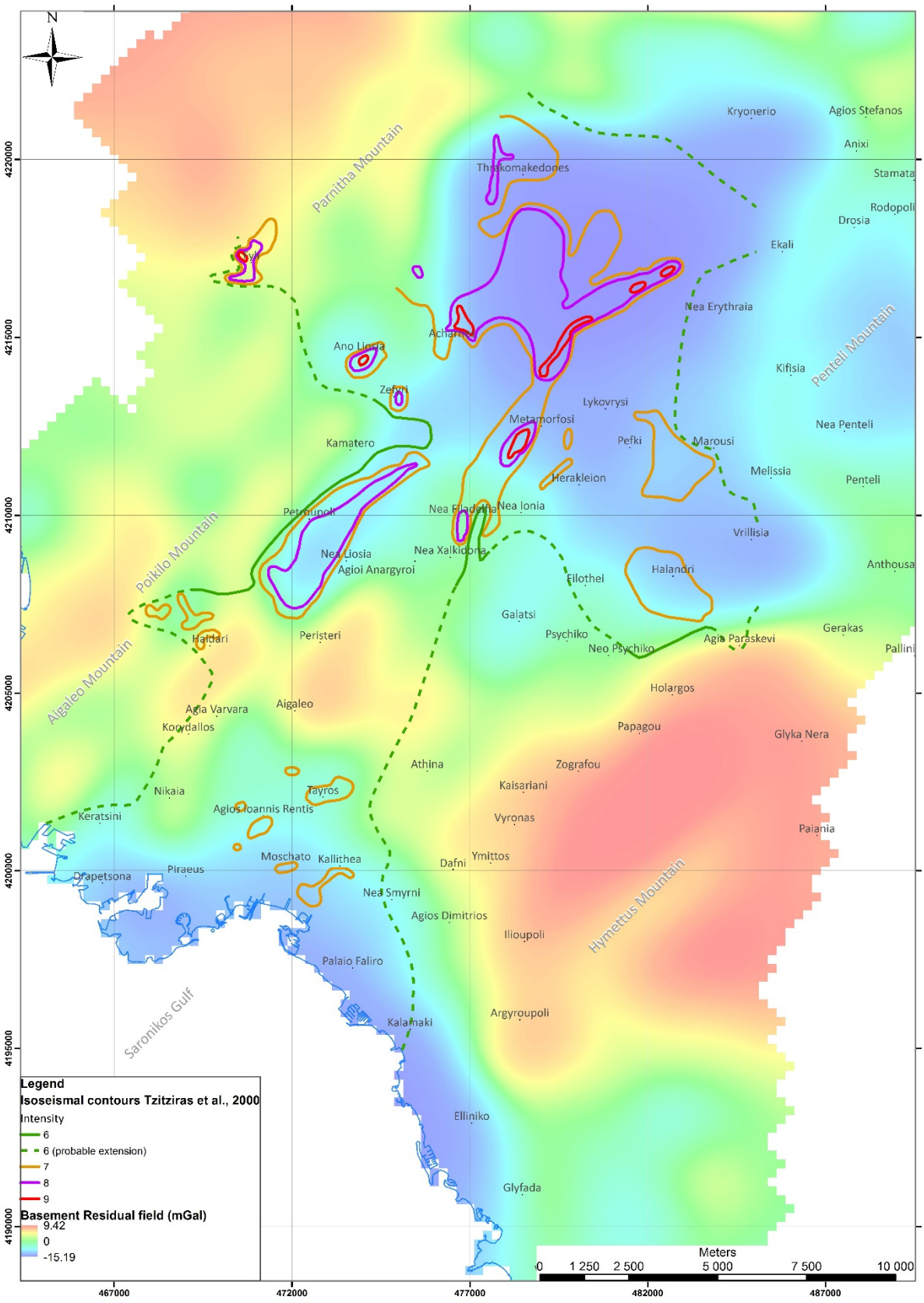

Figure 5.6. Basement Residual Anomaly map (0.02 cycles/km) and isoseismal contours by *Tzitziras et al.* (2000).

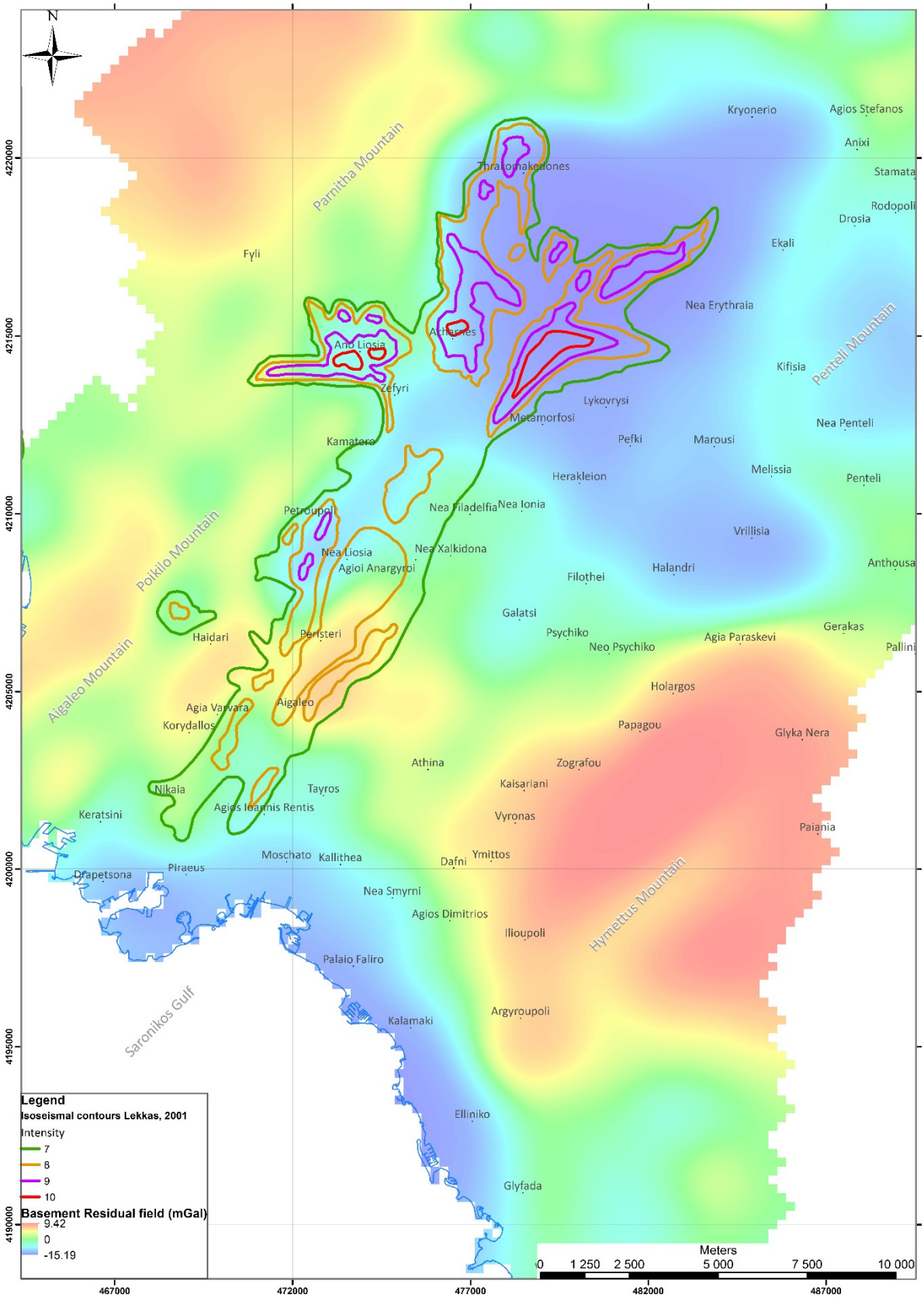

Figure 5.7. Basement Residual Anomaly map (0.02 cycles/km) and isoseismal contours by *Lekkas* (2001).

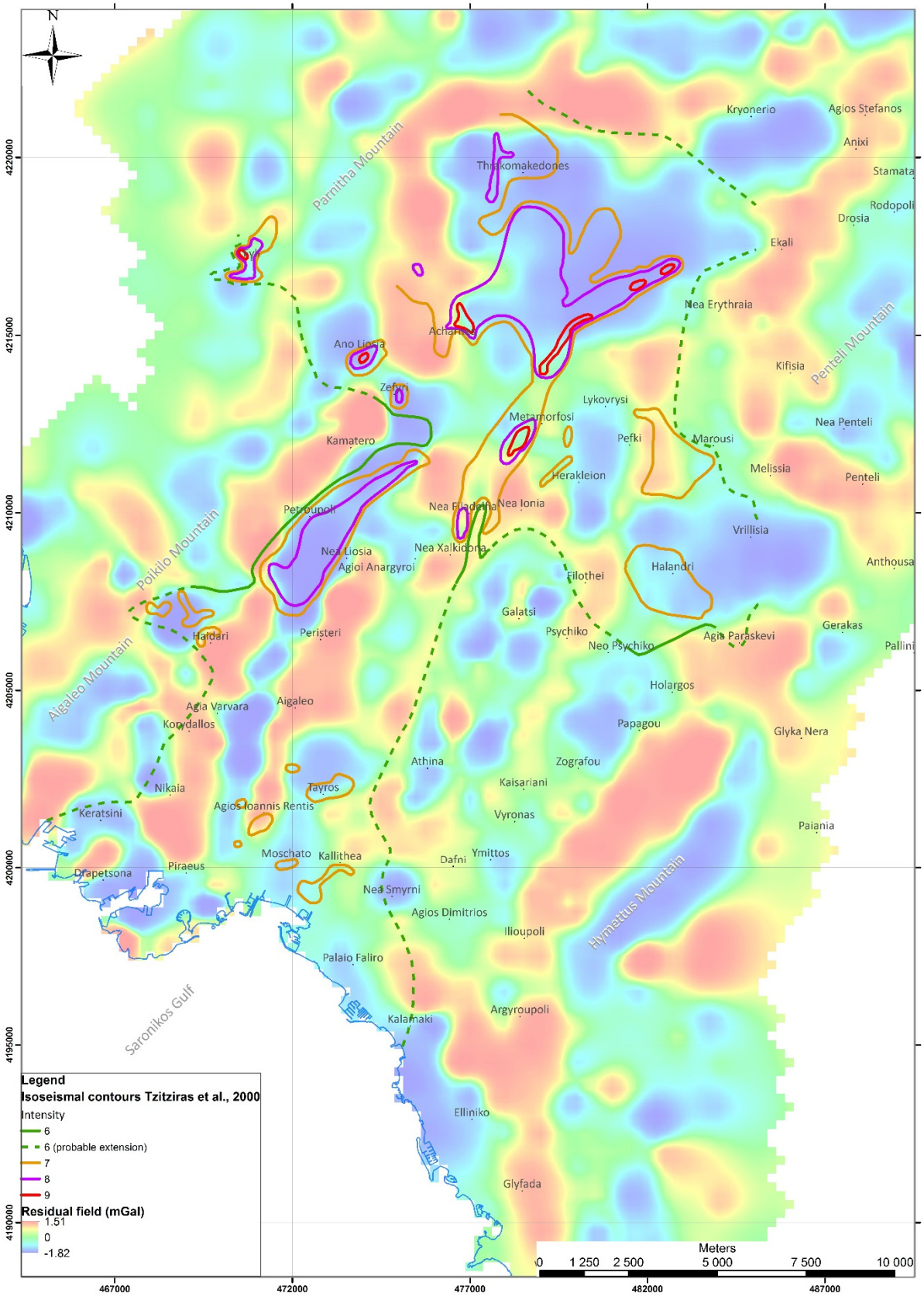

Figure 5.8. Residual Anomaly map (0.25 cycles/km) and isoseismal contours by *Tzitziras et al*. (2000).

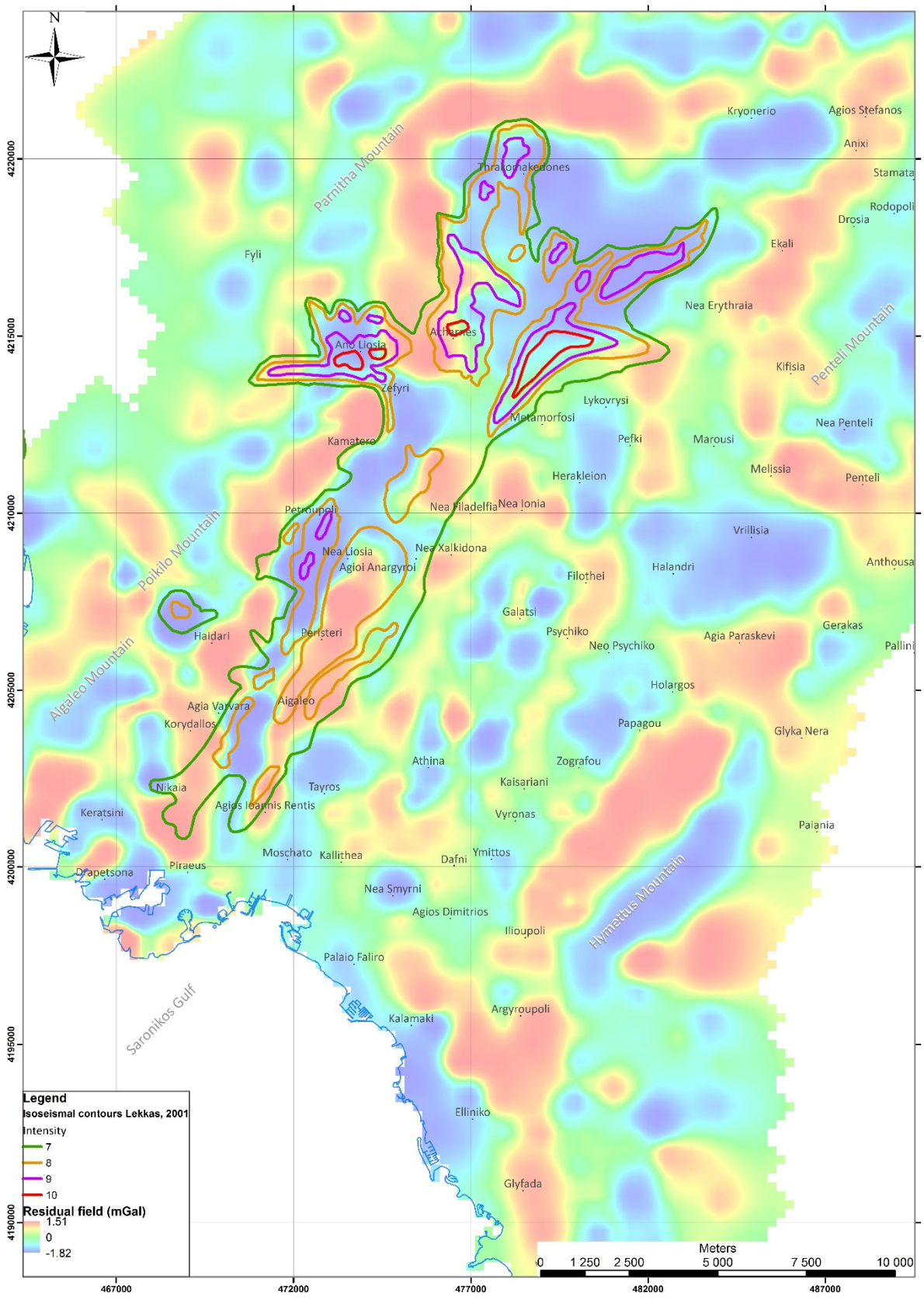

Figure 5.9. Residual Anomaly map (0.25 cycles/km) and isoseismal contours by *Lekkas* (2001).

The most impressive images for the identicalness between the gravity data and the isoseismal contours are the ones for the shallow structures (Figs. 5.8-5.9), where we can observe that the restricted areas of low gravity values enclose the isoseismal contours from both publications. These zones are considered to have thick layers of post alpine sediments (§4.4.c) that affect the propagation of the seismic waves of the earthquakes and by enhancing them. Of course, the geometry of the fault zones plays an important role.

5.3. NEW DATA FOR THE GEOLOGICAL AND TECTONIC STRUCTURE OF ATHENS BASIN

The results of the extensive gravity campaign carried out in the context of this Ph.D. thesis, revealed new subsurface information for the Athens basin, both for its geological and tectonic structure for depths more than 2,500 meters. The results have already been presented in the previous chapter (§4) in detail.

More specifically, the qualitative structural maps (§4.3.e) seems to contribute a lot to the identification of the fault zones providing impressive images, easy to interpret. This means that we can either identify and propose new locations of blind faults or we can verify and modify the location of already proposed as concealed faults zones from other researches.

Beyond that, we managed to interpret and quantify geologically the results by constructing the 2.75D geological models (§4.4.c), based on the gravity response of the collected data. Based on Figures 4.63-4.68 and their analysis, important data regarding the thickness of the geological formations covering the basin were recovered. Therefore, we investigated the following geological formations with their corresponding maximum thickness.

- ✓ Alluvium deposits (*Al*) up to of 40-50 meters.
- ✓ Pleistocene Talus and Screes (*Pt.sc*) up to 310 meters, below *Thrakomakedones, Kryoneri* and *Agios Stefanos* areas.
- ✓ Neogene deposits (*Msl* and *Pll*) up to a total of 550 meters, below the areas of *Thrakomakedones, Acharnes, Lykovrysi* and *Metamorfosi*.
- ✓ The formation of Athens Schists (*SchA*), covering great extent of the Athens basin, up to 600 meters
- ✓ The Schists of *Alepovouni Unit* (*Sch-Al*), up to 270 meters.
- ✓ The Dolomites (*D*), up to 1,300 meters
- ✓ The Schists (*Sch*) close to 1,750 meters.

The geological models illustrated in Figures 4.63-4.68, reveal additional information regarding the subsurface tectonic structure of Athens basin. At first, several possible neotectonic faults have been adumbrated, mainly along the contact line of the post-alpine sediments and their underlying alpine formations, that are usually either the Athens Schists (*SchA*) or the Triassic-Jurassic Limestones (*T-J*) of the *Ypopelagoniki* Unit.

Furthermore, the extent of a major overthrust has been detected, with the Athens Schists (SchA), overlying the Triassic-Jurassic Limestones (*T-J*) of the *Ypopelagoniki* Unit. Likewise, the major detachment zone between the metamorphic and non-metamorphic (*Ypopelagoniki*) units, known as part of the *West Cycladic Detachment System* (Iglseder *et al.*, 2011), has been identified in most of interpretative geological profiles (Figs. 4.63-4.68). Beyond these, the existence of 3-4 different upthrusts in the mass of the Ypopelagoniki Unit seems to have been adumbrated, based on the interpretation of the gravity results. Along these upthrusts, layers of the Shales and Sandstones alterations (*C-P*) appear.

Through some of the interpretative geological profiles (Figs. 4.64-4.66), we can observe the existence of extended parallel folds (Avigad *et al*., 2001) that have been delineated across the formations of in the Metamorphic Unit, especially below the *Hymettus Mt.* These folds are located along the contact of the underlying Dolomites (*D*) and the overlying layers of Schists (*Sch*) and Marbles (*M*). Finally, a supra-detachment basin (Diamantopoulos *et al.*, 2009), filled with 800-900 meters post-alpine sediments has been revealed, at the area between *Thrakomakedones* and *Metamorfosi* (Fig. 4.66).

Additionally to the qualitative structural maps (Figs. 4.32-4.41), the 3D density models (§4.4.b) contribute to the determination of the geometry of the anomalous source bodies as well as to the verification of possible concealed fault zones that have been investigated.

The most ambiguous and important zone that has set many researchers thinking about its existence and precise location, is the one between the non-metamorphic (*Ypopelagoniki Unit*) and the metamorphic formations. As already discussed in §2, it is expected to be identical to the *Kifisos River* (Fig. 2.2). In this point, we have to take into consideration that it is a low-angle displacement fault (*detachment*), which means that it may not be delineated with great detail.

A first approach is illustrated in the structural maps (Figs. 4.32- 4.41) but also in Figure 4.49, where a ground plan of certain isodensity surfaces (-0.03 and 0.03 gr/cm^3), derived from the 3D density inversion models, is presented along with the fault zones of the area (visible and probable ones). We could say that in general, this major tectonic zone does exist, but its trace needs to be redefined [*1*]. The southern part seems to have been identified by the gravity results but restricted in length, between *Tavros* and *Metamorfosi* (Fig. 5.10). Regarding its northern part and more specifically between *Thrakomakedones* and *Acharnes*, it has been relocated a few kilometers westernmost, following the southern foothills of *Parnitha* Mountain (Fig. 5.10). This approach can also be supported by the 3D models presented in Figures 4.50-4.53 and the geological 2.75D sections of Figures 4.63-4.68.

The other perpendicular major probable fault zone, from *Zefyri* to *Agia Paraskevi* [*2*], is also partially revealed from the structural maps (Figs. 4.32- 4.41), between *Halandri* and *Kokkinos Mylos* areas (Fig. 5.10) and slightly relocated to the southern. On the other hand, its western

extension along the western foothills of *Aigaleo-Poikilo* Mountains has not been verified for all its length and has also been relocated a couple kilometers easternmost.

Moreover, two significant probable fault zones seem to have also been identified undoubtedly in the western suburbs of the basin (Fig. 5.10). These fault zones are along *Kamatero-Petroupoli* [*3*] and *Agioi Anargyroi-Peristeri* [*4*], with estimated throws of at least 80 meters. The first one could be extended to southern-easternmost.

At the north-west expanse of the basin (Fig. 5.10), a few smaller covered faults, at the areas of *Ano Liosia, Zefyri* and *Acharnes* [*5*] are also adumbrated in the gravity maps with estimated throws ranging between 40-90 meters. Furthermore, close to westward of *Thrakomakedones*, at the southern foothills of *Parnitha* Mountain [*6*], a few faults mapped as probable, seem to have been verified with throws up to 220-250 meters.

At the south-west part of Athens basin (Fig. 5.10), several other fault zones have been identified. One is located at *Haidari* [*7*], one at *Keratsini* [*8*] but extended southern to *Drapetsona* based on the new data and the other one along *Keratsini-Piraeus* [*9*], with estimated throw of 150 meters. Additionally, the fault of *Korydallos* [*10*] not only has been verified but can also be elongated up to *Nikaia*.

Looking at the central region of Athens basin (Fig. 5.10), the fault zone of *Filothei-Galatsi-Gkyzi* [*11*], with direction almost N-S, has been relocated slightly to the east. The probable fault zones along *Zografou-Fix* [*12*] and *Galatsi-Psychiko* [*13*] provided indications in the gravity data that increase the possibility of their existence.

Furthermore, at the southern suburbs (Fig. 5.10), the zone of *Kalamaki* [*14*] has also been identified, but beyond that, we have severe indications based on the gravity results for a great extension towards the areas of *Elliniko-Glyfada-Voula*, along which the direction will alter from NW-SE to almost N-S.

Northernmost, along the western and southern foothills of *Penteli* Mountain (Fig. 5.10), the probable overthrust of Upper Cretaceous [*15*] has been delineated undoubtedly by the gravity measurements almost at the location that was expected to be (*Anixi-Ekali-Nea Erythraia-Marousi-Melissia-Anthousa*).

The fact that several major visible faults zones have also been verified on the mountains of *Hymettus*, *Penteli* and *Parnitha*, increases the credibility of our results. Some examples of them are running along the areas *Glyka Nera-Ilioupoli* [*16*], *Paiania- Ilioupoli* [*17*]*, Rea-Dionysos* [*18*]*, Rapendosa-Nea Penteli* [*19*] (Fig. 5.10).

Apart from the confirmation of already delineated fault zones, either as visible or probable covered, we have indications based on the gravity measurements that allow us to propose additional locations of probable faults. Beginning from the western suburbs, three new fault zones may have been detected, along the areas of *Agia Varvara-Korydallos-Agios Ioannis Rentis-Piraeus* [*20*], *Aigaleo-Agios Ioannis Rentis* [*21*] and *Aigaleo-Votanikos* [*22*] (Fig. 5.10).

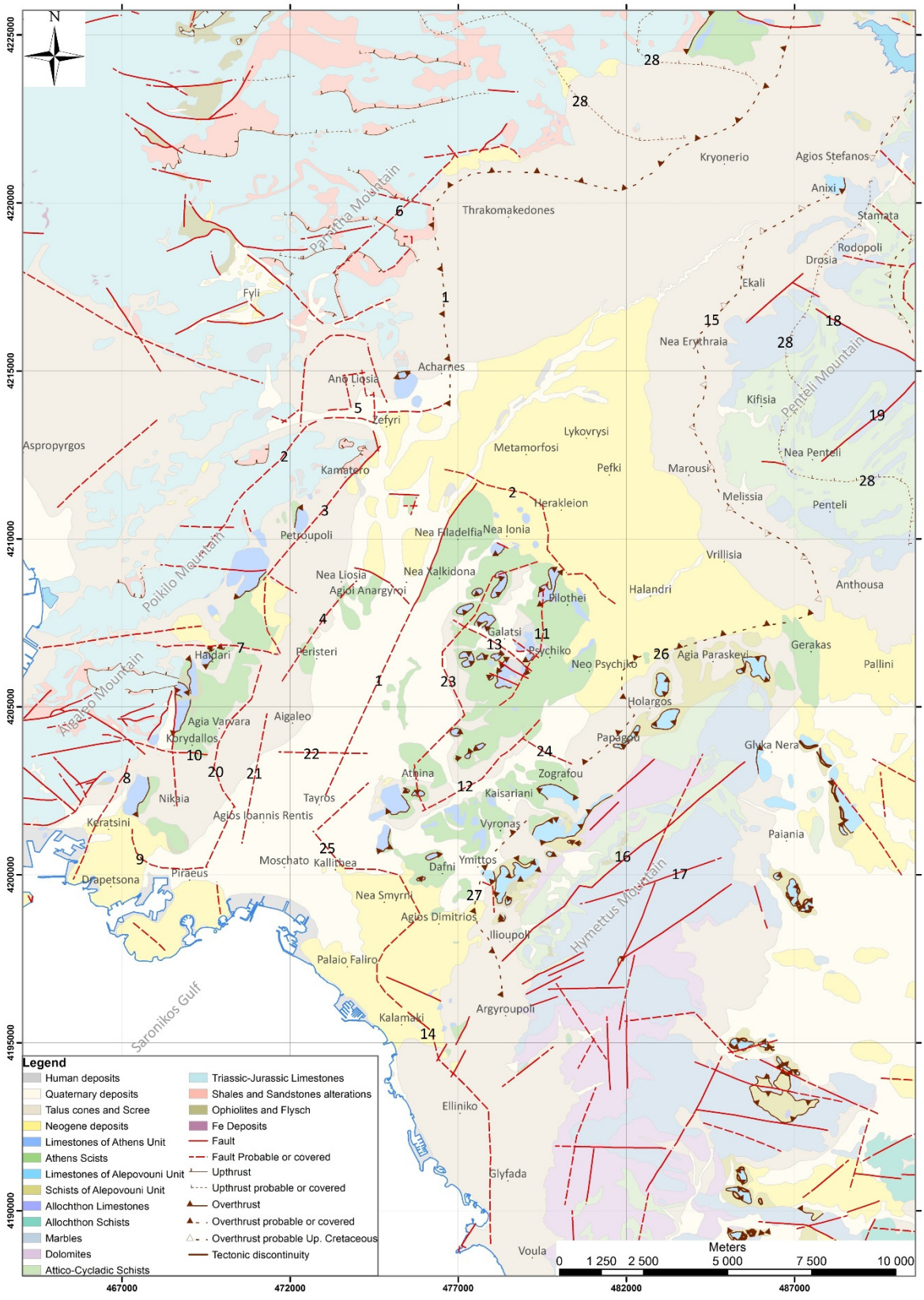

Figure 5.10. Updated geological and tectonic map, based on the results of the gravity survey presented in this Ph.D. Thesis. The modification of older probable concealed faults and the proposal of new ones are illustrated.

Additionally, at the central expanse of the area, more probable fault zones may have been delineated along the areas of *Nea Ionia-Galatsi-Kypseli-Downtown-Fix* [*23*] and a smaller one *Ampelokipoi-Zografou* [*24*] (Fig. 5.10). A few kilometers southern, a new system of fault zones has been revealed, running along *Petralona-Kallithea-Nea Smyrni-Agios Dimitrios-Palaio Faliro* [*25*], with altering directions (NE-SW, NW-SE and W-E). This system could be merged with the one that we have already mentioned, across the areas of *Palaio Faliro-Kalamaki-Elliniko-Glyfada-Voula* [*14*].

Looking at the eastern part of the basin, the gravity results delineate a major tectonic discontinuity along the western foothills of mountain *Hymettus* and more specifically between the areas *Gerakas-Agia Paraskevi-Neo Psychiko-Holargos-Papagou-Zografou* [*26*] and then again along *Vyronas-Ilioupoli-Argyroupoli* [*27*] (Fig. 5.10). This zone could be the overthrust of the *Athens Unit* over the *Alepovouni Unit*.

At the northern suburbs, we can adumbrate a few new upthrust located on the mountains *Penteli* and *Parnitha* (Fig. 5.10). More specifically, for the first one we have a major zone along *Stamata-Rodopoli-Drosia-Kifisia-Nea Penteli* [*28*], while for the second one two or three major ones could be indicated west of *Kryoneri* and *Drosopigi* [*29*]. Beyond these, on the surrounding mountains of Athens basin, there are several other locations indicating the possible existence of smaller fault zones, based on the gravity results.

According to all these updated subsurface data, not only did we obtain new important information for the majority of the geological formations covering the Athens basin, but we also managed to delineate the subsurface structure in order to identify new concealed urban fault zones. These zones may have the potential to generate disastrous earthquakes that will lead to enormous casualties and huge economic loss, especially if we take into consideration the importance of Athens metropolis. Apart from these types of fault zones, we also managed to reveal and adumbrate rare major structural formations, such as the detachment zone (*West Cycladic Detachment System*), the overthrust of the Athens Unit, the extended parallel folds along the Metamorphic Unit, the upthrusts in the Ypopelagoniki Unit and a supra-detachment basin.

5.4. FUTURE PROPOSALS

In the context of this Ph.D. thesis, the application of the gravity method for the adumbration of the tectonic structure in the urban area of Athens basin provided new important scientific information that enriched the already available one. Here, we have to remind that the potential geophysical methods cannot provide unique solutions by themselves.

We could say that the Athens basin is an area that has already been investigated geologically by many researchers from all the specialties, especially after the disastrous earthquake of 7-9-1999.

For the subsurface investigation, with the contribution of geophysical methods there is not much to do, since there are many restrictions as we have already discussed, due to the human infrastructures. Additional seismic profiles, which will be executed at selected sites indicated from our results, could be useful for the confirmation or not of suggested fault zones. The problem is that even this kind of field data can be affected from the cultural noise, reducing the credibility of their results. Additionally, deep geoelectrical soundings might provide extra information. Both of these methods will provide more reliable data and results if applied in the northern suburbs of the basin, where the human infrastructures are minor and rare.

A project of selected deep sampling boreholes would be extremely valuable for our processing and interpretation, since we could minimize a lot the non-uniqueness of the results from this methodology. Not only could we have geological samples from deeper layers that provide more characteristic density values but we could also have several locations of known stratigraphy (type of geological formation and thickness) constraining in that way the inversion results.

Furthermore, the gravity investigation can expand to the surrounding areas of Athens basin, such as the *Mesogeia* and *Thriassio* basins, since they are also covered by several meters of post-alpine deposits that might cover important fault zones.

REFERENCES

1. Abdelrahman E.M., Abo-Ezz E.R., Essa K.S., El-Araby T.M., Soliman K.S., 2006. A least-squares variance analysis method for shape and depth estimation from gravity data. *Journal of Geophysics and Engineering*, 3(2), 143-153. Doi: 10.1088/1742-2132/3/2/005
2. Abbott R.E. & Louie J.N., 2000. Depth to bedrock using gravimetry in the Reno and Carson City, Nevada, area basins. *Geophysics*, 65(2), 340-350. https://doi.org/10.1190/1.1444730
3. Abzalov M.Z., 2013. Measuring and modelling of dry bulk rock density for mineral resource estimation. *Applied Earth Science*, 122(1), 16-29. https://doi.org/10.1179/1743275813Y.0000000027
4. ACI Committee, 2008. *Building Code Requirements for Structural Concrete (ACI 318-08) and Commentary*. American Concrete Institute, 1508p.
5. Adly A., Poggi V., Fäh D., Hassoup A., Omran A., 2017. Combining active and passive seismic methods for the characterization of urban sites in Cairo, Egypt. *Geophysical Journal International*, 210(1), 428-442. https://doi.org/10.1093/gji/ggx176
6. Alawadhi E.M., 2008. Thermal analysis of a building brick containing phase change material. *Energy and Buildings*, 40(3), 351-357. https://doi.org/10.1016/j.enbuild.2007.03.001
7. Alexopoulos J.D, Fountoulis I., Kambouris P., Mariolakos I., Papadopoulos T.D., 2001. Geoelectrical survey for Tatoi (Athens, Greece) blind fault. *Bulletin of the Geological Society of Greece*, 24(1), 121-127 (*In Greek*).
8. Alexouli-Livaditi A., Vouvalidis K., Livaditis G., Pechlivanidou S., 2007. Drainage network characteristics of Athens plain at the end of the 19th century. *Bulletin of the Geological Society of Greece*, 40(4). 1513-1521.
9. Ali M.Y., Fairhead J.D., Green C.M., Noufal A., 2017. Basement structure of the United Arab Emirates derived from an analysis of regional gravity and aeromagnetic database. *Tectonophysics*, 712-713, 503-522. https://doi.org/10.1016/j.tecto.2017.06.006
10. Al-Banna A.S. & Al-Karadaghi S.S., 2018. Integration Study of a New Gravity and Seismic Survey along NE-SW Profilein Al-Najaf Desert. *Iraqi Journal of Science*, 59(1B), 314-328, Doi: 10.24996/ijs.2018.59.1B.10
11. Al-Banna A.S., Daim F.M., Al-Zubaidi A.A., 2017. The Deep Faults in Kut-Hai and Surrounding Area Inferred from Gravity and Magnetic Data. *Iraqi Journal of Science*, 58(3A), 1235-1245. Doi: 10.24996/ijs.2017.58.3A.7
12. Ali H.O. & Whiteley R.J., 1981. Gravity exploration for groundwater in the Bara Basin, Sudan. *Geoexploration*, 19(2), 127-141. https://doi.org/10.1016/0016-7142(81)90025-9

13. Ambraseys N., 1996. Material for investigation of the seismicity of Central Greece. In: *Archaeoseismology,* Publication of the British Archaeological School at Athens, Fitch Laboratory, Occasional paper 7, 23-36.
14. Ameri B., 2000. Automatic Recognition and 3D Reconstruction of Buildings from Digital Imagery. *PhD Thesis*, Institute of Photogrammetry, Stuttgart University, DGK Volume 526.
15. Ammirati J.B., Venerdini A., Alcacer J.M., Alvarado P., Miranda S., Gilbert H., 2018. New insights on regional tectonics and basement composition beneath the eastern Sierras Pampeanas (Argentine back-arc region) from seismological and gravity data. *Tectonophysics*, 740, 42-52. https://doi.org/10.1016/j.tecto.2018.05.015
16. Andersson M. & Malehmir A., 2018. Internal architecture of the Alnö alkaline and carbonatite complex (central Sweden) revealed using 3D models of gravity and magnetic data. *Tectonophysics*, 740-741, 53-71. https://doi.org/10.1016/j.tecto.2018.05.008
17. Andrianakis V., 1999. Disaster response and reconstruction measures after the Athens earthquake of September 7, 1999 (M= 5.9). *Newsletter of the European Centre on Prevention and Forecasting of Earthquakes (Council of Europe)*, 3, 40-44.
18. Antoniou A.A, 2003. HELGEORDAS: a relational geotechnical database management system and the interplay with geographical information system: application of geographical information systems at geotechnical engineering. *PhD Thesis*, National Technical University of Athens, 271p. (*In Greek*). http://hdl.handle.net/10442/hedi/16499
19. Antoniou A.A., Papadimitriou A.G., Tsiambaos G., 2008. A geographical information system managing geotechnical data for Athens (Greece) and its use for automated seismic microzonation. *Natural Hazards*, 47(3), 369-395. https://doi.org/10.1007/s11069-008-9226-6
20. Antoniou V., 2000. Geoenvironmental conditions of Athens basin using geographical information systems. *PhD Thesis*, Agricultural University of Athens, 286p. (*In Greek*). http://hdl.handle.net/10442/hedi/11977
21. Anudu G.K., Stephenson R.A., Macdonald D.I., Oakey G.N., 2016. Geological features of the northeastern Canadian Arctic margin revealed from analysis of potential field data. *Tectonophysics*, 691, 48-64. https://doi.org/10.1016/j.tecto.2016.03.025
22. Apostolopoulos G., Pavlopoulos K., Goiran J.P., Fouache E., 2014. Was the Piraeus peninsula (Greece) a rocky island? Detection of pre-Holocene rocky relief with borehole data and resistivity tomography analysis. *Journal of Archaeological Science*, 42, 412-421. https://doi.org/10.1016/j.jas.2013.11.026
23. Araffa S.A.S., 2012. Delineation of groundwater aquifer and subsurface structures on North Cairo, Egypt, using integrated interpretation of magnetic, gravity, geoelectrical and geochemical data. *Geophysical Journal International*, 192(1), 94-112.

https://doi.org/10.1093/gji/ggs008

24. Araffa S.A.S., Helaly A.S., Khozium A., Lala A.M., Soliman S.A., Hassan N.M., 2015a. Delineating groundwater and subsurface structures by using 2D resistivity, gravity and 3D magnetic data interpretation around Cairo–Belbies Desert road, Egypt. *NRIAG Journal of Astronomy and Geophysics*, 4(1), 134-146. https://doi.org/10.1016/j.nrjag.2015.06.004
25. Araffa S.A.S., Sabet H.S., Gaweish W.R., 2015b. Integrated geophysical interpretation for delineating the structural elements and groundwater aquifers at central part of Sinai Peninsula, Egypt. *Journal of African Earth Sciences*, 105, 93-106. https://doi.org/10.1016/j.jafrearsci.2015.02.011
26. Arfaoui M., Inoubli M.H., Tlig S., Alouani R., 2011. Gravity analysis of salt structures. An example from the El Kef-Ouargha region (northern Tunisia). *Geophysical Prospecting*, 59(3), 576-591. Doi: 10.1111/j.1365-2478.2010.00941.x
27. Arzate J., Corbo-Camargo F., Carrasco G., Hernández J., Yutsis V., 2018. The Los Humeros (Mexico) geothermal field model deduced from new geophysical and geological data. *Geothermics*, 71, 200-211. https://doi.org/10.1016/j.geothermics.2017.09.009
28. Ashby M.F., Johnson K., 2013. *Materials and design: the art and science of material selection in product design*. Butterworth-Heinemann. 389p. ISBN: 978-0-08-0908205-2.
29. ASTM Committee, 1999. *Standard Guide for Using the Gravity Method for Subsurface Investigation*, D6430. ASTM International, West Conshohocken, PA, 9p. Doi: 10.1520/D6430-99R10
30. Assimaki D., 2004. Topography effects in the 1999 Athens earthquake: engineering issues in seismology. *PhD Thesis*, Massachusetts Institute of Technology, 512p. http://hdl.handle.net/1721.1/30048
31. Assimaki D., Gazetas G., Kausel E., 2005a. Effects of local soil conditions on the topographic aggravation of seismic motion: parametric investigation and recorded field evidence from the 1999 Athens earthquake. *Bulletin of the Seismological Society of America*, 95(3), 1059-1089. https://doi.org/10.1785/0120040055
32. Assimaki D., Kausel E, Gazetas G., 2005b. Soil-dependent topographic effects: a case study from the 1999 Athens earthquake. *Earthquake Spectra*, 21(4), 929-966. https://doi.org/10.1193/1.2068135
33. Assimaki D., Kausel E., Gazetas G., 2005c. Wave propagation and soil–structure interaction on a cliff crest during the 1999 Athens Earthquake. *Soil Dynamics and Earthquake Engineering*, 25(7), 513-527. https://doi.org/10.1016/j.soildyn.2004.11.031
34. Avigad D., Ziv A., Garfunkel Z., 2001. Ductile and brittle shortening, extension-parallel folds and maintenance of crustal thickness in the central Aegean (Cyclades, Greece). *Tectonics*, 20(2), 277-287. https://doi.org/10.1029/2000TC001190

35. Ayarza P., Alvarez-Lobato F., Teixell A., Arboleya M.L., Teson E., Julivert M., Charroud M., 2005. Crustal structure under the central High Atlas Mountains (Morocco) from geological and gravity data. *Tectonophysics*, 400(1-4), 67-84. https://doi.org/10.1016/j.tecto.2005.02.009
36. Azab A.A., El-Khadragy A.A., 2013. 2.5-D Gravity/Magnetic Model Studies in Sahl El Qaa Area, Southwestern Sinai, Egypt. *Pure and Applied Geophysics*, 170(12), 2207-2229. https://doi.org/10.1007/s00024-013-0650-5
37. Azizi M. & Saibi H., 2015. Integrating gravity data with remotely sensed data for structural investigation of the Aynak-Logar Valley, eastern Afghanistan, and the surrounding area. *IEEE Journal of Selected Topics in Applied Earth Observations and Remote Sensing*, 8(2), 816-824. Doi: 10.1109/JSTARS.2014.2347375
38. Baba T., Takahashi N., Kaneda Y., Inazawa Y., Kikkojin M., 2014. Tsunami inundation modeling of the 2011 Tohoku earthquake using three-dimensional building data for Sendai, Miyagi Prefecture, Japan. In: Kontar Y., Santiago-Fandino V., Takahashi T. (*Eds*.). *Tsunami Events and Lessons Learned*, 89-98, Springer Verlag.
39. Baltzopoulou A.D., Eleftheriadou A.K., Karabinis A.I., 2012. Seismic vulnerability and risk assessment of the building stock of Attica (Greece) and correlation to the actual repair cost. In: *Proceedings of the 15th World Conference on Earthquake Engineering*, 10p., Lisbon, Portugal.
40. Baptiste J., Martelet G., Faure M., Beccaletto L., Reninger P.A., Perrin J., Chen Y., 2016. Mapping of a buried basement combining aeromagnetic, gravity and petrophysical data: The substratum of southwest Paris Basin, France. *Tectonophysics*, 683, 333-348. http://dx.doi.org/10.1016/j.tecto.2016.05.049
41. Barbosa V.C.F., Silva J.B., Medeiros W.E., 1997. Gravity inversion of basement relief using approximate equality constraints on depths. *Geophysics*, 62(6), 1745-1757. https://doi.org/10.1190/1.1444275
42. Bathrellos G.D., Karymbalis E., Skilodimou H.D., Gaki-Papanastassiou K., Baltas E.A., 2016. Urban flood hazard assessment in the basin of Athens Metropolitan city, Greece. *Environmental Earth Sciences*, 75(4), 319, 14p. https://doi.org/10.1007/s12665-015-5157-1
43. Baumont D., Courboulex F., Scotti O., Melis N.S., Stavrakakis G., 2002. Slip distribution of the Mw 5.9, 1999 Athens earthquake inverted from regional seismological data. *Geophysical Research Letters*, 29(15), 1-4. Doi: 10.1029/2001GL014261
44. Baumont D., Scotti O., Courboulex F., Melis N., 2004. Complex kinematic rupture of the Mw 5.9, 1999 Athens earthquake as revealed by the joint inversion of regional seismological and SAR data. *Geophysical Journal International*, 158(3), 1078-1087. https://doi.org/10.1111/j.1365-246X.2004.02374.x

45. Baziotis I., 2008. Petrology and geochemistry of metamorphic rocks from Attica. *PhD Thesis*, National Technical University of Athens, 410p. (*In Greek*). http://hdl.handle.net/10442/hedi/17835
46. Baziotis I., Mposkos E., Perdikatsis V., 2004. Pre-alpine migmatitic rocks and acid to intermediate orthogneisses in Pentelikon Mountain (NE Attica, Greece). *Bulletin of the Geological Society of Greece*, 36(1), 542-551.
47. Becker D., Dahm T., Schneider F., 2017. Detection and localization capability of an urban seismic sinkhole monitoring network. In: *EGU General Assembly Conference Abstracts*, 19, p.12905.
48. Beiki M., 2010. Analytic signals of gravity gradient tensor and their application to estimate source location. *Geophysics*, 75(6), I59-I74. https://doi.org/10.1190/1.3493639
49. Beltrao J.F., Silva J.B.C., Costa J.C., 1991. Robust polynomial fitting method for regional gravity estimation. *Geophysics*, 56(1), 80-89. https://doi.org/10.1190/1.1442960
50. Berg J.W. & Thiruvathukal J.V., 1965. Gravity base station network, Oregon. *Journal of Geophysical Research,* 70(14), 3325-3330. Doi: 10.1029/JZ070i014p03325
51. Berrocal J., Marangoni Y., de Sá, N.C., Fuck R., Soares J.E., Dantas E., Perosi F., Fernandes C., 2004. Deep seismic refraction and gravity crustal model and tectonic deformation in Tocantins Province, Central Brazil. *Tectonophysics*, 388(1-4), 187-199. https://doi.org/10.1016/j.tecto.2004.04.033
52. Bersi M., Saibi H., Chabou M.C., 2016. Aerogravity and remote sensing observations of an iron deposit in Gara Djebilet, southwestern Algeria. *Journal of African Earth Sciences*, 116, 134-150. https://doi.org/10.1016/j.jafrearsci.2016.01.004
53. Bhattacharyya B.K., 1978. Computer modeling in gravity and magnetic interpretation. *Geophysics*, 43(5), 912-929. https://doi.org/10.1190/1.1440873
54. Birch F., 1960. The velocity of compressional waves in rocks to 10 kilobars: 1. *Journal of Geophysical Research*, 65(4), 1083-1102. Doi: 10.1029/JZ065i004p01083
55. Birch F., 1961. The velocity of compressional waves in rocks to 10 kilobars: 2. *Journal of Geophysical Research*, 66(7), 2199-2224. Doi: 10.1029/JZ066i007p02199
56. Birken R., Miller D.E., Burns M., Albats P., Casadonte R., Deming R., Derubeis T., Hansen T.B., Oristaglio M., 2002. Efficient large-scale underground utility mapping in New York City using a multichannel ground-penetrating imaging radar system. In: *9th International Conference on Ground Penetrating Radar*, 4758, 186-192. International Society for Optics and Photonics. Doi: 10.1117/12.462307
57. Birken R., Deming R., Hansen T., MacIntosh S., Oristaglio M., Zhu Q., 2006. Utility Mapping in Urban Areas with Dual Radar and Induction Arrays. In: *19th EEGS Symposium on the Application of Geophysics to Engineering and Environmental Problems*.

58. Bittner A., 1880. Der geologische Bau von Attica, Boeotien, Lokris und Parnassis. *Denksch*, *Kaiserlichen Akad. Der Wissenschaften Wien*, 40, 1-74 (*In German*)
59. Blaikie T.N., Ailleres L., Betts P.G., Cas R.A.F., 2014. Interpreting subsurface volcanic structures using geologically constrained 3-D gravity inversions: examples of maar-diatremes, Newer Volcanics Province, southeastern Australia. *Journal of Geophysical Research: Solid Earth*, 119(4), 3857-3878. Doi: 10.1002/2013JB010751
60. Blake L.S., 2013. *Civil Engineer's Reference Book*. Elsevier, 775p. ISBN: 0-408-01208-0.
61. Blecha V., Štemprok M., Fischer T., 2009. Geological interpretation of gravity profiles through the Karlovy Vary granite massif (Czech Republic). *Studia Geophysica et Geodaetica*, 53(3), 295-314. https://doi.org/10.1007/s11200-009-0019-5
62. Boszczuk P., Cheng L.Z., Hammouche H., Roy P., Lacroix S., Cheilletz A., 2011. A 3D gravity data interpretation of the Matagami mining camp, Abitibi Subprovince, Superior Province, Québec, Canada: Application to VMS deposit exploration. *Journal of Applied Geophysics*, 75(1), 77-86. https://doi.org/10.1016/j.jappgeo.2011.06.031
63. Bott M.H.P., 1960. The use of rapid digital computing methods for direct gravity interpretation of sedimentary basins. *Geophysical Journal International*, 3(1), 63-67. https://doi.org/10.1111/j.1365-246X.1960.tb00065.x
64. Boubaya D., Allek K., Hamoudi M., 2011. Is there a hidden near surface salt diapir in the Guelma Basin, north-east of Algeria? *Journal of Applied Geophysics*, 73(4), 348-356. https://doi.org/10.1016/j.jappgeo.2011.02.006
65. Bouckovalas G.D. & Kouretzis G.P., 2001. Stiff soil amplification effects in the 7 September 1999 Athens (Greece) earthquake. *Soil Dynamics and Earthquake Engineering*, 21(8), 671-687. http://dx.doi.org/10.1016/S0267-7261(01)00045-8
66. Bouckovalas G.D., Kouretzis G.P., Kalogeras I.S., 2002. Site-specific analysis of strong motion data from the September 7, 1999 Athens, Greece earthquake. *Natural Hazards*, 27(1), 105-131. https://doi.org/10.1023/A:1019960023266
67. Braitenberg C., Wienecke S., Wang Y., 2006. Basement structures from satellite-derived gravity field: South China Sea ridge. *Journal of Geophysical Research: Solid Earth*, 111(B05407). Doi: 10.1029/2005JB003938
68. Brédif M., Tournaire O., Vallet B., Champion N., 2013. Extracting polygonal building footprints from digital surface models: a fully-automatic global optimization framework. *ISPRS Journal of Pphotogrammetry and Remote Sensing*, 77, 57-65. https://doi.org/10.1016/j.isprsjprs.2012.11.007
69. Brenner C., 2000. Towards fully automatic generation of city models. *International Archives of Photogrammetry and Remote Sensing*, 33(B3/1; PART 3), 84-92, Amsterdam.
70. Briggs I.C., 1974. Machine contouring using minimum curvature. *Geophysics*, 39(1), 39-48. https://doi.org/10.1190/1.1440410

71. Brocher T.M., 2005. Empirical relations between elastic wavespeeds and density in the Earth's crust. *Bulletin of the Seismological Society of America*, 95(6), 2081-2092. Doi: 10.1785/0120050077
72. Brunn A. & Weidner U., 1997. Extracting buildings from digital surface models. *International Archives of Photogrammetry and Remote Sensing*, 32(3 SECT 4W2), 27-34.
73. Calvo C., Martín A.M., Carbó A., Bolaño V., 2005. Geophysical Study for the Detection of Voids and Low Density Anomalies in Urban Areas. In: *67th EAGE Conference & Exhibition*, G008.
74. Cara M., 1994. *Geophysik*. Springer Verlag, XI, Berlin, 210p.
75. Carlson R.L. & Herrick C.N., 1990. Densities and porosities in the oceanic crust and their variations with depth and age. *Journal of Geophysical Research: Solid Earth*, 95(B6), 9153-9170. Doi: 10.1029/JB095iB06p09153
76. Carmichael R.S., 1984. *CRC Handbook of Physical Properties of Rocks*. Vol. III. CRC Press.
77. Cheng D., Li Y., Larner K., 2003. Inversion of gravity data for base salt. In: *SEG Technical Program Expanded Abstracts*, 588-591, Society of Exploration Geophysicists. https://doi.org/10.1190/1.1817995
78. Casten U. & Snopek K., 2006. Gravity modelling of the Hellenic subduction zone - A regional study. *Tectonophysics*, 417(3-4), 183-200. https://doi.org/10.1016/j.tecto.2005.11.002
79. Castiello G., Florio G., Grimaldi M., Fedi M., 2010. Enhanced methods for interpreting microgravity anomalies in urban areas. *First Break*, 28(8), 93-98.
80. Cella F., Fedi M., Florio G., Grimaldi M., Rapolla A., 2007. Shallow structure of the Somma–Vesuvius volcano from 3D inversion of gravity data. *Journal of Volcanology and Geothermal Research*, 161(4), 303-317. https://doi.org/10.1016/j.jvolgeores.2006.12.013
81. Chailas S., Tzanis A., Lagios E., 2007. Structure of the Marathon Basin (NE Attica, Greece) based on gravity measurements. Bulletin of the Geological Society of Greece, 40(3), 1063–1073.
82. Charalabakis S., 1952. Contribution to the knowledge of Athens Neogene. *Annales Géologiques des Pays Helléniques*, 4, 1-156 (*In Greek*).
83. Chatoupis Th. & Fountoulis I., 2004. Neotectonic deformation of North Parnis. *Bulletin of the Geological Society of Greece*, 36, 1588-1597 (*In Greek*).
84. Chaubey A.K., Rao D.G., Srinivas K., Ramprasad T., Ramana M.V., Subrahmanyam V., 2002. Analyses of multichannel seismic reflection, gravity and magnetic data along a regional profile across the central-western continental margin of India. *Marine geology*, 182(3-4), 303-323. https://doi.org/10.1016/S0025-3227(01)00241-9

85. Chen S. & Zhou Y., 2005. Classifying depth-layered geological structures on Landsat TM images by gravity data: a case study of the western slope of Songliao Basin, northeast China. *International Journal of Remote Sensing*, 26(13), 2741-2754. https://doi.org/10.1080/01431160500104210
86. Chen Y., Zhang Y., Chen T., Zhao Y., Bao, S., 2011. Preparation of eco-friendly construction bricks from hematite tailings. *Construction and Building Materials*, 25(4), 2107-2111. https://doi.org/10.1016/j.conbuildmat.2010.11.025
87. Chen G., Cheng Q., Zuo R., Liu T., Xi Y., 2015a. Identifying gravity anomalies caused by granitic intrusions in Nanling mineral district, China: a multifractal perspective. *Geophysical Prospecting*, 63(1), 256-270. Doi: 10.1111/1365-2478.12187
88. Chen G., Liu T., Sun J., Cheng Q., Sahoo B., Zhang Z., Zhang H., 2015b. Gravity method for investigating the geological structures associated with W–Sn polymetallic deposits in the Nanling Range, China. *Journal of Applied Geophysics*, 120, 14-25. https://doi.org/10.1016/j.jappgeo.2015.06.001
89. Choi S., Götze H.J., Meyer U., DESIRE Group., 2011. 3-D density modelling of underground structures and spatial distribution of salt diapirism in the Dead Sea Basin. *Geophysical Journal International*, 184(3), 1131-1146. https://doi.org/10.1111/j.1365-246X.2011.04939.x
90. Christensen N.I. & Mooney W.D., 1995. Seismic velocity structure and composition of the continental crust: A global view. *Journal of Geophysical Research: Solid Earth*, 100(B6), 9761-9788. Doi: 10.1029/95JB00259
91. Chromčák J., Grinč M., Pánisová J., Vajda P., Kubová A., 2016. Validation of sensitivity and reliability of GPR and microgravity detection of underground cavities in complex urban settings: Test case of a cellar. *Contributions to Geophysics and Geodesy*, 46(1), 13-32. Doi: 10.1515/congeo-2016-0002
92. Clark S.P., 1966. *Handbook of Physical Constants*, Vol. 97. Geological Society of America, 587p.
93. Clement B., 1976. Essai d'interpretation structurale d'un secteur des zones internes Helleniques; l'Attique-Beotie. *Bulletin de la Société Géologique de France*, 7(2), 309-316 (*In French*).
94. Commer M., 2011. Three-dimensional gravity modelling and focusing inversion using rectangular meshes. *Geophysical Prospecting*, 59(5), 966-979. Doi: 10.1111/j.1365-2478.2011.00969.x
95. Cooper G.R. & Cowan D.R., 2008. Edge enhancement of potential-field data using normalized statistics. *Geophysics*, 73(3), H1-H4. https://doi.org/10.1190/1.2837309
96. Cordell L. & Henderson R.G., 1968. Iterative three-dimensional solution of gravity anomaly data using a digital computer. *Geophysics*, 33(4), 596-601. https://doi.org/10.1190/1.1439955

97. Crossley D., Hinderer J., Boy J.P., 2004. Regional gravity variations in Europe from superconducting gravimeters. *Journal of Geodynamics*, 38(3-5), 325-342. https://doi.org/10.1016/j.jog.2004.07.014
98. Csapó G. & Völgyesi L., 2002. Hungary's new gravity base network (MGH-2000) and it's connection to the European unified gravity net. In: *Vistas for Geodesy in the New Millennium*, 72-77. Springer, Berlin, Heidelberg.
99. Cueto M., Olona J., Fernández-Viejo G., Pando L., López-Fernández C., 2018. Karst-induced sinkhole detection using an integrated geophysical survey: a case study along the Riyadh Metro Line 3 (Saudi Arabia). *Near Surface Geophysics*, 16(3), 270-281. Doi: 10.3997/1873-0604.2018003
100. Curto J.B., Vidotti R.M., Blakely R.J., Fuck R.A., 2015. Crustal framework of the northwest Paraná Basin, Brazil: Insights from joint modeling of magnetic and gravity data. *Tectonophysics*, 655, 58-72. http://dx.doi.org/10.1016/j.tecto.2015.05.011
101. Damaceno J.G., de Castro D.L., Valcácio S.N., Souza Z.S., 2017. Magnetic and gravity modeling of a Paleogene diabase plug in Northeast Brazil. *Journal of Applied Geophysics*, 136, 219-230. https://doi.org/10.1016/j.jappgeo.2016.11.006
102. Danes Z.F., 1960. On a successive approximation method for interpreting gravity anomalies. *Geophysics*, 25(6), 1215-1228. https://doi.org/10.1190/1.1438809
103. Davis K., Li Y., Batzle M., 2008. Time-lapse gravity monitoring: A systematic 4D approach with application to aquifer storage and recovery. *Geophysics*, 73(6), WA61-WA69. https://doi.org/10.1190/1.2987376
104. Debeglia N. & Dupont F., 2002. Some critical factors for engineering and environmental microgravity investigations. *Journal of Applied Geophysics*, 50(4), 435-454. https://doi.org/10.1016/S0926-9851(02)00194-5
105. de Castro D.L., Fuck R.A., Phillips J.D., Vidotti R.M., Bezerra F.H., Dantas E.L., 2014. Crustal structure beneath the Paleozoic Parnaíba Basin revealed by airborne gravity and magnetic data, Brazil. *Tectonophysics*, 614, 128-145. http://dx.doi.org/10.1016/j.tecto.2013.12.009
106. Delibasis N., Papadimitriou P., Voulgaris N., Kassaras I., 2000. The Parnitha fault: a possible relationship with other neighboring faults and causes of larger damages. *Annales Géologiques des Pays Helléniques*, 38(B), 41-50.
107. Deligiannakis G., Papanikolaou I. D., Roberts, G., 2018. Fault specific GIS based seismic hazard maps for the Attica region, Greece. *Geomorphology*, 306, 264-282. https://doi.org/10.1016/j.geomorph.2016.12.005
108. Diamantopoulos A., Krohe A., Mposkos E., 2009. Kinematics of conjugate shear zones, displacement partitioning and fragmentation of the upper rigid crust during denudation of high-P rocks (Pelagonian and Sub-Pelagonian Zones, Greece). *Tectonophysics*, 473(1-2), 84-98. Doi: 10.1016/j.tecto.2008.05.028

109. Dilalos S. & Alexopoulos J.D., 2017. Indications of correlation between gravity measurements and isoseismal maps. A case study of Athens basin (Greece). *Journal of Applied Geophysics*, 140, 62-74. https://doi.org/10.1016/j.jappgeo.2017.03.012
110. Dilalos S., Alexopoulos J.D., Tsatsaris A., 2018. Calculation of Building Correction for urban gravity surveys. A case study of Athens metropolis (Greece). *Journal of Applied Geophysics*. https://doi.org/10.1016/j.jappgeo.2018.09.036
111. Dobrin M.B., 1976. *Introduction to Geophysical Prospecting*. McGraw-Hill, 630p.
112. Dounas A.G. & Gaitanakis P., 1981. Stratigraphical and tectonic observations on the Aigaleos mountain and the western part of the Athens Basin. *Mineral Resources*, 13, 21-32 (*In Greek*).
113. Dounas A., Kallergis G., Morphis A., 1976. Hydrogeological investigation within the framework of the study for the Athens metropolitan underground railway (METRO). *Hydrological and Hydrogeological Investigation*, 19 (*In Greek*).
114. Drakatos G., Karastathis V., Makris J., Papoulia J., Stavrakakis G., 2005. 3D crustal structure in the neotectonic basin of the Gulf of Saronikos (Greece). *Tectonophysics*, 400(1), 55-65. https://doi.org/10.1016/j.tecto.2005.02.004
115. Drakatos G., Melis N., Papanastassiou D., Karastathis V., Papadopoulos G.A., Stavrakakis G., 2002. 3-D crustal velocity structure from inversion of local earthquake data in Attiki (central Greece) region. *Natural Hazards*, 27(1), 1-14. https://doi.org/10.1023/A:1019964408943
116. Dufréchou G., Harris L.B., Corriveau L., Antonoff V., 2011. Gravity evidence for a mafic intrusion beneath a mineralized zone in the Bondy gneiss complex, Grenville Province, Quebec—Exploration implications. *Journal of Applied Geophysics*, 75(1), 62-76. https://doi.org/10.1016/j.jappgeo.2011.06.029
117. Dürr S., Altherr R., Keller J., Okrusch M., Seidel E., 1978. The median Aegean crystalline belt: stratigraphy, structure, metamorphism, magmatism. *Alps, Apennines, Hellenides*, 38, 455-476.
118. Eisenbeiss H. & Zhang L., 2006. Comparison of DSMs generated from mini UAV imagery and terrestrial laser scanner in a cultural heritage application. *International Archives of Photogrammetry, Remote Sensing and Spatial Information Sciences*, 36(5), 90-96.
119. Eleftheriadou A.K. & Karabinis A.I., 2012. Seismic vulnerability assessment of buildings based on damage data after a near field earthquake (7 September 1999 Athens- Greece). *Earthquake and Structures*, 3(2), 117-140. Doi: 10.12989/eas.2012.3.2.117
120. Elenas A., 2003. Athens earthquake of 7 September 1999: Intensity measures and observed damages. *ISET Journal of earthquake technology*, 40(1), 77-97.
121. Elkhodary S.T. & Youssef M.A.S., 2013. Integrated potential field study on the subsurface structural characterization of the area North Bahariya Oasis, Western Desert, Egypt.

Arabian Journal of Geosciences, 6(9), 3185-3200. https://doi.org/10.1007/s12517-012-0590-x

122. Eshaghzadeh A., 2015. Image edge detection of the total horizontal gradient of gravity data using the normalized tilt angle. *Geodynamic Research International Bulletin*, 3(4), 28-33.
123. Essa K., 2007. A simple formula for shape and depth determination from residual gravity anomalies. *Acta Geophysica*, 55(2), 182-190. https://doi.org/10.2478/s11600-007-0003-9
124. Essa K.S., 2014. New fast least-squares algorithm for estimating the best-fitting parameters due to simple geometric-structures from gravity anomalies. *Journal of Advanced Research*, 5(1), 57-65. https://doi.org/10.1016/j.jare.2012.11.006
125. European Environment Agency, 2012. CORINE Land Cover Project.
126. Fairhead J.D., 2015. *Advances in Gravity and Magnetic Processing and Interpretation*. EAGE Publications, The Netherlands, 338p. ISBN 978-94-6282-175-0
127. Fairhead J., Bennett K.J., Gordon D.R.H., Huang D., 1994. Euler: Beyond the "black box". In: *SEG Technical Program Expanded Abstract*, 422-424. Society of Exploration Geophysicists. https://doi.org/10.1190/1.1932113
128. Fairhead J.D., Green C.M., Masterton S.M., Guiraud R., 2013. The role that plate tectonics, inferred stress changes and stratigraphic unconformities have on the evolution of the West and Central African Rift System and the Atlantic continental margins. *Tectonophysics*, 594, 118-127. https://doi.org/10.1016/j.tecto.2013.03.021
129. Fairhead J.D., Mazur S., Green C.M., Masterton S., Yousif M.E., 2012. Regional plate tectonic controls on the evolution of the West and Central African rift system, with a focus on the Muglad Rift Basin, Sudan. SAPEG. *Journal Sudanese Association of Petroleum Geoscientists*, 3, 14-29.
130. Fais S., Radogna P.V., Romoli E., Matta P., Klingele E.E., 2015. Microgravity for detecting cavities in an archaeological site in Sardinia (Italy). *Near Surface Geophysics*, 13(5), 495-502. Doi: 10.3997/1873-0604.2015036
131. Farangitakis G.P., Brentas O.G., Andreadakis E., Lekkas, E., 2016. Seismic risk assessment in the Attica basin. *Bulletin of the Geological Society of Greece*, 50(3), 1415-1425.
132. Farhi W., Boudella A., Saibi H., Bounif M.O.A., 2016. Integration of magnetic, gravity, and well data in imaging subsurface geology in the Ksar Hirane region (Laghouat, Algeria). *Journal of African Earth Sciences*, 124, 63-74. https://doi.org/10.1016/j.jafrearsci.2016.09.013
133. Fathy K., Zahran K.H., Radwan A.H., Sabet H.S., Hamed D., 2013. Gravity observations at Sinai Peninsula and its geophysical and geodetic applications. *NRIAG Journal of Astronomy and Geophysics*, 2(2), 223-233. https://doi.org/10.1016/j.nrjag.2013.12.003

134. Fenning P.J., McCann D., Veness K., 1994. Urban Geophysics - Seeking the Difficult and Hidden. In: *7th EEGS Symposium on the Application of Geophysics to Engineering and Environmental Problems*. https://doi.org/10.4133/1.2922085
135. Fernandez-Cordoba J., Zamora-Camacho A., Espindola J.M., 2017. Gravity Survey at the Ceboruco Volcano Area (Nayarit, Mexico): a 3-D Model of the Subsurface Structure. *Pure and Applied Geophysics*, 174(10), 3905-3918. https://doi.org/10.1007/s00024-017-1600-4
136. FitzGerald D., Reid A., McInerney P., 2004. New discrimination techniques for Euler deconvolution. *Computers & Geosciences*, 30(5), 461-469. https://doi.org/10.1016/j.cageo.2004.03.006
137. Foumelis M., 2009. Surface deformation study of the broader area of Athens based on differential GPS measurements and radar interferometry. *PhD Thesis*, University of Athens, 358p. (*In Greek*) http://hdl.handle.net/10442/hedi/24231
138. Foumelis M., Fountoulis I., Papanikolaou I.D., Papanikolaou D., 2013. Geodetic evidence for passive control of a major Miocene tectonic boundary on the contemporary deformation field of Athens (Greece). *Annals of Geophysics*, 56(6), S0674, 9p. http://dx.doi.org/10.4401/ag-6238
139. Foumelis M., Parcharidis I., Lagios E., Voulgaris N., 2009. Evolution of post-seismic ground deformation of the Athens 1999 earthquake observed by SAR interferometry. *Journal of Applied Geophysics*, 69(1), 16-23. https://doi.org/10.1016/j.jappgeo.2009.02.007
140. Fountoulis I., 2004. The neotectonic macrostructures and the geological basement, the main factors controlling the spatial distribution of the damage and geodynamic phenomena resulting from the Kalamata (13 September 1986) and Athens (7 September 1999) earthquakes. In: *Earthquake Geodynamics: Advances in Earthquake Engineering*, 45-67.
141. Freyberg B.V., 1951. Das Neogen-Gebiet nordwestlich Athen. *Annales Géologiques des Pays Helléniques*, 3, 65–86 (*In German*).
142. Fries M. & Malagutti Filho W., 2005. Crustal and tectonic features of northeast of São Paulo State and southwest of Minas Gerais State based on gravimetric studies in southeast Brazil. In: *9th International Congress of the Brazilian Geophysical Society*. Extended Abstract.
143. Flinders A.F., Ito G., Garcia M.O., 2010. Gravity anomalies of the Northern Hawaiian Islands: Implications on the shield evolutions of Kauai and Niihau. *Journal of Geophysical Research: Solid Earth*, 115, B08412, 15p. Doi: 10.1029/2009JB006877
144. Gabtni H. & Jallouli C., 2017. Regional-residual separation of potential field: An example from Tunisia. *Journal of Applied Geophysics*, 137, 8-24. https://doi.org/10.1016/j.jappgeo.2016.12.011

145. Gaitanakis P., 1982. Geological map of Greece. Sheet “Athens-Piraeus”, Scale 1:50.000. *Institute of Geology and Mineral Exploration*, Athens.
146. Ganas A., Papadopoulos G., Pavlides S., 2000. The 7 September Athens unexpected earthquake: 3D visualization and field evidence of the seismic fault. *Annales Géologiques des Pays Helléniques*, 38(A), 113-129.
147. Ganas A., Pavlides S., Karastathis V., 2005. DEM-based morphometry of range-front escarpments in Attica, central Greece, and its relation to fault slip rates. *Geomorphology*, 65(3), 301-319. https://doi.org/10.1016/j.geomorph.2004.09.006
148. Ganas A., Pavlides S.B., Sboras S., Valkaniotis S., Papaioannou S., Alexandris G.A., Plessa A., Papadopoulos G.A., 2004. Active fault geometry and kinematics in Parnitha Mountain, Attica, Greece. *Journal of Structural Geology*, 26(11), 2103-2118. https://doi.org/10.1016/j.jsg.2004.02.015
149. García-Pérez T., Marquardt C., Yáñez G., Cembrano J., Gomila R., Santibañez I., Maringue J., 2018. Insights on the structural control of a Neogene forearc basin in Northern Chile: A geophysical approach. *Tectonophysics*. 736, 1-14. https://doi.org/10.1016/j.tecto.2018.04.003
150. Gardner G.H.F., Gardner L.W., Gregory A.R., 1974. Formation velocity and density -The diagnostic basics for stratigraphic traps. *Geophysics*, 39(6), 770-780. https://doi.org/10.1190/1.1440465
151. Geosoft, 2009. GM-SYS Profile Modeling - Gravity and magnetic modeling software for Oasis Montaj, User Guide Ver.4.1.
152. Geosoft, 2010. Montaj Gravity & Terrain Correction – Gravity Data Processing Extension for Oasis Montaj v.7.1. – Tutorial and User Guide.
153. Ghosh G.K., 2016. Interpretation of Gravity Data using 3D Euler Deconvolution, Tilt Angle, Horizontal Tilt Angle and Source Edge Approximation of the North-West Himalaya. *Acta Geophysica*, 64(4), 1112-1138. https://doi.org/10.1515/acgeo-2016-0042
154. Goiran J.P., Pavlopoulos K.P., Fouache E., Triantaphyllou M., Etienne R., 2011. Piraeus, the ancient island of Athens: evidence from Holocene sediments and historical archives. *Geology*, 39(6), 531-534. https://doi.org/10.1130/G31818.1
155. Golub G.H., Heath M., Wahba G., 1979. Generalized cross-validation as a method for choosing a good ridge parameter. *Technometrics*, 21(2), 215-223. Doi: 10.1080/00401706.1979.10489751
156. Gómez-Ortiz D., Tejero-López R., Babín-Vich R., Rivas-Ponce A., 2005. Crustal density structure in the Spanish Central System derived from gravity data analysis (Central Spain). *Tectonophysics*, 403(1-4), 131-149. https://doi.org/10.1016/j.tecto.2005.04.006
157. Gönenç T., 2014. Investigation of distribution of embedded shallow structures using the first order vertical derivative of gravity data. *Journal of Applied Geophysics*, 104, 44-57.

https://doi.org/10.1016/j.jappgeo.2014.02.010
158. Götze H.J., Lahmeyer B., Schmidt S., Strunk S., 1994. The lithospheric structure of the Central Andes (20–26 S) as inferred from interpretation of regional gravity. In: *Tectonics of the southern Central Andes*, 7-21. Springer, Berlin, Heidelberg. https://doi.org/10.1007/978-3-642-77353-2_1
159. Goumas G., 2006. *Study of Thriassio Region Structure with Geophysical Methods*. *M.Sc. thesis*, University of Athens, 178p. (*In Greek*).
160. Gournelos Th. & Maroukian H., 1990. Geomorphological observations concerning the evolution of the Basin of Athens. *Geologica Balcanica*. 20(6), 15-24.
161. Gutenberg B., 1929. *Lehrbuch der Geophysik*, Borntraeger, Berlin, 1017p. (*In German*).
162. Haala N., Brenner C., Anders K.H., 1998. 3D urban GIS from laser altimeter and 2D map data. *International Archives of Photogrammetry and Remote Sensing*, 32, 339-346.
163. Haala N. & Brenner C., 1999. Extraction of buildings and trees in urban environments. *ISPRS Journal of Photogrammetry and Remote Sensing*, 54(2-3), 130-137. https://doi.org/10.1016/S0924-2716(99)00010-6
164. Haddad D., Watts A.B., Lindsay J., 2001. Evolution of the intracratonic Officer Basin, central Australia: implications from subsidence analysis and gravity modelling. *Basin Research*, 13(2), 217-238. Doi: 10.1046/j.1365-2117.2001.00147.x
165. Hamdi-Nasr I., Hédi Inoubli M., Ben Salem A., Tlig S., Mansouri A., 2009. Gravity contributions to the understanding of salt tectonics from the Jebel Cheid area (dome zone, Northern Tunisia). *Geophysical Prospecting*, 57(4), 719-728. Doi: 10.1111/j.1365-2478.2009.00788.x
166. Hammer S., 1939. Terrain corrections for gravimeter stations. *Geophysics*, 4(3), 184-194. https://doi.org/10.1190/1.1440495
167. Hammer S., 1950. Density determinations by underground gravity measurements. *Geophysics*, 15(4), 637-652. https://doi.org/10.1190/1.1437625
168. Henderson R.J., 1992. Urban geophysics - A review. *Exploration Geophysics*, 23(4), 531-542. https://doi.org/10.1071/EG992531
169. Henderson R.G. & Zietz I., 1948. Analysis of total magnetic-intensity anomalies produced by point and line sources. *Geophysics*, 13(3), 428-436. https://doi.org/10.1190/1.1437414
170. Hinze W.J., 2003. Bouguer reduction density, why 2.67? *Geophysics*, 68(5), 1559-1560. https://doi.org/10.1190/1.1620629
171. Hinze W.J., Von Frese R.R., Saad A.H., 2013. *Gravity and magnetic exploration: Principles, practices, and applications*. Cambridge University Press. 511p., ISBN: 978-0-521-87101-3.
172. Hipkin R.G., Lagios E., Lyness D., Jones P., 1988. Reference gravity stations on the IGSN71 standard in Britain and Greece. *Geophysical Journal International*, 92(1), 143-148.

https://doi.org/10.1111/j.1365-246X.1988.tb01128.x
173. Hjelt S.E., 1974. The gravity anomaly of a dipping prism. *Geoexploration*, 12(1), 29-39. https://doi.org/10.1016/0016-7142(74)90004-0
174. Hong W.T., Kang S., Lee S.J., Lee J.S., 2018. Analyses of GPR signals for characterization of ground conditions in urban areas. *Journal of Applied Geophysics*, 152, 65-76. https://doi.org/10.1016/j.jappgeo.2018.03.005
175. Hood P., 1965. Gradient measurements in aeromagnetic surveying. *Geophysics*, 30(5), 891-902. https://doi.org/10.1190/1.1439666
176. Hosseini A.A., Doulati Ardejani F., Tabatabaie S.H., Hezarkhani A., 2013. Edge detection in gravity field of the Gheshm sedimentary basin. *International Journal of Mining & Geo-Engineering*, 47(1), 41-50. Doi: 10.22059/IJMGE.2013.50089
177. Hsu S.K., Sibuet J.C., Shyu C.T., 1996. High-resolution detection of geologic boundaries from potential-field anomalies: An enhanced analytic signal technique. *Geophysics*, 61(2), 373-386. https://doi.org/10.1190/1.1443966
178. Hu Y., Liu W., Wang J., Zhang G., Zhou Z., Han R., 2017. Basin-scale structure control of Carlin-style gold deposits in central Southwestern Guizhou, China: Insights from seismic reflection profiles and gravity data. *Ore Geology Reviews*, 91, 444-462. https://doi.org/10.1016/j.oregeorev.2017.09.011
179. Hutchings L., Ioannidou E., Foxall W., Voulgaris N., Savy J., Kalogeras I., Scognamiglio L., Stavrakakis G., 2007. A physically based strong ground-motion prediction methodology; application to PSHA and the 1999 M w= 6.0 Athens earthquake. *Geophysical Journal International*, 168(2), 659-680. https://doi.org/10.1111/j.1365-246X.2006.03178.x
180. Hutchinson P., Teschke B., King J.M., 2009. Seismic Reflection Imaging in Urban Settings. In: *22nd EEGS Symposium on the Application of Geophysics to Engineering and Environmental Problems*.
181. Iglseder C., Grasemann B., Rice A.H.N., Petrakakis K., Schneider D.A., 2011. Miocene south directed low-angle normal fault evolution on Kea Island (West Cycladic Detachment System, Greece). *Tectonics*, 30(4), TC4013, 1-31. Doi: 10.1029/2010TC002802
182. Ioannidou E., Voulgaris N., Kalogeras I., Hutchings L., Stavrakakis G., 2001. Analysis of site response in the Athens area from the 7 September 1999, Mw. *Bollettino di Geofisica Teorica ed Applicata*, 42(3-4), 183-208.
183. Jacobsen B.H., 1987. A case for upward continuation as a standard separation filter for potential-field maps. *Geophysics*, 52(8), 1138-1148. https://doi.org/10.1190/1.1442378
184. Jacobshagen V., Dürr S., Kockel F., Kopp K.O., Kowalczyk G., Berckhemer H., Büttner D. (1978). Structure and geodynamic evolution of the Aegean region. *Alps, Apennines, Hellenides*, 537-564.

185. Jacoby W. & Smilde P.L., 2009. *Gravity Interpretation: Fundamentals and Application of Gravity Inversion and Geological Interpretation*. Springer-Verlag Berlin Heidelberg. 395p. ISBN: 978-3-540-85328-2.
186. Jochem A., Höfle B., Rutzinger M., Pfeifer N., 2009. Automatic roof plane detection and analysis in airborne lidar point clouds for solar potential assessment. *Sensors*, 9(7), 5241-5262. Doi:10.3390/s90705241
187. Jung K., 1961. *Schwerkraftverfahren in der Angewandten Geophysik*. Akademische Verlagsgesellschaft Geest & Portig, Leipzig, 348p.
188. Kadirov F.A., 2000. Application of the Hartley transform for interpretation of gravity anomalies in the Shamakhy–Gobustan and Absheron oil-and gas-bearing regions, Azerbaijan. *Journal of Applied Geophysics*, 45(1), 49-61. https://doi.org/10.1016/S0926-9851(00)00018-5
189. Kane M.F., 1962. A comprehensive system of terrain corrections using a digital computer. *Geophysics*, 27(4), 455-462. https://doi.org/10.1190/1.1439044
190. Karastathis V.K., Karmis P., Novikova T., Roumelioti Z., Gerolymatou E., Papanastassiou D., Liakopoulos S., Tsombos G.A., Papadopoulos G.A., 2010. The contribution of geophysical techniques to site characterisation and liquefaction risk assessment: Case study of Nafplion City, Greece. *Journal of Applied Geophysics*, 72(3), 194-211. https://doi.org/10.1016/j.jappgeo.2010.09.003
191. Karfakis J. & Loupasakis C., 2006. Geotechnical characteristics of the formation of "Tourkovounia" Limestones and their influence on urban construction-City of Athens, Greece. In: *IAEG2006*, Paper number 794.
192. Karner G.D., Studinger M., Bell R.E., 2005. Gravity anomalies of sedimentary basins and their mechanical implications: Application to the Ross Sea basins, West Antarctica. *Earth and Planetary Science Letters*, 235(3-4), 577-596. https://doi.org/10.1016/j.epsl.2005.04.016
193. Kater H., 1818. An account of experiments for determining the length of the pendulum vibrating seconds in the latitude of London. *Philosophical Transactions of the Royal Society of London*, 108, 33-102.
194. Katsikatsos G., 1977. La structure tectonique d'Attique et de l'île d'Eubée. In: *Proceedings of the 6th Colloquium of the Geology of the Aegean Region*, 1, 211-228, IGME publications (*In French*).
195. Katsikatsos G., 2002. Geological map of Greece. Sheet "Kifisia", Scale 1:50.000. *Institute of Geology and Mineral Exploration*, Athens.
196. Katsikatsos G., Migiros G., Triantaphyllis M., Mettos A., 1986. Geological structure of internal Hellenides (E. Thessaly–SW Macedonia–Euboea–Attica–Northern Cyclades islands and Lesvos). *Geological and Geophysical Research*, Special Issue, 191-212. IGME publications.

197. Kay M. & Dimitrakopoulos R., 2000. Integrated interpolation methods for geophysical data: applications to mineral exploration. *Natural Resources Research*, 9(1), 53-64. https://doi.org/10.1023/A:1010161813931
198. Keating P.B., 1998. Weighted Euler deconvolution of gravity data. *Geophysics*, 63(5), 1595-1603. https://doi.org/10.1190/1.1444456
199. Khalil M.A., Santos F.M., Farzamian M., 2014. 3D gravity inversion and Euler deconvolution to delineate the hydro-tectonic regime in El-Arish area, northern Sinai Peninsula. *Journal of Applied Geophysics*, 103, 104-113. https://doi.org/10.1016/j.jappgeo.2014.01.012
200. Khalil M.A., Santos F.M., Farzamian M., El-Kenawy A., 2015. 2-D Fourier transform analysis of the gravitational field of Northern Sinai Peninsula. *Journal of Applied Geophysics*, 115, 1-10. https://doi.org/10.1016/j.jappgeo.2015.01.022
201. Khamies A.A. & El-Tarras M.M., 2010. Surface and subsurface structures of Kalabsha area, southern Egypt, from remote sensing, aeromagnetic and gravity data. *The Egyptian Journal of Remote Sensing and Space Science*, 13(1), 43-52. https://doi.org/10.1016/j.ejrs.2010.07.006
202. Kilias S., Voudouris P., Katerinopoulos A., Kavouri S., 2004. Fluid inclusion study in alpinotype quartz crystals from fissures in Pendelikon mountain. *Bulletin of the Geological Society of Greece*, 36(1), 526-533 (*In Greek*).
203. Kim Y.M., Lee S.M., Okino K., 2009. Comparison of gravity anomaly between mature and immature intra-oceanic subduction zones in the western Pacific. *Tectonophysics*, 474(3-4), 657-673. https://doi.org/10.1016/j.tecto.2009.05.004
204. Kim C., Kang W., Son J., Jeong S., 2017. GPR Experiments of the Simulated Cavity Detection in Urban Areas. In: *EGU General Assembly Conference Abstracts*, 19, p.4314.
205. Kobe M., Gabriel G., Weise A., Krawczyk C., Vogel D., 2017. Time-lapse gravity and levelling in the sinkhole-endangered urban area of Bad Frankenhausen, Germany. In: *EGU General Assembly Conference Abstracts*, 19, p.17812.
206. Kontoes C., Elias P., Sykioti O., Briole P., Remy D., Sachpazi M., Veis G., Kotsis I., 2000. Displacement field and fault model for the September 7, 1999 Athens earthquake inferred from ERS2 satellite radar interferometry. *Geophysical Research Letters*, 27(24), 3989-3992. Doi: 10.1029/2000GL008510
207. Koukis G. & Sabatakakis N., 2000. Engineering geological environment of Athens, Greece. *Bulletin of Engineering Geology and the Environment*, 59(2), 127-135. https://doi.org/10.1007/s100640000058
208. Koumantakis I. and collaborators, 1997. Research of hydrogeological conditions and subsurface waters operation status of Athens basin. *Organization of Athens regulatory plan and environment protection – National Technical University of Athens*. Applied research program, Athens (*In Greek*).

209. Koumetio F., Njomo D., Tabod C.T., Noutchogwe T.C., Manguelle-Dicoum E., 2012. Structural interpretation of gravity anomalies from the Kribi–Edea zone, South Cameroon: a case study. *Journal of Geophysics and Engineering*, 9(6), 664. Doi: 10.1088/1742-2132/9/6/664
210. Krahenbuhl R.A. & Li Y., 2006. Inversion of gravity data using a binary formulation. *Geophysical Journal International*, 167(2), 543-556. https://doi.org/10.1111/j.1365-246X.2006.03179.x
211. Krahenbuhl R.A. & Li Y., 2008. Joint inversion of surface and borehole 4D gravity data for continuous characterization of fluid contact movement. In: *SEG Annual International Meeting* Expanded Abstracts, 726-730. https://doi.org/10.1190/1.3063750
212. Krawczyk C.M., Polom U., Trabs S., Dahm T., 2012. Sinkholes in the city of Hamburg—new urban shear-wave reflection seismic system enables high-resolution imaging of subrosion structures. *Journal of Applied Geophysics*, 78, 133-143. https://doi.org/10.1016/j.jappgeo.2011.02.003
213. Krohe A., Mposkos E., Diamantopoulos A., Kaouras G., 2010. Formation of basins and mountain ranges in Attica (Greece): The role of Miocene to Recent low-angle normal detachment faults. *Earth-Science Reviews*, 98(1), 81-104. https://doi.org/10.1016/j.earscirev.2009.10.005
214. Krynski J., Olszak T., Barlik M., Dykowski P., 2013. New gravity control in Poland–needs, the concept and the design. *Geodesy and Cartography*, 62(1), 3-21. https://doi.org/10.2478/geocart-2013-0001
215. Kober L., 1929). Beiträge zur Geologie von Attika. 31p. (*In German*).
216. Kounis G., 1981. Athens metro hydrogeological research. Part II: Analysis of hydrogeological conditions. *Hydrological and Hydrogeological investigations*, 34, IGME publications, Athens (*In Greek*).
217. Kounis G.D., 1998. A study for the hydrogeology of Attica. IGME publications, Athens (*In Greek*).
218. Kounis G.D. & Kounis K.G., 2010. Relationship between the transmissibility of the "Athens Schists" and the percentage of their competent rock component. *Bulletin of the Geological Society of Greece*, 43(4), 1767-1776. http://dx.doi.org/10.12681/bgsg.11362
219. Ktenas C., 1923. Les plissements d'age primaire dans la region central de la mer Egee. *Comptes-Rendus du 13^{e} Congrès Géologique International*, 571-583, Liege (*In French*).
220. Kuranchie F.A., Shukla S.K., Habibi D., 2016. Utilisation of iron ore mine tailings for the production of geopolymer bricks. *International Journal of Mining, Reclamation and Environment*, 30(2), 92-114. https://doi.org/10.1080/17480930.2014.993834
221. Kynigalaki M., Nikolaou N., Karfakis J., Koutsouveli An., Poyiadji El., Pyrgiotis L., Konstantopoulou G., Bellas M., Apostolidis Em., Loupasakis K., Spanou N., Sabatakakis N., Koukis G., 2010. Digital engineering geological map of the Athens prefecture area

and related database management system. *Bulletin of the Geological Society of Greece*, 43(3), 1619-1626.

222. LaFehr T.R., 1980. Gravity method. *Geophysics*, 45(11), 1634-1639. https://doi.org/10.1190/1.1441054
223. LaFehr T.R., 1983. Rock density from borehole gravity surveys. *Geophysics*, 48(3), 341-356. https://doi.org/10.1190/1.1441472
224. LaFehr T.R. & Nabighian, M.N., 2012. *Fundamentals of Gravity Exploration*. Society of Exploration Geophysicists, Tulsa, 218p. ISBN: 978-1-56080-298-3
225. Latsoudas Ch., 1992. Geological map of Greece. Sheet "Koropi-Plaka", Scale 1:50.000. *Institute of Geology and Mineral Exploration*, Athens
226. Lagios E., 1985. A gravity network in central Greece for secular gravity studies. *Pure and Applied Geophysics*, 123(1), 81-90. https://doi.org/10.1007/BF00877050
227. Lamontagne M., Thomas M., Silliker J., Jobin D., 2011. Detailed gravity survey to help seismic microzonation: Mapping the thickness of unconsolidated deposits in Ottawa, Canada. *Journal of Applied Geophysics*, 75(3), 444-454. https://doi.org/10.1016/j.jappgeo.2011.06.019
228. Leader L.D., Rawling T.J., Wilson C.J.L., 2006. Structural transect and forward modelling of geophysical data across the St Arnaud Group, Victoria. *Australian Journal of Earth Sciences*, 53(5), 863-873. https://doi.org/10.1080/08120090600827504
229. Lekkas E., 2001. The Athens earthquake (7 September 1999): intensity distribution and controlling factors. *Engineering Geology*, 59(3-4), 297-311. http://dx.doi.org/10.1016/S0013-7952(00)00119-8
230. Lekkas S. & Lozios S., 2000. Tectonic structure of Mt. Hymittos. *Annales Géologiques des Pays Helléniques*, 38, 47-62.
231. Lekkas E.L., Lozios S.G., Danamos G.D., 2001. Geological and tectonic structure of the area between Aigaleo and Parnitha Mt. (Attica, Greece) and their importance to antiseismic planning. *Bulletin of the Geological Society of Greece*, 34(1), 19-27 (*In Greek*).
232. Lekkas E., Papanikolaou D., Lozios S., Papoulia I., Vasilopoulou S., Vassilakis Em., 1998. Neotectonic map of East Attiki, Scale 1:100.000. Section of Dynamic, Tectonic and Applied Geology, University of Athens – East Attiki Prefecture.
233. Leoutsakos G., Le Van C., Doulakis I., 2008. Elliniko Extension of Athens Metro–Project Description, Structuring and Implementation. *Geomechanics and Tunnelling*, 1(3), 197-206. Doi: 10.1002/geot.200800023
234. Lepsius R., 1893. Geologie von Attika. Ein Beitrag zur Lehre von Metamorphismus der Gesteine, *Berlin Zeitschr. f. partkt. Geol*., 4, 196S, 592p. (*In German*).
235. Leucci G. & De Giorgi L., 2010. Microgravimetric and ground penetrating radar geophysical methods to map the shallow karstic cavities network in a coastal area (Marina Di Capilungo, Lecce, Italy). *Exploration Geophysics*, 41(2), 178-188.

236. Li Y. & Krahenbuhl R., 2015. *Gravity and Magnetic Methods in Mineral and Oil & Gas Exploration and Production*. EAGE Publications, The Netherlands, 155p. ISBN: 978-9-46282-159-0.
237. Li Y. & Oldenburg D.W., 1996. 3-D inversion of magnetic data. *Geophysics*, 61(2), 394-408. https://doi.org/10.1190/1.1443968
238. Li Y. & Oldenburg D.W., 1998. 3-D inversion of gravity data. *Geophysics*, 63(1), 109-119. https://doi.org/10.1190/1.1444302
239. Li Y. & Oldenburg D.W., 2000. Joint inversion of surface and three-component borehole magnetic data. *Geophysics*, 65(2), 540-552. https://doi.org/10.1190/1.1444749
240. Li Y. & Oldenburg D.W., 2003. Fast inversion of large-scale magnetic data using wavelet transforms and a logarithmic barrier method. *Geophysical Journal International*, 152(2), 251-265. https://doi.org/10.1046/j.1365-246X.2003.01766.x
241. Lillie R.J., 1999. *Whole Earth Geophysics: An Introductory Textbook for Geologists*. Prentice Hall, New Jersey, 361p. ISBN: 978-0-13490-517-4
242. Liu L. & Chan L.S., 2007. Sustainable urban development and geophysics. *Journal of Geophysics and Engineering*, 4(3), p.243. https://doi.org/10.1088/1742-2140/4/3/E01
243. Long L.T. & Kaufmann R.D., 2013. *Acquisition and Analysis of Terrestrial Gravity Data*. Cambridge University Press, 169p. ISBN: 978-1-107-02413-7
244. Louis I.F., Karastathis V.K., Vafidis A.P., Louis F.I., 2002a. Resistivity modelling and imaging methods for mapping near-surface features: Application to a site characterization at the ancient Temple of Olympian Zeus in Athens. *Journal of the Balkan Geophysical Society*, 5(4), 135-144.
245. Louis I.F., Raftopoulos D., Goulis I., Louis F.I., 2002b. Geophysical Imaging of faults and fault zones in the urban complex of Ano Liosia Neogene basin, Greece: Synthetic simulation approach and field investigations. In: *International Conference on Earth Sciences and Electronics*, 269-285
246. Louro V.H.A. & Mantovani M.S.M., 2012. 3D inversion and modeling of magnetic and gravimetric data characterizing the geophysical anomaly source in Pratinha I in the southeast of Brazil. *Journal of Applied Geophysics*, 80, 110-120. https://doi.org/10.1016/j.jappgeo.2012.01.013
247. Louvari E. & Kiratzi A., 2001. Source parameters of the 7 September 1999 Athens (Greece) earthquake based on teleseismic data. *Journal of the Balkan Geophysical Society*, 4(3), 51-60.
248. Lowrie W., 2007. *Fundamentals of Geophysics*. Cambridge University Press, 393p. ISBN-13 978-0-511-35447-2
249. Lozios S., 1990. Observations on the minor structures of the metamorphic rocks of Varnavas-Ramnounda area, NE Attica. *Bulletin of the Geological Society of Greece*, 25, 439-453 (*In Greek*).

250. Lozios S., 1993. Tectonic analysis of the metamorphic formations of NE Attica. *PhD Thesis*, University of Athens, 299p. (*In Greek*) http://hdl.handle.net/10442/hedi/2925
251. Lozios S.G., Lekkas E.L., Chatzistavrou L.C., 2004. Surficial expression of seismic faults and urban planning. In: *Earthquake Geodynamics: Seismic Case Studies*, WIT Press, 91-104.
252. Ludwig W.J., Nafe J.E., Drake C.L., 1970. Seismic refraction. *The Sea*, 4(1), 53-84.
253. Macau A., Benjumea B., Gabàs A., Bellmunt F., Figueras S., 2018. Geophysical measurements for site effects characterisation in the urban area of Girona, Spain. *Near Surface Geophysics*, 16(3), 340-355. Doi: 10.3997/1873-0604.2018004
254. Madon M.B. & Watts A.B., 1998. Gravity anomalies, subsidence history and the tectonic evolution of the Malay and Penyu Basins (offshore Peninsular Malaysia). Basin *Research*, 10(4), 375-392. Doi: 10.1046/j.1365-2117.1998.00074.x
255. Makris J., Papoulia J., Yegorova T., 2013. A 3-D density model of Greece constrained by gravity and seismic data. *Geophysical Journal International*, 194(1), 1-17. https://doi.org/10.1093/gji/ggt059
256. Makris J. & Yegorova T., 2006. A 3-D density–velocity model between the Cretan Sea and Libya. *Tectonophysics*, 417(3-4), 201-220. https://doi.org/10.1016/j.tecto.2005.11.003
257. Mallick K. & Sharma K.K., 1999. A finite element method for computation of the regional gravity anomaly. *Geophysics*, 64(2), 461-469. https://doi.org/10.1190/1.1444551
258. Mallick K., Vasanthi A., Sharma K.K., 2012. *Bouguer Gravity Regional and Residual Separation: Application to Geology and Environment*. Springer, 288p. ISBN: 978-94-007-0406-0
259. Marinos G., 1937. The tectonic position of the Athens Schists formation at its west zone. *Proceedings of Athens Academy*, 12, 16-21.
260. Marinos G., 1955. The age of metamorphic layers of Attica. *Bulletin of the Geological Society of Greece*, 2(1), 1-13 (*In Greek*).
261. Marinos G., Katsikatsos G., Georgiadou-Dikeoulia E., Mirkou E., 1971. The Athens' schist formation I. Stratigraphy and Structure. *Annales Géologiques des Pays Helléniques*, 23, 183-212 (*In Greek*).
262. Marinos G., Katsikatsos G., Mirkou E., 1974. The Athens' schist formation II. Stratigraphy and Structure. *Annales Géologiques des Pays Helléniques*, 25, 439-444 (*In Greek*).
263. Marinos G. & Petrascheck W.E., 1956. Laurium. Geological and geophysical research. IGME Publications, Research, 4(1), 247p., Athens.
264. Marinos P., Bouckovalas G., Tsiambaos G., Sabatakakis N., Antoniou A., 2001. Ground zoning against seismic hazard in Athens, Greece. *Engineering Geology*, 62(4), 343-356. https://doi.org/10.1016/S0013-7952(01)00035-7

265. Marinos P., Marinos V., Stoumpos G., Novak M., Korkaris K., Benissi M., 2004. Behaviour of the "Athenian Schist" in excavation by an open face shield boring machine. Extension line to Peristeri of the metropolitan railway of Athens. *Bulletin of the Geological Society of Greece*, 36(4), 1790-1795 (*In Greek*).
266. Marinos P., Novack M., Benissi M., Panteliadou M., Papouli D., Stoumpos G., Marinos V., Korkaris, K., 2006. Crossing the Kifissos old river bed in the extension of the metro of Athens. Predicted and encountered water inflows. In: *IAEG2006*, Paper 310.
267. Marinos P.G., Novack M., Benissi M., Stoumpos G., Papouli D., Panteliadou M., Marinos V., Boronkay K., Korkaris, K., 2009. Assessment of ground conditions with respect to mechanised tunnelling for the construction of the extension of the Athens Metro to the city of Piraeus. *Bulletin of Engineering Geology and the Environment*, 68(1), 17-26. Doi: 10.1007/s10064-008-0183-9
268. Marinos P., Papouli D., Panteliadou M., 2008. The underground water of Kifissos basin. *1st Scientific Two-day meeting for Kifissos-Integrated approach for Kifissos problems*, National Technological University of Athens.
269. Mariolakos I. & Fountoulis I., 2000a. The Athens earthquake September 7, 1999 neotectonic regime and geodynamic phenomena. *Annales Géologiques des Pays Helléniques*, 38(B), 165-174.
270. Mariolakos I. & Fountoulis I., 2000b. The Athens earthquake September 7, 1999 neotectonic regime and geodynamic phenomena. In: *Integration of Earth Sciences Research on the 1999 Turkish and Greek earthquakes*, Kluwer Academic Publishers (Eds. Gorur *et al.*), NATO Science Series, Earth and Environment Sciences, IV(9), 113-126.
271. Mariolakos I., Fountoulis I., Mariolakos D., Andreadakis E., Georgakopoulos A., 2000. Geodynamic phenomena observed during the Athens earthquake (Ms= 5.9) 7-9-1999. *Annales Géologiques des Pays Helléniques*, 38, 175-186.
272. Mariolakos I., Fountoulis I., Theocharis D., 2001a. Neotectonic structure and evolution of Salamis island (Greece). *Bulletin of the Geological Society of Greece*, 34(1), 165-173 (*In Greek*).
273. Mariolakos I., Fountoulis I., Sideris Ch., Chatoupis Th., 2001b. Morphoneotectonic structure of Parnis Mt. (Attica, Greece). *Bulletin of the Geological Society of Greece*, 34(1), 183-190 (*In Greek*).
274. Mariolakos I. & Papanikolaou D.I., 1987. Deformation pattern and relation between deformation and seismicity in the Hellenic arc. *Bulletin of the Geological Society of Greece*, 19, 59-76 (*In Greek*).
275. Mariolakos I. & Theocharis D., 2001. Shorelines displacement in the Saronic Gulf area during the last 18.000 yrs and the Kihrea paleolake. *Bulletin of the Geological Society of Greece*, 34(1), 405-413 (*In Greek*).

276. Marquardt D.W., 1963. An algorithm for least-squares estimation of nonlinear parameters. Journal of the Society for Industrial and Applied Mathematics, 11(2), 431-441. https://doi.org/10.1137/0111030
277. Martelet G., Calcagno P., Gumiaux C., Truffert C., Bitri A., Gapais D., Brun J.P., 2004. Integrated 3D geophysical and geological modelling of the Hercynian Suture Zone in the Champtoceaux area (south Brittany, France). *Tectonophysics*, 382(1-2), 117-128. https://doi.org/10.1016/j.tecto.2003.12.009
278. Martinez C., Li Y., Krahenbuhl R., Braga M.A., 2013. 3D inversion of airborne gravity gradiometry data in mineral exploration: A case study in the Quadrilátero Ferrífero, Brazil. *Geophysics*, 78(1), B1-B11. Doi: 10.1190/geo2012-0106.1
279. Martínez K. & Mendoza J.A., 2011. Urban seismic site investigations for a new metro in central Copenhagen: Near surface imaging using reflection, refraction and VSP methods. *Physics and Chemistry of the Earth*, 36(16), 1228-1236. https://doi.org/10.1016/j.pce.2011.01.003
280. Martínez-Moreno F.J., Galindo-Zaldívar J., Pedrera A., Teixidó T., Peña J.A., González-Castillo L., 2015. Regional and residual anomaly separation in microgravity maps for cave detection: the case study of Gruta de las Maravillas (SW Spain). *Journal of Applied Geophysics*, 114, 1-11. https://doi.org/10.1016/j.jappgeo.2015.01.001
281. Martínez-Pagán P., Navarro M., Pérez-Cuevas J., Alcalá F.J., García-Jerez A., Vidal F., 2018. Shear-wave velocity structure from MASW and SPAC methods: The case of Adra town, SE Spain. *Near Surface Geophysics*, 16(3), 356-371. Doi: 10.3997/1873-0604.2018012
282. Martins-Ferreira M.A.C., Campos J.E.G., Von Huelsen M.G., Neri B.L.,2018. Paleorift structure constrained by gravity and stratigraphic data: The Statherian Araí rift case. *Tectonophysics*, 738-739, 64-82. https://doi.org/10.1016/j.tecto.2018.05.014
283. Matikainen L., Hyyppä J., Hyyppä H., 2003. Automatic detection of buildings from laser scanner data for map updating. *International Archives of Photogrammetry, Remote Sensing and Spatial Information Sciences*, 34(3/W13), 218-224.
284. Mendonca C.A. & Silva J.B., 1995. Interpolation of potential-field data by equivalent layer and minimum curvature: A comparative analysis. *Geophysics*, 60(2), 399-407. https://doi.org/10.1190/1.1443776
285. Miller R., 2013. Introduction to this special section: Urban geophysics. *The Leading Edge*, 32(3), 248-249. https://doi.org/10.1190/tle32030248.1
286. Miller H.G. & Singh V., 1994. Potential field tilt - A new concept for location of potential field sources. *Journal of Applied Geophysics*, 32(2-3), 213-217. https://doi.org/10.1016/0926-9851(94)90022-1
287. Milsom J. & Eriksen A., 2011. *Field Geophysics*, Vol. 36, Wiley - John Wiley & Sons, 287p. ISBN: 978-0-470-74984-5

288. Mishra D.C., Chandrasekhar D.V., Singh B., 2005. Tectonics and crustal structures related to Bhuj earthquake of January 26, 2001: based on gravity and magnetic surveys constrained from seismic and seismological studies. *Tectonophysics*, 396(3-4), 195-207. https://doi.org/10.1016/j.tecto.2004.12.007
289. Mongus D., Lukač N., Žalik B., 2014. Ground and building extraction from LiDAR data based on differential morphological profiles and locally fitted surfaces. *ISPRS Journal of Photogrammetry and Remote Sensing*, 93, 145-156. http://dx.doi.org/10.1016/j.isprsjprs.2013.12.002
290. Morelli C., Gantar C., Honkasalon T., McConnel K., Tanner J.G., Szabo B., Uotila U., Whalen C.T., 1974. *The International Standardization Net 1971 (IGSN71)*. IUGG-IAG Publ. Spec. 4. Int. Union of Geod. and Geophysics.
291. Mushayandebvu M.F., Reid A.B., Fairhead, J.D., 2000. Grid Euler Deconvolution with constraints for 2D structures. In: *SEG Technical Program Expanded Abstracts*, 398-401. https://doi.org/10.1190/1.1816077
292. Nabighian M.N., Ander M.E., Grauch V.J.S., Hansen R.O., LaFehr T.R., Li Y., Pearson W.C., Peirce J.W., Phillips J.D., Ruder M.E., 2005. Historical development of the gravity method in exploration. *Geophysics*, 70(6), 63ND-89ND. https://doi.org/10.1190/1.2133785
293. Nabighian M.N. & Hansen R.O., 2001. Unification of Euler and Werner deconvolution in three dimensions via the generalized Hilbert transform. *Geophysics*, 66(6), 1805-1810. https://doi.org/10.1190/1.1487122
294. Nafe J.E. & Drake C.L., 1957. Variation with depth in shallow and deep water marine sediments of porosity, density and the velocities of compressional and shear waves. *Geophysics*, 22(3), 523-552. https://doi.org/10.1190/1.1438386
295. Nafe J.E. & Drake C.L., 1961. *Physical Properties of Marine Sediments*. Technical Report No.2, Lamont Geological Observatory, Palisades, New York. 45p.
296. Nagihara S. & Hall S.A., 2001. Three-dimensional gravity inversion using simulated annealing: Constraints on the diapiric roots of allochthonous salt structures. *Geophysics*, 66(5), 1438-1449. https://doi.org/10.1190/1.1487089
297. Nagy D., 1966. The gravitational attraction of a right rectangular prism. *Geophysics*, 31(2), 362-371. https://doi.org/10.1190/1.1439779
298. Nakada M., Tahara M., Shimizu H., Nagaoka S., Uehira K., Suzuki S., 2002. Late Pleistocene crustal uplift and gravity anomaly in the eastern part of Kyushu, Japan, and its geophysical implications. *Tectonophysics*, 351(4), 263-283. https://doi.org/10.1016/S0040-1951(02)00161-0
299. Naouali B.S., Inoubli M.H., Amiri A., Chaqui A., Hamdi I., 2011. Subsurface geology of the Ariana region (Diapir Zone, northern Tunisia) by means of gravity analysis. *Geophysical Prospecting*, 59(6), 983-997. Doi: 10.1111/j.1365-2478.2011.01004.x

300. Narayanpethkar A.B., Vasanthi A., Mallick K., 2007. Demarcation of liquefaction zones by Bouger gravity and electrical resistivity method. *J Indian Geophys Union*, 11(4), 175-180.
301. Nasr I.H., Amiri A., Inoubli M.H., Salem A.B., Chaqui A., Tlig S., 2011. Structural setting of northern Tunisia insights from gravity data analysis Jendouba case study. *Pure and Applied Geophysics*, 168(10), 1835-1849. https://doi.org/10.1007/s00024-010-0189-7
302. Nasuti A., Pascal C., Ebbing J., 2012. Onshore–offshore potential field analysis of the Møre–Trøndelag Fault Complex and adjacent structures of Mid Norway. *Tectonophysics*, 518, 17-28. https://doi.org/10.1016/j.tecto.2011.11.003
303. Negris Ph., 1912. Sur l'age des schistes d'Athenes. *Comptes Rendus de l'Académie des Sciences*, 154, 1838-1840 (*In French*).
304. Negris Ph., 1913. Contribution à la géologie de l'Attique. *Comptes Rendus de l'Académie des Sciences*, 156, 1286-1288 (*In French*).
305. Nettleton L.L., 1939. Determination of density for reduction of gravimeter observations. *Geophysics*, 4(3), 176-183. https://doi.org/10.1190/1.0403176
306. Nettleton L.L., 1954. Regionals, residuals, and structures. *Geophysics*, 19(1), 1-22. https://doi.org/10.1190/1.1437966
307. Niedermayer J., 1971. Die geologische Karte von Athen 1:10.000. *Bulletin of the Geological Society of Greece*, 8(2), 117-134 (*In German*).
308. Nouraliee J., Porkhial S., Mohammadzadeh-Moghaddam M., Mirzaei S., Ebrahimi D., Rahmani M.R., 2015. Investigation of density contrasts and geologic structures of hot springs in the Markazi Province of Iran using the gravity method. *Russian Geology and Geophysics*, 56(12), 1791-1800. https://doi.org/10.1016/j.rgg.2015.11.011
309. Nowell D.A.G., 1999. Gravity terrain corrections - An overview. *Journal of Applied Geophysics*, 42(2), 117-134. https://doi.org/10.1016/S0926-9851(99)00028-2
310. Oldenburg D.W., 1974. The inversion and interpretation of gravity anomalies. *Geophysics*, 39(4), 526-536. https://doi.org/10.1190/1.1440444
311. Onal K.M., Buyuksarac A., Aydemir A., Ates A., 2008. Investigation of the deep structure of the Sivas Basin (innereast Anatolia, Turkey) with geophysical methods. *Tectonophysics*, 460(1), 186-197. http://dx.doi.org/10.1016/j.tecto.2008.08.006
312. Oruç B., 2011. Edge detection and depth estimation using a tilt angle map from gravity gradient data of the Kozaklı-Central Anatolia region, Turkey. *Pure and Applied Geophysics*, 168(10), 1769-1780. https://doi.org/10.1007/s00024-010-0211-0
313. Papadeas G., 2002. Geological investigations on Attiki. 159p., University of Athens, Athens (*In Greek*).
314. Papadimitriou P., Kaviris G., Voulgaris N., Kassaras I., Delibasis N., Makropoulos K., 2000. The September 7, 1999 Athens earthquake sequence recorded by the Cornet Network:

preliminary results of source parameters determination of the mainshock. *Annales Géologiques des Pays Helléniques*, 38(B), 29-39.

315. Papadimitriou P., Voulgaris N., Kassaras I., Kaviris G., Delibasis N., Makropoulos K., 2002. The M_w= 6.0, 7 September 1999 Athens earthquake. *Natural Hazards*, 27(1), 15-33. https://doi.org/10.1023/A:1019914915693
316. Papadopoulos G.A., Drakatos G., Papanastassiou D., Kalogeras I., Stavrakakis G., 2000a. Preliminary results about the catastrophic earthquake of 7 September 1999 in Athens, Greece. *Seismological Research Letters*, 71(3), 318-329. Doi: 10.1785/gssrl.71.3.318
317. Papadopoulos G.A., Drakatos G., Papanastassiou D., Kalogeras I., Stavrakakis G., 2001b. Erratum: Preliminary Results about the Catastrophic Earthquake of 7 September 1999 in Athens, Greece. *Seismological Research Letters*, 72(1), 76-76. https://doi.org/10.1785/gssrl.72.1.76
318. Papadopoulos T., Alexopoulos J., Kambouris P., Tolis S., Kavounidis S., 2001. Contribution of modern seismic methods for subsurface investigations. An application at Kalogreza area (Athens). *Bulletin of the Geological Society of Greece*, 34(4), 1317-1323 (*In Greek*).
319. Papadopoulos T.D. and collaborators, 2003. Investigation of the deep structure of Central-west Attica with the contribution of geophysical soundings. *OASP Applied research program*, 90p., Athens (*In Greek*).
320. Papadopoulos T.D., Goulty N., Voulgaris N.S., Alexopoulos J.D., Fountoulis I., Kambouris P., Karastathis V., Peirce C., Chailas S., Kassaras J., Pirli M., 2007. Tectonic structure of Central-Western Attica (Greece) based on geophysical investigations-preliminary results. *Bulletin of the Geological Society of Greece*. 40(3), 1207-1218.
321. Papaioannou M., 2002. The use of geophysics in the detection of underground structures in urban environment. *PhD Thesis*, University of Patras, 125p. (*In Greek*). http://hdl.handle.net/10442/hedi/13562
322. Papanastassiou D., Stavrakakis G., Drakatos G., Papadopoulos G., 2000. The Athens, September 7, 1999, Ms= 5.9, earthquake: first results on the focal properties of the main shock and the aftershock sequence. *Annales Géologiques des Pays Helléniques*, 38, 73-88.
323. Papanikolaou D., 1986. Geology of Greece. *Heptalofos*, 240p., Athens (*In Greek*).
324. Papanikolaou D. and collaborators, 2002. Geological – Geotechnical study of Athens basin. *OASP Applied research program*, 152p., Athens (*In Greek*).
325. Papanikolaou D., Bassi E.K., Kranis H., Danamos G., 2004a. Paleogeographic evolution of the Athens basin from upper Miocene to present. *Bulletin of the Geological Society of Greece*, 36(2), 816-825 (*In Greek*).

326. Papanikolaou D., Chronis G., Lykousis V., Pavlakis P., Roussakis G., Syskakis D., 1989a. Submarine Neotectonic Map of Saronikos Gulf, Scale 1:100.000. Publication of Earthquake, Planning and Protection Organization-University of Athens, Athens.
327. Papanikolaou D., Chronis G., Lykousis V., Pavlakis P., Roussakis G., Syskakis D., 1989b. Submarine Neotectonic Map of Southern Evoikos Gulf, Scale 1:100.000. Publication of Earthquake, Planning and Protection Organization-University of Athens, Athens.
328. Papanikolaou D., Lekkas E., Sideris Ch., Fountoulis I., Danamos G., Kranis Ch., Lozios S., Antoniou I., Vassilakis E., Vasilopoulou S., Nomikou P., Papanikolaou I., Skourtsos E., Soukis K., 1999. Geology and tectonics of Western Attica in relation to the 7-9-99 earthquake. *Newsletter of the European Centre on Prevention and Forecasting of Earthquakes (Council of Europe)*, 3, 30-34.
329. Papanikolaou D. & Lozios S., 1990. Comparative neotectonic structure of high (Korinthia-Beotia) and low rate (Attica-Cyclades) activity. *Bulletin of the Geological Society of Greece*, 26, 47-65 (*In Greek*).
330. Papanikolaou D.I., Lozios S.G., Soukis K., Skourtsos E., 2004b. The geological structure of the allochthonous 'Athens Schists'. *Bulletin of the Geological Society of Greece*, 36(4), 1550-1559 (*In Greek*).
331. Papanikolaou D., Mariolakos I., Lekkas E.L., Lozios S.G., 1988. Morphotectonic observations on the Asopos basin and the Coastal zone of Oropos. Contribution to the Neotectonic of Northern Attica. *Bulletin of the Geological Society of Greece*, 20(1), 251-267 (*In Greek*).
332. Papanikolaou D. & Papanikolaou I., 2007. Geological, geomorphological and tectonic structure of NE Attica and seismic hazard implications for the northern edge of the Athens plain. *Bulletin of the Geological Society of Greece*, 40, 425-438.
333. Papanikolaou I.D., Papanikolaou D.I., Lekkas E.L., 2008. Low slip-rate faults around big cities: a challenging threat. The Afidnes fault as a case study for the city of Athens. In: *Proceedings of the 14th World Conference on Earthquake Engineering*, 12-17, Beijing, China.
334. Papazachos C.B., Karakostas B.G., Karakaisis G.F., Papaioannou Ch.A., 2001. The Athens 1999 mainshock (Mw=5.9) and the evolution of its aftershock sequence. *Bulletin of the Geological Society of Greece*, 34(4), 1581-1586.
335. Paraskevaidis H. & Chorianopoulou P., 1978. The Aegaleos mountain and the Athens schists. *Bulletin of the Geological Society of Greece*, 13(2), 116-136 (*In Greek*).
336. Parasnis D.S., 1952. A study of rock densities in the English Midlands. *Geophysical Supplements to the Monthly Notices of the Royal Astronomical Society*, 6(5), 252-271. https://doi.org/10.1111/j.1365-246X.1952.tb03013.x

337. Parcharidis I. & Foumelis M., 2005. On the assessment of co-seismic InSAR images of different time span associated to Athens (Greece) 1999 earthquake. In: *Proceedings of International Geoscience and Remote Sensing Symposium (IGARSS'05)*, 7, 5251-5254.
338. Parcharidis I., Lagios E., Sakkas V., Raucoules D., Feurer D., Le Mouélic S., King C., Carnec C., Novali F., Ferretti A., Capes R., Cooksley G., 2006. Subsidence monitoring within the Athens Basin (Greece) using space radar interferometric techniques. *Earth, Planets and Space*, 58(5), 505-513. http://doi.org/10.1186/BF03351947
339. Park C.H., Kim J.W., Isezaki N., Roman D.R., von Frese R.R., 2006. Crustal analysis of the Ulleung Basin in the East Sea (Japan Sea) from enhanced gravity mapping. *Marine Geophysical Researches*, 27(4), 253-266. Doi: 10.1007/s11001-006-9006-1
340. Pamukçu O., Gönenç T., Uyanik O., Sözbilir H., Çakmak O., 2014. A microgravity model for the city of İzmir (Western Anatolia) and its tectonic implementations. *Acta Geophysica*, 62(4), 849-871. https://doi.org/10.2478/s11600-014-0203-z
341. Parker R.L., 1973. The rapid calculation of potential anomalies. *Geophysical Journal International*, 31(4), 447-455. https://doi.org/10.1111/j.1365-246X.1973.tb06513.x
342. Pavlopoulos K.P., 1992. Geomorphological evolution of South Attica. *PhD Thesis*, University of Athens, 390p. (*In Greek*). http://hdl.handle.net/10442/hedi/2059
343. Pavlopoulos K.P., Kotabasi X., Skentos A., 2005. Geomorphological evolution of the basin of Athens. *Bulletin of the Geological Society of Greece*, 38, 1-13 (*In Greek*).
344. Panisova J., Pašteka R., Papco J., Fraštia M., 2012. The calculation of building corrections in microgravity surveys using close range photogrammetry. *Near Surface Geophysics*, 10(5), 391-399. Doi:10.3997/1873-0604.2012034
345. Pawlowski R.S., 1994. Green's equivalent-layer concept in gravity band-pass filter design. *Geophysics*, 59(1), 69-76. https://doi.org/10.1190/1.1443535
346. Pazzi V., Tapete D., Cappuccini L., Fanti R., 2016. An electric and electromagnetic geophysical approach for subsurface investigation of anthropogenic mounds in an urban environment. *Geomorphology*, 273, 335-347. https://doi.org/10.1016/j.geomorph.2016.07.035
347. Pearson-Grant S.C., Franz P., Clearwater J., 2018. Gravity measurements as a calibration tool for geothermal reservoir modelling. *Geothermics*, 73, 146-157. https://doi.org/10.1016/j.geothermics.2017.06.006
348. Pedersen L.B., 1977. Interpretation of potential field data: A generalized inverse approach. *Geophysical Prospecting*, 25(2), 199-230. Doi: 10.1111/j.1365-2478.1977.tb01164.x
349. Peters L.J., 1949. The direct approach to magnetic interpretation and its practical application. *Geophysics*, 14(3), 290-320. https://doi.org/10.1190/1.1437537
350. Petrascheck W.E. & Marinos G., 1953. Zur Geologie von Attika. *Kober Festschr*, 52-59, Univ. Wien. (*In German*).

351. Philippson A., 1898. La tectonique de l'Égéide (Grèce, Mer Egée, Asie Mineure Occidentale). *Annales de Géographie*, 7(32), 112-141 (*In French*). http://www.jstor.org/stable/23443914
352. Photiades A. & Carras N., 2001. Statigraphy and geological structure of the Lavrion area (Attica, Greece). *Bulletin of the Geological Society of Greece*, 34(1), 103-109.
353. Pilkington M. & Shamsipour P., 2014. Noise reduction procedures for gravity-gradiometer data. *Geophysics*, 79(5), G69-G78. https://doi.org/10.1190/geo2014-0084.1
354. Pirli M., 2001. Seismic characteristics of the aftershock sequence of Athens earthquake (07/09/1999, M_S=5.9). *MSc. Thesis*, University of Athens, 141p. (*In Greek*).
355. Piroddi L., Ranieri G., Manconi M., Piga C., Deidda G.P., Loddo F., Belghazal H., 2009. Synergical use of passive and active methods to reconstruct the subsoil in urban areas. In: *Near Surface 2009-15th EAGE European Meeting of Environmental and Engineering Geophysics*, P01. Doi: 10.3997/2214-4609.20147075
356. Poll K. & Theodoropoulos D., 1971 Anwendung von Computern in des Tektonik an Beispilen aus den Helleniden und aus den Ostalpen. *Annales Géologiques des Pays Helléniques*, 23, 23-57 (*In German*).
357. Pomonis A., 2002. The mount Parnitha (Athens) earthquake of September 7, 1999: a disaster management perspective. *Natural Hazards*, 27(1-2), 171-199. https://doi.org/10.1023/A:1019989512220
358. Priestnall G., Jaafar J., Duncan A., 2000. Extracting urban features from LiDAR digital surface models. *Computers, Environment and Urban Systems*, 24(2), 65-78. https://doi.org/10.1016/S0198-9715(99)00047-2
359. Prutkin I., Vajda P., Tenzer R., Bielik M., 2011. 3D inversion of gravity data by separation of sources and the method of local corrections: Kolarovo gravity high case study. *Journal of Applied Geophysics*, 75(3), 472-478. https://doi.org/10.1016/j.jappgeo.2011.08.012
360. Radogna P.V., Olivier R., Logean P., 2003. Micro-gravity survey in urban environment: modelling, evaluation and correction of buildings influence. In: *9th EAGE/EEGS Meeting*, P-006.
361. Radogna P.V., Olivier R., Logean P., 2004. A Subway Project in Lausanne, Switzerland, As an Urban Microgravimetry Test Site: Acquisition, Correction of Buildings Influence and Modeling. In: *17th EEGS Symposium on the Application of Geophysics to Engineering and Environmental Problems*.
362. Rajasekhar R.P. & Mishra D.C., 2008. Crustal structure of Bengal basin and Shillong plateau: extension of Eastern Ghat and Satpura mobile belts to Himalayan fronts and seismotectonics. *Gondwana Research*, 14(3), 523-534. https://doi.org/10.1016/j.gr.2007.10.009

363. Rasmussen R. & Pedersen L.B., 1979. End corrections in potential field modeling. *Geophysical Prospecting*, 27(4), 749-760. Doi: 10.1111/j.1365-2478.1979.tb00994.x
364. Raum T., Mjelde R., Digranes P., Shimamura H., Shiobara H., Kodaira S., Haatvedt G., Sørenes N., Thorbjørnsen T., 2002. Crustal structure of the southern part of the Vøring Basin, mid-Norway margin, from wide-angle seismic and gravity data. *Tectonophysics*, 355(1-4), 99-126. https://doi.org/10.1016/S0040-1951(02)00136-1
365. Re D.L., Florio G., Ferranti L., Lalongo S., Castiello G., 2016. Self-constrained inversion of microgravity data along a segment of the Irpinia fault. *Journal of Applied Geophysics*, 124, 148-154. https://doi.org/10.1016/j.jappgeo.2015.12.002
366. Reamer S.K. & Ferguson J.F., 1989. Regularized two-dimensional Fourier gravity inversion method with application to the Silent Canyon caldera, Nevada. *Geophysics*, 54(4), 486-496. https://doi.org/10.1190/1.1442675
367. Reid A.B., Allsop J.M., Granser H., Millett A.T., Somerton I.W., 1990. Magnetic interpretation in three dimensions using Euler deconvolution. *Geophysics*, 55(1), 80-91. https://doi.org/10.1190/1.1442774
368. Reid A.B., Ebbing J., Webb S.J., 2012. Comment on 'A crustal thickness map of Africa derived from a global gravity field model using Euler deconvolution'by Getachew E. Tedla, M. van der Meijde, AA Nyblade and FD van der Meer. *Geophysical Journal International*, 189(3), 1217-1222. https://doi.org/10.1111/j.1365-246X.2012.05353.x
369. Reid A.B., Ebbing J., Webb S.J., 2014a. Avoidable Euler errors–the use and abuse of Euler deconvolution applied to potential fields. *Geophysical Prospecting*, 62(5), 1162-1168. Doi: 10.1111/1365-2478.12119
370. Reid A.B. & Thurston J. B., 2014b. The structural index in gravity and magnetic interpretation: Errors, uses, and abuses. *Geophysics*, 79(4), J61-J66. https://doi.org/10.1190/geo2013-0235.1
371. Remondino F., Barazzetti L., Nex F., Scaioni M., Sarazzi D., 2011. UAV photogrammetry for mapping and 3D modeling–current status and future perspectives. *International Archives of the Photogrammetry, Remote Sensing and Spatial Information Sciences*, 38(1), C22.
372. Renz C., 1908. Sur les preuves de l'existence du Carbonifère et du Trias dans l'Attique. *Bulletin de la Societe Geologique de France*, 8, 519-523 (*In French*).
373. Renz C., 1909. Der Nachweis von Carbon und Trias in Attika. *Zentr. Miner*, 84-87, Stuttgart (*In German*).
374. Renz C., 1940. Die Tektonik der Griechischen Gebirge. *Proceedings of Athens Academy*, 8, 255-257 (*In German*).
375. Ring U., Glodny J., Will T., Thomson S., 2007. An Oligocene extrusion wedge of blueschist-facies nappes on Evia, Aegean Sea, Greece: Implications for the early exhumation of high-pressure rocks. *Journal of the Geological Society*, 164(3), 637-652.

https://doi.org/10.1144/0016-76492006-041

376. Roach M.J., Leaman D.E., Richardson R.G., 1993. A comparison of regional–residual separation techniques for gravity surveys. *Exploration Geophysics*, 24(3/4), 779-784.
377. Robertson E.I., 1965. Gravity base stations in the south-west Pacific Ocean. *New Zealand Journal of Geology and Geophysics*, 8(3), 424-439. https://doi.org/10.1080/00288306.1965.10426414
378. Rondoyanni T., Mettos A., Galanakis D., Georgiou C., 2000. The Athens earthquake of September 7, 1999: its setting and effects. *Annales Géologiques des Pays Helléniques*, 38, 131-144.
379. Rossi M., Dahlin T., Olsson P.I., Günther T., 2018. Data acquisition, processing and filtering for reliable 3D resistivity and time-domain induced polarisation tomography in an urban area: field example of Vinsta, Stockholm. *Near Surface Geophysics*, 16(3), 220-229. Doi: 10.3997/1873-0604.2018014
380. Rossi M., Olsson P.I., Dahlin T., 2017. Mapping Bedrock Lithology in Urban Environment via Large Scale Time Domain Induced Polarization Tomography. In: *23rd European Meeting of Environmental and Engineering Geophysics*.
381. Roumelioti Z., Dreger D., Kiratzi A., Theodoulidis N., 2003a. Slip distribution of the 7 September 1999 Athens earthquake inferred from an empirical Green's function study. *Bulletin of the Seismological Society of America*, 93(2), 775-782. https://doi.org/10.1785/0120020053
382. Roumelioti Z., Kiratzi A., Theodoulidis N., Kalogeras I., Stavrakakis G., 2003b. Rupture directivity during the September 7, 1999 (M W 5.9) Athens (Greece) earthquake inferred from forward modeling of strong ground motion. *Pure and Applied Geophysics*, 160(12), 2301-2318. https://doi.org/10.1007/s00024-003-2395-z
383. Roumelioti Z., Kiratzi A., Theodulidis N., 2004. Stochastic strong ground-motion simulation of the 7 September 1999 Athens (Greece) earthquake. *Bulletin of the Seismological Society of America*, 94(3), 1036-1052. https://doi.org/10.1785/0120030219
384. Sabatakakis N., 1991. Engineering geological setting of Athens basin. *PhD Thesis*, University of Patras, 216p. (*In Greek*). http://hdl.handle.net/10442/hedi/1734
385. Saibi H. & Aboud E., 2013. Gravity Analysis for Geothermal Reconnaissance in Costa Rica. In: *2nd EAGE International Conference on Engineering Geophysics*. Doi: 10.3997/2214-4609.20131872
386. Sainz-Maza S., Montesinos F.G., Martí J., Arnoso J., Calvo M., Borreguero A., 2017. Structural interpretation of El Hierro (Canary Islands) rifts system from gravity inversion modelling. *Tectonophysics*, 712, 72-81. https://doi.org/10.1016/j.tecto.2017.05.010

387. Salem A.S.K., Campell S., Derek J.D., Dickinson J., Murphy C., 2011. Interpretation of Tensor Gravity Data Using an Adaptive Tilt Angle Technique. In: *73rd EAGE Conference and Exhibition*, Extended Abstract – P283, Vienna, Austria.
388. Saltus R.W. & Blakely R.J., 1983. *HYPERMAG: An interactive, two-dimensional gravity and magnetic modeling program*. US Geological Survey, Open-file Report No. 83-241.
389. Sambridge M., Braun J., McQueen H., 1995. Geophysical parametrization and interpolation of irregular data using natural neighbours. *Geophysical Journal International*, 122(3), 837-857. https://doi.org/10.1111/j.1365-246X.1995.tb06841.x
390. Sampath A. & Shan J., 2007. Building boundary tracing and regularization from airborne LiDAR point clouds. *Photogrammetric Engineering & Remote Sensing*, 73(7), 805-812. https://doi.org/10.14358/PERS.73.7.805
391. Sanchez-Rojas J. & Palma M., 2014. Crustal density structure in northwestern South America derived from analysis and 3-D modeling of gravity and seismicity data. *Tectonophysics*, 634, 97-115. https://doi.org/10.1016/j.tecto.2014.07.026
392. Sandwell D.T. & Smith W.H., 1997. Marine gravity anomaly from Geosat and ERS 1 satellite altimetry. *Journal of Geophysical Research: Solid Earth*, 102(B5), 10039-10054. Doi: 10.1029/96JB03223
393. Sander B.K. & Cawthorn R.G., 1996. 2.5-D gravity model of the Ni-Cu-PGM mineralized Mount Ayliff Intrusion (Insizwa Complex), South Africa. *Journal of Applied Geophysics*, 35(1), 27-43. https://doi.org/10.1016/0926-9851(95)00027-5
394. Sargeant S.L., Burton P.W., Douglas A., Evans J.R., 2002. The source mechanism of the Athens earthquake, September 7, 1999, estimated from P seismograms recorded at long range. *Natural Hazards*, 27(1), 35-45. https://doi.org/10.1023/A:1019924508035
395. Saribudak M., 2010. Urban Geophysics: A Mapping of Mount Bonnell Fault and Its Karstic Features in Austin, Tx. In: *23rd EEGS Symposium on the Application of Geophysics to Engineering and Environmental Problems*.
396. Schmoker J.W., 1978. Accuracy of borehole gravity data. *Geophysics*, 43(3), 538-542. https://doi.org/10.1190/1.1440834
397. Sevil J., Gutiérrez F., Zarroca M., Desir G., Carbonel D., Guerrero J., Linares R., Roque C., Fabregat, I., 2017. Sinkhole investigation in an urban area by trenching in combination with GPR, ERT and high-precision leveling. Mantled evaporite karst of Zaragoza city, NE Spain. *Engineering Geology*, 231, 9-20. https://doi.org/10.1016/j.enggeo.2017.10.009
398. Shafie N.H., Hamzah U., Samsudin A.R., 2014. 2D gravity inversion technique in the study of Cheshire basin. *Electronic Journal of Geotechnical Engineering*, 19, 4381-4394.
399. Shafie N.H., Hamzah U., Samsudin A.R., Ibrahim A., 2016. Basement depth estimation of Cheshire Basin in Northwest England by power spectrum analysis of gravity data. *Electronic Journal of Geotechnical Engineering*, 21(1), 395-408.

400. Sharma P.V., 1986. *Geophysical Methods in Geology*. Elsevier, 428p. ISBN: 978-0-44441-235-5
401. Sindowski K.H., 1949. Der geologische Bau von Attika. *Annales Géologiques des Pays Helléniques*, 2, 163-218 (*In German*).
402. Sindowski K.H., 1950. Zur Geologie des Lykabettos-Turkovuni_Gebietes bei Athen. *Annales Géologiques des Pays Helléniques*, 3, 11-21 (*In German*).
403. Sirles P., Batchko Z., Pullammanappallil S., Shawver J.B., 2009. Mapping top-of-rock and soft-soil zones beneath high-traffic areas using 2D ReMi. In: *22nd EEGS Symposium on the Application of Geophysics to Engineering and Environmental Problems*.
404. Skounakis S., 1972. The volcanic rocks of Athens basin and the connected metallogenesis. *PhD Thesis*, University of Athens, 96p. (*In Greek*). http://hdl.handle.net/10442/hedi/6396
405. Skylodimou H., 2002. Geomorphologic and environmental study of the coastal zone of southwestern Attica. *PhD Thesis*, University of Athens, 267p. (*In Greek*). http://hdl.handle.net/10442/hedi/17035
406. Slack H.A., Lynch V.M., Langan L., 1967. The geomagnetic gradiometer. *Geophysics*, 32(5), 877-892. https://doi.org/10.1190/1.1439897
407. Smith N., Cassidy J., Locke C.A., Mauk J.L., Christie A.B., 2006. The role of regional-scale faults in controlling a trapdoor caldera, Coromandel Peninsula, New Zealand. *Journal of Volcanology and Geothermal Research*, 149(3-4), 312-328. https://doi.org/10.1016/j.jvolgeores.2005.09.005
408. Sokolov K.P., 1956. *Geological Interpretation of Magnetic Surveys*. Soviet Government Pub., Agency for Scientific Technical Literature on Geology and the Conservation of Mineral Resources, Gosgeoltechizdat, Moscow, 127p.
409. Son S.W., Tandon N.F., Polvani L.M., Waugh D.W., 2009. Ozone hole and Southern Hemisphere climate change. *Geophysical Research Letters*, 36(15), L15705, 5p. Doi: 10.1029/2009GL038671
410. Spanos D., 2012. Geodynamic evolution of Attica. *PhD Thesis*, University of Patras, 216p. (*In Greek*). http://hdl.handle.net/10442/hedi/28050
411. Spector A. & Grant F.S., 1970. Statistical models for interpreting aeromagnetic data. *Geophysics*, 35(2), 293-302. https://doi.org/10.1190/1.1440092
412. Srivastava R.P., Vedanti N., Dimri V.P., 2015. New gravity bases in Jabera-Damoh Vindhyan basin, central India. *Journal of the Geological Society of India*, 85(3), 359-366. https://doi.org/10.1007/s12594-015-0225-4
413. Stamatis G., Antoniou V., Migkiros G., 1994. Hydrogeological and geotechnical conditions of Athens central area. *Bulletin of the Geological Society of Greece*, 30(4), 367-380 (*In Greek*).

414. Stavrakakis G.N., Chouliaras G., Panopoulou G., 2002. Seismic source parameters for the M L= 5.4 Athens earthquake (7 September 1999) from a new telemetric broad band seismological network in Greece. *Natural Hazards*, 27(1), 47-60. https://doi.org/10.1023/A:1019939628612
415. Stoulos S., Manolopoulou M., Papastefanou C., 2003. Assessment of natural radiation exposure and radon exhalation from building materials in Greece. *Journal of Environmental Radioactivity*, 69(3), 225-240. https://doi.org/10.1016/S0265-931X(03)00081-X
416. Sultan S.A., Mekhemer H.M., Santos F.A.M., Alla M.A., 2009a. Geophysical measurements for subsurface mapping and groundwater exploration at the central part of the Sinai Peninsula, Egypt. *Arabian Journal for Science and Engineering*, 34(1A), 103-119.
417. Sultan S.A., Mohameden M.I., Santos F.M., 2009b. Hydrogeophysical study of the El Qaa Plain, Sinai, Egypt. *Bulletin of Engineering Geology and the Environment*, 68(4), 525-537. https://doi.org/10.1007/s10064-009-0216-z
418. Sultan S.A., Santos F.A., Helaly A.S., 2011. Integrated geophysical interpretation for the area located at the eastern part of Ismailia Canal, Greater Cairo, Egypt. *Arabian Journal of Geosciences*, 4(5-6), 735-753. https://doi.org/10.1007/s12517-009-0085-6
419. Syberg F.J.R., 1972. A Fourier method for the regional-residual problem of potential fields. *Geophysical Prospecting*, 20(1), 47-75. Doi: 10.1111/j.1365-2478.1972.tb00619.x
420. Symeonidis K., Papadopoulos T.D., Alexopoulos J., 2005. Use of surface waves for geotechnical characterization of neogene deposits - The Glyfada, Athens case study. In: *Near Surface 2005-11th European Meeting of Environmental and Engineering Geophysics*.
421. Szeto A., 2006. How Well Can One Determine the Density of a Box-Like Building Using Gravity Measurements? In: *19th EEGS Symposium on the Application of Geophysics to Engineering and Environmental Problems*.
422. Talwani M. & Ewing M., 1960. Rapid computation of gravitational attraction of three-dimensional bodies of arbitrary shape. *Geophysics*, 25(1), 203-225. https://doi.org/10.1190/1.1438687
423. Talwani M. & Heirtzler J.R., 1964. Computation of magnetic anomalies caused by two-dimensional bodies of arbitrary shape. In: *Parks G.A., (Ed.), Computers in the Mineral Industries*, Part 1. Stanford Univ. Publ., Geological Sciences, 9. 464-480.
424. Talwani M., Worzel J.L., Landisman M., 1959. Rapid gravity computations for two-dimensional bodies with application to the Mendocino submarine fracture zone. *Journal of Geophysical Research*, 64(1), 49-59. Doi: 10.1029/JZ064i001p00049

425. Tataris A.A., 1966. Observations on the structure of Skaramaga-Aegaleo Mountain-Piraeus-Athens area (Attica). *Bulletin of the Geological Society of Greece*, 7(1), 52-58 (*In Greek*).
426. Tataris A.A., 1972. Recent results on the geology of Salamis island and Attiki area. *Bulletin of the Geological Society of Greece*, 9(2), 482-514 (*In Greek*).
427. Tataris A.A & Sideris Ch., 1989. Geology of S. Aegaleo Mt. and correlation with the opposite part of Salamis Island. *Bulletin of the Geological Society of Greece*, 23(1), 303-320 (*In Greek*).
428. Tedla G.E., Van Der Meijde M., Nyblade A.A., Van der Meer F.D., 2011. A crustal thickness map of Africa derived from a global gravity field model using Euler deconvolution. *Geophysical Journal International*, 187(1), 1-9. https://doi.org/10.1111/j.1365-246X.2011.05140.x
429. Telford W.M., Geldart L.P., Sheriff R.E., 1990. *Applied Geophysics.* Cambridge University Press. 770p. ISBN 0-521-33938-3
430. ten Brink U.S., Coleman D.F., Dillon W.P., 2002. The nature of the crust under Cayman Trough from gravity. *Marine and Petroleum Geology*, 19(8), 971-987. https://doi.org/10.1016/S0264-8172(02)00132-0
431. Theocharis D., 2001. Neotectonic Fault system of Salamina Island. *MSc. Thesis*, University of Athens (*In Greek*).
432. Thierry P., Debeblia N., Bitri A., 2005. Geophysical and geological characterisation of karst hazards in urban environments: application to Orléans (France). *Bulletin of Engineering Geology and the Environment*, 64(2), 139-150. https://doi.org/10.1007/s10064-004-0247-4
433. Thompson D.T., 1982. EULDPH: A new technique for making computer-assisted depth estimates from magnetic data. *Geophysics*, 47(1), 31-37. https://doi.org/10.1190/1.1441278
434. Tikhonov A.N. & Arsenin V.I., 1977. *Solutions of ill-Posed Problems*. John-Wiley & Sons, New York.
435. Tokunaga M., 2015. Accuracy verification of DSM obtained from UAV using commercial software. In: Geoscience and Remote Sensing Symposium (IGARSS), IEEE International, 3022-3024. Doi: 10.1109/IGARSS.2015.7326452
436. Tontini F.C., de Ronde C.E., Scott B.J., Soengkono S., Stagpoole V., Timm C., Tivey M., 2016. Interpretation of gravity and magnetic anomalies at Lake Rotomahana: geological and hydrothermal implications. *Journal of Volcanology and Geothermal Research*, 314, 84-94. https://doi.org/10.1016/j.jvolgeores.2015.07.002
437. Triantaphyllou M.V., Pavlopoulos K.P., Kouli K., Koukousioura O., Dimiza M.D., Aidona, E., Syrides G., Pallikarakis A., Goiran J.P., Fouache E., 2016. Multiproxy

paleoenvironmental reconstruction: The Piraeus coastal plain case study. *Bulletin of the Geological Society of Greece*, 50(1), 478-488. http://dx.doi.org/10.12681/bgsg.11749

438. Trogu A., Ranieri G., Piga C., Piroddi L., 2012. Gravity survey: a tool for urban planning. In: *Proceedings of the 7th International Conference on Informatics and Urban Regional Planning INPUT*, 811-820.
439. Tselentis G.A. & Zahradnik J., 2000a. The Athens earthquake of 7 September 1999. *Bulletin of the Seismological Society of America*, 90(5), 1143-1160. https://doi.org/10.1785/0119990168
440. Tselentis G.A. & Zahradnik J., 2000b. Aftershock monitoring of the Athens earthquake of 7 September 1999. *Seismological Research Letters*, 71(3), 330-337. Doi: 10.1785/gssrl.71.3.330
441. Tsokas G.N., Tsourlos P.I., Vargemezis G., Novack M., 2008. Non-destructive electrical resistivity tomography for indoor investigation: the case of Kapnikarea Church in Athens. *Archaeological Prospection*, 15(1), 47-61. Doi: 10.1002/arp.321
442. Tsourlos P.I. & Tsokas G.N., 2011. Non-destructive Electrical Resistivity Tomography Survey at the South Walls of the Acropolis of Athens. *Archaeological Prospection*, 18(3), 173-186. Doi: 10.1002/arp.416
443. Tzitziras A., Rozos D., Vakondios I., Elias P., Kynigalaki M., Nikolaou N., Konstantopoulou G., 2000. Macroseismic observations from the earthquake of 7/9/99 in Attiki area. *Annales Géologiques des Pays Helléniques*, 38, 145-152. (*In Greek*).
444. Vacquier V., Steenland N.C., Henderson R.G., Zietz I., 1951. Interpretation of aeromagnetic maps. *Geological Society of America Memoirs*, 47, 1-150. Doi: 10.1130/MEM47-p1
445. Vandarakis D., 2013. The palaeogeographical evolution of the Athenian basin the last 6.000 years. *PhD Thesis*, Harokopio University, 238p., Athens (*In Greek*)
446. Vandarakis D., Pavlopoulos K., Vouvalidis K., Fouache E., 2016. Holocene lithostratigraphy and its implementation in the geoarchaeological research of the Athenian Basin, Greece. *Archaeological and Anthropological Sciences*, 8(3), 441-452. https://doi.org/10.1007/s12520-014-0203-6
447. Vosselman G. & Dijkman S., 2001. 3D building model reconstruction from point clouds and ground plans. *International Archives of Photogrammetry Remote Sensing and Spatial Information Sciences*, 34(3/W4), 37-44.
448. Voulgaris N., Kassaras I., Papadimitriou P., Delibasis N., 2000. Preliminary results of the Athens September 7, 1999 aftershock sequence. *Annales Géologiques des Pays Helléniques*, 38(B), 51-62.
449. Voulgaris N., Pirli M., Papadimitriou P., Kassaras J., Makropoulos K., 2001. Seismotectonic characteristics of the area of western Attica derived from the study of

the September 7, 1999 Athens earthquake aftershock sequence. *Bulletin of the Geological Society of Greece*, 34(4), 1645-1651.

450. Wahba G., 1990. Spline models for observational data. In: *CBMS-NSF Regional Conference Series in Applied Mathematics*., Vol. 59, Society for industrial and applied mathematics, Philadelphia.
451. Wang G., Zhang S., Yan C., Song Y., Sun Y., Li D., Xu F., 2011. Mineral potential targeting and resource assessment based on 3D geological modeling in Luanchuan region, China. *Computers & Geosciences*, 37(12), 1976-1988. https://doi.org/10.1016/j.cageo.2011.05.007
452. Wang W., Zhao J., Cheng Q., 2013. Application of singularity index mapping technique to gravity/magnetic data analysis in southeastern Yunnan mineral district, China. *Journal of Applied Geophysics*, 92, 39-49. https://doi.org/10.1016/j.jappgeo.2013.02.012
453. Warsi W.E., 1989. Gravity bases in the State of Kuwait. *Journal of the University of Kuwait-Science*, 16(2), 433-447.
454. Webring M., 1985. *SAKI: a FORTRAN Program for Generalized Linear Inversion of Gravity and Magnetic Profiles*. US Geological Survey, Open-file Report No. 85-122.
455. Wehr H., Chevrot S., Courrioux G., Guillen A., 2018. A three-dimensional model of the Pyrenees and their foreland basins from geological and gravimetric data. *Tectonophysics*, 734, 16-32. https://doi.org/10.1016/j.tecto.2018.03.017
456. Weidmann C., Gimenez M., Klinger F.L., Alvarez O., 2016. Anomalous values of gravity and magnetism in the western margin of Gondwana. *Tectonophysics*, 667, 1-15. https://doi.org/10.1016/j.tecto.2015.11.017
457. Whetton J.T., Myers J.O., Watson I.J., 1956. A gravimeter survey in the Craven district of north-west Yorkshire. *Proceedings of the Yorkshire Geological Society*, 30(3), 259-287. https://doi.org/10.1144/pygs.30.3.259
458. Williams R.A., Stephenson W.J., Pratt T.L., Odum J.K., 2006. Seismic imaging in urban areas: examples and lessons learned. In: *19th EEGS Symposium on the Application of Geophysics to Engineering and Environmental Problems*.
459. Whiteley R.J. & Stewart S.B., 2008. Engineering geophysics in Australia: urban case studies from downunder. In: *21st EEGS Symposium on the Application of Geophysics to Engineering and Environmental Problems*.
460. Wiener J., Galikeev T., Richardson C., Korotkov I., 2014. Optimizing Niobrara horizontal drilling through wireless urban 3D seismic survey. In: *2014 SEG Annual Meeting. Society of Exploration Geophysicists*. Denver, Colorado, USA.
461. Won I.J. & Bevis M., 1987. Computing the gravitational and magnetic anomalies due to a polygon: Algorithms and Fortran subroutines. *Geophysics*, 52(2), 232-238. https://doi.org/10.1190/1.1442298

462. Wu H., Li L., Xing C., Zhang S., 2017. A new method of edge detection based on the total horizontal derivative and the modulus of full tensor gravity gradient. *Journal of Applied Geophysics*, 139, 239-245. https://doi.org/10.1016/j.jappgeo.2017.02.026
463. Xu Y., Hao T., Li Z., Duan Q., Zhang L., 2009. Regional gravity anomaly separation using wavelet transform and spectrum analysis. *Journal of Geophysics and Engineering*, 6(3), 279-287. Doi:10.1088/1742-2132/6/3/007
464. Xu C., Wang H.H., Luo Z.C., Ning J.S., Liu H.L., 2015. Multilayer stress from gravity and its tectonic implications in urban active fault zone: A case study in Shenzhen, South China. *Journal of Applied Geophysics*, 114, 174-182. https://doi.org/10.1016/j.jappgeo.2015.01.017
465. Xu C., Wang H., Luo Z., Liu H., Liu X., 2017. Insight into urban faults by wavelet multi-scale analysis and modeling of gravity data in Shenzhen, China. *Journal of Earth Science*, 1-9. https://doi.org/10.1007/s12583-017-0770-4
466. Xypolias P., Kokkalas S., Skourlis K., 2003. Upward extrusion and subsequent transpression as a possible mechanism for the exhumation of HP/LT rocks in Evia Island (Aegean Sea, Greece). *Journal of Geodynamics*, 35(3), 303-332. https://doi.org/10.1016/S0264-3707(02)00131-X
467. Yan W.Y., Shaker A., El-Ashmawy N., 2015. Urban land cover classification using airborne LiDAR data: A review. *Remote Sensing of Environment*, 158, 295-310. https://doi.org/10.1016/j.rse.2014.11.001
468. Yan Y., Gao F., Deng S., Su N., 2017. A Hierarchical Building Segmentation in Digital Surface Models for 3D Reconstruction. *Sensors*, 17(2), 222, 14p., Doi:10.3390/s17020222
469. Yegorova T., Maystrenko Y., Bayer U., Scheck-Wenderoth M., 2008. The Glueckstadt Graben of the North-German Basin: new insights into the structure from 3D and 2D gravity analyses. *International Journal of Earth Sciences*, 97(5), 915-930. https://doi.org/10.1007/s00531-007-0228-5
470. Yu D., 2014. The Influence of Buildings on Urban Gravity Surveys. *Journal of Environmental and Engineering Geophysics*, 19(3), 157-164. Doi: 10.2113/JEEG19.3.157
471. Yu B., Liu H., Wu J., Hu Y., Zhang L., 2010. Automated derivation of urban building density information using airborne LiDAR data and object-based method. *Landscape and Urban Planning*, 98(3-4), 210-219. https://doi.org/10.1016/j.landurbplan.2010.08.004
472. Yuan B., Xie W., Liu G., Zhang C., 2012. Gravity field and tectonic features of Block L2 in the Lamu basin, Kenya. *Geophysical Prospecting*, 60(1), 161-178. Doi: 10.1111/j.1365-2478.2011.00961.x
473. Yu-shan Y., & Yuan-yuan L., 2018. Crustal structure of the Dabie orogenic belt (eastern China) inferred from gravity and magnetic data. *Tectonophysics*, 723, 190-200. https://doi.org/10.1016/j.tecto.2017.12.016

474. Zahra H.S. & Oweis H.T., 2016. Application of high-pass filtering techniques on gravity and magnetic data of the eastern Qattara Depression area, Western Desert, Egypt. *NRIAG Journal of Astronomy and Geophysics*, 5(1), 106-123. https://doi.org/10.1016/j.nrjag.2016.01.005
475. Zeng H., Xu D., Tan H., 2007. A model study for estimating optimum upward-continuation height for gravity separation with application to a Bouguer gravity anomaly over a mineral deposit, Jilin province, northeast China. *Geophysics*, 72(4), I45-I50. https://doi.org/10.1190/1.2719497
476. Zheng T., Chen L., Zhao L., Xu W., Zhu R., 2006. Crust–mantle structure difference across the gravity gradient zone in North China Craton: seismic image of the thinned continental crust. *Physics of the Earth and Planetary Interiors*, 159(1-2), 43-58. https://doi.org/10.1016/j.pepi.2006.05.004

Websites

1. DeepEarthScience (2013, October 22). T*he geoid.* Retrieved from: http://deepearthscience.blogspot.gr/search?q=geoid
2. National Geospatial-Intelligence Agency (2008). *EGM2008 2.5 Minute Geoid* Heights. Retrieved from: http://earth-info.nga.mil/GandG/wgs84/gravitymod/egm2008/egm08_wgs84.html

APPENDIX A – TABLE OF CALCULATED CORRECTIONS

Station	Tidal Correction	FreeAir Correction	Bouguer Correction	Terrain Correction	Building Correction
1001	0.029	43.232	15.691	0.866	0.066
1002	0.016	34.659	12.579	0.705	0.116
1003	0.002	25.871	9.389	0.603	0.064
1004	-0.011	29.167	10.586	0.805	0.051
1005	-0.026	37.611	13.650	0.696	0.123
1006	-0.031	42.629	15.471	0.816	0.088
1007	-0.033	41.568	15.087	0.661	0.102
1008	-0.032	44.338	16.092	0.624	0.057
1009	-0.030	33.867	12.291	0.757	0.053
1010	-0.028	16.795	6.096	0.543	0.072
1011	-0.028	12.113	4.396	0.561	0.034
1012	-0.029	36.179	13.130	0.777	0.104
1013	0.075	14.187	5.149	0.466	0.055
1014	0.059	21.923	7.956	0.514	0.114
1015	0.040	30.696	11.141	0.654	0.103
1016	0.017	45.822	16.630	1.289	0.078
1017	-0.010	13.616	4.942	0.450	0.054
1018	-0.030	22.171	8.047	0.491	0.069
1019	-0.042	24.346	8.836	0.632	0.004
1020	-0.049	7.467	2.710	0.430	0.016
1021	-0.052	8.869	3.219	0.374	0.027
1022	-0.052	6.481	2.352	0.369	0.064
1023	-0.049	14.842	5.387	0.464	0.030
1024	-0.046	22.888	8.307	0.601	0.103
1025	0.112	6.016	2.183	0.359	0.022
1026	0.100	5.644	2.048	0.335	0.107
1027	0.086	3.079	1.117	0.310	0.008
1028	0.065	6.011	2.181	0.335	0.001
1029	0.020	11.327	4.111	0.424	0.021
1030	-0.008	10.751	3.902	0.400	0.017
1031	-0.028	9.398	3.411	0.420	0.064
1032	-0.043	12.044	4.371	0.447	0.062
1033	-0.063	6.847	2.485	0.375	0.009
1034	-0.069	7.099	2.576	0.382	0.012
1035	-0.071	6.161	2.236	0.407	0.013
1036	-0.068	4.512	1.638	0.346	0.004
1037	-0.064	3.176	1.153	0.300	0.022
1038	0.132	78.184	28.376	1.363	0.015
1039	0.132	66.506	24.137	1.371	0.044
1040	0.125	49.556	17.986	1.011	0.013

1041	0.109	22.247	8.074	0.528	0.076
1042	0.092	22.200	8.057	0.511	0.170
1043	0.051	67.662	24.557	0.915	0.045
1044	0.015	57.052	20.706	1.024	0.081
1045	-0.013	30.839	11.192	0.562	0.142
1046	-0.035	23.682	8.595	0.525	0.048
1047	-0.064	48.302	17.530	0.465	0.042
1048	-0.077	55.662	20.202	0.462	0.007
1049	-0.083	48.606	17.641	0.477	0.003
1050	-0.085	43.007	15.609	0.592	0.020
1051	-0.082	47.725	17.321	0.692	0.030
1052	0.133	16.829	6.108	0.472	0.034
1053	0.143	14.501	5.263	0.474	0.024
1054	0.143	16.678	6.053	0.516	0.101
1055	0.132	19.873	7.212	0.639	0.056
1056	0.092	12.750	4.627	0.451	0.019
1057	0.061	12.146	4.408	0.436	0.009
1058	0.028	13.636	4.949	0.451	0.023
1059	-0.004	18.214	6.610	0.476	0.058
1060	-0.041	19.511	7.081	0.524	0.019
1061	-0.064	18.428	6.688	0.505	0.036
1062	-0.083	18.396	6.676	0.507	0.025
1063	-0.093	23.505	8.531	0.530	0.023
1064	-0.094	23.270	8.445	0.544	0.018
1065	0.122	92.938	33.730	0.750	0.011
1066	0.138	94.145	34.169	0.939	0.005
1067	0.146	93.392	33.895	0.975	0.019
1068	0.144	80.848	29.342	0.821	0.014
1069	0.135	83.970	30.476	0.792	0.020
1070	0.109	75.869	27.535	0.669	0.022
1071	0.077	75.800	27.510	0.634	0.006
1072	0.041	68.251	24.770	0.561	0.056
1073	0.007	69.629	25.271	0.555	0.048
1074	-0.041	81.117	29.440	0.571	0.025
1075	-0.068	78.524	28.499	0.520	0.061
1076	-0.086	73.764	26.771	0.537	0.057
1077	-0.097	60.153	21.832	0.496	0.029
1078	0.070	42.799	15.533	0.636	0.004
1079	0.096	50.486	18.323	0.583	0.044
1080	0.120	56.725	20.588	0.550	0.016
1081	0.134	68.008	24.683	0.643	0.034
1082	0.139	59.963	21.762	0.543	0.014
1083	0.129	40.001	14.518	0.531	0.045
1084	0.108	48.394	17.564	0.557	0.040

1085	0.086	47.157	17.115	0.525	0.027
1086	0.058	41.273	14.980	0.585	0.014
1087	0.027	53.333	19.356	0.636	0.028
1088	-0.021	36.685	13.314	0.577	0.062
1089	-0.048	45.760	16.608	0.567	0.060
1090	-0.069	29.638	10.757	0.565	0.013
1091	-0.088	24.320	8.827	0.553	0.030
1092	-0.098	30.820	11.186	0.554	0.092
1093	0.021	62.021	22.510	0.478	0.047
1094	0.056	67.574	24.525	0.931	0.005
1095	0.088	49.192	17.854	0.818	0.010
1096	0.105	34.411	12.489	0.541	0.046
1097	0.122	54.087	19.630	0.452	0.057
1098	0.120	61.864	22.453	0.438	0.017
1099	0.110	63.004	22.866	0.494	0.014
1100	0.092	61.467	22.308	0.427	0.037
1101	0.064	59.292	21.519	0.471	0.020
1102	0.023	50.592	18.361	0.475	0.063
1103	-0.007	53.845	19.542	0.454	0.031
1104	-0.035	60.727	22.040	0.587	0.056
1105	-0.061	71.938	26.109	0.886	0.001
1106	-0.085	56.707	20.581	0.513	0.047
1107	-0.010	1.359	0.493	0.264	0.032
1108	0.025	2.182	0.792	0.265	0.052
1109	0.055	1.332	0.484	0.293	0.016
1110	0.078	3.173	1.152	0.314	0.039
1111	0.100	0.631	0.229	0.250	0.065
1112	0.099	0.503	0.182	0.262	0.096
1113	0.089	1.044	0.379	0.334	0.024
1114	0.061	0.691	0.251	0.249	0.007
1115	0.026	3.358	1.219	0.229	0.074
1116	-0.005	2.631	0.955	0.295	0.039
1117	-0.038	6.793	2.465	0.358	0.033
1118	-0.061	2.626	0.953	0.310	0.079
1119	-0.040	7.816	2.837	0.389	0.041
1120	-0.017	13.359	4.848	0.494	0.035
1121	0.016	17.444	6.331	0.618	0.043
1122	0.037	19.476	7.069	0.610	0.058
1123	0.066	14.118	5.124	0.432	0.037
1124	0.075	20.461	7.426	0.544	0.055
1125	0.071	40.300	14.626	1.338	0.018
1126	0.057	68.362	24.811	2.663	0.005
1127	0.028	14.419	5.233	0.517	0.024
1128	0.007	24.266	8.807	0.693	0.017

1129	-0.027	30.595	11.104	0.874	0.041
1130	-0.055	64.864	23.542	2.417	0.004
1131	-0.057	17.672	6.414	0.527	0.063
1132	-0.037	27.497	9.980	0.788	0.029
1133	-0.015	72.430	26.287	1.773	0.019
1134	0.003	38.398	13.936	0.860	0.036
1135	0.033	23.851	8.656	0.556	0.019
1136	0.047	30.312	11.001	0.617	0.052
1137	0.050	44.532	16.162	0.907	0.046
1138	0.044	34.228	12.422	0.721	0.009
1139	0.028	19.344	7.021	0.562	0.069
1140	0.014	29.669	10.768	0.636	0.045
1141	-0.004	44.576	16.178	1.163	0.029
1142	-0.025	30.465	11.057	0.695	0.078
1143	-0.041	24.900	9.037	0.596	0.049
1144	-0.047	26.331	9.556	0.580	0.027
1145	-0.041	25.917	9.406	0.578	0.010
1146	-0.032	31.488	11.428	0.608	0.067
1147	-0.019	30.470	11.059	0.675	0.037
1148	0.002	31.334	11.372	0.595	0.023
1149	0.015	30.191	10.957	0.635	0.042
1150	0.022	33.671	12.220	0.723	0.056
1151	0.025	42.008	15.246	0.806	0.038
1152	0.026	59.650	21.649	1.377	0.005
1153	0.020	36.269	13.163	0.672	0.006
1154	0.012	34.422	12.493	0.667	0.004
1155	0.002	34.718	12.600	0.726	0.010
1156	-0.012	39.685	14.403	0.830	0.017
1157	-0.030	33.704	12.232	0.591	0.060
1158	0.004	53.913	19.567	0.468	0.014
1159	0.005	63.831	23.166	0.661	0.028
1160	0.002	83.078	30.152	1.573	0.005
1161	-0.002	71.656	26.007	0.955	0.021
1162	-0.008	55.481	20.136	0.562	0.012
1163	-0.018	56.706	20.581	0.486	0.043
1164	-0.028	57.744	20.957	0.568	0.052
1165	-0.039	58.124	21.095	0.753	0.006
1166	-0.013	48.122	17.465	0.647	0.006
1167	-0.013	59.566	21.619	1.029	0.051
1168	-0.014	67.822	24.615	1.512	0.023
1169	-0.017	50.134	18.195	0.855	0.028
1170	-0.023	59.155	21.470	1.160	0.081
1171	-0.031	65.478	23.764	1.547	0.009
1172	-0.040	61.361	22.270	1.544	0.010

1173	-0.027	29.475	10.697	0.796	0.041
1174	-0.028	28.968	10.513	0.651	0.033
1175	-0.028	39.175	14.218	0.914	0.048
1176	-0.029	53.270	19.334	1.341	0.078
1177	-0.031	45.560	16.535	1.026	0.050
1178	-0.033	71.832	26.070	1.854	0.006
1179	-0.035	84.907	30.816	2.653	0.010
1180	-0.037	20.203	7.333	0.491	0.073
1181	-0.040	22.135	8.034	0.546	0.060
1182	-0.041	32.163	11.673	0.740	0.071
1183	-0.040	50.616	18.370	1.204	0.019
1184	-0.038	61.387	22.279	2.099	0.007
1185	-0.036	87.495	31.755	3.284	0.027
1186	-0.036	27.054	9.819	0.859	0.067
1187	-0.043	39.327	14.273	1.300	0.035
1188	-0.049	55.162	20.020	2.122	0.033
1189	-0.052	65.819	23.888	3.694	0.043
1190	-0.052	35.188	12.771	1.474	0.018
1191	-0.048	19.732	7.161	0.563	0.041
1192	-0.043	24.931	9.048	0.919	0.029
1193	-0.038	22.126	8.030	0.637	0.030
1194	0.101	7.892	2.864	0.293	0.067
1195	0.096	7.570	2.748	0.296	0.045
1196	0.084	10.028	3.640	0.308	0.019
1197	0.066	9.769	3.545	1.798	0.015
1198	0.049	4.292	1.558	0.811	0.024
1199	0.022	14.282	5.183	0.446	0.028
1200	0.002	19.574	7.104	0.862	0.078
1201	-0.023	39.168	14.215	1.952	0.021
1202	-0.042	36.645	13.300	1.883	0.003
1203	-0.061	1.136	0.412	0.327	0.023
1204	-0.067	7.852	2.850	0.414	0.064
1205	-0.069	8.239	2.990	0.370	0.057
1206	-0.068	16.320	5.923	0.482	0.094
1207	-0.062	4.141	1.503	0.227	0.050
1208	-0.005	78.917	28.642	1.252	0.047
1209	-0.027	73.024	26.503	0.770	0.078
1210	-0.048	65.434	23.748	0.533	0.028
1211	-0.062	67.099	24.352	0.496	0.018
1212	-0.076	68.498	24.860	0.726	0.058
1213	-0.073	61.554	22.340	0.514	0.058
1214	-0.065	63.112	22.906	0.443	0.040
1215	-0.003	77.895	28.271	0.594	0.021
1216	-0.031	68.371	24.814	0.778	0.030

1217	-0.052	59.745	21.684	0.600	0.012
1218	-0.066	65.514	23.777	0.575	0.029
1219	-0.079	73.653	26.731	0.557	0.040
1220	-0.086	80.641	29.267	0.636	0.028
1221	-0.081	94.047	34.133	0.699	0.066
1222	0.028	106.525	38.662	0.913	0.023
1223	0.001	117.196	42.534	1.332	0.004
1224	-0.044	133.751	48.543	2.043	0.011
1225	-0.064	107.849	39.142	1.155	0.052
1226	-0.086	95.733	34.745	0.768	0.036
1227	-0.089	84.640	30.719	0.662	0.121
1228	-0.079	108.854	39.507	1.265	0.032
1229	-0.088	128.630	46.684	1.927	0.004
1230	-0.023	55.093	19.995	0.618	0.013
1231	0.005	53.781	19.519	0.653	0.016
1232	0.027	49.425	17.938	0.717	0.007
1233	0.044	46.860	17.007	0.628	0.016
1234	0.061	43.967	15.957	0.652	0.016
1235	0.063	45.195	16.403	0.732	0.006
1236	0.058	41.849	15.189	0.793	0.011
1237	0.042	60.419	21.928	1.308	0.005
1238	-0.007	36.454	13.230	0.752	0.038
1239	-0.031	64.370	23.362	1.299	0.007
1240	-0.054	67.613	24.539	2.182	0.002
1241	-0.074	53.502	19.418	1.187	0.049
1242	-0.084	72.718	26.392	2.361	0.002
1243	-0.050	48.772	17.701	0.999	0.011
1244	-0.023	53.207	19.310	0.848	0.033
1245	0.032	45.844	16.638	1.249	0.001
1246	0.040	45.718	16.593	0.873	0.008
1247	0.042	46.099	16.731	1.017	0.006
1248	0.039	49.189	17.852	1.310	0.011
1249	0.030	48.948	17.765	1.443	0.000
1250	0.007	47.820	17.355	1.260	0.015
1251	-0.009	53.729	19.500	1.277	0.010
1252	-0.026	52.392	19.015	1.446	0.002
1253	-0.047	66.216	24.032	1.636	0.000
1254	-0.074	67.134	24.365	1.872	0.003
1255	-0.025	15.696	5.697	0.447	0.060
1256	-0.024	5.691	2.066	0.390	0.051
1257	-0.024	0.522	0.189	0.297	0.011
1258	-0.028	3.258	1.182	0.287	0.113
1259	-0.036	5.997	2.177	0.376	0.088
1260	-0.043	4.743	1.721	0.356	0.041

1261	-0.045	9.549	3.466	0.484	0.026
1262	-0.042	3.962	1.438	0.378	0.008
1263	-0.040	13.539	4.914	0.516	0.025
1264	-0.040	4.143	1.504	0.495	0.014
1265	-0.062	9.002	3.267	0.414	0.018
1266	-0.055	15.048	5.462	0.582	0.014
1267	-0.049	26.845	9.743	1.254	0.002
1268	-0.043	15.683	5.692	0.844	0.062
1269	-0.039	20.519	7.447	0.902	0.012
1270	0.053	73.885	26.815	0.609	0.052
1271	0.034	64.736	23.495	0.646	0.003
1272	0.015	58.887	21.372	0.716	0.010
1273	-0.010	56.654	20.562	0.738	0.014
1274	-0.044	75.268	27.317	0.672	0.062
1275	-0.058	66.782	24.237	0.738	0.006
1276	-0.068	58.321	21.167	0.968	0.002
1277	-0.074	60.369	21.910	0.832	0.000
1278	-0.076	67.063	24.339	0.896	0.005
1279	-0.071	86.650	31.448	0.717	0.049
1280	-0.066	77.050	27.964	0.744	0.006
1281	-0.058	73.598	26.711	0.754	0.012
1282	-0.045	68.639	24.912	0.894	0.004
1283	0.109	87.048	31.593	0.946	0.106
1284	0.103	95.075	34.506	0.868	0.024
1285	0.089	106.120	38.514	1.477	0.023
1286	0.068	121.022	43.923	2.627	0.022
1287	0.049	130.934	47.520	2.810	0.004
1288	0.011	77.130	27.993	0.855	0.064
1289	-0.007	75.165	27.280	0.820	0.001
1290	-0.033	71.930	26.106	1.074	0.004
1291	-0.050	82.400	29.906	1.283	0.000
1292	-0.079	107.242	38.922	1.362	0.080
1293	-0.085	92.894	33.714	0.967	0.068
1294	-0.085	84.216	30.565	0.850	0.065
1295	-0.082	72.795	26.420	0.873	0.003
1296	-0.071	81.001	29.398	1.157	0.007
1297	0.026	68.309	24.792	0.492	0.013
1298	-0.004	68.529	24.872	0.523	0.045
1299	-0.033	74.467	27.027	0.637	0.021
1300	-0.062	95.807	34.772	1.270	0.016
1301	-0.085	82.766	30.039	0.792	0.002
1302	-0.097	70.225	25.487	0.543	0.020
1303	-0.096	69.752	25.315	0.510	0.025
1304	-0.090	77.990	28.305	1.255	0.009

1305	-0.022	90.729	32.929	0.838	0.045
1306	0.022	81.176	29.462	0.953	0.003
1307	0.035	87.520	31.764	0.788	0.002
1308	0.039	84.762	30.763	0.817	0.008
1309	0.040	99.817	36.227	0.904	0.062
1310	0.034	123.703	44.896	2.196	0.003
1311	0.025	145.338	52.748	3.913	0.010
1312	0.010	152.933	55.505	3.107	0.011
1313	-0.005	141.407	51.322	2.102	0.074
1314	-0.035	121.820	44.212	1.597	0.077
1315	-0.051	142.181	51.602	1.417	0.056
1316	-0.065	165.480	60.058	2.711	0.015
1317	-0.077	127.475	46.265	0.967	0.029
1318	-0.057	110.888	40.245	0.893	0.049
1319	-0.044	117.481	42.638	0.909	0.115
1320	-0.027	112.958	40.996	0.800	0.009
1321	-0.011	121.924	44.251	0.850	0.037
1322	0.002	104.898	38.071	0.704	0.057
1323	0.017	115.015	41.743	0.757	0.020
1324	0.021	106.756	38.746	0.826	0.054
1325	0.022	103.407	37.530	0.748	0.028
1326	0.019	110.178	39.987	0.576	0.012
1327	0.013	123.277	44.741	0.799	0.010
1328	-0.005	95.317	34.594	0.765	0.014
1329	-0.019	108.095	39.231	0.603	0.003
1330	-0.036	105.265	38.204	0.672	0.012
1331	-0.050	116.372	42.235	0.744	0.022
1332	-0.063	106.755	38.745	0.751	0.015
1333	-0.071	97.690	35.455	0.729	0.006
1334	-0.062	116.910	42.431	1.296	0.058
1335	-0.065	122.952	44.623	1.523	0.007
1336	-0.067	148.672	53.958	2.270	0.004
1337	-0.070	156.971	56.970	3.157	0.044
1338	-0.069	73.163	26.553	0.611	0.012
1339	-0.065	69.761	25.318	0.544	0.013
1340	-0.027	48.383	17.560	0.868	0.002
1341	-0.006	49.223	17.865	0.810	0.015
1342	0.014	54.824	19.897	0.759	0.012
1343	0.028	57.990	21.046	0.943	0.016
1344	0.038	64.259	23.322	1.028	0.001
1345	0.043	64.837	23.531	1.189	0.010
1346	0.043	55.883	20.282	1.252	0.012
1347	0.039	66.108	23.993	1.725	0.010
1348	0.028	81.552	29.598	2.306	0.013

1349	0.014	77.637	28.177	1.778	0.006
1350	-0.002	66.427	24.109	1.449	0.017
1351	-0.020	58.044	21.066	1.114	0.002
1352	-0.046	75.410	27.369	1.449	0.002
1353	-0.062	72.210	26.207	1.234	0.002
1354	-0.076	86.856	31.523	1.560	0.002
1355	-0.086	89.673	32.545	1.814	0.005
1356	-0.094	92.049	33.408	2.336	0.003
1357	-0.096	95.789	34.765	3.746	0.002
1358	-0.069	108.115	39.239	0.855	0.011
1359	-0.052	92.556	33.592	0.786	0.002
1360	-0.027	129.483	46.994	1.088	0.005
1361	-0.008	128.129	46.502	1.581	0.001
1362	0.010	106.212	38.548	1.046	0.002
1363	0.019	91.880	33.347	0.892	0.025
1364	0.028	91.184	33.094	1.095	0.073
1365	0.024	104.172	37.808	1.304	0.010
1366	0.014	127.173	46.155	1.602	0.004
1367	-0.001	114.492	41.553	2.053	0.001
1368	-0.015	103.832	37.684	1.675	0.042
1369	-0.066	89.084	32.332	1.291	0.003
1370	-0.082	105.668	38.350	2.135	0.009
1371	-0.091	119.696	43.442	3.222	0.002
1372	-0.095	92.422	33.543	1.591	0.050
1373	0.047	51.206	18.584	1.641	0.004
1374	0.033	53.567	19.441	1.807	0.004
1375	0.018	61.211	22.215	1.648	0.002
1376	0.001	67.040	24.331	2.105	0.002
1377	-0.016	78.861	28.621	2.760	0.000
1378	-0.042	67.287	24.421	2.508	0.002
1379	-0.059	81.701	29.652	2.926	0.001
1380	-0.067	78.046	28.326	2.730	0.001
1381	-0.070	110.606	40.143	4.466	0.004
1382	-0.064	91.504	33.210	3.555	-0.001
1383	-0.052	69.467	25.212	1.982	0.006
1384	-0.037	116.441	42.260	4.250	0.002
1385	0.052	115.186	41.805	2.976	0.002
1386	0.034	145.965	52.976	6.108	0.007
1387	0.016	138.910	50.415	4.013	0.006
1388	-0.004	171.755	62.336	7.482	0.013
1389	-0.023	216.547	78.592	8.026	0.003
1390	-0.049	111.470	40.456	2.363	0.049
1391	-0.062	129.329	46.938	3.104	0.028
1392	-0.073	178.324	64.720	6.249	0.021

1393	-0.078	115.771	42.017	2.551	0.047
1394	-0.077	100.086	36.325	1.866	0.010
1395	-0.057	124.127	45.050	0.856	0.008
1396	-0.048	143.989	52.258	1.398	0.006
1397	-0.010	10.273	3.729	0.714	0.035
1398	-0.031	4.819	1.749	0.517	0.002
1399	-0.039	3.657	1.327	0.474	0.001
1400	-0.047	12.198	4.427	0.624	0.007
1401	-0.054	19.208	6.971	1.008	0.024
1402	-0.056	25.029	9.084	1.443	0.031
1403	-0.056	34.894	12.664	1.489	0.054
1404	-0.054	72.685	26.380	3.770	0.002
1405	-0.050	50.218	18.226	3.072	0.003
1406	-0.041	40.428	14.673	1.930	0.004
1407	-0.034	78.475	28.481	4.206	0.001
1408	-0.027	54.842	19.904	2.425	0.006
1409	0.045	21.008	7.625	0.822	0.029
1410	0.040	17.286	6.274	0.781	0.041
1411	0.031	10.623	3.855	0.613	0.004
1412	0.019	1.279	0.464	0.423	0.004
1413	0.006	4.145	1.504	0.510	0.004
1414	-0.013	9.113	3.307	0.673	0.030
1415	-0.024	1.824	0.662	0.534	0.011
1416	-0.038	0.620	0.225	0.474	0.028
1417	-0.046	7.779	2.823	0.535	0.024
1418	-0.054	4.955	1.798	0.550	0.022
1419	-0.060	10.947	3.973	0.655	0.011
1420	-0.063	7.793	2.828	0.844	0.026
1421	-0.062	17.871	6.486	0.813	0.026
1422	-0.057	42.474	15.415	1.409	0.007
1423	-0.049	61.614	22.362	2.947	0.005
1424	-0.039	37.207	13.504	1.586	0.004
1425	-0.062	14.501	5.263	1.051	0.010
1426	-0.070	8.771	3.183	0.943	0.006
1427	-0.076	35.161	12.761	2.074	0.000
1428	-0.078	38.804	14.083	2.353	0.001
1429	-0.076	46.624	16.922	3.093	0.002
1430	-0.067	50.269	18.244	1.860	0.039
1431	-0.058	31.319	11.367	1.197	0.019
1432	-0.045	25.050	9.091	1.211	0.033
1433	-0.011	144.004	52.264	2.495	0.008
1434	0.005	161.800	58.723	3.673	0.010
1435	0.017	169.106	61.374	5.178	0.016
1436	0.020	127.150	46.147	1.672	0.008

1437	0.017	118.685	43.075	1.263	0.110
1438	-0.013	141.326	51.292	1.679	0.002
1439	-0.028	161.448	58.595	1.731	0.032
1440	-0.050	161.104	58.470	2.786	0.036
1441	-0.066	130.914	47.513	2.075	0.044
1442	-0.091	106.110	38.511	0.754	0.047
1443	-0.097	108.825	39.496	0.847	-0.001
1444	-0.095	116.232	42.185	1.436	0.001
1445	-0.060	148.326	53.832	1.344	0.003
1446	-0.043	159.948	58.051	1.859	0.004
1447	-0.025	166.526	60.438	1.850	0.052
1448	-0.010	181.802	65.982	2.345	0.009
1449	0.000	173.249	62.878	2.726	0.035
1450	0.007	155.489	56.432	1.912	0.016
1451	0.001	121.824	44.214	1.305	0.009
1452	-0.009	117.947	42.807	0.831	0.005
1453	-0.021	98.375	35.703	1.270	0.003
1454	-0.034	97.363	35.336	0.964	0.007
1455	-0.050	112.638	40.880	0.810	0.005
1456	-0.074	112.170	40.710	0.765	0.045
1457	-0.086	112.935	40.988	1.149	0.014
1458	-0.097	81.835	29.701	1.160	0.002
1459	-0.101	101.810	36.950	1.096	0.002
1460	0.017	132.103	47.945	2.179	0.008
1461	0.009	146.122	53.033	2.084	0.027
1462	-0.009	178.220	64.682	2.599	0.029
1463	-0.044	158.241	57.431	3.357	0.003
1464	-0.055	195.256	70.865	5.602	0.007
1465	-0.075	166.478	60.420	4.932	0.011
1466	-0.075	127.803	46.384	5.313	0.019
1467	-0.070	71.633	25.998	2.472	-0.002
1468	0.016	54.298	19.707	0.457	0.018
1469	-0.021	77.539	28.141	0.581	0.018
1470	-0.038	86.190	31.281	0.710	0.039
1471	-0.069	131.939	47.885	2.494	0.033
1472	-0.075	98.793	35.855	1.073	0.002
1473	-0.078	85.086	30.881	0.736	0.003
1474	-0.078	72.849	26.440	0.616	-0.001
1475	-0.074	63.694	23.117	0.585	0.012
1476	0.027	83.235	30.209	1.725	0.000
1477	0.023	74.665	27.098	2.298	0.003
1478	0.015	75.770	27.499	1.659	0.001
1479	-0.001	70.435	25.563	2.406	0.043
1480	-0.015	48.914	17.753	1.845	0.006

1481	-0.054	63.265	22.961	1.546	0.001
1482	-0.068	18.678	6.779	1.554	0.003
1483	-0.077	8.967	3.254	0.450	0.021
1484	-0.082	2.914	1.058	0.251	0.008
1485	-0.083	26.731	9.702	1.480	0.037
1486	-0.076	4.723	1.714	0.241	0.065
1487	-0.066	9.544	3.464	0.358	0.044
1488	-0.056	13.181	4.784	0.546	0.085
1489	-0.040	10.324	3.747	0.480	0.065
1490	-0.018	108.916	39.530	4.331	0.006
1491	-0.005	134.137	48.683	4.603	0.006
1492	0.005	133.566	48.476	3.871	0.015
1493	0.010	117.963	42.813	2.968	0.015
1494	0.000	90.557	32.866	3.307	0.008
1495	-0.018	76.682	27.830	3.559	0.020
1496	-0.035	69.071	25.068	3.297	0.016
1497	-0.058	58.547	21.249	2.662	0.004
1498	-0.084	82.771	30.040	1.644	0.005
1499	-0.089	132.376	48.044	3.937	0.005
1500	-0.082	65.818	23.888	0.459	0.032
2001	0.123	46.819	16.992	1.529	0.004
2002	0.138	45.777	16.614	1.094	0.002
2003	0.138	36.994	13.426	0.747	0.031
2004	0.129	88.211	32.015	2.233	0.006
2005	0.097	31.786	11.536	1.939	0.015
2006	0.078	27.870	10.115	1.642	0.014
2007	0.049	96.044	34.858	4.115	0.017
2008	0.028	118.227	42.909	4.230	0.002
2009	0.004	91.669	33.270	2.750	0.005
2010	0.004	102.316	37.134	2.416	0.003
2011	0.020	110.266	40.019	2.858	0.002
2012	0.046	124.844	45.310	5.780	0.005
2013	0.084	52.801	19.163	1.086	0.010
2014	0.094	48.637	17.652	1.455	0.011
2015	0.123	155.517	56.442	3.768	0.007
2016	0.128	101.287	36.760	3.188	0.002
2017	0.128	144.628	52.490	5.551	0.016
2018	0.123	85.939	31.190	5.086	0.033
2019	0.112	114.081	41.404	2.875	0.003
2020	0.062	49.191	17.853	1.294	-0.001
2021	0.039	31.917	11.584	2.528	0.000
2022	0.013	29.301	10.635	1.499	0.001
2023	-0.008	25.363	9.205	1.459	0.002
2024	-0.024	25.494	9.253	1.834	0.001

2025	0.023	3.602	1.307	0.844	0.008
2026	0.014	36.017	13.072	2.567	0.002
2027	0.008	48.908	17.750	2.634	0.015
2028	0.003	37.547	13.627	1.916	0.001
2029	-0.002	31.323	11.368	1.815	0.000
2030	-0.008	43.512	15.792	2.076	0.001
2031	-0.009	18.120	6.576	1.127	0.000
2032	-0.009	10.286	3.733	1.203	0.002
2033	-0.007	8.120	2.947	1.106	0.000
2034	-0.005	12.612	4.577	1.049	0.000
2035	-0.002	3.845	1.396	0.869	0.009
2036	0.001	1.423	0.516	0.694	0.005
2037	0.006	1.370	0.497	1.041	0.005
2038	0.009	3.073	1.115	1.468	0.001
2039	0.011	23.617	8.571	2.640	0.002
2040	0.011	65.970	23.943	1.526	0.005
2041	0.009	46.402	16.841	1.708	0.012
2042	0.055	97.822	35.503	2.927	0.034
2043	0.051	117.047	42.480	4.964	0.000
2044	0.045	128.748	46.727	5.442	0.004
2045	0.035	104.720	38.007	3.106	0.005
2046	0.026	97.169	35.266	3.949	0.001
2047	0.016	89.106	32.340	4.678	0.001
2048	0.002	78.905	28.637	2.015	0.000
2049	-0.017	42.420	15.396	1.336	0.001
2050	-0.021	22.151	8.039	1.681	0.013
2051	-0.023	5.985	2.172	0.453	0.010
2052	-0.022	2.501	0.908	0.309	0.035
2053	-0.021	0.671	0.243	0.244	0.040
2054	-0.017	20.490	7.436	0.904	0.056
2055	-0.015	7.466	2.710	0.382	0.038
2056	-0.012	11.304	4.103	0.799	0.035
2057	-0.010	23.782	8.631	0.658	0.005
2058	-0.009	30.812	11.183	0.770	0.031
2059	-0.008	35.944	13.045	1.011	0.005
2060	0.046	2.156	0.782	0.300	0.062
2061	0.073	3.995	1.450	0.337	0.010
2062	0.102	6.091	2.211	0.400	0.010
2063	0.127	10.303	3.739	0.477	0.034
2064	0.144	20.818	7.556	0.569	0.008
2065	0.157	34.323	12.457	0.852	0.034
2066	0.170	21.035	7.634	0.559	0.046
2067	0.171	24.590	8.924	0.697	0.034
2068	0.167	23.459	8.514	0.562	0.034

2069	0.156	24.873	9.027	0.612	0.039
2070	0.138	18.414	6.683	0.476	0.047
2071	0.114	14.308	5.193	0.440	0.061
2072	0.077	7.757	2.815	0.384	0.020
2073	0.046	9.166	3.327	0.397	0.006
2074	0.022	8.323	3.021	0.411	0.046
2075	-0.005	6.453	2.342	0.357	0.007
2076	-0.042	6.436	2.336	0.372	0.061
2077	-0.062	11.026	4.002	0.424	0.046
2078	-0.081	16.591	6.022	0.465	0.029
2079	-0.096	33.842	12.282	1.012	0.029
2080	-0.003	11.875	4.310	0.453	0.025
2081	0.025	18.161	6.591	0.465	0.080
2082	0.057	26.662	9.677	0.531	0.117
2083	0.090	20.278	7.359	0.666	0.045
2084	0.121	29.728	10.789	0.681	0.041
2085	0.139	40.443	14.678	0.719	0.131
2086	0.158	70.909	25.735	2.584	0.009
2087	0.163	18.324	6.650	0.479	0.101
2088	0.161	18.471	6.704	0.484	0.049
2089	0.153	28.773	10.443	0.556	0.059
2090	0.139	39.657	14.393	0.751	0.079
2091	0.117	68.933	25.018	1.375	0.090
2092	0.061	61.374	22.275	0.647	0.020
2093	0.031	98.804	35.859	3.426	0.003
2094	0.003	55.994	20.322	0.813	0.089
2095	-0.026	50.863	18.460	0.877	0.005
2096	-0.046	50.670	18.390	0.625	0.008
2097	-0.065	45.927	16.669	0.519	0.009
2098	-0.083	73.837	26.798	1.010	0.009
2099	0.035	154.733	56.158	2.219	0.034
2100	0.020	154.001	55.892	2.688	0.024
2101	0.010	141.189	51.242	2.140	0.003
2102	-0.002	132.893	48.231	1.943	0.002
2103	-0.013	193.076	70.074	5.118	0.000
2104	-0.016	283.964	103.060	11.541	0.001
2105	-0.020	239.359	86.872	7.314	-0.001
2106	-0.018	97.785	35.489	0.902	0.027
2107	-0.012	179.196	65.036	5.356	0.009
2108	-0.007	111.588	40.499	0.720	0.027
2109	-0.006	110.463	40.091	0.695	0.006
2110	-0.006	88.401	32.084	0.656	0.067
2111	-0.006	81.035	29.410	0.547	0.059
2112	0.037	0.454	0.165	0.401	0.043

2113	0.067	82.157	29.818	4.063	0.000
2114	0.099	163.630	59.387	8.373	0.001
2115	0.117	106.655	38.709	2.728	0.001
2116	0.128	43.803	15.898	3.096	0.001
2117	0.125	82.166	29.821	3.716	0.001
2118	0.118	52.725	19.136	3.190	0.004
2119	-0.021	313.796	113.887	7.602	0.000
2120	-0.022	325.988	118.312	9.652	0.023
2121	-0.020	342.071	124.149	7.724	0.016
2122	-0.018	365.050	132.489	11.331	0.017
2123	-0.002	128.211	46.532	2.366	0.007
2124	0.006	193.750	70.319	2.816	0.003
2125	0.012	171.349	62.189	3.433	0.013
2126	0.016	143.393	52.042	4.707	0.015
2127	0.021	137.113	49.763	3.145	0.043
2128	0.022	98.357	35.697	2.157	0.039
2129	0.021	91.334	33.148	1.211	0.034
2130	0.015	80.960	29.383	0.946	0.032
2131	0.006	76.032	27.594	0.782	0.011
2132	-0.003	98.746	35.838	0.991	0.004
2133	0.092	48.655	17.658	0.636	0.013
2134	0.112	47.265	17.154	0.513	0.004
2135	0.131	54.352	19.726	0.496	0.003
2136	0.145	65.511	23.776	0.510	0.060
2137	0.152	63.243	22.953	0.511	0.086
2138	0.154	69.516	25.230	0.590	0.092
2139	0.150	75.123	27.265	0.659	0.018
2140	0.118	64.579	23.438	0.482	0.020
2141	0.093	91.934	33.366	1.529	0.001
2142	0.057	140.877	51.129	4.184	0.022
2143	0.020	156.314	56.732	5.167	0.002
2144	-0.030	85.164	30.909	4.341	0.011
2145	0.076	103.729	37.647	4.061	0.007
2146	0.093	102.961	37.368	5.398	0.002
2147	0.109	93.635	33.983	4.526	0.001
2148	0.125	117.245	42.552	4.942	0.003
2149	0.134	115.872	42.054	5.355	0.004
2150	0.139	148.622	53.940	6.656	0.003
2151	0.138	92.121	33.434	4.663	0.007
2152	0.108	86.669	31.455	4.682	0.002
2153	0.087	126.024	45.739	6.305	0.004
2154	0.057	148.136	53.764	8.349	0.002
2155	0.020	96.241	34.929	4.446	0.001
2156	0.087	28.308	10.274	0.692	0.249

2157	0.048	22.681	8.232	0.703	0.059
2158	-0.035	208.837	75.794	10.480	0.003
2159	-0.026	225.395	81.804	9.827	0.006
2160	-0.018	237.468	86.185	10.458	0.001
2161	-0.011	223.845	81.241	9.801	0.001
2162	-0.007	240.651	87.340	10.908	0.015
2163	-0.005	250.507	90.917	10.392	0.002
2164	-0.017	264.339	95.938	12.984	0.001
2165	-0.031	199.946	72.567	8.815	0.003
2166	-0.049	229.724	83.375	12.587	0.001
2167	-0.059	196.798	71.425	7.673	0.008
2168	-0.086	120.321	43.668	3.582	0.004
2169	-0.094	129.933	47.157	6.348	0.002
2170	-0.061	21.862	7.934	0.504	0.127
2171	-0.050	27.515	9.986	0.579	0.053
2172	-0.039	33.794	12.265	0.633	0.180
2173	-0.029	27.130	9.846	0.535	0.040
2174	-0.020	21.586	7.834	0.585	0.084
2175	-0.013	32.084	11.644	0.647	0.071
2176	-0.014	31.761	11.527	0.589	0.095
2177	-0.019	36.231	13.149	0.639	0.047
2178	-0.026	49.766	18.062	0.672	0.050
2179	-0.034	47.461	17.225	0.631	0.031
2180	-0.051	84.680	30.733	2.518	0.004
2181	-0.063	65.136	23.640	1.202	0.003
2182	-0.071	64.442	23.388	0.764	0.001
2183	-0.086	67.450	24.480	0.810	0.058
2184	-0.092	50.738	18.414	0.617	0.023
2185	-0.074	266.328	96.659	7.566	0.001
2186	-0.078	296.996	107.790	8.973	0.012
2187	-0.080	322.006	116.867	6.919	0.008
2188	-0.079	354.249	128.569	12.705	0.021
2189	-0.078	351.918	127.723	8.830	0.005
2190	-0.074	343.218	124.566	9.021	0.006
2191	-0.048	302.295	109.713	5.975	0.005
2192	-0.041	305.633	110.924	5.416	0.010
2193	-0.033	306.303	111.168	6.244	0.029
2194	-0.025	345.491	125.391	14.263	0.007
2195	-0.019	321.902	116.829	10.458	0.008
2196	-0.009	235.156	85.346	5.883	0.009
2197	-0.005	179.401	65.111	6.404	0.031
2198	-0.015	272.078	98.746	5.346	0.020
2199	-0.026	265.455	96.343	5.892	0.001
2200	-0.035	289.655	105.126	5.333	0.008

2201	-0.045	286.560	104.002	6.543	0.021
2202	-0.054	258.047	93.654	4.680	0.040
2203	-0.061	233.122	84.608	6.514	0.018
2204	-0.068	247.215	89.723	7.229	0.012
2205	-0.074	272.436	98.876	7.765	0.001
2206	-0.080	213.055	77.325	4.012	0.006
2207	-0.077	242.469	88.000	4.284	0.002
2208	-0.071	214.140	77.719	4.412	0.017
2209	-0.064	173.833	63.090	4.733	0.004
2210	-0.054	143.406	52.047	3.672	0.006
2211	-0.027	246.888	89.604	8.847	-0.004
2212	-0.008	202.357	73.442	5.269	0.001
2213	-0.006	334.080	121.249	21.956	0.012
2214	-0.030	211.948	76.923	5.746	0.001
2215	-0.054	165.833	60.186	3.758	0.002
2216	-0.068	206.271	74.863	4.703	-0.002
2217	-0.081	259.969	94.351	8.635	0.008
2218	-0.083	247.554	89.846	7.516	0.001
2219	-0.078	174.138	63.200	6.754	0.011
2220	-0.073	142.240	51.624	3.574	0.004
2221	-0.059	146.594	53.204	2.504	0.006
2222	-0.043	163.503	59.341	2.955	0.000
2223	-0.031	123.645	44.875	1.014	0.002
2224	-0.021	118.165	42.886	0.978	0.017
2225	0.000	142.874	51.854	5.084	0.009
2226	0.002	161.577	58.642	6.425	0.005
2227	0.003	173.564	62.992	7.410	0.006
2228	0.000	129.006	46.821	6.248	0.000
2229	-0.004	121.226	43.997	7.073	0.001
2230	-0.011	147.750	53.624	9.645	-0.001
2231	-0.027	161.596	58.649	4.076	-0.001
2232	-0.037	142.718	51.797	5.312	0.003
2233	-0.049	122.705	44.534	5.004	0.003
2234	-0.075	118.065	42.850	1.988	0.002
2235	-0.082	105.960	38.456	1.229	0.004
2236	-0.090	118.902	43.154	4.301	0.001
2237	-0.092	107.821	39.132	3.678	0.013
2238	-0.092	79.765	28.949	2.288	0.008
2239	-0.090	71.676	26.014	1.139	0.006
2240	-0.079	78.249	28.399	1.571	0.013
2241	-0.063	55.132	20.009	1.103	0.009
2242	-0.011	52.333	18.993	0.764	0.010
2243	-0.006	44.179	16.034	0.748	0.079
2244	-0.004	45.796	16.621	0.877	0.062

2245	-0.004	47.100	17.094	1.022	0.077
2246	-0.012	27.987	10.158	0.644	0.048
2247	-0.024	43.136	15.655	0.932	0.055
2248	-0.036	45.182	16.398	0.930	0.056
2249	-0.047	37.789	13.715	0.741	0.076
2250	-0.061	77.904	28.274	1.904	0.002
2251	-0.059	1.498	0.544	1.118	0.016
2252	-0.050	6.003	2.179	1.117	0.032
2253	-0.038	65.227	23.673	3.347	0.001
2254	-0.028	32.882	11.934	2.616	0.003
2255	-0.018	53.564	19.440	1.298	0.001
2256	-0.014	37.947	13.772	0.875	0.000
2257	-0.012	41.281	14.982	1.780	0.004
2258	-0.011	21.669	7.865	2.590	0.002
2259	-0.014	13.486	4.894	1.542	0.021
2260	-0.022	119.944	43.532	2.932	0.006
2261	-0.030	129.471	46.990	6.838	0.038
2262	-0.038	143.662	52.140	5.645	0.013
2263	-0.050	255.672	92.792	4.714	0.005
2264	-0.060	250.501	90.915	2.515	0.038
2265	-0.091	214.182	77.734	2.759	0.030
2266	-0.092	205.051	74.420	3.158	0.088
2267	-0.060	375.917	136.433	9.315	0.009
2268	-0.048	395.691	143.610	11.568	0.006
2269	-0.042	379.235	137.637	11.879	0.006
2270	-0.033	326.707	118.573	7.559	0.007
2271	-0.024	343.986	124.844	7.628	0.008
2272	-0.020	342.588	124.337	8.976	0.024
2273	-0.015	308.168	111.845	5.401	0.000
2274	-0.030	328.013	119.047	7.525	0.006
2275	-0.041	272.619	98.943	4.775	0.020
2276	-0.051	294.585	106.915	6.118	0.016
2277	-0.062	315.379	114.462	5.484	0.030
2278	-0.071	312.406	113.383	6.310	0.006
2279	-0.041	96.683	35.089	5.518	0.000
2280	-0.051	99.961	36.279	6.199	0.002
2281	-0.057	99.625	36.157	4.299	0.006
2282	-0.061	91.132	33.075	5.311	0.005
2283	-0.064	121.374	44.051	4.588	0.001
2284	-0.063	47.977	17.413	1.485	0.002
2285	-0.062	32.373	11.749	1.079	-0.001
2286	-0.048	73.390	26.636	1.944	0.001
2287	-0.041	117.007	42.466	4.654	0.018
2288	-0.029	196.484	71.311	10.107	0.000

2289	-0.023	177.219	64.319	8.663	0.003
2290	-0.009	104.889	38.068	3.157	0.000
2291	0.001	50.675	18.392	1.731	0.000
2292	0.003	29.842	10.831	1.219	0.002
2293	0.005	17.375	6.306	1.048	0.011
3001	-0.043	3.015	1.094	0.428	0.086
3002	-0.012	0.706	0.256	0.256	0.053
3003	0.013	4.104	1.489	0.281	0.021
3004	0.036	11.715	4.252	0.672	0.040
3005	0.057	0.850	0.308	0.715	0.023
3006	0.090	37.786	13.714	0.983	0.035
3007	0.106	29.127	10.571	0.638	0.047
3008	0.117	20.496	7.439	0.544	0.034
3009	0.119	28.145	10.215	0.600	0.024
3010	0.113	46.132	16.743	0.502	0.064
3011	0.101	53.481	19.410	0.466	0.052
3012	0.088	70.417	25.557	0.866	0.046
3013	0.070	62.239	22.588	0.770	0.047
3014	0.052	48.339	17.544	0.607	0.111
3015	0.029	63.072	22.891	0.540	0.058
CA-101	0.075	47.419	17.210	0.796	0.054
CA-102	0.086	51.027	18.520	0.968	0.064
CA-103	0.096	54.689	19.849	1.193	0.088
CA-104	0.105	52.191	18.942	1.270	0.081
CA-105	0.111	49.863	18.097	1.108	0.127
CA-106	0.115	43.848	15.914	0.848	0.105
CA-201	0.000	80.572	29.242	1.443	0.011
CA-202	-0.002	84.153	30.542	1.621	0.011
CA-203	-0.006	87.755	31.849	1.891	0.023
CA-204	-0.010	90.759	32.940	2.245	0.018
CA-205	-0.017	94.249	34.206	2.831	0.015
CA-206	-0.023	90.987	33.022	3.152	0.010
CA-207	-0.029	81.451	29.561	2.505	0.011
CA-301	-0.018	47.809	17.351	1.117	0.054
CA-302	-0.021	53.553	19.436	1.282	0.019
CA-303	-0.024	57.897	21.013	1.407	0.005
CA-304	-0.029	61.325	22.257	1.334	0.002
CA-305	-0.038	68.807	24.972	1.528	0.010
CA-306	-0.045	69.493	25.221	1.288	0.034
CA-307	-0.053	66.812	24.248	1.210	0.018
CA-401	-0.068	30.205	10.963	0.642	0.025
CA-402	-0.066	36.079	13.094	1.009	0.010
CA-403	-0.062	38.865	14.105	1.224	0.005
CA-404	-0.059	41.647	15.115	1.598	0.020

CA-405	-0.055	44.958	16.317	2.391	0.008
CA-406	-0.050	42.284	15.346	2.348	0.008
CA-407	-0.045	39.099	14.190	1.993	0.015
CA-408	-0.041	34.128	12.386	1.487	0.017
CA-409	-0.037	29.072	10.551	1.034	0.042
Cal-101	0.118	62.646	22.736	1.778	0.044
Cal-102	0.126	66.799	24.244	1.813	0.012
Cal-103	0.128	72.090	26.164	1.974	0.007
Cal-104	0.129	80.404	29.181	2.358	0.003
Cal-105	0.127	84.866	30.801	2.740	0.002
Cal-106	0.121	92.288	33.495	3.717	0.002
Cal-107	0.115	89.497	32.482	3.110	0.005
Cal-108	0.106	85.067	30.874	2.728	0.002
Cal-109	0.092	77.647	28.181	2.191	0.003
Cal-110	0.075	71.043	25.784	1.906	0.009
Cal-111	0.058	65.563	23.795	1.843	0.020
Cal-201	-0.050	43.041	15.621	1.177	0.035
Cal-202	-0.040	46.577	16.904	1.269	0.066
Cal-203	-0.031	49.887	18.106	1.325	0.071
Cal-204	-0.023	52.796	19.162	1.408	0.050
Cal-205	-0.012	55.603	20.180	1.646	0.022
Cal-206	-0.004	54.435	19.756	1.546	0.040
Cal-207	0.002	49.750	18.056	1.320	0.032
Cal-208	0.006	46.206	16.770	1.233	0.041
Cal-209	0.008	44.051	15.988	1.201	0.100
CmA-101	0.006	34.111	12.380	0.745	0.064
CmA-102	0.006	36.364	13.198	0.868	0.069
CmA-103	0.005	38.186	13.859	0.910	0.140
CmA-104	0.003	39.879	14.473	1.013	0.085
CmA-105	0.000	38.808	14.085	0.920	0.108
CmA-106	-0.003	36.644	13.299	0.781	0.165
CmA-107	-0.009	33.383	12.116	0.629	0.126
CmA-201	-0.010	32.897	11.939	0.663	0.073
CmA-202	-0.018	34.756	12.614	0.757	0.069
CmA-203	-0.026	36.767	13.344	0.884	0.029
CmA-204	-0.036	39.008	14.157	1.087	0.017
CmA-205	-0.044	40.968	14.869	1.396	0.022
CmA-206	-0.051	38.693	14.043	1.167	0.047
CmA-207	-0.061	36.952	13.411	1.056	0.041
CmA-208	-0.068	33.356	12.106	0.935	0.028
CmA-209	-0.075	29.764	10.802	0.863	0.044
CmA-301	0.024	38.429	13.947	0.961	0.039
CmA-302	0.014	39.755	14.428	1.117	0.020
CmA-303	0.005	40.142	14.569	1.228	0.030

CmA-304	-0.004	38.919	14.125	1.168	0.085
CmA-305	-0.014	34.458	12.506	0.948	0.074
CmA-306	-0.024	31.437	11.410	0.901	0.029
CP-101	0.063	200.424	72.741	3.424	0.007
CP-102	0.076	202.346	73.438	3.425	0.008
CP-103	0.091	204.193	74.109	3.466	0.005
CP-104	0.103	207.365	75.260	3.597	0.002
CP-105	0.113	209.479	76.027	3.658	0.002
CP-106	0.122	212.116	76.984	3.876	0.003
CP-107	0.129	213.863	77.618	4.130	0.004
CP-108	0.132	211.804	76.871	3.850	0.013
CP-109	0.134	209.142	75.905	3.563	0.004
CP-110	0.133	207.604	75.346	3.428	0.003
CP-111	0.129	204.951	74.384	3.307	0.004
CP-201	0.071	257.504	93.457	3.883	0.009
CP-202	0.053	260.713	94.622	4.181	0.005
CP-203	0.036	263.196	95.523	4.477	0.005
CP-204	0.017	265.837	96.481	4.877	0.006
CP-205	0.000	264.411	95.964	4.791	0.007
CP-206	-0.014	262.587	95.302	4.674	0.008
CP-207	-0.031	257.089	93.307	4.300	0.008
D-101	0.087	70.699	25.659	3.479	0.022
D-102	0.086	80.053	29.054	3.885	0.017
D-103	0.083	85.089	30.882	3.851	0.016
D-104	0.078	86.536	31.407	3.889	0.010
D-105	0.071	84.636	30.717	3.747	0.011
D-106	0.061	72.157	26.188	3.237	0.007
D-107	0.052	62.133	22.550	3.320	0.012
D-201	0.009	38.543	13.988	1.676	0.021
D-202	-0.007	43.877	15.924	1.607	0.018
D-203	-0.019	51.652	18.746	1.893	0.022
D-204	-0.031	46.123	16.740	1.643	0.021
D-205	-0.041	41.393	15.023	1.449	0.044
D-206	-0.050	36.873	13.382	1.264	0.020
DL-101	0.064	53.691	19.486	2.260	0.021
DL-102	0.073	58.695	21.302	2.056	0.022
DL-103	0.082	61.217	22.218	2.083	0.021
DL-104	0.085	63.715	23.124	2.127	0.012
DL-105	0.086	60.736	22.043	2.071	0.031
DL-106	0.085	57.685	20.936	1.916	0.022
DL-107	0.082	53.958	19.583	1.816	0.057
DL-108	0.076	49.689	18.034	1.757	0.040
DL-201	0.047	61.517	22.327	2.349	0.049
DL-202	0.035	64.377	23.364	2.622	0.034

DL-203	0.024	66.932	24.292	2.740	0.020
DL-204	-0.011	73.111	26.534	3.018	0.005
DL-205	0.003	70.204	25.479	2.896	0.005
DL-206	-0.024	69.584	25.255	2.781	0.022
DL-207	-0.037	63.921	23.199	2.500	0.052
M-101	-0.077	129.002	46.819	2.480	0.028
M-102	-0.076	138.534	50.279	2.432	0.016
M-103	-0.073	147.964	53.701	2.835	0.014
M-104	-0.069	146.317	53.104	2.858	0.018
M-105	-0.062	138.616	50.308	2.532	0.030
M-201	-0.037	99.010	35.934	1.299	0.038
M-202	-0.029	107.439	38.993	1.551	0.050
M-203	-0.021	109.366	39.693	1.532	0.070
M-204	-0.014	113.889	41.334	1.689	0.061
M-205	-0.008	118.608	43.047	1.964	0.019
M-206	-0.004	115.811	42.032	1.838	0.017
M-207	0.002	110.585	40.135	1.540	0.018
M-208	0.000	104.864	38.059	1.293	0.041
Msl-101	-0.059	52.494	19.052	0.595	0.037
Msl-102	-0.062	51.134	18.558	0.642	0.026
Msl-103	-0.063	55.720	20.223	0.719	0.010
Msl-104	-0.063	58.622	21.276	0.618	0.047
Msl-105	-0.061	55.351	20.089	0.565	0.081
Msl-106	-0.058	52.212	18.949	0.600	0.042
Msl-107	-0.054	50.236	18.232	0.588	0.053
Msl-108	-0.048	48.532	17.614	0.555	0.038
Msl-109	-0.042	46.704	16.950	0.555	0.108
Msl-110	-0.036	45.870	16.648	0.556	0.052
Msl-201	0.046	60.940	22.117	0.562	0.029
Msl-202	0.050	65.221	23.671	0.631	0.022
Msl-203	0.053	67.948	24.661	0.633	0.010
Msl-204	0.054	79.343	28.796	0.692	0.020
Msl-205	0.052	78.781	28.592	0.610	0.036
Msl-206	0.050	76.586	27.795	0.579	0.035
Msl-207	0.045	73.816	26.790	0.551	0.031
Msl-208	0.039	72.512	26.317	0.548	0.017
Msl-209	0.031	69.944	25.385	0.550	0.036
Msl-210	0.025	68.009	24.683	0.558	0.028
Msl-301	-0.069	40.917	14.850	0.770	0.003
Msl-302	-0.064	44.756	16.243	0.821	0.008
Msl-303	-0.058	47.155	17.114	0.833	0.007
Msl-304	-0.052	51.440	18.669	0.874	0.004
Msl-305	-0.045	53.316	19.350	0.905	0.011
Msl-306	-0.040	51.398	18.654	0.898	0.002

Msl-307	-0.030	46.753	16.968	0.863	0.001
Msl-308	-0.025	41.900	15.207	0.836	0.002
Msl-309	-0.021	38.907	14.121	0.842	0.007
Msm-101	0.127	18.810	6.827	0.585	0.027
Msm-102	0.129	21.486	7.798	0.616	0.044
Msm-103	0.129	27.996	10.161	0.749	0.053
Msm-104	0.124	28.637	10.393	0.724	0.099
Msm-105	0.117	34.604	12.559	1.109	0.075
Msm-106	0.059	30.793	11.176	0.863	0.089
Msm-107	0.106	26.090	9.469	0.797	0.038
Msm-108	0.095	24.235	8.796	0.870	0.048
Msm-109	0.081	24.320	8.826	0.905	0.049
Msm-201	0.016	10.177	3.694	0.645	0.042
Msm-202	0.000	12.702	4.610	0.664	0.069
Msm-203	-0.094	18.726	6.796	0.818	0.032
Msm-204	-0.021	23.379	8.485	0.948	0.005
Msm-205	-0.044	20.032	7.270	0.793	0.007
Msm-206	-0.058	14.897	5.407	0.684	0.029
Msm-207	-0.071	9.173	3.329	0.600	0.064
Msm-208	-0.081	7.242	2.628	0.588	0.015
Msm-209	-0.088	5.523	2.005	0.564	0.033
Msm-300	-0.044	3.345	1.214	0.287	0.115
Msm-301	-0.083	3.736	1.356	0.298	0.096
Msm-302	-0.057	4.927	1.788	0.309	0.078
Msm-303	-0.082	6.424	2.332	0.321	0.061
Msm-304	-0.079	7.850	2.849	0.344	0.101
Msm-305	-0.075	6.781	2.461	0.310	0.059
Msm-306	-0.070	6.099	2.213	0.304	0.050
Msm-307	-0.064	5.476	1.987	0.307	0.059
Pll-101	0.002	57.774	20.968	0.462	0.009
Pll-102	-0.009	56.902	20.652	0.469	0.026
Pll-103	-0.019	56.676	20.570	0.474	0.019
Pll-104	-0.028	54.858	19.910	0.513	0.012
Pll-105	-0.036	54.744	19.868	0.512	0.019
Pll-106	-0.044	56.122	20.369	0.496	0.032
Pll-107	-0.052	57.500	20.869	0.478	0.016
Pll-201	-0.067	62.381	22.640	0.550	0.063
Pll-202	-0.067	60.867	22.091	0.533	0.077
Pll-203	-0.057	61.091	22.172	0.518	0.096
Pll-204	-0.052	61.522	22.328	0.510	0.063
Pll-205	-0.065	60.589	21.990	0.512	0.058
Pll-206	-0.063	61.135	22.188	0.492	0.065
Plm-101	-0.029	3.742	1.358	0.300	0.087
Plm-102	-0.032	6.794	2.466	0.376	0.089

Plm-103	-0.034	23.069	8.372	1.278	0.035
Plm-104	-0.034	26.772	9.716	1.486	0.031
Plm-105	-0.033	23.546	8.546	1.411	0.013
Plm-106	-0.031	14.771	5.361	1.088	0.080
Plm-107	-0.028	5.890	2.138	0.757	0.015
Plm-108	-0.024	1.094	0.397	0.372	0.015
Plm-201	-0.011	0.325	0.118	0.505	0.013
Plm-202	-0.008	8.847	3.211	0.451	0.021
Plm-203	-0.004	14.576	5.290	0.472	0.054
Plm-204	0.000	14.120	5.125	0.459	0.061
Plm-205	0.002	10.101	3.666	0.442	0.033
Plm-206	0.004	5.209	1.891	0.336	0.031
Plm-301	-0.022	2.363	0.858	0.419	0.048
Plm-302	-0.036	6.946	2.521	0.602	0.104
Plm-303	-0.047	11.011	3.996	0.836	0.059
Plm-304	-0.060	15.584	5.656	1.085	0.032
Plm-305	-0.070	23.798	8.637	1.498	0.039
Plm-306	-0.078	26.067	9.461	1.448	0.044
Plm-307	-0.084	25.739	9.341	1.443	0.034
Plm-307B	-0.087	26.245	9.525	1.461	0.032
Plm-308	-0.089	24.695	8.963	1.321	0.033
Plm-309	-0.086	21.579	7.832	1.243	0.034
Plm-310	-0.081	18.554	6.734	1.028	0.045
Plm-311	-0.076	15.598	5.661	0.895	0.050
Plm-312	-0.069	12.791	4.642	0.926	0.047
Plm-313	-0.060	8.466	3.073	0.795	0.030
Plm-314	-0.048	1.620	0.588	0.556	0.012
Ptsc-101	-0.022	87.410	31.724	0.829	0.087
Ptsc-102	-0.018	82.559	29.964	0.902	0.066
Ptsc-103	-0.014	80.754	29.308	0.920	0.070
Ptsc-104	-0.013	81.152	29.453	0.853	0.021
Ptsc-105	-0.012	81.613	29.620	0.886	0.027
Ptsc-106	-0.012	85.041	30.864	0.796	0.028
Ptsc-107	-0.013	84.769	30.766	0.792	0.015
Ptsc-201	0.054	98.254	35.660	0.758	0.130
Ptsc-202	0.055	100.481	36.468	0.744	0.081
Ptsc-203	0.054	102.009	37.023	0.731	0.058
Ptsc-204	0.051	102.239	37.106	0.752	0.080
Ptsc-205	0.047	102.246	37.108	0.859	0.131
Ptsc-206	0.040	98.647	35.802	0.925	0.082
Ptsc-207	0.034	95.424	34.633	1.011	0.096
Sch-101	-0.027	82.692	30.012	3.676	0.066
Sch-102	-0.021	76.307	27.694	3.413	0.056
Sch-103	-0.016	67.985	24.674	3.050	0.047

Sch-104	-0.010	75.912	27.551	2.690	0.034
Sch-105	-0.002	78.218	28.388	2.584	0.034
Sch-201	-0.002	129.720	47.080	2.015	0.063
Sch-202	-0.006	137.157	49.779	2.133	0.053
Sch-203	-0.012	141.147	51.227	2.211	0.031
Sch-204	-0.020	143.617	52.124	2.282	0.031
Sch-205	-0.035	138.865	50.399	2.160	0.048
Sch-206	-0.044	133.135	48.319	2.105	0.065
Sch-207	-0.053	129.385	46.958	2.140	0.093
Sch-301	-0.007	100.276	36.394	1.027	0.029
Sch-302	-0.015	103.176	37.446	1.062	0.059
Sch-303	-0.026	106.001	38.471	1.143	0.049
Sch-304	-0.038	108.254	39.289	1.203	0.093
Sch-305	-0.046	111.538	40.481	1.248	0.049
Sch-306	-0.054	114.412	41.524	1.246	0.064
Sch-307	-0.068	116.899	42.427	1.336	0.073
Sch-308	-0.071	119.209	43.265	1.405	0.035
Sch-309	-0.073	116.499	42.281	1.354	0.058
Sch-310	-0.073	113.160	41.070	1.328	0.070
Sch-311	-0.071	111.495	40.465	1.440	0.083
Sch-312	-0.067	109.127	39.606	1.516	0.070
SchA-101	-0.045	53.180	19.301	0.618	0.079
SchA-102	-0.040	54.158	19.656	0.637	0.088
SchA-103	-0.035	55.451	20.125	0.686	0.065
SchA-104	-0.030	59.774	21.694	0.908	0.077
SchA-105	-0.023	64.395	23.371	1.080	0.083
SchA-106	-0.013	71.914	26.100	1.447	0.106
SchA-107	-0.007	67.037	24.330	1.066	0.068
SchA-108	0.001	60.735	22.043	0.933	0.055
SchA-109	0.007	57.215	20.765	0.918	0.054
SchA-110	0.013	54.937	19.938	0.786	0.079
SchA-111	0.018	47.811	17.352	0.786	0.052
SchA-201	0.026	49.633	18.014	0.833	0.074
SchA-202	0.026	58.543	21.247	1.194	0.073
SchA-203	0.025	58.820	21.348	1.054	0.051
SchA-204	0.020	54.640	19.831	1.097	0.087
SchA-205	0.016	49.457	17.950	0.910	0.068
SchA-206	0.009	47.546	17.256	0.912	0.131
SchA-301	-0.028	39.266	14.251	0.786	0.132
SchA-302	-0.028	50.428	18.302	1.171	0.126
SchA-303	-0.028	54.183	19.665	1.691	0.085
SchA-304	-0.034	59.219	21.493	2.003	0.010
SchA-305	-0.031	62.429	22.657	1.892	0.008
SchA-306	-0.037	59.470	21.584	1.579	0.020

SchA-307	-0.041	54.092	19.632	1.227	0.037
SchA-308	-0.044	51.819	18.807	1.132	0.069
SchA-309	-0.047	47.875	17.376	0.986	0.064
SchA-310	-0.052	43.461	15.774	0.747	0.072
SchAL-101	-0.020	48.561	17.625	1.725	0.046
SchAL-102	-0.029	60.036	21.789	1.960	0.067
SchAL-103	-0.038	49.884	18.105	1.771	0.039
SchAl-201	-0.051	58.118	21.093	1.973	0.085
SchAl-202	-0.052	54.618	19.823	2.021	0.093
SchAl-203	-0.051	51.802	18.801	2.022	0.064
SchAl-204	-0.049	53.598	19.453	2.038	0.099
SchAl-205	-0.046	59.383	21.552	2.078	0.056
TJ-101	-0.027	54.443	19.759	1.089	0.045
TJ-102	-0.019	56.110	20.364	1.105	0.024
TJ-103	-0.013	59.761	21.689	1.225	0.003
TJ-104	-0.008	62.913	22.833	1.431	0.010
TJ-105	-0.006	65.134	23.639	1.519	-0.002
TJ-106	-0.005	64.731	23.493	1.474	-0.002
TJ-107	-0.006	61.926	22.475	1.352	0.000
TJ-108	-0.008	59.236	21.499	1.249	0.001
TJ-201	-0.023	62.446	22.664	1.667	0.027
TJ-202	-0.035	81.138	29.448	2.619	0.006
TJ-203	-0.047	99.637	36.162	3.336	0.007
TJ-204	-0.056	93.577	33.962	2.714	0.010
TJ-205	-0.064	89.908	32.631	2.529	0.004
TJ-206	-0.073	69.602	25.261	1.987	0.006

APPENDIX B – LABORATORY DENSITY MEASUREMENTS

Sample code	W_1 (dry specimen measured in air)	W_2 (saturated specimen measured in air)	W_3 (saturated specimen measured in the water)	Dry density ρd (gr/cm^3)	Saturation density ρs (gr/cm3)	Grain density ρg (gr/cm3)
TJ-1	64.525	64.741	40.747	2.684	2.693	2.709
TJ-2	27.497	27.535	17.353	2.696	2.699	2.706
TJ-3	52.005	53.096	33.400	2.636	2.691	2.790
TJ-4	27.560	27.714	17.364	2.658	2.673	2.698
TJ-5	40.758	40.880	25.670	2.675	2.683	2.696
TJ-6	61.418	61.696	38.759	2.673	2.685	2.706
TJ-7	60.203	60.434	38.103	2.691	2.701	2.719
TJ-8	52.841	53.030	33.281	2.671	2.680	2.697
TJ-9	28.856	29.276	18.155	2.590	2.628	2.692
TJ-10	42.456	42.760	26.609	2.624	2.643	2.674
TJ-11	46.424	46.633	29.348	2.681	2.693	2.714
TJ-12	22.916	23.092	14.420	2.638	2.658	2.692
TJ-13	18.470	18.627	11.646	2.641	2.663	2.702
TJ-14	22.147	22.233	13.990	2.682	2.692	2.710
TJ-15	20.345	20.468	12.821	2.656	2.672	2.699
TJ-16	44.020	44.141	27.803	2.689	2.697	2.710
TJ-17	42.728	42.998	26.962	2.660	2.677	2.705
TJ-18	60.245	60.455	38.080	2.688	2.697	2.713
TJ-19	56.327	56.427	35.602	2.700	2.705	2.713
TJ-20	26.252	26.533	16.591	2.636	2.664	2.712
TJ-21	32.414	32.486	20.444	2.687	2.693	2.703
TJ-22	26.213	26.295	16.510	2.674	2.682	2.697
TJ-23	39.013	39.240	24.541	2.649	2.665	2.691
TJ-24	26.010	26.219	16.374	2.637	2.658	2.694
TJ-25	23.039	23.096	14.556	2.693	2.700	2.711
TJ-26	28.639	28.696	18.055	2.687	2.692	2.701
TJ-27	15.104	15.229	9.511	2.637	2.659	2.696
TJ-28	11.539	11.685	7.281	2.615	2.648	2.705
TJ-29	34.535	34.696	21.802	2.674	2.686	2.707
TJ-30	12.518	12.623	7.879	2.634	2.656	2.694
TJ-31	31.978	32.057	20.130	2.676	2.683	2.694
TJ-32	68.447	68.583	42.435	2.613	2.618	2.627
TJ-33	59.318	59.417	37.452	2.696	2.700	2.708
TJ-34	16.943	16.970	10.722	2.707	2.711	2.719
TJ-35	40.995	41.137	24.689	2.488	2.497	2.510

TJ-36	51.086	51.310	32.550	2.718	2.730	2.751
TJ-37	32.935	33.027	20.792	2.687	2.695	2.707
TJ-38	61.103	61.225	38.518	2.686	2.691	2.701
TJ-39	43.344	43.480	27.543	2.715	2.723	2.738
TJ-40	56.283	56.622	35.946	2.717	2.734	2.763
TJ-41	33.965	34.135	21.642	2.714	2.727	2.751
TJ-42	48.552	48.685	30.612	2.682	2.689	2.701
TJ-43	43.085	43.168	27.138	2.683	2.688	2.697
TJ-44	36.335	36.470	22.937	2.680	2.690	2.707
TJ-45	44.506	44.694	28.006	2.662	2.673	2.692
TJ-46	22.236	22.390	13.966	2.635	2.653	2.684
TJ-47	27.069	27.140	17.055	2.679	2.686	2.698
TJ-48	44.806	44.912	28.230	2.681	2.687	2.698
TJ-49	17.184	17.259	10.793	2.653	2.664	2.684
TJ-50	49.570	49.829	31.303	2.671	2.685	2.709
TJ-51	50.525	50.719	31.462	2.619	2.629	2.646
TJ-52	22.255	22.517	13.885	2.574	2.604	2.654
TJ-53	57.618	57.946	36.052	2.627	2.642	2.667
TJ-54	32.331	32.552	20.366	2.648	2.666	2.697
TJ-55	41.366	41.535	26.031	2.663	2.674	2.693
TJ-56	16.689	16.792	10.524	2.658	2.674	2.702
TJ-57	44.032	44.245	27.760	2.666	2.679	2.701
D-1	42.136	42.374	26.580	2.663	2.678	2.704
D-2	44.037	44.443	27.903	2.658	2.682	2.725
D-3	39.192	39.580	24.708	2.631	2.657	2.701
D-4	64.412	64.833	41.533	2.759	2.778	2.810
D-5	49.566	49.918	31.198	2.643	2.662	2.694
D-6	50.126	50.548	32.380	2.754	2.777	2.820
D-7	30.968	31.036	20.017	2.805	2.812	2.823
D-8	35.858	35.947	23.317	2.834	2.841	2.854
D-9	34.739	35.046	22.572	2.780	2.804	2.850
D-10	40.723	41.225	26.442	2.750	2.784	2.846
D-11	51.853	52.019	33.616	2.813	2.822	2.838
D-12	21.903	22.044	14.215	2.793	2.811	2.844
D-13	21.707	22.041	14.022	2.702	2.744	2.820
D-14	63.489	63.865	40.106	2.667	2.683	2.710
D-15	59.483	59.938	37.455	2.641	2.661	2.695
D-16	30.593	30.788	19.299	2.658	2.675	2.704
D-17	61.653	61.816	40.078	2.831	2.839	2.852
D-18	21.197	21.353	13.780	2.794	2.815	2.853
D-19	14.488	14.554	9.406	2.809	2.822	2.846
M-1	74.600	74.855	46.766	2.651	2.660	2.675

M-2	23.526	23.645	14.835	2.666	2.679	2.702
M-3	41.934	42.440	26.478	2.622	2.654	2.708
M-4	21.121	21.215	13.312	2.668	2.680	2.700
M-5	36.656	36.826	23.102	2.666	2.678	2.700
M-6	12.888	13.023	8.102	2.614	2.642	2.688
M-7	24.753	24.839	15.591	2.672	2.681	2.697
M-8	52.901	53.107	33.290	2.665	2.675	2.693
M-9	29.782	29.963	18.764	2.655	2.671	2.698
M-10	18.671	18.733	11.760	2.673	2.682	2.697
M-11	29.616	29.875	18.579	2.617	2.640	2.679
M-12	21.026	21.128	13.168	2.637	2.649	2.671
M-13	11.023	11.076	6.913	2.643	2.656	2.677
M-14	31.710	31.940	19.883	2.625	2.644	2.676
M-15	18.326	18.495	11.483	2.609	2.633	2.673
M-16	13.585	13.655	8.565	2.664	2.678	2.701
M-17	55.535	55.762	35.049	2.676	2.687	2.706
M-18	27.923	28.780	18.346	2.671	2.753	2.910
M-19	61.503	61.764	38.856	2.680	2.691	2.711
M-20	50.845	50.985	32.126	2.691	2.699	2.711
M-21	33.992	34.211	21.424	2.654	2.671	2.700
M-22	18.631	18.743	11.735	2.654	2.670	2.697
M-23	23.129	23.263	14.664	2.685	2.700	2.727
M-24	48.675	48.889	30.793	2.685	2.697	2.717
M-25	16.098	16.204	10.269	2.708	2.725	2.757
M-26	40.512	40.711	25.514	2.661	2.674	2.696
M-27	34.765	34.904	21.905	2.670	2.680	2.698
S-1	30.125	31.171	19.169	2.505	2.592	2.745
S-2	18.385	19.422	11.801	2.408	2.544	2.787
S-3	12.222	12.817	7.763	2.414	2.531	2.736
S-4	14.231	14.984	9.073	2.403	2.530	2.754
S-5	19.890	21.046	12.699	2.379	2.517	2.761
S-6	30.318	31.515	19.552	2.530	2.630	2.811
S-7	8.794	9.332	5.623	2.367	2.512	2.768
S-8	9.153	9.701	5.808	2.347	2.487	2.731
S-9	9.240	9.583	5.992	2.568	2.664	2.840
S-10	16.496	17.879	11.612	2.627	2.848	3.371
S-11	13.691	14.298	8.785	2.479	2.589	2.786
S-12	9.961	10.408	6.348	2.449	2.559	2.752
S-13	6.114	6.398	3.886	2.430	2.542	2.739
S-14	38.502	40.129	24.704	2.492	2.597	2.785
S-15	52.586	52.882	33.127	2.657	2.672	2.698
S-16	25.536	25.805	16.120	2.632	2.660	2.707

S-17	50.757	50.952	32.002	2.674	2.684	2.701
S-18	30.722	30.920	19.372	2.656	2.673	2.702
S-19	30.966	31.156	19.500	2.652	2.668	2.696
S-20	11.864	12.010	7.482	2.615	2.648	2.703
S-21	26.242	26.580	16.559	2.614	2.648	2.705
S-22	13.855	14.043	8.748	2.612	2.647	2.708
CP-1	42.709	43.359	26.771	2.570	2.609	2.675
CP-2	38.048	38.824	23.965	2.556	2.608	2.697
CP-3	40.057	40.865	25.009	2.522	2.573	2.657
CP-4	27.122	27.655	16.982	2.537	2.586	2.670
CP-5	18.578	19.239	11.620	2.434	2.521	2.665
CP-6	9.227	9.603	5.805	2.425	2.524	2.692
CP-7	24.525	24.959	15.230	2.516	2.561	2.634
CP-8	18.602	18.971	11.763	2.576	2.627	2.715
CP-9	38.544	39.168	24.115	2.556	2.597	2.666
CP-10	20.323	20.713	12.592	2.498	2.546	2.624
CP-11	12.967	13.272	8.142	2.523	2.582	2.683
CP-12	6.855	7.056	4.319	2.500	2.573	2.698
CP-13	54.561	55.108	33.855	2.563	2.588	2.630
CP-14	34.096	34.516	21.154	2.547	2.578	2.630
CP-15	11.786	12.074	7.347	2.489	2.550	2.650
CA-1	54.020	54.216	34.113	2.682	2.692	2.709
CA-2	30.293	30.443	19.077	2.660	2.674	2.696
CA-3	33.824	33.940	21.335	2.679	2.688	2.703
CA-4	36.844	37.098	23.255	2.657	2.675	2.706
CA-5	36.605	36.746	23.092	2.676	2.686	2.704
CA-6	34.896	35.120	22.025	2.660	2.677	2.706
CA-7	41.838	42.120	26.405	2.658	2.675	2.706
CA-8	14.690	14.853	9.237	2.611	2.640	2.689
CA-9	21.260	21.424	13.416	2.650	2.671	2.705
CA-10	22.653	22.765	14.284	2.666	2.679	2.702
CA-11	18.206	18.379	11.475	2.632	2.657	2.700
CA-12	9.113	9.242	5.737	2.595	2.632	2.694
CA-13	31.418	31.682	19.763	2.631	2.653	2.691
CA-14	16.607	16.788	10.430	2.607	2.636	2.684
CA-15	10.767	10.950	6.783	2.579	2.623	2.698
CA-16	51.065	51.332	32.287	2.676	2.690	2.715
CA-17	18.219	18.325	11.489	2.660	2.676	2.702
CA-18	16.465	16.606	10.332	2.620	2.642	2.680
CA-19	14.211	14.295	8.966	2.662	2.678	2.705
CA-20	34.424	34.612	21.730	2.667	2.682	2.707
CA-21	20.215	20.394	12.743	2.637	2.661	2.701

CA-22	25.639	25.952	16.154	2.612	2.644	2.698
CA-23	14.438	14.577	9.072	2.618	2.643	2.686
CA-24	4.917	4.958	3.097	2.637	2.659	2.697
CA-25	27.469	27.803	17.302	2.611	2.643	2.697
CA-26	8.267	8.414	5.081	2.476	2.520	2.590
CA-27	18.166	18.337	11.451	2.633	2.658	2.700
CA-28	37.233	37.550	23.515	2.648	2.671	2.709
CmA-1	66.496	67.282	41.788	2.604	2.634	2.686
CmA-2	45.142	45.450	28.132	2.602	2.620	2.649
CmA-3	26.469	26.770	16.587	2.595	2.624	2.674
CmA-4	19.168	19.674	12.013	2.498	2.563	2.674
CmA-5	14.481	14.694	9.065	2.568	2.606	2.669
CmA-6	21.894	22.102	13.630	2.580	2.604	2.645
CmA-7	21.463	21.694	13.437	2.595	2.623	2.669
CmA-8	16.221	16.524	10.129	2.532	2.579	2.658
SA-1	45.899	46.360	28.832	2.614	2.640	2.685
SA-2	28.106	28.693	17.570	2.522	2.575	2.663
SA-3	34.538	34.980	21.880	2.632	2.665	2.724
SA-4	13.483	13.783	8.484	2.540	2.596	2.692
SA-5	24.811	25.334	15.527	2.525	2.579	2.668
SA-6	11.958	12.139	7.521	2.585	2.624	2.690
SA-7	23.336	23.731	14.632	2.560	2.603	2.676
SA-8	8.763	9.020	5.498	2.484	2.556	2.679
SA-9	33.416	34.546	20.958	2.455	2.538	2.677
SA-10	18.401	19.031	11.505	2.441	2.524	2.664
SA-11	43.170	43.490	27.068	2.624	2.644	2.676
SA-12	13.741	14.126	8.510	2.442	2.511	2.622
SA-13	21.314	21.620	13.503	2.621	2.659	2.724
SA-14	20.405	20.888	12.692	2.485	2.544	2.641
SA-15	22.187	22.973	13.858	2.430	2.516	2.659
SA-16	39.242	40.901	25.530	2.548	2.656	2.857
SA-17	17.955	18.808	11.689	2.518	2.637	2.860
SA-18	35.510	36.605	22.219	2.464	2.540	2.667
SA/B1 - 1	23.936	24.817	15.009	2.436	2.526	2.676
SA/B1 - 2	52.180	52.983	32.834	2.585	2.625	2.692
SA/B1 - 3	44.944	45.563	28.210	2.585	2.621	2.681
SA/B1 - 4	62.120	63.055	39.645	2.649	2.689	2.759
SA/B1 - 5	17.479	17.695	11.013	2.611	2.643	2.698
SA/B1 - 6	26.035	26.394	16.299	2.574	2.610	2.669
SA/B1 - 7	20.508	20.725	12.792	2.580	2.608	2.653
SA/B1 - 8	22.259	22.955	13.847	2.439	2.516	2.641
SA/B1 - 9	20.396	20.555	12.763	2.613	2.633	2.667

SA/B1 - 10	19.189	19.701	12.044	2.502	2.568	2.681
SA/B1 - 11	33.955	34.468	21.360	2.586	2.625	2.691
SchA/SER - 1	50.490	51.723	31.565	2.500	2.561	2.663
SchA/SER - 2	62.908	63.192	39.238	2.621	2.633	2.653
SchA/SER - 3	39.985	40.514	25.230	2.611	2.646	2.705
SchA/SER - 4	27.293	27.585	17.175	2.617	2.645	2.693
SchA/SER - 5	15.268	15.650	9.615	2.525	2.589	2.696
SchA/SER - 6	13.356	13.645	8.441	2.562	2.617	2.713
Sal-1	11.529	12.110	7.069	2.283	2.398	2.580
Sal-2	31.656	34.027	19.653	2.198	2.363	2.633
Sal-3	13.651	14.895	8.339	2.078	2.268	2.565
Sal-4	14.299	14.960	8.363	2.164	2.264	2.405
SAl/B2 - 1	63.683	71.265	39.904	2.027	2.268	2.673
SAl/B2 - 2	52.110	56.143	32.517	2.202	2.372	2.655
SAl/B2 - 3	41.710	44.599	26.095	2.250	2.406	2.666
SAl/B2 - 4	54.746	58.714	34.926	2.297	2.464	2.757
SAl/B2 - 5	39.634	42.448	24.830	2.246	2.405	2.672
SAl/B2 - 6	32.639	35.336	20.392	2.180	2.360	2.660
SAl/B2 - 7	35.357	38.039	22.034	2.205	2.372	2.649
SAl/B2 - 8	14.751	15.881	8.742	2.063	2.221	2.450
Plm-1	91.716	93.354	57.249	2.536	2.581	2.656
Plm-2	57.130	59.286	35.512	2.399	2.489	2.638
Plm-3	66.447	68.074	40.994	2.449	2.509	2.606
Plm-4	60.414	61.957	37.466	2.462	2.525	2.628
Plm-5	35.020	35.752	21.754	2.497	2.549	2.635
Plm-6	24.521	25.140	15.181	2.458	2.520	2.621
Plm-7	45.379	46.470	28.009	2.454	2.513	2.608
Plm-8	27.590	28.750	17.278	2.401	2.502	2.671
Plm-9	26.725	27.400	16.565	2.462	2.524	2.626
Plm-10	19.008	19.591	11.725	2.412	2.486	2.605
Plm-11	25.117	26.105	15.573	2.381	2.474	2.627
Plm-12	23.040	23.455	14.417	2.545	2.590	2.667
Plm-13	66.169	67.173	40.723	2.497	2.535	2.596
Plm-14	78.459	79.776	49.000	2.545	2.587	2.659
Plm-15	37.051	37.641	23.029	2.531	2.571	2.638
Plm-16	44.383	45.109	27.733	2.550	2.591	2.661
Plm-17	26.500	27.083	16.967	2.615	2.672	2.775
Pll -1	-	8.303	4.447	-	2.149	-
Pll -2	-	9.316	5.106	-	2.209	-
Pll -3	-	10.241	5.563	-	2.185	-
Pll -4	-	15.106	8.116	-	2.157	-
Pll -5	-	5.105	2.691	-	2.111	-

Msm-1	21.993	25.924	13.235	1.730	2.039	2.507
Msm-2	61.538	71.651	27.844	1.402	1.633	1.823
Msm-3	41.362	48.065	22.711	1.628	1.892	2.214
Msm-4	33.742	40.586	18.480	1.524	1.833	2.207
Msm-5	42.848	49.662	24.110	1.674	1.940	2.283
Msm-6	18.347	22.267	9.944	1.486	1.804	2.179
Msm-7	22.723	26.684	12.690	1.621	1.903	2.261
Msm-8	34.893	42.595	21.502	1.651	2.016	2.601
Msm-9	49.887	50.575	31.281	2.581	2.617	2.676
Msm-10	44.980	53.096	24.660	1.579	1.864	2.210
Msm-11	16.370	19.614	8.262	1.439	1.725	2.015
Msm-12	45.994	55.609	27.798	1.651	1.996	2.523
Msm-13	22.834	27.856	14.099	1.657	2.021	2.609
Msm-14	17.613	20.759	9.276	1.531	1.805	2.109
Msm-15	17.923	22.235	11.051	1.600	1.985	2.603
Msm-16	36.970	44.665	22.677	1.678	2.028	2.582
Msm-17	36.362	45.008	22.185	1.590	1.968	2.560
Msm-18	32.700	40.002	19.929	1.626	1.989	2.556
Msm-19	58.745	59.906	36.738	2.531	2.581	2.665
Msm-20	34.224	35.127	21.118	2.439	2.503	2.607
Msm-21	41.867	44.022	25.891	2.305	2.424	2.616
Msm-22	52.543	53.081	32.757	2.581	2.607	2.651
Msm-23	17.889	18.221	11.176	2.535	2.582	2.660
Msm-24	15.778	19.277	9.691	1.643	2.007	2.587
Msl-1	68.820	69.062	43.347	2.671	2.681	2.697
Msl-2	30.361	30.717	19.111	2.611	2.642	2.694
Msl-3	29.015	29.258	18.228	2.626	2.648	2.685
Msl-4	28.320	28.723	17.768	2.580	2.617	2.679
Msl-5	10.133	10.242	6.328	2.584	2.612	2.658
Msl-6	17.960	18.522	11.257	2.468	2.545	2.675
Msl-7	30.175	30.989	18.923	2.496	2.564	2.677
Msl-8	29.574	30.261	18.575	2.526	2.585	2.684
Msl-9	36.285	37.427	22.801	2.476	2.554	2.686
Msl-10	27.881	28.608	17.582	2.524	2.590	2.702
Msl-11	41.425	42.876	25.904	2.436	2.522	2.664
M.L./B1-1	77.211	80.676	47.644	2.333	2.438	2.607
M.L./B1-2	20.884	22.846	12.477	2.010	2.199	2.480
M.L./B1-3	56.281	58.546	34.740	2.360	2.455	2.608
M.L./B1-4	78.754	82.373	33.787	1.618	1.692	1.748
M.L./B1-5	24.673	27.605	14.852	1.931	2.161	2.508
M.L./B1-6	18.167	19.996	9.688	1.759	1.936	2.139
M.L./B1-7	28.270	29.448	17.394	2.341	2.439	2.595

M.L./B1-8	44.691	48.105	26.845	2.098	2.259	2.500
M.L./B1-9	16.378	18.056	9.802	1.981	2.184	2.486
M.L./B1-10	26.346	27.667	16.292	2.312	2.428	2.616
M.L./B1-11	30.267	32.700	18.159	2.078	2.245	2.495
M.L./B1-12	46.055	55.587	27.937	1.663	2.007	2.537
M.L./B1-13	30.009	32.282	17.880	2.080	2.237	2.470
M.L./B1-14	54.996	61.715	31.296	1.805	2.025	2.316
M.L./B1-15	54.752	62.916	32.141	1.776	2.041	2.417
M.L./B1-16	34.065	37.706	20.294	1.953	2.162	2.469
M.L./B1-17	90.081	99.235	54.075	1.991	2.193	2.497
M.L./B1-18	49.628	55.171	29.252	1.911	2.125	2.431
M.L./B1-19	20.481	24.468	12.495	1.708	2.040	2.560
M.L./B1-20	35.808	38.108	21.509	2.153	2.292	2.500
M.L./B1-21	47.386	49.787	28.750	2.248	2.362	2.538
O-1	32.012	32.413	22.186	3.125	3.164	3.252
O-2	30.403	30.856	20.914	3.053	3.098	3.198
O-3	48.902	49.489	33.663	3.084	3.121	3.203
O-4	21.800	22.208	15.007	3.022	3.078	3.203
O-5	23.663	24.037	16.308	3.056	3.104	3.211
O-6	23.193	23.550	15.935	3.040	3.087	3.190
O-7	16.466	16.776	11.314	3.009	3.066	3.190
O-8	35.222	35.700	24.203	3.058	3.100	3.191
O-9	24.106	24.478	16.467	3.004	3.050	3.150

APPENDIX C – SUPPLEMENTARY NETTLETON PROFILES

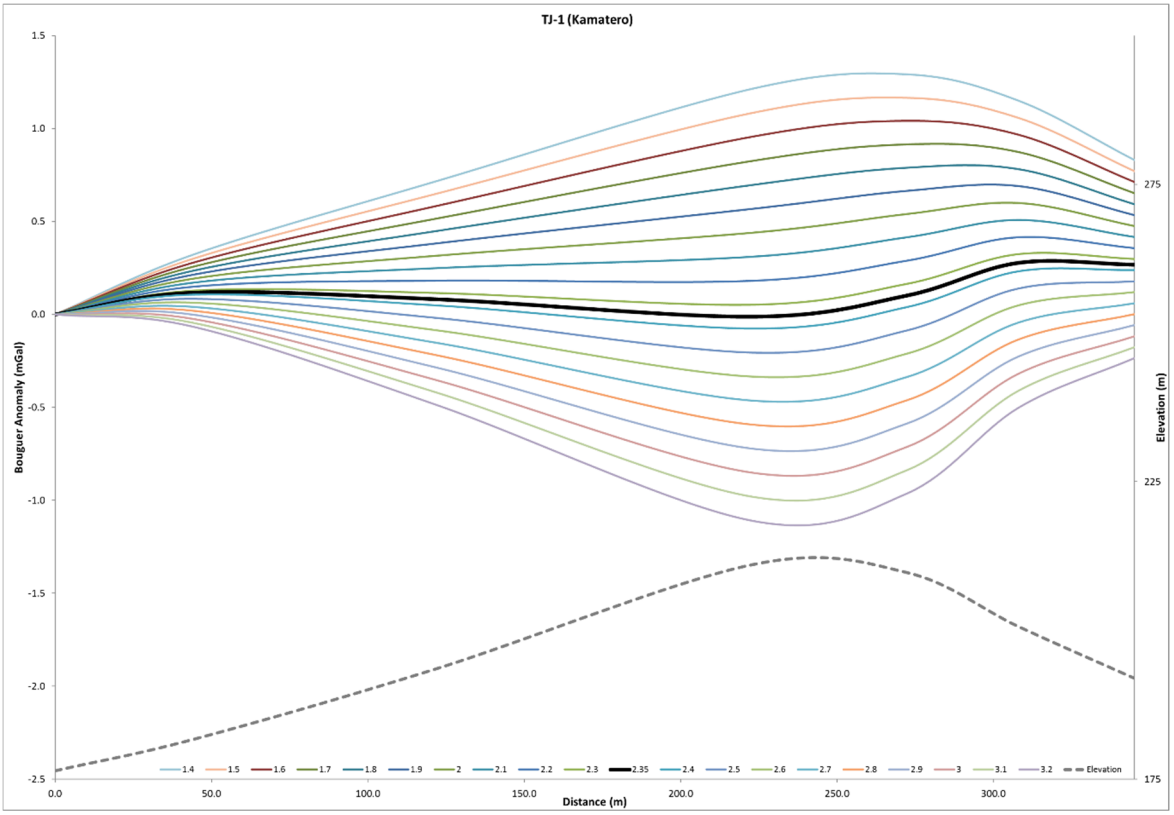

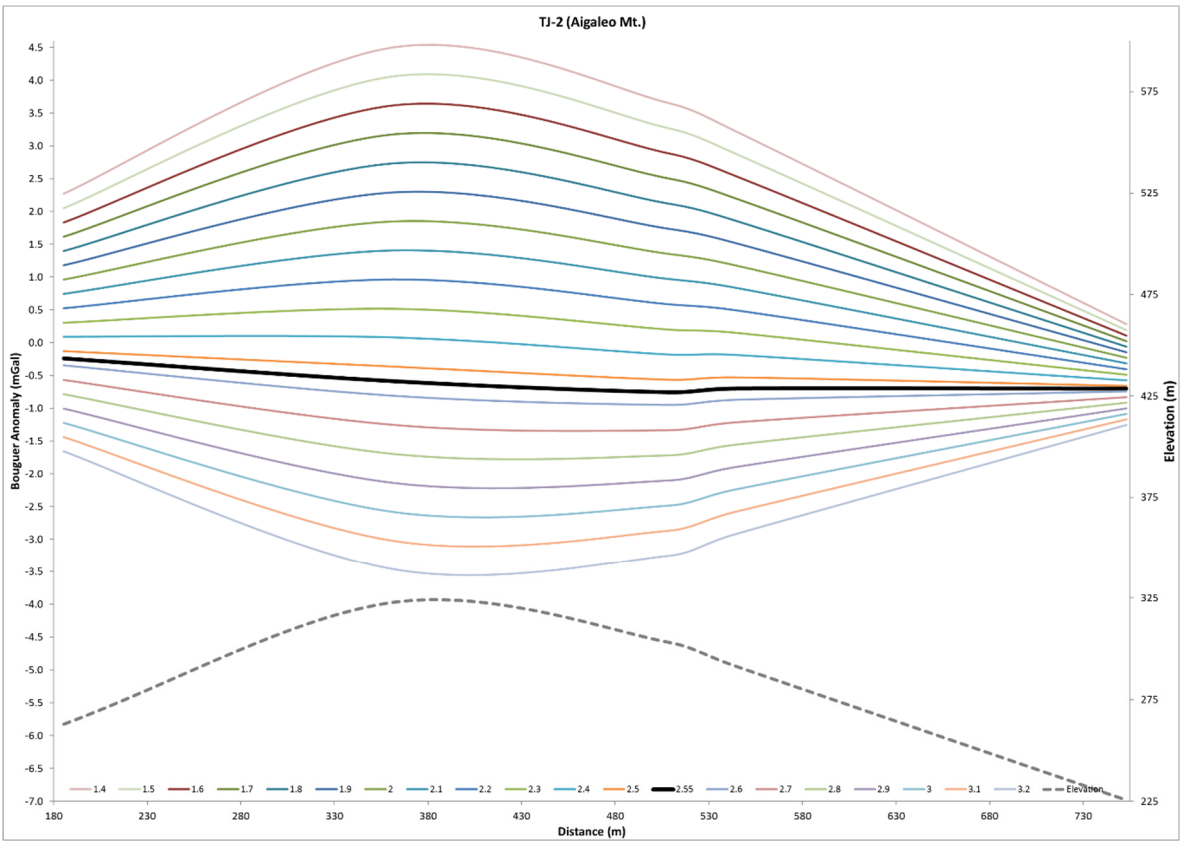

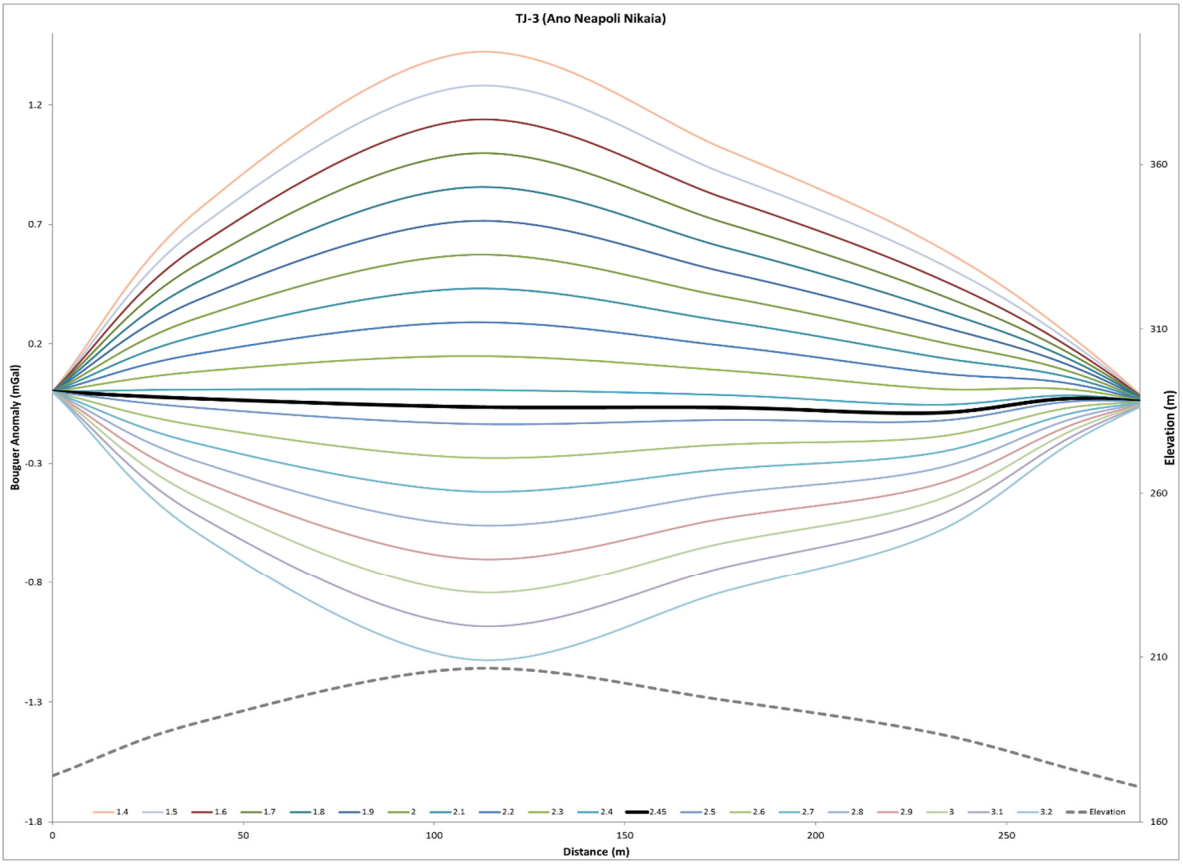
TJ-3 (Ano Neapoli Nikaia)
Bouguer Anomaly (mGal)
Elevation (m)
Distance (m)
1.2
0.7
0.2
-0.3
-0.8
-1.3
-1.8
360
310
260
210
160
0
50
100
150
200
250
1.4 1.5 1.6 1.7 1.8 1.9 2 2.1 2.2 2.3 2.4 2.45 2.5 2.6 2.7 2.8 2.9 3 3.1 3.2 Elevation

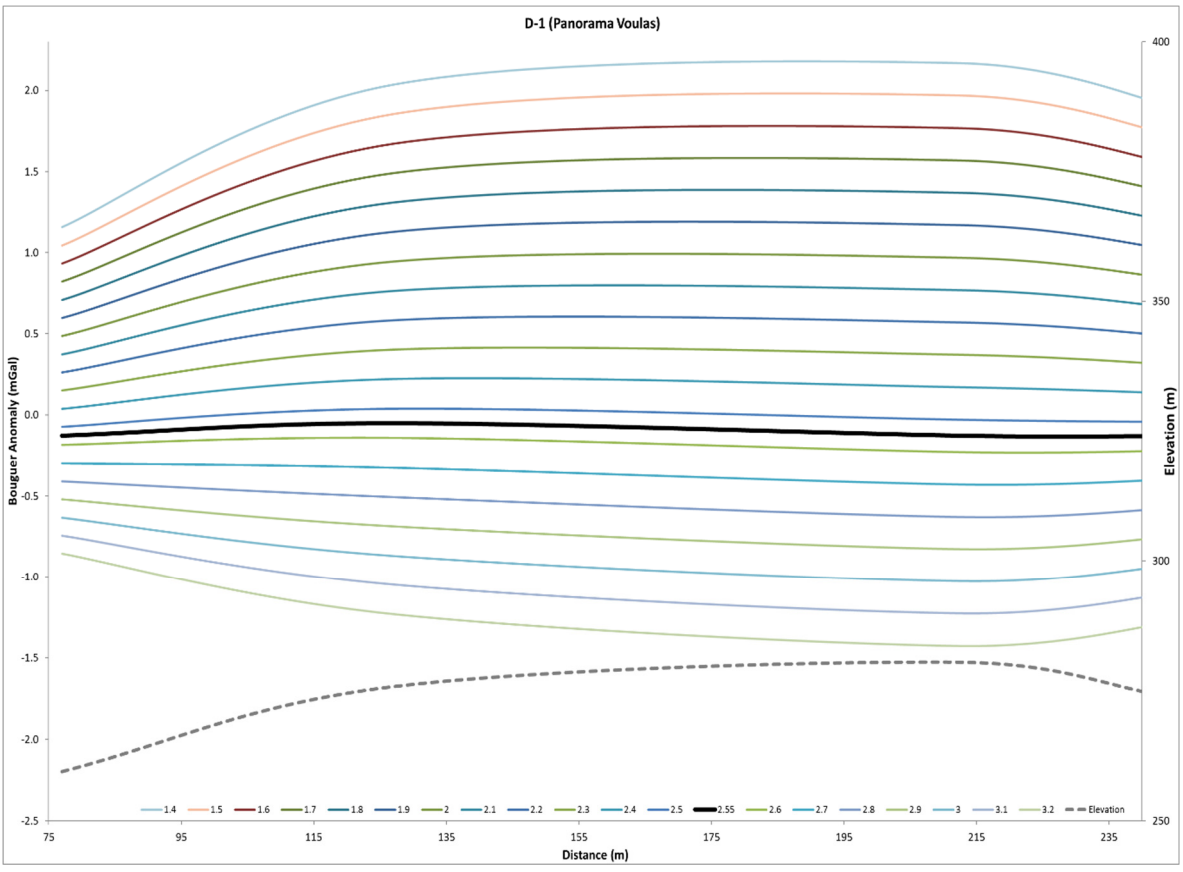
D-1 (Panorama Voulas)
Bouguer Anomaly (mGal)
Elevation (m)
Distance (m)
2.0
1.5
1.0
0.5
0.0
-0.5
-1.0
-1.5
-2.0
-2.5
400
350
300
250
75
95
115
135
155
175
195
215
235
1.4 1.5 1.6 1.7 1.8 1.9 2 2.1 2.2 2.3 2.4 2.5 2.55 2.6 2.7 2.8 2.9 3 3.1 3.2 Elevation

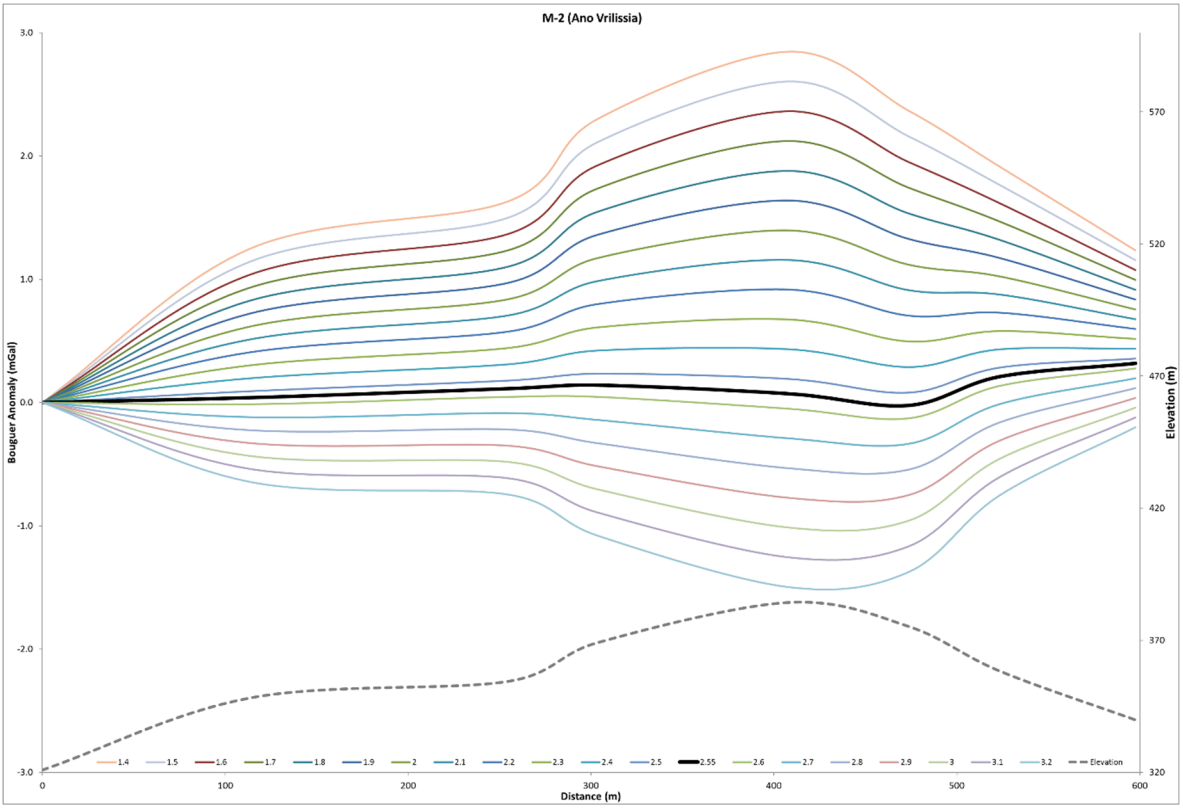
M-2 (Ano Vrilissia)
Bouguer Anomaly (mGal)
Elevation (m)
Distance (m)
1.4 1.5 1.6 1.7 1.8 1.9 2 2.1 2.2 2.3 2.4 2.5 2.55 2.6 2.7 2.8 2.9 3 3.1 3.2 Elevation

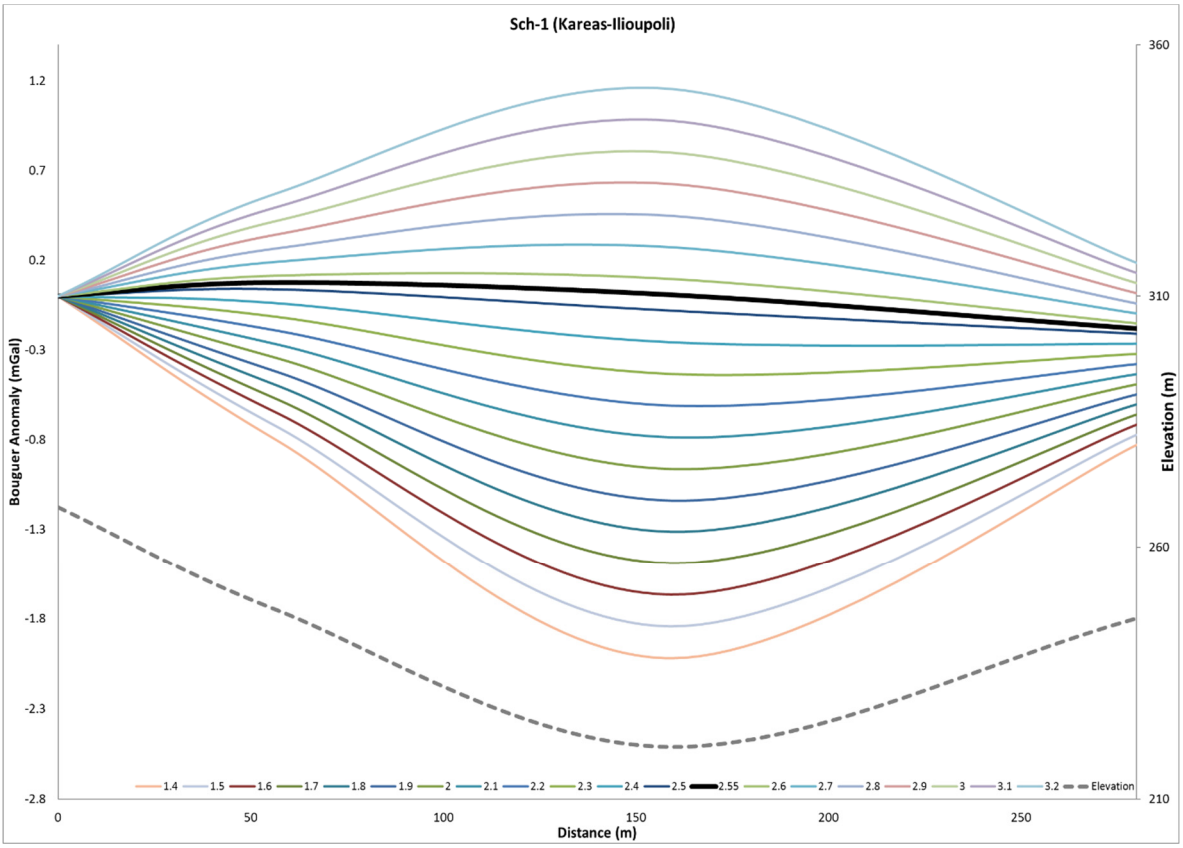
Sch-1 (Kareas-Ilioupoli)
Bouguer Anomaly (mGal)
Elevation (m)
Distance (m)
1.4 1.5 1.6 1.7 1.8 1.9 2 2.1 2.2 2.3 2.4 2.5 2.55 2.6 2.7 2.8 2.9 3 3.1 3.2 Elevation

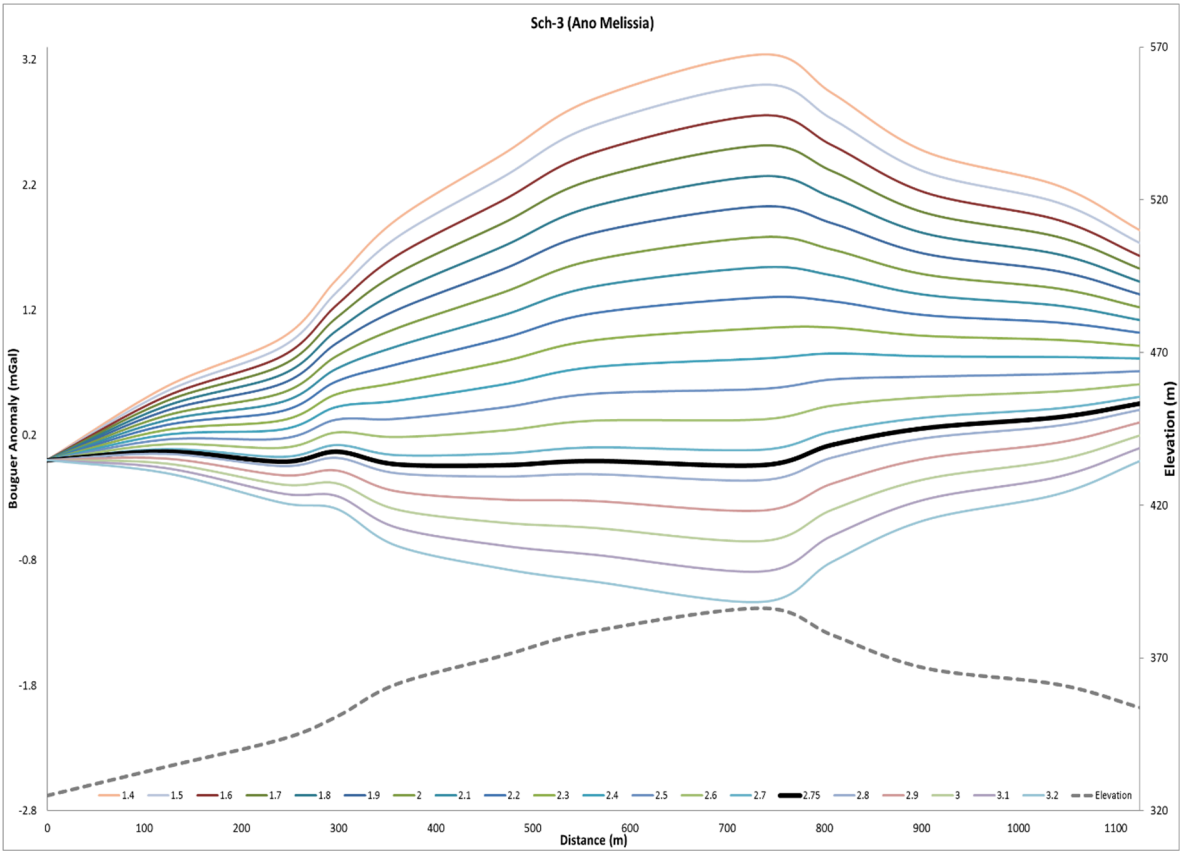
Sch-3 (Ano Melissia)
Bouguer Anomaly (mGal)
Elevation (m)
Distance (m)
3.2
2.2
1.2
0.2
-0.8
-1.8
-2.8
570
520
470
420
370
320
0
100
200
300
400
500
600
700
800
900
1000
1100
1.4 1.5 1.6 1.7 1.8 1.9 2 2.1 2.2 2.3 2.4 2.5 2.6 2.7 2.75 2.8 2.9 3 3.1 3.2 Elevation

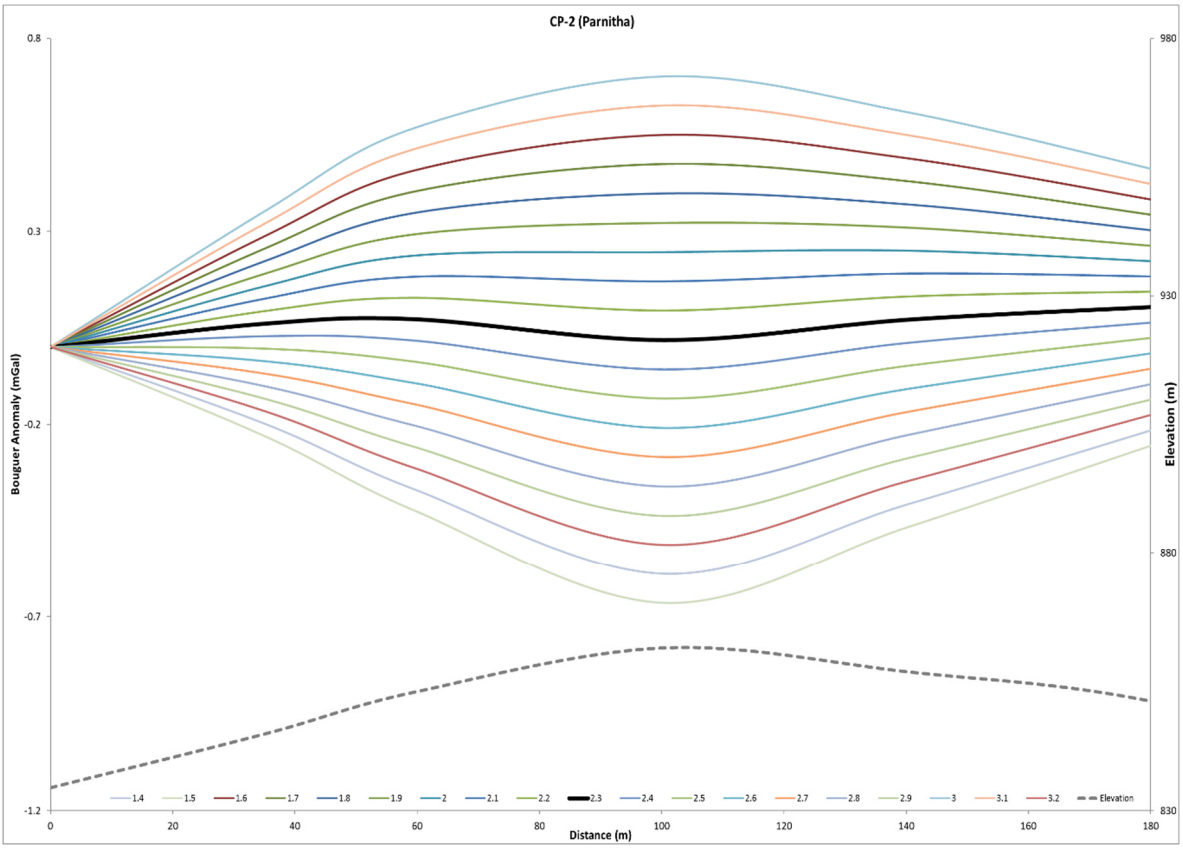
CP-2 (Parnitha)
Bouguer Anomaly (mGal)
Elevation (m)
Distance (m)
0.8
0.3
-0.2
-0.7
-1.2
980
930
880
830
0
20
40
60
80
100
120
140
160
180
1.4 1.5 1.6 1.7 1.8 1.9 2 2.1 2.2 2.3 2.4 2.5 2.6 2.7 2.8 2.9 3 3.1 3.2 Elevation

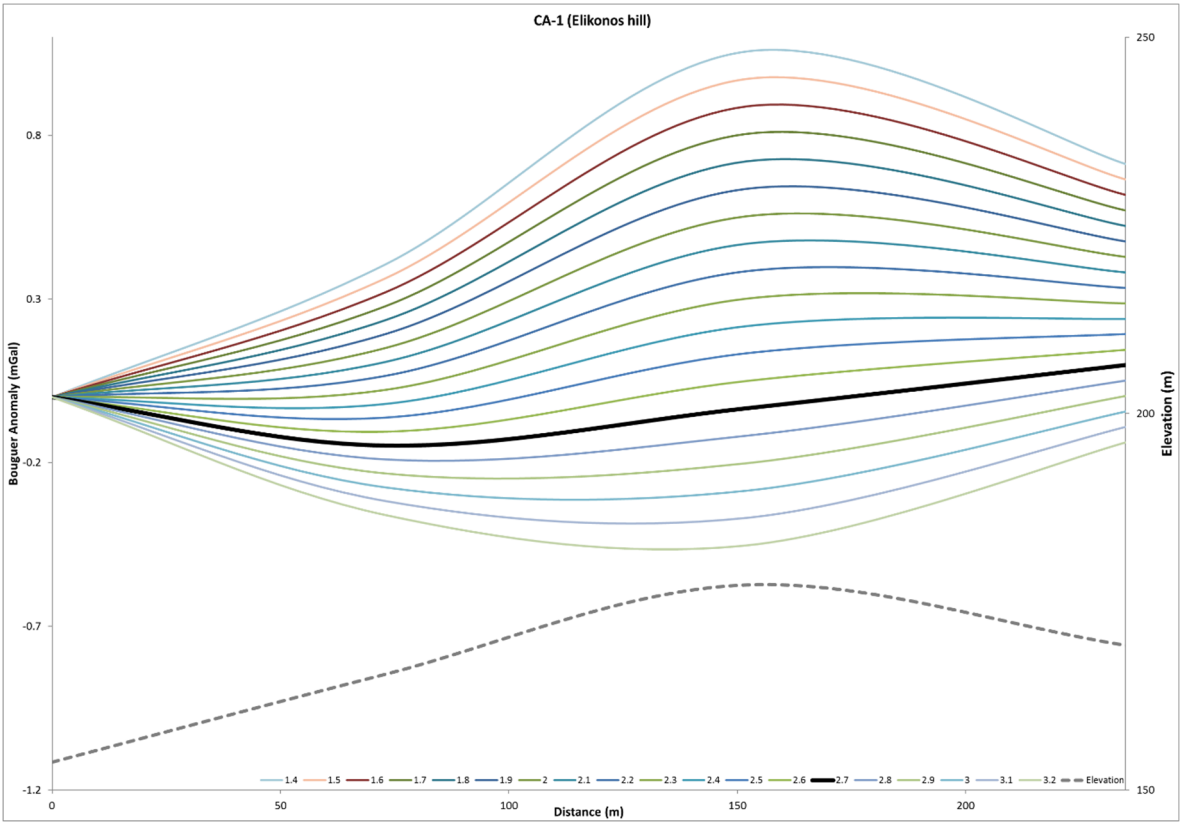
CA-1 (Elikonos hill)
Bouguer Anomaly (mGal)
0.8
0.3
-0.2
-0.7
-1.2
Elevation (m)
250
200
150
0
50
100
150
200
Distance (m)
1.4 1.5 1.6 1.7 1.8 1.9 2 2.1 2.2 2.3 2.4 2.5 2.6 2.7 2.8 2.9 3 3.1 3.2 Elevation

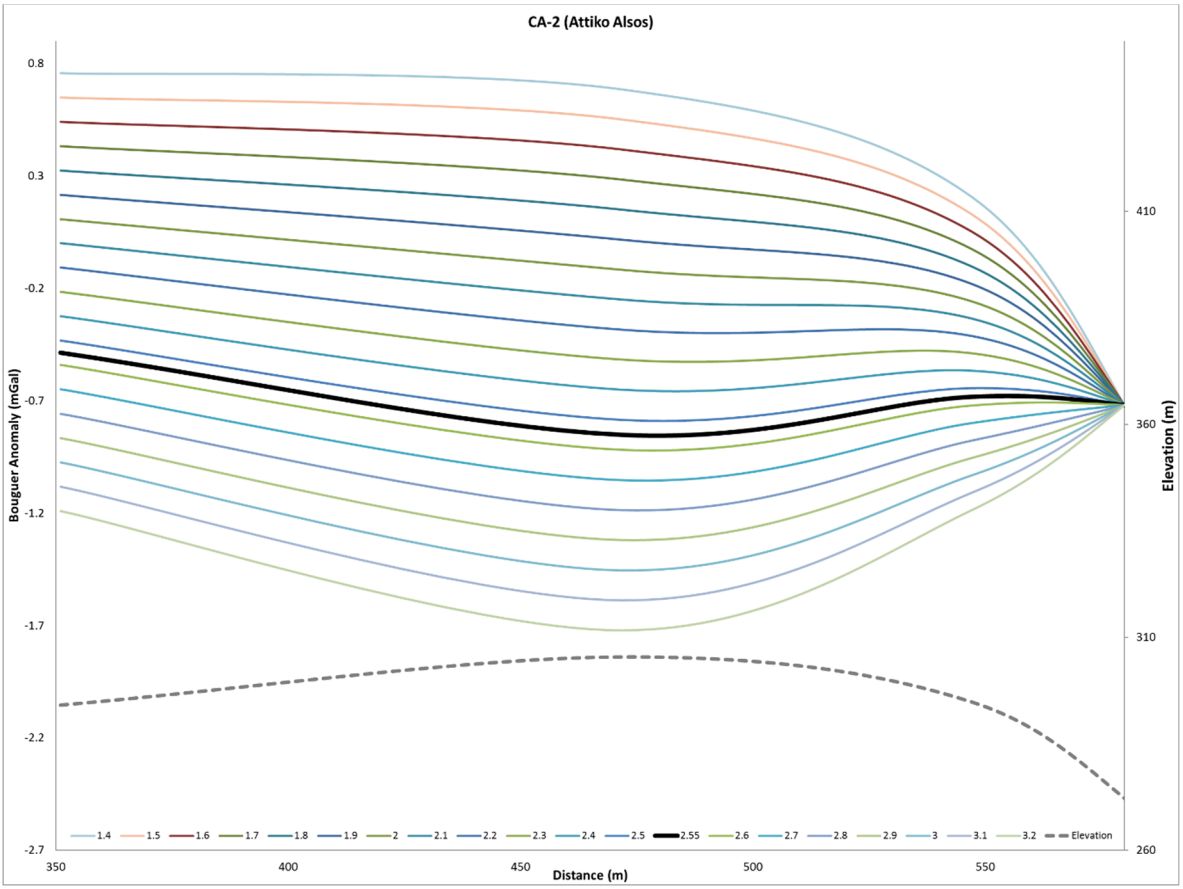
CA-2 (Attiko Alsos)
Bouguer Anomaly (mGal)
0.8
0.3
-0.2
-0.7
-1.2
-1.7
-2.2
-2.7
Elevation (m)
410
360
310
260
350
400
450
500
550
Distance (m)
1.4 1.5 1.6 1.7 1.8 1.9 2 2.1 2.2 2.3 2.4 2.5 2.55 2.6 2.7 2.8 2.9 3 3.1 3.2 Elevation

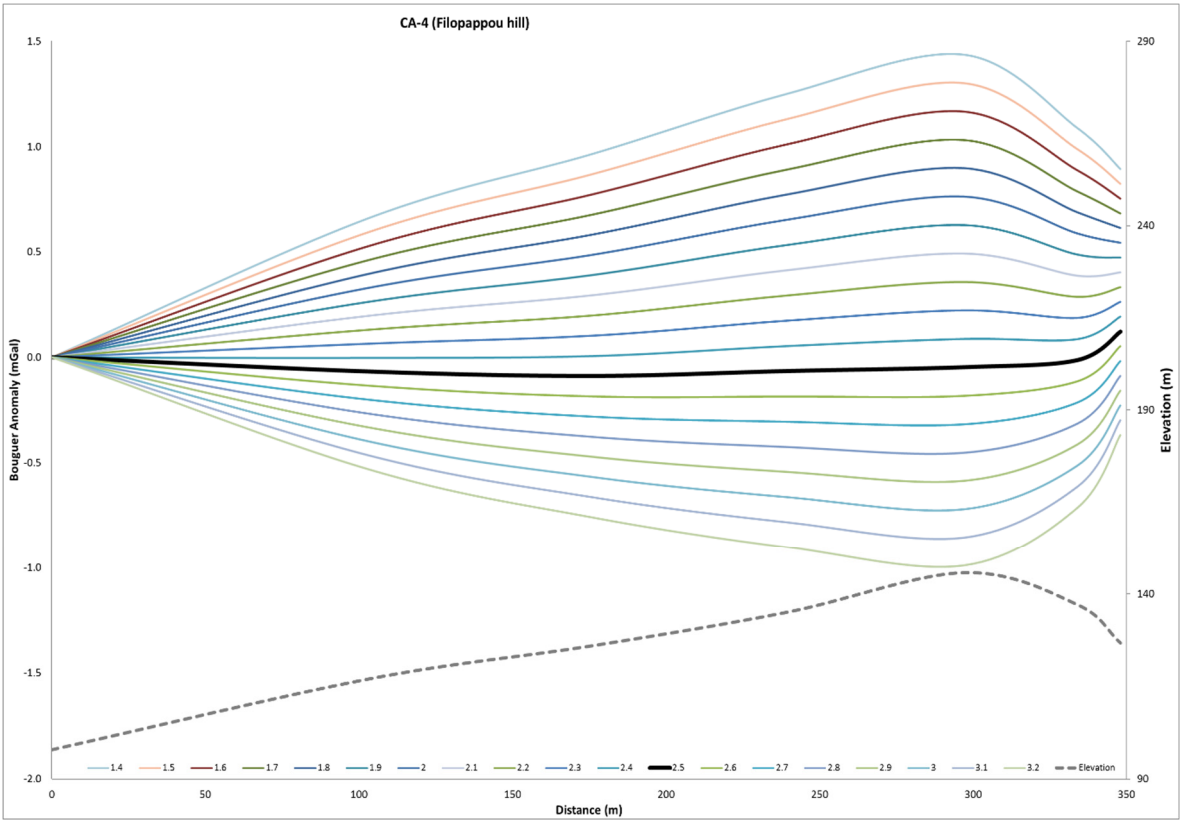
CA-4 (Filopappou hill)
Bouguer Anomaly (mGal)
Elevation (m)
Distance (m)
1.4 1.5 1.6 1.7 1.8 1.9 2 2.1 2.2 2.3 2.4 2.5 2.6 2.7 2.8 2.9 3 3.1 3.2 Elevation

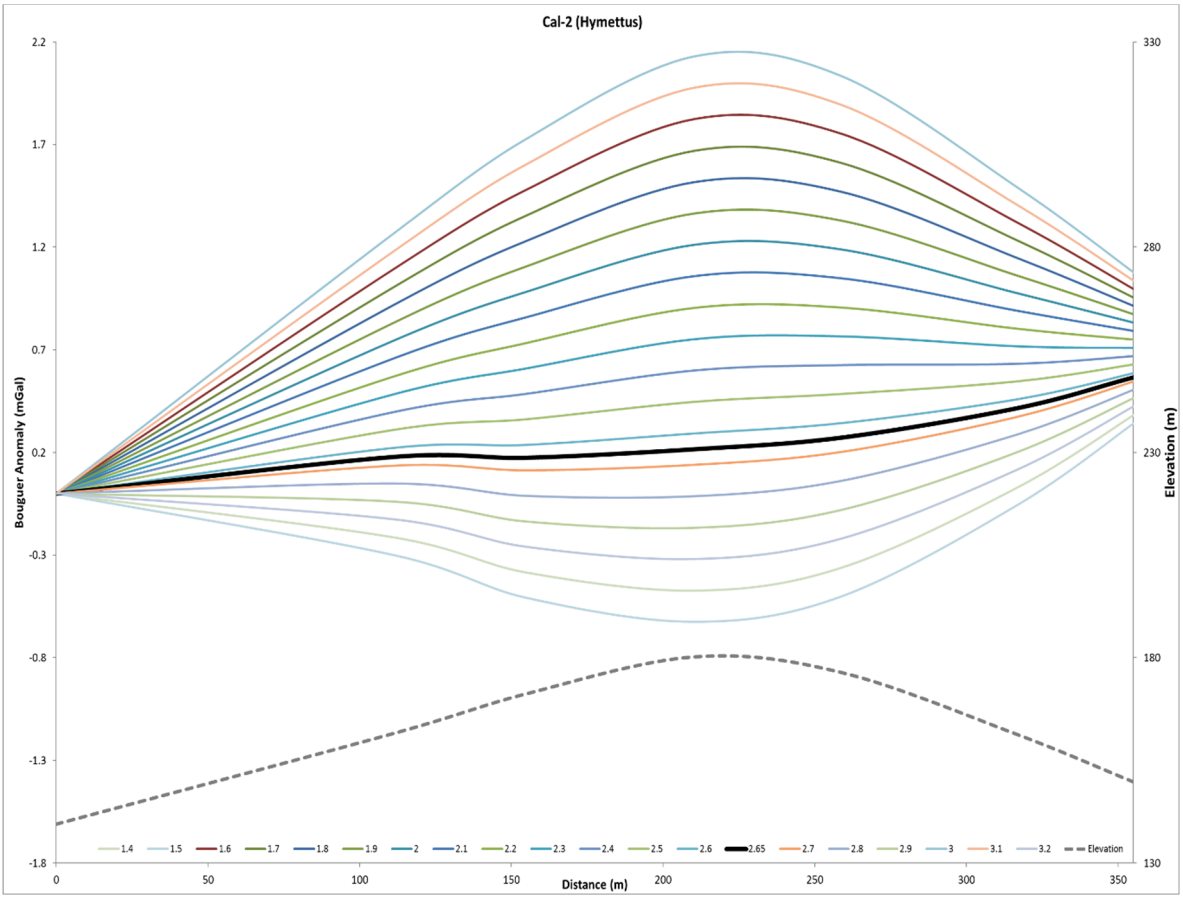
Cal-2 (Hymettus)
Bouguer Anomaly (mGal)
Elevation (m)
Distance (m)
1.4 1.5 1.6 1.7 1.8 1.9 2 2.1 2.2 2.3 2.4 2.5 2.6 2.65 2.7 2.8 2.9 3 3.1 3.2 Elevation

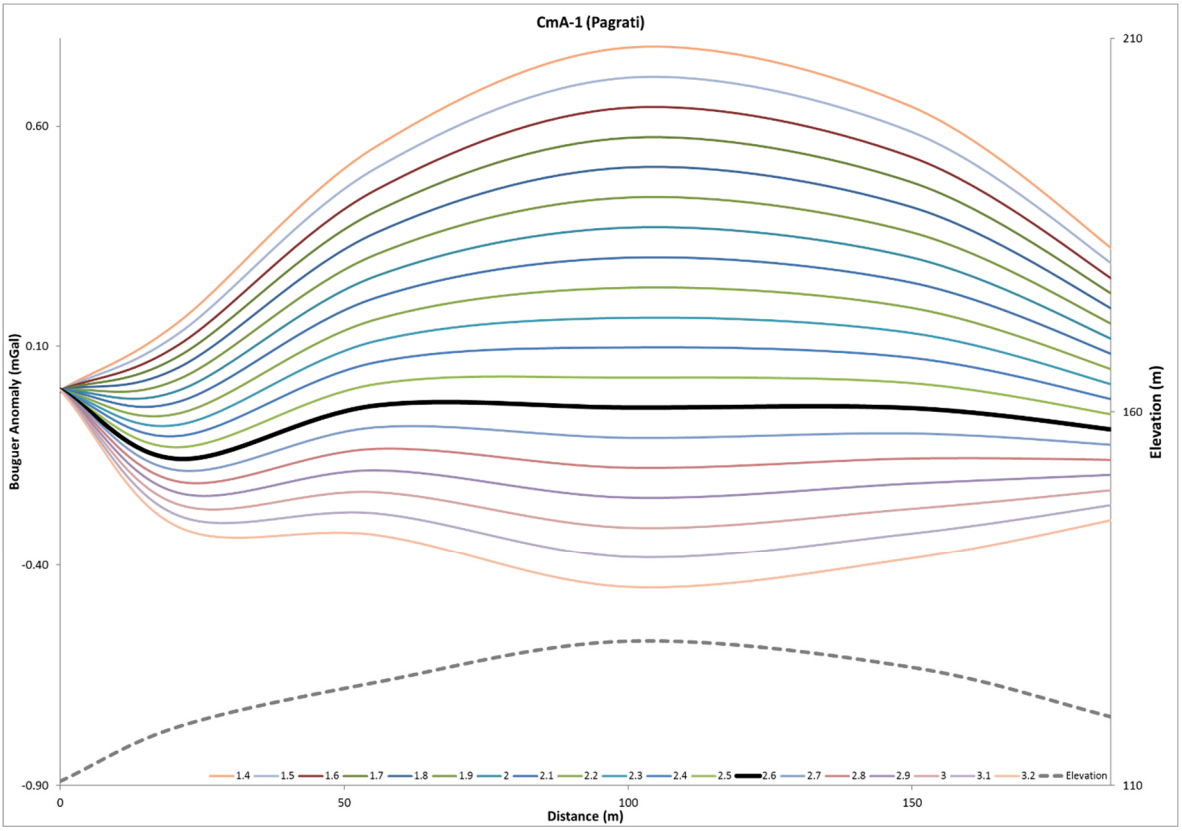
CmA-1 (Pagrati)
Bouguer Anomaly (mGal)
0.60
0.10
-0.40
-0.90
Elevation (m)
210
160
110
0
50
100
150
Distance (m)
1.4 1.5 1.6 1.7 1.8 1.9 2 2.1 2.2 2.3 2.4 2.5 2.6 2.7 2.8 2.9 3 3.1 3.2 Elevation

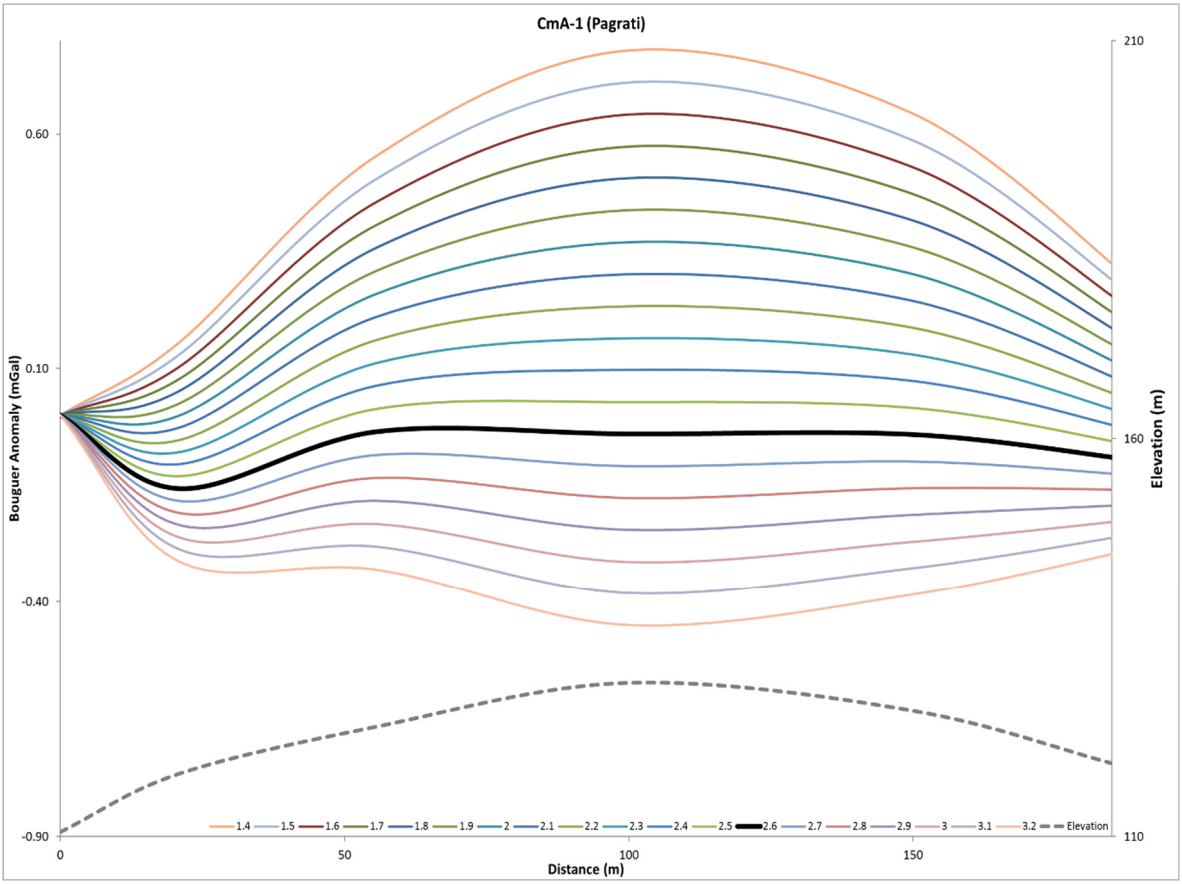
CmA-1 (Pagrati)
Bouguer Anomaly (mGal)
0.60
0.10
-0.40
-0.90
Elevation (m)
210
160
110
0
50
100
150
Distance (m)
1.4 1.5 1.6 1.7 1.8 1.9 2 2.1 2.2 2.3 2.4 2.5 2.6 2.7 2.8 2.9 3 3.1 3.2 Elevation

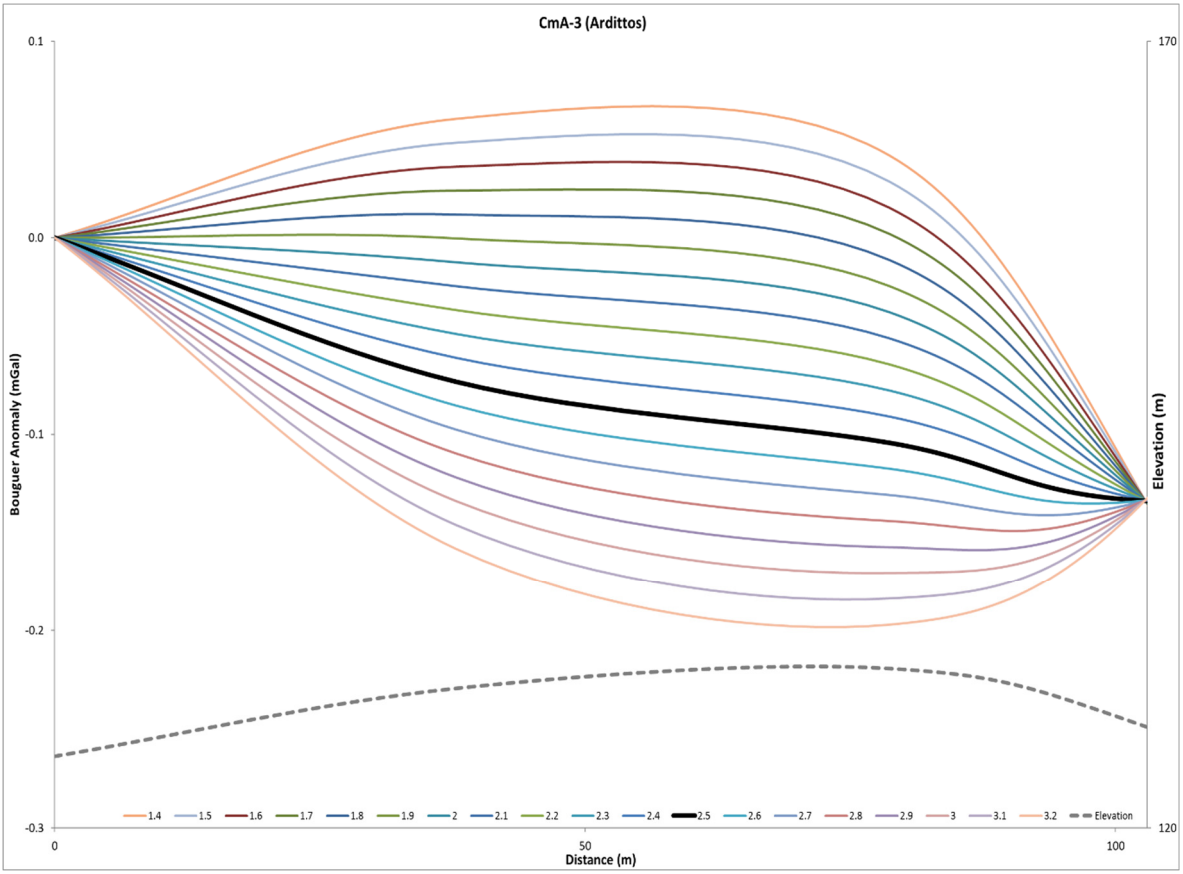
CmA-3 (Arditos)
Bouguer Anomaly (mGal)
Elevation (m)
Distance (m)
0.1
0.0
-0.1
-0.2
-0.3
170
120
0
50
100
1.4 1.5 1.6 1.7 1.8 1.9 2 2.1 2.2 2.3 2.4 2.5 2.6 2.7 2.8 2.9 3 3.1 3.2 Elevation

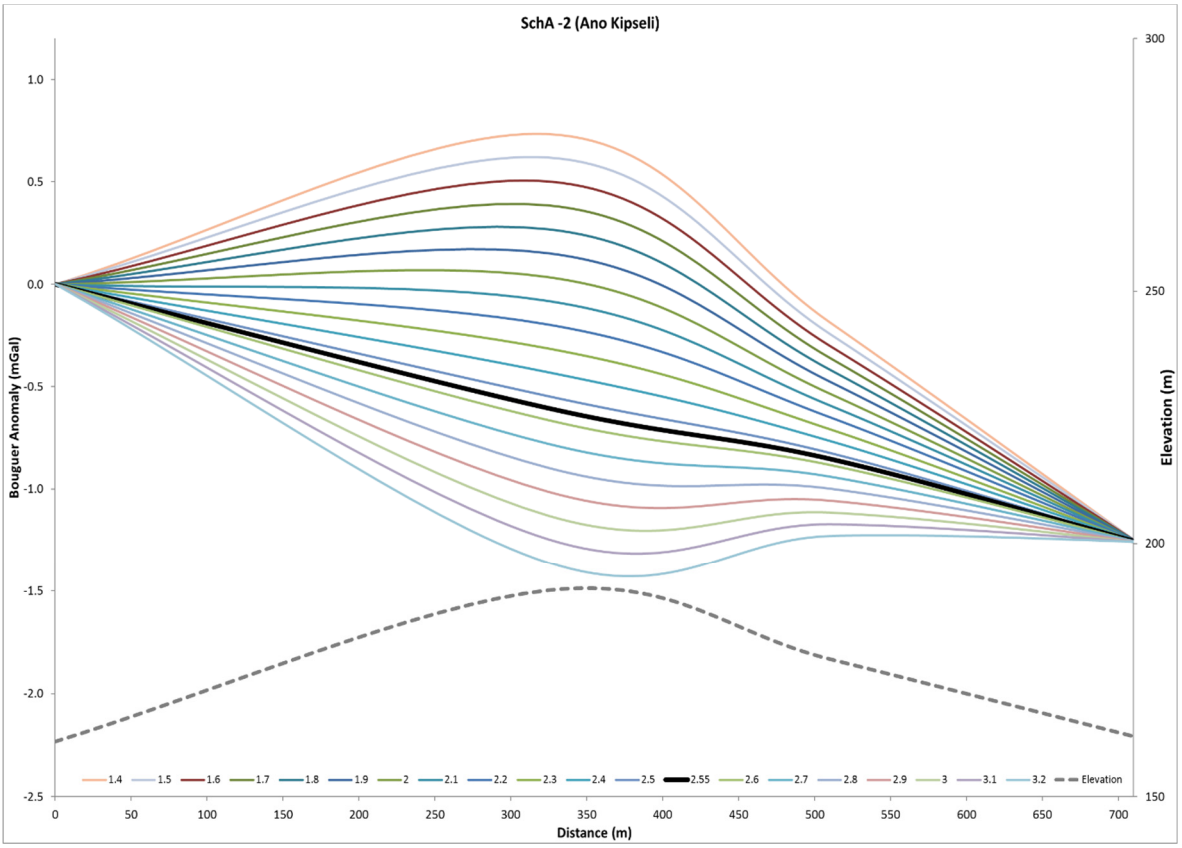
SchA -2 (Ano Kipseli)
Bouguer Anomaly (mGal)
Elevation (m)
Distance (m)
1.0
0.5
0.0
-0.5
-1.0
-1.5
-2.0
-2.5
300
250
200
150
0
50
100
150
200
250
300
350
400
450
500
550
600
650
700
1.4 1.5 1.6 1.7 1.8 1.9 2 2.1 2.2 2.3 2.4 2.5 2.55 2.6 2.7 2.8 2.9 3 3.1 3.2 Elevation

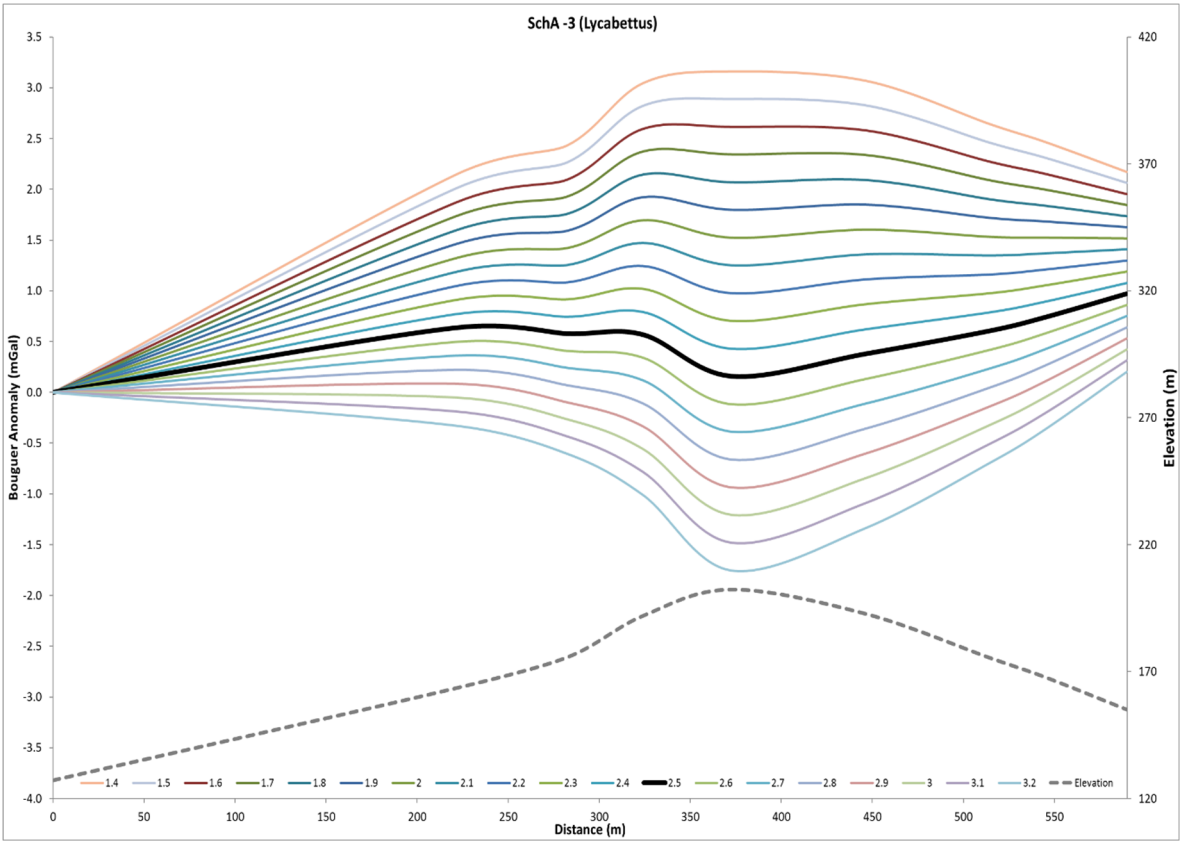
SchA -3 (Lycabettus)
Bouguer Anomaly (mGal)
Elevation (m)
Distance (m)
1.4 1.5 1.6 1.7 1.8 1.9 2 2.1 2.2 2.3 2.4 2.5 2.6 2.7 2.8 2.9 3 3.1 3.2 Elevation

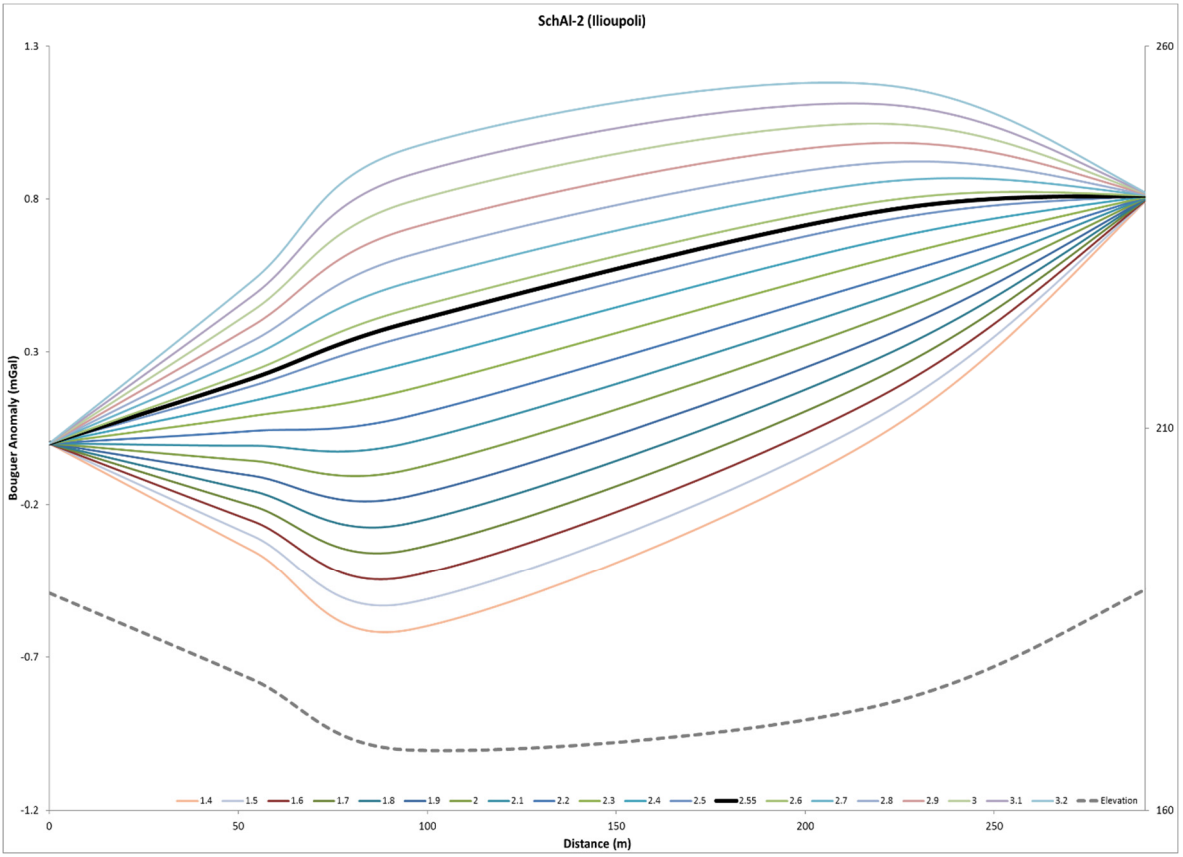
SchAl-2 (Ilioupoli)
Bouguer Anomaly (mGal)
Distance (m)
1.4 1.5 1.6 1.7 1.8 1.9 2 2.1 2.2 2.3 2.4 2.5 2.55 2.6 2.7 2.8 2.9 3 3.1 3.2 Elevation

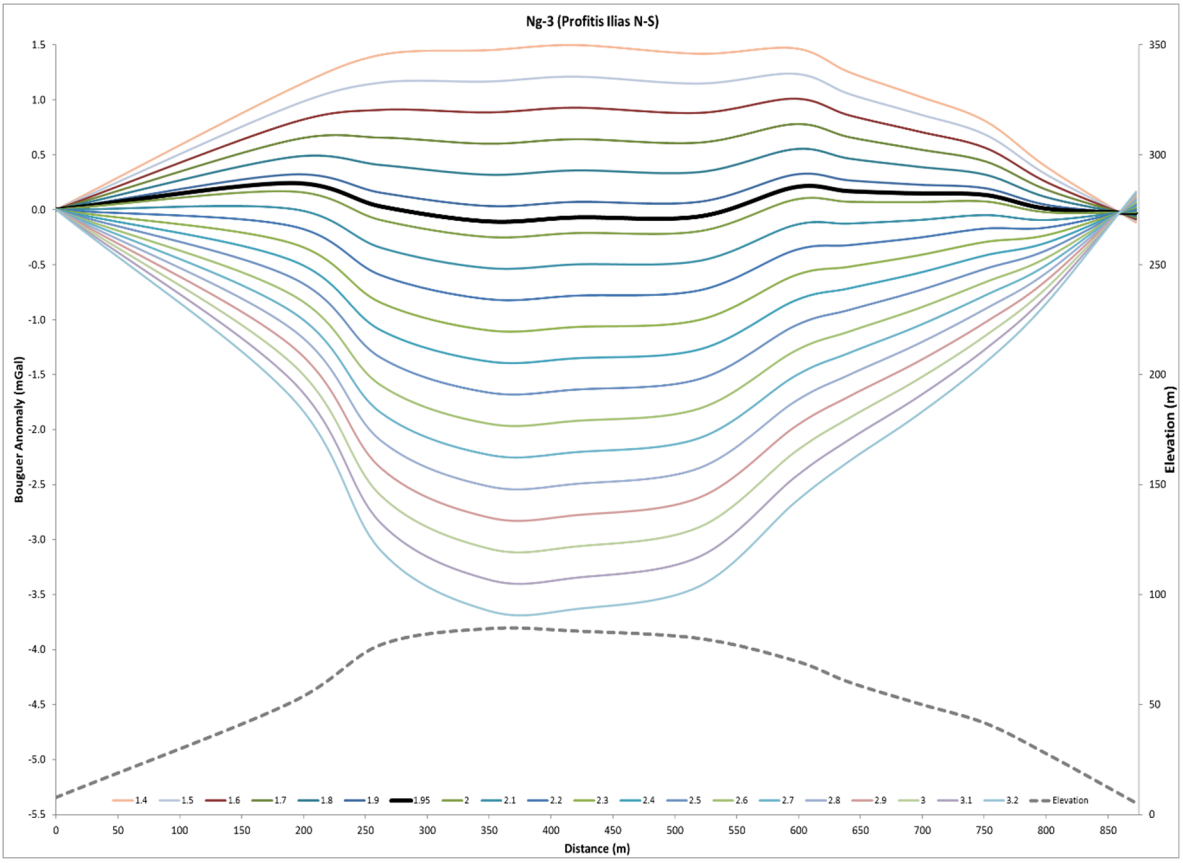
Ng-3 (Profitis Ilias N-S)
Bouguer Anomaly (mGal)
Elevation (m)
Distance (m)
1.4 1.5 1.6 1.7 1.8 1.9 1.95 2 2.1 2.2 2.3 2.4 2.5 2.6 2.7 2.8 2.9 3 3.1 3.2 Elevation

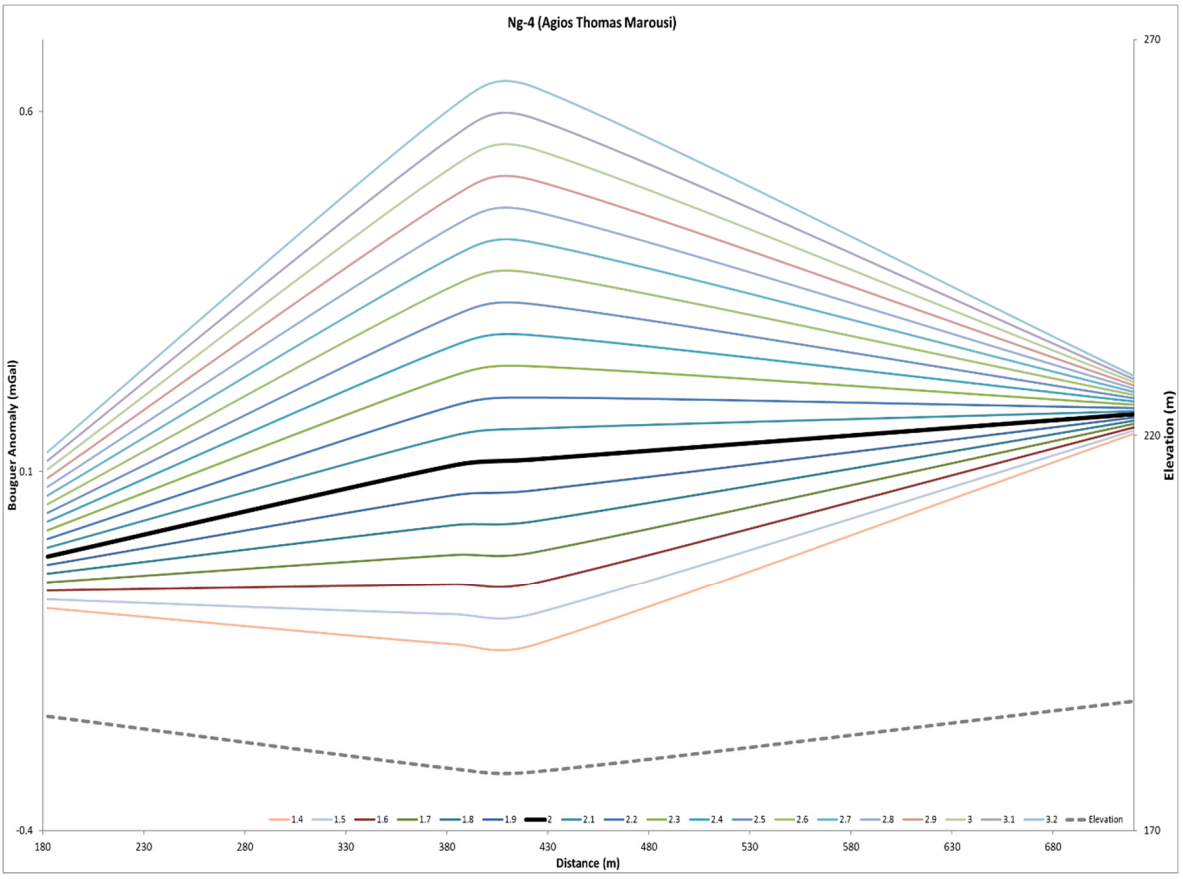
Ng-4 (Agios Thomas Marousi)
Bouguer Anomaly (mGal)
Elevation (m)
Distance (m)
1.4 1.5 1.6 1.7 1.8 1.9 2 2.1 2.2 2.3 2.4 2.5 2.6 2.7 2.8 2.9 3 3.1 3.2 Elevation

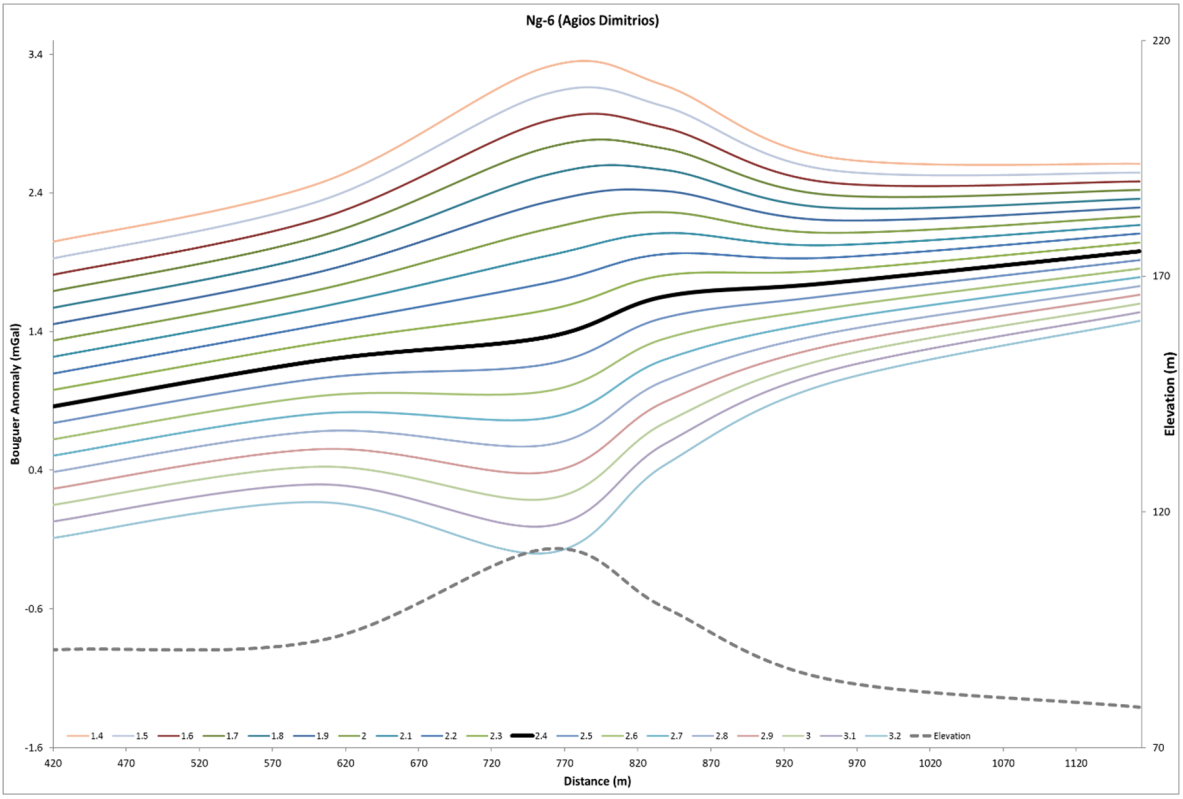
Ng-6 (Agios Dimitrios)
Bouguer Anomaly (mGal)
Elevation (m)
Distance (m)
3.4
2.4
1.4
0.4
-0.6
-1.6
220
170
120
70
420
470
520
570
620
670
720
770
820
870
920
970
1020
1070
1120
1.4 1.5 1.6 1.7 1.8 1.9 2 2.1 2.2 2.3 2.4 2.5 2.6 2.7 2.8 2.9 3 3.1 3.2 Elevation

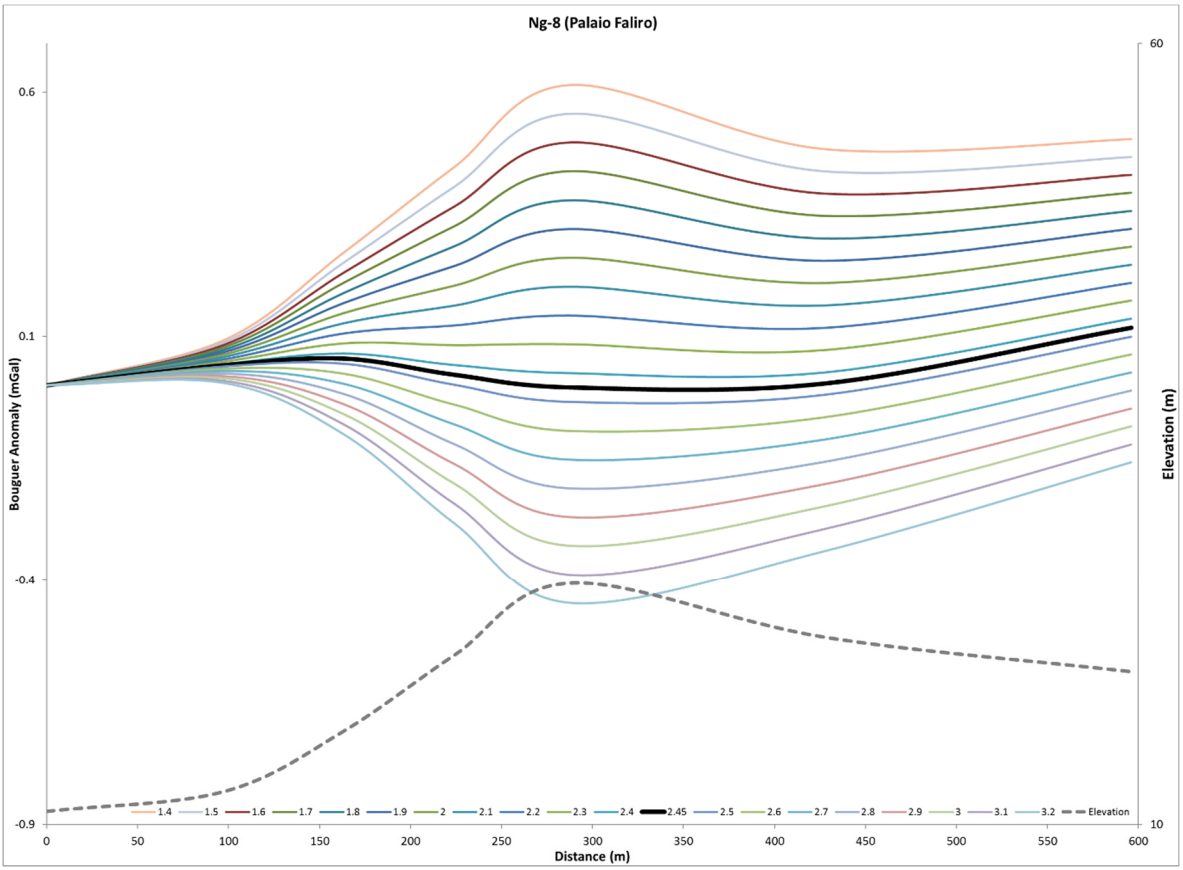
Ng-8 (Palaio Faliro)
Bouguer Anomaly (mGal)
Elevation (m)
Distance (m)
0.6
0.1
-0.4
-0.9
60
10
0
50
100
150
200
250
300
350
400
450
500
550
600
1.4 1.5 1.6 1.7 1.8 1.9 2 2.1 2.2 2.3 2.4 2.45 2.5 2.6 2.7 2.8 2.9 3 3.1 3.2 Elevation

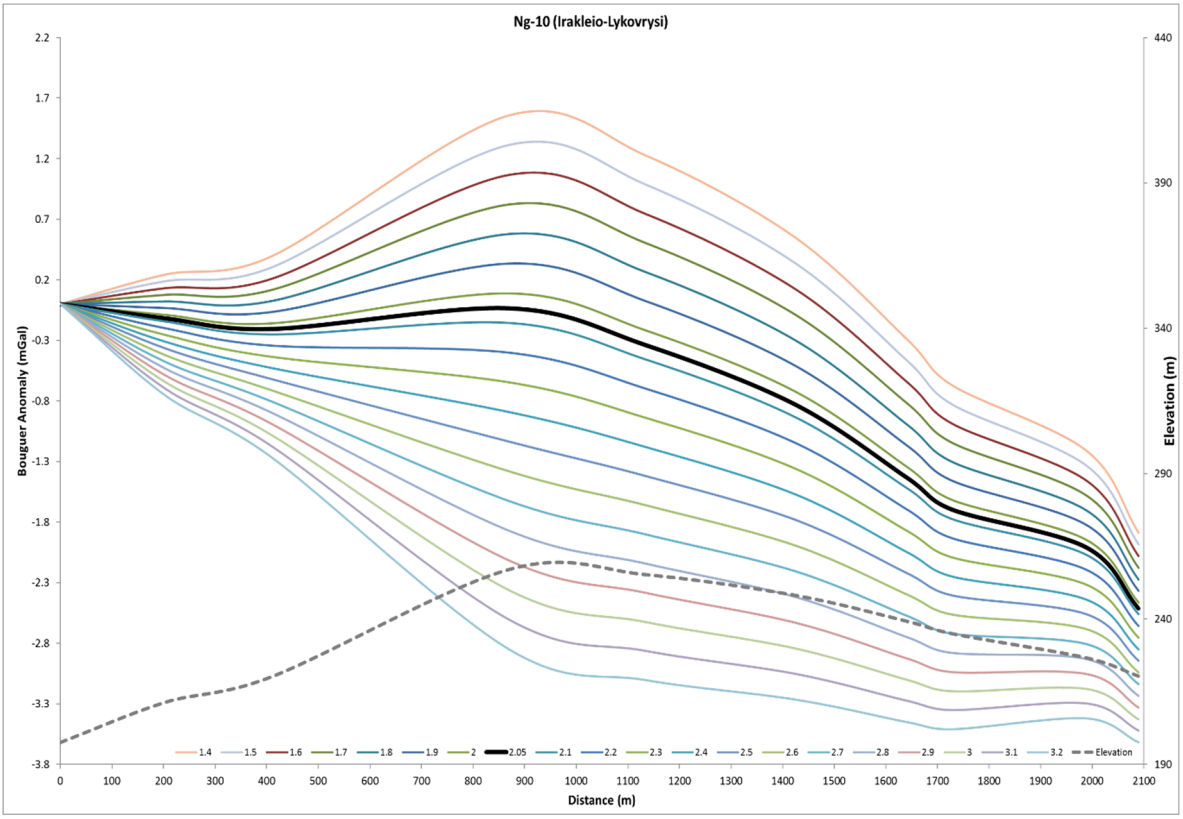
Ng-10 (Irakleio-Lykovrysi)
Bouguer Anomaly (mGal)
Elevation (m)
Distance (m)
1.4 1.5 1.6 1.7 1.8 1.9 2 2.05 2.1 2.2 2.3 2.4 2.5 2.6 2.7 2.8 2.9 3 3.1 3.2 Elevation

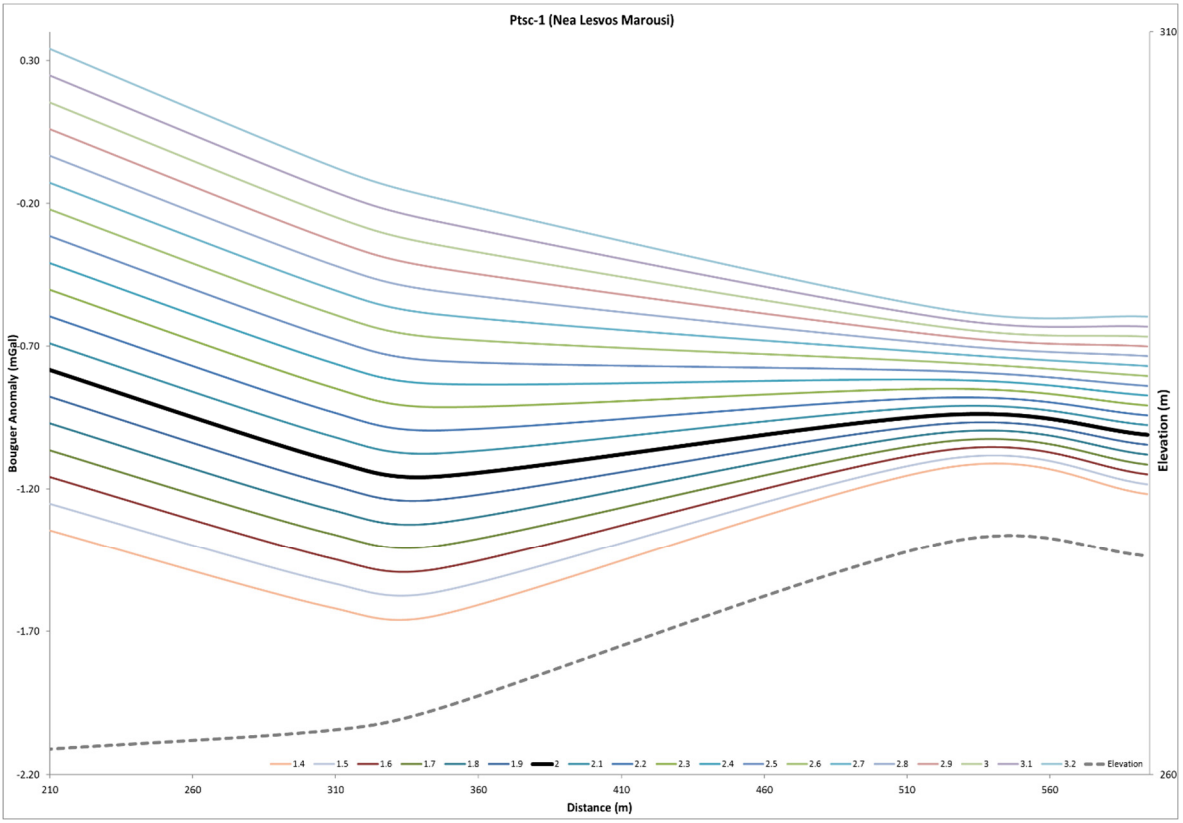
Ptsc-1 (Nea Lesvos Marousi)
Bouguer Anomaly (mGal)
Elevation (m)
Distance (m)
1.4 1.5 1.6 1.7 1.8 1.9 2 2.1 2.2 2.3 2.4 2.5 2.6 2.7 2.8 2.9 3 3.1 3.2 Elevation

APPENDIX D – GEOLOGICAL SAMPLES FOR DENSITY MEASUREMENT

Triassic-Jurassic Limestones (*T-J*)

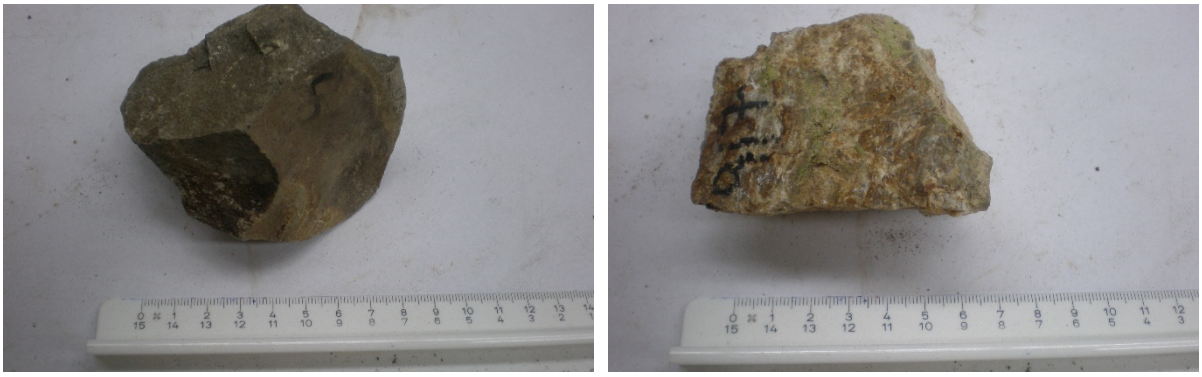

Shales and Sandstones Alterations (*C-P*)


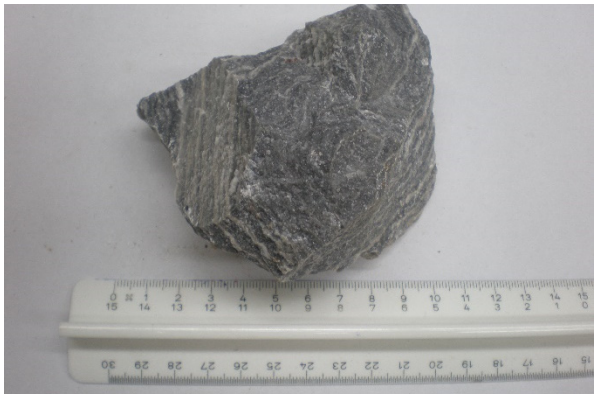

Marbles (*M*)




Schists (*Sch*)

Dolomites (*D*)

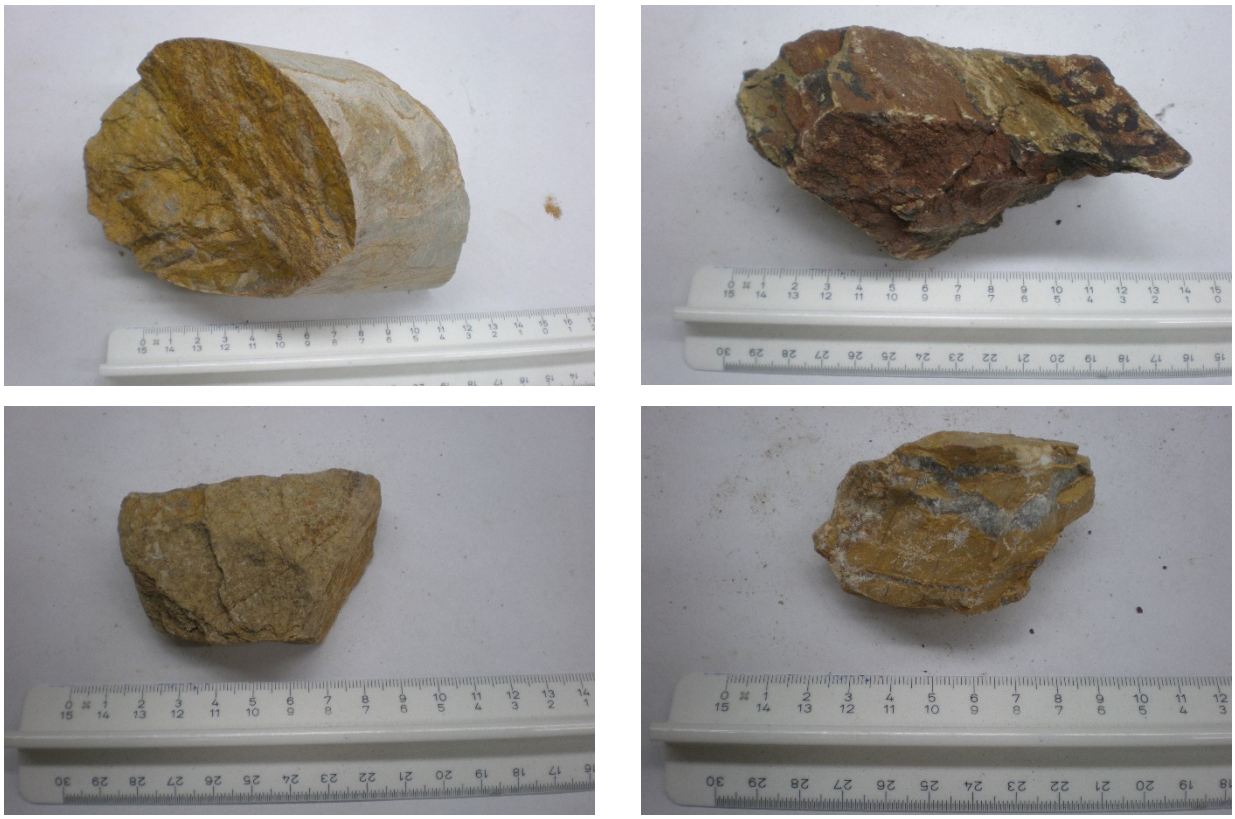

Athens Schist mélange (*SchA*)

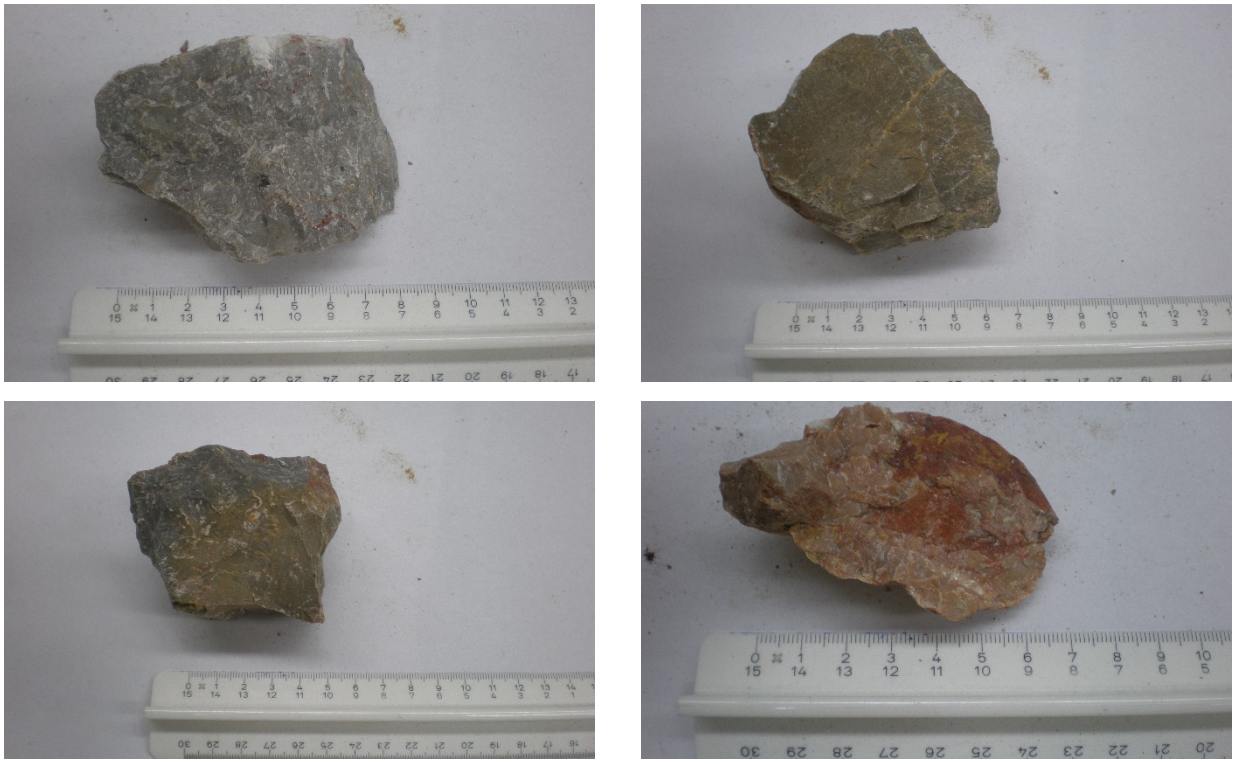

Limestones of Athens Unit (*CA*)

Schists of Alepovouni Unit (*CAl*)

Limestones of Alepovouni Unit (*CAl*)

Upper Miocene Terrestrial and Lacustrine deposits (*Msl*)

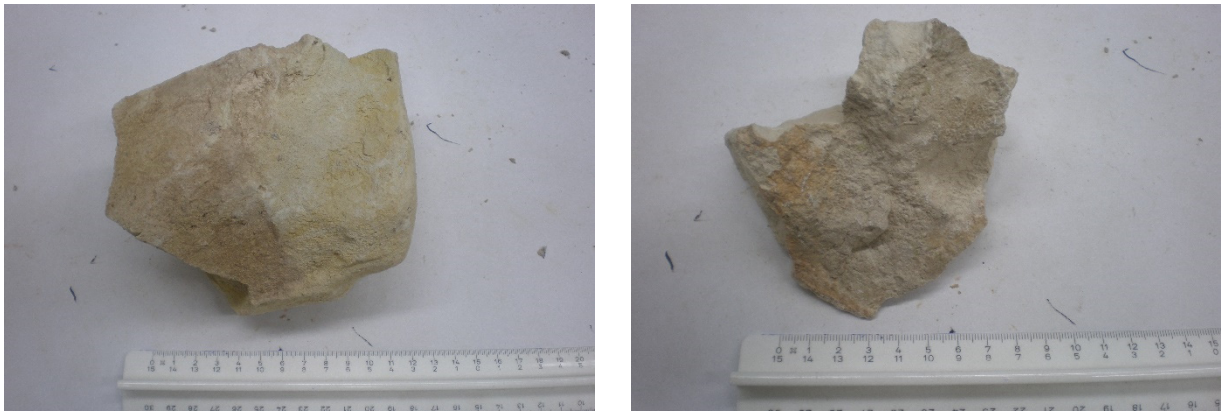

Upper Miocene Coastal deposits (*Msm*)

Pliocene Marine deposits (*Plm*)